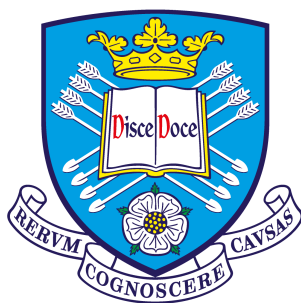


A Bioinspired Approach to the Synthesis and Scale-up of Bespoke Magnetite Nanoparticles

University of Sheffield



The
University
Of
Sheffield.

Laura Norfolk

*A thesis submitted to the University of Sheffield in partial fulfilment of the requirements
for the Degree of Doctor of Philosophy*

August 2021

Abstract

Magnetic nanoparticles (MNP) comprised of magnetite are fast gaining interest in the scientific research community due to their vast and widely varied applications in industry. These applications include waste water treatments, carbon capture, data storage, magnetic inks, and importantly, the biomedical industry. For biomedical applications, it is important for particles to be synthesised in a manner that makes them uniform in shape and size, and is suitable for industrial scale-up.

Currently many synthetic methodologies for magnetite rely on energy intensive processes and toxic precursors to synthesise high quality magnetic nanoparticles with narrow size distributions and consistent defined shapes. In an age of increased environmental awareness, it is critical to address these concerns before the large scale manufacture of magnetite nanoparticles is further established. Room temperature co-precipitation (RTCP) is a synthetic methodology which does not require environmentally harsh conditions, instead using water as a solvent and non-toxic iron salts as reagents, with no additional heating costs and expenditure required in the process. This process however does not currently offer fine control over the properties of particles formed, with wide variation in shape and size observed between reactions.

In Nature, the synthesis of sophisticated biominerals is commonplace with the nucleation and directed assembly of these materials being facilitated and templated by various proteins and biomolecules. The presence of these biological entities allows for bespoke high quality biominerals to be formed under ambient conditions, such as neutral pH and low temperature. The identification and study of how these 'bioadditives' function has allowed herein an investigation into the use of simpler compounds and molecules to aid the mineralisation of magnetite under greener reaction conditions.

This thesis covers the bioinspired application of additives to producing tailored nanomaterials, spanning three different systems of particle synthesis to ascertain the effect of batch and continuous production, as well as lay the groundwork for the scale-up of MNP produc-

tion with the addition of additives. The papers within have explored the use of additives, as well as two fluidic systems to tune the shape and size of MNP in an environmentally sustainable manner.

A screening study based on the active functionalities from bioadditives was conducted to search for chemical functional groups which may control the shape and size distribution of particles formed. A series of ethylenediamine (EDA) based additives capable of tightly modulating the shape of particles formed were identified, acting as a starting point for further study. The addition of the longer chain EDA-based additives triethylenetetramine (TETA), tetraethylenepentamine (TEPA), and pentaethylenehexamine (PEHA) produced 96, 97, and 91 % faceted particles respectively, showcasing the excellent morphological control these additives display.

This initial screening was built upon, with molecular dynamics modelling (MD) of the EDA series of amines revealing a preference for adsorption to the [111] crystal facet of magnetite. This face-specific adsorption enables the formation of primarily octahedral Fe_3O_4 particles, opening the door to the formation of shape-mediated particles under ambient conditions. TEPA was identified as the most effective of the EDA series at modulating the shape of particles formed, with a concentration study showing a 1:62.5 - 1:125 additive to Fe ratio produces the most highly faceted particles.

An iterative Design of Experiment (DoE) process was then conducted on the effect of TEPA, investigating the significance of three factors influencing the shape and magnetism of MNP formed with the addition of TEPA: i) the Fe/additive ratio, ii) the ferric/ferrous iron ratio, and iii) the timepoint of additive addition. Three rounds of DoE were conducted, comprised of two factorial designs (FFD), and a path of steepest ascent optimisation (PSA). The time-point of additive addition was found to be insignificant, suggesting TEPA acts to interact with forming magnetite particles rather than with aqueous Fe ions. Further FD narrowed down the ideal ferric and iron to additive ratios which produce MNP with the highest proportion of faceted particles and saturation magnetisation. The use of a PSA optimisation design allowed a compromise to be found between percentage of faceted particles formed and the saturation magnetisation, with ideal conditions found at a 1:50 and

1:59 additive to Fe ratio to produce near homogeneously faceted MNP.

A co-axial macrofluidic system was investigated for its potential to produce highly reproducible particles utilising highly controlled laminar flow. The biomineralisation protein Mms6 was found to be unable to exert control over the size of particles formed within this system. The millifluidic system however, allows for the tuning of particle size between a 20.5 and 6.5 nm range via simple adjustment of the ferric ion ratio. This millifluidic system was then used alongside the the EDA series of additives (EDA-PEHA) finding particle shape morphology was controllable, with a 1:100 ratio of TEPA to iron producing 58 % faceted particles.

Furthermore, a continuous flow static mixer was designed capable of producing 311 g day⁻¹ (where day covers a 24 hour period) of MNP under co-precipitation conditions, five times higher than previously reported for MNP synthesis. The EDA series of additives was found to be highly effective within this system, producing 84 % faceted particles on addition of a 1:100 ratio of TEPA to iron. Optimisation was conducted on the continuous flow static mixer, varying the Fe and NaOH feed concentrations, and ferric ratio to tune the size of particles produced. TEPA was used as an additive across a 0.4 - 0.6 ferric range, and was found to consistently produce a high proportion of faceted particles (73 - 81 %), showcasing the robustness of TEPA as an additive across multiple systems and ferric ranges.

As this thesis is presented in paper format, the introductions to each paper may be similar and use the same references due to the need to present each paper as a stand alone body of work for publication.

Dedication

Dedicated to my cats Kylo and Phoenix, who have frustrated me, walked on my keyboard, and brought me unending joy every day for the past four years. You are, and shall remain, the lights of my life.

Declaration

This candidate confirms that the work submitted is her own. The contribution of others to this work has been explicitly indicated below, and throughout the thesis. As the work has been submitted in publication format, each results chapter is preceded by author contributions, outlining what each author has contributed to the work. The candidate also confirms that appropriate credit has been given within the thesis where reference has been made to the work of others.

Chapter 2: Methods All protein expression and purification work including their methodologies has been conducted and written by Andrea Rawlings. ICP analyses have been performed by Heather Grievson. The machining of the PDMS device methodology was written by Jonathan Bramble.

Acknowledgements

I would first like to thank Dr. Sarah Staniland and Professor Siddharth Patwardhan for giving me this opportunity. Whilst the PhD process has been tough, and at times a great deal of stress, they have always acted to reassure and guide me throughout these years. They have made the completion of my doctorate possible, and have been two of the best supervisors a student could ask for. Sarah and Sidd have always been the first to tell me not to worry, and to point me in the right direction when things look like they're going awry. I will always be grateful to them for the past 4 years, and the kindness with which they have acted as my academic supervisors.

The Staniland research group has been a lovely working environment, and thanks goes to Rosie, Chris, Sam, and Lukas for the many hours spent chatting and commiserating over research in the office and lab over the years. I would like to pay special recognition to Andrea Rawlings, an excellent researcher, whose ideas and support helped me find my feet during the first year of my PhD. To my wonderful summer students Katy, Klaudia, and Michael, your hard work has been appreciated and I wish all of you the best for your futures, and hope that you find much success in whatever you wish to do!

Thanks also goes to the many staff and kind souls throughout the University of Sheffield who have offered assistance in training, adjusting bits of equipment, and all sorts. Craig Robertson who got me set-up on XRD, Chris Hill and Svetomir Tzokov who taught me TEM, and Nicola Morley and Zhao Leong who helped me run my first VSM, their teachings have become the backbone of my research project. Another thanks goes to Garry Turner and Richard Truswell for their assistance in removing damaged screws, and adjusting odds and ends by fractions of a millimeter... Their skills and patience in teaching me some DIY basics were much appreciated!

To Georgina Zimbitas, you are one of the hardest working people I have ever met, and a brilliant academic. It was a pleasure to work with you in Glasgow, and the kindness you showed me when I was worried about my kittens surgery will always be remembered. I truly

wish you all the success and happiness you deserve in whichever venture you choose!

A special thanks goes to Luc Dewulf for his hard work on our Design of Experiment paper, and being nothing but understanding when I've wanted to re-run data, or re-analyse pieces of the work. You're the smartest young academic I've ever met, and I'm sure you have a great career awaiting you!

Thank you to my Mum and Dad for their support, especially in my first year of my PhD. Your support when I have been struggling has gone a long way. I'll make you read my thesis one of these days! Thanks also goes to my brother Andrew for his clever insights and re-imagining of the macrofluidic flow system. Further thanks go to my brother Chris and his lovely wife Lucy for keeping me in their thoughts, and being a source of kindness and brightness throughout a difficult few years.

I would like to thank the friends I have met throughout my time in Sheffield, and the huge impact they have had on my life. When I came to Sheffield years ago, I had no idea that I was moving to the city where I'd build my life. Thanks goes to the University of Sheffield Video Gaming society, where I've met some of the best and unlikeliest friends I've ever known. To my dear friend Chris, you were the first PhD student I ever met, and your advice on writing and friendship has meant the world to me over the years I have spent here. To Ash H, you have been a cheerleader to my writing and research struggles through the past year, and remain one of the most optimistic people I know through a hard couple of years, and for that I thank you sincerely for your motivation and inspiration. To my old flatmates Dale, Ash, and Jamie thank you for two great years in the Broomhall flat, even if Kylo didn't make it easy at times! To Jamie and Ash, you have always had more belief in me than I have myself, and I thank you for your support in times I have desperately needed it throughout my university career. Your friendship has always been appreciated and cherished. I would also like to thank the University of Sheffield Jiu Jitsu society. It's been wonderful to train with you all, and I can't wait to see you all back on the mat!

I would like to thank my fellow PhD students, Ben and Shiv. Complaining about data analysis, running experiments, and research has kept me going through the past years, and I can't wait for the day we all reminisce on these times!

A huge thank you goes to one of my best friends Jack, for not only convincing me to use LaTeX for my thesis, but also helping me with my endless LaTeX woes from tables, to fonts, to all sorts! You've made the thesis writing process so much less stressful with your help, and you are personally responsible for my bibliography working. Your friendship has been a constant throughout the past 4 years, and I look forward to many more evenings discussing our cats, plants, cooking, and Dokapon/Mario Party!

I would finally like to thank my best friend and partner, Matt. Every time I have doubted myself, you've been there to cheer me up and keep me going. Your support and kindness from the moment I met you, to all throughout the thesis writing process has been above and beyond. This wouldn't have been possible without your love and support, and I'll always appreciate everything you have done for me throughout this time. I can't wait for our next chapter together.

Contents

1	Introduction	1
1.1	Overview	2
1.2	The Nanoscale, Nanoparticles, and the Nanoindustry	3
1.2.1	<i>The Developing Nanomaterials Industry</i>	5
1.2.2	<i>The Sustainability of Nanomaterials</i>	7
1.2.3	<i>Bioinspired Nanomaterials</i>	9
1.3	Magnetism	10
1.3.1	<i>Background of Magnetism</i>	10
1.3.2	<i>Magnetic Ordering</i>	11
1.3.3	<i>Magnetic Hysteresis</i>	13
1.3.4	<i>Magnetic Domains</i>	15
1.4	Magnetite: Properties and Applications	17
1.4.1	<i>Magnetite</i>	17
1.4.2	<i>Industrial Application of Magnetite Nanoparticles</i>	19
1.4.2.1	<i>Biomedical Applications</i>	19
1.5	Crystal Growth and Formation	23
1.5.1	<i>Crystal Nucleation</i>	23
1.5.2	<i>Crystal Growth Mechanisms</i>	26
1.5.3	<i>Influencing Crystal Growth and Morphology</i>	29
1.6	Synthesis of Magnetic Nanoparticles	30
1.6.1	<i>Thermal Decomposition</i>	31
1.6.2	<i>Hydrothermal Synthesis</i>	32
1.6.3	<i>Microemulsion</i>	32
1.6.4	<i>Room Temperature Co-Precipitation</i>	33
1.6.5	<i>Synthetic Summary</i>	37
1.7	Biom mineralisation and Biomimetics	38

1.7.1	<i>Biologically Induced Mineralisation and Biologically Controlled Mineralisation</i>	39
1.7.2	<i>Biomimetics, Biokleptics, and Bioinspired Research</i>	41
1.7.3	<i>Magnetotactic Bacteria</i>	42
1.7.3.1	<i>Magnetosomes</i>	45
1.7.3.2	<i>Magnetosome Formation</i>	46
1.7.4	<i>Key Biomineralisation Proteins</i>	48
1.7.4.1	<i>Mms6</i>	48
1.7.4.2	<i>MmsF</i>	50
1.7.5	<i>Magnetite Interacting Adhirones</i>	51
1.8	The Role of 'Additives'	54
1.8.1	<i>Proteins, Peptides, and Bio-Molecule Based Additives</i>	56
1.8.2	<i>Carboxyl and Hydroxyl Based Additives</i>	58
1.8.3	<i>Templating Additives</i>	59
1.8.4	<i>Surfactants as Additives</i>	61
1.8.5	<i>Amine Based Additives</i>	62
1.8.6	<i>Summary of Additives</i>	64
1.9	Production Systems for Magnetite Synthesis and Scale-Up	65
1.9.1	<i>Batch and Continuous Processes</i>	65
1.9.2	<i>Magnetite Scale-Up</i>	66
1.9.3	<i>Microfluidics for Magnetite Synthesis</i>	67
1.10	Experimental Design and Optimisation	69
1.10.1	<i>One Factor at a Time</i>	69
1.10.2	<i>Design of Experiment</i>	69
1.10.2.1	<i>DoE of Magnetite</i>	71
1.11	Project Aims and Objectives	72
2	Methods	76
2.1	Methods Overview	77
2.2	Room Temperature Co-Precipitation	77

2.2.1	<i>Standard Reaction Set-up</i>	77
2.3	Macrofluidic Synthesis	79
2.3.1	<i>Macrofluidic Device Fabrication</i>	79
2.3.2	<i>Protein Expression and Purification</i>	81
2.3.3	<i>Macrofluidic MNP Synthesis</i>	82
2.3.3.1	<i>Macrofluidic MNP Synthesis Modified with Mms6</i>	83
2.4	Continuous Flow Static Mixing Synthesis of MNP	83
2.4.1	<i>Experimental Set-up</i>	83
2.4.2	<i>Experimental Set</i>	85
2.5	Characterisation	86
2.5.1	<i>Transmission Electron Microscopy</i>	86
2.5.1.1	<i>Sample Preparation and Analysis</i>	87
2.5.2	<i>X-Ray Diffraction</i>	87
2.5.2.1	<i>Sample Preparation and Analysis</i>	90
2.5.3	<i>Vibrating Sample Magnetometry</i>	90
2.5.3.1	<i>Sample Preparation and Analysis</i>	91
2.5.4	<i>Inductively Coupled Plasma Optical Emission Spectrometry</i>	92
2.5.4.1	<i>Sample Preparation and Analysis</i>	92
2.5.5	<i>Fourier-Transform Infrared Spectroscopy</i>	92
2.5.5.1	<i>Sample Preparation and Analysis</i>	94
2.5.6	<i>Thermal Gravimetric Analysis</i>	94
2.5.6.1	<i>Sample Preparation and Analysis</i>	95
2.5.7	<i>Particle Size Analysis</i>	95
2.5.8	<i>Particle Shape Analysis</i>	96
3	Screening Additives	99
3.1	The Role of Biological and Bioinspired Additives in the Green Synthesis of Magnetite Nanoparticles	100
3.1.1	<i>Author Contributions</i>	100
3.1.2	<i>Research Paper</i>	101

3.1.3	<i>Supplementary</i>	116
4	Ethylenediamine Additives	122
4.1	Ethylenediamine Series as Additives to Control the Morphology of Magnetite Nanoparticles Using Green Reaction Conditions	123
4.1.1	<i>Author Contributions</i>	123
4.1.2	<i>Research Paper</i>	124
4.1.3	<i>Supplementary</i>	136
5	TEPA Design of Experiment	146
5.1	A Design of Experiment (DoE) Approach to the Optimisation of Bioinspired Magnetite Nanoparticles Using an Affordable Amine Additive	147
5.1.1	<i>Author Contributions</i>	147
5.1.2	<i>Research Paper</i>	148
5.1.3	<i>Supplementary</i>	158
6	Millifluidics	166
6.1	Macrofluidic Coaxial Flow Platforms to Produce Tunable Magnetite Nanoparticles: A Study of the Effect of Reaction Conditions and Biom mineralisation Protein Mms6	167
6.1.1	<i>Author Contributions</i>	167
6.1.2	<i>Research Paper</i>	169
6.1.3	<i>Supplementary</i>	184
6.2	Adapting the Morphology of Magnetite Nanoparticles Synthesised in a Coaxial Flow Device Using Affordable Amine Additives	195
6.2.1	<i>Author Contributions</i>	195
6.2.2	<i>Research Paper</i>	196
6.2.3	<i>Supplementary</i>	201
7	Large Scale Flow Mixing and Optimisation	204
7.1	Robust Scalable Continuous Flow Bioinspired Synthesis of Magnetite Nanoparticles Using Ethylenediamine Additives	205

7.1.1	<i>Author Contributions</i>	205
7.1.2	<i>Research Paper</i>	206
7.1.3	<i>Supplementary</i>	228
7.2	Optimisation of a Scalable Continuous Flow Synthesis of Magnetite Nanoparticles Using Tetraethylenepentamine as an Additive	234
7.2.1	<i>Author Contributions</i>	234
7.2.2	<i>Research Paper</i>	235
7.2.3	<i>Supplementary</i>	244
8	Conclusions and Future Work	245
8.1	Conclusions	246
8.1.1	<i>Screening Additives</i>	246
8.1.2	<i>Additive Optimisation and Understanding</i>	249
8.1.3	<i>Fluidic Systems and Scale-up</i>	251
8.2	Final Remarks	255
	Bibliography	257

Abbreviations and Definitions

3D: Three-dimensional

acac: Acetylacetonate

AC: Alternating current

AFM: Atomic force microscopy

AMB-1: *Magnetospirillum magneticum*, strain AMB-1

ATR: Attenuated total reflectance

BCM: Biologically controlled mineralisation

BIM: Biologically induced mineralisation

CNT: Classical nucleation theory

CTAB: N-Cetyl-N,N,N-trimethylammonium bromide

DETA: Diethylenetriamine

DLS: Dynamic light scattering

DoE: Design of Experiment

EDA: Ethylenediamine

EDTA: Ethylenediaminetetraacetic acid

EMA: European Medicines Agency

EPR: Electron paramagnetic resonance

FD: Factorial design

FDA: U.S. Food and Drug Administration

FFD: Full factorial design

FTIR: Fourier-transform infrared spectroscopy

FWHM: Full width at half maximum intensity

GG: Gellan gum

HA: High-acyl

HRTEM: High-resolution transmission electron microscopy

ICP-OES: Inductively coupled plasma optical emission spectrometry

ID: Inner-diameter

IR: Infrared

LA: Low-acyl

Mam: Magnetosome associated membrane

MD: Molecular dynamics

MDDS: Magnetic drug delivery system

mg: Milligram

mmol: Millimoles

Mms: Magnetosome membrane specific

MNP: Magnetic nanoparticle

MRI: Magnetic resonance imaging

MTB: Magnetotactic bacteria

NIH: National Institute of Health

OD: Outer-diameter

OATZ: Oxic anoxic transition zone

OFAT: One factor at a time

PAMAM: Polyamidoamine

PAPMA: Poly(N-(3-aminopropyl)methacrylamide)

PDMS: Polydimethylsiloxane

PEEK: Polyether ether ketone

PEG: Polyethylene glycol

PEHA: Pentaethylenehexamine

PSA: Path of steepest ascent

PTFE: Polytetrafluoroethylene

RBF: Round bottom flask

RCP: Reverse co-precipitation

RTCP: Room temperature co-precipitation

SD: Standard deviation

SDS: Sodium dodecylsulphate

SEM: Scanning electron microscope

SD: Standard deviation

SPION: Superparamagnetic iron oxide nanoparticles

STY: Space-time-yield

SynBio: Synthetic biology

TEM: Transmission electron microscopy

TETA: Triethylenetetramine

TEPA: Tetraethylenepentamine

TGA: Thermal gravimetric analysis

TMS: Transmembrane spanning

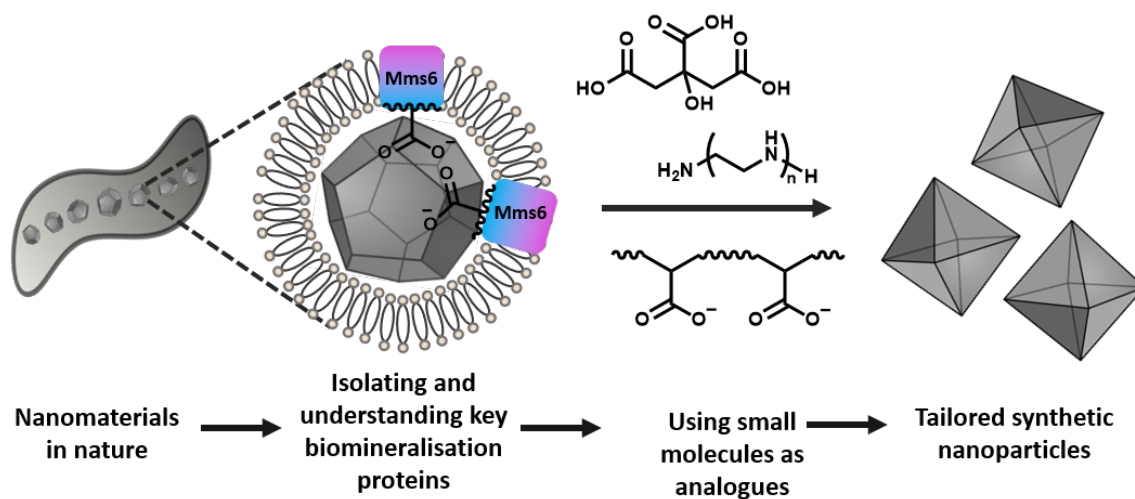
Tris: Tris(hydroxymethyl)aminomethane

UV-vis: Ultraviolet visible

VSM: Vibrating-sample magnetometry

Chapter 1.

Introduction



This chapter is a scientific introduction to this thesis, and consists of a systematic review of the literature, the overall project aims and overview, and a project map of the work conducted alongside their chapter numbers.

1.1 Overview

Magnetism is a unique phenomenon that has seen many industrial applications throughout history. From its humble beginnings as lodestone in navigational compasses, the use of magnetism in industrial fields has risen, with magnetic nanoparticles offering not only a possible bespoke method of data-storage in the form of bit-patterned media on the nanoscale,¹ but also a potential cancer treatment,² diagnostic tool,³ or targeted drug delivery system.⁴ The biomedical industry is investing heavily into the use of nanomaterials due to their compatibility with the human body and similar sizing to cells, proteins, and genes, allowing them to get close to biological entities and effectively interact with them.⁴ The unique magnetic properties of magnetite nanoparticles (MNPs) offer advantages over conventional medical treatments which will be later discussed.

For a product to be approved in the biomedical industry by the U.S. Food and Drug Administration (FDA) or European Medicines Agency (EMA) it must meet rigorous criteria on specifications and safety.⁵ As such it is favourable to be able to select the properties desired for particles to be used in medical applications, and synthesise particles to meet the individual demands of each application. The synthesis of complicated structures via chemical methods however remains a challenge to be addressed. As chemists persevere at formulating synthetic methodologies capable of producing high quality nanomaterials, reliance on highly energy intensive processes has remained. The current synthesis techniques of magnetite are often reliant on the use of high temperatures, organic solvents, toxic pre-cursors, and extensive vacuum use with these practices becoming standard for the manufacture of monodisperse MNPs as discussed in detail in section 1.6.⁶

The global market for inorganic nanomaterials was estimated at approximately \$8.5 billion in 2019, and expected to grow to over \$9.5 billion in 2020.⁷ Current nanomaterial synthesis techniques are notoriously wasteful, with up to 100,000 kg of waste being produced in the synthesis of 1 kg of nanomaterial product.⁸ For MNPs to become viable as a widespread therapeutic treatment it is critical to not only be able to scale-up the synthesis of nanoparticles, but also address the key issues negatively affecting the environmental

impact of the synthetic methods. For this, we can look to Nature for inspiration. Complex and hierarchical displays of mineralisation are seen throughout Nature, from skeletons and teeth in the animal kingdom, to complex silica structures in the cell walls of diatoms, and finally defined nanoparticles in water-dwelling bacteria, each occurring via complicated protein-mediated processes known as biomineralisation.⁹

Biomineralisation in Nature shows that it is possible for high quality nanomaterials to be formed at ambient conditions, with many cases of biomineralisation occurring at low temperatures and milder pH. By drawing inspiration from the proteins and chemical moieties identified through extensive research to enable the formation of these nanomaterials, it may be possible to utilise simpler compounds displaying the most important functionalities for use as 'additives' to aid in structure-direction under milder conditions which are deemed more suitable for scale-up.¹⁰

The purpose of this thesis is to build upon the past body of work and research delving into the biomineralisation processes enabling the formation of uniform MNPs in Nature, and apply these principles to lab synthesised particles with the addition of additives inspired by the function of proteins found to be effective for tailoring MNPs in Nature. When additives are identified that can influence the properties of forming nanomaterials, these processes must then be optimised in the path toward industrial use and scale-up.

1.2 The Nanoscale, Nanoparticles, and the Nanoindustry

In 1959 the now renowned lecture by Richard Feynman "There's Plenty of Room at the Bottom" opened discussion on the development of nanotechnology, and the advantages of working on a smaller scale to create denser electronics and microscopes capable of resolutions much higher than that which was possible with current microscope technology.¹¹ While this talk had little influence on the development of nanotechnology over the following two decades, interest in his speech rose in the late 1990s, when the term 'nanotechnology' began to garner greater attention.¹² Feynman's status as a Nobel laureate is believed to have aided

in the increased funding seen in the nanotechnology industry from the early 2000s, when the US National Nanotechnology Initiative worth \$500 million was established.¹³

Whilst nanotechnology is a relatively new field in the history of chemistry, its primary growth and development can be traced to the development of electron microscopy, with Max Knoll and Ernst Ruska developing the first transmission electron microscope (TEM) capable of a higher resolution than the wavelength of light in 1933.¹⁴ The development of a microscope capable of giving structural and morphological information on the nanoscale was of great importance for the progression of nanomaterials, allowing these newly developing materials to be imaged and characterised. In 1937 Manfred von Ardenne invented a microscope that scanned samples in a small raster pattern using a finely focused electron beam in an attempt to improve upon the current resolution achievable via TEM.¹⁵

Whereas TEM microscopes operate by using transmitted electrons that have passed through a sample to generate an image, scanning electron microscopes (SEM) produce images of the surface topography of samples by detecting secondary reflected or back-scattered electrons. As such, TEM can reveal internal crystallographic information of samples, whereas SEM cannot. TEM offers a higher resolution than that afforded by SEM,¹⁶ and is typically the preferred method of imaging nanoparticles of smaller dimensions. Figure 1.1 shows an example of the variation in resolution and image type between the two most used methods of visualising nanoparticles, TEM and SEM.

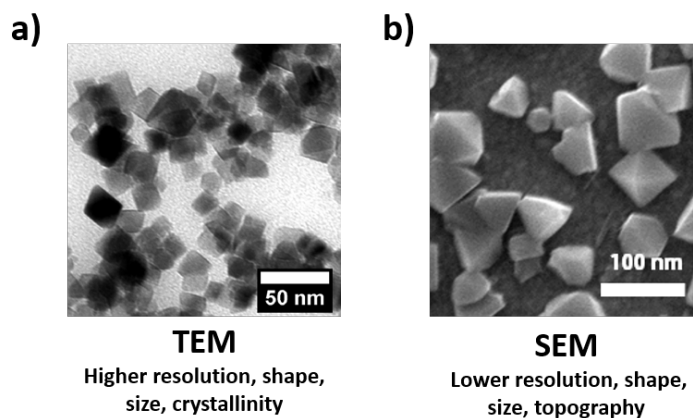


Figure 1.1: a) Example TEM image and b) SEM image of magnetite (Fe₃O₄) nanoparticles (SEM image from Staniland group).

For a material to be classed as a nanomaterial it must fit the definition of one or more of its dimensions being in the nanoscale ($1 \text{ nm} = 1 \times 10^{-9} \text{ m}$).¹⁷ From the classification of the nanoscale, a nanoparticle is a type of particle typically smaller than 100 nm in diameter.¹⁸ Nanoparticles come in many forms, both amorphous or crystalline, with different structures and composition resulting in the formation of diverse types of nanomaterials with various practical purposes depending on their properties.¹⁹ The dimensions of a particle (shape and size) have a significant influence on the range of applications they are suitable for, i.e. a needle shaped particle is less suitable in biomedical applications due to increased cytotoxicity as a result of cell perforation.²⁰

There are challenges associated with work at this scale due to the interplay of properties of a material as it goes from majority bulk effects to surface effects having the largest influence as the surface area to volume ratio rapidly increases with decreasing material size. These surface effects place greater importance on Van der Waals forces,²¹ electrostatic interactions,²² aggregation,²³ and quantum effects.²⁴ A direct result of increased surface area is the degree to which nanomaterials can be functionalised is also greatly increased, which makes nanomaterials promising for industrial purposes where surface functionalisation is key.²⁵

1.2.1 The Developing Nanomaterials Industry

Research into nanoparticles and nanomaterials is of increasing interest,^{26,27,28} with novel nanomaterials and technology being developed at a rapid rate.²⁹ The global market for these materials is significant, with a conservative estimate valued at ~\$4.1 billion in 2015, and expected to rise to more than \$9.5 billion by 2020.⁷ An inventory conducted in 2015 has documented more than 1800 consumer products containing nanomaterials from 622 companies,³⁰ whereas a Danish inventory of products containing nanomaterials accessed in November 2020 contains approximately 5000 products, showing the growth and normalisation of nanomaterials in everyday life.³¹ The climb in industry value and rise of products containing nanomaterials is highly indicative of the need to develop methods of synthesising these materials in an affordable and environmentally friendly manner if demand is to be met

without negative environmental repercussions.

Nanoparticles offer properties that bulk materials are incapable of offering in consumer goods, with their smaller size allowing them to be easily utilised in fluidic products, allowing for a diverse range of products to be developed.¹⁹ Nanoparticles improved surface area is a governing factor in the industrial importance of nanomaterials, due to the highly economical ratio of material to functional surface area.³² This increased surface area allows nanomaterials to offer superior surface activity in the fields of gas storage, catalysis, and wastewater treatment.² As such, synthetic nanomaterials are already commercially viable and are present in a range of industries from nanoparticulate titanium,³³ amorphous nanosilica as both anti-caking agents in food and a rheology additive designed to improve flow of powders,¹⁹ to carbon nanotubes for increasing the durability of concrete.²⁷ This type of material is classed as the 'first generation' of nanomaterials, focused on the enhancement of material properties.³⁴

More developed nanomaterial systems are being investigated and developed often known as 'second generation' nanomaterials, comprised of targeted drug delivery systems,³⁵ nanoparticle actuators capable of converting chemical energy into mechanical energy,³⁶ and the use of peptide tagged nanoparticles encapsulated with photodynamic sensitisers and imaging agents to target tumour vasculature.³⁷ The 'third' and 'fourth' generation systems are predicted to be the future pathway of nanotechnology, and are comprised of 'systems of nanosystems' and 'molecular nanosystems' as outlined in Figure 1.2.

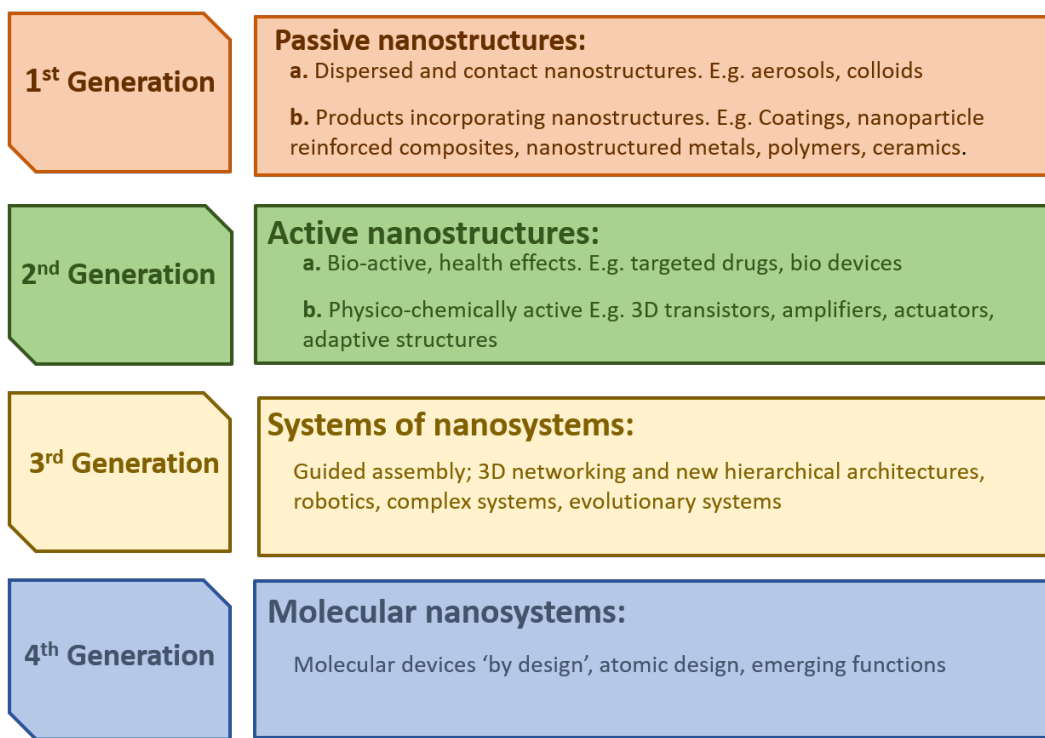


Figure 1.2: The four generations of nanotechnology as outlined by the United States National Nanotechnology Initiative. (Redrawn from Roco et al.³⁴)

Some more lucrative uses of nanoparticles in industry are bio-imaging,³⁸ carbon capture,³⁹ and ultra-high density data storage.⁴⁰ For industrial purposes homogeneous particle size and quality is strongly favoured, and in many cases such as drug delivery, essential for functionality.⁴¹

1.2.2 The Sustainability of Nanomaterials

Whilst the properties of nanomaterials have opened the door to many interesting chemical developments, it is also key to consider how they may affect the world around us. Many studies into the sustainability of nanomaterials have focused primarily on the impact of nanomaterials post-production,⁴² such as the impact of nanowaste and how these materials interact and even react with humans and the environment.^{43,44,45} As nanomaterials become increasingly commonplace in both consumer products and bespoke medical treatments, it is also crucial to consider how the production and synthetic methodologies of these materials impacts the environment and begin to consider both long term implications and

sustainability.⁴⁶

When it comes to the manufacture of nanomaterials, two key process pathways can be established.⁴⁷ Top-down processes entail either the milling of larger bulk material into smaller bodies of nanomaterial or lithography and etching to create nanoscale patterns. The top-down approach is fast reaching its resolution limit in the field of lithography, whereas milling processes are sub-optimal for producing particles of uniform size.⁴⁸ Bottom up approaches focus on synthesis from starting reagents to selectively develop tailored nanomaterials with smaller and more complicated geometries than those currently achievable via top-down processing. The bottom-up approach is seen in Nature,⁴⁹ with many biological entities mineralising complex and intricate materials within from chemical starting blocks such as aqueous ions.^{50,51}

Many current nanomaterial synthesis techniques have recurring issues relating to sustainability.⁵² To create high quality materials, expensive conditions are often required such as high temperature and heavy vacuum usage, raising both costs and energy expenditure in the synthesis of these materials. Toxic pre-cursors and by-products are yet another issue, requiring either proper disposal at extra cost or running the risk of pollution and environmental irresponsibility.⁴⁹

An environmental impact and sustainability analysis based on the waste to product ratio in six nanomaterial syntheses found that between 1000-100,000 kg of undesired material may be produced while synthesising 1 kg of desired nanomaterial, up to 1000 times higher than the production of fine, bulk, or pharmaceutical chemicals.⁸ To address these sustainability issues it is instead possible to look toward altering the synthetic methodologies, choosing less toxic starting materials and energy intensive techniques. By refining these greener techniques over time, the aim of this area of research is the production of high quality nanomaterials that no longer exhibit a substantially negative environmental profile.

However, green nanomaterials and nanotechnologies still face challenges, namely a slow progression from lab discovery and synthesis to commercial scale synthesis and application.⁵³ Getting nanomaterials approved is a costly process, which is impeded by the unclear toxicological implications of many of these materials, as well as time-consuming regulatory

barriers involved in changing the methods of production of materials.⁵⁴ As many less environmentally friendly synthetic methodologies have already been approved and commercial infrastructure designed around these processes, it is expensive and therefore less lucrative to adapt these or design new mechanisms by which to synthesise the same product, albeit in a greener manner.

For this financial hurdle to be overcome, the collaboration of both academic research and private sector will be key.⁵³ Government subsidies for green nanomaterial research and regulations for greener production of nanomaterials may also aid in the pathway to attainable and sustainable nanomaterials.

1.2.3 Bioinspired Nanomaterials

An effective approach to improving the sustainability of nanomaterial synthesis is to look to Nature and its effective production of nanomaterials under mild conditions. One example of inspiration and further research is the production of silica nanomaterials, SiO_2 .^{35,55}

Finely controlled silica materials are seen in multiple species of aquatic single-celled organisms known as diatoms, a type of microalgae.⁵⁶ Investigation of these diatoms found specific proteins and biomolecules played a key role, with silicatein, an enzyme which catalyses the formation of biosilica, and sillafins, a protein rich in a series of the cationic basic amino acids, serine and lysine appearing crucial to the mineralisation process.^{57,58} These biomolecules were further studied with amine analogues being discovered which enable the rapid condensation of silica nanoparticles under ambient conditions.^{59,60} This directly led to success in the process of synthesising bioinspired silica which can be synthesised under mild conditions, with water as a solvent, neutral pH, and a reaction time of only 5 minutes.⁶¹

This highly developed bioinspired silica process is further along the developmental pipeline than the synthesis of magnetite, but allows us to observe the process and apply these principles to the magnetite pipeline. As will be further detailed in this chapter, while magnetite is behind in the development process, biomolecules and proteins found within a bacteria that produces MNPs natively have been extensively studied.¹⁰ Research into the design of additives is now a key priority to push for greener MNPs and is the next step required to

move along the development pipeline of green MNP production which is further discussed in section 1.7.

Figure 1.3 shows the planned development pipeline for magnetite nanomaterials, from i) observing the formation of magnetite nanomaterials in Nature, ii) studying their function (proteins, templating, etc.), iii) understanding their mechanism of biomineralisation, iv) designing additives incorporating the active chemical functionalities from biomineralisation mechanisms, v), producing custom bespoke NP (low polydispersity, specific shapes, enhanced properties, etc.), vi) scale-up of said particles, and vii) the large scale manufacture of custom nanoparticles.

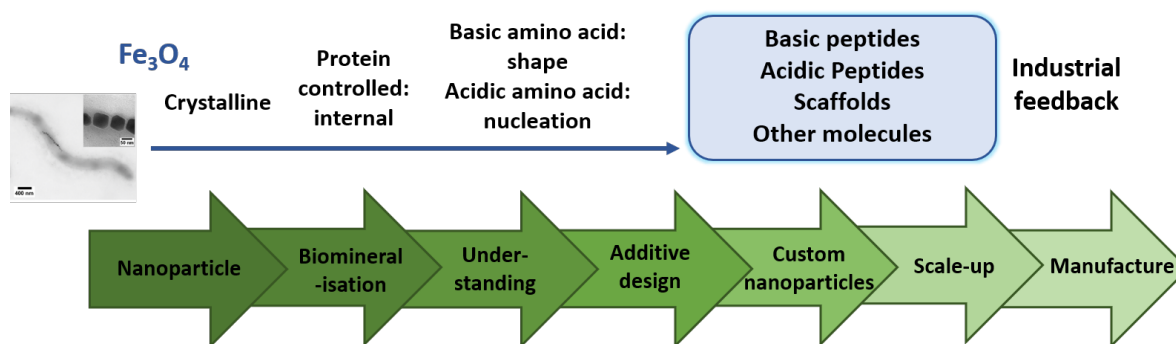


Figure 1.3: SynBio overview of the planned development process for industrial magnetite nanoparticle production.

1.3 Magnetism

After considering the industrial perspective of MNPs, it is time to focus on the properties which make these particles desirable. Magnetism is defined as an attractive or repulsive force generated in matter by the motion of electrons within its atoms. Simply, a magnetic field is generated by the movement of electric charges.

1.3.1 Background of Magnetism

The effect of magnetism is a principle that society has been familiar with for thousands of years. The ancient Greeks were among the first to utilise magnetism, with the uncommon naturally magnetised form of the magnetic iron ore magnetite, Fe₃O₄, being used as the first

magnetic compasses. Their importance to navigation is reflected in the moniker lodestone, meaning 'course stone'. By suspending an elongated piece of magnetite so it could rotate, the stone would align itself as a pointer to magnetic North. It was found that this naturally magnetised mineral not only attracted iron but could also magnetise it via gentle rubbing. William Gilbert, an English physician and scientist was the first to publish research on the properties of magnetite in 'De Magnete' published in 1600, suggesting magnetism was the root of the Earth's rotation on its axis, and that the Earth itself is magnetic, hence compasses pointing North.⁶²

1.3.2 Magnetic Ordering

Magnetism is an inherent property of all materials, due to the presence of electrons in their substituent atoms. Electrons have a property known as spin angular momentum, where an electron can either be 'spin-up' or 'spin-down', hence cancelling out their magnetic moment when in a pair. When a magnetic field is applied to atoms, the electrons within the atoms orient themselves to align directionally parallel or antiparallel to this magnetic field, with magnetism itself being determined by the susceptibility of a material to this external magnetic field.

The different orientation of electrons in response to a magnetic field results in different forms of magnetism. There are four variations of electron arrangement giving rise to the differing types of magnetism shown in Figure 1.4.

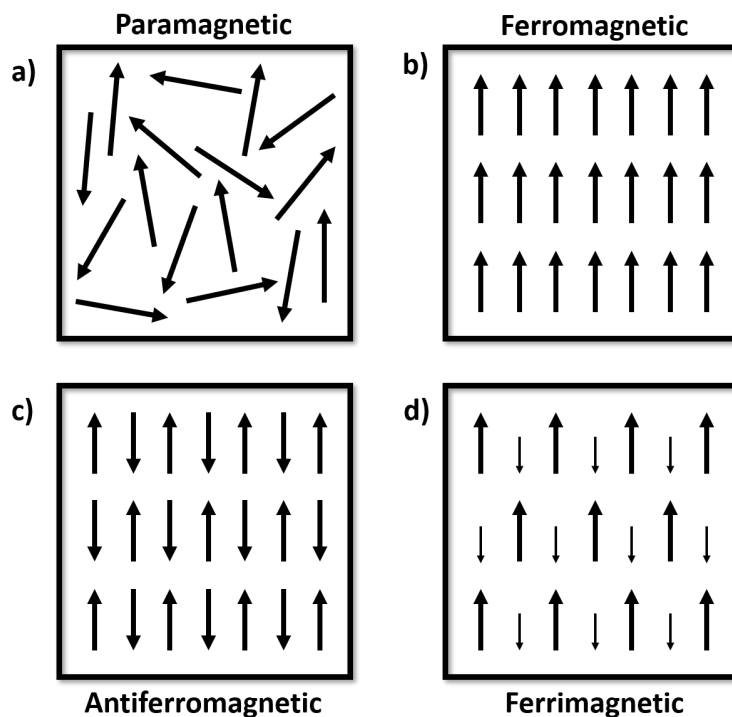


Figure 1.4: Magnetic dipole ordering occurring in each type of magnetism, where the arrows represent the alignment of magnetic moments; **a)** Paramagnetic: unpaired electron spins which are attracted in an applied external magnetic field; **b)** Ferromagnetic: parallel spins in a lattice-type structure; **c)** Antiferromagnetic: anti-parallel spins in a lattice-type structure; **d)** Ferrimagnetic: unequal anti-parallel spins.

Diamagnetism is an intrinsic property in all substances and occurs when two electrons are paired in an orbital, resulting in their spins cancelling out and no net magnetic moment. These electrons are known as diamagnetic electrons, and when subjected to a magnetic field, there is an insignificant negative magnetisation. If a material contains only atoms with diamagnetic electrons, the material itself is classified as diamagnetic (non-magnetic).

Paramagnetism (Figure 1.4a) is the result of unpaired electrons which impart a magnetic dipole moment upon the material. Hence, when an external magnetic field is applied, the spin of this unpaired electron will align with the field, and the paramagnetic material will be attracted.

Ferromagnetism (Figure 1.4b) and antiferromagnetism (Figure 1.4c) are cases of para-

magnetism where the system can be considered magnetically concentrated and each paramagnetic atom is in close proximity, such as in an atomic lattice. Consequently, they can interact and in the case of ferromagnetism the magnetic moments align in the same direction and a net magnetic moment is observed in the absence of an external magnetic field. These areas of aligned long-range ordering are known as magnetic domains.

In the case of anti-ferromagnetic materials, the spins align in an antiparallel configuration, decreasing the magnetic susceptibility of the substance as there is no net magnetic moment. These forms of atomic ordering only occur below the material-specific Curie temperature, the temperature at which the permanent magnetic properties are lost, and they can be considered effectively paramagnetic.

Ferrimagnetism (Figure 1.4d) is a special case of antiferromagnetism, where the spins still align in an antiparallel fashion, however due to the difference in magnitude of the magnetic moments on adjacent atoms there is still remnant magnetism without the presence of an external magnetic field.

1.3.3 Magnetic Hysteresis

An MH curve (Figure 1.5) is used to show the relationship between magnetisation, M , and magnetic field strength, H . When H is increased linearly, the resulting relationship between M and H is not linear, instead being sigmoidal (s-shaped). The magnetic susceptibility of a material, χ , is a dimensionless proportionality constant that is indicative of the degree of magnetisation of a substance when a magnetic field is applied (eq 1.1).⁶³

$$M = \chi H \tag{1.1}$$

In the case of ferromagnetic materials, when they are magnetised in one direction they do not return to zero magnetisation when the external magnetic field is removed, with this phenomenon being known as hysteresis. The cause of hysteresis is due to the presence of magnetic domains aligning under a magnetic field. A hysteresis loop is developed by increasing the magnetic field strength until the material reaches saturation magnetisation

(when all domains are aligned and magnetisation is no longer increasing), and then reversing the magnetic field, to align the magnetic moments in the opposite orientation. This reversal of the magnetic field from positive to negative allows the hysteresis loop to be generated, with the saturation magnetism being located at the tips of the loop.⁶³

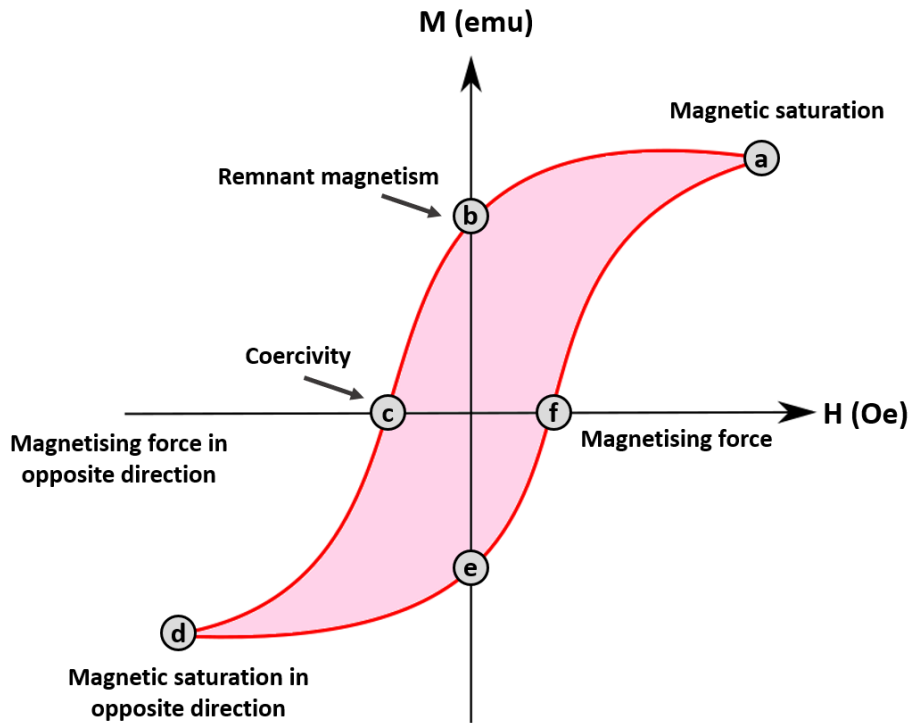


Figure 1.5: Diagram of a magnetic hysteresis loop of a ferromagnetic material, showing the saturation magnetisation (**a, d**), coercivity (**c, f**), and remnant magnetism (**b, e**). (Adapted from a diagram by the Florida State University High Energy Physics Group.⁶⁴)

Coercivity is a measure of the resistance of a ferromagnetic material to being demagnetised from a fully magnetised state. When a ferromagnetic material is magnetised in one direction, removing the external magnetic field does not demagnetise the material, and a reverse magnetic field must be applied to coerce the materials magnetism back to zero. Coercivity can be found from a materials hysteresis loop by observing the the magnetic field strength when magnetism is at zero (point c and f on Figure 1.5). In the case of MNPs, the size of the particles has a significant effect on their coercivity, with the coercivity increasing to a maximum as the particle size decreases due to the disappearance of domain walls.⁶⁵

1.3.4 Magnetic Domains

As previously touched upon, a magnetic domain is a region inside an overall ferromagnetic structure in which the individual magnetic moments within the material align in a uniform direction. Whilst each domain points in a certain direction, the different domains will point in varying directions and counteract each other, with magnetic domains acting to minimise the internal energy of a particle. A single large domain with constant magnetisation must maintain a large amount of magnetostatic energy (magnetic potential energy), which past a certain size becomes unstable. Domains form to lower this internal energy, with opposing magnetisation in each domain.⁶³ The formation of multi-domain structures and their alignment with external magnetic fields is represented schematically in Figure 1.6.

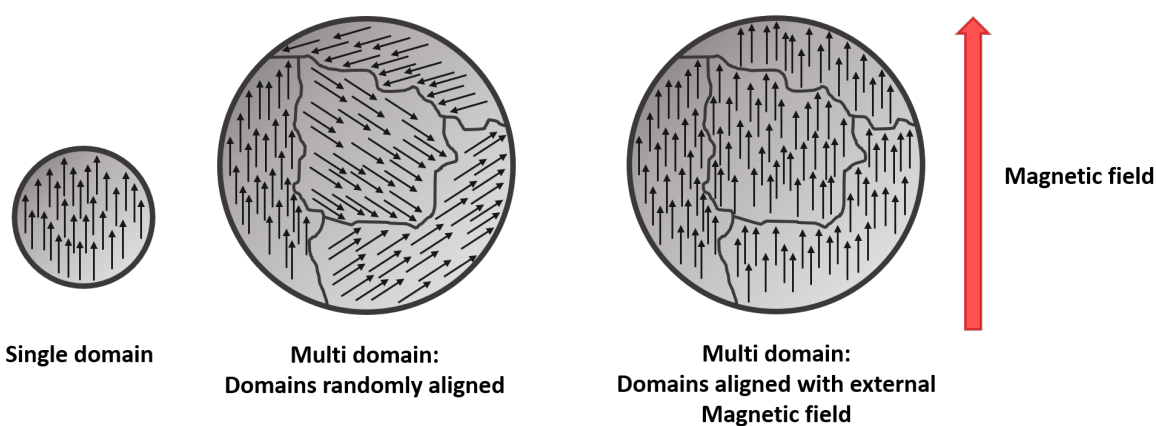


Figure 1.6: Spin ordering of ferromagnetic materials showing domain alignment when exposed to an external magnetic field.

Superparamagnetism is a property that occurs when a particles diameter is sufficiently small enough that the particle both contains only a single domain, and is small enough that the magnetisation can spontaneously flip alignment under the influence of temperature. The time between these relaxations is known as the Néel relaxation time and is highly temperature dependent as higher temperatures provide more thermal energy for magnetic fluctuation. The blocking temperature T_b , is the temperature below which these magnetic fluctuations do not occur and the material has similar magnetic properties as its bulk material.⁶⁶ Particles below this critical size (~ 25 nm⁶⁷) are often referred to as superparamagnetic iron oxide

nanoparticles (SPIONs), and are said to be magnetically unstable at room temperature as ambient thermal energy alone is sufficient to change their magnetic alignment, making them appear to be paramagnetic.⁶⁸ When an external magnetic field is applied to SPIONs, they align with this field and behave in a ferromagnetic/ferrimagnetic manner.⁶⁹

Multi-domain particles have lower coercivity due to the domains counteracting each other, with coercivity increasing as particle size decreases and the particles become single domain. At the superparamagnetic region the thermal agitation energy is larger than the magnetic energy of the sample and coercivity falls to zero (Figure 1.7). This also allows for the interesting potential for SPIONs to be introduced into the body as superparamagnetic, and then later magnetised utilising an external field. Consequently, the size of MNPs influences and controls their physicochemical properties and is therefore a crucial factor to consider and control in synthesis.

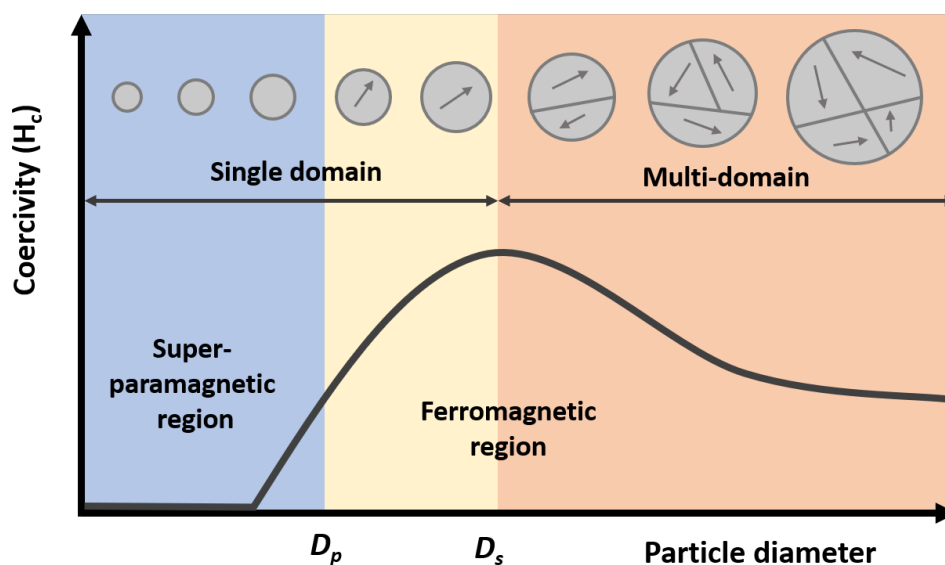


Figure 1.7: Schematic showing the development of multiple domains in magnetic nanoparticles, and coercivity behaviour as a function of particle diameter. (Redrawn from Lee et al.⁶⁵)

1.4 Magnetite: Properties and Applications

1.4.1 Magnetite

Magnetite, Fe_3O_4 , or ferrous-ferric oxide, is a naturally occurring abundant iron oxide comprised of ferric (Fe^{3+}) and ferrous (Fe^{2+}) ions in a 2:1 stoichiometric ratio. The material is ferrimagnetic due to its inverse spinel structure, with the O^{2-} ions within its crystal structure forming a face-centred cubic lattice, with iron cations at the interstices between these oxygen ions. As shown in Figure 1.8, there are two types of interstices the iron ions can fill, octahedral (red) or tetrahedral (yellow), with twice the number of octahedral sites available.

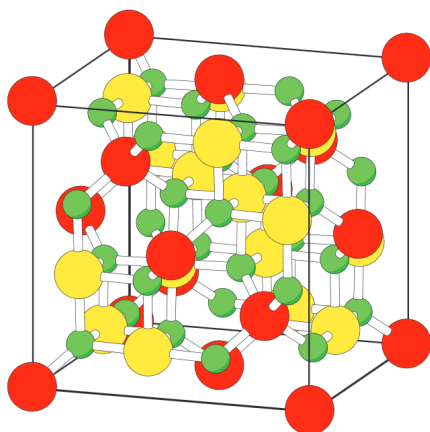


Figure 1.8: Crystal structure of magnetite (face-centered cubic spinel) with oxygen atoms shown in green, octahedral iron sites in red, and tetrahedral iron sites in yellow. (Reproduced from Friak et al.⁷⁰)

All tetrahedral sites are occupied by Fe^{3+} (ferric) ions, and half the octahedral sites occupied by Fe^{3+} with the other half occupied by Fe^{2+} (ferrous) ions.⁷¹ The tetrahedral and octahedral sites can be considered to form two magnetic sublattices with anti-parallel magnetic moments due to superexchange,^{72,73} a strong antiferromagnetic coupling which occurs between ferric ions in the octahedral lattice and is facilitated by the presence of the anionic O^{2-} which allows for the long-range interaction shown in Figure 1.9.

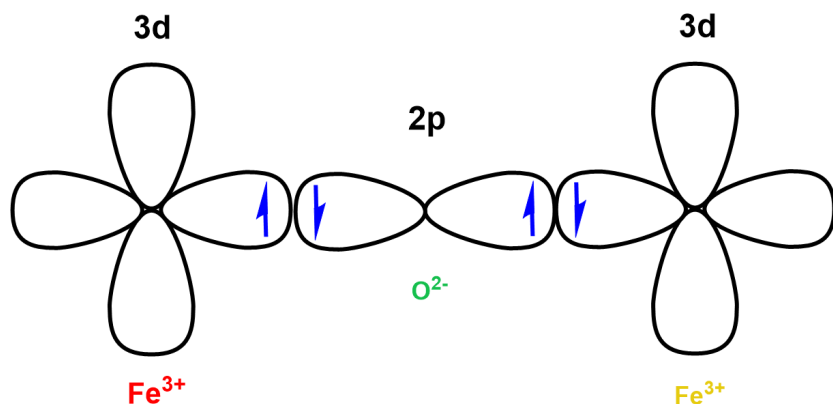


Figure 1.9: Diagram of the superexchange interaction between octahedral (red) and tetrahedral (yellow) ferric iron.

The hybridised orbitals are oriented anti-parallel following the Pauli exclusion principle, resulting in the antiparallel coupling between the octahedral and tetrahedral Fe³⁺ ions, thus leaving the only overall contribution to the magnetic moment as the octahedral Fe²⁺ ions.

Table 1.1: Physicochemical properties of magnetite at room temperature.

Property	Value
Chemical formula	Fe ²⁺ Fe ³⁺ ₂ O ₄
Crystal structure	Inverse spinel/face-centered cubic
Unit cell	8.3963 Å
Density	5.175 g cm ⁻³
Magnetism state	Ferrimagnetic
Curie temperature	858 K

The magnetic properties of magnetite crystals are highly dependent on both the shape and size of the crystalline particles, with coercivity and blocking temperature being heavily influenced. Saturation magnetisation is influenced by several features, including the crystallite size, with larger crystallites having smaller spin disorder layers.^{74,75} Imperfectly crystallised magnetite, irregular morphologies,⁷⁶ and the agglomeration of MNPs via magnetostatic interactions each negatively influence saturation magnetisation.⁷⁷

1.4.2 Industrial Application of Magnetite Nanoparticles

Whilst magnetic nanoparticles have found applications across a range of industries such as catalysis,⁷⁸ water purification,⁷⁹ data storage,¹ and ferrofluids,⁸⁰ the primary applications explored for the future usage of magnetic nanoparticles have centred around the biomedical industry, which will be expanded on within this section.

The internal use of magnetite for medical purposes have been reported as far back as the 10th Century A.D, when Egyptian physician and philosopher Avicenna recommended the use of a singular magnetite grain as an antidote for the ingestion of rust.⁸¹ In modern times, magnetite is seeing a wider range of applications, due to the improved understanding of the medical use of magnetism.

1.4.2.1 Biomedical Applications

Biomedical research is highly funded compared to many fields and industries, with a high margin of profit available for successful research breakthroughs. In 2012 alone 268.4 billion dollars of biomedical research and development expenditures accrued worldwide, showing the vast scale of this sector.⁸² Inorganic nanomaterials offer several advantages over classical organic compounds; i) the ability to modify nanomaterial surfaces with various functionalities makes them highly versatile,⁸³ ii) their capability to adsorb and deliver drug compounds,⁸⁴ and iii) nanomaterials may offer additional properties not exhibited by organic compounds such as magnetism, and energy absorption. Nanomaterials also have the additional advantage of being on a similar size-scale to biological entities, facilitating interactions with cells and their constituents.⁸⁵

One already utilised application for MNPs in biomedicine is their use as Magnetic Resonance Imaging (MRI) contrast agents, with multiple FDA approved iron oxide nanoparticles in active use as of 2011.³ For use as contrast agents it is key for particles to exhibit high relaxivity, the degree by which a magnetic compound can enhance the relaxation rate of nearby water proton spins. MNPs have been synthesised for MRI purposes in both biocompatible and biodegradable manners.^{86,87}

Another biomedical application for MNPs currently being explored is the possibility of magnetic hyperthermia to treat malignant tumours without damaging healthy tissue.^{85,88,2} In magnetic hyperthermia, MNPs are exposed to an alternating current (AC) magnetic field, which results in the generation of heat through either hysteresis loss in ferrimagnetic particles, or Néel relaxation in SPIONs.^{89,90} Heating as a result of hysteresis loss occurs when domain walls are displaced and hence occurs only in larger particles,⁹¹ whereas heating loss due to relaxation occurs in superparamagnetic nanoparticles as a result of the particles doing work against the applied magnetic field, leading to the loss of energy as heat. The particles are then introduced to the tumour site, often by injection, at which point thermal ablation of the tumour can occur (Figure 1.10). There are however still safety concerns that if the particles are exceptionally small they may be capable of diffusing through cell membranes and damaging intracellular organelles, or distribute widely around the body through the blood to undesired locations.⁹²

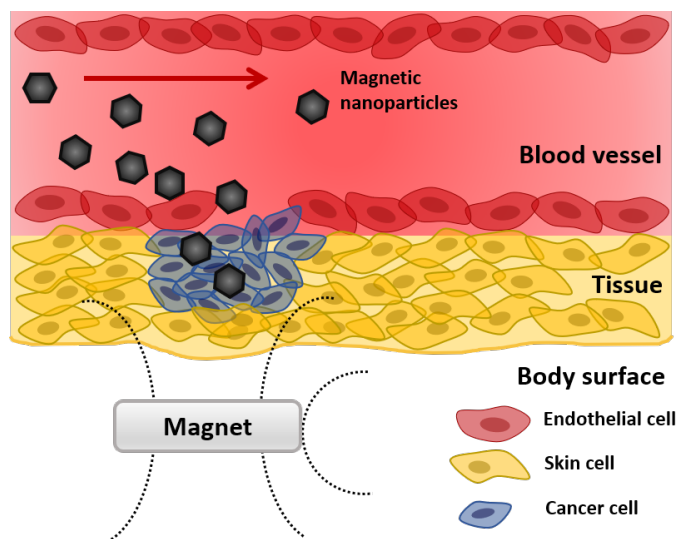


Figure 1.10: Schematic of magnetic hyperthermia showing the magnetic direction of injected magnetic nanoparticles to cancerous cells via an external magnet. (Redrawn from Park et al.⁹³)

Techniques of coating MNPs in various materials such as silica,⁹⁴ heavy metals,⁹⁵ and carbon⁹⁶ have allowed the development of particulate drug delivery systems. These can be

further functionalised by coating with a biocompatible polymer such as dextran, chitosan,⁹³ or polyethylene glycol (PEG),⁹⁷ which then provide a favourable surface for the binding of biological molecules to the nanoparticles.⁹² In traditional drug delivery, biodistribution is uncontrolled with general systemic distribution occurring in most cases,⁹⁷ which can be harmful to the organs. The use of magnetic drug delivery systems (MDDS) has the potential to remedy this, with the idea of an external magnetic field guiding functionalised SPIONs to their target.

The shape and size of particles employed for MDDS is a crucial factor with the influences of shape, size, and surface properties summarised in Figure 1.11.⁹²

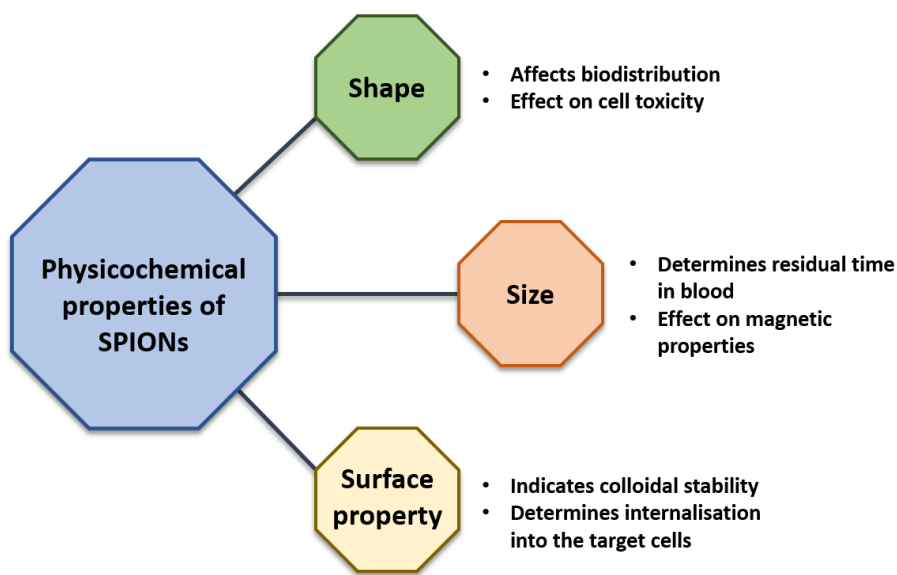


Figure 1.11: Physicochemical considerations of SPIONs for drug delivery. (Redrawn from Wahajuddin et al.⁹²)

For many of the above proposed applications of MNPs, particles have the highest efficacy when their size is around 10-20 nm,⁹⁸ with shape homogeneity and control also being preferable for applications such as MRI and heating. Colloidal nanoparticles offer varying physical properties dependent on the composition, size, and shape, and as such a homogeneous solution is preferable for a high degree of control over both the magnetic and surface properties of the magnetic nanomaterial. Particle size influences the biodistribution of MNPs, with particles <10 nm in diameter being rapidly cleared via the kidneys, whereas particles

>200 nm concentrate in the spleen, or are uptaken in phagocytosis, lowering their overall concentration in the blood plasma.⁹⁹ Another hazardous effect of exceptionally small (<2 nm) nanoparticles is their potential to diffuse through cell walls and damage the organelles within resulting in increased cytotoxicity. Particles between 10-100 nm in size appear to have optimal properties due to their ability to both penetrate through small capillaries and evade macrophages more effectively than larger particles.¹⁰⁰

Whilst currently less studied than the effect of size, the shape of a nanomaterial has been reported by researchers to influence the blood circulation time of nanoparticles, with rod-shaped and non-spherical mesoporous silica particles exhibiting longer circulation times.¹⁰¹ In the case of rod-shaped particles, short rods were noted to primarily build-up within the liver, whereas longer particles spread to the spleen. The excretion of shorter rods was observed via silica detection in urine and faeces to occur on a significantly faster timescale than long rods,¹⁰¹ with rod-shaped particles in general having been observed to invoke lower phagocytic activity in macrophages than their spherical counterparts.¹⁰²

Cubic MNPs are reported to perform better as MRI contrast agents compared to their spherical counterparts with comparable particle diameters due to their higher degree of crystallinity, increased crystallite size, and higher saturation magnetisation resulting in higher relaxivity (Figure 1.12).^{103,104}

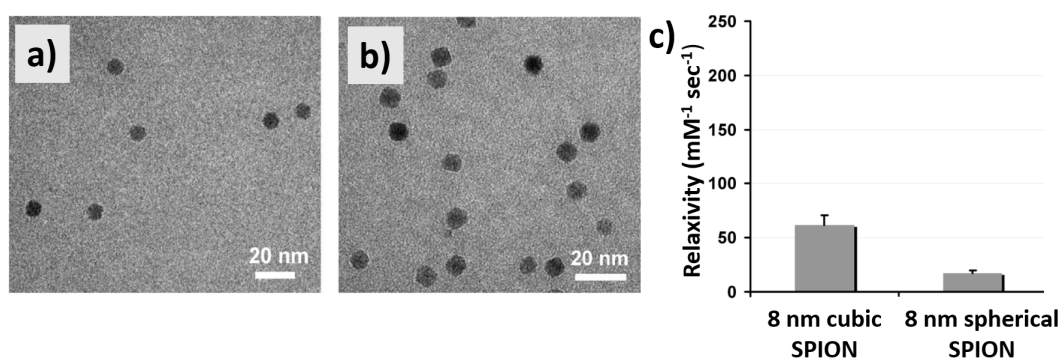


Figure 1.12: TEM images comparing **a)** spherical and **b)** cubic SPIONs; **c)** comparison of relaxivity of cubic and spherical SPIONs. (Reproduced from Zhen et al.¹⁰⁴)

Shape was once again observed to enhance the magnetic properties of MNPs with the synthesis of small (6 - 14 nm) octahedral particles which exhibited higher saturation mag-

netisation than spherical MNPs of a similar size.¹⁰⁵ Octahedral MNPs were also found to have enhanced specific absorption rates for magnetic hyperthermia treatment, and improved relaxivity for MRI applications,¹⁰⁶ further highlighting the importance of producing shape-controlled MNPs.

1.5 Crystal Growth and Formation

For crystalline inorganic materials such as MNPs, it is required to understand how crystal growth occurs and is controlled to replicate conditions synthetically. Nanoparticles are a kinetically determined product, with reasonably complicated mechanisms of nucleation and growth that can be difficult to consistently reproduce.

1.5.1 Crystal Nucleation

Crystallisation begins with the formation of presence of nuclei (seed crystals), which act as the template for further crystal growth. It is the emergence of a distinct thermodynamic phase via a first-order phase transition from a prior phase with high Gibbs free energy to form a highly ordered crystalline structure with reduced free energy.¹⁰⁷ Homogeneous nucleation is the phenomenon of nucleation occurring uniformly throughout the parent phase without a set nucleation site, whereas heterogeneous nucleation typically occurs on a surface within the system such as added seed crystals or impurities, and occurs comparatively easier as the nucleating surface is already present.¹⁰⁸

One of the most common theoretical models used to understand nucleation is classical nucleation theory (CNT). CNT when applied to the nucleation of nanoparticles considers the change in free energy of a system during homogeneous nucleation of a spherical nucleus/particle. The free energy of a nanoparticle is defined as the sum of the particles surface free energy and the bulk free energy.¹⁰⁸ For a spherical particle with radius r , the surface energy γ , and the crystal free energy ΔG_v , gives the total free energy ΔG (eq 1.3).¹⁰⁸

The crystal free energy ΔG_v , is defined by the temperature T , Boltzmann's constant k_B , the supersaturation of the solution S , and its molar volume, v (eq 1.4).

$$\Delta G = \frac{-4\pi r^3}{3} \Delta G_v + 4\pi r^2 \gamma \quad (1.2)$$

$$\Delta G_v = \frac{-k_B T \ln(S)}{v} \quad (1.3)$$

Surface free energy is always positive due to surfaces not having all bonding possibilities satisfied, and are hence energetically unfavourable, whereas crystal free energy is negative due to the high stability afforded by the bond saturation in a crystalline structure. There is a maximum free energy ΔG_{crit} (eq 1.5), which a nucleus must pass through to be stable in solution that occurs at the critical radius (eq 1.6); the minimum size at which a particle can exist in solution without being redissolved, shown on Figure 1.13 below.

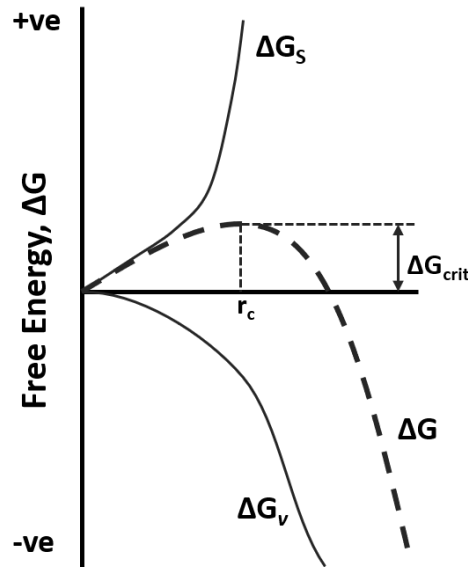


Figure 1.13: A free energy diagram of classical nucleation theory, explaining the existence of a 'critical nucleus'. (Reproduced from Thanh et al.)¹⁰⁸

$$\Delta G_{crit} = \frac{4\pi\gamma r_{crit}^2}{3} \quad (1.4)$$

$$r_{crit} = \frac{-2\gamma}{\Delta G_v} = \frac{2\gamma v}{k_B T \ln(S)} \quad (1.5)$$

CNT makes the simplifying assumptions that i) the formed nucleus has the same macroscopic properties (density, structure, and composition) as the stable phase, ii) the nucleus is spherical and the interface between the nucleus and solution is a distinct boundary, iii) surface tension is isotropic.¹⁰⁷

When considering the growth of nanocrystals, a widely accepted model which has built upon CNT is the LaMer theory of burst nucleation followed by a period of particle growth.¹⁰⁹ LaMer has previously described a reaction system in terms of monomer concentration versus time, where a monomer is defined as a species that is dissolved in solution, unstable, and able to form particles without a significant energy barrier.¹⁰⁹

The LaMer mechanism (Figure 1.14) considers the nucleation and growth of nanoparticles with time as a function of monomer concentration. Three distinct stages occur in the nucleation and growth of nanoparticles; i) monomer concentration increases until the critical supersaturation concentration required for nucleation is achieved (C_{\min}), ii) monomer concentration lowers after the nucleation event as some monomer has been consumed, and iii) monomer concentration is too low for further nucleation to be energetically favourable, at which point particle growth occurs via addition of the remaining monomer to the nucleated particle surfaces. As the concentration of monomer lowers past the lower solubility limit (the lowest concentration at which nucleation can occur, C_s), additional growth occurs via Ostwald ripening, resulting in wide size distributions.¹¹⁰

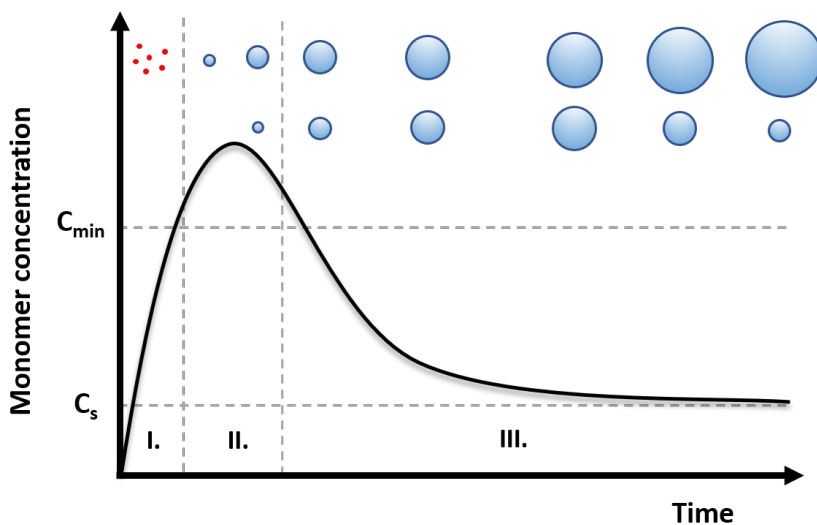


Figure 1.14: A diagram of the classic LaMer mechanism of nanoparticle growth. (Redrawn from Vreeland et al.)¹¹⁰

1.5.2 Crystal Growth Mechanisms

As the LaMer model suggests for the synthesis of monodisperse particles that nucleation and growth must be separate processes, then models for the growth of particles are required to predict final size distributions. Crystal growth is considered a secondary nucleation process due to it entailing the clustering of ions at the crystal surface in a comparable manner to primary heterogeneous nucleation.¹¹¹

The primary mechanism of particle growth is by diffusion of monomers to the particle surface, and their subsequent integration into lattice sites in a layer-by-layer fashion (Figure 1.15).¹¹² The crystal growth is driven by higher energy active sites on the crystal surface, which are favourably filled by binding ions. These sites enable the growth of crystals at relatively low supersaturations, with the highest energy sites being kinks and steps in the surface of the crystal. As kinks and steps are coordinatively unsaturated compared to the flat surface of a growing crystal, the surface binding of aqueous ions is higher, and more energy is released from binding to these growth sites.

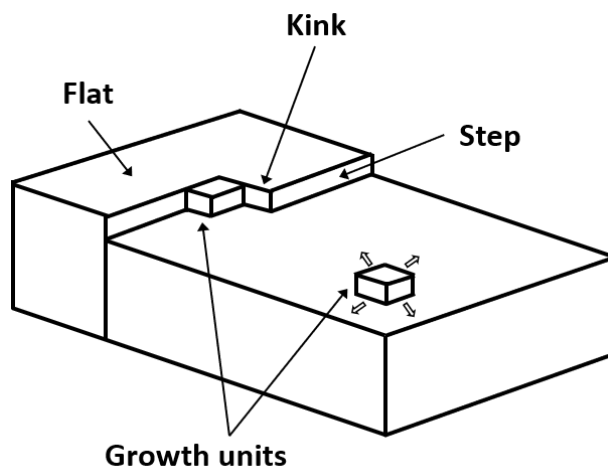


Figure 1.15: A three-dimensional crystal surface showing growth units and the three types of growth sites. (Adapted from Mann, 1993)⁹

The LaMer mechanism explains how growth is also achieved through Ostwald ripening; A thermodynamically-driven process in which smaller, less stable particles are dissolved and re-deposited onto the surface of larger particles in order to lower the overall energy of the system (Figure 1.16a).¹¹³ The overall effect is a ‘coarsening’ of the particles, where the size distribution is shifted toward larger particles.

Coalescence can also result in particle growth and is the process of primary particles aggregating on a crystal and fusing to form larger overall particles (Figure 1.16b). The crystallinity is often lowered in coalesced particles as no crystallographic alignment is required.¹¹⁴ Both Ostwald ripening and coalescence are reversible reactions.

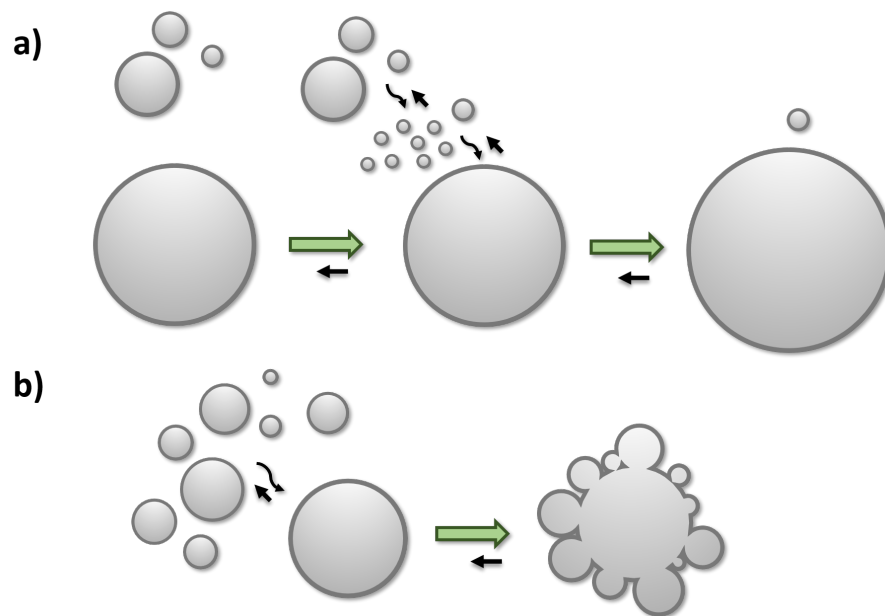


Figure 1.16: Schematics of two mechanisms of particle growth; **a)** Ostwald ripening, and **b)** Coalescence.

Significant research on biomineralisation mechanisms has indicated crystallisation is not only occurring via the classical crystallisation pathway of ions/monomers to a particle surface to form a single crystal (Figure 1.17a). Crystallisation is also possible through a non-classical mechanism via a particle mediated process, where preformed crystalline building blocks aggregate. This often occurs at the mesoscale (>100 nm), with iso-oriented crystals (Figure 1.17b) forming from the oriented attachment of primary particles (~ 3 nm particles). Crystallographic alignment minimises the highest energy surfaces, while formation of larger particles lowers the overall energy of the system.^{115,116} Internal restructuring and fusion can then result in the formation of a crystallographically aligned single crystal.¹¹⁷

The other non-classical pathway occurs via mesoscale assembly, where the primary particles are stabilised by the addition of an organic additive. These stabilised nanocrystals coated in organic ligands self-assemble and undergo aggregation, forming a mesocrystal which can fuse into a textured mosaic iso-oriented crystal through oriented attachment.¹¹⁶ This is the mechanism by which many biominerals are stabilised and formed, and will be discussed further in section 1.7 and 1.8.

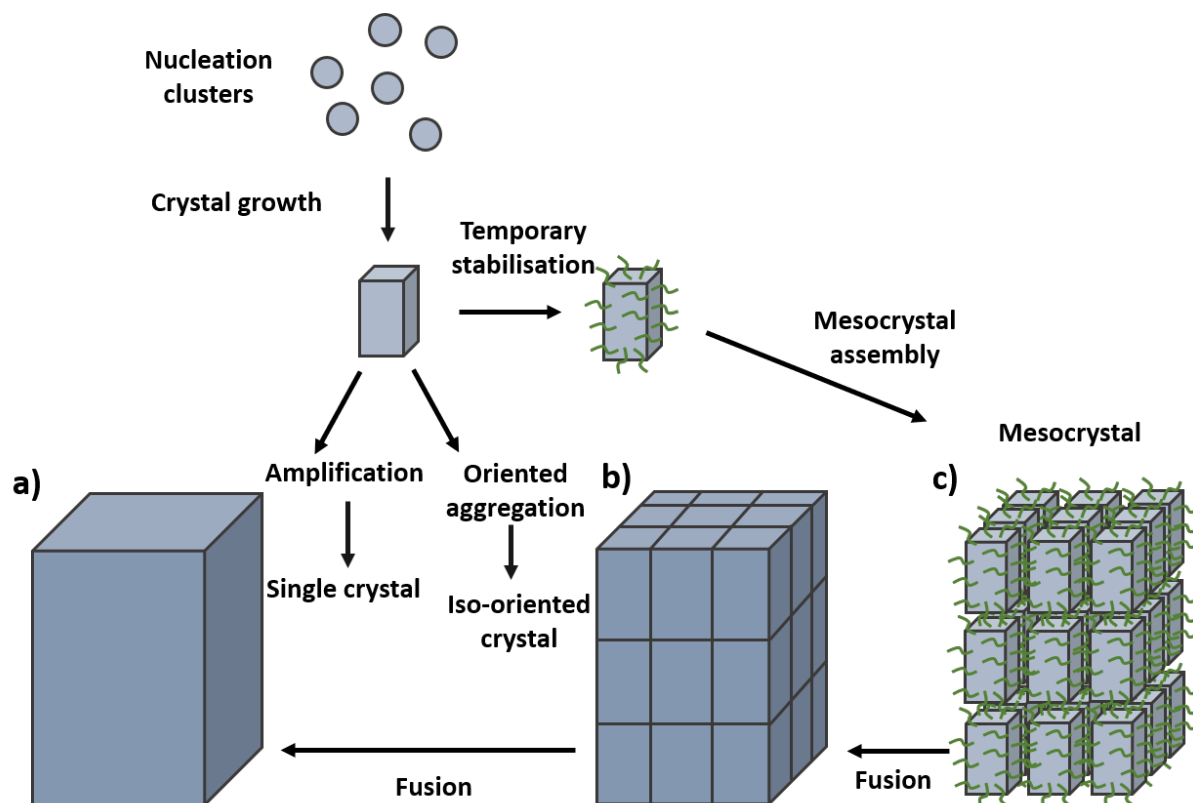


Figure 1.17: Schematic representation of both classical and non-classical crystallisation: **a)** Classical crystallisation pathway, **b)** Oriented attachment of primary nanoparticles forming an iso-oriented crystal upon fusion, **c)** Mesocrystal formation via self-assembly of primary nanoparticles covered/stabilised with organics. (Redrawn from Niederberger et al.⁵⁰)

1.5.3 Influencing Crystal Growth and Morphology

A growing particle is typically spherical when it is nucleating as a primary particle or small cluster of atoms, as this shape has the lowest surface energy (lowest surface area for a given volume).

When an organic molecule adsorbs to and interacts with a crystal surface, it lowers the surface's interfacial energy and the growth of the face is slowed as a result.⁹ Ions and other molecules can interact with and inhibit the kinks and steps present on a crystalline surface, drastically lowering their growth rate and changing the morphology of crystals formed, as the slowest growing crystal faces are more expressed in the final crystal habit. Additive-mediated crystallisation has been observed across a range of minerals including calcite,^{118,119} silica,¹²⁰

aragonite,¹²¹ and magnetite.^{122,123} By inhibiting different crystallographic axes different morphologies are expressed, e.g. a crystal with rapid growth along a single axis would afford a needle shaped crystal, fast growth along two axes would produce plates, and equivalent growth in all three axes would lead to an isotropic morphology such as cuboid or octahedral. As such, morphology is determined by growth rate, with soluble additives playing a crucial role in the types of crystals producible.

Figure 1.18 shows the effect of an additive binding to different crystal faces, altering the final morphology of a forming crystal and producing different shapes.

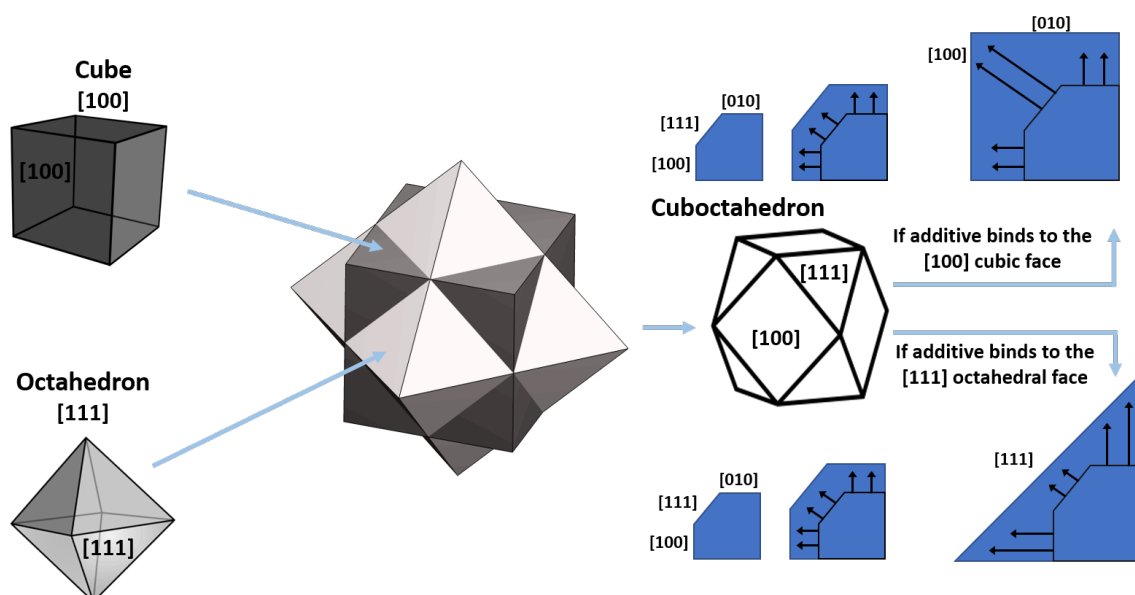


Figure 1.18: Schematic showing a cuboctahedron forming from the combination of cubic [100] and octahedral [111] faces (by cutting off the corners). An adsorbed additive can direct the formation back to either cubic or octahedral morphology via growth inhibition of the bound facet. (Redrawn from Staniland and Patwardhan.¹⁰)

1.6 Synthesis of Magnetic Nanoparticles

When it comes to the synthesis of MNPs, there are various diverse synthetic techniques utilised in the literature over the years, with many well refined processes capable of producing particles of differing polydispersities and morphologies.¹²⁴ The size and magnetic

properties are a direct result of the particle synthesis technique, and as such understanding how synthetic conditions influence particle nucleation and growth is of utmost importance.

A key issue across most established magnetite synthetic methods has been reproducibility due to both the kinetic nature of crystal formation, and the sensitivity of ferrous (2^+) ions to oxidise, forming ferric (3^+) ions. This is generally circumvented by synthesising MNPs under an inert atmosphere and storing the particles dry to prevent and slow further oxidation.

1.6.1 Thermal Decomposition

Thermal decomposition has been cited as one of the most effective methods of synthesising magnetic nanoparticles whilst exerting a degree of control over the morphology of the particles generated. Typically, an iron precursor such as iron pentacarbonyl, $[\text{Fe}(\text{CO})_5]$, or iron (III) acetylacetonate, $\text{Fe}(\text{acac})_3$, is decomposed in a high boiling organic solvent in the presence of both stabilising surfactants such as oleic acid and oleylamine, and reducing agents. The solution is then dehydrated at $\sim 110^\circ\text{C}$ and then subjected to high temperature ($>280^\circ\text{C}$) under an inert atmosphere.^{22,125} The particles are extracted in ethanol, and centrifuged to obtain the final magnetite product.

This results in the formation of organic soluble nanoparticles due to the surfactant layer on the particle surface. For many purposes, including biomedical applications, it is preferred to have water soluble MNPs. This has led to the development of an adapted methodology wherein water soluble surfactants are used in the synthesis such as poly(ethylene glycol) (PEG).¹²⁵ The particles formed from thermal decomposition can have highly tailored geometries, including nanoflowers, cubic, and octahedral morphologies.¹²⁶

The requirement of large quantities of toxic and expensive precursors, organic surfactants, alongside high boiling organic solvents and sustained elevated temperatures makes the thermal decomposition methodology ecologically unfriendly.¹²⁷ Safety concerns have also been raised due to the associated risks of high temperature organic liquid and vapour phases.^{125,128}

Another downside to this technique is that due to the juxtaposition of synthesising a

metal oxide in the absence of oxygen, many particles synthesised with this methodology were found to contain crystal defects, undesired iron oxides, and poor magnetic properties compared to pure magnetite.¹²⁵ These poor properties were the result of the formation of a 'magnetically dead layer' of non-magnetic iron oxides several nanometres thick rather than the expected single unit cell diameter.^{129, 130}

A novel solvent free technique has also been reported, with low particle sizes of 9 nm, and well-established particle magnetism of 76 emu g⁻¹.²² This synthesis however still uses the toxic reagent Fe(acac)³, and is highly energy intensive with both long reaction times and high temperatures.

1.6.2 Hydrothermal Synthesis

The hydrothermal process of synthesising magnetite is highly successful for growing crystals of iron oxides at larger particle sizes than other methods offer. In a typical hydrothermal synthesis, iron salts are dissolved in deionised water to form a solution and the pH of this solution slowly increased from acidic to pH ~10 via dropwise addition of a base. The mixture is then heated in a high pressure and temperature autoclave for an extended period (hours to days) to allow for magnetite crystallisation.

The particles obtained from this synthesis are typically more polydisperse than those formed in thermal decomposition.¹²⁷ Hydrothermal syntheses are reasonably cost-effective, with no use of organic reagents.¹³¹ They however still require heating and pressure, preventing the process from being considered a green synthetic technique.

1.6.3 Microemulsion

A microemulsion is a transparent thermodynamically stable mixture of two immiscible liquids such as oil and water, which is stabilised by a surfactant.¹³² Thermodynamic stability is the defining characteristic of a microemulsion, with the dispersed aqueous microdroplets (typically less than 100 nm in diameter) stabilised by a monolayer of surfactant molecules.^{98,133} The diameter of these reverse micelles can be controlled and tuned by the ratio of water and surfactant, with higher proportions of surfactant allowing a greater quantity of smaller

micelles to form.

Two identical microemulsions are formed with one containing dissolved iron salts and the other base. The size limited aqueous drops act as nanoreactors with the mixing and coalescing of microdroplets from the solutions leading to the precipitation of iron oxide within the aqueous phase.¹³⁴ This precipitate is then extracted by the addition of solvent to break up the micelles, such as acetone or ethanol, and then extracting or centrifuging the mixture.⁹⁸

The use of microemulsions to synthesise magnetite is a complicated process, requiring organic solvents and capping-agents to produce a stable solution. A relatively poor yield of nanoparticles is produced, albeit with a relatively narrow size distribution due to the physical constraint of the reverse micelle nanoreactors. While the reaction occurs at ambient conditions, the complexity, low yields, and organic solvents make it unsuitable as a sustainable large-scale manufacturing process.

1.6.4 Room Temperature Co-Precipitation

The room temperature co-precipitation (RTCP) method of particle synthesis is a straightforward wet route of synthesising MNPs wherein a base such as NaOH, KOH, or tetraethylammonium hydroxide,¹³⁵ is added to an aqueous mixture of ferric and ferrous iron under an inert atmosphere at room temperature, producing iron oxides without the need for toxic pre-cursors or environmentally unfriendly solvents.¹³⁶ The ferric:ferrous iron ratio is important for the quality of the final products formed, with a stoichiometric ratio of 2:1 favouring magnetite formation. These reactions proceed at low temperatures and are considered industrially important due to their cheap reagents and ecologically friendly reaction conditions. Many factors can influence the products formed in RTCP which will be discussed further in this section.

When iron sulphate salts are used for RTCP, there are several reactions simultaneously occurring within the solution of mixed valence iron salts that can result in the precipitation of iron minerals. Equations below show the iron oxides formed from pure ferrous to pure ferric minerals.

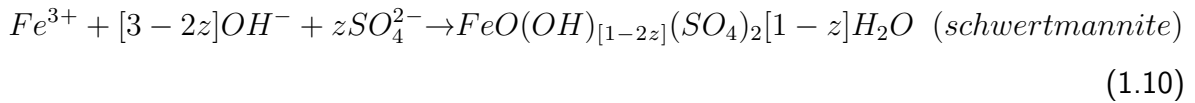
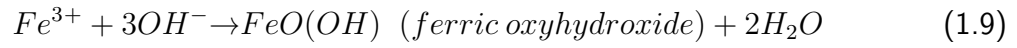
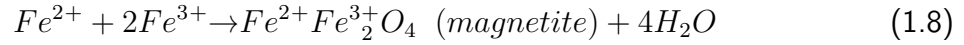
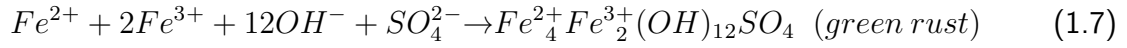
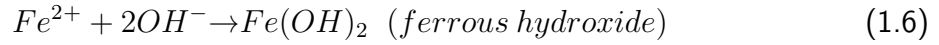


Figure 1.19a shows titration curves for the RTCP of ferric and ferrous sulphate with sodium hydroxide. The molar ratio of Fe^{3+} to total iron is denoted by X , with the ratio of hydroxide ions and total iron being R . The rate of addition of NaOH was $0.05 R \text{ min}^{-1}$, meaning R increased linearly with time as the reaction progressed. The titration curves are characterised by three plateaus separated by two equivalence points, denoted as E_1 (circles) and E_2 (crosses).

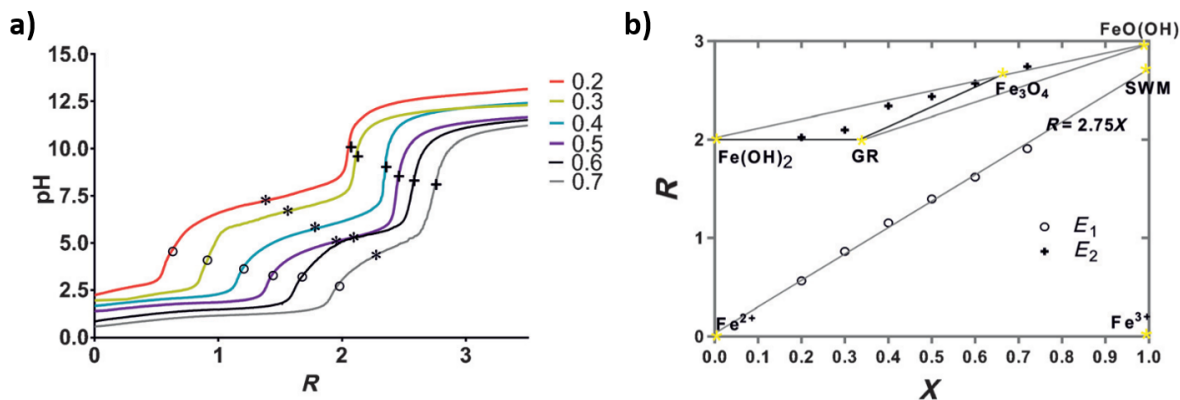


Figure 1.19: a) pH measurements recorded during RTCP reactions for total iron concentrations of 50 mM at a rate of 0.05 R min^{-1} ; b) Mass balance diagram of the formation of various iron oxides showing the equivalence points from a), (GR = green rust, SWM = schwertmannite). (Reproduced from Rawlings et al.¹³⁷)

The three plateaus are indicative of the mechanism of iron oxide formation, with the first plateau (between $\sim\text{pH } 1.4 - 2.6$) showing hydroxide consumption as ferric rich basic salts precipitate (ferric oxyhydroxide, schwertmannite) and free Fe^{3+} in solution is consumed. As ferric ions are less soluble than ferric ions in base, these salts precipitate first. The middle plateau (between $\text{pH } \sim 6.5 - 6.9$) shows the conversion and formation of a range of iron minerals in the form of ferrous hydroxide, green rust, magnetite, and goethite in varying amounts, shifting toward the latter minerals in experiments with higher X ratios. This is indicative of free Fe^{2+} being consumed. At this stage, ferrous ions are incorporated into the ferric oxyhydroxide present, forming green rust and magnetite. When this process is complete, excess ferrous ions are precipitated as ferrous hydroxide, with the mixture of oxides remaining to the end of the titration ($\sim\text{pH } 12.5$), at which point the solution was left overnight to convert remaining ferrous rich iron oxides into magnetite. Figure 1.19b shows the mass balance diagram, with the obtained experimental values of E_1 and E_2 plotted for the various ranges of X .

The most critical factor for the production of magnetite in a RTCP system is the Fe^{3+} to Fe^{2+} ratio. As presented in eq 1.7 - 1.11 and Figure 1.19b, a wide range of iron oxides form throughout the reaction pipeline. As the Fe^{3+} ratio increased, mean size is decreased

as yield improves, up to the stoichiometric 2:1 ferric to ferrous ratio (0.66) natively observed in magnetite.^{138,139,140} The only particles suitable for use as MRI contrast agents are those formed between a 0.4 and 0.6 ferric ratio.¹⁴¹ Iron concentration is also of high importance, with an optimum concentration between 39 and 78 mM.¹⁴¹

The formation of magnetite from the concomitant precipitation of ferrous and ferric iron with a base under reverse RTCP conditions at a set pH has been investigated utilising high-resolution cryogenic TEM (HRTEM).¹⁴² It was found that the particles form through the rapid agglomeration of nanoscale primary particles (~2 nm in size), with these aggregates becoming denser and spheroidal particles of 5-15 nm forming. The forming magnetic nanoparticles exhibited surface roughness consistent with particle growth via attachment and coalescence, with the primary particles exhibiting no significant crystal lattice fringes pre-attachment to a larger growing particle. This is indicative that the primary particles do not have high crystallinity and is proposed to be the result of the interaction of ferrous iron ions with an amorphous ferrihydrite hydrogel formed in the initial stages of the co-precipitation. As such, oriented attachment is not necessary in this case.¹⁴²

Another study into the formation pathways of magnetite under standard RTCP reactions found through XRD (x-ray diffraction) analysis that when a base was added over time to an iron chloride solution, a complex series of iron transformations occurs.¹³⁶ Akaganeite (β -FeOOH) nucleates and transforms through ferric rich goethite (α -FeOOH) to magnetite via arrow shaped nanoparticle intermediates. At higher addition rates, the addition of base altered this pathway with two different nucleation pathways initiating as ferrous hydroxide nucleates and transforms through lepidocrocite (γ -FeOOH) to magnetite with both pathways competing. This study provides insights into how MNPs form in a co-precipitation via the phase transformation of iron oxyhydroxides in a topotactic transition to magnetite, and not through the direct reaction of aqueous ferrous and ferric ions.¹³⁶

Stirring velocity is another factor seen to play a role in the morphology of particles precipitated, particle size, distribution, and even iron oxides formed being affected.¹⁴³ Vigorous magnetic stirring or 10,000 rpm stirring produced magnetite particles primarily spherical or ellipsoidal in shape. The magnetic stirring led to particles ~19 nm in size with a broad size

distribution, whereas stirring at 10,000 rpm produced particles which were notably smaller at ~10 nm, with a narrower size distribution. Increasing the rpm to 18,000 led to varied shapes and sizes including nanorods (speculated to be hydrated goethite rods),¹⁴⁴ and reduced particle magnetism. A further increase in stirring rate to 25,000 rpm resulted in a rise in temperature from 20.0 to 37.3 °C and produced a mixture of non-magnetic iron compounds.¹⁴³

Particle size is influenced by the choice of base,¹³⁵ as well as the pH of reaction and rate of addition of base.¹³⁶ The counter cation of the base exerts influence on MNP size in the order of $\text{Na}^+ > \text{K}^+ > \text{N}(\text{C}_2\text{H}_4)^+_4$. This size response is attributed to steric effects, with larger cations inhibiting the agglomeration of nanoparticles.¹³⁵

Magnetite easily oxidises to maghemite in acidic media and water leading to reduced magnetism.¹⁴⁵ Bubbling nitrogen through the RTCP reaction solution both protects against this oxidation, and produces smaller and more uniform particles than in reactions with no oxygen removal.^{100,146}

Reverse RTCP is also feasible, with a dissolved iron salt solution being added dropwise to a solution of base. The particles formed from reverse RTCP tend to be smaller than those obtained from a standard RTCP reaction.¹⁴⁷ This difference in size is due to the pH of the reaction being kept consistently high, and iron never being in excess. As such, the particles are not given the opportunity to mass nucleate as pH increases and cannot grow over time.

1.6.5 Synthetic Summary

Of each of the four common methods of synthesising MNPs, there are various benefits and drawbacks Table 1.2 shows a summary of the synthetic methodologies, detailing the complexity, timescale, reagents, as well as particle properties.

Table 1.2: Summary comparison of the common methods used to synthesise magnetite.(Reproduced from Lu et al.⁹⁸)

Synthetic method	Synthesis	Reaction temp (°C)	Reaction period	Solvent	Surface-capping agents	Size distribution	Shape control	Yield
thermal decomposition	complicated, inert atmosphere	100-320	hours - days	organic compound	added during reaction	very narrow	very good	high/scalable
hydrothermal synthesis	simple, high pressure	220	hours - days	water-ethanol	added during reaction	very narrow	very good	medium
microemulsion	complicated, ambient conditions	20-50	hours	organic compound	added during reaction	relatively narrow	good	low
room temperature co-precipitation	very simple, ambient conditions	20-90	minutes	water	added during or after reaction	relatively narrow	not good	high/scalable

From this review, RTCP is the only synthetic system which is simple, produces a high-yield of particles, and does not require high temperature, pressure, or long reaction times. The key disadvantage of this technique stems from the poor shape control currently achievable. The particles formed from this technique tend to lack defined shape, and as such there is much scope for improvement in this key area.

By influencing the formation of particles *in vitro*, it may be possible to positively influence the shape profile of MNPs produced using RTCP. This would allow the large-scale production of fine magnetite particles without the heavy energy and environmental expenditure that is currently associated with their production.

1.7 Biomineralisation and Biomimetics

Biomineralisation is the process in which biological organisms crystallise or precipitate inorganic minerals from metal ions which are selectively up-taken from the environment and formed into complex, functional structures. The types of material synthesised vary greatly depending on the genus and size of organism, with single celled bacteria able to create nanoscale particles and intricate silica structures, and mammals forming complete skeletons and teeth. Around sixty different minerals are known to be formed by bio-organisms, comprising of a wide range of materials including amorphous, crystalline, and hybrid mate-

rials such as organic crystals.¹²⁴ The subject of biomineralisation is truly interdisciplinary, spanning biology, chemistry, computational modelling, and their further disciplines such as materials chemistry, physical chemistry, microbiology, and crystallography.

1.7.1 Biologically Induced Mineralisation and Biologically Controlled Mineralisation

There are two forms of biomineralisation observed in Nature: biologically induced mineralisation (BIM) and biologically controlled mineralisation (BCM). In the case of BIM, minerals tend to both nucleate and grow external to the cell as a result of the mineral deposition being a side effect of interactions between the metabolic process of the organism and surrounding environment.¹²⁴ This can occur through the excretion of a metabolic by-product, which then goes on to react with compounds or ions in the surrounding environment leading to the precipitation of biominerals. The poor crystallinity, size distribution, and lack of defined crystal shape suggests that these minerals are an uncontrolled aspect of the metabolic process of the mother organism.¹⁴⁸ Whilst this type of particle growth is often free in solution from the metabolic products diffusing, it can also occur on bacterial cell walls or other surfaces as adsorption sites for nucleation.

In the process of BCM, the organism has intentionally developed the mineral for a specific function (i.e. protection, support). Each of these mineral formation processes is dictated in some manner by proteins and/or macromolecules which control the nucleation and propagation of the inorganic materials formed. These materials tend to be species specific, more intricate and controlled, and with features in common such as i) uniform particle sizes, ii) defined crystal structures in the case of crystalline nanomaterials, iii) high spatial organisation, iv) further assembly into hierarchical structures, v) well-defined chemical compositions, and vi) controlled levels of aggregation for amorphous and crystalline nanomaterials.¹¹¹

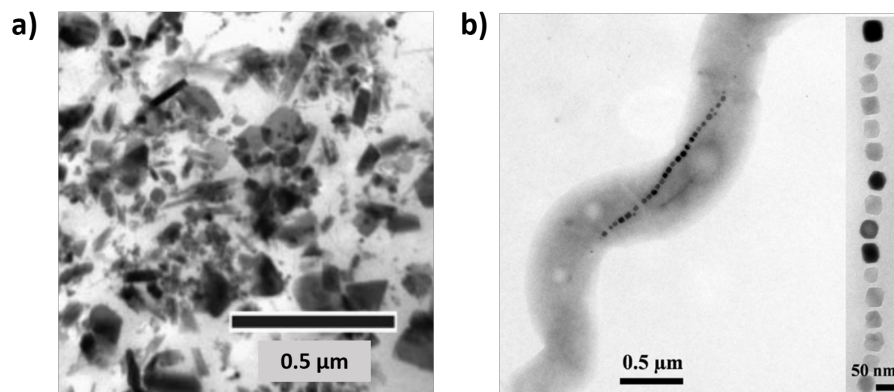


Figure 1.20: Comparison of iron biominerals formed in; **a)** BIM (*Geobacter metallireducens* strain GS-15), and **b)** BCM (*Magnetospirillum* strain CB-1). (Reproduced from Vali et al.¹⁴⁹ and Lefevre et al.¹⁵⁰)

These properties contrast with the far less controlled Nature of BIM (Figure 1.20), befitting of the evolutionary design of materials with a set functionality. Mineralisation sites such as organic frameworks and vesicles have four identifying requirements: spatial delimitation, diffusion-limited ion flow, chemical regulation, and organic surface templating.¹⁵¹

In most cases bacterial BCM is a two-step process where in the first step metal cations interact electrostatically with the anionic surfaces of the bacteria cell wall or organic polymers acting as a templating matrix, which then go on to act as nucleation sites for the final nanoparticle crystals in the second step. These high-quality materials are reproducible across the species, and materials formed under a BCM process will tend to be of a higher quality than the corresponding material formed either artificially or under BIM. An example of the type of complex structures which can be formed under BCM is shown in Figure 1.21, with four species of diatoms producing high quality biogenic silica structures.

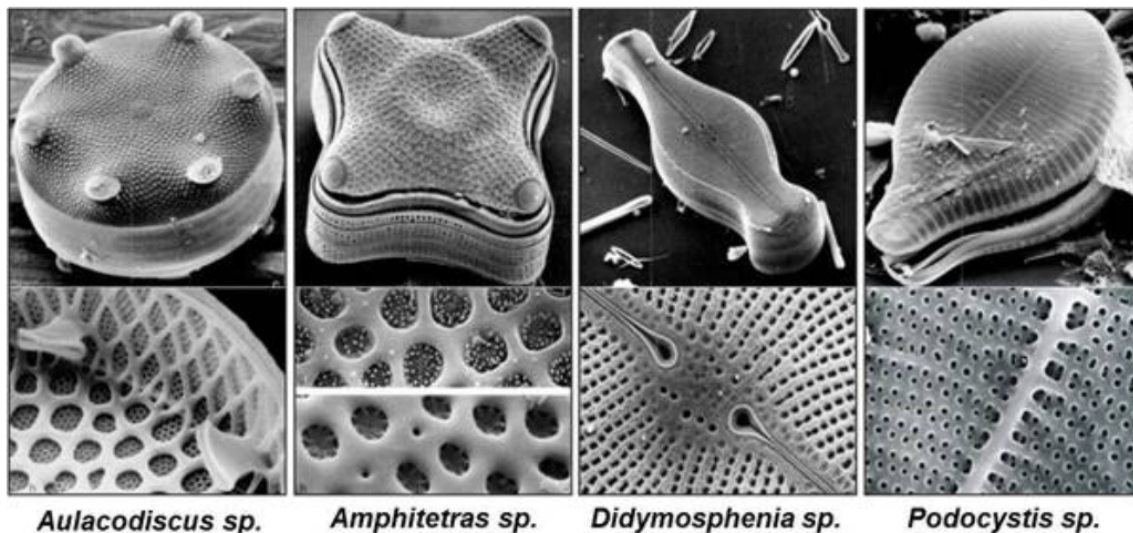


Figure 1.21: SEM images of the structure of four different diatom cell walls (top) and further detailing (bottom) showing the high order of structural control achievable by BCM. (Reproduced from R. F. E. Round, 1990.¹⁵²)

1.7.2 Biomimetics, Biokleptics, and Bioinspired Research

Through the process of natural selection, living organisms have evolved countless inventive processes and biomaterials from which it is possible to draw inspiration. Emulating biological forms and processes synthetically can lead to greater success than attempting to develop a system from scratch, as it has already evolved to function effectively in Nature.¹⁵³ There are several closely related fields of research dedicated to using biological organisms as a basis for research, each utilising the study of biology in subtly varying manners.

Biomimetics, also known as biomimicry, pertains to imitating designs that are observed in Nature. Designs forged in Nature have resulted in some of the most effective and unique materials. Examples of this span from observing the scales of butterfly wings to create iridescent fabric,¹⁵⁴ to forming adhesives based around the chemical composition of a mussels foot,¹⁵⁵ and designing artificial solar cells mimicking chlorophyll found in plant leaves.¹⁵⁶ These processes mimic the forms occurring in Nature by creating a synthetic alternative that does not contain the original biological components.

Biokleptics is the act of 'stealing' a biological component or reagent (e.g. enzymes,

proteins) to use in a non-biological environment to aid a synthetic process.¹⁵³ Biokleptics is often the first step of developing a biomimetic system, as it garners information on the biological mechanisms of the reagent. An example of a biokleptic system is the use of alkaline proteases from a strain of *Bacillus brevis*, which were found to exhibit compatibility with commercial detergents, and improve their efficiency at removing protein based staining.¹⁵⁷ This fits the definition of biokleptic, as the protein is taken directly from Nature and used in an artificial environment.

Taking inspiration from biology in the form of bioinspired research overlaps closely with biomimicry and is hence harder to define. Where biomimetics aims to directly imitate a product formed in Nature, bioinspired research is only influenced by biology and does not endeavour to entirely replicate the form or function of the subject from which it is drawing inspiration. By instead drawing inspiration from the process and key functionalities found to be effective in Nature, bioinspired research seeks to build upon our understanding of a process but modify it to fit our requirements. Biokleptics and biomimicry may both be considered as subcategories of bioinspiration, with a large degree of overlap between the fields.

By observing the forms of nanoparticles developed in Nature it becomes possible to study their formation and attempt to imitate the control observed in BCM processes using biomimetic and bioinspired design. Multiple approaches can be taken to this problem in the context of observing and analysing the proteins and mechanisms utilised *in vivo* to form nanoparticles with a comparable level of control. The two main approaches are either the biokleptic approach of extracting the proteins from their parent organism to use as additives, or the biomimetic approach of mimicking the protein functionality using synthetic biology (SynBio). A third approach is the use of molecules with similar chemical functionality as the binding sites in the native proteins, but without imitating the protein structure itself.

1.7.3 Magnetotactic Bacteria

Iron biominerals occur naturally in a diverse range of organisms, from bacteria to mammals across most phyla of life.¹⁵⁸ Over sixty different iron minerals alone have been observed in

Nature, granting a wide range of functionalities and purposes, making iron a truly essential element for life.

Many organisms have evolved the ability to utilise iron through the evolution of a range of proteins capable of transporting, precipitating, and co-ordinating iron ions.¹⁵⁹ Applications of iron in Nature include ferritin as iron storage proteins,¹⁶⁰ heme groups in both myoglobin and haemoglobin,¹⁶¹ and iron-containing enzymes crucial to photosynthesis.¹⁶² A remarkable type of prokaryote found worldwide, magnetotactic bacteria (MTB), are one of the oldest and simplest organisms capable of biomineralising iron oxide nanocrystals, utilising protein mounted linear chains of these crystals as navigational systems (Figure 1.22).¹⁶³

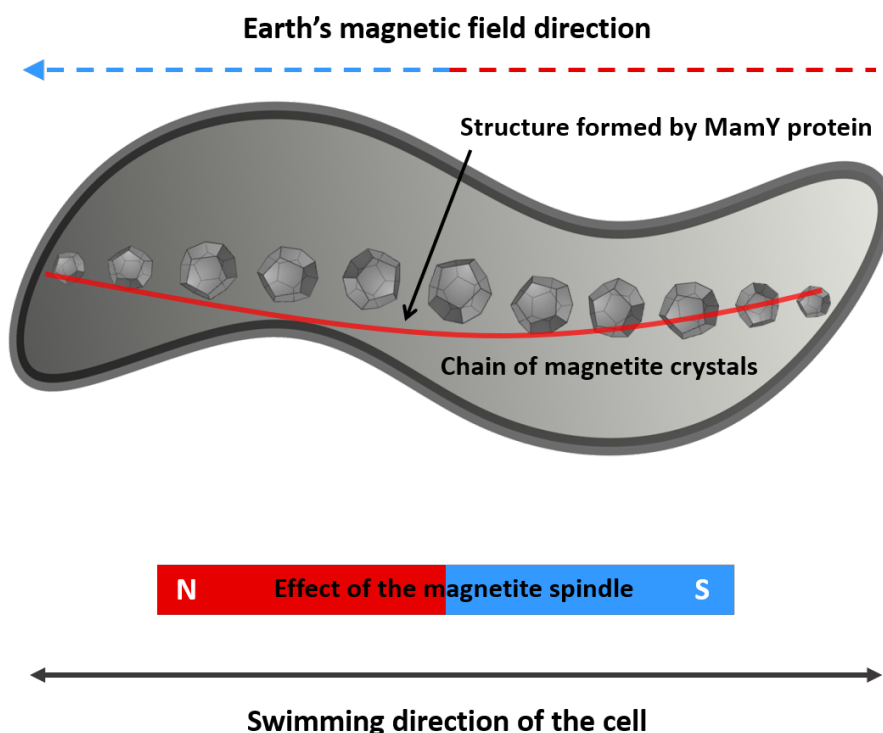


Figure 1.22: Schematic of magnetotactic bacteria (MTB) showing the effect of the Earth's magnetic field on the swimming direction of the cell. (Redrawn from image by Frank-Dietrich Müller.¹⁶⁴)

Magnetotactic bacteria are motile microorganisms that have the unique ability of migrating along geomagnetic field lines via a spindle of MNPs running along the cell of the bacterium.¹⁶⁵ The existence of these bacteria was first discovered in 1958,¹⁶⁶ when the phe-

nomenon of these magnetically moving bacteria was first observed by Salvatore Bellini and discussed in two unpublished papers. These bacteria were independently rediscovered at a later date by Richard Blakemore, who published his findings to the larger scientific community in 1975.¹⁶⁷ It was found that these bacteria did not react to external stimuli such as light, however swam rapidly in the same direction, each appearing to travel only in a straight line. Upon placement of a magnet nearby, the swimming direction of the cells were altered, leading to the revelation that each bacterium contained a chain of iron oxide nanocrystals.

While many organisms are capable of biomineralisation and the creation of intricate 3D (three-dimensional) structures,¹⁶⁸ MTB are believed to date back billions of years,¹⁶³ with fossilised magnetite chains and crystals being discovered in numerous terrestrial samples dating back millions of years, and Earth sediments up to two billions years old.^{169,170} Whilst MTB habituate globally, they thrive in highly specific conditions with higher concentrations of the bacterium found at the oxic-anoxic interface or the anoxic regions of sediments or water.¹⁷¹ This region, known as the oxic-anoxic transition zone (OATZ), forms as the result of opposing gradients of dissolved oxygen from above the water surface and sulphide from sediments at the bottom (Figure 1.23) wherein the oxygen levels are extremely low.¹⁶³

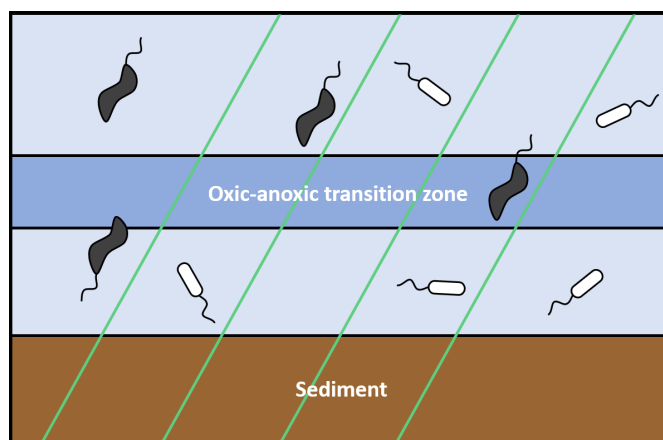


Figure 1.23: Schematic representation of magnetotaxis. In many aquatic environments, opposing redox gradients create an oxygen-poor oxic anoxic transition zone (OATZ). Magnetotactic bacteria (black) use the Earth's magnetic field (green lines) as guides to efficiently localise to the OATZ. Other organisms (white) must rely on a three-dimensional, and presumably slower, method for finding the same region. (Adapted from Komeili.¹⁶³)

MTB foster the interesting ability of synthesising high-quality MNPs, whilst exhibiting greater control than that usually achievable under synthetic lab conditions. The nanoparticles are formed inside a MTB specific organelle called a magnetosome, an internal lipid vesicle which acts as a nanoreactor, resulting in a nanoscale sized iron oxide crystal enveloped and bound to a membrane. These membrane-bound particles of iron minerals (Fe_3O_4 or Fe_3S_4) then line up in a chain via an internal dedicated cytoskeleton, allowing them to act as compass needles that direct the bacteria by applying torque to the surrounding bacterial tissue resulting in movement of the cell.¹⁵¹

1.7.3.1 Magnetosomes

Mature magnetosome crystals are typically 35-120 nm in size,¹⁷² mostly falling in the single-domain size range of magnetic nanoparticles.¹⁷³ This is an exhibition of biological optimisation of magnetisation of the particles, with the particles formed being highly homogeneous between members of the same species of bacteria.

Different strains of MTB result in different morphologies of particles, dependent on the biomineralisation proteins present which result in different biochemical and genetic control of the particles formed. Many nanoparticle shapes have been observed, from bullet shaped, to cubic, cubo-octahedral, and other elongated forms (Figure 1.24).

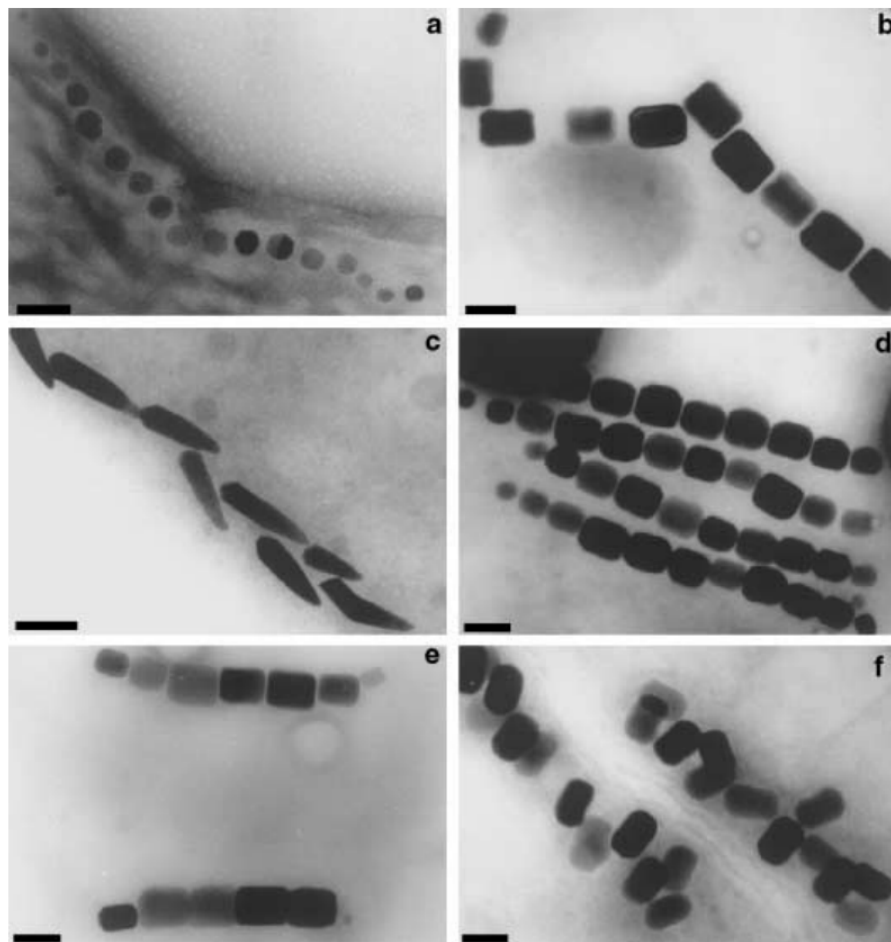


Figure 1.24: TEM images of crystal morphologies and intracellular organisation of magnetosomes found in various magnetotactic bacteria. Shapes of magnetic crystals include **a)** cubo-octahedral, **[b), d), e), f)]** elongated hexagonal prismatic, **c)** bullet-shaped morphologies. The particles are arranged in **[a), b), c)]** one, **e** two, **e)** multiple chains, or **f)** irregularly. The scale bar is equivalent to 100 nm. (Reproduced from Safariki et al.¹⁷⁴)

1.7.3.2 Magnetosome Formation

Whilst the mechanism of intracellular MNP formation and the role of macromolecules in this process is not yet fully understood, mechanisms have been proposed that fit our current understanding of MTB (Figure 1.25).

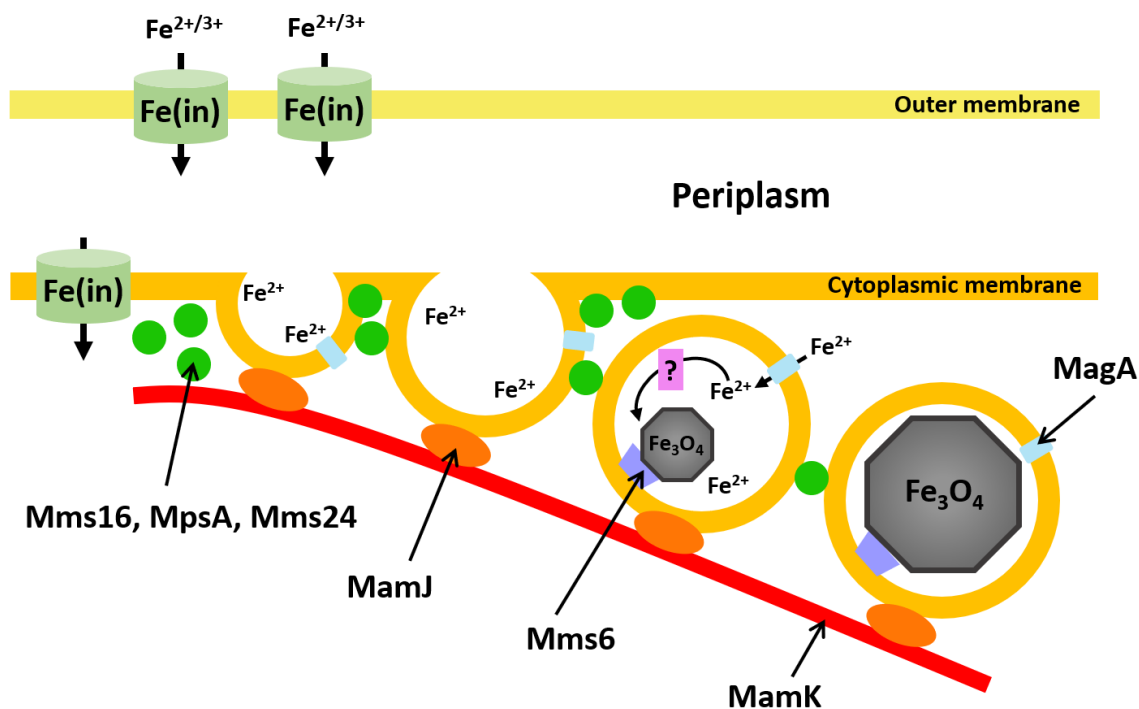


Figure 1.25: A schematic representation of the process carried out in magnetosomes for nanoparticle formation. (Redrawn from Yan et al.¹⁷⁵)

One such mechanism hypothesises that magnetite formation occurs in magnetosomes and is proposed to involve three major steps, beginning with the lipid vesicle forming from the invagination of the cytoplasmic membrane of the bacterium and the arrangement of the developed vesicles in a linear chain along cytoskeletal (MamK) filaments. Ferrous and ferric iron is uptaken through the periplasm via transport proteins and siderophores, a class of molecules which act as small high-affinity iron chelators,¹⁷⁶ wherein it is accumulated in the vesicles by transmembrane iron transporters. In the final step, tightly bound magnetosome membrane specific (Mms)/magnetosome associated membrane (Mam) proteins induce magnetite nucleation and regulate the morphology of the forming particles. The vesicle acts as a size limiter during the formation of the nanoparticle, guiding the crystal growth in a controlled manner. Many proteins play crucial roles in the build-up of ferrous and ferric iron, the nucleation of the magnetosomes, and keeping reductive conditions to prevent cell damage.

It has been shown that magnetosome formation is highly sensitive to environmental

conditions, with external factors such as oxygen and iron concentration also having an important influence, as well as the expected biological and genetic control. The cultivation of MTB is challenging due to the highly specific growth conditions required, making the use of them for industrial nanoparticle production unfeasible for cost and environmental reasons.

1.7.4 Key Biomineralisation Proteins

Biomineralisation is facilitated by a complex suite of proteins, with many proteins influencing the formation of highly defined magnetosomes, as shown in Figure 1.25.¹⁷⁵ In this section two of the key proteins responsible for the nucleation and shape control of magnetosomes will be discussed in detail.

1.7.4.1 Mms6

Magnetosome membrane specific6 (Mms6) is a small (6 kDa) acidic protein (isoelectric point of the binding region = 4.2)¹³⁷ found tightly associated with the magnetosome membrane, and is considered one of the most important biomineralisation proteins present in MTB for the function of controlling magnetosome morphology.¹⁷⁷ Biomineralisation proteins are found localised to magnetosomes and tightly bind magnetite crystals, therefore suggesting a key role in the BCM process. Mms6 however has been successfully isolated and used *in vitro* to control particle formation reactions, with a marked positive effect on the particles formed compared to protein free reactions (an increase in size and incidence of cubo-octahedral morphology).^{137,178}

To understand the function of Mms6, its structure has been carefully considered from the truncated amino acid sequence from *Magnetospirillum magneticum* (AMB-1) in Figure 1.26. It is found to exhibit a net negative charge at neutral pH, which contrasts with all other magnetosome membrane proteins recovered so far.¹³⁷

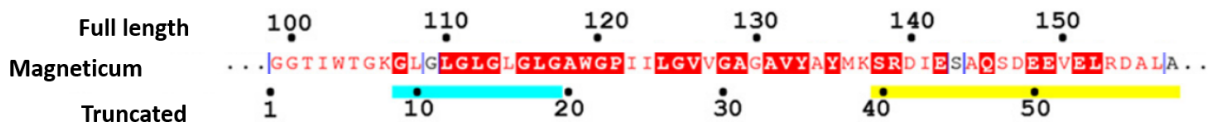


Figure 1.26: Amino acid sequence alignment of truncated Mms6 from AMB-1. Cyan bar highlights the glycine-leucine repeat sequence, and the yellow bar highlights the hydrophilic region. (Reproduced from Rawlings et al.¹³⁷)

The presence of both a hydrophobic N-terminal comprised of multiple repeat leucine and glycine units and a highly acidic C-terminal imparts amphiphilic character onto the protein. Mms6 has been shown to form micelles of 10.2 ± 3 nm size in aqueous solution,¹⁷⁹ with the addition of iron leading to the formation of higher-order structures (Figure 1.27a). From the similar effect of the presence of Mms6 on particle formation *in vivo* and *in vitro*, it can be postulated that self-assembly must be occurring in some form in the magnetosome membrane.¹⁷⁹

It is proposed that Mms6 self-assembles in the magnetosome membrane to form a protein raft which displays the negatively charged C-terminal region, similar to the micelles formed *in vitro* but with reversed curvature (Figure 1.27b). Mms6 shows negligible activity at acidic pHs, however upon deprotonation forms 10-12 nm sized negatively charged Mms6 micelles which can bind ferric and ferrous iron.^{178,137} It has been proposed that the highly acidic C-terminus aids precipitation of magnetite via the concentration of ferric and ferrous iron on the surface of Mms6 micelles in the stoichiometric 2:1 ratio found in magnetite.¹⁷⁸

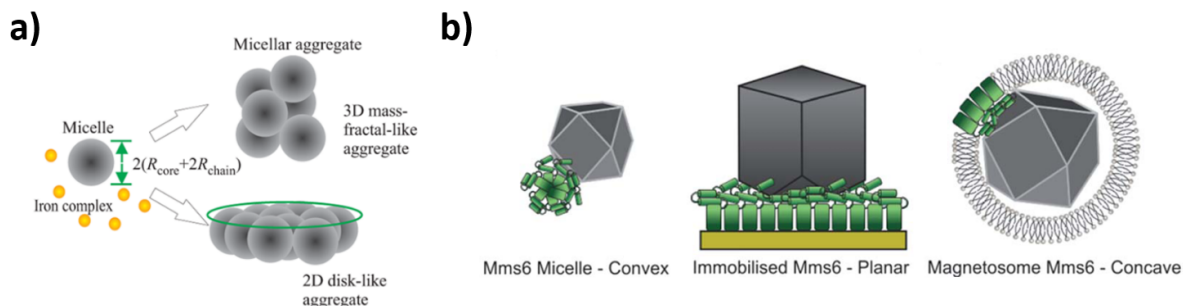


Figure 1.27: a) The micellar structure and aggregates formed in the presence of iron,¹²³ b) the assembly of Mms6 under varying conditions (N-terminal region of Mms6 represented by a green rectangle, and the Fe binding C-terminal region by two green cylinders). (Reproduced from Rawlings et al.^{137,123})

A modified C-terminal peptide (C20Mms6) consisting of the 20 amino acid chain closest to the C-terminal, removing the N-terminal and the leucine-glycine repeat sequence has been found not to nucleate and control magnetite formation.¹⁷⁸ This suggests the glycine-leucine repeat sequence appears to be key to self-assembly, with the knob and hole arrangement of these hydrophobic residues potentially interlocking Mms6 sub-units together into a 3D structure. This would result in the distribution of the iron nucleating C-terminals across an Mms6 surface. As such, it has been determined that Mms6 can regulate both the nucleation and growth direction of the particles formed along preferred crystal faces.¹²³

1.7.4.2 MmsF

A second magnetosome membrane protein, MmsF, has recently been found to play a dominant role in the regulation of magnetite biomineralisation.¹⁸⁰ It was observed in a gene deletion study of an AMB-1 mutant that when eight genes (including *mms6*) were removed severe biomineralisation defects producing small and misshapen magnetosome crystals resulted.¹⁸¹ However, once the gene for MmsF was reintroduced it was found to be sufficient for restoring the magnetite biosynthesis without the presence of Mms6 or other biomineralisation candidates.¹⁸⁰

Whilst the function itself of MmsF in biomineralisation is not yet fully understood, the results presented thus far are indicative that the activity of MmsF is likely required during the

maturation of the magnetite crystal, and after the initial nucleation of the particle. MmsF consists of three transmembrane spanning helices (TMS) with green fluorescent protein tagging experiments suggesting the C-terminus projects into the magnetosome and the N-terminus into the bacterial cytoplasm (Figure 1.28).¹⁸²

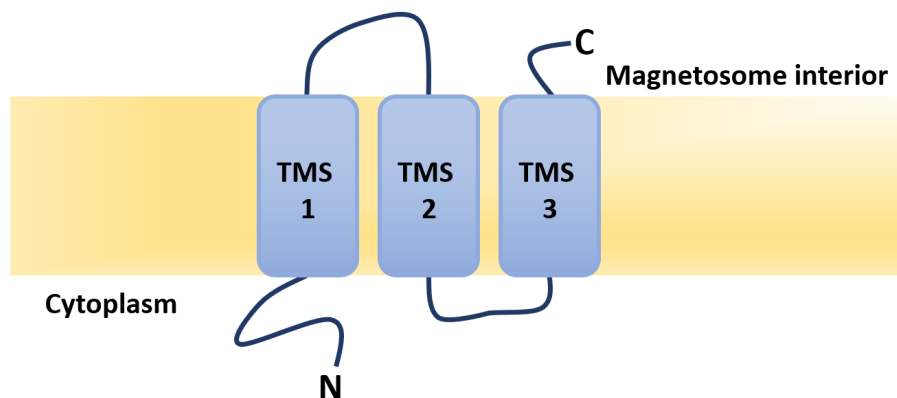


Figure 1.28: Topology diagram of MmsF spanning the magnetosome membrane. (Reproduced from Rawlings et al.¹⁸²)

The loop projecting into the magnetosome interior connecting TMS region 1 and 2 is believed to govern the biomineralisation properties of MmsF. The loop is rich in amino acids with acidic side chains which are thought to operate similarly to the acidic residues found in Mms6, and interact with the iron ions in solution and the growing magnetite crystal facets to direct crystal growth.¹⁸² This once more highlights the necessity of charged residues in magnetosome development. It is speculated that MmsF self-assembles within the magnetosome membrane, tightly packing, and creating regions with the magnetosome where the active loops are displayed in a specific manner to interact with a maturing magnetosome crystal.¹⁸² This loop has been noted to be conserved between MmsF and two homologous proteins, further indicating the importance of this protein loop.¹⁸²

1.7.5 Magnetite Interacting Adhirons

Aside from native biomineralisation proteins, another type of protein which shows effective interactions in the formation of MNPs are Adhirons, commercially known as affirmers. Adhirons are a robust class of small peptide displaying scaffold proteins, comprised of a compact

low molecular weight body based on a cystatin consensus sequence (an amino acid sequence in which each amino acid selected is the most common found at that position in similar naturally occurring protein motifs), displaying exceptional thermal stability. Consensus sequences follow the logic that if an amino acid is conserved between variations of a protein, that amino acid is likely to contribute to the proteins stability.¹⁸³ It exhibits two variable peptide loops capable of displaying nine amino acids each.¹⁸⁴ The utilisation of biopanning with Adhiron has been used to determine the binding sequences most attuned to cubic magnetite.

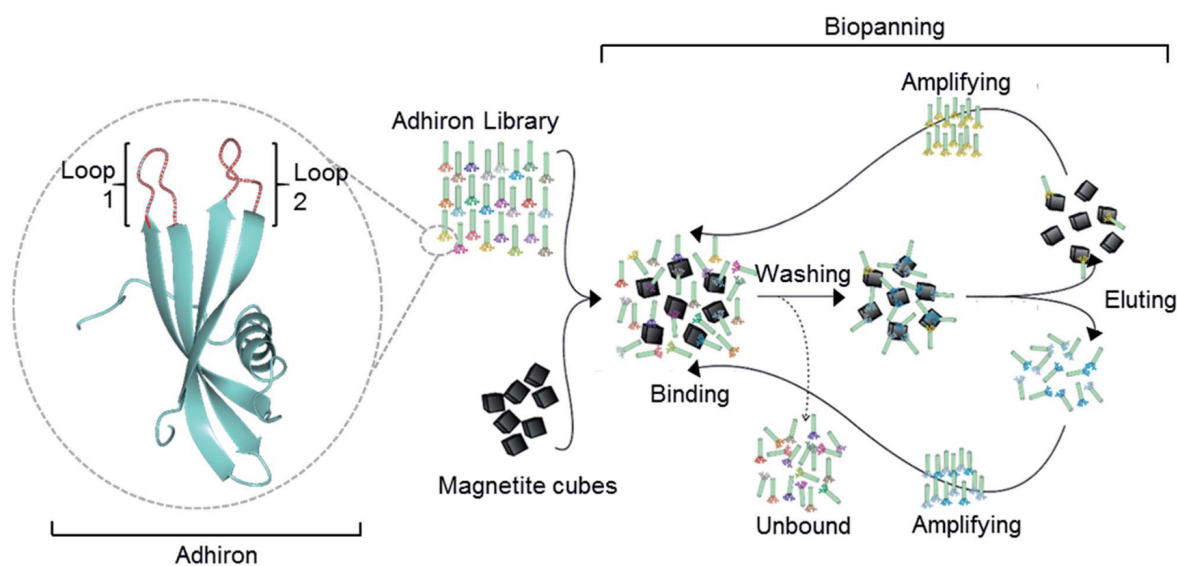


Figure 1.29: Schematic of the magnetite interacting Adhiron (MIA) selection process. The structure of an Adhiron is shown in turquoise, with the two variable binding loops shown in red. (Reproduced from Rawlings et al.¹²³)

The biopanning process (Figure 1.29) is the process of using a combinatorial peptide library to screen for affinity to a given target, in this case cubic magnetite. A large Adhiron library of 1.3×10^{10} varying sequences was exposed to the MNPs, through three sequential rounds of peptide binding, substrate washing, peptide elution, and sequence amplification to ascertain the strongest magnetite binding proteins.¹²³

DNA sequencing revealed that the Adhiron loops were enriched in basic residues, with a 26.4% predominance of lysine and 9.3% of histidine in loop 1, with almost no incidence of

acidic amino acids. Loop 1 was determined to be the primary magnetite interacting loop, due to the fact that many of the enriched sequences contained only the first binding loop after amplification.¹²³ As these proteins are playing no role in the nucleation of magnetite, instead acting to specifically bind the [100] face of magnetite, it follows that minimal acidic amino acids are present.

This was further corroborated by simulated adsorption of amino acids on the [100] surface of magnetite (Figure 1.30) shown in Table 3, displaying that the adsorption energy of both lysine and arginine were significantly higher than that of glutamic or aspartic acid (Figure 1.30).¹²³ This suggests the strong role of basic residues in controlling the shape of particles formed, as binding to a surface slows the growth of that surface, as discussed in section 1.5. The use of MIA proteins as additives is further detailed in section 1.8.5.

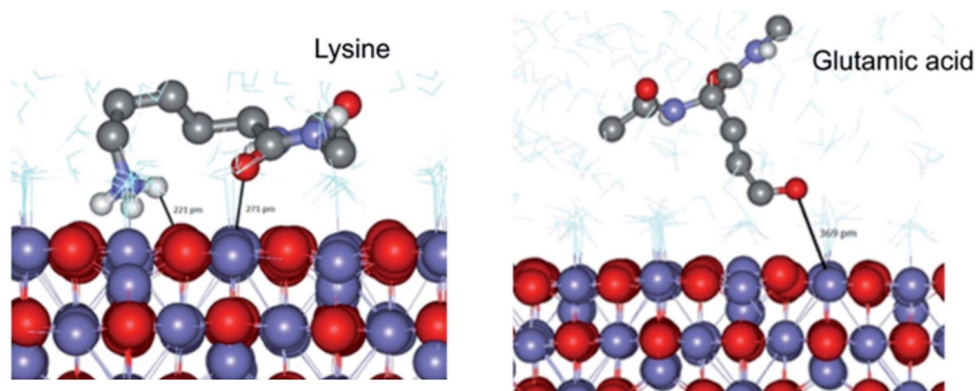


Figure 1.30: Simulated adsorption of amino acids on a magnetite [100] surface. A snapshot from the MD simulation of capped-lysine on the left and capped-glutamic acid on the right, on the [100] surface of magnetite. Hydrogen atoms bonded to carbon have been removed for clarity. (Reproduced from Rawlings et al.¹²³)

Table 1.3: Comparison of simulated amino acid to [100] magnetite adsorption energy.
(Table values taken from Rawlings et al.¹²³)

Amino acid	Adsorption energy (kJ mol ⁻¹)
Lysine (K)	-52
Arginine (R)	-45
Leucine (L)	-31
Glutamic acid (G)	-3
Aspartic acid (D)	2

1.8 The Role of ‘Additives’

In literature, many terms are used to describe a compound which can be added to a reaction to improve the properties of the materials synthesised. Additives,¹⁸⁵ control agents,¹⁸⁶ modifiers,²⁵ stabilising agents,⁷⁴ surfactants,¹⁴⁶ ligands,¹⁸⁷ and capping agents¹⁸⁸ are all terms used to describe various additions to the synthesis mixture which are not required for the reaction to take place, but can impact the final product.

During the nucleation period of crystal growth, macromolecules and other compounds can interact with ferrous and ferric iron, self-assemble to provide a surface on which magnetite can nucleate, or bind to the forming surfaces of magnetite, altering the reaction products. The presence of additives in the starting solutions affect the magnetite formation processes and have been shown to have significant impacts on the final nanomaterial products formed. An additive may inhibit growth and nucleation, or promote them.¹⁸⁹ Additives may also regulate the formation of imperfections within a crystal structure, and in some cases alter the chemical and physical properties of ion solutions as well as crystals and their aggregates, with the largest current industrial application of additives seen in the reduction of scale formation in industrial processes via the addition of low molecular weight phosphonates or polymeric carboxylates.^{190,191}

The ability to influence the crystal nucleation and growth events detailed in the LaMer mechanism open the door to the ability to produce tailored nanomaterials. Through face-

specific adsorption, macromolecules and other additives interact with crystalline materials such as forming magnetite particles and modify the resultant products. This face specificity is a result of ‘lattice matching’ where the charged functionalities of an additive may align with charged surfaces of an inorganic crystal via electrostatic forces or hydrogen bonds in a more energetically favourable manner (i.e. improved alignment with a cubic [100] face than an octahedral [111] face).¹⁹² Molecular modelling, also known as molecular dynamics (MD), studies into these systems are typically simplistic models of *in vacuo* additive adsorption at a flat crystal surface. Nonetheless, these studies have typically shown positive correlation with experimental results, allowing them to provide valuable insight into crystal development and growth.^{193,194} The effect of the growth rate of different crystallographic planes on the final morphology of a nanoparticle can be seen in Figure 1.31.

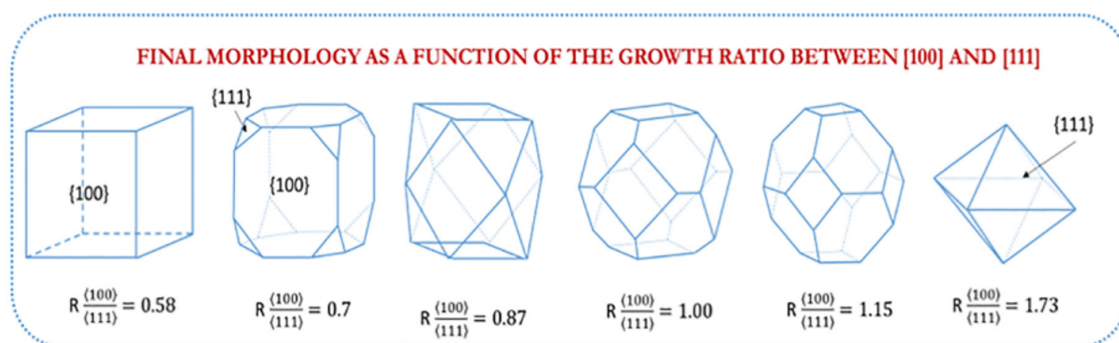


Figure 1.31: Final morphology of a nanoparticle as a function of R (ratio between the growth rate along the [100] and [111] crystal planes). (Reproduced from Roca et al.¹⁹⁵)

Further understanding of crystallisation has led to the knowledge that crystal growth can occur via the accretion of smaller crystals (primary particles) with either similar crystallinity through oriented attachment, or amorphous precursors.¹⁹⁶ Additive coating on a crystal surface can promote this aggregation, depending on both additive adsorption, and additive-additive interactions.¹⁸⁹ If additive concentration is high the surface coverage of a growing crystal will also be high, which can inhibit further crystal growth.¹⁸⁹ Larger additives such as macromolecules present the additional issue of incorporation into growing crystals, occurring when the growing crystal effectively grows over an adsorbed macromolecule. This can lead to reduced crystallinity and worsen the properties of a material.

While great success has been seen in producing highly tailored MNPs under environmentally unfriendly reaction conditions, primarily with the addition of oleic acid and oleylamine additives,^{197,198,199,126,200} these additives are insoluble in water and thus are unsuitable for RTCP. As such, this section will focus on additives that exhibit applicability or future scope in water based syntheses.

1.8.1 Proteins, Peptides, and Bio-Molecule Based Additives

The interactions of biomolecules with inorganic materials at the molecular level are commonplace in Nature, as discussed earlier. Both Mms6 and MmsF have been used in RTCP reactions as additives, yielding higher quality particles of increased homogeneity and size in comparison to particles formed without the presence of these proteins, as shown in Figure 1.32.

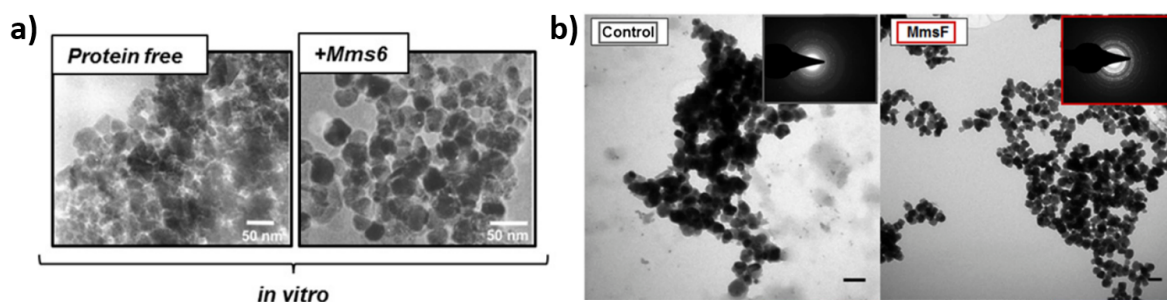


Figure 1.32: Comparison of protein-free control particles and MNPs formed with **a)** Mms6 as an additive,¹⁷⁸ **b)** MmsF as an additive.¹⁸² (Reproduced from Rawlings et al.^{178,182})

A third biomineralisation protein, MamC, has been shown to influence the size of magnetite particles formed *in vitro* by locally enhancing the supersaturation of iron and promoting the formation of magnetite.²⁰¹ Using a biomimetic co-precipitation reaction showed the presence of MamC resulted in larger ($\sim 33 \pm 11$ nm) highly faceted crystals forming compared to smaller ($\sim 19 \pm 11$ nm) particles formed in a control reaction (Figure 1.33).²⁰¹

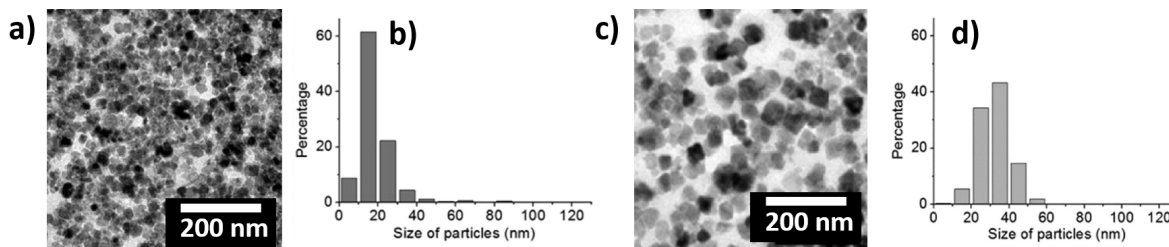


Figure 1.33: Comparison of **a)** protein-free control particles and **b)** control particles size distribution, and **c)** particles formed with the addition of MamC and **d)** MamC particles size distribution. (Reproduced from Lopez-Moreno et al.²⁰¹)

Two co-polypeptide libraries were designed and synthesised consisting of one containing aspartic acid and serine, and the other glutamic acid, lysine, and alanine monomeric units, with each polypeptide being of equal length and exhibiting a random monomer sequence with varying hydrophobicity and charge.^{202,186} The size, shape, and therefore magnetic properties of the crystal could be systematically regulated via variation of the aspartic or glutamic acid content of the polypeptides. Acidic functionalities acted to regulate the nucleation of magnetite via controlling the pH at which the ferric precursor converts to magnetite. When higher concentrations of poly-L-glutamic acid and poly-L-aspartic acid were present in the co-polypeptides, a higher number of rounded and less defined crystals were observed, suggesting that aspecific binding of the carboxylate groups to Fe ions at the crystal surface inhibited faceted growth.¹⁵¹

Artificial peptide cages capable of self-assembly to act as space constrained nanoreactors for magnetite are being investigated further, with the end goal of utilising peptide assemblies to template MNP synthesis.²⁰³

The inherent disadvantage of many biomolecules lies in both the high labour and time costs of production, and their poor stability and solubility compared to simpler compounds. For these compounds to be suitable in industrial manufacture they must be easy to produce, stable, and cost-effective. Due to the highly specific conditions required for MTB to thrive and grow effectively (precise O₂ and N₂ requirements), the difficulty in isolating and purifying specific proteins, and the relatively low yield of protein garnered from the bacteria, these proteins are unsuitable for larger scale work. Therefore, despite their positive impact on

the properties of particles formed with the presence of bio additives, they are unfeasible for industrial scale manufacture of nanoparticles.

1.8.2 Carboxyl and Hydroxyl Based Additives

When considering the mechanism by which Mms6 and MmsF interact with magnetite via highly acidic charged regions, it follows that additives presenting carboxyl and hydroxyl may influence MNP nucleation. Some compounds such as citric acid and ethylenediaminetetraacetic acid (EDTA) are known for their ability to sequester iron ions.^{204,205} The presence of multiple acidic functionalities with a high affinity for iron cations allows these compounds to act as chelators, which can form two or more bonds with a metal ion.

When considering the manner by which Mms6 and MmsF nucleate and control magnetosome formation via highly acidic charged regions in their amino acid sequence, it follows that additives presenting carboxyl and hydroxyl functionalities may influence MNP nucleation. In a literature example using RTCP, citrate ions (Figure 1.34) were added to the iron solution prior to heating for particle growth, and found to decrease the average size of particles formed from 10.5 to 4.4 nm.²⁰⁶ Size control has been exhibited in maghemite particles by tuning the molar ratio of citrate to iron, with particle sizes varying between 2 and 8 nm being formed.²⁰⁷

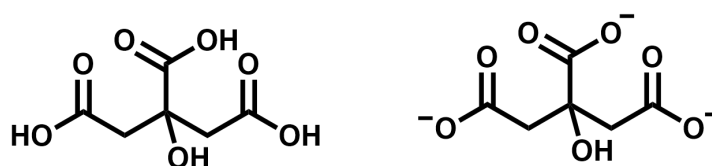


Figure 1.34: Chemical structure of citric acid (left) and a citrate ion (right).

It has been hypothesised that this effect may be due to the charged carboxyl groups of citric acid binding to multiple iron ions creating a region of high iron concentration and acting as a point of nucleation from which nanoparticles can further grow. This leads to an increased number of nucleations, resulting in more particles of smaller size being produced. Other nucleators shown to influence the size of magnetite particles include oxalic acid, and

hydroxyl-containing diethylene glycol which was observed to decrease both the crystallite size (10nm \rightarrow 5 nm) and overall particle size (50 nm \rightarrow 20 nm).²⁰⁸

Contrary to these results was the use of tris(hydroxymethyl)aminomethane (Tris) as an additive which was found to inhibit the nucleation of magnetite.¹⁸⁵ This was postulated to be due to two molecules of Tris being capable of complexing with an iron ion (Figure 1.35a), which promoted oxidation of ferrous iron within the complex, leading to the formation of needle like akaganeite particles (Figure 1.35b). This suggests that consideration must be made to the iron ion-organic molecule complex forming in the reaction mixture.

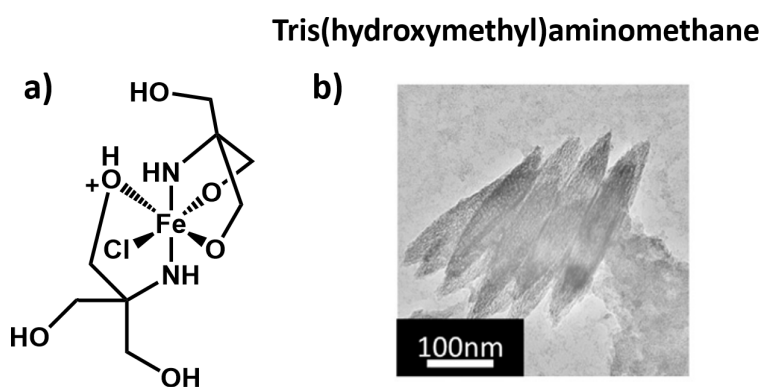


Figure 1.35: a) Complex formed between iron and Tris, b) TEM of particles formed with 4% by mass addition of Tris. (Reproduced from Kuwahara et al.¹⁸⁵)

Plant leaf extracts have been utilised as additives in an endeavour to develop green syntheses that do not require environmentally harmful chemicals.²⁰⁹ Many plants have shown an affinity for sequestering heavy metal ions, with plant extracts containing many compounds with polysaccharide,²¹⁰ carboxyl,²¹¹ and hydroxyl²¹² functionalities capable of acting as both nucleators and capping agents on the formation of nanoparticles. These extracts however are comprised of many compounds, and the active molecules/moieties are not identified in the literature.

1.8.3 Templating Additives

Magnetosomes control the size of the particles they template via physical limitation of the particle within a vesicle. Some additives have been seen to control particle formation in a

similar manner, whether within layers, or nano-reactors, in a principle similar to microemulsion synthesis.

A slightly more unusual additive detailed in literature is a form of naturally occurring clay, montmorillonite. Capable of templating particles in a co-precipitation synthesis, MNPs are nucleated between the layers of clay, which act as limiters to the size of particle formed (Figure 1.36).²¹³ The limited space between the layers, combined with the regular repeat structure between layers of clay allowed particles to form in set sizes due to physical size constraint, exhibiting an increased degree of control over particles formed with no additive. As montmorillonite is insoluble, it acts as a mould for the particle to grow within and fill.

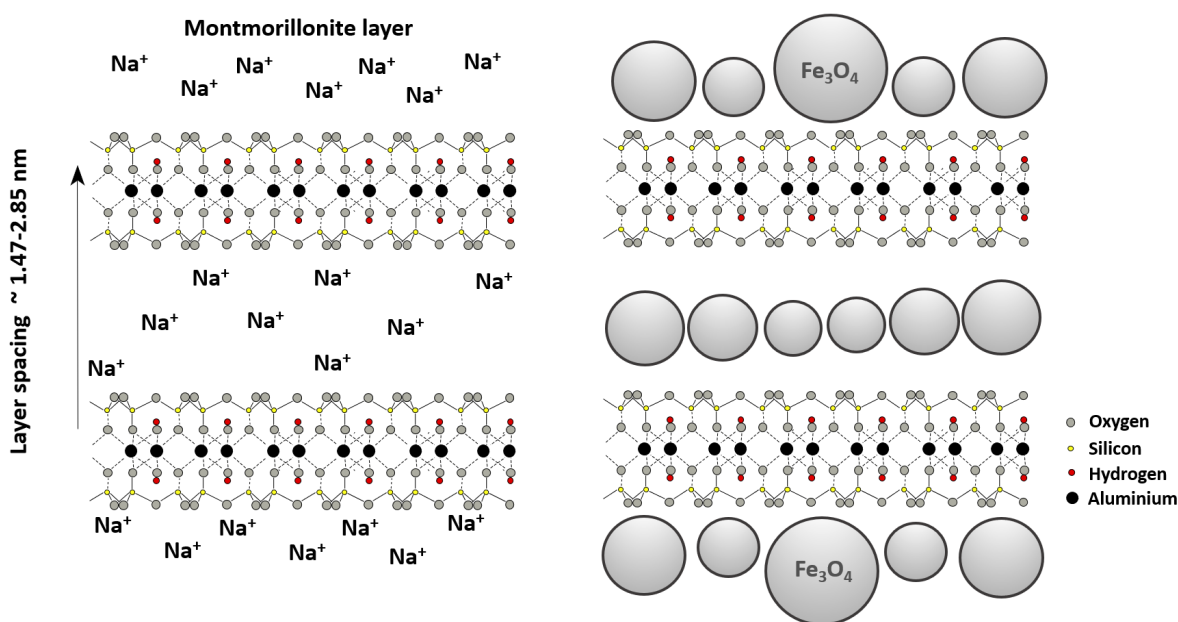


Figure 1.36: Schematic illustration of synthesised magnetite nanoparticles in the inter-layer space of montmorillonite via chemical co-precipitation. (Adapted from Li et al.²¹³, montmorillonite structure adapted from public domain image by Andreas Trepte.²¹⁴)

Heparin, a naturally occurring glycosaminoglycan (or mucopolysaccharide), has also been used to regulate particle growth in RTCP reactions via a templating effect. The regular repeating structure (Figure 1.37) featuring a negatively charged backbone, strong biocompatibility, and ability to reduce particle agglomeration making heparin highly suitable as a MNP stabilising reagent for biomedical applications.²¹⁵

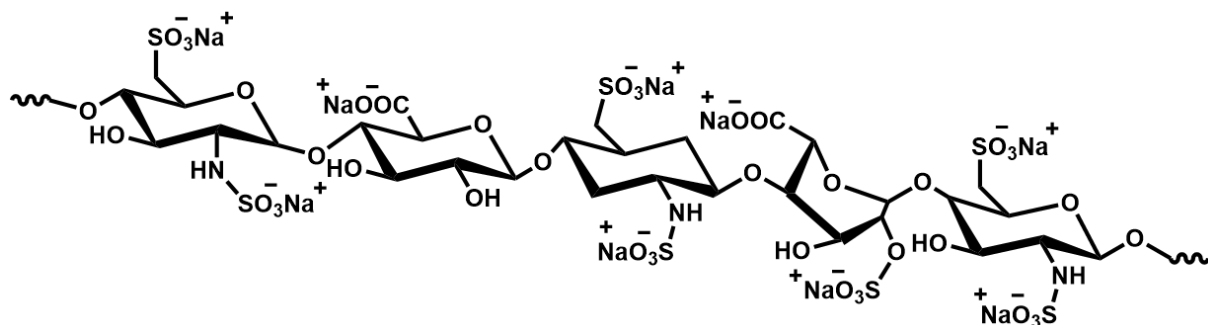


Figure 1.37: Chemical structure of heparin-sulphate.

The particles formed with the addition of heparin as an additive exhibited both a tight size distribution, and reduced agglomeration due to the polymers ability to stabilise the surface of the particles in water.²¹⁵ Particle sizes reduced from 8.9 ± 2.5 nm with no heparin present to 6.7 ± 1.1 nm at a 100:1 iron to additive ratio.²¹⁵

1.8.4 Surfactants as Additives

A class of additives which has found success in influencing the formation of MNPs are surfactants, which function by stabilising the surface of the particle in either water or organic medium depending on the surfactant used. The amphiphilic structure of surfactants consisting of a charged head and a long hydrocarbon chain allows this structure to manipulate the size of particles formed in several manners depending on the type of surfactant. The long hydrocarbon chain present in surfactants sterically hinder particles, restricting their growth. Anionically charged surfactants complex with ferrous iron, preventing the close contact of MNPs via ionic repulsion. While cationic surfactants are incapable of forming complexes with ferrous iron they still adsorb onto magnetite, preventing the agglomeration of MNPs.²¹⁶ The presence of these surface stabilising molecules prevent agglomeration and allow for size control of particles formed.⁹⁸

A study using the surfactants stearic acid, N-Cetyl-N,N,N-trimethylammonium bromide (CTAB), Triton X-100 (a non ionic surfactant), sodium dodecylsulphate (SDS) (Figure 1.38) as additives in a heated reaction were found to decrease particle size from 57.2 ± 74.9 nm to < 44 nm and produce narrower standard deviations (SD) of < 18 nm, showcasing

the effectiveness of surfactants in size control.²¹⁶ Interestingly, Triton X-100 is still able to influence the size of particles formed via dipole-ion interactions with magnetite.²¹⁶

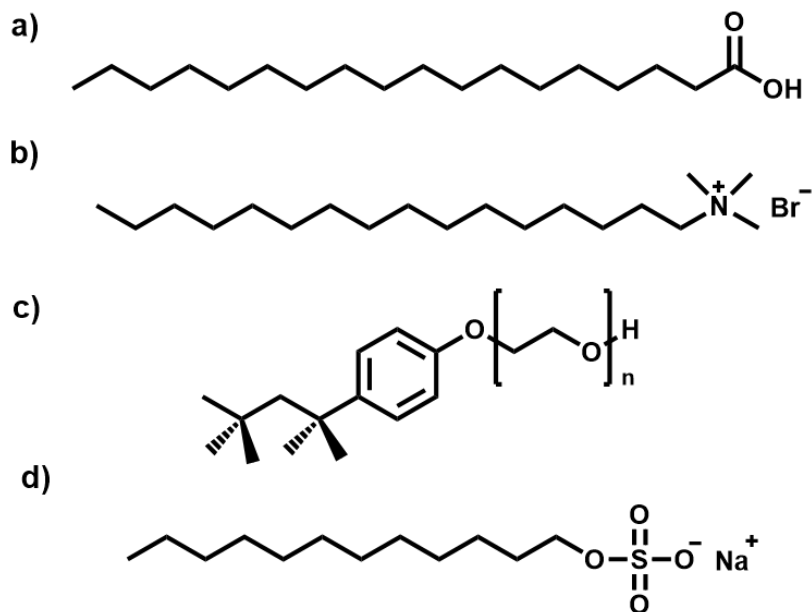


Figure 1.38: Chemical structures of **a)** stearic acid, **b)** CTAB, **c)** Triton X-100, **d)** SDS.

Polyethylene glycol (PEG) is a synthetic polymer frequently used for the surface modification of magnetite particles.^{25,100,217,218} Particles synthesised with PEG in situ were highly effective at improving the colloidal stability of MNPs in a basic solution (pH = 10) for up to 21 days of stability. The morphology of these particles also changed with an increasing proportion of PEG, with the crystallite size decreasing from 13.6 nm to 9.3 nm at the highest concentration of PEG.²¹⁹

1.8.5 Amine Based Additives

Further expanding on the biopanning work conducted by Rawlings et al, magnetite interacting Adhirons (MIAs) were successfully used as additives (Figure 1.39). The biopanning process selected for binding loops with an affinity for cubic magnetite faces, with DNA sequencing revealing a preference for basic residues in the strongest cubic face binders. The sequence of these MIAs can be seen in Table 1.4.

Table 1.4: Binding loops sequences of selected Adhirons. (Taken from Rawlings et al.¹²³)

Adhiron	Loop1	Loop2	Protein pI ^a
MIA-1	QKFVPKSTN	PKKSKIELK	9.6
MIA-2	IKKKKKYKY	ETLTHKVIR	9.7
Control	DWWEAGVFM	WNEINYMFD	5.5

* Letters in Loop1 and Loop2 refer to standard amino acid codes. The prevalence of basic amino acids is exhibited through the excess of K (lysine) residues.

It followed on from this that the MIA proteins would influence particle formation to favour the presence of the [100] crystal face, which was experimentally observed. HRTEM confirmed the presence of the [400] cubic crystal plane. An ideal concentration was observed for the addition of the MIA additive, which was calculated to be roughly consistent with the formation of a mono-layer of protein. Too little additive resulted in particles comparable to the control with no additive present, whereas too much protein resulted in rough particles, speculated to be due to the sensitivity of iron oxide precipitation reactions to changes in reaction conditions.¹²³

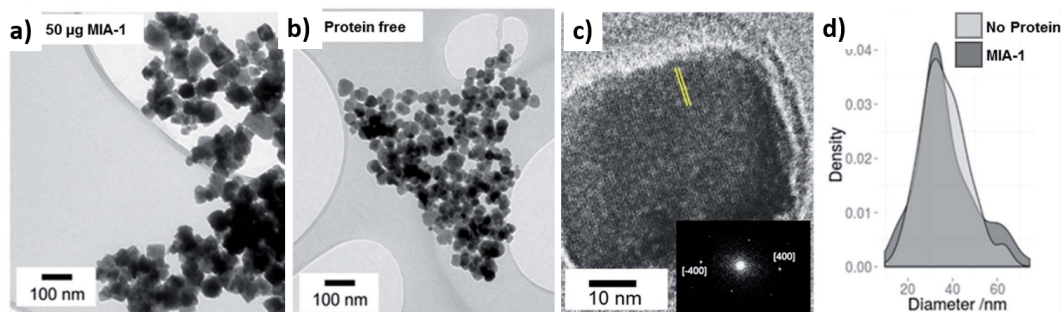


Figure 1.39: TEM analysis of magnetite nanoparticles. **a)** Particles prepared with MIA-1 at 50 mg per 10 ml reaction. **b)** Particles prepared in the absence of MIA-1. **c)** HRTEM analysis of a representative MIA-1 prepared MNP. A region of the lattice fringe is highlighted with yellow lines and the Fourier transform is shown inset with the [400] peaks identified. **d)** Particle size analysis of MNPs prepared with and without addition of MIA-1. (Reproduced from Rawlings et al.¹²³)

Ethylenediamine (EDA) has been used in a hydrothermal synthesis as an additive to produce

magnetite nanowires.¹²² The N-chelation behaviour of EDA makes it a strong donor ligand, and it is speculated that EDA forms complexes with ferrous iron, lowering the concentration of free Fe^{3+} in solution, lowering reaction rate and favouring the growth of nanowires.²²⁰

1.8.6 Summary of Additives

From the examples throughout this section it can be seen many additives have been found thus far that promote or inhibit particle nucleation and growth. The field of additive controlled magnetite synthesis has much room for expansion, with the need to discover effective additives to further enable green scalable synthesis becoming a key issue in this field. Many additives which have been observed to greatly influence higher temperature reactions may not retain their effect in RTCP syntheses, or may simply be too cost ineffective to produce on a significant scale such as in the case of many bioadditives. A table summarising the effect of the additives discussed can be seen below .

Table 1.5: Summary table of additives types and their effects on particles formed.

Additive class	Active functionality	Effect	Mode of action
Proteins + peptides	Varies	Varies	Mms6 + MmsF: Nucleation Magnetosomes: Size control
Carboxyl + hydroxyl	-COOH	Size control	Nucleation
	-OH	Surface stabilisation	Surface interactions
Templating	Varies	Size control	Mould for growth
Surfactants	Charged head	Size control	Steric hinderance
	Aliphatic tail	Surface Stabilisation	Surface interactions
Amines	-NH ₂	Shape control	Adsorption onto growing magnetite surface

1.9 Production Systems for Magnetite Synthesis and Scale-Up

For MNPs to successfully see further use in industry, it is important to be able to produce large quantities of particles. As well as considering the methodology used for forming these MNPs (RTCP, thermal decomposition, etc.) and the compounds that can aid the reaction, it is also imperative to consider the future scalability of the synthesis method. When making design considerations, manufacturing is typically achieved in either a batch or continuous flow manner. Both these techniques offer advantages and disadvantages which must be carefully considered.

1.9.1 Batch and Continuous Processes

A batch process is one that involves processing the reagents in batches through each step of the manufacturing process, with synthesis being fully completed at each step before carrying the batch of material through to the next. Batch processing can be preferable for smaller quantities of material where production is not needed all the time, and often utilises simpler, widely available equipment. These processes tend to be further developed in industry due to high monetary and research investment into these plant systems.²²¹ Batch processes, however, have limitations that can complicate large scale industrial scale-up (temperature control and profiles, mixing, reproducibility). Mixing is often a source of inconsistency in batch set-ups, with complicated mixing regimes not often being considered on the laboratory-scale.²²²

Continuous flow processes can run for 24 hours a day with fewer workers and a higher rate of production compared to a batch process. Whilst the initial cost of equipment tends to be higher for specialised continuous manufacturing processes, their operational costs are lower, lending continuous flow processes to being a promising synthetic procedure for scale-up.²²³ Continuous manufacturing processes offer the advantages of higher consistency and reproducibility compared to batch methods, however often require specialised set-ups including highly developed process monitoring and control strategies. As such, the financial

and time costs of large-scale flow processes may offset the benefits in some cases.²²² A hurdle that can arise for industrial manufacture is the difficulty in changing a synthetic process once it has been established. As most established processes are batch, this is an additional obstacle to overcome for flow processes to become commonplace.

1.9.2 Magnetite Scale-Up

Magnetite is used extensively in several industries, and as such the future scalability of reaction is a key factor to be considered. The reduction of an iron pre-cursor solution is currently the favoured method for scale-up due to the greater control exerted over reaction products. Co-precipitation has been successfully used to scale-up both titanium oxide nanoparticles at a low temperature,²²⁴ and MNPs with heating.²²⁵ A waste reduction algorithm conducted on a theoretical scaled-up magnetite co-precipitation process established that the process is not environmentally harmful.²²⁶ As such, co-precipitation is a promising avenue for the green scale-up of MNPs if the products can be further controlled without the use of heating.^{83,227} Our primary research focus for feasibly scaling the RTCP process is improving the space-time-yield (STY), the amount of tailored nanomaterials produced in a given time (24 hours) by looking at various production systems with the addition of additives.

Two methods are typically used for increasing the production of a material, scale-up and scale-out (Figure 1.40). Scale-up involves taking a chemical process which has been experimentally observed to operate as intended on the small-scale, and performing this reaction with higher amounts of reagents and/or in a larger vessel to produce larger quantities of product. Scale-up is not as simple as linearly scaling the reagents used in a reaction, as the dimensions of a vessel play a major role in heat transfer, mixing, reaction safety, and other factors. For systems which rely on millifluidic channels such as the confined channels of microfluidic magnetite synthesis, it is not possible to scale-up these to increased volumes without impacting laminar flow. As such, scale-out is instead considered, utilising multiple systems to increase overall production.²²⁸ Scale-out offers the advantage of requiring no further research to operate compared to scale-up which requires significant research to understand the chemistry of scale. However, when reaching larger scales the capital cost

rises drastically due to the small modular design of scale-out, compared to scale-out where cost generally reduces as production increases.

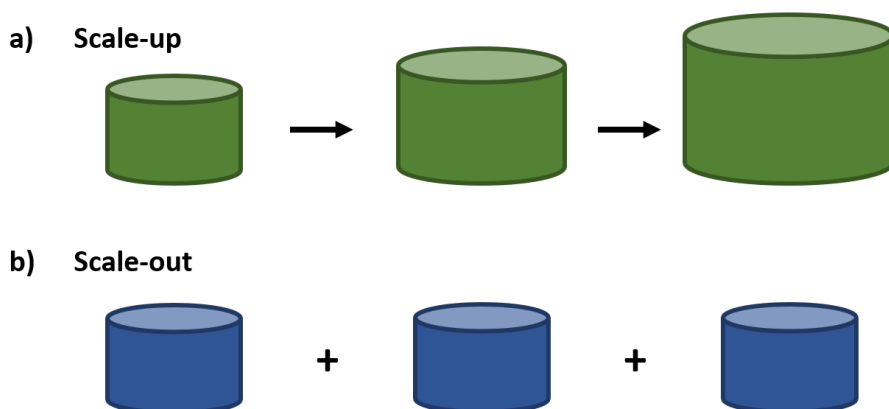


Figure 1.40: Schematic representation of **a)** scale-up and **b)** scale-out.

1.9.3 Microfluidics for Magnetite Synthesis

Microfluidics is a field of study pertaining to the control of fluidics that are often geometrically constrained in a microchannel with at least one-dimension of the channel being sub-milliscala. Microfluidics have been utilised in the analysis of blood samples,²²⁹ cell sorting,²³⁰ and the detection of mycotoxins,²³¹ but only recently begun to be considered for synthetic purposes, as the practical possibility of conducting reactions with small volumes whilst consuming minimal reagents is highly promising for chemical syntheses.

When forming MNPs, a challenge across all synthetic methods is the struggle in producing reproducible products which are highly controlled due to both the kinetic nature of crystallisation products, and small variations in reaction conditions (stirring rate, N₂ sparging rate, etc.).

Microfluidic reactors such as a coaxial flow device allow laminar sheath flow throughout their entire system. The small dimensions of the microchannels typically result in a Reynolds number of < 100, where Reynolds number is a dimensionless quality used in fluid mechanics which predicts flow patterns by considering the viscous and inertial forces. A low Reynolds number is indicative of laminar (sheet-like) flow, whereas a high value suggests turbulent flow. The Reynolds number is defined by the density of fluid, ρ , velocity of fluid, u , the

characteristic length, L (channel diameter and length), dynamic viscosity of fluid, μ , and kinematic viscosity of fluid, ν (eq 1.12).²³²

$$Re = \frac{\rho u L}{\mu} = \frac{u L}{\nu} \quad (1.11)$$

Theoretically, the use of a microfluidic reactor allows several problems with the RTCP batch synthesis method to be addressed. In a microfluidic system all particles are exposed to the same reaction conditions with every particle being formed at an identical pH, in a system entirely devoid of air, as the entire reaction ‘vessel’ is filled with reaction solution, with no mixing required due to the laminar flow.

The idea of synthesising magnetite in a flow device has only occurred in the last two decades, with Hassan et al. using a coaxial flow device to form maghemite nanoparticles in 2008.²³³ Y-shaped microreactors led to channel clogging due to precipitation adsorbing to the channel walls. A coaxial flow device cast from polydimethylsiloxane (PDMS), with concentric flows creating a sheath flow of base around a core flow of iron solution (Figure 1.41).

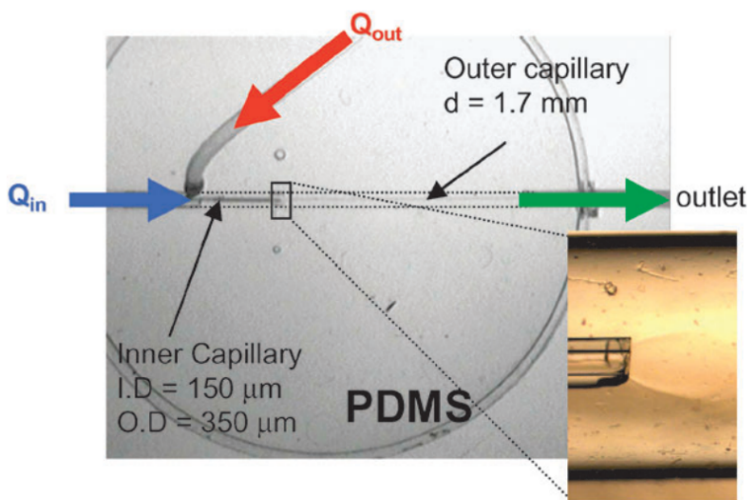


Figure 1.41: A coaxial flow device used for the synthesis of magnetite. The inset image shows the outlet of the inner capillary, with Q_{in} representing the core flow of iron, and Q_{out} representing the sheath flow of base solution. (Reproduced from Hassan et al.²³³)

Several variations of microfluidic synthesis of MNPs exist,²³⁴ with continuous flow reactors,²³⁵ drop-wise flow reactors,²³⁶ and gas-segmented flow reactors²³⁷ each being used to produce MNPs.

Drop-wise flow reactors and gas-segmented flow reactors both minimise reaction volume, resulting in low output of particles formed.²³⁴ Continuous flow reactors often utilise pre-built chip reactors,²³⁸ however the internal volume of these chips is very low. Whilst they offer highly reproducible particles between batches,²³⁴ producing a large quantity of particles would require a significant monetary investment to scale-out the synthesis.

Ideally, microfluidic principles could be learnt from and extrapolated to produce tightly defined particles on a larger scale. The concept of microfluidic particle synthesis opens the door for the further development of tightly controlled microfluidic MNP synthesis systems, and further study into flow chemistry for the synthesis of magnetite particles.

1.10 Experimental Design and Optimisation

1.10.1 One Factor at a Time

One factor at a time (OFAT) is considered the standard method of running experiments, keeping each factor consistent while changing a single variable (independent variable) and measuring a response (dependent variable). Multiple responses can be measured for each variation of the independent variable to develop an understanding of the effect the level (high or low concentration/temperature etc.) of a factor on the output of a process or reaction.²³⁹

1.10.2 Design of Experiment

Design of experiments (DoE), also referred to as designed experiments or experimental design, is the systematic procedure of determining the relationship of multiple factors influencing a process, and the output of said process. The primary purpose of DoE is to optimise experiments in a time efficient manner by varying multiple factors at once to iden-

tify significant factors, and the relationships, if any, between the factors and responses.²³⁹

In an OFAT experiment it is not possible to estimate interactions among the factors, and it is harder to identify the optimum synthetic conditions if multiple factors are being varied in a reaction landscape. As such it is possible to miss key information as only a small area of the experimental possibilities will be explored.²³⁹ The concept of DoE operates on the principle of covering the established landscape in fewer experiments, offering more reliable results.

The principles of DoE centre around removing experimenter bias (randomised experimental order), minimising external hard to control factors (blocking), replicating experiments to confirm results, factorial experiments, and if required further optimisation.²³⁹ By performing experiments in similar groups (blocks) the effect of nuisance factors, a factor that may influence the response but is not of research interest, can be minimised.

DoE is ideally an iterative process, working toward identifying the optimum conditions within set guidelines. A common iteration for DoE is to identify important factors, and then conduct a full factorial design (FFD), whose design consists of minimum two factors tested at high and low values.²³⁹ Therefore, a 2^3 design (3 factors, 2 levels) as shown in Figure 1.42a will result in 8 experiments. The addition of centre points (Figure 1.42c) to a design allows for curvature in a response to also be measured, and 3D visualisations of the factor responses to be generated. Fractional designs are also possible, where a subset of the experimental runs from a FFD are selected.

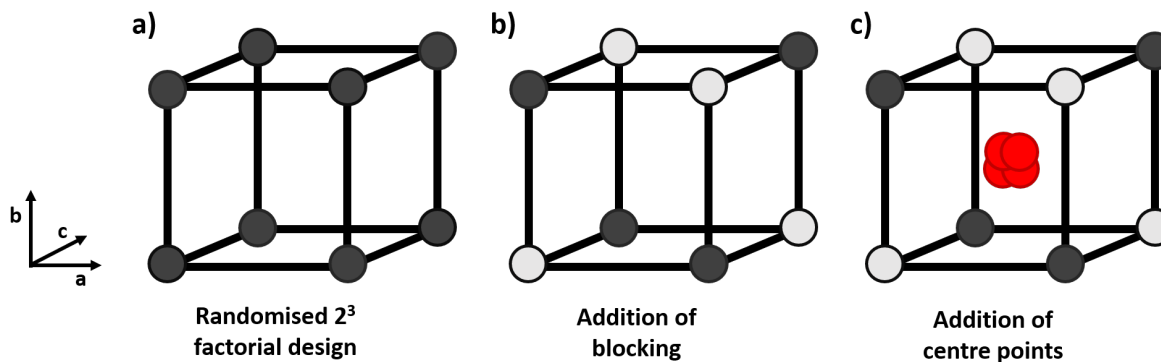


Figure 1.42: Schematic of the DoE process showing **a)** a randomised 2^3 factorial design; **b)** the addition of experimental blocking (experiments split into two sets of 4 to be conducted on the same days); and **c)** the addition of centre points in the design.

If a factor is found through analysis to be insignificant, a second FFD may be conducted to focus in on the conditions required to produce the optimum output.

Manufacturing industries are increasingly relying on the DoE technique to improve the efficiency of their research and processes.²⁴⁰ To further progress the pipeline of green magnetite synthesis toward industrial scale, it is judicious to integrate DoE into the experimental development process to further optimise synthesis. Many nanoscale syntheses are not yet fully understood, and often have complex relationships between reaction parameters and product outputs, and hence DOE is a powerful strategy.

1.10.2.1 DoE of Magnetite

Several FFD DoE studies have been conducted on the synthesis of magnetite to investigate the relationship between synthesis factors across various synthesis techniques such as electrochemical synthesis,²⁴¹ and microwave-assisted hydrothermal synthesis,^{242,243} and the properties of the particles synthesised. Two studies have been conducted on the co-precipitation of magnetite. The co-precipitation of magnetite has been investigated using a 2^6 fractional design, consisting of 2 factors (molarity of iron solution and stirring rate) and 6 levels for each. Particle shape, formation, size, and magnetic properties were found to be affected by these factors, with the use of DoE deemed to provide a unique insight into the

influence these factors exerted on the particles formed.²⁴⁴

Optimisation studies focusing on the co-precipitation of magnetite have also been conducted covering a variety of designs.^{245,246,247,248} Whilst these designs were effective in optimising the size and saturation magnetisation of the particles formed, these designs consisted of a single iteration without optimising or building upon their findings. As such, they did not benefit from the advantage of iterative DoE.

Further investigation of the RTCP of magnetite utilising additives is important to understand the influence additives exert on the morphology and composition of particles formed, with plenty of scope for further research and development in this area. By using iterative DoE incorporating multiple designs, it allows for the reaction landscape of the complicated co-precipitation system to be investigated in detail.

1.11 Project Aims and Objectives

The overall aim of this project is to synthesise MNPs using bioinspired approaches that lower the manufacturing carbon footprint, and energy-usage required to produce bespoke MNP, hence providing a significant cost benefit and competitive advantage to industry. Current nanomaterial synthesis methods are at least 1000 times more wasteful in comparison to the production of fine and bulk chemicals. As such, the need to develop green production methods is pressing.

One of the finer aims of the project is to develop the knowledge to enable larger-scale production of tunable nanomaterials using an eco-friendly SynBio (synthetic biology) approach. Instead of using bacteria or cells to form materials, synthetic molecules referred to as additives inspired from biomineralisation proteins and research will be used to produce a range of well-defined and tunable products under ambient conditions with minimal waste generation.

This approach has previously been applied to the development of silica nanomaterials over the course of 11 years, with their formation being mediated by the addition of additives. In the case of silica, silaffins in diatoms were found to contain a series of propylamine

containing peptides, which were used as a basis for the development of a series of poly-amine additives able to control both the particle and pore-size in green synthesis. Drawing inspiration from this approach, the biomineralisation proteins of magnetotactic bacteria are to be used as a starting point to develop a series of molecules which can interact with ferrous and/or ferric iron, or developing magnetite faces on growing MNPs and control the properties of the materials formed. The project has been divided into 3 objectives, each with their own hypothesis:

1. To screen and identify synthetic additives for MNP synthesis. Ideally, a series of additives will be discovered through a screening process to act as a 'molecular toolkit' capable of creating bespoke MNPs that fit the criteria of being environmentally friendly, and readily available/easy to synthesise at a reasonable cost. This was to be achieved by screening multiple classes of compounds with comparable functionalities to those observed in Nature in Mms6, MmsF, and artificially in MIAs. The hypothesis is that by learning from the form and function of these bio-additives, a range of compounds can be tested for their effect as additives within a RTCP reaction, and lead additives identified for further study.

2. To optimise the synthesis of MNPs with additives through further studies and application of DoE principles. On identification of an additive or additives that can tailor the physicochemical attributes of MNPs, research will go into optimising the products formed. This will be achieved thorough investigation into the factors which influence the properties of MNPs, such as the ferric ratio, the timepoint of additive addition, and the concentration of additive, with the aim of further understanding the role additives play in tailoring the properties of magnetite. The hypothesis is that DoE will aid in the understanding of how additives interact with magnetite to produce high quality tailored MNPs.

3. To utilise bioinspired additives in various production systems to ascertain suitability for tailored MNP synthesis, and identify a promising route to large-scale production of tailored MNPs. As previously discussed, different synthetic methodologies offer various advantages, disadvantages, and even particle properties. This also applies within the realm of co-precipitation, with batch reactions not necessarily producing particles with identical qualities as those formed within a low volume fluidic system, or those formed in a large-

scale system. The hypothesis is that by testing the efficacy of additives within several RTCP systems a methodology capable of scale-up will be identified, with the overall goal of producing > 100 g a day of tailored nanoparticles.

Figure 1.43 shows a schematic of the work conducted on this project, and the corresponding chapters in which that work can be found.

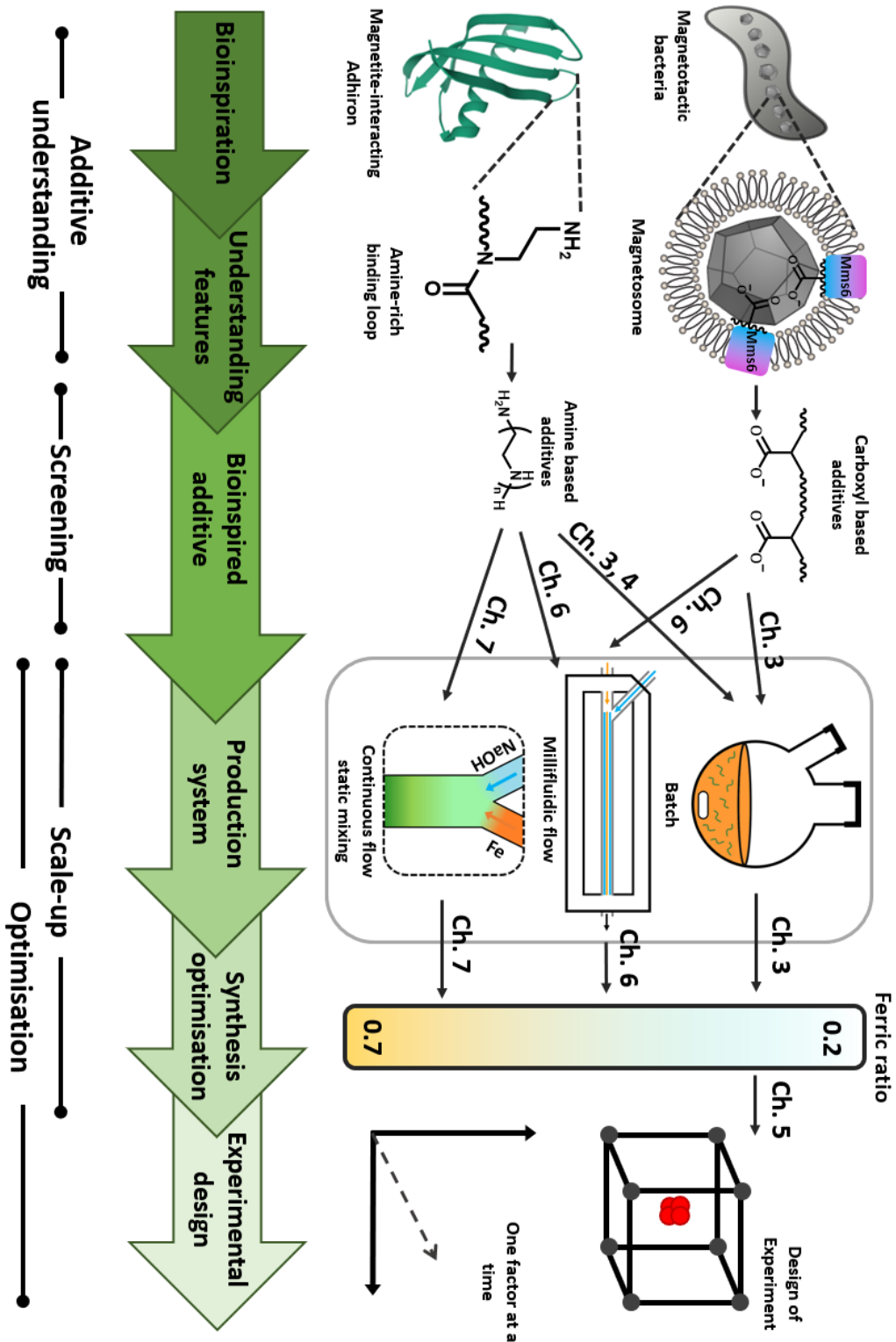
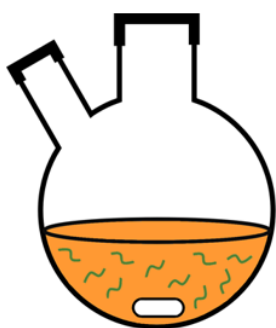


Figure 1.43: Schematic of the project pipeline from bioinspiration through to scale-up and optimisation, alongside a research summary, and the corresponding results chapters.

Chapter 2.

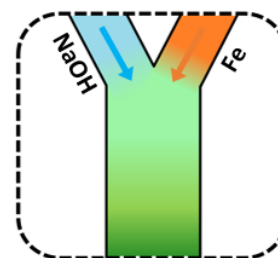
Methods



Batch



Millifluidic flow



Continuous flow
static mixing

This chapter contains the methods and analytical techniques used throughout this body of work, alongside descriptions on how the analysis techniques function and the benefit of using these techniques.

2.1 Methods Overview

Due to this thesis being presented in paper format, the methodologies have also been compiled here for ease of reading and presentation. Several synthetic techniques for the production of MNP have been utilised throughout this project. All solutions used in each synthetic methodology were sparged with N₂ for a minimum of 30 minutes prior to use, and carried out under an inert atmosphere to prevent oxidation of magnetite to other iron oxides.

Iron (II) sulphate, iron(III) sulphate, and sodium hydroxide were purchased from Sigma-Aldrich (Gillingham, United Kingdom) and used without further purification. Iron contents of the iron salts were confirmed via inductively coupled plasma optical emission spectrometry (ICP-OES) analysis when calculating iron solution molarities.

Each sample was characterised with transmission electron microscopy (TEM) and x-ray diffraction (XRD), with vibrating-sample magnetometry being used for all samples past the initial additive screening.

2.2 Room Temperature Co-Precipitation

To favour the formation of magnetite nanoparticles, all reactions were carried out under an inert atmosphere of N₂ for a minimum of 30 minutes prior to use. Ultrapure water (Milli-Q) (Merck, Milli-Q integral purification system) was used. Reagents were purchased from Sigma Aldrich unless otherwise stated and used as purchased.

2.2.1 Standard Reaction Set-up

Particles were formed using a room temperature co-precipitation technique. Iron(II) sulphate (0.3 mM) and iron(III) sulphate (0.4 mM) were dissolved in N₂ sparged MilliQ water (20 mL), under an inert atmosphere of N₂ to form a 1 mM Fe solution in a two-necked round bottom flask (RBF) as shown in Figure 2.1. A set amount of additive was added to the iron solution, and left to stir to ensure dissolution of additive and iron salts. When adding

a small amount of additive, it was pre-dissolved in the 20 mL aliquot of water for ease of preparation. N_2 sparged 0.5 M NaOH (8 mL) was added at a rate of 50 μ L a minute with magnetic stirring, for a total of 160 minutes using a Harvard Apparatus 11 plus syringe pump driver.

The reaction was then left to age for an hour under the inert atmosphere with stirring maintained. The reaction mixture was then magnetically separated, washed 5 times with sparged MilliQ to remove any unreacted pre-cursors, non-magnetic iron oxides and NaOH, and the particles dried in a vacuum oven at 40 $^{\circ}$ C overnight. The particles were then ground with a pestle and mortar for analysis.

The amount of additive used is detailed in each chapter, stated alongside the data with differences in amounts of additive clearly stated.

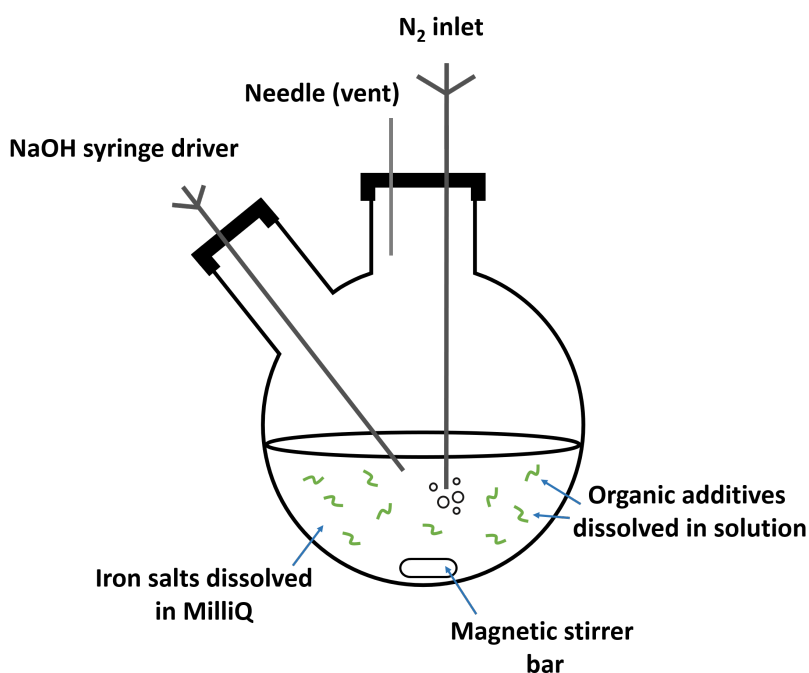


Figure 2.1: Diagram of the standard reaction set up used for room temperature co-precipitation of MNPs.

2.3 Macrofluidic Synthesis

2.3.1 Macrofluidic Device Fabrication

PDMS Device

The device was constructed from a polytetrafluoroethylene (PTFE) hollowed out block with a long channel milled from the centre, and machined for a screw fitting at one end. Initially a stiff metal wire with a diameter of 1.6 mm was pushed through the two holes along the axis of the device. A second input hole intersected the main channel at an angle of 45° as shown in Figure 2.2.

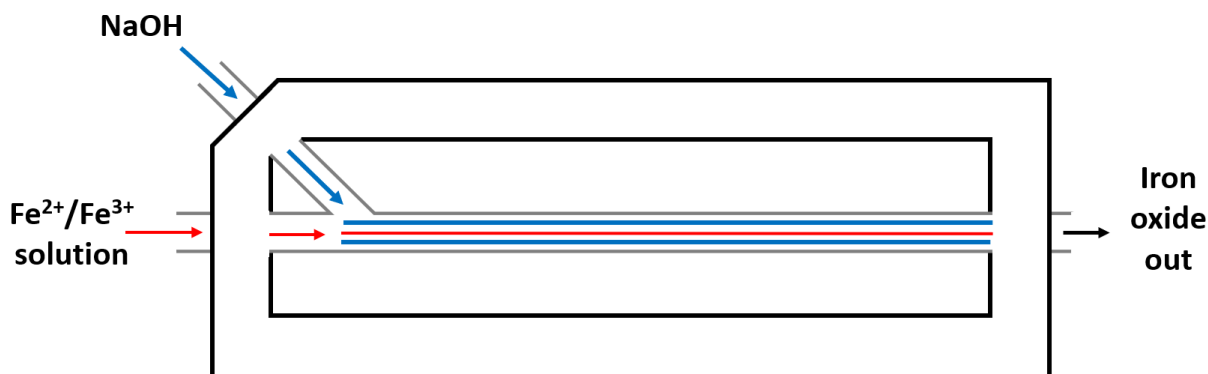


Figure 2.2: Schematic of the macrofluidic room temperature co-precipitation system, showing the sheath outer flow of NaOH in blue and the core inner flow of mixed valence iron salts in red.²⁴⁹

The blunt end of a needle was shaped using a drill bit to meet and fit the shape of the central wire and enable a smooth transition. Triton X-100 was wiped over the wires/needle so they could be easily removed from the device after casting. The space was then filled with liquid polydimethylsilane (PDMS) and cured at 60 °C for 24 hours. When cured, the central wire and needle were carefully removed, leaving behind a central channel and side inlet cast in PDMS. The materials and equipment required to create this device are cheap and readily available, and the PTFE block is reusable for many castings. The block was fastened via screw fittings to a heavy object to prevent lateral movement when connected to stiff fluidic tubes. The fluid from the central channel was fed into a polyether ether ketone

(PEEK) tube with an inner diameter of 0.02" attached via appropriate fittings. The internal hole was expanded using a shaped drill bit to ensure a smooth transition in diameter. This experimental excerpt was written by Jonathan Bramble, who also designed the PTFE block used to cast the PDMS device.²⁴⁹

PEEK Device

The device was designed and modelled in SolidWorks, comprising of 6 individual components; (i) Fe inlet, (ii) NaOH inlet, (iii) inlet faceplate, (iv) capillary, (v) outlet faceplate, and (vi) outlet (Figure 2.3).

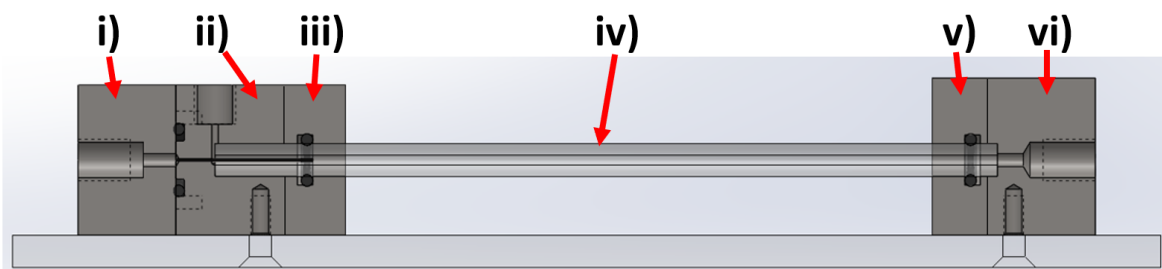


Figure 2.3: Cross-section of the PEEK system illustrating the different components.²⁴⁹

The rig was machined from PEEK, with PTFE o-ring seals between components i-ii, ii-iii, and v-vi to ensure no leakage of solution, a problem often observed in PDMS cast systems. A 27 gauge blunt-end needle (0.41 mm outer-diameter (OD), 0.016 inner-diameter (ID)) was set through component i) with the use of epoxy resin. This needle was sprayed with Teflon spray to increase hydrophobicity and aid flow of reagents. The capillaries used were 0.5 m in length, with a 5 mm OD and 1.5 mm ID. The capillary tube was inserted between components ii/iii (inlet) and components v/vi (outlet) to form the reaction channel. The system was locked in position with clamp stands to prevent movement when connected to the fluidic tubing. This PEEK device was designed by Andrew Norfolk and machined by Stefan Waterson of the Cambridge Design Partnership.²⁴⁹

Fluidic connectors for both devices (Upchurch Scientific, purchased from Kinesis (Cambridge United Kingdom) or Fischer Scientific (Loughborough, United Kingdom)) and PEEK tubing with an OD of 1/16" and ID of 0.02" were used. All tubes were cut with tube

cutters (Upchurch Scientific A-327, A-350) to ensure clean and perpendicular cuts. Two syringe drivers (Harvard Apparatus, Cambridge, United Kingdom) were used to control the flow rate of iron and base into the system. Luer lock syringes with volumes of 1 mL and 10 mL were used for the inner (iron) and outer (NaOH) flows respectively. Luer lock fittings were used to connect PEEK tubing to the syringes.

2.3.2 Protein Expression and Purification

The *mms6* sequence from AMB-1 was introduced into a pTTQ8 based expression vector by cohesive end cloning with the resulting plasmid, pHis8mms6, encoding N-terminally octahistidine tagged Mms6. The protein was produced in E.coli BL21 star (DE3) cells (Invitrogen, Waltham, MA, United States) harbouring a pRARE (Merck, Nottingham, United Kingdom) plasmid to compensate for codon bias in the *mms6* sequence. Cells were cultured in autoinducing Superbroth (Formedium, Hunstanton, United Kingdom) at 37 °C with shaking for 24 hours in the presence of carbenicillin and chloramphenicol to select for the pHis8mms6 and pRARE plasmids respectively. Cells were lysed by sonication in 25 mM Tris pH 7.4, 100 mM NaCl. The insoluble material, containing the His8-Mms6 inclusion bodies, was collected by centrifugation at 16,000x *g* and re-suspended in 6 M Guanidine Hydrochloride, 25 mM Tris pH 7.4 to solubilise the proteins. Further centrifugation at 16,000x *g* was performed to remove any material not solubilised by the Guanidine treatment. The supernatant was mixed with nickel charged nitrilotriacetic acid resin (Amintra resin, Expedeon, Cambridge, United Kingdom) to allow binding of the histidine tagged Mms6. The resin was subsequently packed into a gravity flow column and washed extensively with Wash Buffer (6 M Guanidine hydrochloride, 25 mM Tris pH 7.4, 10 mM Imidazole) before elution of the bound protein in 300 mM Imidazole supplemented Wash Buffer. The eluted protein was refolded by rapidly diluting into a large volume of Refolding Buffer (500 mM NaCl, 25 mM Tris pH 7.4) before being concentrated using a 10 kDa molecular weight cut off centrifugal concentrator (Sartorius, Binbrook, United Kingdom). The concentrated material was subjected to centrifugation to remove any small amounts of precipitated protein before dialysis against 500 mM NaCl using a 3.5 kDa molecular weight cut off slide-a-lyser (Thermo Scientific, Waltham, Ma, United States). The refolded His9-Mms6 was quantified by absorbance at

280 nm and stored at 193 K.

This experimental excerpt was written by Andrea Rawlings, who also conducted all protein expression and purification work.²⁴⁹

2.3.3 Macrofluidic MNP Synthesis

The coaxial fluidic device was cleaned with MilliQ water, and each solution deoxygenated by sparging with N₂ for a minimum of 30 minutes. The outer flow syringe pump driver was loaded with a 10 mL Luer lock syringe of NaOH (1 M) and connected to the co-axial fluidic device via PEEK capillary tubing. This was set at a continuous rate of 360 µL/min. This syringe was refilled with N₂ sparged NaOH solution as required. The inner flow syringe pump driver was loaded with a 10 mL Luer lock syringe containing 8 mL of a mixed ratio of Fe²⁺ and Fe³⁺ salts (ferrous sulphate pentahydrate and ferric sulphate heptahydrate respectively) varied from a 4:1 (0.2 ferric) to ~1:2 (0.7 ferric) Fe²⁺:Fe³⁺ ratio with a total iron concentration of 0.05 M and connected to the co-axial fluidic device inner channel via capillary tubing. This was set at a continuous rate of 90 µL/min. The solutions were prepared immediately prior to the experiment to avoid ferrous iron oxidation.

The iron oxide material formed and flowed to the end of the device where it reached the exit port and dripped into a round bottom flask which was kept under a continuous atmosphere of nitrogen. The iron oxide product was magnetically separated and washed 3x in deoxygenated MilliQ water and subsequently dried in a vacuum oven at 40 °C overnight. The particles were then ground with a pestle and mortar for analysis.

Further improvements to the initial experiments performed in the PDMS device included magnetically collecting the iron oxide as it exited the device using a magnetic trap. These particles were also washed 3x with deoxygenated MilliQ water and dried overnight in a vacuum oven as before. In the case of the PEEK device the particles were collected as detailed above.

2.3.3.1 Macrofluidic MNP Synthesis Modified with Mms6

The iron oxide synthesis was further modified with the addition of Mms proteins, where 50 μg of protein was added to the 8 mL Fe salt solution before the reaction. The experiment then proceeded as before.

2.4 Continuous Flow Static Mixing Synthesis of MNP

2.4.1 Experimental Set-up

2 Watson Marlow 520DuN (Zwijnaarde, Belgium) cased peristaltic pumps were used, with one being the NaOH feed and the other being the Fe solution feed, with each pump set at 10 rounds per minute. The feeds from both pumps were connected via a plastic Y mixer, from which plastic tubing was directed to the collection vessel. When running the pumps concurrently this setup resulted in a residence time for the mixed solution (from the Y mixer to the collection vessel) of approximately 2 seconds.

Fe solution was fed through one pump, whereas NaOH solution was fed concurrently from the second pump. Feed solutions each contained a magnetic stirrer with the solutions placed on magnetic stirrer plates so as to be under constant mild stirring conditions throughout the experimental run. All solutions (feeds and collected) were constantly sparged with N_2 throughout the duration of the experiment, ensuring thorough deoxygenation of the solutions, and thus minimising the possibility of undesired oxidation occurring at any stage of the precipitation process. The feed solutions were left to stir under an inert atmosphere of N_2 prior to mixing in iron salts to prevent their oxidation (Figure 2.4).

Modified lids were used to avoid the re-dissolution of O_2 in to the solutions during the experimental runs. Both feed vessels and the collection vessel were sealed with the modified lids that incorporated 3 openings: one for the pump feed tubing, one for the N_2 supply, and the third had tubing that allowed for pressure to escape the vessel.

Once the initial 5 minute stirring of the feed solutions was completed, both peristaltic pumps were turned on (counter clockwise flow) for mixing to occur. The flow of the mixed

solution after the Y-mixer junction was collected only after the flow became constant. Timing the collection of 15-20 mL mixed solution resulted in a calculated flow rate of approximately 110-115 ml/min.

To minimise the possibility of cross-contamination from a previous run the system was flushed out with MilliQ water until the water ran clear from the collection tube for a couple of minutes. The flow was then reversed on both pumps (clockwise) and MilliQ water was then left to run out of the feeding tubes, again, until the water ran clear for approximately 1-2 minutes.

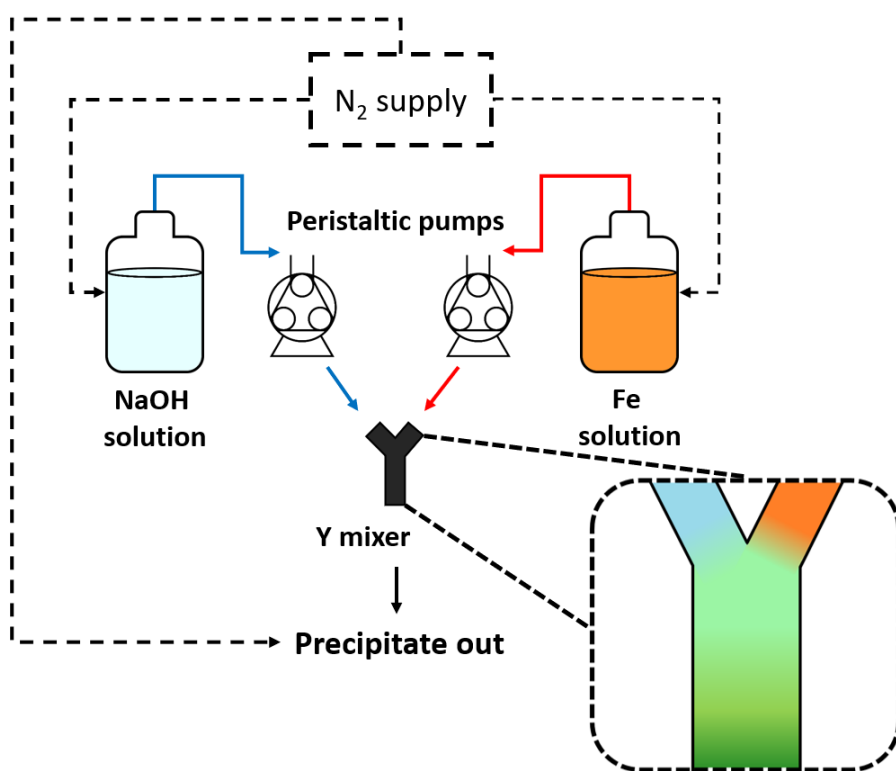


Figure 2.4: Schematic representation of the continuous flow static mixing set-up, including peristaltic pumps, 2 feed solutions, orange (Fe salts) and pale blue (NaOH), a collected precipitate solution, and a Y-mixer. Supply routes are designated with arrows: feed and collection routes are solid lines and N_2 gas supply in dashed lines.

2.4.2 Experimental Set

A total of 42 experiments were performed, with variables being NaOH concentration, $\text{Fe}^{3+}:\text{Fe}^{2+}$ ratio, total Fe:additive ratio, and type of additive used.

The first two sets of experiments were performed without the addition of an amine additive. Specifically, the first set of experiments were performed to see if altering the ratio between the ferric and ferrous ions affected properties of the precipitate formed. Ratios of 0.2-0.7 $\text{Fe}^{3+}:\text{Fe}^{2+}$ were used. The total iron concentration for each solution was kept at 50 mmol, and the concentration of NaOH used at 500 mmol. Additional focus was given to the ratios close to 0.6, which is considered the ideal ratio for magnetite precipitation from published literature.

The second set of experiments were performed to see if varying the NaOH concentration and Fe concentration affected precipitate properties. The total iron ratio was kept constant at 0.6 (total iron concentration of 20 mmol) for experiments 8-10 but the NaOH concentration tested at 3 different levels, 300, 500, and 1000 mmol. For experiment 11 and 12 a reduced iron concentration of 10 mmol was tested at the 2 higher NaOH concentrations (500 mmol and 1 M).

The third set of experiments were all performed with the presence of an amine (EDA based) additive. The amines used were initially added to the iron salt solution at different amine: total iron ratios, with these ratios being 1:100, 1:1000, and 1:10000. The experiments were then repeated by adding the additives to the NaOH solution at the same additive:total iron ratios. Amines were added to the feed solutions after the initial 5 minute stirring with N_2 sparging, and the solutions allowed to continue stirring for a couple more minutes prior to the pumps being turned on to allow for mixing. For this set of experiments, the ferric (Fe^{3+}) to total iron ratio was 0.6 with a total iron concentration of 50 mmol, and 500 mmol NaOH used. A full list of conditions can be seen in Chapter 7.

2.5 Characterisation

2.5.1 Transmission Electron Microscopy

Transmission Electron Microscopy (TEM) operates by firing a beam of electrons through a sample to produce a highly magnified image of a section of the sample (Figure 2.5). An electron gun (typically fit with a tungsten filament to generate electrons) produces a high voltage electron beam, which is then accelerated by an anode. The beam is then focused by electrostatic and electromagnetic lenses, and transmitted through the very thin specimen leading to some electrons scattering on the sample, and others passing through to a fluorescent or phosphorescent viewing screen at the bottom of the set-up.^{250,251} Condenser lenses (two or three) comprised of magnetic coils gather the electrons and focus them onto the sample to screen only the area being imaged. The sample is inserted into or by the objective lens which is used to focus or magnify the image, and finally projector lenses are used to further enlarge the image.²⁵²

The electron beam on the other side of the sample carries information about the sample, which is then magnified by the objective lens of the microscope, and finally hits the phosphorescent viewing screen at the bottom of the microscope to form an image. This gives a silhouette type view of the sample in monochrome, effectively showing an area of a specimen that has the ability to repel electrons. As electrons pass through the material they can diffract and give structural information about the sample.²⁵³

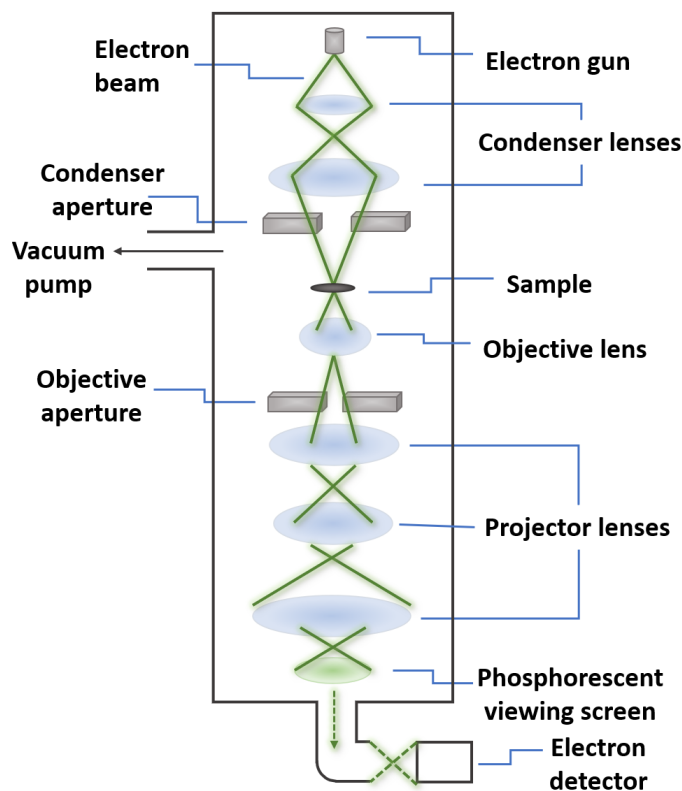


Figure 2.5: Schematic of a transmission electron microscope (TEM). (Adapted from Kelsall et al., 2005.²⁵¹)

2.5.1.1 Sample Preparation and Analysis

For TEM analysis of magnetic nanoparticles, a 10 μL of a 1 mg/mL suspension of nanoparticles sonicated for 1 minute in hexane was dropped onto a carbon coated copper TEM grid and allowed to dry down for a minimum of 1 hour. Grids were imaged using a FEI Tecnai G2 Spirit electron microscope (Thermo Scientific, Waltham, MA, United States) and the TEM images were analysed using Image-J software (v1.52, public domain, National Institute of Health, MD, USA). >200 particles per sample were randomly selected for measurement.

2.5.2 X-Ray Diffraction

X-ray diffraction (XRD) is a technique used to determine the crystallographic planes present in a sample, allowing for structural identification based on the diffraction pattern.²⁵¹ Powder X-ray diffraction operates on the concept of atoms in a crystal scattering X-rays as they

interact with the electrons of these atoms in a process known as constructive interference. Crystals are generally highly ordered arrays of atoms with regular spacing between the atoms forming a crystal lattice. This defined lattice of atoms acts as a diffraction grating, with most scattered X-rays cancelling each other out through destructive interference, and simultaneously producing constructive interference at a few set angles. These angles are determined by Bragg's Law (equation 2.1) where d is the interplanar distance between layers of lattice atoms, θ is the incident angle at which the X-ray hits the sample, n is an integer number of the incident wavelength, and λ is the wavelength.²⁵⁴

$$2d\sin\theta = n\lambda \quad (2.1)$$

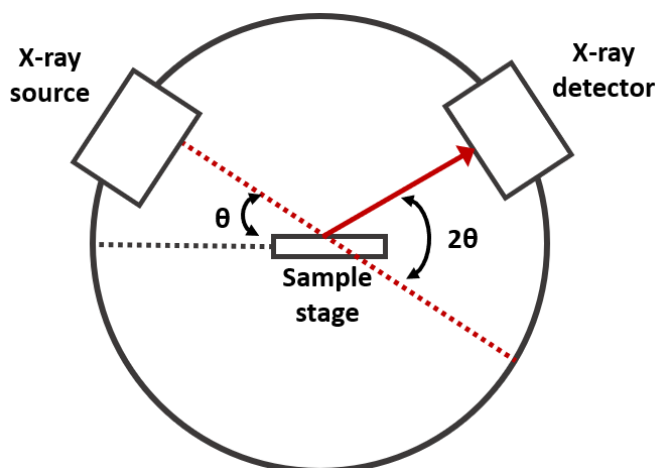


Figure 2.6: Schematic of an X-ray diffractometer (XRD). (Adapted from Epp, 2016.²⁵⁵)

Powder X-ray diffractometers detect the intensity of the diffracted X-rays between a user-specified range of angles of incident rays by rotating the x-ray source and detector with respect to the sample and recording the response (Figure 2.6). The 2θ value a peak occurs at can then be converted to d -spacing (Figure 2.7).²⁵⁴ Once the distance between planes of atoms is known, the data can be compared to mineral databases to identify which iron oxide is responsible for the peak.

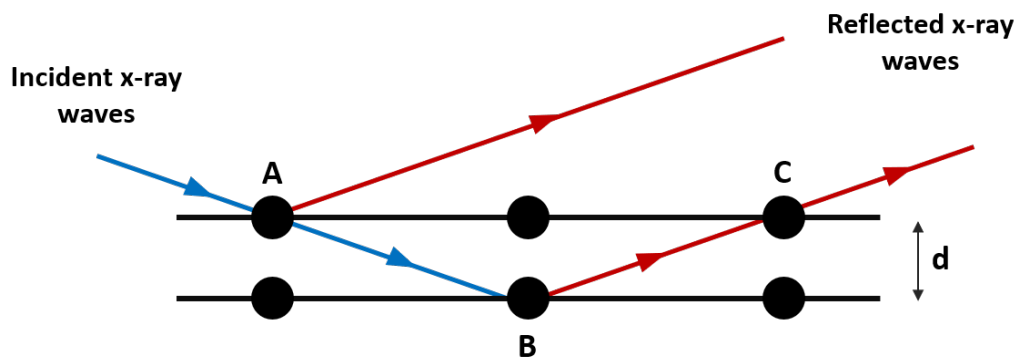


Figure 2.7: Bragg's diffraction occurring as incident x-rays (blue) reflect or are transmitted to the next layer of atoms, allowing d-spacing to be derived. (Adapted from Stanjek et al.²⁵⁴)

As there are many layers of atoms present in a crystalline sample, there is a sharp transition between constructive and destructive interference as many waves interact, leading to the presence of defined peaks.

The grain size of MNPs can also be analysed via XRD,²⁵⁶ and is calculated with the Scherrer equation (equation 2.2) where τ is the mean size of the crystalline domain, K is a dimensionless shape factor, (typically around 0.9), λ is the X-ray wavelength, β is the full width at half maximum intensity (FWHM), and θ is the Bragg angle:

$$\tau = \frac{K\lambda}{\beta \cos\theta} \quad (2.2)$$

In the case of magnetite, this analysis was conducted on the highest intensity [311] peak occurring at approximately $2\theta = 35.5$ with a sample XRD spectra of magnetite shown in Figure 2.8.

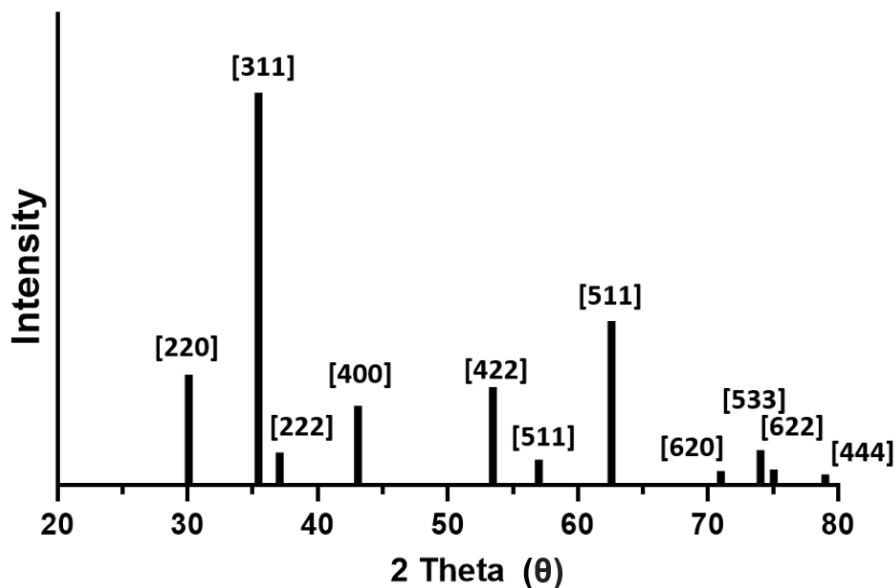


Figure 2.8: Theoretical magnetite XRD data between 20-80 2θ showing the crystallographic planes responsible for each peak. Crystallographic data was acquired from the crystallography open database.

2.5.2.1 Sample Preparation and Analysis

For XRD data of samples was collected by analysis of dry iron oxide nanoparticles in a Bruker D8 powder diffractometer (Bruker, Coventry, United Kingdom). Samples were analysed in either capillary or flat plate mode, dependent on the mass of particles available. Diffraction images were collected at 0.022 degree increments from 20–80 degrees, with a fixed wavelength at $\lambda = 1.54178 \text{ \AA}$ at 1.2 seconds per step from a Cu $K\alpha$ X-ray source.

2.5.3 Vibrating Sample Magnetometry

Vibrating sample magnetometry (VSM) measures the magnetic properties of a sample by vibrating a sample in a uniform magnetic field.²⁵⁷ Based on Faraday's Law of induction stating that a changing magnetic field will produce an electric field, a sample is magnetised in a uniform magnetic field and then vibrated perpendicular to this applied field. As the magnetic domains in the sample align with the external field, an increased voltage is induced in the pick-up coils relative to the magnetisation of the sample (Figure 2.9) The strength of

the uniform magnetic field is varied over time to create a hysteresis loop as magnetisation at various applied field strengths is measured for a sample.²⁵⁷

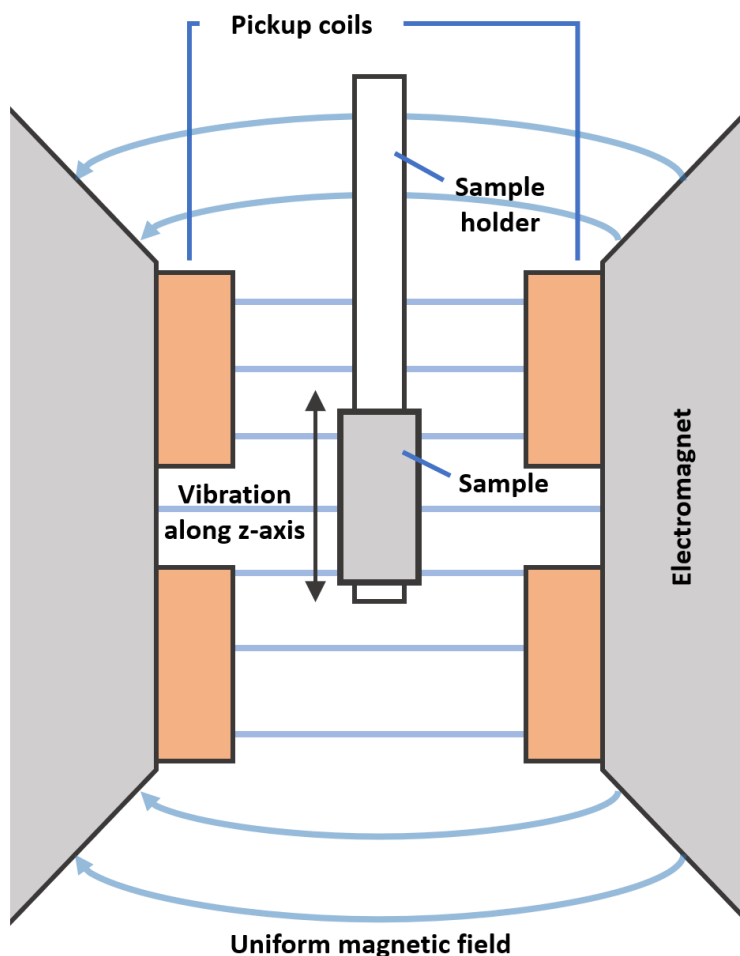


Figure 2.9: Schematic of a vibrating sample magnetometer (VSM). (Redrawn from a public domain image.²⁵⁸)

2.5.3.1 Sample Preparation and Analysis

Magnetic susceptibility was performed on a known quantity (1–5 mg) of dry iron oxide nanoparticles on a MPMS 3 SQUID magnetometer (Quantum Design, Surrey, United Kingdom) in vibrating sample mode, with the samples packed in size 3 gelatine capsules. The samples were run at 300 K between -3 and 3 T with a sweep rate of 0.01 T/s. The data shown is cropped at saturation magnetisation.

2.5.4 Inductively Coupled Plasma Optical Emission Spectrometry

Inductively coupled plasma optical emission spectrometry (ICP-OES) is a form of elemental analysis which allows the elemental content of a sample to be determined down to trace presence of elements at highly dilute concentrations (mg per L). Argon plasma is generated by exposing argon gas to a plasma torch, producing a high temperature plasma (~7000k).²⁵⁹ The sample to be analysed is delivered via peristaltic pump to a nebuliser and ionised using this argon plasma. Atoms and ions can absorb energy exciting an electron from the ground state to an excited state. As this excited electron returns to its ground state, the absorbed energy is released as a photon of light of a specific wavelength of light unique to different elements. The intensity of the light emitted is measured, and the concentration of specific elements present is then calculated based on a calibration graph.

2.5.4.1 Sample Preparation and Analysis

ICP was used to determine the amount of Fe present in synthesised MNPs via dissolution in 2.5 M HCl and diluted in ultrapure MilliQ water. Samples were analysed using a Spectro-Ciros-Vision Inductively Coupled Plasma Optical Emission Spectrometer, with all samples being processed by Heather Grievson at the University of Sheffield.

2.5.5 Fourier-Transform Infrared Spectroscopy

Fourier-transform infrared spectroscopy (FTIR) is an analytical technique which measures infrared absorption and emission spectra. An infrared (IR) spectra allows the visualisation of the bond types present in a sample by measuring the absorption of IR radiation. Different bonds absorb radiation at characteristic frequencies matching the vibrational frequency of the bond. For a bond vibration to be IR active it must change the overall dipole moment, with multiple vibrational modes being possible from a single bond.²⁶⁰

In a Fourier-transform system there are three components, a radiation source, interferometer, and a detector. An interferometer (Figure 2.10) takes a beam of light or other electromagnetic radiation and splits it using a beam-splitter, a piece of glass thinly coated in silver which reflects half the light that hits it and transmits the other half such that the

paths of the two beams differ. Path 1's length varies due to a moving mirror, whereas path 2 is consistent. The two beams are then recombined at the beam splitter and travel into a detector. Constructive and destructive interference occur when the beams recombine, resulting in maxima and minima. This modulates the optical radiation by altering the path difference between the two paths, producing a target spectra of light of varying wavelengths. The frequencies a sample absorb can then be measured and recorded.²⁶⁰

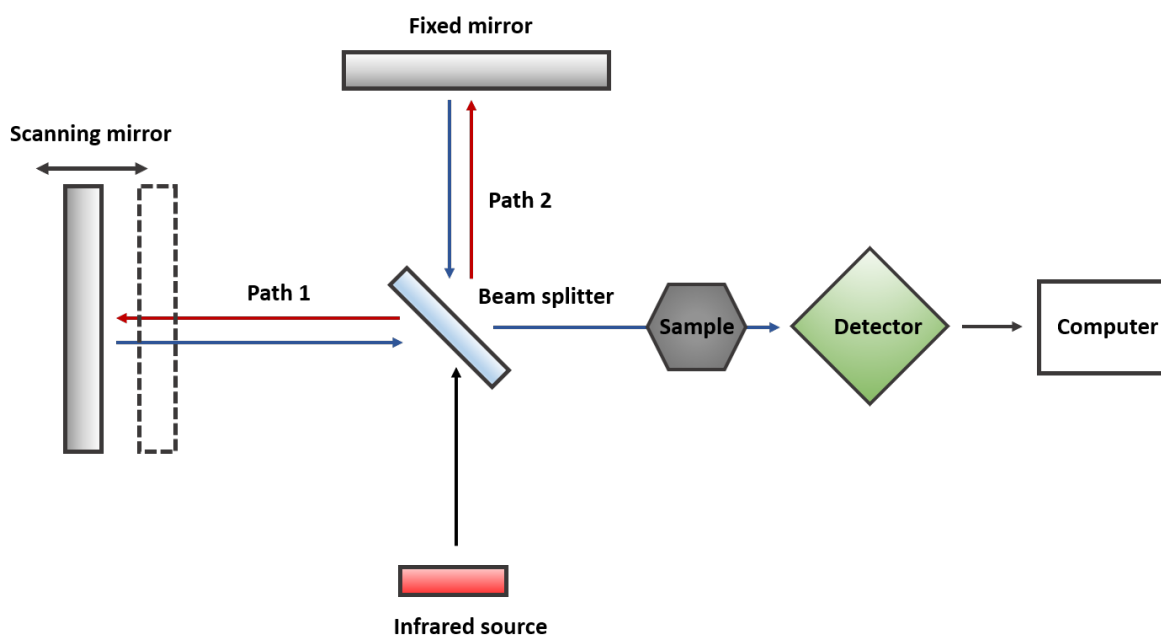


Figure 2.10: Schematic of an interferometer used in a Fourier Transform Infrared Spectrometer (FTIR). (Adapted from Blum et al.²⁶¹)

Attenuated total reflectance (ATR) is a sampling technique in infrared spectroscopy which allows for samples to be analysed as a solid or liquid without further sample preparation. The sample is placed onto an internal reflection element comprised of a material with a high refractive index such as ZnSe, and hit with an IR beam which is directed onto the reflection element such that the IR light undergoes internal reflection. An evanescent wave is produced at each of the internal points of reflection, with the sample absorbing radiation from being in contact with the internal reflection element (Figure 2.11).^{262,261}

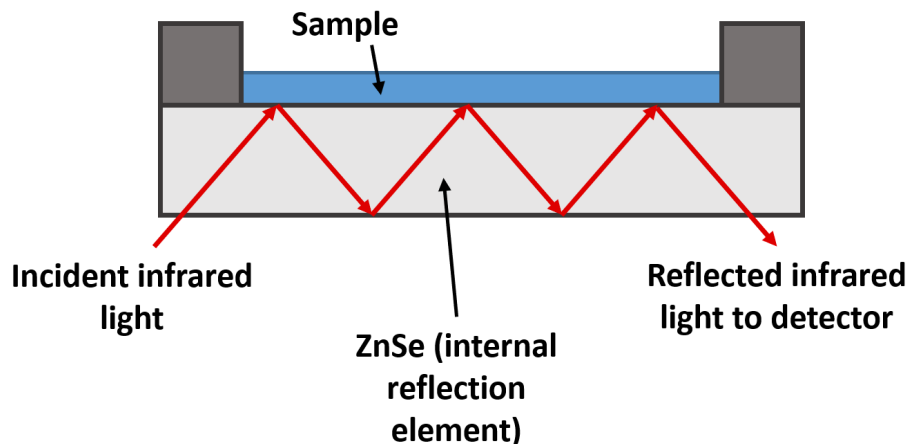


Figure 2.11: Schematic of an attenuated total reflection (ATR) adaption of infrared (IR) spectroscopy showing the internal reflections through the internal reflection element made of a high refractive index material. (Adapted from Schuttlefield et al.²⁶²)

2.5.5.1 Sample Preparation and Analysis

FTIR was performed on a small quantity (5-10 mg) of dry iron oxide nanoparticles using a Perkin Elmer FTIR and Golden Gate Diamond ATR spectrometer. Data collection and analysis was performed using SpectrumTM 10, with scans being made between 450 and 4000 cm^{-1} . Baseline correction was performed on all spectra.

2.5.6 Thermal Gravimetric Analysis

Thermogravimetric analysis (TGA) is a technique by which the mass of a sample is measured over time as the temperature increases. This allows for the presence of adsorbed molecules and the percentage mass of the product they comprise to be determined.

TGA is operated using a thermobalance, an instrument which can accurately measure the weight of a sample under high temperatures. A sample is placed on an analytical balance inside a sample pan, at which point a furnace is raised to encase the sample and heat it according to a user programmed routine. The heating occurs under an atmosphere of N_2 to reduce undesired oxidation of the heated compound.

2.5.6.1 Sample Preparation and Analysis

To ascertain the presence of organic material on iron oxide nanoparticles, a small amount (10-20 mg) of particles were washed with ethanol and acetone to remove any residual surface groups and dried in a vacuum oven. These clean particles were then dispersed in a 0.05 M solution of TEPA in ultrapure MilliQ and sonicated for 10 minutes. The solution pH was adjusted to ~pH 7 using 0.5 M HCl and rotated for 1 hour using a Lab net Mini Labroller. The particles were then magnetically separated and washed using ultrapure water to remove excess unbound amine and dried overnight in a vacuum desiccator. TGA was performed on these dry particles between 20-800 °C at a heating rate of 10°C per minute under a 2/3 N₂ and 1/3 O₂ atmosphere. Control particles were also tested, which were simply washed with ethanol and acetone and left to dry overnight in a vacuum desiccator.

2.5.7 Particle Size Analysis

In order to analyse the grain size of particles formed in each reaction, TEM images were analysed using ImageJ software. Particle size measurements were taken across the longest axis of each particle to ensure consistency between samples and measurements. A minimum of 200 measurements were taken per sample to get an accurate measure of mean size given the variation in particles formed. To aid in avoiding human bias in which particles were selected for analysis, particles were analysed from a single starting point of a TEM image to prevent small or large particles being selectively measured as shown in Figure 2.12. Several images, and hence 'areas' were analysed for each sample to ensure a representative sample was taken.

These data points were fit with a Gaussian distribution in GraphPad Prism to generate a size distribution, with exceptions to this being noted where relevant.

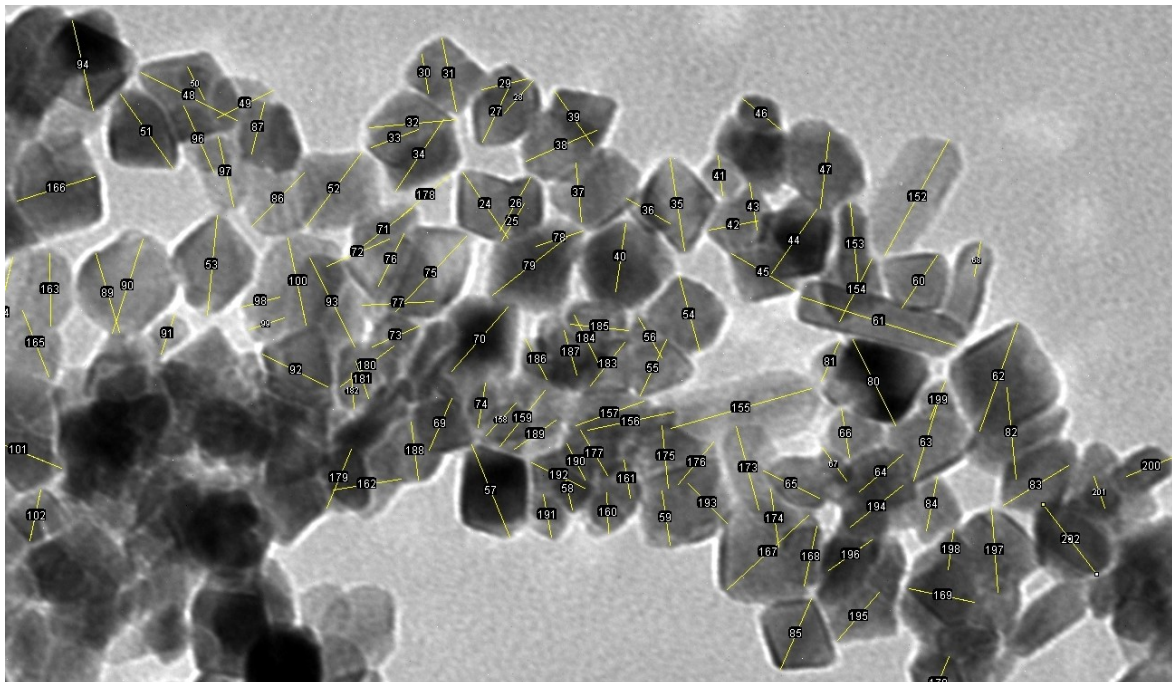


Figure 2.12: Screenshot of ImageJ particle sizing showing particles are analysed in clusters from a starting point. (Reproduced from Norfolk et al.²⁶³)

2.5.8 Particle Shape Analysis

To ascertain the distribution of shapes in a sample, TEM images were manually analysed using drawing software (Inkscape, Paint.net, etc) by marking each particle with a set colour corresponding to its shape, shown in Figure 2.13.

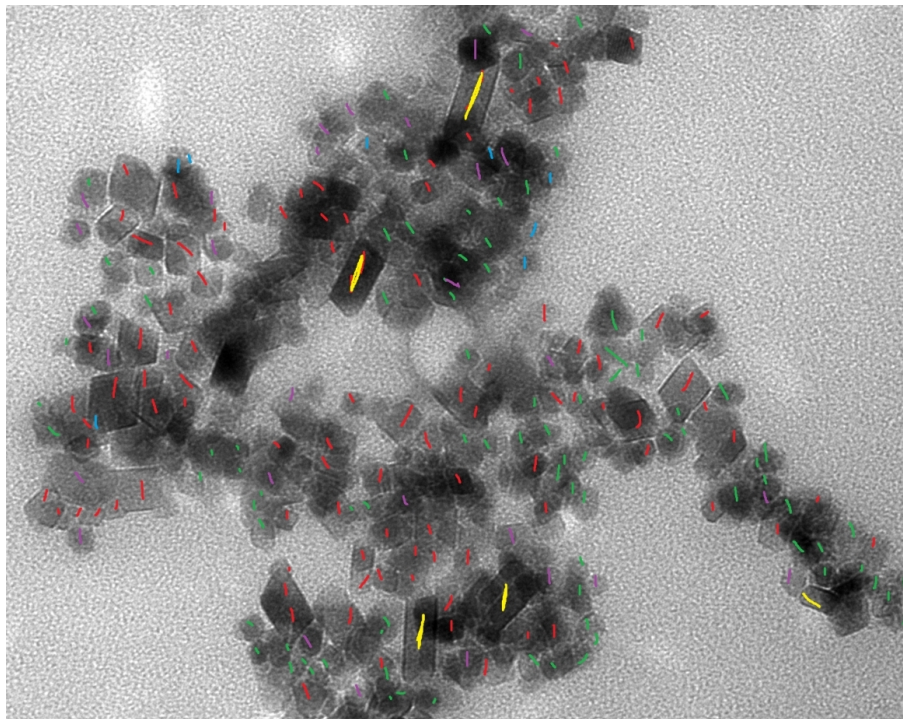


Figure 2.13: Example particle shape analysis showing undefined particles (green), diamond (red), square (blue), hexagonal (purple), and elongated (yellow).

A minimum of 300 particles are marked from several images to ensure a representative sample is selected and analysed. The numbers of particles of each shape are then counted, at which point the shape assignment is checked a second time to maximise accuracy. As the analysis is performed manually and may vary slightly due to human interpretation, each sample is analysed by the same person. Sample particle shaped can be seen in Figure 2.14 showing the most commonly observed particle shapes.

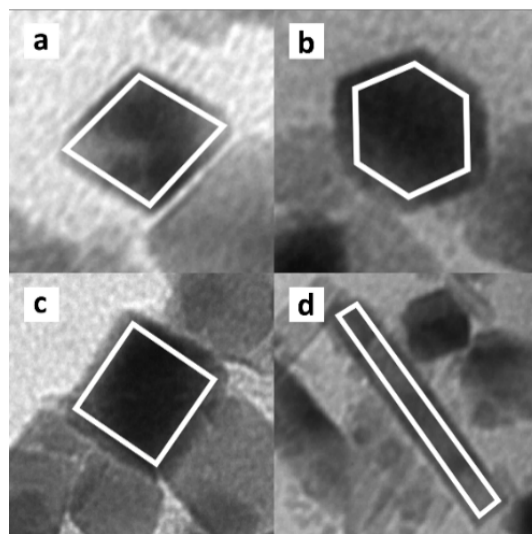
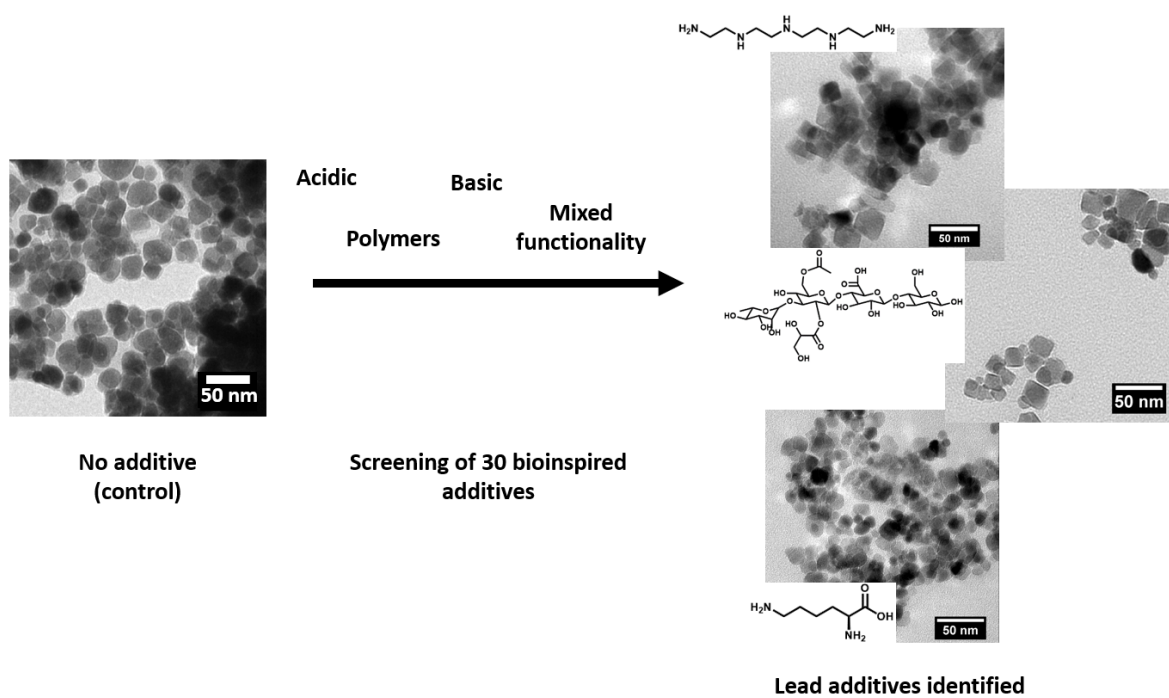


Figure 2.14: Sample particle shapes from TEM analysis; **a)** diamond; **b)** hexagonal; **c)** square; and **d)** rod/elongated. (Reproduced from Norfolk et al.²⁶³)

Chapter 3.

Screening Additives



This chapter covers the preliminary screening of a range of 30 additives spanning a variety of functionalities inspired by the function of Mms6, MmsF, and magnetite interacting Adhiron.

3.1 The Role of Biological and Bioinspired Additives in the Green Synthesis of Magnetite Nanoparticles

3.1.1 Author Contributions

Laura Norfolk (first author): Planned work, selected additives, synthesised and analysed particles (XRD, TEM, shape and size analysis), designed and created figures, wrote first draft, and edited the final paper version.

Siddharth Patwardhan: Supervisor, conceptualised the project, acquired project funding, and anprovided feedback on first draft.

Sarah Staniland (principal investigator): Supervisor, conceptualised the project, acquired project funding, and provided feedback on the first draft and restructuring.

ARTICLE

The role of biological and bioinspired additives in the green synthesis of magnetite nanoparticles

Laura Norfolk,^a Siddharth Patwardhan,^b Sarah Staniland^{a*}

Received 00th January 20xx,
Accepted 00th January 20xx

DOI: 10.1039/x0xx00000x

As industrial demand for magnetite nanoparticles (MNP) rises, it has become clear there is not yet an environmentally friendly route to synthesise precision particles on a large scale. Drawing inspiration from biomineralisation proteins found to modulate MNP synthesis in Nature, a set of 30 compounds with a wide range of properties and functionalities were screened for use as additives in a room-temperature co-precipitation (RTCP) reaction, measuring their effect on particle size and shape. As a preliminary study detailing the effect of various functionalities on the RTCP of magnetite, several lead additives have been successfully identified. Additives containing either acidic or basic groups such as L-lysine and 7-aminoheptanoic acid produced particles with a reduced size distribution, increased mean size, and proportion of faceted particles. Specifically, high-acyl gellan gum (HA-GG) produced highly faceted particles, with 74% of particles formed exhibiting a faceted particle shape. Triethylenetetramine (TETA) and tetraethylenepentamine (TEPA) were found to aid the synthesis of >84% faceted particles, a significant increase over the ~6% faceted particles exhibited in an additive-free control reaction. The ethylenediamine and glycolic functionalities have hence been identified as points of interest for further studies. These findings are significant as they begin to shed light on the mechanism on bioinspired additive controlled nanoparticles crystallisation, while also providing the first step to fully realising synthetic, controlled and scalable synthesis of MNP.

Introduction

Magnetite (Fe₃O₄) is a naturally occurring abundant iron oxide with ferric (Fe³⁺) and ferrous (Fe²⁺) ions in a 2:1 ratio. Magnetite nanoparticles (MNP) are seeing an increasing range of applications in industry, with their use spanning carbon-capture sorbents,¹ magnetic inks,² water purification,³ and critically, the biomedical industry. Research on magnetic nanoparticles (MNPs) is on the rise, with much of this research being centred on the future use of MNP in biomedical applications.⁴

The requirements for use in biomedical applications is stringent,⁵ with a particular emphasis on control over the shape and size of particles due to the impact of these factors on their action in the body as well as their magnetic properties. Superparamagnetic iron oxide nanoparticles (SPIONs) are a class of MNPs so small, typically less than 20nm,⁶ that they do not exhibit bulk magnetic properties, and rather behave like a paramagnetic atom. SPIONs and larger MNPs can be used for a range of magnetic nanomedicine, such as: targeted drug delivery (by magnetically directing drug-conjugated MNPs to a treatment site within the body);⁷ targeted magnetic hyperthermia^{8,9,10} and photothermia¹¹ therapy (once directed to

site, heating is induced by an alternating electromagnetic field or a laser respectively); contrast agents for magnetic resonance imaging (MRI) (with several Food and Drug Administration (FDA) approved iron oxide nanoparticle in medical use).¹²

Particles of specific morphologies have been noted in literature to offer enhanced nanomedical properties over particles which are either spherical or undefined in shape.¹³ For example, octahedral particles have been found to exhibit both increased relaxivity for MRI applications and higher heat absorbance for hyperthermic cancer treatment, offering a significant advantage over spherical particles.¹⁴

Mono-dispersed particles (same shape and size) are favoured due to the particle population having consistent magnetic and heating properties and consistent effect on the body.

While methods exist to synthesise faceted monodisperse magnetite in a range of shapes from cubic, octahedral, tetrahedral, to nanoflowers and nanorods,¹⁵ it remains a synthetic challenge to emulate these results under greener reaction conditions. Many known methodologies utilise high temperatures exceeding 100 °C, toxic-precursors, high boiling-point organic solvents,¹⁶ and costly vacuum procedures. When producing functional nanomaterials on an increased scale a sustainable manufacture route is essential for cost and the environment whilst it is also important to maintain morphological and size control.

Room temperature co-precipitation (RTCP) utilises greener reaction conditions, with water as a solvent and minimal use of energy intensive conditions.¹⁷ However, RTCP offers poor

^a Department of Chemistry, The University of Sheffield, Dainton Building, Brook Hill, Sheffield, S3 7HF, United Kingdom

^b Department of Chemical and Biological Engineering, The University of Sheffield, Mappin Street, Sheffield, S1 3JD, United Kingdom

Electronic Supplementary Information (ESI) available: [details of any supplementary information available should be included here]. See DOI: 10.1039/x0xx00000x

control over size, morphology, and iron oxide phase, with highly polydispersed populations of mixed iron oxides, unsuitable for biomedical use.¹⁸ Ideally a RTCP method must be improved to offer definition and control over particle crystallisation.

To achieve this, we need to look to Nature. Magnetotactic bacteria (MTB) are a diverse group of prokaryotes that create a unique magnetic organelle called a magnetosome, a lipid bound vesicle containing a single magnetic nanoparticle. MTB biomineralise these magnetosomes under ambient conditions facilitated by proteins to produce highly homogeneous MNPs. Such proteins like Mms6 controls the formation of MNP via nucleation of the forming mineral in the acidic -DEEVE C-terminus region of the protein.¹⁹ MmsF interacts with forming magnetite crystals through an acidic transmembrane loop which is thought to act similarly to Mms6, interacting with both iron ions and the forming magnetite crystals to control the particle shape.²⁰

When isolated these proteins have been used *in vitro* as additives to control RTCP reactions, facilitating the formation of more monodispersed, high-quality particles.^{18,20} Proteins, particularly membrane proteins, are both costly and difficult to produce and purify, making them unsuitable for industrial scale MNP production.

As well as native biomineralisation proteins, artificial proteins called magnetite interacting Adhirons (MIA) have also been used as additive to control the shape of MNPs, directing them to a cubic morphology under a RTCP route.¹⁹ A large quantity of basic residues such as lysine and histidine are present in the magnetite surface binding site. Modelling confirmed a preference for lysine to the [100] cubic face of magnetite, suggesting the control towards cubic particles is driven by preferential basic-protein/magnetite-surface binding.¹⁹

Protein additives have been used to control and enhance the quality of MNPs formed using RTCP reactions, with acidic residues being shown to aid nucleation of magnetite, and basic residues being found to bind to the magnetite surface to direct the final morphology. It therefore follows that other (non-protein) additives with similar chemical functional groups, may be able to control the crystallisations of MNPs. A bioinspired pipeline of: observing nature; using proteins *in vitro*; understanding the biomineralisation process; translating knowledge to identify simpler molecular bioinspired additives can thus be developed. Such a pipeline has been successfully demonstrated bioinspired silica production, with amine-based additives mimicking amine rich silaffins.²¹

Several other additives have also been shown to alter particle size in magnetite syntheses such as, heparin,²² montmorillonite clay,²³ plant leaf extracts,^{24–27} citric acid,²⁸ and other compounds.^{29–31} It is thus critical to fully understand how these additives are controlling particle formation and discover more additives capable of controlling the formation of tailored MNP, providing a toolbox of additives capable of producing a range of desired MNP products.

In this study we use Mms6 and MIA as a starting point to identify a range of new bioinspired additive to screen. Here, it is critical to cover a wide range of molecular additives spanning

a range of, functionalities, size, and structures to begin building the body of knowledge.

Experimental

Materials and methods

All reactions were carried out under an inert atmosphere of N₂, and all solutions sparged with N₂ for 30 minutes prior to use. Ultrapure Milli-Q water (Merck Milli-Q integral purification system) was used. Reagents were purchased from either Merck or Sigma Aldrich unless otherwise stated and used as purchased.

Room temperature co-precipitation

Iron(II) sulphate (111 mg, 0.4 mmol) and iron(III) sulphate (163 mg, 0.3 mmol) were dissolved in N₂ sparged Milli-Q water (20 mL) in a two-neck round bottom flask to form a 1 mmol Fe solution (Figure 1). A set amount of additive was added to the reaction mixture and left to stir for 5 minutes to ensure dissolution of additive and iron salts under an N₂ atmosphere. N₂ sparged 0.5 M NaOH (8 mL) was added at a rate of 50 μ L a minute with stirring, for a total of 160 minutes using a Harvard Apparatus 11 plus syringe pump driver. The reaction was left to age for an hour under the inert atmosphere, then magnetically separated, washed five times with sparged Milli-Q water to remove any non-magnetic iron oxide by-products, and the particles dried in a 40 °C vacuum oven overnight.

Characterisation

Transmission electron microscopy (TEM) 10 μ L of a 1mg/mL suspension of nanoparticles in hexane was dropped onto a carbon coated copper TEM grid and allowed to dry down. Grids were imaged using a FEI Technai G2 Spirit electron microscope and the TEM images were analysed using ImageJ software. > 200 particles per sample were randomly selected and measured (supplementary information S1 and S2 for full protocol on sample analysis).

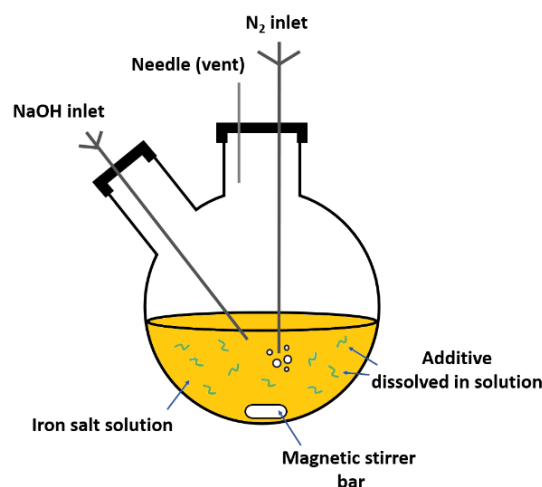


Figure 1. Schematic of the experimental set-up for the RTCP of magnetite.⁶¹

X-ray diffraction (XRD) XRD data was collected for dry nanoparticle samples in a Bruker D8 powder diffractometer. Diffraction images were collected at 0.022-degree increments from 20–80 degrees, with a fixed wavelength at $\lambda = 1.54178 \text{ \AA}$ from a Cu K α X-ray source.

Results

Lead additive screening

When tackling the task of designing a bioinspired molecular toolkit capable of tailoring the properties of magnetite MNPs, it is important to cover a range of functionalities based on the understanding and knowledge gained from natural systems and their derivatives.

Ideal additives would have the greatest positive impact on controlling shape, size, and composition, while also being non-toxic, environmentally friendly, and readily synthesisable or cheap and easy to procure. However, it is difficult to emulate the functionality of a highly specific three-dimensional folded protein in simpler compounds. The inherent lack of structured binding sites makes the design of a screening set of additives fit for the task challenging. As such, the set of selected additives have been inspired by the structure and functionalities of proteins found natively within MTB which exert control over the formation of uniform magnetosomes. The full list of bioinspired additives and their structures are shown in Table 1.

The nucleation and growth regime of crystallisation are known to be affected by a set of proteins in biomineralisation, which facilitate the formation of highly uniform particles.^{20,32,33} In general terms, acidic protein residues in larger numbers (assemblies of negatively charged protein surface) are known to bind to metal cations and aid nucleation of magnetite.^{34,35} We will therefore screen acidic amino acids and homopeptides to assess the importance of multiple acidic groups together.

Expanding the additive range to non-proteins, but still biological polymers, a series of polysaccharides were selected. The high number of hydroxy and carboxyl functionalities present in polysaccharides, coupled with the reduced flexibility of the sugar ring leads to the potential for these compounds to act as nucleators for magnetite nanoparticles. Hydroxy and carboxyl functionalities can bind metal ions,^{36,37} aiding the nucleation of minerals through local regions of high iron concentration.

Simpler polymers comprised of a simple chain with sp³ carbons in their backbone will also be investigated. These polymers will exhibit a greater degree of rotation than peptide

and sugar backbones, with three polymers being selected to observe the effects of alkyl and polyether backbones.

Small acidic molecules such as citric acid maintain the acidic properties which are favourable for MNP control in Mms6 and MmsF and have previously been observed to alter the properties of MNP formed under RTCP conditions.³⁰ Biomineralisation proteins aggregate to form regions of negative charge,³⁸ however, have been found to retain activity when the key functionalities of the biomineralisation proteins are displayed as active loops on a coiled coil. This suggests these regions of acidity remain effective when discrete, further directing us to screen small acidic compounds.

Basic residues and amine-rich molecules have been shown to bind to specific magnetite surfaces ([100]¹⁹ and [111]³⁹ respectively) offering control over the preferential growth of individual magnetite faces, defining a particles shape. The binding of homohexamers of each amino acid to bare MNP across multiple buffers revealed strong binding for both arginine and lysine.⁴⁰ Therefore, basic amino acids and homopeptides have been selected as potential additives.

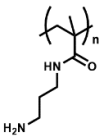
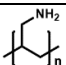
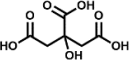
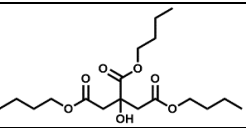
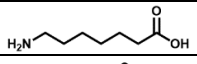
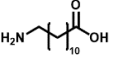
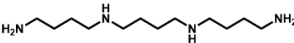
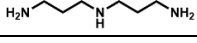
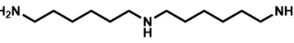
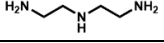
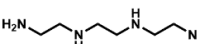
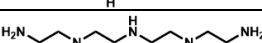
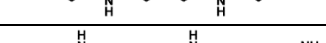
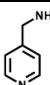
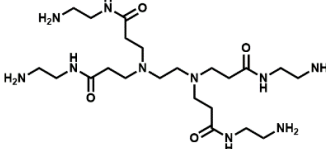
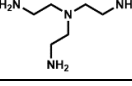
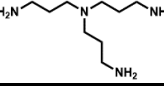
As monomeric L-lysine and L-arginine show affinity for magnetite binding and hence, shape-control,¹⁹ investigating alkylamines containing a range of chain length, N-N spacing, and C:N ratios allow for the influence of amine properties on morphological control to be assessed. An ethylenediamine (EDA) based range of amines each increasing in length by a singular C₂H₂(NH₂)₂ unit have been included in the screening to directly compare the effect of increasing chain length alongside identical functionalities and spacing.

Biomineralisation proteins play a significant role in modulating both the size and shape of magnetosomes. As these proteins contain a wide range of functionalities, both acidic and basic simultaneously, small molecule mixed functionality compounds containing both carboxyl and amine functionalities were included to probe whether it is possible to utilise a singular additive to control both shape and size of MNP.

The quantity of additive initially used in each precipitation reaction was relative to the number of functional groups present in the tested additive to ensure the same molar quantity of functionalities between reactions ($8 \times 10^{-8} \text{ mol}$). This additive concentration was determined from previous research wherein 5.6 $\mu\text{g/mL}$ of Mms6 was used as an additive to regulate the shape and size of MNP in a RTCP reaction.⁴¹ As the screening progressed, a concentration study was conducted on a simple amine additive to determine whether this concentration was still appropriate for tailoring particle shape. As nucleation and shape-control operate under different mechanisms, it was found a higher concentration of additive by a factor of 1000 was more appropriate for shape-controlling additives.

Table 1. Table of characterisation of magnetic nanoparticles formed with the addition of various bioinspired additives.

Sample (additive)	Structure	Mean particle size TEM (nm)	Percentage faceted particles (%)
Control A	N/A	22.5 ± 6.5	7
Control B		19.6 ± 6.2	5
Control C		20.8 ± 6.8	5
Average of control data		21.0 ± 6.5	6
8 × 10⁻⁸ mol of additive			
Poly-L-aspartic acid		14.7 ± 5.9	16
Poly-L-glutamic acid		33.2 ± 22.7	29
L-aspartic acid		18.5 ± 9.7	12
L-glutamic acid		19.9 ± 9.3	21
Poly-L-lysine		18.8 ± 9.4	23
Poly-L-arginine		17.4 ± 10.1	41
L-lysine		13.9 ± 4.2	55
L-arginine		18.5 ± 6.5	39
Gellan gum (high acyl)		21.4 ± 7.4	74
Dextrin		16.7 ± 5.8	16
Chitosan		13.6 ± 4.9	15
Alginate acid		11.8 ± 5.4	20
Polyethylene glycol (PEG)		15.2 ± 5.8	11

Poly(N-(3-Aminopropyl)methacrylamide) (PAPMA)		15.0 ± 5.1	18
Poly(allylamine)		15.5 ± 5.3	27
Citric acid		17.7 ± 9.2	15
Tributyl citrate		19.2 ± 8.4	17
7-Aminoheptanoic acid		17.9 ± 6.3	29
12-Aminododecanoic acid		18.3 ± 8.2	42
8 x 10⁻⁵ mol of additive			
Spermine, 5 µg		20.4 ± 7.1	25
Spermine, 50 µg		16.0 ± 5.5	32
Spermine, 500 µg		17.9 ± 6.2	40
Spermine, 5000 µg		22.6 ± 7.5	52
Spermine		17.5 ± 5.0	50
3'3-Diaminopropylamine		17.8 ± 6.3	48
Bis(hexamethylene)triamine		17.1 ± 6.8	90
Diethylenetriamine (DETA)		22.0 ± 6.6	42
Triethylenetetramine (TETA)		18.2 ± 5.4	96
Tetraethylenepentamine (TEPA)		22.4 ± 6.2	97
Pentaethylenhexamine (PEHA)		22.4 ± 7.7	91
4-(Aminomethyl)pyridine		15.4 ± 4.7	22
PAMAM, Gen 0		19.8 ± 5.9	31
Tris(2-aminoethyl)amine		14.3 ± 5.7	5
Tris(3-aminopropyl)amine		16.8 ± 5.2	14

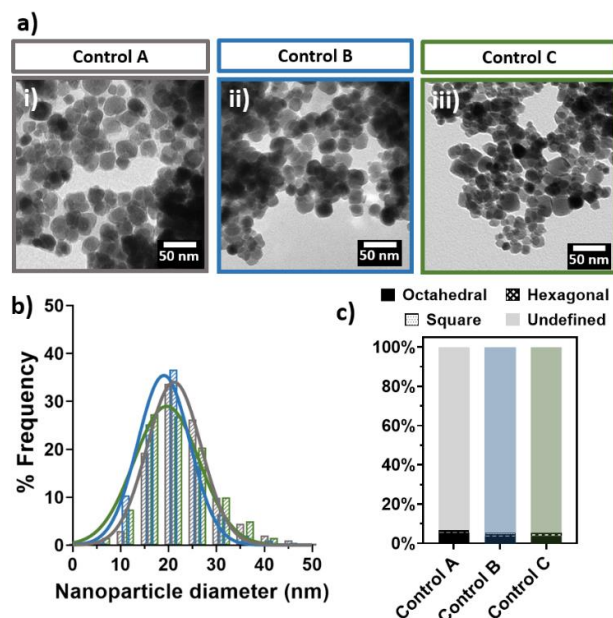


Figure 2. Comparison of three sets of magnetite nanoparticles formed with no additive. a) representative TEM images; b) particle size frequency distribution; c) comparison of shape analysis results.

Control reactions: Control reactions with no additive present were performed to produce particles without additives influencing the reaction pathway and products. The control reactions were conducted in triplicate to assess the inherent uncertainty in the RTCP process, and to increase the reliability of the result.

The particles collected were analysed via TEM and XRD to determine shape, size, and iron oxides present within the synthesised material. The TEM images were used to generate a frequency distribution and shape distribution of each sample, with the method of this further detailed in the supplementary. Three sets of control particles were synthesised to ensure reliability as these are the basis to which future particles will be compared, and as such it is crucial to establish a baseline by which to compare.

An average particle size of 21.0 ± 6.5 nm was observed across the triplicate reactions (Figure 2), with a high degree of polydispersity, and shape analysis suggesting most particles formed were undefined in morphology, and a poor degree of shape and size control was observed. Size and shape data of the three repeats can be seen in Table 1. Minor variations in control reactions are ascribed to the kinetic regime of the reaction leading to the synthesis of varied particles. Due to the time constraints of each synthesis and full set of analysis, the additive studies were not replicated

Homopeptides and amino acids: When considering Nature as inspiration from which to select and design additives, amino acids and homopeptides are a logical choice to observe the effects of the individual amino acid functionalities that comprise larger biomineralisation proteins.

Aspartic and glutamic acid play a crucial role in the -DEEVE nucleating section of Mms6,¹⁸ and co-polypeptide libraries used

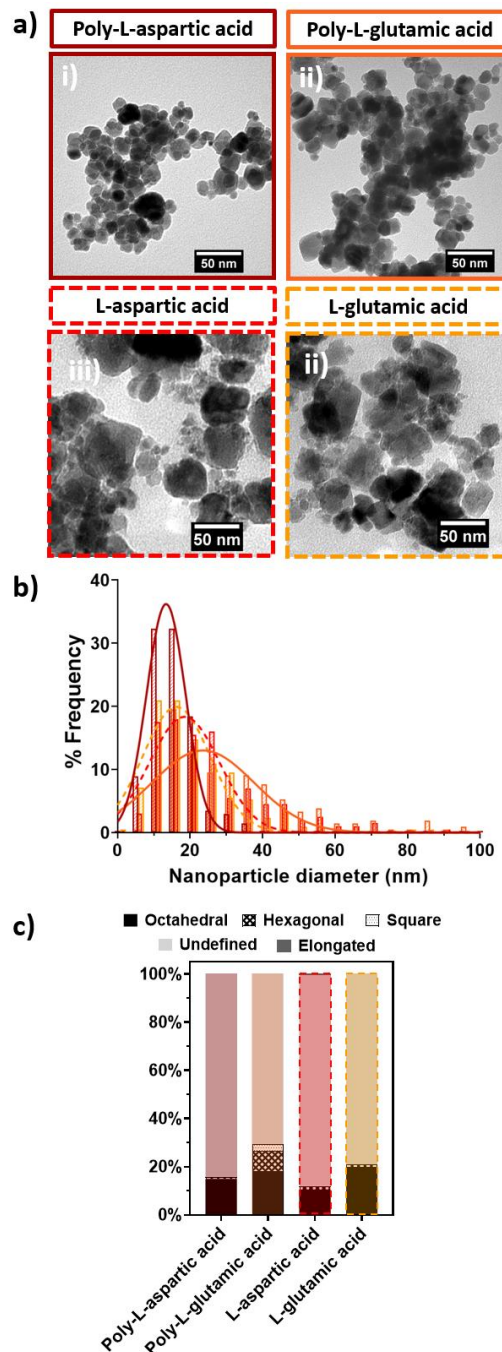


Figure 3. Comparison of effect of additives on magnetite nanoparticles formed with the addition of acidic homopeptides and amino acids a) representative TEM images; b) particle size frequency distribution; c) comparison of shape analysis results.

as additives in the synthesis of MNP have found the magnetic properties of the magnetite crystals can be regulated via the proportion of these key acidic functionalities.^{42,43} Lysine and arginine have been chosen to observe their potential influence on final particle morphology due to previous research and modelling studies showing basic amino acids bind the cubic

[100] face of magnetite, promoting shape-controlled particle growth.¹⁹

Both the homopeptide and amino acid forms have been selected to compare the effects of the presence of additional functionalities in the monomers as the additional carboxyl and amino groups present may play a different rule in influencing the reaction products, and to investigate the potential importance or effect of the peptide backbone. Due to being comprised of single repeat amino acids the homopeptides secondary structures have not been assumed. The chemical structures of the additives and properties of the particles formed with the addition of each additive used can be seen in Table 1.

TEM images (Figure 3a) show the change in particle response upon addition of the acidic homopeptides and amino acids. A general increase in standard deviation (SD) occurred (Figure 3b) with the exception of poly-aspartic acid which produced particles with a reduced mean diameter of 14.7 nm

and a SD of 5.9 nm. Interestingly, poly-L-glutamic acid, despite only differing in structure by a single $-CH_2$, produced the largest particles with the highest polydispersity of any additive increasing from 21.0 ± 6.5 to 33.2 ± 22.7 nm. This particularly diverse distribution occurred as the result of two types of particles being present leading to the appearance of a bimodal distribution. Particles greater than 100 nm in diameter and particles akin to those formed in control reactions were both observed. Each of the four acidic additives showed a small increase in percentage of faceted particles formed compared to the controls (Figure 3c), producing between 12-29 % faceted particles. Both the homopeptide and monomeric form of glutamic acid produced a higher percentage of faceted particles than their aspartic acid counterparts.

In the case of basic amino acids and homopeptides, TEM images (Figure 4a) and size distributions (Figure 4b) revealed both basic homopeptides also increased the polydispersity of particles formed, however did not increase the average size of particle formed. L-lysine reduced the particle size and SD to 13.3 ± 4.3 nm, the lowest polydispersity of the 30 additives screened. Whilst each of the four basic biological additives exhibited increased shape control (Figure 4c), this effect was most pronounced in L-lysine, producing 55% faceted particles.

The monomeric amino acids were found to impart a greater influence on the synthesised MNP than their homopeptide counterparts, simultaneously reducing the size range of particles produced, whilst aiding the formation of significantly more faceted particles than reactions with no additive.

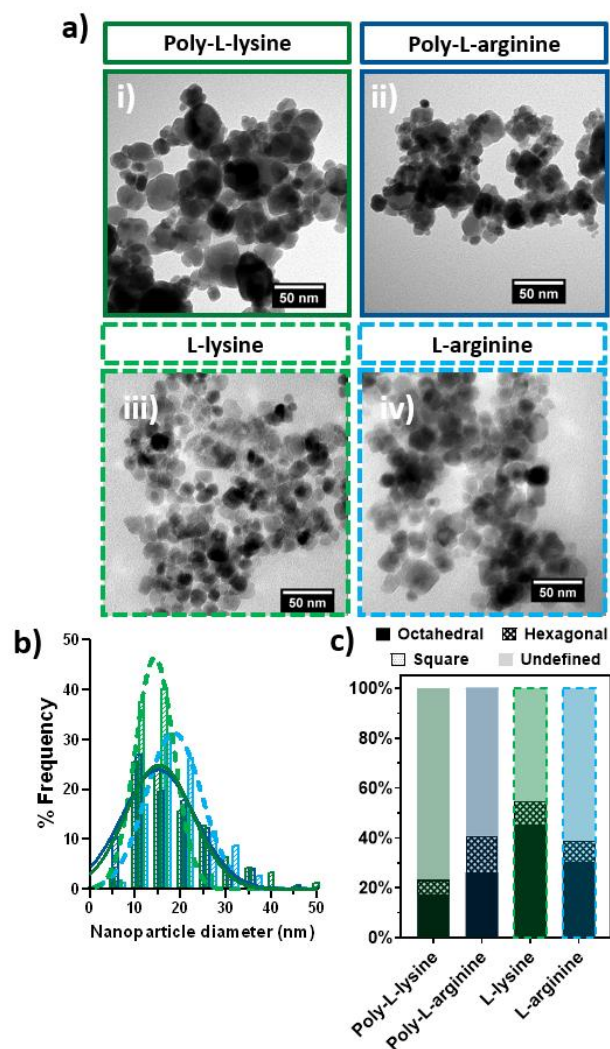


Figure 4. Comparison of effect of additives on magnetite nanoparticles formed with the addition of basic homopeptides and amino acids **a)** representative TEM images; **b)** particle size frequency distribution; **c)** comparison of shape analysis results.

Polysaccharides: Polysaccharides are polymeric carbohydrate molecules comprised of long chains of monosaccharides (sugars) connected via glycosidic bonds. Their linear regular repeating structure has previously been shown to template nanoparticles as in the case of heparin.²² Composites of MNPs and polysaccharides have been synthesised⁴⁴ and complexes of polysaccharides with iron have been observed to affect goethite, FeOOH, recrystallisation^{45,46} making them interesting candidates for influencing Fe₃O₄ particle formation. A range of polysaccharides were selected based on their differing properties and functional groups.

Gellan gum (GG) naturally occurs in a high-acyl (HA) form with a linear tetrasaccharide repeat unit consisting of D-glucose, D-glucuronic acid, and L-rhamnose repeat units. The high acyl form used in this study contains two acyl groups, acetate and glycerate, which are present on one of the glucose residues.

Dextrin has been selected as a relatively simple low molecular-weight polysaccharide consisting of only D-glucose units. The sugar backbone displays three hydroxy functionalities per repeat unit. Chitosan was selected due to its similarity in structure to dextrin, with one hydroxy functionality per sugar on the saccharide backbone being replaced with an amine group allowing for a direct comparison of the effect of the additional $-NH_2$ group. This allows for the biopolymer to serve as both cationic and anionic binding sites depending on pH.

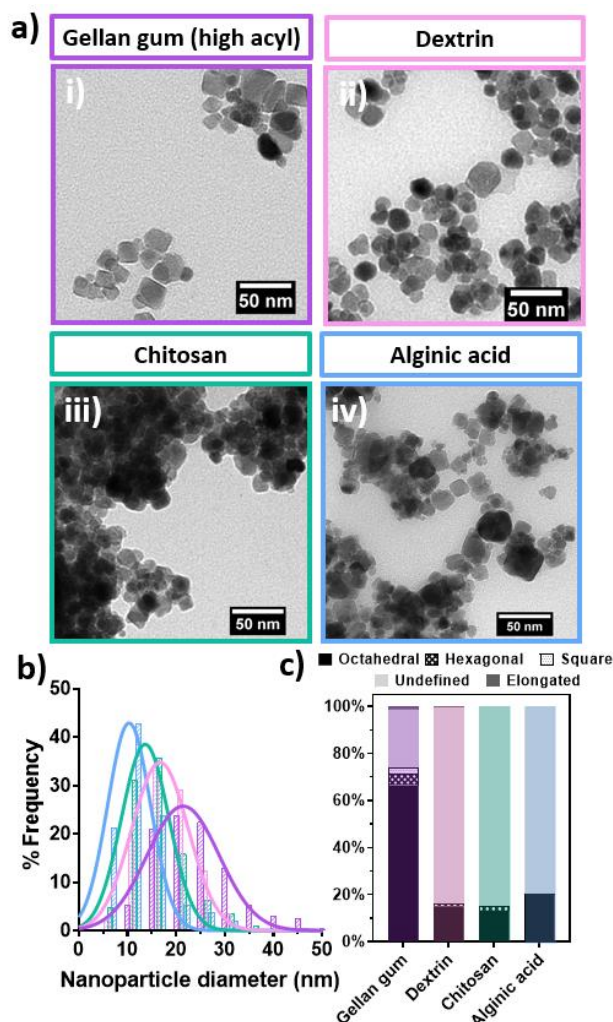


Figure 5. Comparison of effect of additives on magnetite nanoparticles formed with the addition of various polysaccharides. **a)** representative TEM images; **b)** particle size frequency distribution; **c)** comparison of shape results.

Chitosan is biocompatible and has the potential to be further functionalised to form cross-linked networks,⁴⁷ or by modification of its hydroxy and amino functionalities.⁴⁸

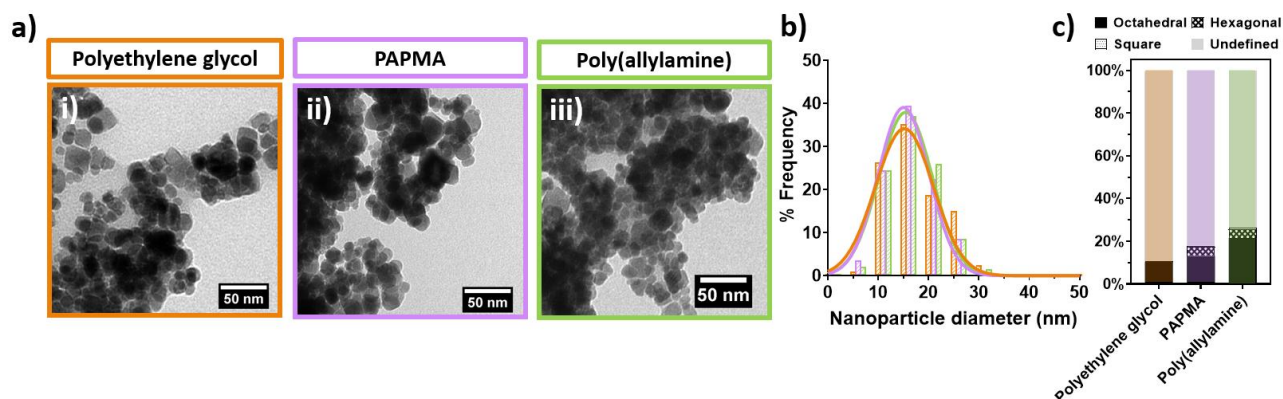


Figure 6. Comparison of effect of additives on magnetite nanoparticles formed with the addition of various polymers. **a)** representative TEM images; **b)** particle size frequency distribution; **c)** comparison of shape results.

Alginate is an unbranched glycuronan consisting of D-mannuronic acid (M-block), and its epimer L-glucuronic acid (G block), with alternating sequences of both D-mannuronic and L-glucuronic acid (MG-block) also occurring. The two monosaccharides are structurally identical, differing only in conformation (axial/equatorial).

Figure 5a-c shows a comparison of the particles formed in the presence of polysaccharide. Polysaccharide additives resulted in a general reduction in particle size, with dextrin, chitosan, and alginate each producing smaller particles than the control reactions. Chitosan and alginate each exhibited tighter size distributions than control particles. Alginate exhibited the most significant mean particle diameter decrease of 44% from 21.0 nm to 11.8 nm. HA-GG however, produced particles with a slight increase in size and SD.

Addition of HA-GG produced the highest proportion of faceted particles of the polysaccharide additives, with 74% of particles having a defined faceted shape. The other polysaccharides exhibited no significant increase in faceted particles.

Other Polymers: Due to the complexity in structure of homopeptides and polysaccharides, it is also prudent to test simpler polymers to observe if promising results can be achieved without the polymer backbone rigidity observed in proteins.

Polyethylene glycol (PEG) has previously been used as a surface stabilising agent and as a surface modifier for MNPs.⁴⁹ As this additive has an inherent lack of functional groups it has been selected to observe the effect of an inert polymer with no highly charged functionalities.

Poly(N-(3-aminopropyl)methacrylamide) (PAPMA) is designed to emulate the properties of basic polypeptides with decreased rigidity, potentially allowing for increased interaction of amine groups with forming magnetite particle surfaces.

Poly(allylamine) was also selected to see the effect of a polyamine on particle morphology as a cheap and readily available basic polymer with a simple $-NH_2$ side chain.

Each of the three polymers led to the production of smaller particles of 15.0-15.5 nm size range (Figure 6a-b), and an average polydispersity of ~ 5.4 nm. Minimal shape-control over control reactions was observed, with PAPMA (18% faceted) and poly(allylamine) (27% faceted) each showing a mild increase in shape-control over no additive being used.

Carboxyl and mixed functionality compounds: The possibility of additives capable of both nucleating and controlling the final morphology of particles would be promising for industry due to the increased economy and convenience of using a singular additive for multiple purposes. 7-aminoheptanoic acid and 12-aminododecanoic acid are readily available dual functionality

compounds, containing both a nucleating carboxylic acid group and an amine group.

Citric acid, a weak organic acid which is known to act as a chelator of iron ions^{50,51} was chosen to observe its nucleating effects in comparison to tributyl citrate, a similar compound replacing the carboxylic acid groups with esters which should have minimal effect on the size of particles formed and reinforce the necessity of acidic groups to modulate particle size.

TEM images and frequency distributions of the particles formed on addition of citric acid (Figure 7a-b) shows the formation of both large and significantly smaller particles within the sample. This is reflected in the increased SD of 9.2 nm, suggesting a wide range of particle sizes. Notably, tributyl citrate induced a similar effect with an increased size distribution also present despite no nucleating functionalities.

Both 7-aminoheptanoic acid and 12-aminododecanoic acid showed both an improvement in the morphology of particles formed, with 29% and 42% of faceted particles formed respectively (Figure 7c). The mixed functionality compounds however did not significantly affect either the polydispersity or size of particles formed.

Alkylamines: The success of monomeric L-lysine in modulating the shape of particles formed inspired the selection of a series of alkylamine additives with multiple amine functionalities. Varying chain lengths, N-N spacing, and C:N ratios have been selected to assess the influence of amine properties on morphological control. Polyamine compounds have the potential to act as iron chelators, with multiple amine functionalities forming co-ordination bonds to a charged iron centre to form a complex.

Spermine, 3'3-diaminopropylamine (3'3-DAPA), and bis(hexamethylene)triamine (BHETA) were selected due to their varying N-N spacing and C:N ratios which contrast with the ethylenediamine-based series to be screened, which have a repeat structure varying only by length. This allows the effect of these various factors to be observed.

Due to the differing modes of actions of additives nucleating vs modulating the surface properties of particles, different concentrations will be optimum for various additive functionalities. Additives designed to nucleate particles require lower concentrations on the μg scale, with previous additive quantities being calculated relative to prior research utilising proteins, as too many sites of nucleation will lead to significantly reduced particle size from the mass formation of nuclei. Amines which require interaction with surfaces to inhibit crystal growth will possibly require higher concentrations to optimally interact. However, if the amine concentration is too high there may be unselective binding and sub-optimal conditions for specific magnetite face formation. A large quantity of basic additive may also alter the reaction conditions negatively by altering the pH and chemical environment too significantly.

As such, spermine was tested at four concentrations (5-5000 μg) to ascertain whether there is a requirement for higher concentrations of alkylamine additives as a simple concentration study (Figure 8).

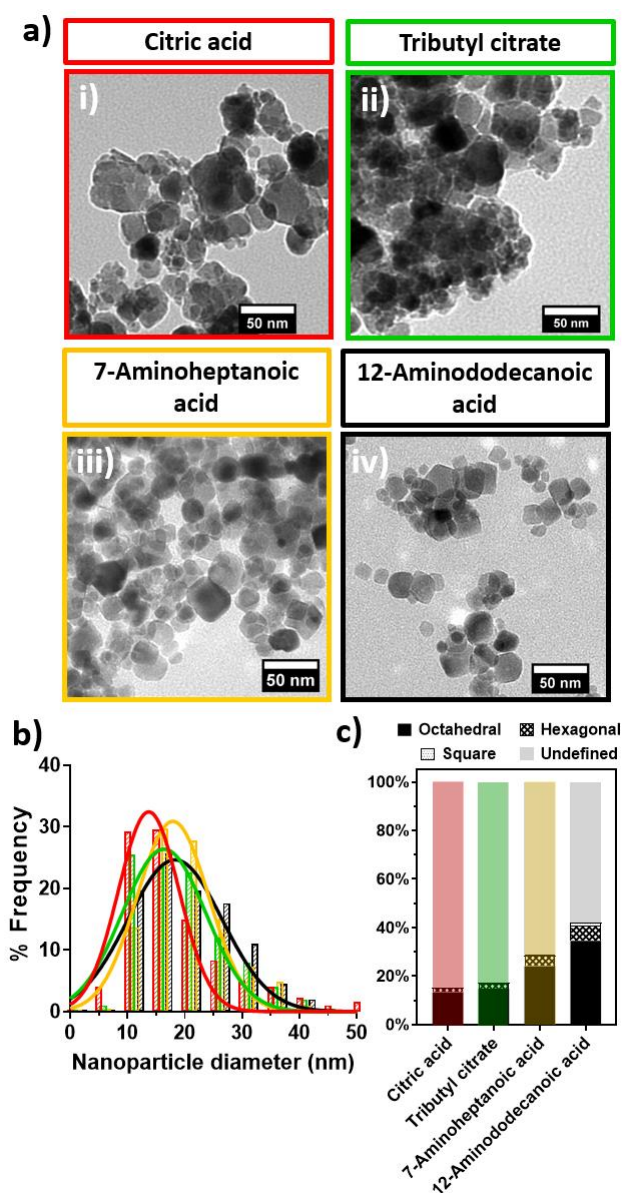


Figure 7. Comparison of effect of additives on magnetite nanoparticles formed with the addition of various carboxyl or mixed functionality additives a) representative TEM images; b) particle size frequency distribution; c) comparison of shape results.

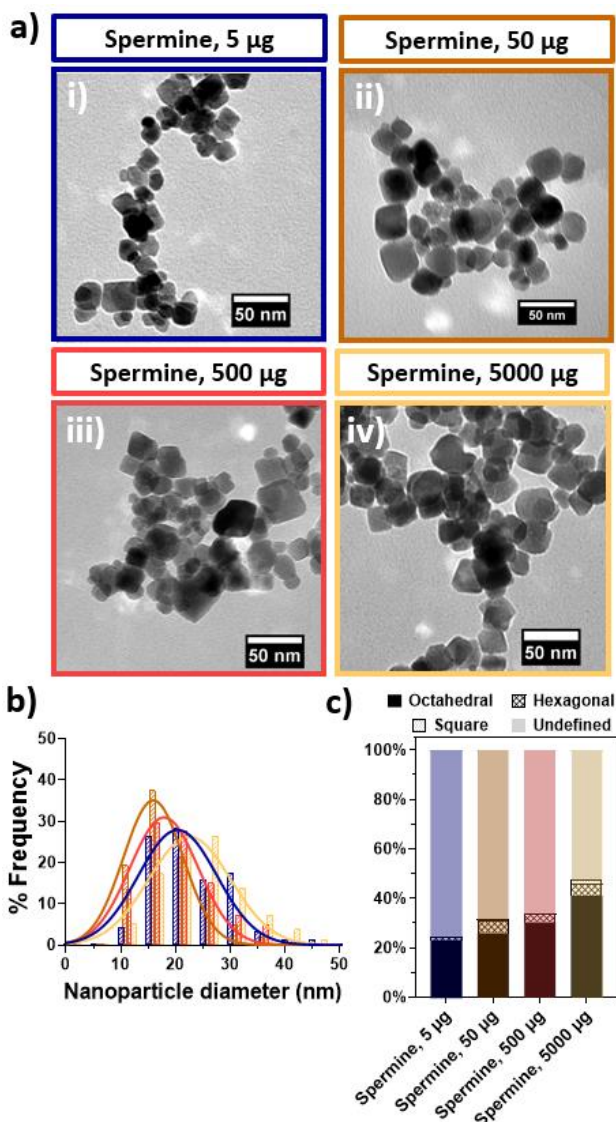


Fig 8. Comparison of effect of additives on magnetite nanoparticles formed with the addition of various quantities of spermine. **a)** representative TEM images; **b)** particle size frequency distribution; **c)** comparison of shape results.

The shape distribution of particles formed with spermine (Figure 8c) shows a steady increase in percentage of faceted particles as the amount of amine additive is also increased. As such, the following amine reactions have been carried out at a higher additive functionality concentration of 8×10^{-5} mol (Table 1).

Spermine, 3'3-DAPA, and BHETA (Figure 9) each produced particles comparable to control data in size, and polydispersity. Each of the amines, however, exhibited a significant rise in faceted particles, with 48-50 % for spermine and 3'3-DAPA and highly homogeneous faceted particles for BHETA (90% faceted) showcasing the promise of amines for shape modulation.

Ethylenediamine (EDA) series of amines: Diethylenetriamine (DETA), triethylenetetramine (TETA), tetraethylenepentamine (TEPA), and pentaethylenhexamine (PEHA) are a series of linear ethylenediamines which have found success in modulating the properties of mesoporous silica nanomaterials.⁵² EDA has been used as an additive to form magnetite nanowires, with a proposed theory that the chelation of iron ions lowers the concentration of free Fe ions in solution, slowing the reaction rate, which is favourable for the growth of nanowires.^{31,53} The DETA-PEHA series has been selected due to their homologous nature, making it possible to quantify the effect of increasing chain length.

The addition of any of the EDA based series of amines shows a marked increase in the formation of faceted particles (Figure 13), whilst having minimal impact on particle size. A sharp transition is observed from DETA to TETA with the addition of an extra EDA functionality having a substantial influence of 42% to 96% faceted particles formed. In the case of TEPA, some rod-shaped particles were also observed in the reaction, which can be typical of a goethite impurity.⁵⁴ This however was not supported by the XRD data (Figure 10) which showed only minor maghemite and hematite impurities. Morphological control drops minimally as the chain length increases, with TETA, TEPA, and PEHA each producing >95% faceted particles. The EDA series as additives led to a higher proportion of nanorod formation than other additives.

Morphological control drops minimally as the chain length increases, with TETA, TEPA, and PEHA each producing >95% faceted particles, making the ethylenediamine series a point of interest for further research.

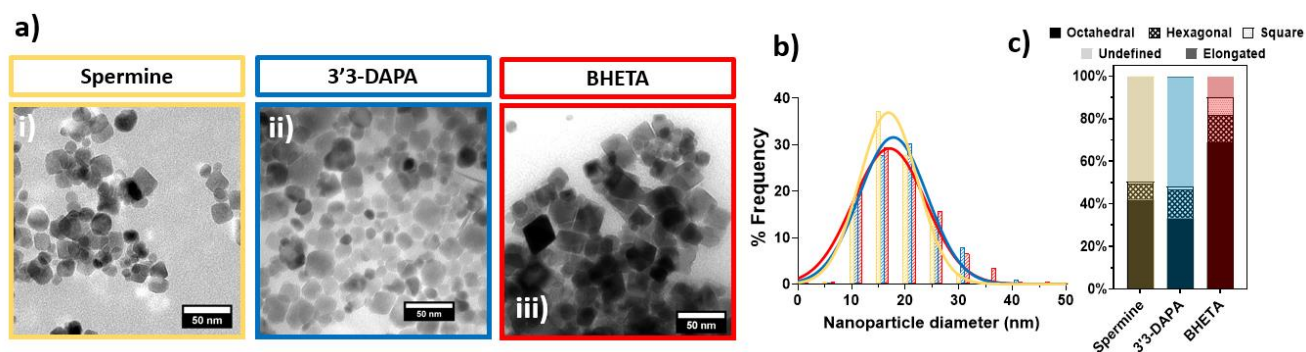


Figure 9. Comparison of effect of additives on magnetite nanoparticles formed with the addition of various alkylamines. **a)** representative TEM images; **b)** particle size frequency distribution; **c)** comparison of shape results.

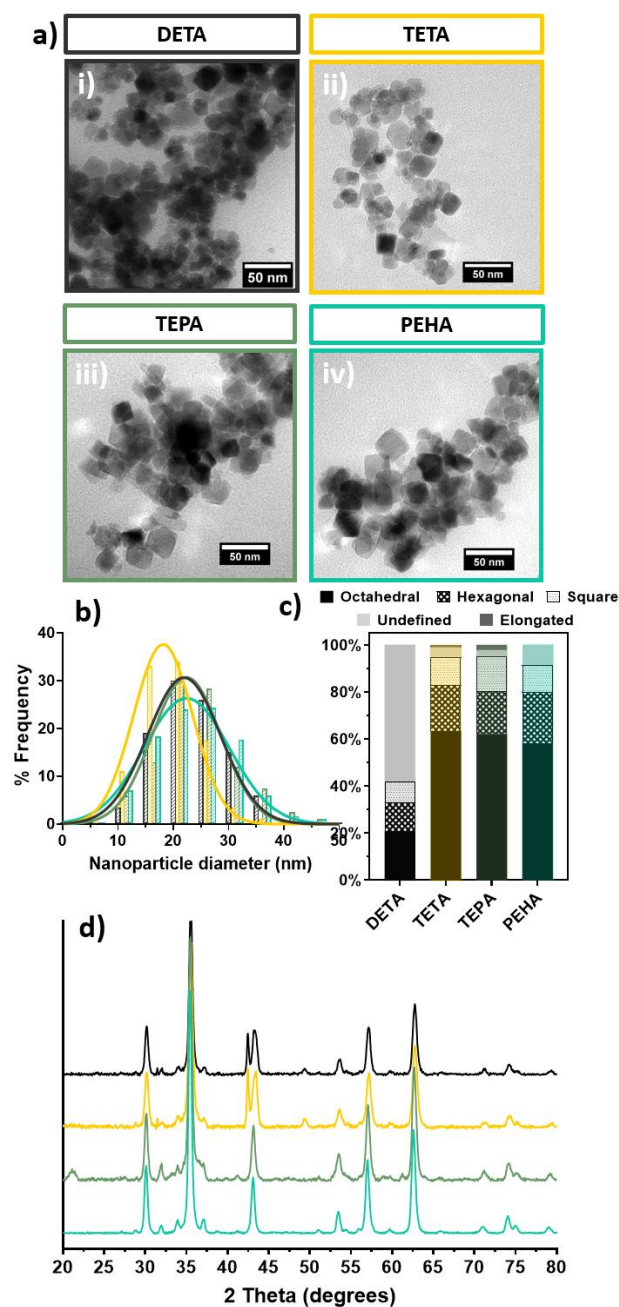


Figure 10. Comparison of effect of additives on magnetite nanoparticles formed with the addition of basic homopeptides and amino acids a) representative TEM images; b) particle size frequency distribution; c) comparison of shape analysis results, d) XRD data.

Branched and Other Amines: As primary, secondary, and tertiary amines will each interact differently with a magnetite surface, it is important to screen additives with different binding properties and structures.

4-(Aminomethyl)pyridine was chosen as an amine with vastly different properties to those screened thus far, with little similarity to the bioinspired additives selected thus far. Due to the aqueous nature of RTCP highly aromatic additives are incompatible with the methodology, however 4-(Aminomethyl)pyridine is water soluble.

Hydroxy-terminated polyamidoamine (PAMAM) dendrimers have been observed in literature to act as iron chelators, with the core tertiary amine functionalities coordinating to ferric iron centres.⁵⁵ PAMAM Gen 0 consists of an EDA core, functionalised with amidoamine branches each terminating in a primary amine group. This additive has been selected due to its uniform branched structure, amide functionalities (similar structure to homopeptide backbones), and potential for strong amine interactions with forming magnetite surfaces to tailor particle shape.

Tris(2-aminoethyl)amine and tris(3-aminopropyl)amine were selected to expand on the linear amines and investigate the effect of a branched structure in comparison to their straight chain analogues.

4-(Aminomethyl)pyridine showed no significant difference from control particles, with minimal shape control and a slight reduction in particle size ($15.4 \text{ nm} \pm 4.7 \text{ nm}$) (Figure 11).

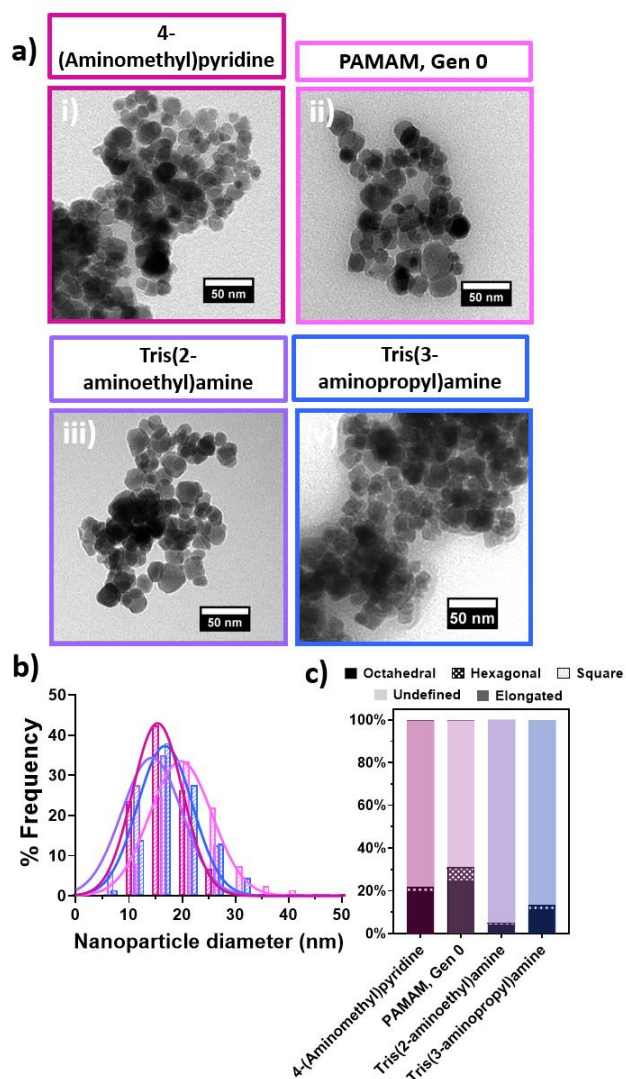


Figure 11. Comparison of effect of additives on magnetite nanoparticles formed with the addition of branched and other amines a) representative TEM images; b) particle size frequency distribution; c) comparison of shape analysis results.

Despite the success of EDA homologues at modulating the shape of particles produced, tris(2-aminoethyl)amine did not exhibit the same properties with 95% of particles formed appearing smooth and undefined in shape. A similar decrease in shape control was observed for tris(3-aminopropyl)amine compared to 3-3'-diaminopropylamine, which produced 48% faceted particles compared to 14% with the branched analogue.

The use of PAMAM dendrimer Gen 0 as an additive led to the formation of a higher proportion of faceted particles compared to a control (31% faceted), however not as efficient as any of the linear amines previously screened.

Discussion

When taking inspiration from MTB and their formation of magnetosomes, it is critical to consider the functionalities which make them effective in nature. In this study we drew inspiration from the structure and functionalities present in biomineralisation proteins,^{32,56} magnetite interacting Adhirons,¹⁹ and coiled coil proteins³³ to further our understanding of the role additives play in the development of environmentally sustainable yet highly homogeneous MNP.

On addition of the acidic homopeptides, the two homopeptides produced vastly different particles despite their similarity in structure, with only a single $-CH_2$ unit different on the side chain. Whilst addition of poly-L-aspartic acid produced MNP of reduced mean diameter and slightly reduced SD, addition of poly-L-glutamic acid produced particles with a wide size distribution and increased mean size. The TEM and size distribution (Figure 2a-b) of poly-L-glutamic acid suggest the formation of two particles types, with many particles resembling those formed in the control reaction, but also the presence of larger more faceted particles. The presence of multiple acidic groups may be acting as a preferential nucleation site, allowing early and specific nucleation leading to the presence of larger particles. This early nucleation would allow growth to occur over a longer timescale, leading to the formation of the unusually large crystals which are not commonly observed in the RTCP of magnetite.

The increased range of particle sizes formed with poly-L-glutamic acid suggests the additional flexibility afforded to the $-COOH$ group attached to the peptide backbone via the additional carbon atom (see Table 1 for structures) has a major effect on the function of the additive and how it can interact with constituents of the co-precipitation process. It is a possibility that the carboxyl functionalities on longer carbon chains have more freedom of movement to effectively space out from each other and bind iron ions in solution with less specificity. Molecular modelling studies to gauge the interactions of additives with magnetite would shed light on this difference in properties.

The two differing functional groups present on L-lysine (amine side chain and carboxyl) may be allowing L-lysine to simultaneously aid nucleation in the early stages of the reaction through the carboxyl functionality, and later interact with the growing surface of the MNPs to produce more highly faceted particles. The other two mixed-functionality additives, 7-

aminoheptanoic acid and 12-dodecanoic acid, each exhibit a rise in faceted particles, however produce wider size distributions than both L-lysine and control particles. L-Lysine and poly-L-aspartic acid are promising candidates for further research due to their reduced polydispersity, with the idea of using these additives in conjunction with L-lysine being added at a later point in the reaction than poly-L-aspartic acid to observe its effect on shape control when magnetite has already been nucleated.

Citric acid did not significantly alter the properties of MNP formed, however did increase the size distribution with several significantly larger particles being observed by TEM (Figure 7a). This was also observed for tributyl citrate, despite a lack of iron chelating groups. While the reason for this is not clear, perhaps the hydroxy groups are still able to bind iron ions, aiding the nucleation of larger particles, widening the resultant size distribution despite the presence of no carboxyl groups.

As carboxyl functionalities are easily deprotonated compared to hydroxy groups, alginic acid is more acidic than dextrin and chitosan, and hence has more deprotonated groups as the RTCP reaction progresses from low to high ($\sim 2-12$) pH on addition of base. As such, alginic acid may be able to nucleate a higher number of particles simultaneously, resulting in the reduced size of particles formed. Alginic acid has unusual conformations due to it being a copolymer comprised of block regions of mannuronic acid, guluronic acid, or regions of an alternating diblock copolymer, which may be allowing the additive to interact with the forming particles more effectively, with sugar groups aligned at differing angles.

In comparison to other polysaccharides, the percentage of faceted particles produced on addition of GG is exceptionally high (74%). Interestingly, GG contains no functionalities typically associated with the modulation of particle shape. Instead, the increased complexity of groups attached to the GG polysaccharide backbone may govern the shape control the additive offers with the longer glycerate group having the potential to flexibly interact with forming magnetite surfaces easier than groups attached directly to the sugar backbone. The glycerol functionality may be able to bind to a magnetite facet through its two alcohol groups, in a manner comparable to the function of the EDA based additives.⁵⁷ Another possibility is the ethylene spaced $-OH$ groups along the sugar backbone interacting with growing magnetite faces. This could be tested by using low-acyl GG as an additive to observe the difference in additive effect.

In the case of the simpler polymers, the three carbon backbone polymers are either basic or contain no strong nucleating functionalities such as $-OH$ or $-COOH$ groups, and as such it is consistent that the mean particle sizes and distributions would be comparable to reactions formed with no additive. Poly(allylamine) offered the highest percentage of shape-controlled particles (27%), however, performed worse than all of the shorter chain amines (DETA-PEHA, other alkylamines) The lack of shape control afforded by either of the basic polymers suggests that some backbone rigidity or structure may be required in polymers if shape is to be influenced.

The general increase in the percentage faceted particles formed on addition of amine-based additives is consistent with amine functionalities influencing MNP formation by binding to developing magnetite crystal faces, requiring a higher concentration to form a monolayer over the particle surface for a maximised effect. This mode of action is suggested by the spermine concentration study, with an increasing proportion of faceted particles forming as more spermine is available to bind growing magnetite faces. Our further concentration study shows an optimal concentration of additive is achieved, whereby too much additive results in the formation of less defined particles.⁵⁷

The EDA series of additives led to a higher proportion of nanorod formation than other additives. Morphological control drops minimally as the chain length increases, with TETA, TEPA, and PEHA each producing >95% faceted particles, making the ethylenediamine series a point of interest for further research. Further studies have been performed which include investigating the mechanism by which these additives interact with magnetite through molecular modelling, showing their ability to selectively bind the [111] magnetite face.⁵⁷

3'-Diaminopropylamine performed comparably to DETA, with each amine being similar in length and number of functionalities. This correlation appears to be more related to overall amine length rather than the number of amine functionalities present, as bis(hexamethylene)triamine also containing 3 amines performed similarly to PEHA, displaying enhanced morphological control. Bis(hexamethylene)triamine has a backbone length of 15 atoms, yet only 3 amine groups compared to PEHA's chain length of 16 with 6 amine functionalities. The similarity in results corroborates the idea of an optimum chain length rather than number of amine groups.

Despite the success of EDA homologues at modulating the shape of particles produced, tris(2-aminoethyl)amine did not exhibit the same properties with 95% of particles formed appearing smooth and undefined in shape. Compared to DETA, which produced 42% particles with faceted morphology, tris(2-aminoethyl)amine exhibited a significant decrease in shape control. The binding of tris(2-aminoethyl)amine to the particle

third amine primary amine group, leading to no preferential inhibition of a particular crystal face, and less control of particle morphology. A similar decrease in shape control was observed for tris(3-aminopropyl)amine compared to 3-3'-DAPA, which produced 48% faceted particles compared to only 14% with the branched analogue. This is speculated to be the result of similar reasons as discussed for tris(2-aminoethyl)amine.

The use of PAMAM dendrimer Gen 0 as an additive led to the formation of a higher proportion of faceted particles compared to a control (31% faceted), however not as efficient as any of the linear amines for producing highly faceted particles. The high number of branched amines may lead to more generalised facet binding, and hence less tailored morphological control compared to additives which selectively bind a single crystal face as there will be no selective growth inhibition. As such, none of these additives are considered points of interest for further research.

Conclusions

When planning scale-up of functional nanomaterials such as bespoke MNP, it is key to consider both the cost and environmental impact of the synthetic method. Taking inspiration from the high-quality materials formed in Nature and learning from the principles exhibited in Mms6 and MIA, several lead points have been identified for further research. This screening study compiles a range of structures and functionalities to ascertain solid starting points for further research into the green production of bioinspired MNP.

An initial additive study was conducted, with the aim of building on the current understanding of how compounds influence the RTCP of magnetite and select several starting lead additives for further work. The key additives found to influence the formation of MNP under RTCP conditions are outlined in Figure 12.

The dual functionality additive L-lysine appears promising, with L-lysine producing particles with the lowest polydispersity observed thus far of 4.3 nm and enabling the synthesis of particles of reduced diameter compared to those typically

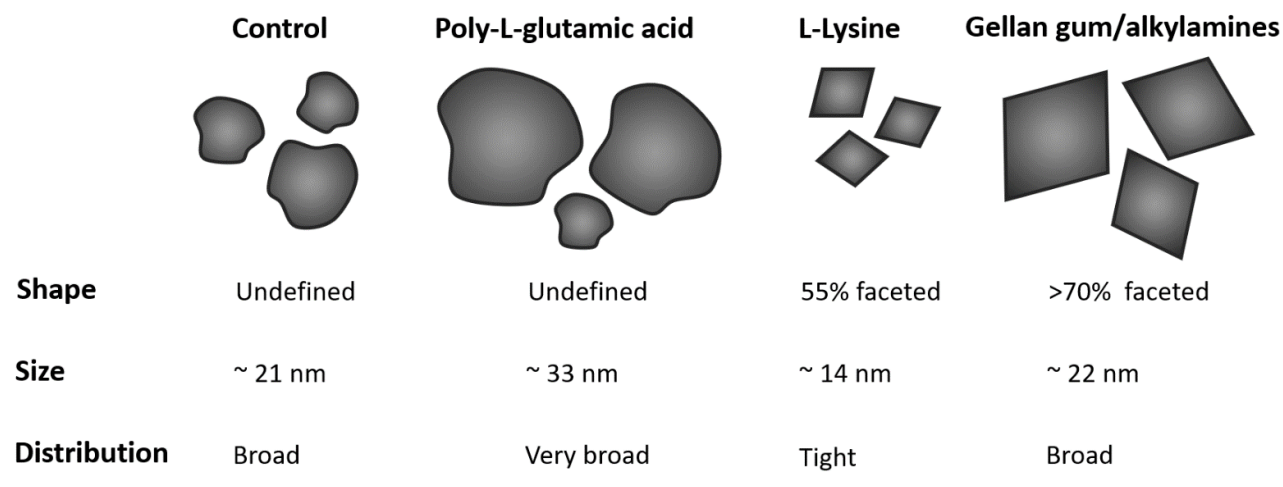


Figure 12. Summary of the key additives found to influence the properties of magnetic nanoparticles formed within room-temperature co-precipitation reactions.

producibile in RTCP, alongside significant shape control, forming 55% faceted particles.

HA-GG was found to exhibit an exceptionally high degree of morphological control, with 74% of particles formed exhibiting faceted morphology, whilst maintaining particle size. The high efficacy of HA-GG at low concentrations (8×10^{-8} mol per 20 mL reaction), and structure containing no amine groups typical of forming faceted particles suggest the morphological control of this additive is occurring through either the binding of other functional groups to forming magnetite surfaces, or a different mechanism.

TETA, TEPA, and PEHA each produced highly faceted particles, a significant increase from the 6% displayed in control reactions. Further research has been conducted on the effect of the EDA series of amines, finding they are proficient at modulating the shape of forming MNP and producing octahedral particles.³⁹

Conflicts of interest

There are no conflicts to declare.

Abbreviations

3'3-DAPA: 3'3-diaminopropylamine
BHETA: bis(hexamethylene)triamine
DETA: diethylenetriamine
EDA: ethylenediamine
FDA: Food and Drug Association
GG: gellan gum
HA: high-acyl;
MIA: magnetite interacting Adhiron
Mms: magnetosome membrane specific
MNP: magnetic nanoparticle
MRI: magnetic resonance imaging
MTB: magnetotactic bacteria
PAMAM: poly(amidoamine)
PAPMA: poly(N-(3-aminopropyl)methacrylamide)
PEG: polyethylene glycol
PEHA: pentaethylenhexamine
RTCP: room temperature co-precipitation
SD: standard deviation
SPION: super paramagnetic iron oxide
TEM: transmission electron microscopy
TETA: triethylenetetramine
TEPA: tetraethylenepentamine
XRD: X-ray powder diffraction

Acknowledgements

This work was supported by funding from the EPSRC (grant number EP/P006892/1) and the University of Sheffield's EPSRC DTP allowance (grant number EP/M508135/1) funds Laura Norfolk's PhD. We thank S. Tsokov, C. Hill (Sheffield Electron Microscopy unit) for TEM training, and Craig Robertson for support with powder XRD.

References

- 1 E. Y. Mora Mendoza, A. Sarmiento Santos, E. Vera López, V. Drozd, A. Durygin, J. Chen and S. K. Saxena, *J. Mater. Res. Technol.*, 2019, **8**, 2944–2956.
- 2 R. E. Rosensweig, *Sci. Am.*, 1982, 136–145.
- 3 R. Gregory, R. J. Maloney and M. Stockley, *Water Environ. J.*, 1988, **2**, 532–544.
- 4 Q. A. Pankhurst, J. Connolly, J. S. K and J. Dobson, *J. Phys. D. Appl. Phys.*, 2003, **36**, 167–181.
- 5 Y. Z. Joy Wolfram, Motao Zhu, Yong Yang, Jianliang Shen, Emanuela Gentile, Donatella Paolino, Massimo Fresta, Guangjun Nie, Chunying Chen, Haifa Shen, Mauro Ferrari, *Curr. Drug Targets*, 2015, **16**, 1671–1681.
- 6 J. Dulińska-Litewka, A. Łazarczyk, P. Hałubiec, O. Szafranski, K. Karnas and A. Karewicz, *Materials (Basel)*, 2019, **12**, 1–26.
- 7 Wahajuddin and S. Arora, *Int. J. Nanomedicine*, 2012, **7**, 3445–3471.
- 8 S. Laurent, S. Dutz, U. O. Häfeli and M. Mahmoudi, *Adv. Colloid Interface Sci.*, 2011, **166**, 8–23.
- 9 S. Mornet, S. Vasseur, F. Grasset and E. Duguet, *J. Mater. Chem.*, 2004, **14**, 2161–2175.
- 10 E. C. Vreeland, J. Watt, G. B. Schober, B. G. Hance, M. J. Austin, A. D. Price, B. D. Fellows, T. C. Monson, N. S. Hudak, L. Maldonado-Camargo, A. C. Bohorquez, C. Rinaldi and D. L. Huber, *Chem. Mater.*, 2015, **27**, 6059–6066.
- 11 J. Estelrich and M. Antònia Busquets, *Molecules*, 2018, **23**, 1–26.
- 12 Z. R. Stephen, F. M. Kievit and M. Zhang, *Mater. Today*, 2011, **14**, 330–338.
- 13 A. G. Roca, L. Gutiérrez, H. Gavilán, M. E. Fortes Brollo, S. Veintemillas-Verdaguer and M. del P. Morales, *Adv. Drug Deliv. Rev.*, 2019, **138**, 68–104.
- 14 J. Mohapatra, A. Mitra, M. Aslam and D. Bahadur, *IEEE Trans. Magn.*, 2015, **51**, 1–4.
- 15 W. Li, S. S. Lee, J. Wu, C. H. Hinton and J. D. Fortner, *Nanotechnology*, 2016, **27**, 1–7.
- 16 D. Maity, S. N. Kale, R. Kaul-Ghanekar, J. M. Xue and J. Ding, *J. Magn. Magn. Mater.*, 2009, **321**, 3093–3098.
- 17 M. C. Mascolo, Y. Pei and T. A. Ring, *Materials (Basel)*, 2013, **6**, 5549–5567.
- 18 A. E. Rawlings, J. P. Bramble, A. M. Hounslow, M. P. Williamson, A. E. Monnington, D. J. Cooke and S. S. Staniland, *Chem. - A Eur. J.*, 2016, **22**, 7885–7894.
- 19 A. E. Rawlings, J. P. Bramble, A. A. S. Tang, L. A. Somner, A. E. Monnington, D. J. Cooke, M. J. McPherson, D. C. Tomlinson and S. S. Staniland, *Chem. Sci.*, 2015, **6**, 5586–5594.
- 20 A. E. Rawlings, J. P. Bramble, R. Walker, J. Bain, J. M. Galloway and S. S. Staniland, *Proc. Natl. Acad. Sci.*, 2014, **111**, 16094–16099.
- 21 D. J. Belton, S. V. Patwardhan, V. V. Annenkov, E. N. Danilovtseva and C. C. Perry, *Proc. Natl. Acad. Sci. U. S. A.*, 2008, **105**, 5963–5968.
- 22 L. Ternent, D. A. Mayoh, M. R. Lees and G. L. Davies, *J. Mater. Chem. B*, 2016, **4**, 3065–3074.

- 23 C. Li, Y. Wei, A. Liivat, Y. Zhu and J. Zhu, *J. Nanomater.*, 2014, **2014**, 1–9.
- 24 V. V. Makarov, A. J. Love, O. V. Sinitysyna, S. S. Makarova, I. V. Yaminsky, M. E. Taliansky and N. O. Kalinina, *Acta Naturae*, 2014, **6**, 35–44.
- 25 Y. P. Yew, K. Shameli, M. Miyake, N. Kuwano, N. B. Bt Ahmad Khairudin, S. E. Bt Mohamad and K. X. Lee, *Nanoscale Res. Lett.*, 2016, **11**, 1–7.
- 26 A. M. Awwad and N. M. Salem, *Nanosci. Nanotechnol.*, 2013, **2**, 208–213.
- 27 I. P. Sari and Y. Yulizar, *IOP Conf. Ser. Mater. Sci. Eng.*, 2017, **191**, 1–5.
- 28 H. KAZEMZADEH, A. ATAIE and F. RASHCHI, *Int. J. Mod. Phys. Conf. Ser.*, 2012, **05**, 160–167.
- 29 Y. Kuwahara, T. Miyazaki, Y. Shirosaki, G. Liu and M. Kawashita, *Ceram. Int.*, 2016, **42**, 6000–6004.
- 30 W. L. Tan and M. A. Bakar, *J. Phys. Sci.*, 2006, **17**, 37–50.
- 31 D. Zhang, J. Zheng and Z. Tong, *J. Exp. Nanosci.*, 2010, **5**, 162–168.
- 32 A. Arakaki, J. Webb and T. Matsunaga, *J. Biol. Chem.*, 2003, **278**, 8745–8750.
- 33 A. E. Rawlings, L. A. Somner, M. Fitzpatrick-Milton, T. P. Roebuck, C. Gwyn, P. Liravi, V. Seville, T. J. Neal, O. O. Mykhaylyk, S. A. Baldwin and S. S. Staniland, *Nat. Commun.*, 2019, **10**, 1–9.
- 34 S. M. Bird, A. E. Rawlings, J. M. Galloway and S. S. Staniland, *RSC Adv.*, 2016, **6**, 7356–7363.
- 35 A. Bürger, U. Magdans and H. Gies, *J. Mol. Model.*, 2013, **19**, 851–857.
- 36 S. J. Armistead, A. E. Rawlings, C. C. Smith and S. S. Staniland, *Environ. Sci. Technol.*, 2020, **54**, 13963–13972.
- 37 F. M. Al-Sogair, B. P. Operschall, A. Sigel, H. Sigel, J. Schnabl and R. K. O. Sigel, *Chem. Rev.*, 2011, **111**, 4964–5003.
- 38 S. S. Staniland and A. E. Rawlings, *Biochem. Soc. Trans.*, 2016, **44**, 883–90.
- 39 S. S. S. Laura Norfolk, Klaudia Kapusta, David Cooke, .
- 40 S. P. Schwaminger, S. A. Blank-Shim, I. Scheifele, P. Fraga-García and S. Berensmeier, *Faraday Discuss.*, 2017, **204**, 233–250.
- 41 Y. Amemiya, A. Arakaki, S. S. Staniland, T. Tanaka and T. Matsunaga, *Biomaterials*, 2007, **28**, 5381–5389.
- 42 V. Dmitrović, J. J. M. Lenders, H. R. Zope, G. De With, A. Kros and N. A. J. M. Sommerdijk, *Biomacromolecules*, 2014, **15**, 3687–3695.
- 43 J. J. M. Lenders, H. R. Zope, A. Yamagishi, P. H. H. Bomans, A. Arakaki, A. Kros, G. De With and N. A. J. M. Sommerdijk, *Adv. Funct. Mater.*, 2015, **25**, 711–719.
- 44 G. A. Kloster, D. Muraca, C. Meiorin, K. R. Pirota, N. E. Marcovich and M. A. Mosiewicki, *Eur. Polym. J.*, 2015, **72**, 202–211.
- 45 C. S. Chan, S. C. Fakra, D. C. Edwards, D. Emerson and J. F. Banfield, *Geochim. Cosmochim. Acta*, 2009, **73**, 3807–3818.
- 46 M. Nesterova, J. Moreau and J. F. Banfield, *Geochim. Cosmochim. Acta*, 2003, **67**, 1185–1195.
- 47 Ş. Öztöp, H.N., Saraydin, D. & Cetinus, *Appl. Biochem. Biotechnol.*, 2002, **101**, 239–249.
- 48 A. Jain, A. Gulbake, S. Shilpi, A. Jain, P. Hurkat and S. K. Jain, *Crit. Rev. Ther. Drug Carrier Syst.*, 2013, **30**, 91–181.
- 49 M. M. Yallapu, S. P. Foy, T. K. Jain and V. Labhasetwar, *Pharm. Res.*, 2010, **27**, 2283–2295.
- 50 N. Mobarra, M. Shanaki, H. Ehteram, H. Nasiri, M. Sahmani, M. Saeidi, M. Goudarzi, H. Pourkarim and M. Azad, *Int. J. Hematol. Stem Cell Res.*, 2016, **10**, 239–247.
- 51 I. Gautier-Luneau, P. Bertet, A. Jeunet, G. Serratrice and J. L. Pierre, *BioMetals*, 2007, **20**, 793–796.
- 52 D. J. Belton, S. V. Patwardhan and C. C. Perry, *J. Mater. Chem.*, 2005, **15**, 4629–4638.
- 53 J. J. Zhu, Q. F. Qiu, H. Wang, J. R. Zhang, J. M. Zhu and Z. Q. Chen, *Inorg. Chem. Commun.*, 2002, **5**, 242–244.
- 54 T. Ahn, J. H. Kim, H. M. Yang, J. W. Lee and J. D. Kim, *J. Phys. Chem. C*, 2012, **116**, 6069–6076.
- 55 M. R. Mankbadi, M. A. Barakat, M. H. Ramadan, H. L. Woodcock and J. N. Kuhn, *J. Phys. Chem. B*, 2011, **115**, 13534–13540.
- 56 D. Murat, V. Falahati, L. Bertinetti, R. Csencsits, A. Körnig, K. Downing, D. Faivre and A. Komeili, *Mol. Microbiol.*, 2012, **85**, 684–699.
- 57 L. Norfolk, K. Kapusta, D. J. Cooke and S. S. Staniland, *Green Chem.*, 2021, **23**, 1–12.

The role of biological and bioinspired additives in the green synthesis of magnetite nanoparticles

Laura Norfolk,^a Siddharth Patwardhan,^b Sarah Staniland^a

Supplementary information

Particle Sizing Methodology:

This methodology has previously been published in Norfolk et al.¹

Particle measurements are taken across the longest axis of each particle to ensure consistency between measurements using ImageJ software. Approximately 200 measurements are taken from each sample to get an accurate measure of mean size given the variety in particles per sample. To avoid human bias in which particles are selected for analysis, particles are analysed from a single “area” of a TEM image to prevent small or large particles being selectively measured. Several images are analysed for each sample to ensure a representative sample is taken.

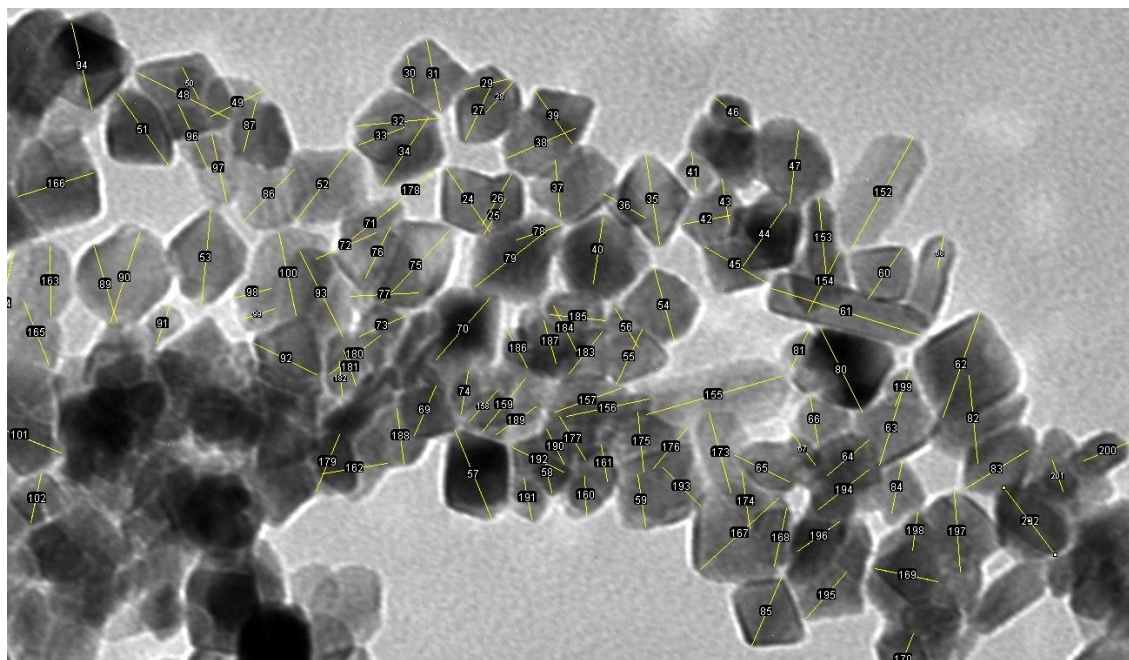


Figure S1: Screenshot of ImageJ particle sizing showing particles are analysed in clusters.

Particle Shape Analysis Methodology:

Images are manually analysed using drawing software (Inkscape, Paint.net, etc) by marking each particle a shape with a set colour (figure S2). A minimum of 300 samples are marked from several different images to ensure a representative sample is selected. The particles are then counted, at which point the shape assignment is checked a secondary time to maximise accuracy. Sample particle shapes can be seen in figure S3.

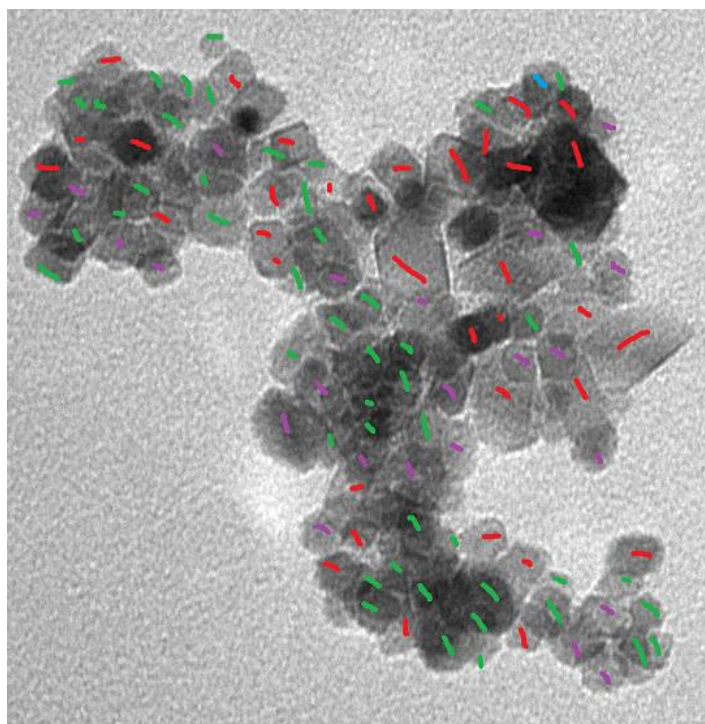


Figure S2. Example image analysis showing octahedral (red), undefined (green), and hexagonal (purple) particles.

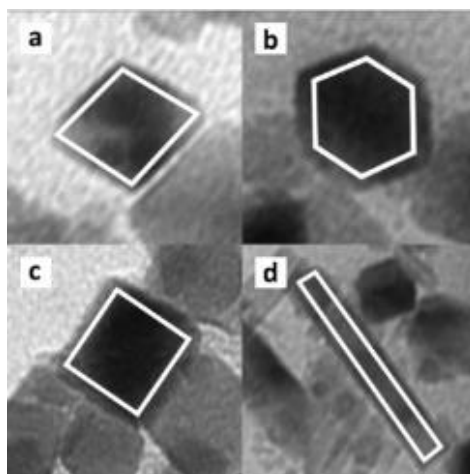
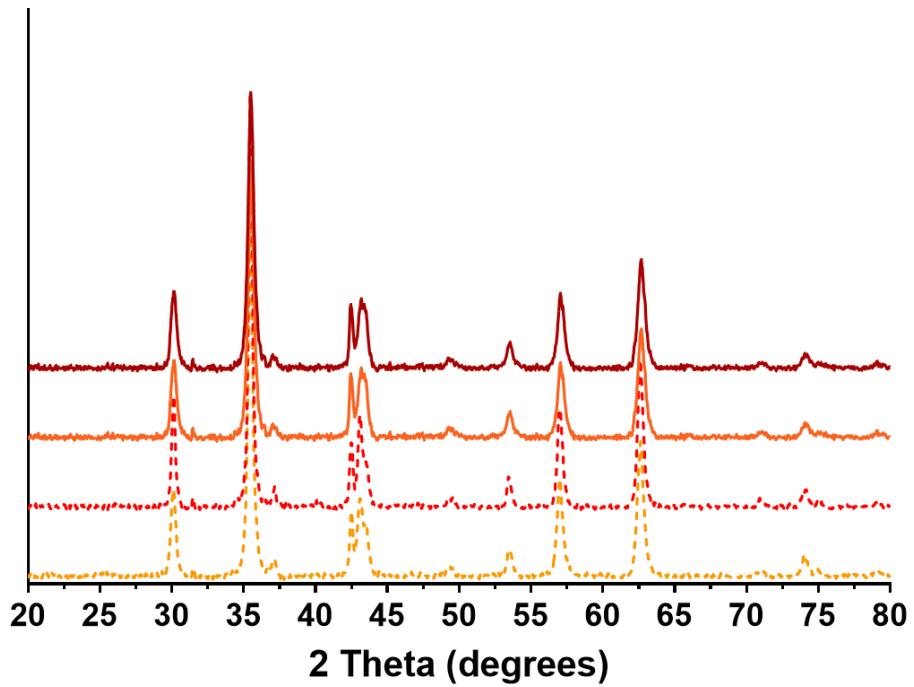
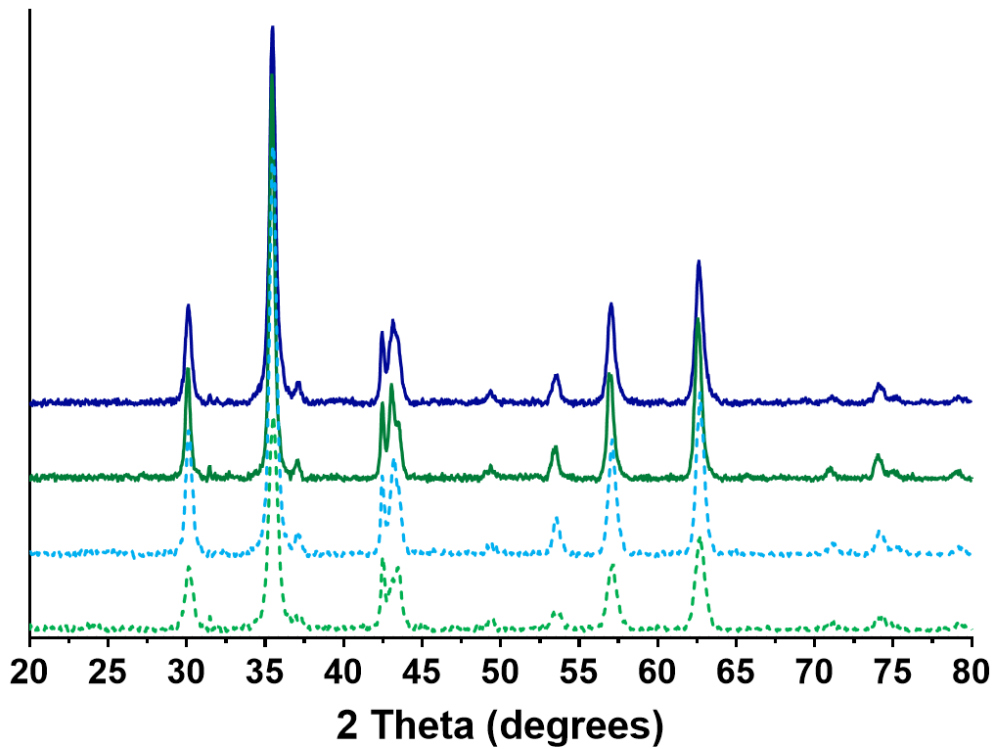


Figure S3. Sample particle shapes from TEM analysis; **a)** Octahedral; **b)** Hexagonal; **c)** square; **d)** rod/elongated.



— Poly-L-aspartic acid — Poly-L-glutamic acid - - - L-Aspartic acid - - - L-Glutamic acid
 Figure S4. XRD data of particles formed with the addition of acidic homopeptide and amino acid additives.



— Poly-L-arginine — Poly-L-lysine - - - L-Arginine - - - L-Lysine
 Figure S5. XRD data of particles formed with the addition of acidic homopeptide and amino acid additives.

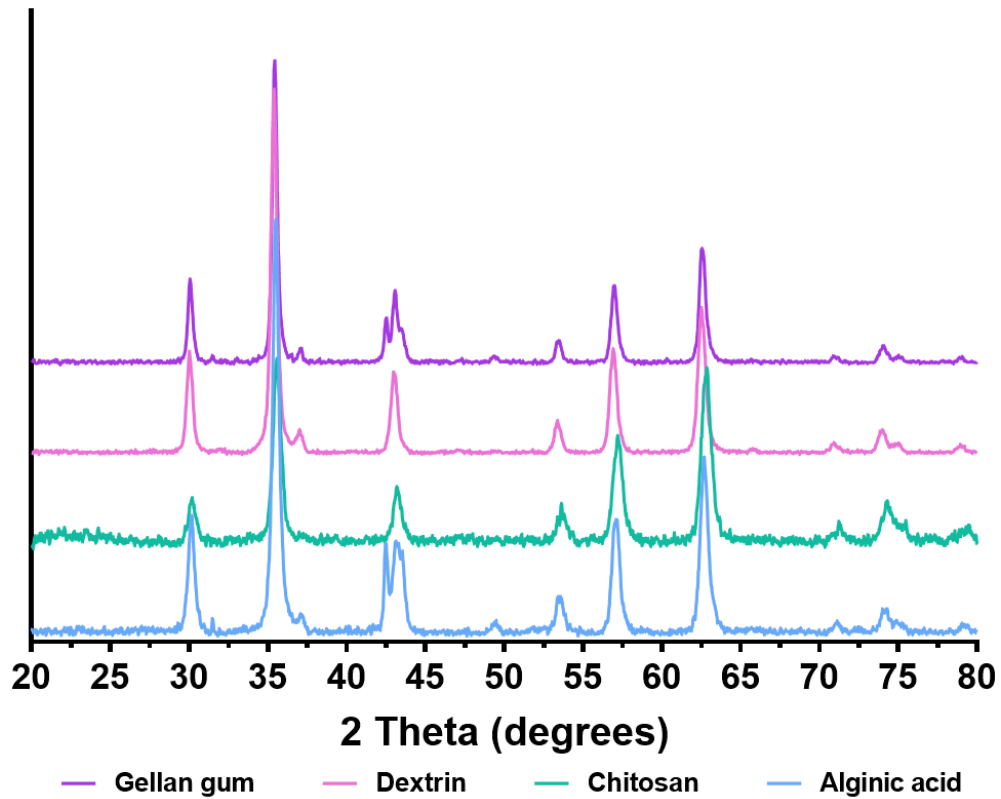


Figure S6. XRD data of particles formed with the addition of polysaccharide additives.

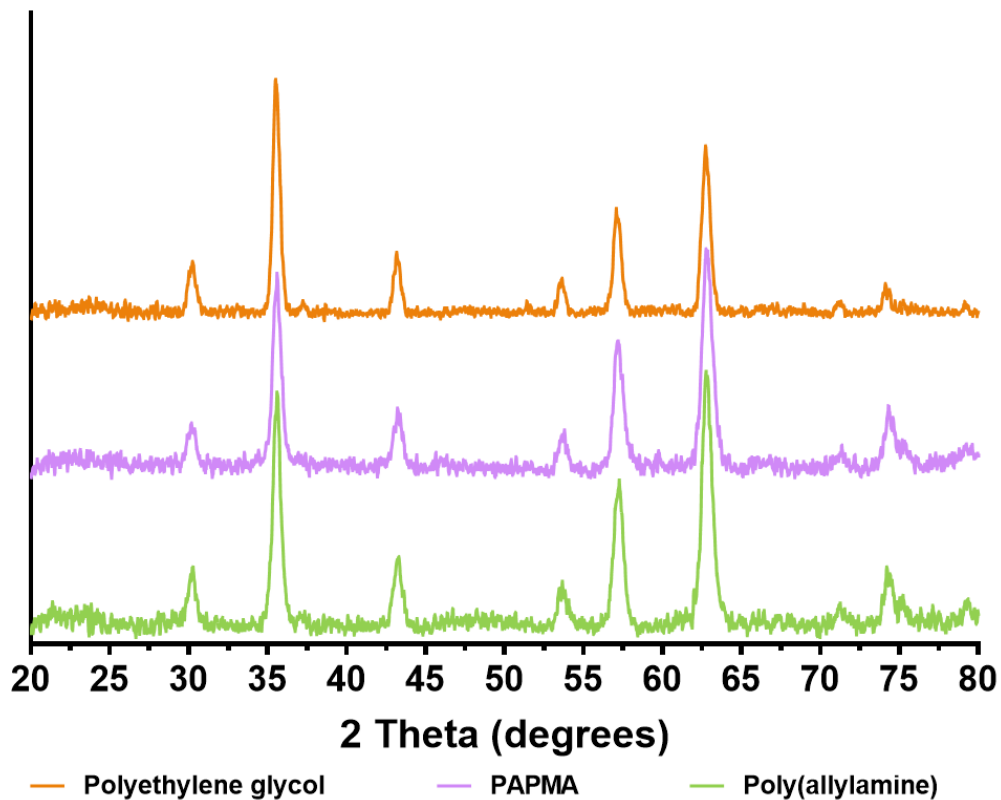


Figure S7. XRD data of particles formed with the addition of carbon backbone polymer additives.

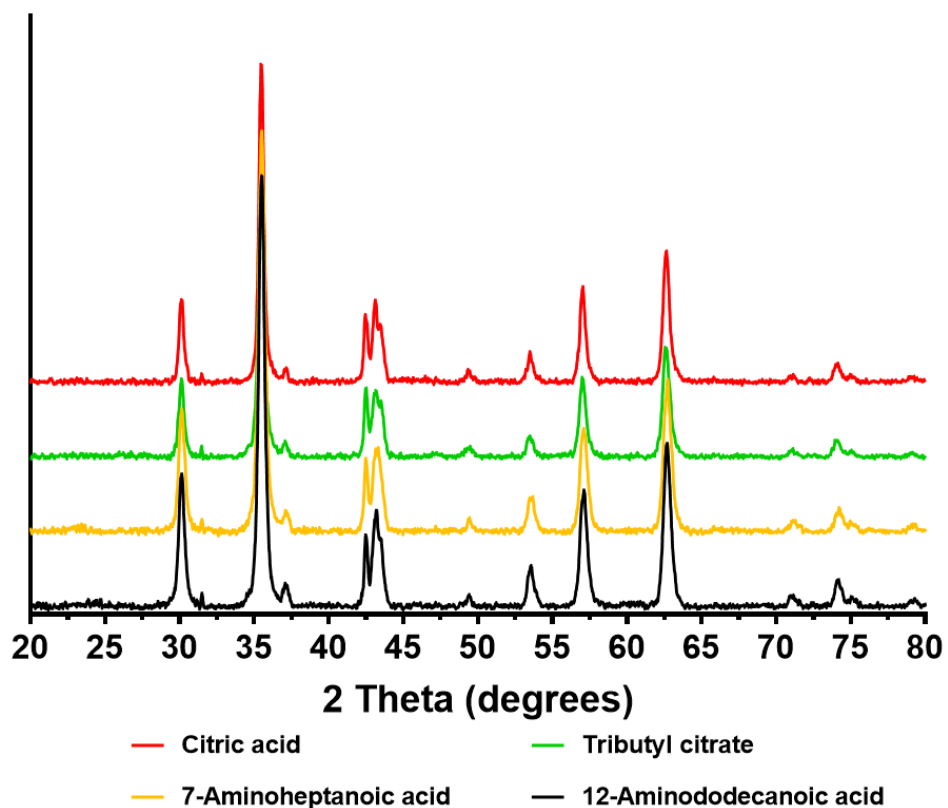


Figure S8. XRD data of particles formed with the addition of carboxyl and mixed functionality based additives.

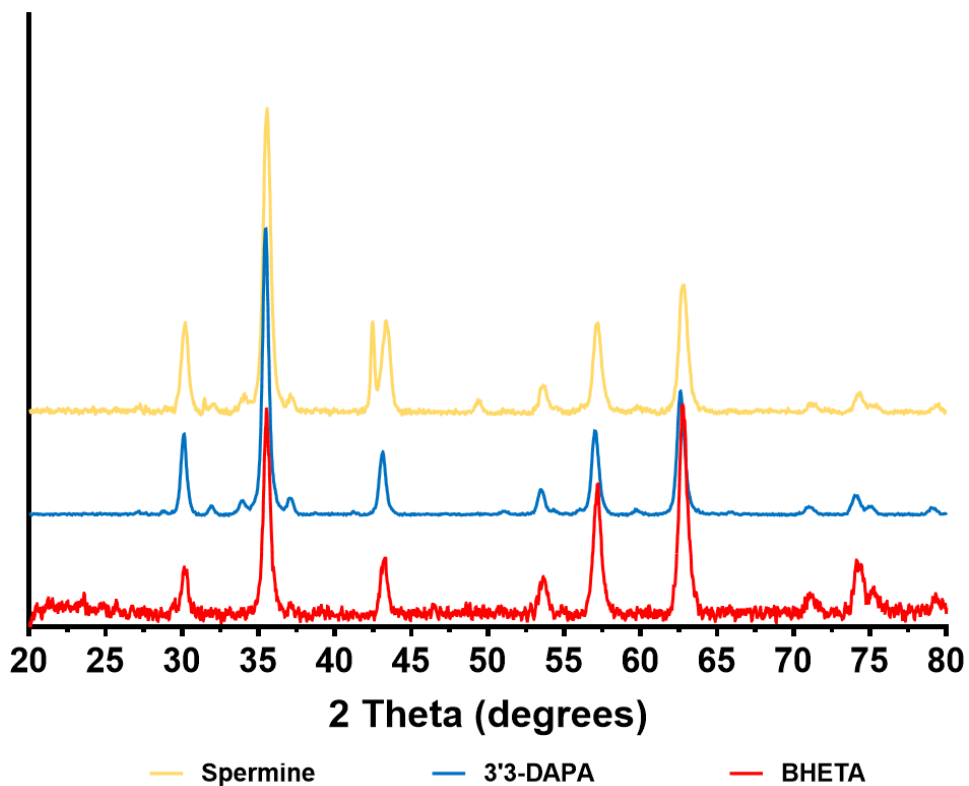


Figure S9. XRD data of particles formed with the addition of alkylamine additives.

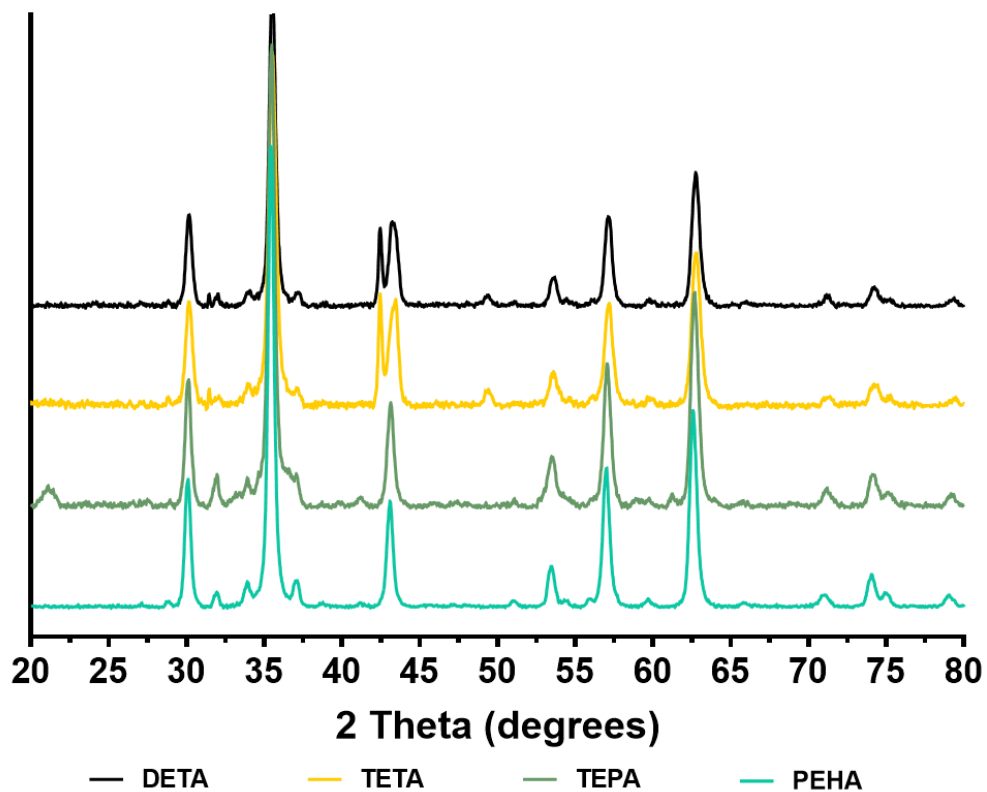


Figure S10. XRD data of particles formed with the addition of ethylenediamine series additives.

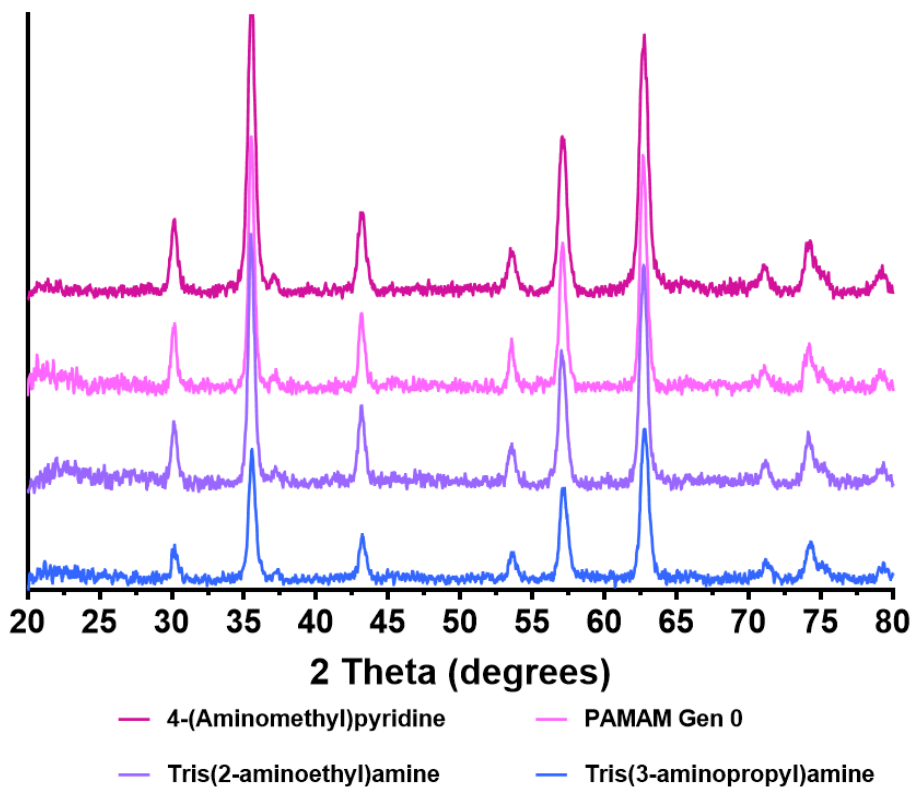
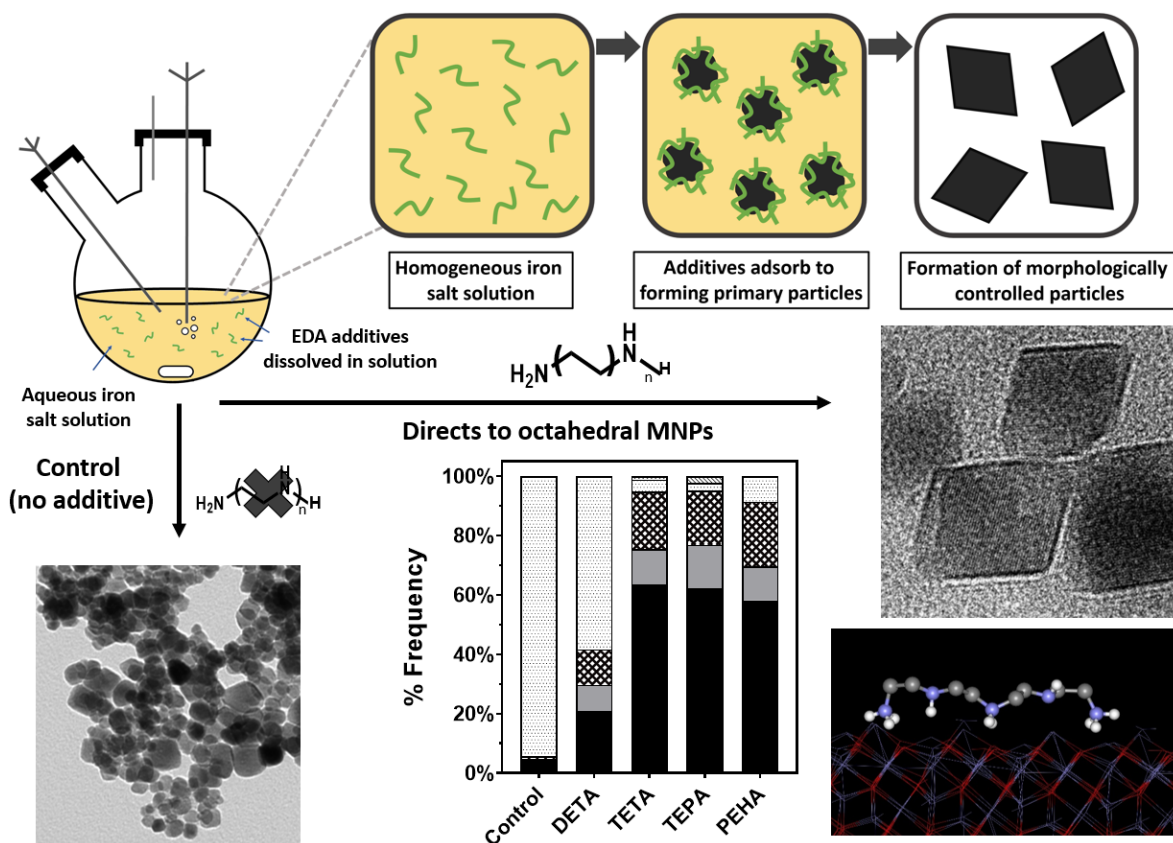


Figure S11. XRD data of particles formed with the addition of branched and other amine additives.

Chapter 4.

Ethylenediamine Additives



This chapter is a published paper for RSC Green Chemistry titled 'Ethylenediamine Series as Additives to Control the Morphology of Magnetite Nanoparticles Using Green Reaction Conditions'.

DOI: 10.1039/D1GC01539G

4.1 Ethylenediamine Series as Additives to Control the Morphology of Magnetite Nanoparticles Using Green Reaction Conditions

4.1.1 Author Contributions

Laura Norfolk (first author): Selected additives for research, carried out experimental work, analysed particles formed (XRD, TEM, HRTEM, TGA, FTIR, shape analysis, and size analysis), designed and created figures, wrote first draft of paper, and created the supplementary and figures.

Klaudia Kapusta: Summer student, assisted with molecular dynamics modelling of DETA-PEHA.

David Cooke: Wrote computational modelling section, ran molecular dynamics modelling for the paper, and calculated adsorption energies.

Sarah Staniland (principal investigator): Supervisor, acquired project funding, assisted in re-drafting, partially wrote the introduction and discussion, as well as helping with editing the manuscript and supplementary.



Ethylenediamine series as additives to control the morphology of magnetite nanoparticles†

Cite this: DOI: 10.1039/d1gc01539g

Laura Norfolk,^a Klaudia Kapusta,^a David Cooke^b and Sarah Staniland^a

Magnetite nanoparticles play a key role in the nano-industry, with crucial importance in the developing nanomedicine sector. Such particles must be homogeneous, with a consistent shape and size, due to the growing need to tailor particles to more defined faceted morphologies. Here an ethylenediamine series ($\text{H}_2\text{N}-(\text{--CH}_2\text{CH}_2\text{N--})_n\text{H}_2$, $n = 2$ (DETA), 3 (TETA), 4 (TEPA), and 5 (PEHA)), of additives have been successfully used to control the morphology of nanomagnetite produced *via* a green ambient co-precipitation method. Whilst DETA showed less control, TETA, TEPA and PEHA mediated the near universal synthesis of faceted particles (91–97%) suggesting a near pure octahedral population (compared to only 6% of control particles). The particle size was ≈ 22 nm for all the samples and was not affected by the addition of additives. Computational molecular dynamic modelling shows the binding to the octahedral [111] face to be preferred for all additives with binding to the [100] face unfavourable for TETA, TEPA and PEHA, showing a preference to bind and direct an octahedral morphology for these 3 additives. This is further explained by the increased numbers of interactions of the longer additives with the [111] surface through O and Fe in the magnetite surface bonding to H and N in the additive which is better able to lie flat on the [111] surface. An optimum concentration of a 1 : 125 additive : iron ion ratio was determined which shows that a relatively small quantity of a cheap, organic bioinspired amine-rich additive can have a massive impact on the morphological quality of the magnetite nanoparticles. This powerful, additive-directed, green synthesis approach could be universally applied to a vast range of nanomaterial syntheses to great impact.

Received 2nd May 2021,
Accepted 24th June 2021

DOI: 10.1039/d1gc01539g

rsc.li/greenchem

Introduction

In recent years, magnetite (Fe_3O_4) nanoparticles (MNPs) have been extensively researched for their widespread applications in industry such as their use in magnetic inks¹ and carbon capture,² and importantly, their wide potential in the biomedical industry.^{3–6} Their use is being realised as Magnetic Resonance Imaging (MRI) contrast agents,⁷ drug delivery systems,⁸ and hyperthermic cancer treatments.⁹

For any application, control over the size, shape, composition, mono-dispersity and reproducibility is beneficial, but it is critical with MNPs for nanomedicine, with the ability to precisely tune the particles to specific requirements – a much sought-after feature of production. Monodispersity is key to ensure uniform, consistent and predictable magnetic properties, anatomical uptake, anatomical distribution and therapeutic dosing/effects.

Control over the size is essential (1) to understand the surface area and thus dosing levels; (2) to direct the anatomical location (as different sized MNPs concentrate in different parts of the body); and (3) to tune the magnetic response, with smaller MNPs exhibiting superparamagnetism with profound effects on hyperthermic heating.¹⁰

Control over the shape also varies the properties of the nanomedicine. Due to particle nuclei formation requiring a low surface area to volume ratio, the smallest MNPs will be spherical. While being highly dependent on the reaction conditions, as the MNP grows, magnetite's low index crystal faces ($\gamma[111] < \gamma[100] < \gamma[110]$) tend to be favoured in the final crystal form.¹¹ As such, a typical equilibrium morphology is cubo-octahedral (a truncated cube which appears spherical) incorporating a reduced surface area and the most stable [111] and [100] facets.¹² However, more faceted (non-spherical) MNPs have been shown to offer the most promise across a range of nanomedicines. For example, cubic nanoparticles have been found to be preferable for contrast agents compared to spherical particles (with similar volumes),^{13,14} while angular “nanoflower” shaped MNPs have been found to have higher hyperthermic heating compared to spherical MNPs.^{15,16} This is thought to be due to the physical effect of the points and edges.^{15,16} As such, the demand for non-spherical faceted

^aDepartment of Chemistry, The University of Sheffield, Dainton Building, Brook Hill, Sheffield, S3 7HF, UK. E-mail: s.s.staniland@sheffield.ac.uk

^bDepartment of Chemical Sciences, The University of Huddersfield, Huddersfield, HD1 3DH, UK

† Electronic supplementary information (ESI) available. See DOI: 10.1039/d1gc01539g



MNPs in the biomedical industry is on the rise with synthetic control over the size, shape, and crystal quality of particles being crucial.

Whilst many syntheses exist to carefully tailor the morphology (shape and size) of MNPs, most of these techniques require environmentally unsustainable reaction conditions, increasing the negative environmental impact of the syntheses. The manufacture of cubic or nanoflower MNPs currently requires high temperature,^{17,18} alongside a range of organic reagents, or microwaves,¹⁹ while octahedral MNPs require an elevated temperature to allow the kinetically favoured [111] facet to dominate.²⁰ These synthetic routes are not green, demonstrating a general problem with inorganic nanomaterial synthesis: precisely faceted nanomaterial production requires highly wasteful and less environmentally friendly synthesis.

Magnetite can be easily synthesized on a large scale using a room-temperature co-precipitation (RTCP) reaction (Fig. 1a). The addition of a base such as NaOH, KOH, or Et₄NOH to an aqueous solution of ferric and ferrous iron under an inert atmosphere at room temperature produces iron oxides without the use of toxic solvents/reagents.²¹ This is a fast and straightforward green synthesis, with no use of high energy processes such as heating or vacuum pressure allowing for large volumes of particles to be produced. The disadvantage of this green synthesis is that there is very little control over the final product, with a broad size distribution (5–40 nm) of an undefined/pseudo-spherical shape with little opportunity to tailor the morphology.

Within the green chemistry remit (ambient conditions), some control can be offered by changing the reaction conditions, using such systems as micro-²² and milli-fluidic flow synthesis²³ or pH-regulated synthesis;²⁴ however, these methods are not currently scalable to large-scale production and offer less control over the particle shape.

The use of additives in a green RTCP is an established method to offer control over nanoparticle synthesis.²⁵ Grafted co-polymer additives have been used to control the size of magnetite MNPs²⁶ while there are many examples of green/natural additives being used such as unrefined seaweed²⁷ and plant leaf extracts in the synthesis of MNPs,^{28–30} as well as citrate,³¹ oxalic acid³² and chitosan.³³ Green additives such as fruit juice and sea buckthorn have also been used to control the size of gold³⁴ and silver^{35,36} nanoparticles. However, all these examples produce spherical particles or particles of undefined morphology. Clearly, shape is more difficult to control with additive synthesis, with the green synthesis of tailored faceted MNPs offering a greater challenge.

Highly uniform, morphologically controlled MNPs are observed in nature, for example within magnetotactic bacteria. These unique bacteria foster the ability to precisely control the synthesis of MNPs using magnetosome membrane specific (Mms) biomineralisation proteins such as Mms6^{37–41} and MmsF.⁴² This has translated to the successful use of several Mms proteins as biological additives to mediate the formation of enhanced MNPs in simple RTCP syntheses. Purified Mms6, MmsF and an MmsF protein mimic⁶⁰ have been used *in vitro* to control particle formation in RTCP reactions, with increased control over the size (Mms6) and morphology (MmsF) and magnetite mineral purity (both) compared to protein free reactions.^{38,39,41,42,60}

Recently, by screening an (Adhiron) affimer protein phage-display library against cubic [100] magnetite (labelled MIA (Magnetite Interacting Adhiron)), we identified a protein additive that specifically directs the formation of cubic MNPs. The resulting MIAs were found to contain high levels of basic residues, particularly lysine.⁴³ Molecular dynamics simulations showed the amino acid lysine to have the lowest adsorption energy to the magnetite [100] surface through amine inter-

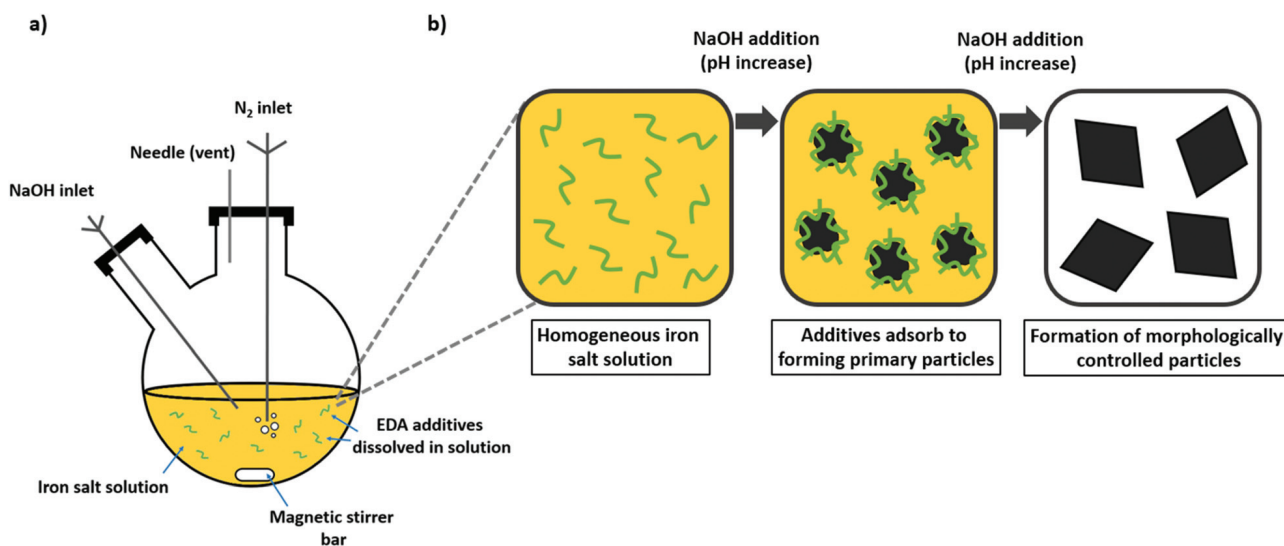


Fig. 1 (a) Schematic of the experimental setup for an RTCP reaction containing an organic additive or protein *in vitro*. (b) The reaction progression on addition of NaOH is shown, with the role of additives adsorbing to the surface of forming primary particles, and finally the production of morphologically controlled particles.



actions with the surface.⁴³ Adsorption of MIA additives to the magnetite [100] surface of a developing crystal results in stabilizing and propagating that surface allowing it to dominate the final (cubic) particle structure. This was seen in RTCP reactions where cubic MNPs were formed when mediated by an MIA protein additive, a morphology previously only accessible using organic solvents and high-temperature methods. From this work, we saw that the amine rich additive controlled the MNP morphology through adsorption to the magnetite surface.⁴³

Whilst complex proteins are green additives capable of specific crystal face binding to control morphology, they are very expensive to produce compared to the other additives cited above. For example, a commonly used arginine based synthetic protein costs £49 per mg,⁴⁴ with more bespoke and membrane proteins costing multiple times more. In this study, we take a systematic approach to understand morphology controlling protein additives and use this to develop cheaper bioinspired additives to mediate the RTCP of faceted MNPs.

We identify the importance of amine groups for interacting with magnetite surfaces to control their morphology. In this study, we screen an ethylenediamine series (amines linked with aliphatic CH₂CH₂ spacers of various lengths) as bioinspired additives for RTCP of faceted MNPs. Ethylenediamines are small, simple and cheap additives for a green RTCP synthesis that pose a more realistic commercially viable proposition for scale-up and green manufacture at a millionth of the cost of a protein additive (tetraethylenepentamine is £55.30 per kg (ref. 45)), demonstrating that this method could be used for the green production of magnetite on an industrially viable scale.

If the nanomaterial industries, particularly biomedical, are to continue to expand and precisely faceted MNPs are required on a larger scale, it is critical to develop synthetic methods that offer substantial reductions in energy usage and manufacturing carbon footprint whilst still offering precise control over the nanomaterial properties. Here we demonstrate that ethylenediamine additives in green RTCP have the ability to control morphology with the precision of proteins at a fraction of the cost.

Experimental

Materials and methods

All reactions were carried out under an inert atmosphere of N₂, and all solutions were sparged with N₂ for 30 minutes prior to use. Ultrapure Milli-Q water (Merck Milli-Q integral purification system) was used. All reagents were purchased from Sigma Aldrich.

Room temperature co-precipitation

Iron(II) sulphate (111 mg, 0.4 mmol) and iron(III) sulphate (179 mg, 0.3 mmol) were dissolved in N₂ sparged Milli-Q (20 mL) in a two-neck round bottomed flask. A set amount of the additive was added to the reaction mixture and left to stir for 5 minutes to ensure dissolution of the additive and iron

salts under an N₂ atmosphere. N₂ sparged 0.5 mol NaOH (8 mL) was added at a rate of 50 µL a minute with stirring, for a total of 160 minutes using a Harvard Apparatus 11 plus syringe pump driver. The reaction was left to age for an hour under the inert atmosphere. The reaction mixture was then magnetically separated, washed five times with sparged Milli-Q to remove any non-magnetic iron oxide by-products, and the particles dried in a 40 °C vacuum oven overnight. All reactions produced a high yield of particles (>85%).

Characterisation

Transmission electron microscopy (TEM). 10 µL of a 1 mg ml⁻¹ suspension of nanoparticles in hexane was dropped onto a carbon coating copper TEM grid and allowed to dry down. Grids were imaged using an FEI Technai G2 Spirit electron microscope and the TEM images were analysed using the ImageJ software. >200 particles per sample were randomly selected and measured (see ESI S1 and S2† for the full protocol of sample analysis). For HRTEM and selected-area electron diffraction, an FEI Titan microscope was used.

X-ray diffraction (XRD). The XRD data were collected by the analysis of dry iron oxide nanoparticles in a Bruker D8 powder diffractometer. The diffraction images were collected in 0.022-degree increments from 20 to 80 degrees, with a fixed wavelength at $\lambda = 1.54178 \text{ \AA}$ from a Cu K α X-ray source.

Fourier-transform infrared spectrometry (FTIR). FTIR was performed on a small quantity (5–10 mg) of dry iron oxide nanoparticles using a PerkinElmer FTIR and Golden Gate Diamond ATR spectrometer. The particles were dispersed in a 0.05 M solution of TEPA in ultrapure Milli-Q and sonicated for 10 minutes. The solution pH was adjusted to the desired pH using 0.5 M HCl/0.5 M NaOH and rotated for 1 hour using a Lab net Mini Labroller. The particles were then magnetically separated, washed with pH adjusted Milli-Q (adjusted to the same desired pH), and dried overnight in a vacuum desiccator. Data collection and analysis were performed using Spectrum 10, with scans being made between 450 and 4000 cm⁻¹. Baseline correction was performed on all the spectra.

Thermal gravimetric analysis (TGA). To ascertain the binding of organic material to iron oxide nanoparticles, a small amount (10–20 mg) of particles were washed with ethanol and acetone to remove any residual surface organic debris and dried in a vacuum oven. The cleaned particles were then dispersed in a 0.05 M solution of TEPA in ultrapure Milli-Q and sonicated for 10 minutes. The solution pH was adjusted to ~pH 7 using 0.5 M HCl and rotated for 1 hour using a Lab net Mini Labroller. The particles were then magnetically separated and washed using ultrapure water to remove excess unbound amine and dried overnight in a vacuum desiccator.

TGA was performed on these dry particles between 20 and 800 °C at a heating rate of 10 °C per minute under a 2/3 N₂ and 1/3 O₂ atmosphere.

Computational modelling

The computational study used an approach similar to our previous study of magnetite surfaces.⁴³ The DL_POLY Classic



code⁴⁶ using the Generalised AMBER Force Field (GAFF)⁴⁷ for the ethylenediamine molecules, a modified version of CLAYFF for magnetite^{48,49} with standard, Lorentz–Berthelot^{50,51} mixing rules, was used to define the interaction between the two force-fields. Applying this approach to describe the interface between two very different media is not normally advisable and its reliability should be tested before production runs are performed.⁵² However the similarity in form of the two force-fields and the partial charges associated with the atoms on both sides of the interface meant that our tests showed that the approach adequately described the interface between magnetite and a range of simple organic molecules.⁵³ The approach has also been used by others to study similar systems,^{54–56} including the organic/magnetite interface.⁵⁷

The structures of the ethylenediamine molecules were generated using the AMBERTOOLS package TLEAP, and magnetite slabs terminating with the (100) and (111) surfaces perpendicular to the *x*-axis and approximately 25 Å thick were generated from the pre-relaxed (1 ns of MD simulation at 300 K using the NPT ensemble) bulk structure using the METADISE code.³² pH was incorporated into the modelling by considering several charged examples of each ethylenediamine molecule and using published pK_a values (Hazardous Substances Data Bank) a weighted average could be determined to reflect the results in the chosen conditions.

Except for the initial relaxation of the bulk structure, the MD simulations were performed using the canonical, NVT, ensemble at 300 K, employing the Nose Hoover thermostat with a relaxation time of 0.5 ps. The trajectories were generated using the Verlet leapfrog algorithm⁵⁸ using a time step of 1.0 fs. The long-range coulombic interactions were calculated using the Ewald summation,⁵⁹ and the short-range inter- and intramolecular interactions were described using the potential parameters discussed above. Each production run was performed for 5 ns, during which all the atoms within the system were free to relax. The energetics of the system were recorded every 0.1 ps, and the coordinates were written to the general trajectory file every 1 ps. To better scan the configuration space, 42 simulations were run for each molecule on each surface, where the orientation and position of the molecule at the start of the simulation differed. Thus, the results reported represent statistics collected over 210 ns of MD simulation.

Results

Additive screening

When selecting additives for potential future scale-up, it is important to consider the cost. While a compound may be highly effective at face-specific adsorption (such as the MIA protein), if they are not readily available, easily synthesised or competitively priced, the process will not be commercially viable for industrial scale-up. Additives must be water soluble to be effective in green RTCP reactions, and non-toxic. Ethylenediamine is an inexpensive compound, and known to be a chelating agent. Fig. 1a and b schematically shows the

setup of the RTCP reactions, and the process of additive-directed synthesis.

We have screened a full ethylenediamine series of $H_2N(-CH_2CH_2N-)_nH_2$ (with $n = 2$, diethylenetriamine (DETA); 3, triethylenetetramine (TETA); 4, tetraethylenepentamine (TEPA); and 5, pentaethylenehexamine (PEHA)) (Fig. 2b–e) to assess their effectiveness in controlling the morphology of MNPs compared to additive-free control. These additives were selected due to their relatively low cost, the only factor varied in these reactions was the additive used. The amount of additive used per reaction was relative to the number of amine groups present, *i.e.* twice the amount of DETA was used relative to PEHA to maintain 0.08 mmol of active amine groups. As the reaction contained 1 mmol of iron ions, the ratio of functional groups : iron ions was thus 1 : 12.5. As such, the final ratios of additive : iron ions varied depending on the additive used: DETA (1 : 37.5), TETA (1 : 50), TEPA (1 : 62.5), PEHA (1 : 75).

Fig. 2a–e shows representative TEM images of the nanoparticles formed (ESI Fig. S3† for larger TEM images). From visual inspection, it is clear the additives have had a profound effect on particle morphology. The control particles (Fig. 2a) were found to be consistent with previous magnetite MNPs from the literature formed *via* an RTCP route (mean size 22.2 nm, standard deviation (6.5 nm)).⁶⁰ The sizes of MNPs from TEM analysis (Fig. 2a–e) and crystallite sizing calculated with the Scherrer equation from the full width maximum of the XRD pattern are in agreement and are shown in Table 1. The addition of the amine additives does not have a significant effect on the MNP/crystallite size and the size distributions are similar for all the reactions with only TETA appearing minimally smaller in size (Fig. 2f, (ESI Fig. S4† for individual histograms)), suggesting that the amine additives do not affect the MNP size.

The XRD patterns (Fig. 2g) of MNPs synthesised with additives are consistent with magnetite being the major crystalline component of each sample (semi-quantitative analysis suggests >80% for all samples). Minor contaminants of other iron oxides (wüstite hematite and maghemite) are present. The control sample contains all 3 contaminants, while small quantities of maghemite and hematite (estimated < 6%) are seen in the reactions mediated by the longer chain PEHA and TEPA additives, and wüstite (estimated < 20%) is seen in the reactions mediated by the short chain DETA and TETA additives. The TEPA mediated sample was found to contain the purest magnetite.

From the analysis of TEM images, the particle shape was assigned (Fig. 2h and 3). Remarkably, the addition of all the ethylenediamine additive resulted in an increased formation of faceted particles (diamond, square, hexagonal). The methodology by which a particle's shape is assigned is demonstrated in Fig. 3 (also see Methods and ESI S2†). It should be noted that TEM images are 2D projections of 3D shapes and as such there can be an overlap and error in the assignment (*e.g.* octahedra commonly project a diamond shape in 2D but can also project hexagonal and square shapes if viewed at a different angle.⁴¹ Similarly, cubes commonly look square but



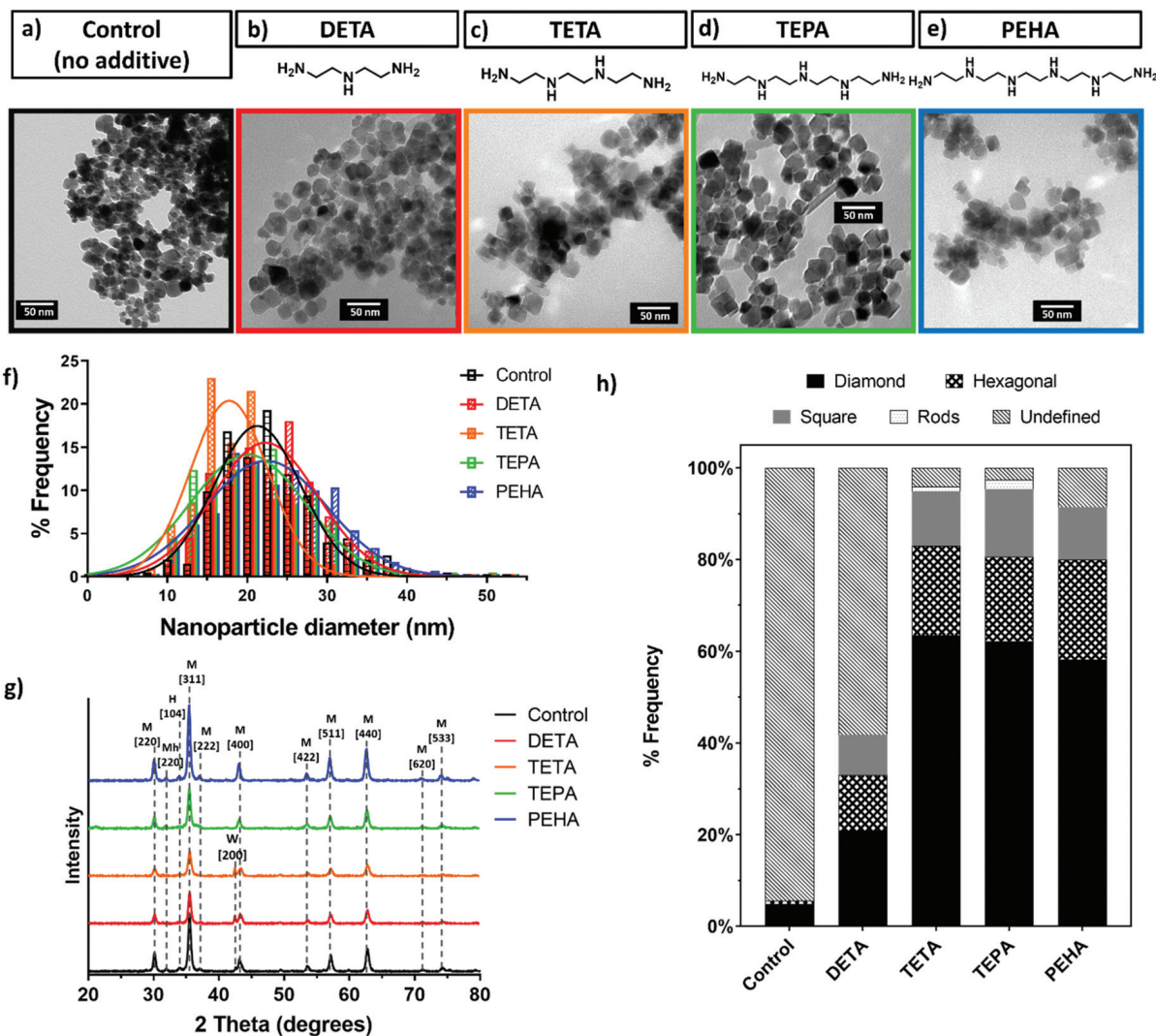


Fig. 2 MNP analysis: Representative TEM images of nanoparticles formed with the addition of various additives. (a) Control (no additive); (b) DETA; (c) TETA; (d) TEPA; (e) PEHA, with scale bars and additive structure. (f) Frequency distribution histogram of particles; (g) annotated XRD data where M = magnetite, Mh = maghemite, H = hematite, and W = wüstite. (h) Shape distribution of particles from TEM images. All scale bars are 50 nm.

Table 1 Table of characterisation of samples from additive screening

Sample	Particle size TEM (nm)	Crystallite size XRD (nm)	% Faceted particles
Control	22.2 ± 6.5	20.4	6
DETA	22.6 ± 6.1	19.3	42
TETA	18.4 ± 5.0	17.5	96
TEPA	23.3 ± 7.2	17.5	97
PEHA	22.9 ± 7.0	18.4	91

can project a hexagon). The populations here show a particular dominance of the octahedral morphology, with mainly diamonds with some square and hexagons. Faceted particles are clearly distinguishable from undefined particles.

A control reaction produced 6% faceted particles, increasing to 42% on addition of DETA, the shortest amine additive tested. The proportion of faceted particles increased with the

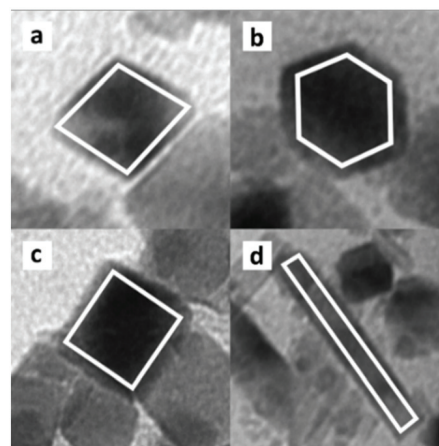


Fig. 3 Sample particle shapes from TEM: (a) diamond, (b) hexagonal, (c) square, and (d) rod.



additive length up to TEPA, with TETA and TEPA producing 96% and 97% of particles with a defined morphology respectively. As the additive chain length increased further for PEHA, 91% of faceted particles were formed. All three TETA, TEPA, and PEHA show highly significant quantities of faceted MNPs with each mediating the production of >60% of diamond particles, assigned to an octahedral morphology. The octahedral nature of these assigned particles was confirmed by the lattice fringe measurement of HRTEM images (Fig. 4). The *d*-spacing of 4.8 Å is indicative of a [111] octahedral plane, confirming a predominantly octahedral morphology in the TEPA additive mediated particle population.

Modelling study

Our previous modelling studies explained why a lysine-rich peptide was able to control the formation of cubic magnetite MNPs by a strong interaction of the amine with the [100] surface of magnetite.⁶¹ In this study we see a series of ethylenediamine molecules of different lengths preferentially mediate the formation of octahedral magnetite MNPs. It is clear the ethylenediamines are not interacting with the [100] and [111] surfaces in the same way as the lysine-rich protein, so again we turned to modelling to explain why these molecules preferentially mediate the formation of octahedral MNPs. We have defined the adsorption energy of the ethylenediamine molecules onto the magnetite surfaces as the difference in the energy of a magnetite slab with an adsorbed molecule and the energy of the same slab and an isolated molecule:⁵²

$$E_{\text{ads}} = E_{\text{slab+molecule}} - (E_{\text{slab}} + E_{\text{molecule}})$$

With the exception of DETA, we find the adsorption is endothermic at the [100] surface and exothermic at the [111] surface (Fig. 5), showing a definite preference for the interaction with the [111] face over the [100] face for these molecules. After this quantity has been normalised, to take into account the varying number of amine groups in the molecule and the overall charge on the molecule, we find that that

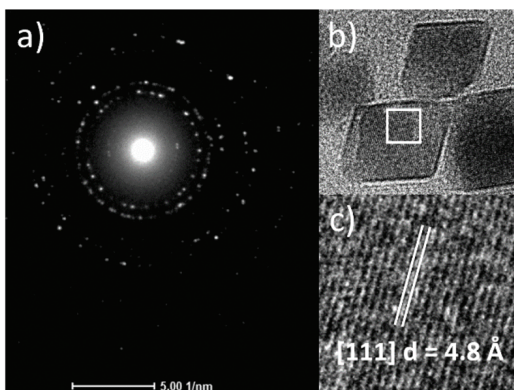


Fig. 4 (a) Selected area electron diffraction of octahedra assigned particles from the TEPA mediated MNP sample, (b) HRTEM of octahedral particles, (c) lattice fringe measurements.

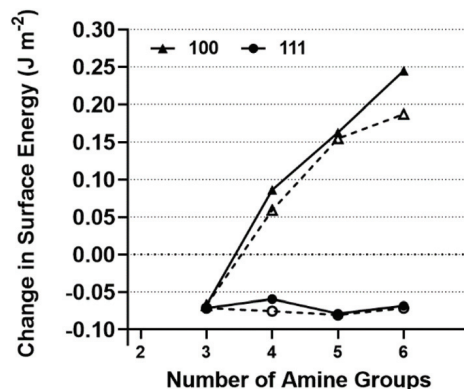


Fig. 5 Calculated changes in the surface energy due to the adsorption polyamine chains of varying lengths. Solid lines at pH 7 and dotted lines at pH 8.

adsorption at the [111] surface is favoured by 100–140 kJ mol⁻¹ per unit charge per amine group. There is no significant difference between the calculated values for TETA, TEPA and PEHA but the difference is greater at pH 7 than at pH 8 (Fig. 5).

The surface energy, after adsorption (γ_{ads}), is defined as the difference in energy per unit area between a magnetite slab with an adsorbed molecule and the sum of a bulk system containing the same number of Fe₃O₄ formula units as the slab and an isolated molecule:

$$\gamma_{\text{ads}} = [E_{\text{slab+molecule}} - (E_{\text{bulk}} + E_{\text{molecule}})]/A$$

As a Wulff construction⁶² assumes that a crystal will arrange itself such that its surface Gibbs free energy is minimized by assuming a shape of low surface energy the reduction in the energy of a particular surface at the expense of another will be directly related to the observed morphology of the resulting particles. This is shown in Fig. 5 and clearly illustrates that the adsorption of the TETA, TEPA or PEHA molecule leads to a small stabilisation of the [111] surface, whereas adsorption destabilises the [100] surface with the effect increasing with chain length and goes some way to explaining the results shown in Fig. 2h, where octahedral particles are the most abundant when TETA, TEPA and PEHA are present. Note there is negligible difference for both adsorption energies to each magnetite surface and thus less preference for octahedral particles when DETA is present.

The nature of the adsorption, and hence the difference in the calculated surface energies can be understood by considering the nature of the bonding at the surface. This is simply achieved by considering the radial distribution functions (RDF) between the iron and oxygen in the magnetite and the nitrogen and hydrogen atoms in the amine groups. Fig. 6 shows this data for a system at pH 8. The sharp peak at ~1.8 Å in Fig. 6a and c indicates that strong hydrogen bonds form between surface oxygen and the hydrogens in the amine groups for both [100] and [111] surfaces.

As would be expected, the peaks are sharpest for the shortest molecules as there fewer degrees of freedom available



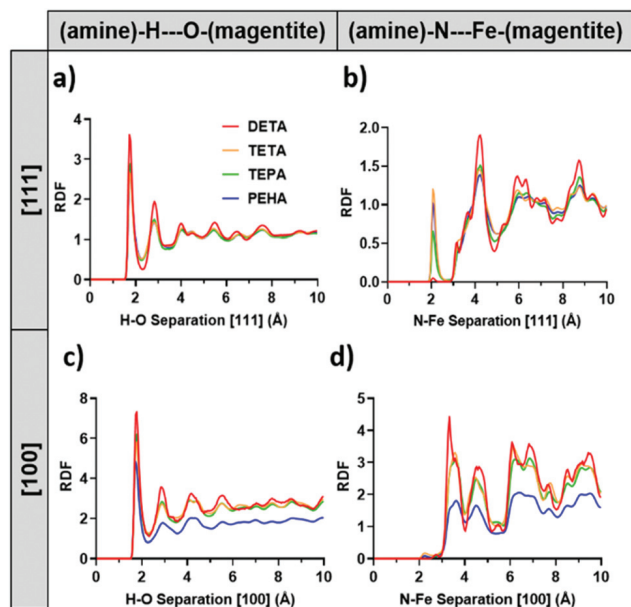


Fig. 6 Radial distribution functions for (a) hydrogen–oxygen interactions and (b) nitrogen–iron interactions at the [111] surface; (c) and (d) show hydrogen–oxygen interactions and nitrogen–iron interactions at the [100] surface.

during the adsorption and thus the range of bond lengths explored will be smaller. More interesting, and also explaining why the adsorption is stronger at the [111] surface, is the lack of an Fe–N bonding peak at 2 Å in Fig. 6d, which is present in Fig. 6b, illustrating that at the [111] surface both adsorption modes are present, whereas only hydrogen bonding is present at the [100] surface. The link of increased binding with increased binding modes is further demonstrated by the fact the adsorption peak for the Fe–N bonding at [111] is missing only for DETA (Fig. 6b) and DETA shows no difference in surface energy absorption (Fig. 5).

Integrating the first peak of the RDF gives the average number of bonds formed between the adsorbed molecule and the surface.⁶³ As would be expected, the number of bonds increases with chain length however, more importantly, the number of bonds is significantly greater for the [111] surface than that for [100]. This implies that the longer molecules are better able to lie flat on the [111] surface, forming a stronger interaction with the surface and reducing the surface energy at the [111] surface. Fig. 7 shows PEHA is able to lie flat on the [111] surface (Fig. 7b), which is not the case for the [100] surface (Fig. 7a). Fig. 7b shows additional interactions between surface Fe and the amine groups and N to surface O interactions. However, the data appear to be independent of both chain length and pH for the [111] surface, whereas increasing chain length and reducing pH have a detrimental effect on the [100] surface energy (Fig. 6 and 7).

To further probe the nature of the adsorption, two angular order parameters were defined that describe the orientation of the molecule on the surface.⁶⁴ The first is the acute angle formed by a vector, parallel to the surface and a vector connect-

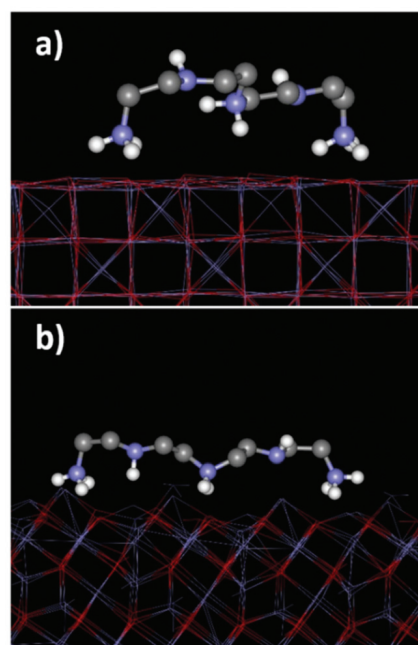


Fig. 7 Atomistic simulations of TEPA interacting with a magnetite surface (a) [100] and (b) with the [111] surface.

Table 2 The variation in the angle in degrees between the molecule and the surface. The median value is tabulated with the interquartile range shown in brackets. The numbers are based on the composition of each molecule at pH 8

	End to end	End to centre
	[100]	
DETA	4 (1.8)	28 (4.1)
TETA	20 (26.8)	38 (10.8)
TEPA	24 (24.8)	20 (17.8)
PEHA	45 (32)	29 (29.7)
	[111]	
DETA	15 (18.5)	30 (25.3)
TETA	16 (15.3)	30 (28.4)
TEPA	14 (15)	29 (29.4)
PEHA	15 (15.1)	29 (30.7)

ing the two terminal amine groups and second, the acute angle formed by the vector, parallel to the surface and a vector joining a terminal amine with the centre of mass of the molecule. The results are shown in Table 2.

The end–end angle increases steadily with chain length, when considering adsorption at the [100] surface, whereas it remains approximately constant ($\sim 15^\circ$) when considering adsorption at the [111] surface. With the exception of DETA the angle is always greater for the [100] surface. This, together with variance in the end to centre parameter shows that the molecules are more mobile on the [100] surface, whereas they adsorb strongly to the [111] surface and remain flat, *i.e.* parallel to surface, further suggesting the molecules' role in promoting the growth of the [111] surface.



Optimising amine additive concentration

The concentration of the additive and thus the ratio of additive to iron ions present in an RTCP reaction is likely to be a critical factor in the effectiveness of MNP control. For this concentration study TEPA was selected owing to it mediating the highest number of faceted particles and the purest magnetite MNPs. 4 different additive:iron ratios were tested, each varying by a factor of 10 (1 : 1250, 1 : 125, 1 : 12.5, 1 : 1.25).

TEM images (Fig. 8a–d) show particles of various sizes and morphologically defined populations (larger images available in ESI Fig. S5†). Fig. 8e and Table 3 (and ESI Fig. S6†) demonstrates that size and size distribution remained consistent at the lower concentrations between the 1 : 1250–1 : 12.5 ratios. At the 1 : 1.25 ratio, there is a significant shift in the profile with respect to both the size and morphology of the particles formed. The mean size of the particles increases from ~22 nm for lower concentrations to 49.4 nm, and the standard deviation increasing from 6.0 to 19.6.

The shape profile (Fig. 8g) shows the particle morphology of the 1 : 1.25 sample to be the poorest too, with 72% of undefined shape (Table 3). It is interesting there are almost equal quantities of diamond and elongated rods (12%) in this poorer 1 : 1.25 sample, showing that high quantities of the additive have a detrimental effect on both the size and morphology. Rod shaped particles are typically associated with the iron oxide goethite, however the XRD (Fig. 8f) shows that for each sample magnetite is the main crystalline product, with only a small quantity of goethite impurity in all samples. In fact, the XRD data remained consistent between all the samples, suggesting the difference in particle morphology is not the result of different iron oxides species being present.

The ratio 1 : 125 was found to produce the most consistently faceted particles, with 81% of the particles formed being faceted with >70% being octahedral (Table 3). The ratios above and below, (1 : 1250 and 1 : 12.5 respectively) display a similar size and shape profile to each other. 1 : 125 TEPA:Fe ratio showing the best shape control is consistent with the previous additive screening results. The initial screening used a concentration of 1 : 62.5 (twice the concentration of 1 : 125, and between 1 : 125 and 1 : 12.5 values). It is interesting to note that the optimum proportion of faceted particles is actually achieved in the initial screening, but this concentration study achieves a more morphologically consistent diamond-shaped population.

To better understand if and when TEPA is binding to the forming particles, FT-IR spectroscopy was performed at a range of pH from 4.5 to 12.8 (ESI Fig. S6†). The magnetite particles give a strong Fe–O peak at 542 cm^{-1} (and a minor one at 691 cm^{-1}). The signal from an amine organic coating (bending frequencies occurring between 1220 and 1747 cm^{-1}) is the most predominant in pH 7.4 and pH 9 samples while only a negligible signal is seen in the extreme pH values of 4.5 and 12.8. This suggests TEPA binds only after the particle has nucleated (above pH 4.5), thus to the surface as opposed to iron ions. Above pH 12, TEPA is exclusively neutral with no

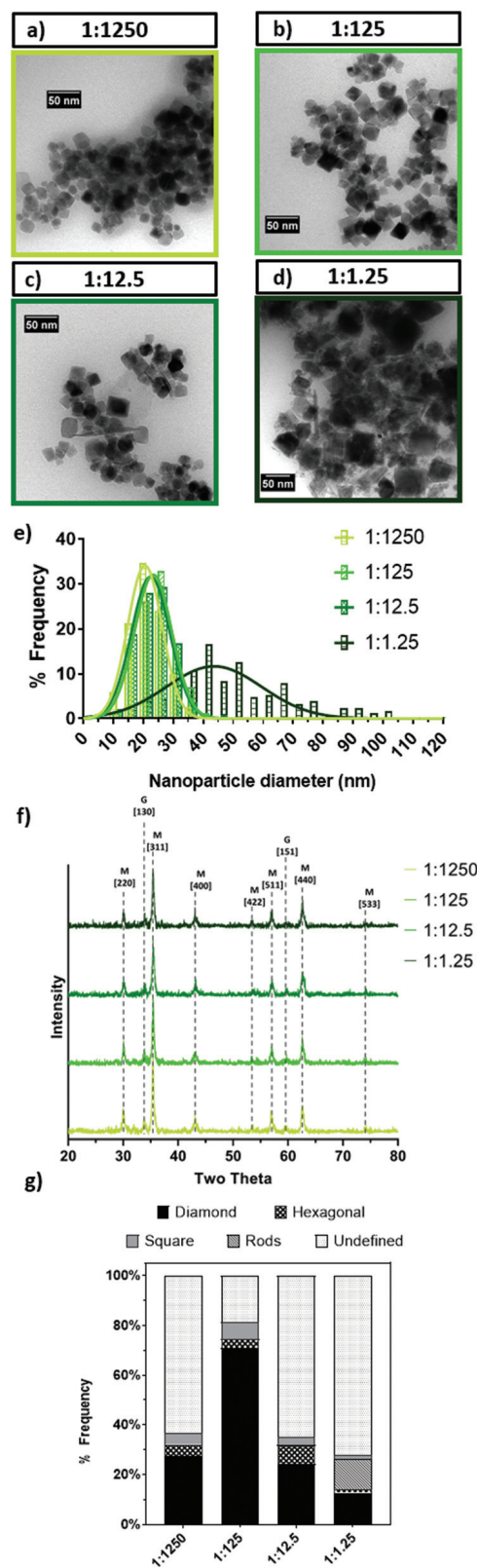


Fig. 8 MNP analysis: Representative TEM images of nanoparticles formed with varying TEPA:iron ion ratios. (a) 1 : 1250; (b) 1 : 125; (c) 1 : 12.5; (d) 1 : 1.25; (e) frequency distribution histogram of particles; (f) annotated XRD data where M = magnetite and G = goethite; (g) shape distribution of particles from TEM images. All scale bars are 50 nm.



Table 3 Table of characterisation of samples from the concentration study

Sample TEPA : Fe	Particle size TEM (nm)	Crystallite size XRD (nm)	% Faceted particles (total)			
			Diamond	Hexagonal	Square	Rod
1 : 1250	21.1 ± 6.0	23.0	37	5	5	—
			28			
1 : 125	23.5 ± 6.0	24.0	81	3	7	—
			71			
1 : 12.5	22.7 ± 6.0	26.2	35	7	3	1
			24			
1 : 1.25	49.4 ± 19.6	23.0	28	1	2	12
			13			

–NH₃⁺ or –NH₂[–] groups for electrostatic interaction, suggesting the TEPA completely disassociates from the particles at above pH 12. TGA (ESI Fig. S6†) suggests the presence of TEPA as an organic coating at pH7.

Discussion

RTCP is a simple, well-studied method of producing large quantities of magnetite nanoparticles, with the drawback that particles produced have an undefined morphology. While a range of natural additives have been used in an RTCP reaction to control the MNP size, the use of biomineralisation proteins and peptides to control both the size and shape as well as produce higher quality particles is well documented,^{38,60,65,66} with varied complexities and functionalities. A molecule that specifically adsorbs to a developing crystal face, reduces its surface energy to slow the growth of the face, resulting in that facet dominating the final morphology of the crystal.³⁸ Peptide and protein control over nanoparticle morphology has been ascribed to precise mapping of the specific surface resulting in multiple interactions. In this study we used the learning from such proteins. They were found to be lysine-rich showing strong amine interactions with the magnetite surface.

EDA is an inexpensive, simple, amine compound and has previously been used as well as DETA as a structure-directing agent (in non-green synthetic conditions).^{67,68} The addition of EDA based additives of all lengths tested (amine groups = 3–6, DETA–PEHA) had an influence on the morphology of the particles, with an increased percentage of faceted particles being observed from DETA to TETA, with TETA to PEHA showing close to pure faceted particles (optimum found at TEPA). Particle size remained consistent (~18–23 nm) between samples synthesised with no additive and the samples produced with all additives, suggesting the additive does not play a role in nucleating the MNPs. This is to be expected as mineral nucleation is usually facilitated by acidic proteins in biomineralisation (containing multiple aspartic and glutamic acid) providing sites for metal ion binding.²¹ An additive that affects nucleation will generally influence the mineral type and/or the particle size, neither of which is seen here. Instead the amine molecules exclusively act to control morphology, preferentially adsorbing to and stabilising the [111] face to

direct the growth of [111] faceted octahedral particles. This is consistent with what is currently understood in the literature and from our modelling studies.²⁹

Production of octahedral MNPs *via* a green additive synthesis is a very important advance for biomedicine. Such faceted particles are very desirable for both therapeutics and diagnostic nanomedicine, while cheap sustainable manufacture will increase accessibility leading to more widespread uses. While it is clear the EDA series of additives primarily acts to direct the morphology of the growing crystal, in doing so the amine chains bind to the surface. This has a secondary feature of forming an organic coating. This helps to stabilise and increase the dispersion of the MNPs in solution. The amine additives could thus be modified to also functionalise the particles if desired, giving the additive a dual purpose. However, the additive does not bind at extreme pH, so can be easily removed with base by continuing the titration if desired.

It is clear from the additive screening that TETA, TEPA and PEHA produce the majority octahedral particles (while DETA is less effective). Computational simulation studies explain why the ethylenediamine series directs the morphology towards octahedral particles. The modelling demonstrates a clear preferential binding to the [111] face over the [100]. Despite the identical functional groups, additive performance is affected by their length, with the shortest DETA showing only a minor effect. While TETA, TEPA, and PEHA are comparable, there is a slight reduction in performance from PEHA, the longest amine molecule. From the modelling data we see DETA shows no preference for [111] or [100] and this explains why it had the least influence over particle morphology.

Modelling also shows the energies of absorption for binding are similar for TETA, TEPA and PEHA for both the [111] and [100] magnetite surfaces. This seems to be driven by a mixture of the positive effect of chelation coupled with the negative effect of entropy for long molecules which may explain the slight fall off for PEHA. The adsorption at the [111] surface is favoured by TETA, TEPA and PEHA because the arrangement of the ions on the surface enables the molecule to adsorb flat and form, not only hydrogen bonds between the magnetite surface oxygen and hydrogens on the amine groups, but also strong interactions between surface iron and nitrogen groups in the amine. Whereas only hydrogen bonding is able to occur at the [100] surface and to a lesser extent to that pre-



dicted at the [111] surface. It should be noted that the energy changes required to favour one surface over the other can be small, thus subtle changes in the form of the additive molecule result in a substantial effect to the MNP morphology. For example, it is noteworthy that the ethylenediamine series was inspired by the basic amino acid rich morphology controlling protein, with a particularly high quantity of lysine. The lysine rich peptide loop directed magnetite MNP morphology towards cubic particles, showing a preference to the [100] face. It is interesting that because these seemingly similar molecules (differ by a carboxylate group) bind differently to the magnetite [111] and [100] surfaces, a dramatically different morphological outcome is achieved. This is something that, carefully designed, computer modelling can probe as the techniques are able to directly compare adsorption at different surfaces and consider a variety of adsorption modes.

From varying the concentration of TEPA by factors of 10, a rough ideal concentration was ascertained as ~1 : 125. This is in line with the results seen for the screening which used a 1 : 62.5 ratio. At 1 : 1250 and 1 : 12.5, similar degrees of morphological control were exerted over the MNP formed, despite the difference in conditions. This may be because below the ideal concentration there may be too little of the additive for surface coverage to have a substantial effect on particle formation, and at high concentrations the reaction conditions such as pH may be altered by the additive, effectively polluting the reaction environment. This seems to be the case at near 1 : 1 additive to iron concentrations. This study was conceived to translate a green bioinspired approach to scale-up. A chief concern with scale is cost. This study demonstrates a vastly cheaper additive compared to protein alternatives and the concentration study reveals that very small quantities of this cheap additive (1 : 125) are the optimum, which is a very positive news for scale-up.

Conclusions

Ethylenediamine based additives have been successfully used to enhance magnetite MNPs formed under a high-yielding, environmentally friendly RTCP, by directing the formation of octahedral particles. A modelling study revealed that the longer EDA series molecules adsorb strongly and lie flatter against a [111] octahedral magnetite surface; conversely adsorption to a [100] surface is unfavourable. As such both modelling and experimental results align to represent the potency of the longer EDA molecules (TETA, TEPA, PEHA) as shape-directing additives for octahedral magnetite. Only a small quantity of the additive is required to offer optimum control. This study realises and explains the power of the bioinspired-additive green chemistry approach to MNP synthesis. Previous work has demonstrated how metal-alloy nanoparticle phase,⁶⁹ silica mesoporosity,⁷⁰ and morphology of many nanoparticles such as magnetite,⁴³ calcite,⁷¹ and platinum⁷² can be controlled using proteins and peptides in similar simple green precipitation reactions. Learning from

biology, here we have used only the specific functionalities and motifs on simpler organic molecular additives. We demonstrated that easily accessible additives can define and control the MNP morphology. More widely, this methodology has the potential to translate to a full range of nanomaterials, most readily those where protein/peptide directed synthesis has already been demonstrated, with a scalable universal green nanomaterial synthesis offering a huge impact for nanomaterial manufacture.

Abbreviations

DETA	Diethylenetriamine
EDA	Ethylenediamine
FCC	Face-centred cubic
FTIR	Fourier-transform infrared spectroscopy
FWHM	Full width half maximum
HRTEM	High resolution transmission electron microscopy
MIA	Magnetite interacting adiron
Mms	Magnetosome membrane specific
MNP	Magnetic nanoparticle
MRI	Magnetic resonance imaging
NaOH	Sodium hydroxide
PEHA	Pentaethylenehexamine
RDF	Radial distribution functions
RTCP	Room temperature co-precipitation
TEM	Transmission electron microscopy
TETA	Triethylenetetramine
TGA	Thermal gravimetric analysis
TEPA	Tetraethylenepentamine
VSM	Vibrating sample magnetometry
XRD	X-ray powder diffraction

Conflicts of interest

There are no conflicts of interest to declare.

Acknowledgements

This work was supported by funding from the EPSRC (grant number EP/P006892/1) and the University of Sheffield's ESRC DTP allowance (grant number EP/M508135/1) funds Laura Norfolk's PhD. The research was supported by David Cooke's membership of the UK's HEC Materials Chemistry Consortium, funded by the EPSRC (EP/L000202, EP/R029431), and used THOMAS, the UK Materials and Molecular Modelling Hub, for computational resources, which is partially funded by the EPSRC (EP/P020194). We thank S. Tsokov and C. Hill (Sheffield Electron Microscopy unit) for TEM training and HRTEM, Nicola Morley and Zhao Leong for support with VSM and Craig Robertson for support with powder XRD.



Notes and references

- R. E. Rosensweig, *Sci. Am.*, 1982, pp. 136–145.
- E. Y. M. Mendoza, A. S. Santos, E. V. López, V. Drozd, A. Durygin, J. Chen and S. K. Saxena, *J. Mater. Res. Technol.*, 2019, **8**, 2944–2956.
- B. Issa, I. M. Obaidat, B. A. Albiss and Y. Haik, *Int. J. Mol. Sci.*, 2013, **14**, 21266–21305.
- C. Y. Haw, F. Mohamed, C. H. Chia, S. Radiman, S. Zakaria, N. M. Huang and H. N. Lim, *Ceram. Int.*, 2010, **36**, 1417–1422.
- M. Mahdavi, M. Bin Ahmad, M. J. Haron, F. Namvar, B. Nadi, M. Z. Ab Rahman and J. Amin, *Molecules*, 2013, **18**, 7533–7548.
- K. Mahmoudi, A. Bouras, D. Bozec, R. Ivkov and C. Hadjipanayis, *Int. J. Hyperthermia*, 2018, 1–13.
- P. Sharma, S. Brown, G. Walter, S. Santra and B. Moudgil, *Adv. Colloid Interface Sci.*, 2006, **123**, 471–485.
- M. Gaumet, A. Vargas, R. Gurny and F. Delie, *Eur. J. Pharm. Biopharm.*, 2008, **69**, 1–9.
- J. Motoyama, T. Hakata, R. Kato, N. Yamashita, T. Morino, T. Kobayashi and H. Honda, *Biomagn. Res. Technol.*, 2008, **6**, 1–9.
- M. Gonzales-Weimuller, M. Zeisberger and K. M. Krishnan, *J. Magn. Magn. Mater.*, 2009, **321**, 1947–1950.
- L. Zhang, R. He and H. C. Gu, *Mater. Res. Bull.*, 2006, **41**, 260–267.
- D. Santos-Carballal, A. Roldan, R. Grau-Crespo and N. H. de Leeuw, *Phys. Chem. Chem. Phys.*, 2014, **16**, 21082–21097.
- G. Zhen, B. W. Muir, B. a. Moffat, P. Harbour, K. S. Murray, B. Moubaraki, K. Suzuki, I. Madsen, N. Agron-Olshina, L. Waddington, P. Mulvaney and P. G. Hartley, *J. Phys. Chem. C*, 2011, **115**, 327–334.
- A. Nikitin, M. Fedorova, V. Naumenko, I. Shchetinin, M. Abakumov, A. Erofeev, P. Gorelkin, G. Meshkov, E. Beloglazkina, Y. Ivanenkov, N. Klyachko, Y. Golovin, A. Savchenko and A. Majouga, *J. Magn. Magn. Mater.*, 2017, **441**, 6–13.
- P. Hugounenq, M. Levy, D. Alloeyau, L. Lartigue, E. Dubois, V. Cabuil, C. Ricolleau, S. Roux, C. Wilhelm, F. Gazeau and R. Bazzi, *J. Phys. Chem. C*, 2012, **116**, 15702–15712.
- S. K. Shaw, A. Biswas, A. Gangwar, P. Maiti, C. L. Prajapat, S. Singh and N. K. Prasad, *J. Magn. Magn. Mater.*, 2019, **484**, 437–444.
- C. H. Ho, C. P. Tsai, C. C. Chung, C. Y. Tsai, F. R. Chen, H. J. Lin and C. H. Lai, *Chem. Mater.*, 2011, **23**, 1753–1760.
- L. Zhang, Q. Li, S. Liu, M. Ang, M. O. Tade and H. C. Gu, *Adv. Powder Technol.*, 2011, **22**, 532–536.
- P. Hugounenq, M. Levy, D. Alloeyau, L. Lartigue, E. Dubois, V. Cabuil, C. Ricolleau, S. Roux, C. Wilhelm, F. Gazeau and R. Bazzi, *J. Phys. Chem. C*, 2012, **116**, 15702–15712.
- A. G. Roca, L. Gutiérrez, H. Gavilán, M. E. Fortes Brollo, S. Veintemillas-Verdaguer and M. del P. Morales, *Adv. Drug Delivery Rev.*, 2019, **138**, 68–104.
- M. C. Mascolo, Y. Pei and T. A. Ring, *Materials*, 2013, **6**, 5549–5567.
- A. Abou Hassan, O. Sandre, V. Cabuil and P. Tabeling, *Chem. Commun.*, 2008, 1783–1785.
- L. Norfolk, A. E. Rawlings, J. P. Bramble, K. Ward, N. Francis, R. Waller, A. Bailey and S. S. Staniland, *Nanomaterials*, 2019, **9**, 1729.
- Â. L. Andrade, D. M. Souza, M. C. Pereira, J. D. Fabris and R. Z. Domingues, *Quím. Nova*, 2010, **33**, 524–527.
- S. Si, A. Kotal, T. K. Mandal, S. Giri, H. Nakamura and T. Kohara, *Chem. Mater.*, 2004, **16**, 3489–3496.
- S. Wan, J. Huang, H. Yan and K. Liu, *J. Mater. Chem.*, 2006, **16**, 298–303.
- Y. P. Yew, K. Shameli, M. Miyake, N. Kuwano, N. B. Bt Ahmad Khairudin, S. E. Bt Mohamad and K. X. Lee, *Nanoscale Res. Lett.*, 2016, **11**, 1–7.
- V. V. Makarov, A. J. Love, O. V. Sinitsyna, S. S. Makarova, I. V. Yaminsky, M. E. Taliany and N. O. Kalinina, *Acta Nat.*, 2014, **6**, 35–44.
- I. P. Sari and Y. Yulizar, *IOP Conf. Ser.: Mater. Sci. Eng.*, 2017, **191**, 1–5.
- N. M. Salem and A. M. Awwad, *Nanosci. Nanotechnol.*, 2013, **3**, 35–39.
- V. L. Kirillov, D. A. Balaev, S. V. Semenov, K. A. Shaikhutdinov and O. N. Martyanov, *Mater. Chem. Phys.*, 2014, **145**, 75–81.
- Y. Kuwahara, T. Miyazaki, Y. Shirosaki, G. Liu and M. Kawashita, *Ceram. Int.*, 2016, **42**, 6000–6004.
- W. L. Tan and M. A. Bakar, *J. Phys. Sci.*, 2006, **17**, 37–50.
- B. Yang, J. Chou, X. Dong, C. Qu, Q. Yu, K. J. Lee and N. Harvey, *J. Phys. Chem. C*, 2017, **121**, 8961–8967.
- A. Kora, S. Beedu and A. Jayaraman, *Org. Med. Chem. Lett.*, 2012, **2**, 17.
- S. Wei, Y. Wang, Z. Tang, J. Hu, R. Su, J. Lin, T. Zhou, H. Guo, N. Wang and R. Xu, *New J. Chem.*, 2020, **44**, 9304–9312.
- A. Arakaki, J. Webb and T. Matsunaga, *J. Biol. Chem.*, 2003, **278**, 8745–8750.
- S. S. Staniland and A. E. Rawlings, *Biochem. Soc. Trans.*, 2016, **44**, 883–890.
- M. Tanaka, E. Mazuyama, A. Arakaki and T. Matsunaga, *J. Biol. Chem.*, 2011, **286**, 6386–6392.
- L. Wang, T. Prozorov, P. E. Palo, X. Liu, D. Vaknin, R. Prozorov, S. Mallapragada and M. Nilsen-Hamilton, *Biomacromolecules*, 2012, **13**, 98–105.
- S. S. S. Johanna, M. Galloway, A. Arakaki, F. Masuda, T. Tanaka and T. Matsunaga, *J. Mater. Chem.*, 2011, **21**, 15244–15254.
- A. E. Rawlings, J. P. Bramble, R. Walker, J. Bain, J. M. Galloway and S. S. Staniland, *Proc. Natl. Acad. Sci. U. S. A.*, 2014, **111**, 16094–16099.
- A. E. Rawlings, J. P. Bramble, A. A. S. Tang, L. A. Somner, A. E. Monnington, D. J. Cooke, M. J. McPherson, D. C. Tomlinson and S. S. Staniland, *Chem. Sci.*, 2015, **6**, 5586–5594.



- 44 UK-Peptides, Buy IGF1 LR3, <https://www.uk-peptides.com/igf1-lr3-1mg>.
- 45 Merck, Tetraethylenepentamine, <https://www.sigmaaldrich.com/catalog/product/aldrich/t11509?lang=en®ion=GB>.
- 46 W. Smith and T. R. Forester, *J. Mol. Graphics*, 1996, **7855**, 136–141.
- 47 J. Wang, R. M. Wolf, J. W. Caldwell, P. A. Kollman and D. A. Case, *J. Comput. Chem.*, 2004, **25**(9), 1157–1174.
- 48 R. T. Cygan, J. Liang and A. G. Kalinichev, *J. Phys. Chem. B*, 2004, **108**(4), 1255–1266.
- 49 S. Kerisit, *Geochim. Cosmochim. Acta*, 2011, **75**, 2043–2061.
- 50 H. A. Lorentz, *Ann. Phys.*, 1881, **248**, 127–136.
- 51 D. Berthelot, *C. R. Hebd. des séances l'Acad. des Sci.*, 1898, **126**, 1703–1855.
- 52 J. H. Harding and D. M. Duffy, *J. Mater. Chem.*, 2006, **16**, 1105–1112.
- 53 A. Monnington, *Magnetite Biomineralisation: The Interactions of Proteins and Fe₃O₄ Surfaces*, Phd Thesis, University of Huddersfield, 2014.
- 54 M. Szczerba and A. G. Kalinichev, *Clays Clay Miner.*, 2016, **64**, 488–502.
- 55 T. V. Shapley, M. Molinari, R. Zhu and S. C. Parker, *J. Phys. Chem. C*, 2013, **117**, 24975–24984.
- 56 J. A. Greathouse, D. B. Hart, G. M. Bowers, R. J. Kirkpatrick and R. T. Cygan, *J. Phys. Chem. C*, 2015, **119**, 17126–17136.
- 57 M. Konuk, K. Sellschopp, G. B. Vonbun-Feldbauer and R. H. Meißner, *J. Phys. Chem. C*, 2021, 4794–4805.
- 58 L. Verlet, *J. Phys. Chem. C*, 1967, **125**, 4794–4805.
- 59 P. P. Ewald, *Ann. Phys.*, 1921, **369**, 253–287.
- 60 A. E. Rawlings, L. A. Somner, M. Fitzpatrick-Milton, T. P. Roebuck, C. Gwyn, P. Liravi, V. Seville, T. J. Neal, O. O. Mykhaylyk, S. A. Baldwin and S. S. Staniland, *Nat. Commun.*, 2019, 2873.
- 61 A. E. Rawlings, J. P. Bramble, A. A. S. Tang, L. A. Somner, A. E. Monnington, D. J. Cooke, M. J. McPherson, D. C. Tomlinson and S. S. Staniland, *Chem. Sci.*, 2015, **6**, 5586–5594.
- 62 G. Wulff, *Z. Kristallogr. Mineral.*, 1901, **34**, 449–530.
- 63 M. P. Allen and D. J. Tildesley, *Computer Simulation of Liquids*, Oxford University Press, Oxford, 1st edn, 1987.
- 64 D. J. Cooke and J. A. Elliott, *J. Chem. Phys.*, 2007, **127**, 1–10.
- 65 R. Lopez-Moreno, A. Fernández-Vivas, C. Valverde-Tercedor, A. I. Azuaga Fortes, S. Casares Atienza, A. B. Rodriguez-Navarro, R. Zarivach and C. Jimenez-Lopez, *Cryst. Growth Des.*, 2017, **17**, 1620–1629.
- 66 J. J. M. Lenders, H. R. Zope, A. Yamagishi, P. H. H. Bomans, A. Arakaki, A. Kros, G. De With and N. A. J. M. Sommerdijk, *Adv. Funct. Mater.*, 2015, **25**, 711–719.
- 67 D. Arndt, V. Zielasek, W. Dreher and M. Bäumer, *J. Colloid Interface Sci.*, 2014, **417**, 188–198.
- 68 D. Zhang, J. Zheng and Z. Tong, *J. Exp. Nanosci.*, 2010, **5**, 162–168.
- 69 R. M. Jarrald, A. W. Liang Alvin, A. E. Rawlings, M. Tanaka, M. Okochi and S. S. Staniland, *Bioconjugate Chem.*, 2020, **31**, 1981–1994.
- 70 D. J. Belton, S. V. Patwardhan and C. C. Perry, *J. Mater. Chem.*, 2005, **15**, 4629–4638.
- 71 D. B. DeOliveira and R. A. Laursen, *J. Am. Chem. Soc.*, 1997, **7863**, 10627–10631.
- 72 C. Y. Chiu, Y. Li, L. Ruan, X. Ye, C. B. Murray and Y. Huang, *Nat. Chem.*, 2011, **3**, 393–399.



Ethylenediamine based Compounds as Additives to Control the Morphology of Magnetite Nanoparticles Using Green Reaction Conditions

Laura Norfolk,^{*a} Klaudia Kapusta^a, David Cooke^b, and Sarah Staniland^a

Supplementary information

Additive study: Individual Histograms

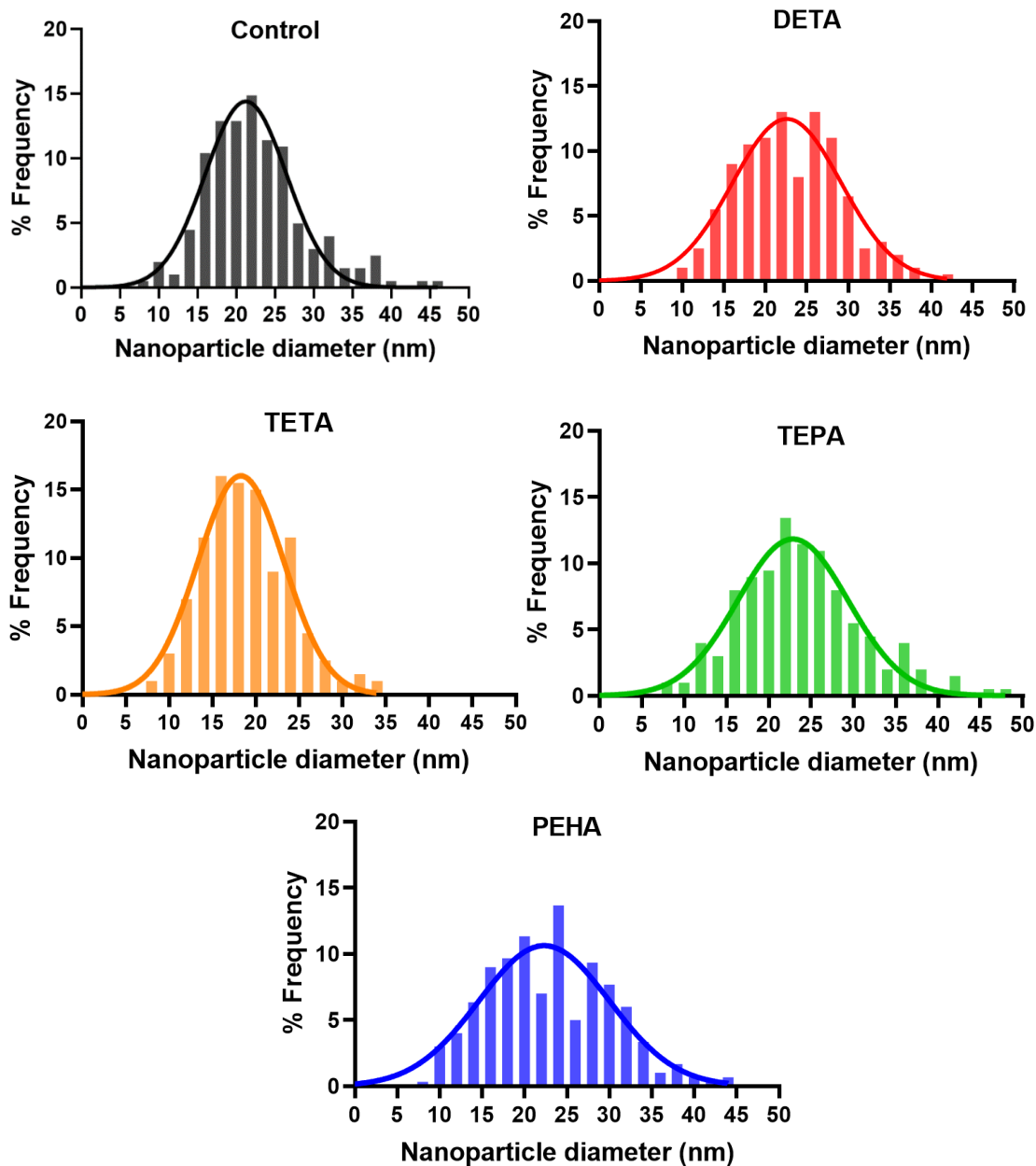


Figure S1. Individual histograms of MNP formed in RTCP reactions with the addition of varying additives: **a)** No additive (control); **b)** DETA; **c)** TETA; **d)** TEPA; **e)** PEHA

Particle Sizing Methodology:

Particle measurements are taken across the longest axis of each particle to ensure consistency between measurements using ImageJ software. Approximately 200 measurements are taken from each sample to get an accurate measure of mean size given the variety in particles per sample. To avoid human bias in which particles are selected for analysis, particles are analysed from a single “area” of a TEM image to prevent small or large particles being selectively measured. Several images are analysed for each sample to ensure a representative sample is taken.

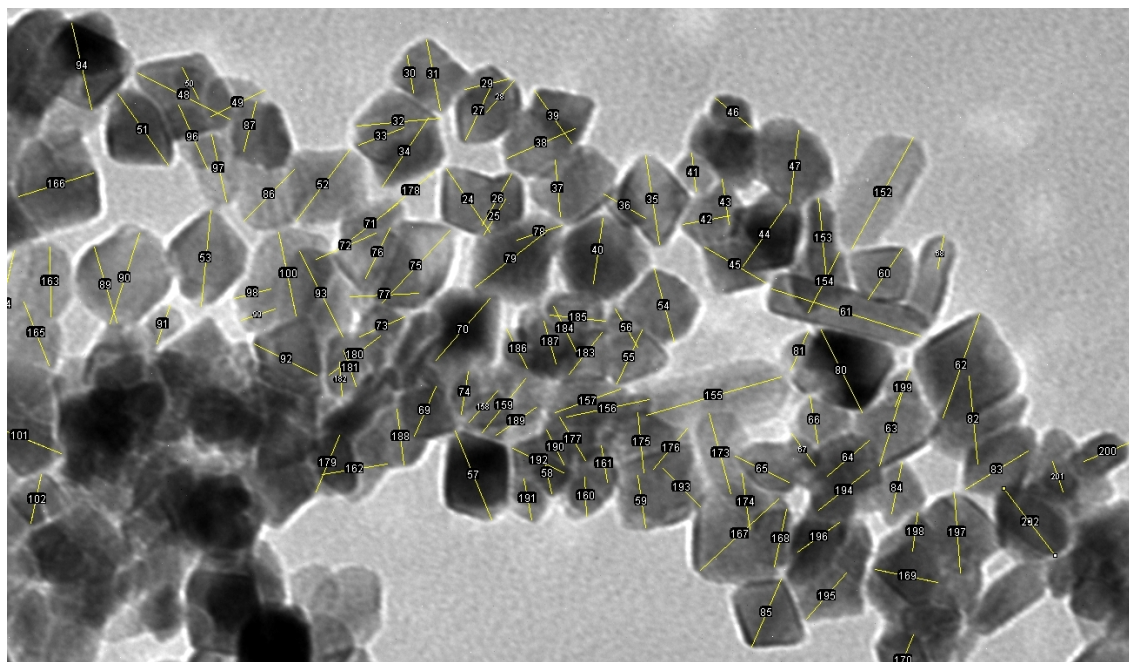


Figure S2: Screenshot of ImageJ particle sizing showing particles are analysed in clusters.

Particle Shape Analysis Methodology:

Images are manually analysed using drawing software (Inkscape, Paint.net, etc) by marking each particle a shape with a set colour (figure S3). A minimum of 300 samples are marked from several different images to ensure a representative sample is selected. The particles are then counted, at which point the shape assignment is checked a secondary time to maximise accuracy. Sample particle shapes can be seen in figure S4.

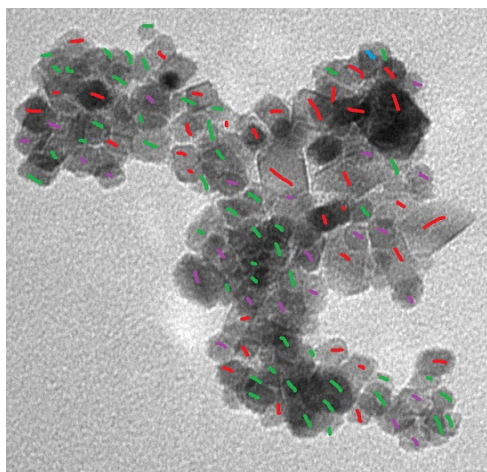


Figure S3. Example image analysis showing octahedral (red), undefined (green), and hexagonal (purple) particles.

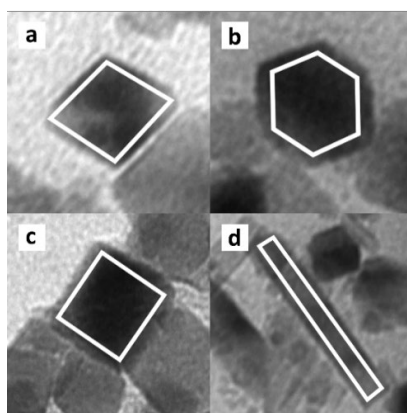


Figure S4. Sample particle shapes from TEM analysis; **a)** Octahedral; **b)** Hexagonal; **c)** square; **d)** rod/elongated.

Faceted Particle Breakdown: Table S1

Sample	Octahedral (%)	Hexagonal (%)	Square %	Rod (%)	Undefined (%)
Control	5	1	-	-	94
DETA	21	12	9	-	58
TETA	64	19	12	1	4
TEPA	62	18	15	2	3
PEHA	58	22	11	-	9

Concentration study: Individual histograms

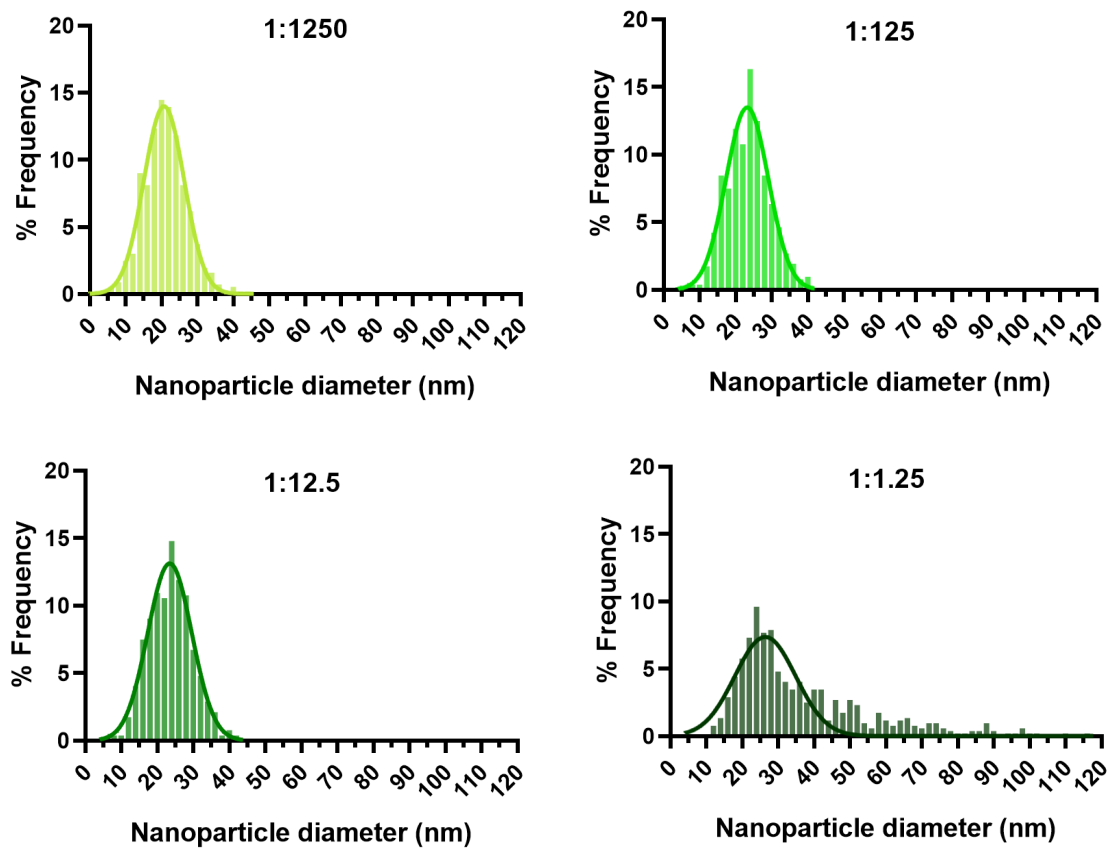


Figure S5. Individual histograms of MNP formed in RTCP reactions with the addition of varying iron:TEPA ratios: **a)** 1:1250; **b)** 1:125; **c)** 1:12.5; **d)** 1:1.25

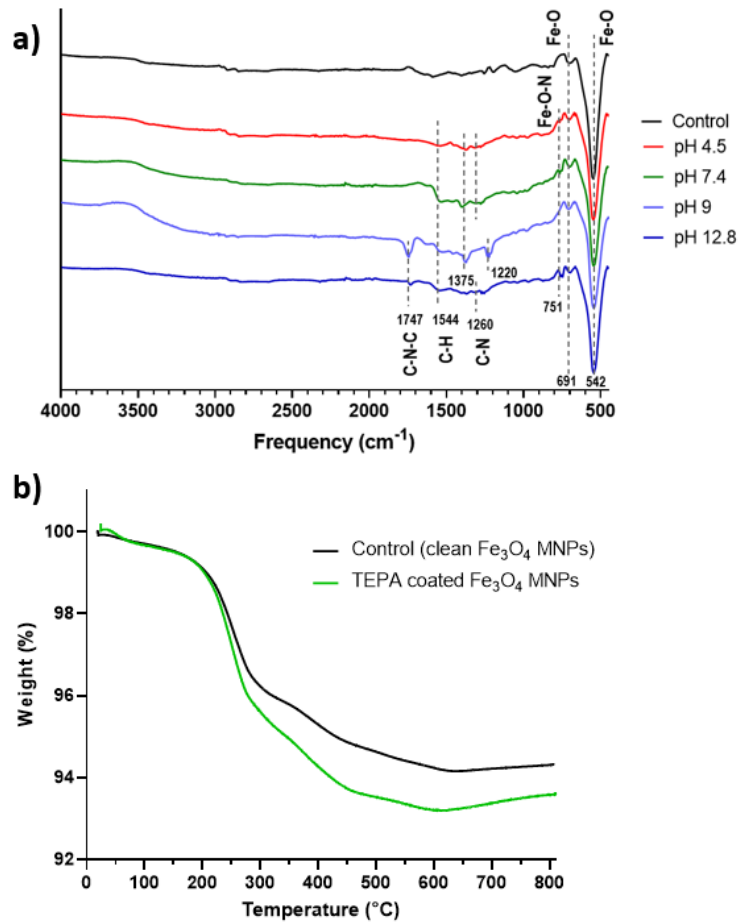
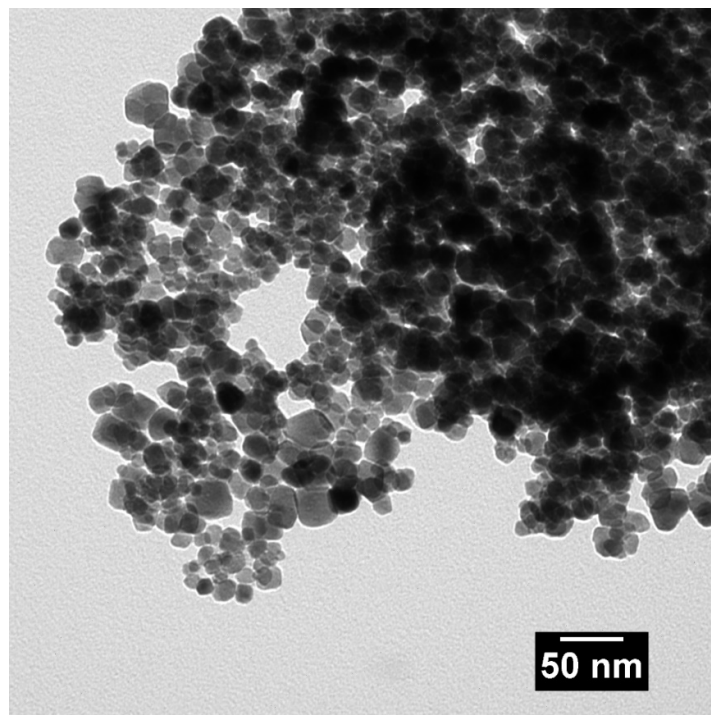


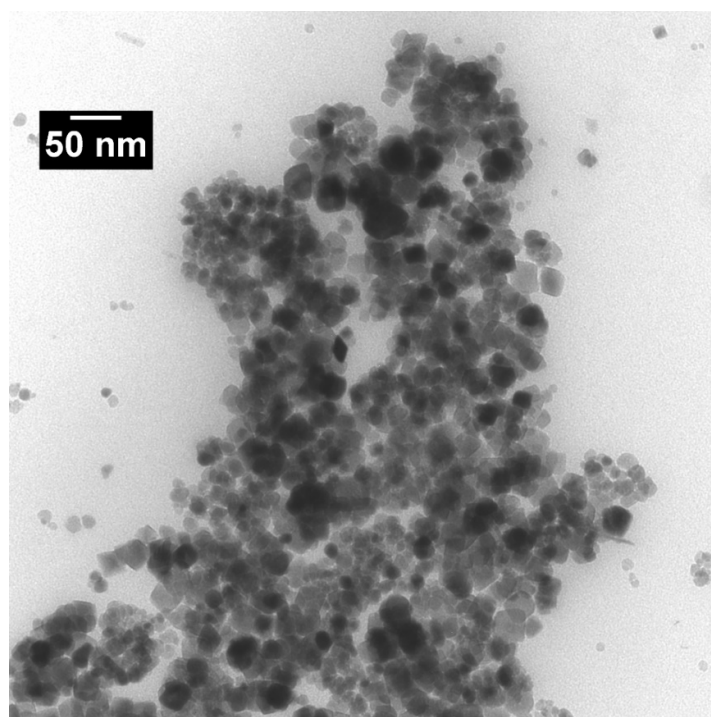
Figure S6. a) FTIR data of TEPA binding to magnetite nanoparticles at various indicated pH's; **b)** TGA of control magnetite nanoparticles (black) and TEPA bound particles (at pH 7).

Full size TEM images

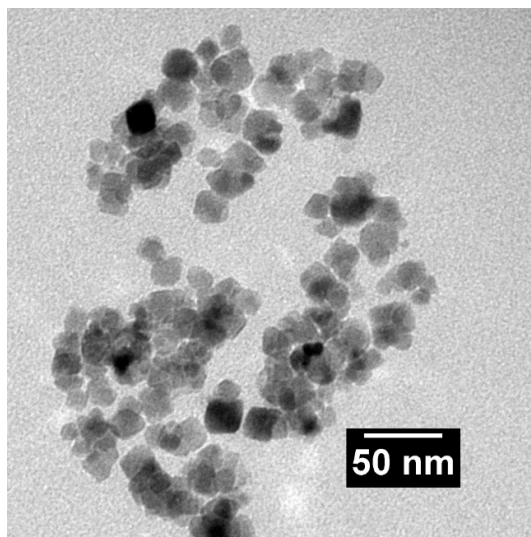
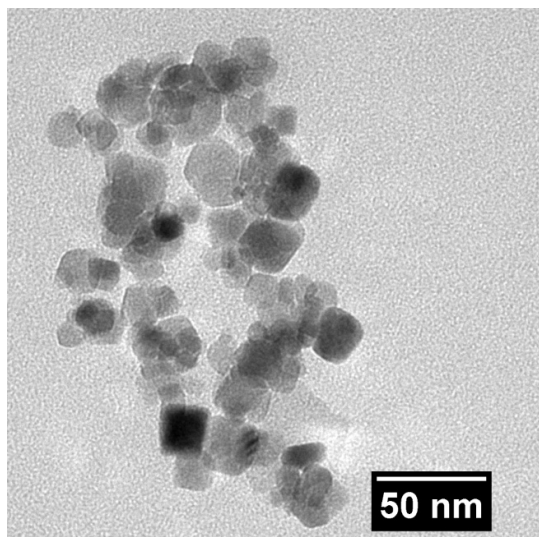
Control particles:



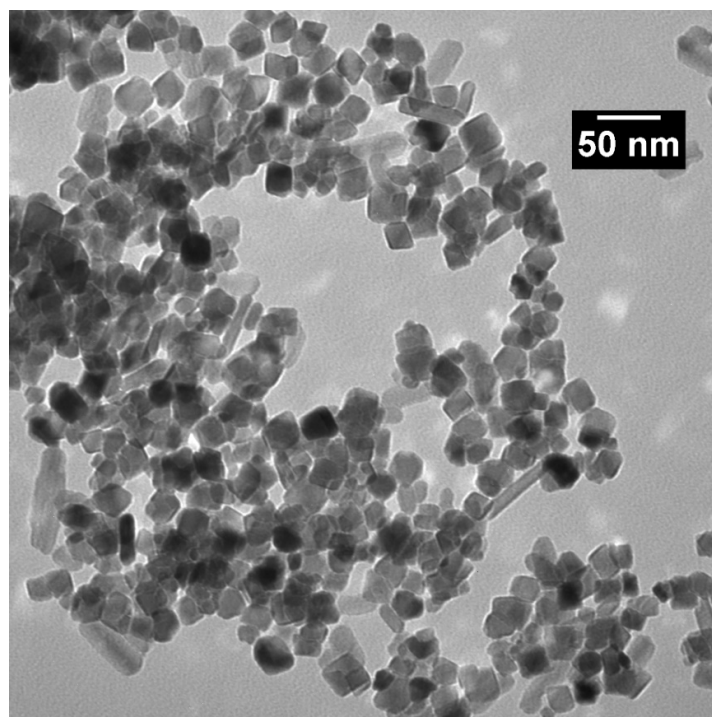
DETA:



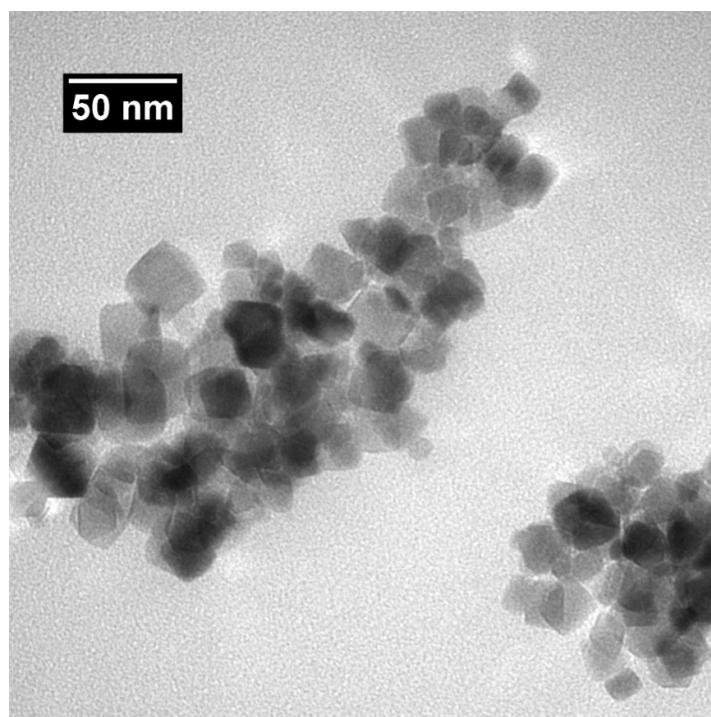
TETA:



TEPA:

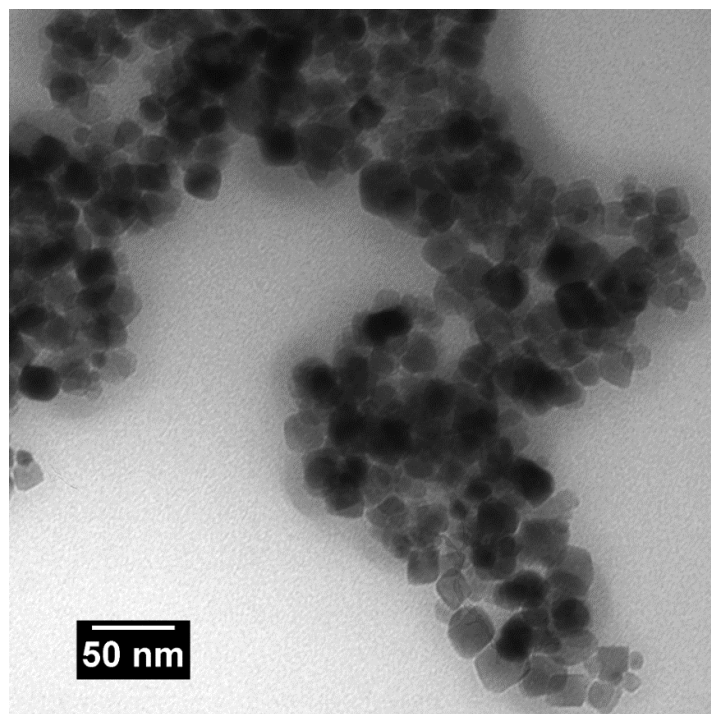


PEHA:

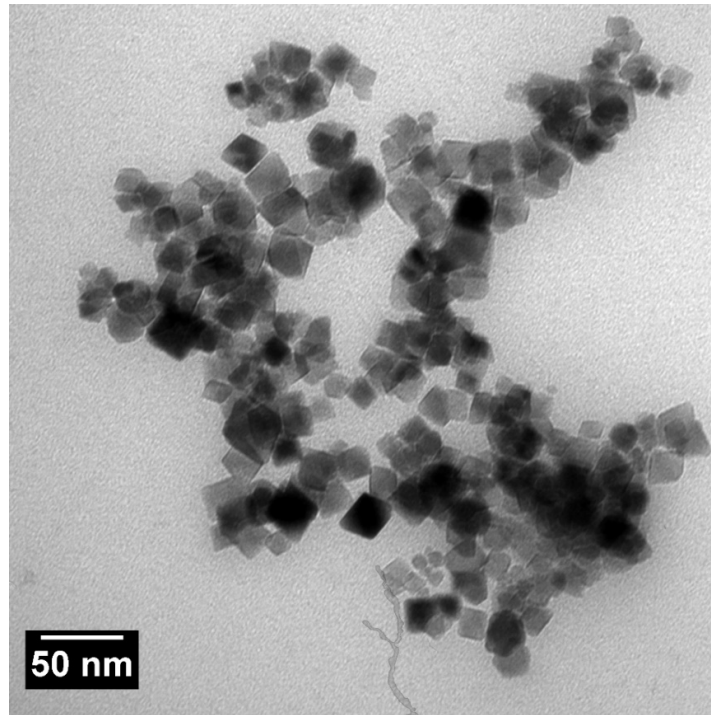


Full size TEM images:

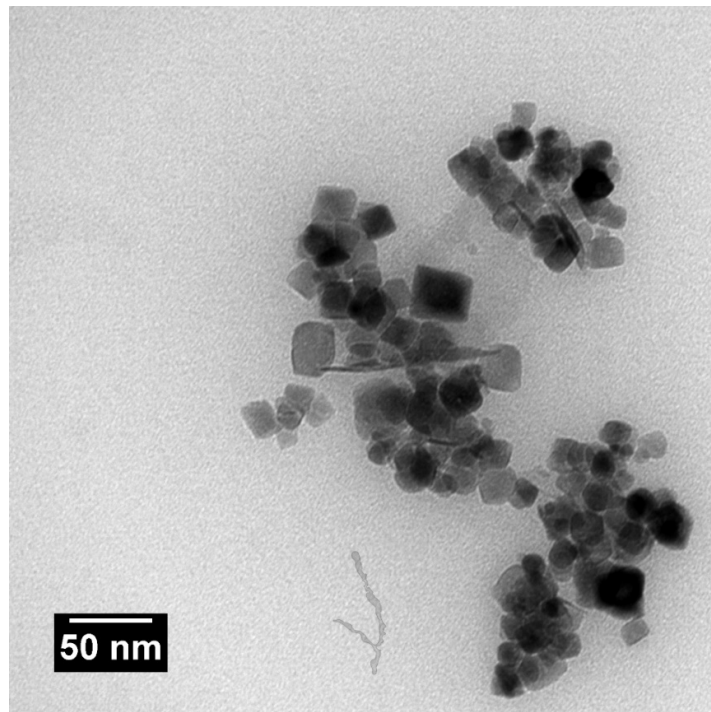
1:1250



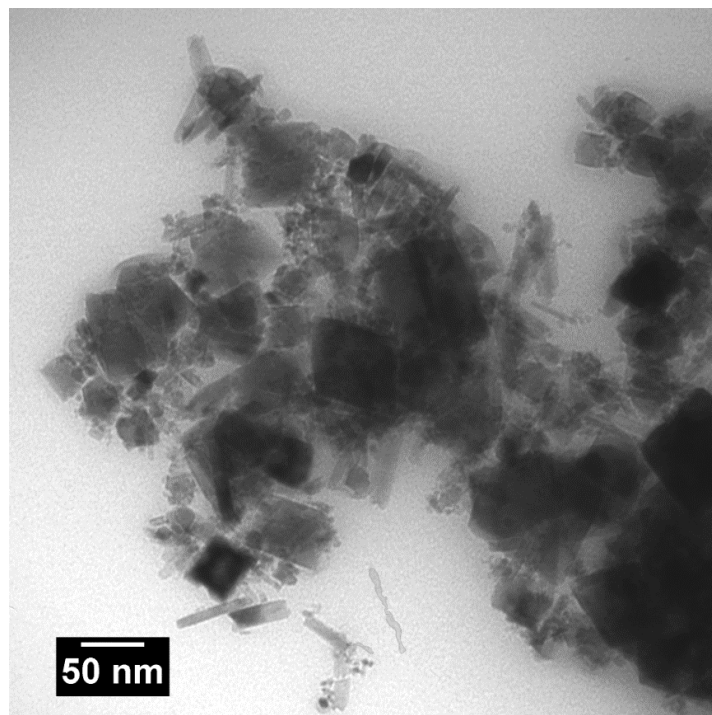
1:125



1:12.5

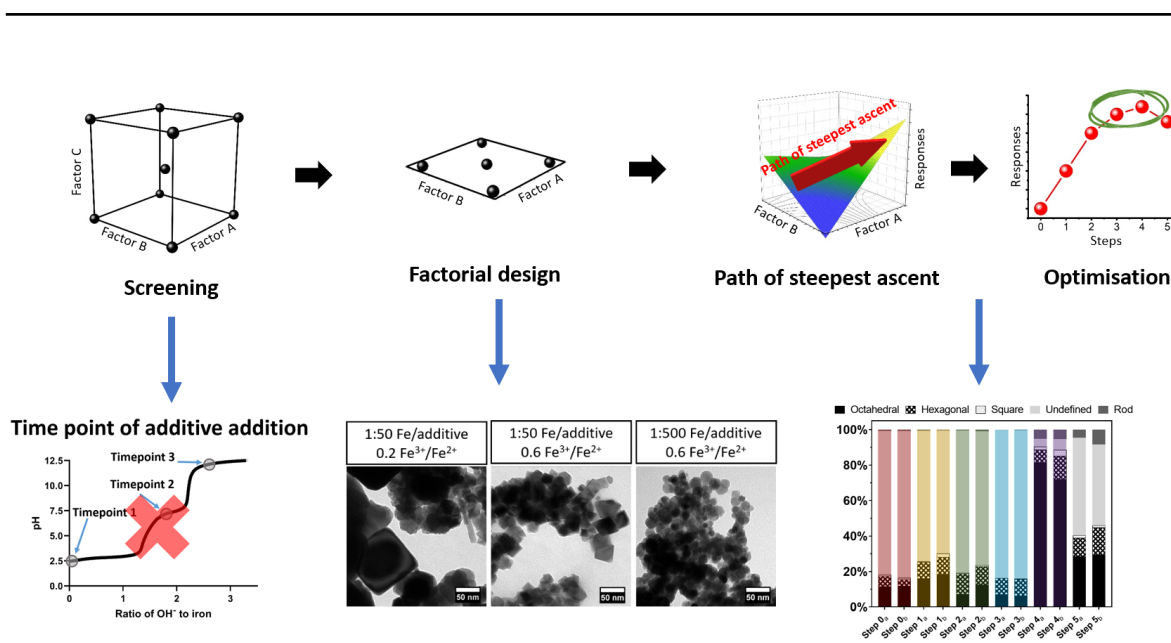


1:1.25



Chapter 5.

TEPA Design of Experiment



This chapter consists of a to-be-submitted paper titled "A Design of Experiment (DoE) approach to the optimisation of bioinspired magnetite nanoparticles using an affordable amine additive".

5.1 A Design of Experiment (DoE) Approach to the Optimisation of Bioinspired Magnetite Nanoparticles Using an Affordable Amine Additive

5.1.1 Author Contributions

Laura Norfolk (first author): Helped design the first factorial design, carried out all experimental work, analysed particles formed (XRD, TEM, VSM, shape analysis, and size analysis), created supplementary and Figure 2, 5b, and 6, and wrote the additives/MNP portion of the introduction, methods, results and discussion.

Luc Dewulf (first author): Designed the second factorial design and the path of steepest ascent, analysed the three sets of data (one from each design), created Figure 1, 3, 5, 5a, and 5c, and wrote the DoE/statistical portion of the introduction, methods and results.

Mauro Chiacchia: Designed the first factorial design, aided with the analysis of initial results and explaining DoE principles.

Siddharth Patwardhan: Helped design the first factorial design, acquired project funding, and provided feedback on the first draft of the paper.

Sarah Staniland (principal investigator): Supervisor, suggested DoE as a means of further analysing MNP formed with TEPA, helped design the first factorial design, acquired project funding, and provided feedback on the first draft of the paper.

ARTICLE

A Design of Experiment (DoE) approach to the optimisation of bioinspired magnetite nanoparticles using an affordable amine additive

Received 00th January 20xx,
Accepted 00th January 20xx
DOI: 10.1039/x0xx00000x

Laura Norfolk,^a Luc Dewulf,^{*b} Mauro Chiacchia,^c Siddharth Patwardhan,^c and Sarah Staniland^{a*}

The bioinspired co-precipitation of magnetite using additives to tailor particle shape is an attractive alternative to the currently favoured environmentally unsustainable methods of producing shape-controlled particles. The effect of tetraethylenepentamine (TEPA) as an additive in the room-temperature co-precipitation (RTCP) of magnetite has been investigated in an iterative Design of Experiments (DoE) strategy, utilising Full Factorial Designs (FFD) and a Path of Steepest Ascent (PSA) optimisation through three designs. Considering the ferric ratio ($\text{Fe}^{3+}/\text{Fe}^{2+}$), Fe/additive ratio, and timepoint of additive addition as factors, the percentage of isotropic faceted particles and saturation magnetisation were measured as responses. After an initial scouting FFD, timepoint of additive addition was found to be insignificant as a factor. A second FFD followed by a PSA optimisation found higher $\text{Fe}^{3+}/\text{Fe}^{2+}$ ratios of 0.6, closer to the ideal 2:1 stoichiometric ferric ratio produced a higher shape response (an increase in isotropic faceted particles). The interaction between ferric and Fe/additive ratio was found to be significant, as the same level of additive concentration was not as effective at lower ferric ratios. An optimum Fe/additive ratio of 50:1 was established, alongside the higher ferric ratio of 0.6 to produce ~90% isotropic faceted particles with a high magnetism of 77 emu g^{-1} , showing it is possible to synthesise MNP which are both highly magnetic and highly faceted. Since it is a requirement of many industries to use homogeneous particles, the production of these magnetite nanoparticles is a significant step toward the industrial production of green magnetite nanoparticles. These conditions can be utilised for further synthesis or as a basis for further optimisation of shape tuned magnetite nanoparticle syntheses. This involved use of DoE shows it is possible to optimise two responses simultaneously to produce high quality MNP.

Introduction

For several decades tailored magnetite nanoparticles (MNP) have been extensively studied¹ for their applications in various industries spanning data storage,² ferrofluids for electronics,^{3,4} and crucially several biomedical applications including hyperthermic cancer treatments,⁵ targeted drug delivery,⁶ and MRI contrast agents.⁷

In these applications, particle properties such as size,⁸ composition,⁹ and shape¹⁰ each play a pivotal role in the performance and potential applications of magnetic particles. As such, it is crucial to be able to modulate these properties in a nanomaterial product. The ability to design and tailor bespoke magnetic nanoparticles controlling these properties has hence been a research goal.

The shape of MNPs has been observed to influence the properties of particles for clinical applications. Octahedral MNPs were found to exhibit higher specific absorption rates and

improved relaxivity for MRI use, showcasing the potential advantages of specific morphologies for medical applications.¹¹

As industrial use of MNPs rise, it is increasingly clear that producing tailored nanomaterials in a sustainable manner is a critical issue to address.¹² Whilst highly shape-controlled MNP have been synthesised, the methodologies require high boiling organic solvents, toxic precursors, and extensive heating and vacuum use^{13,14}, rendering them highly unsustainable. Achieving enhanced morphological control of MNPs under milder reaction conditions such as a room temperature co-precipitation (RTCP) has proved to be a challenge under laboratory conditions.¹⁵

As a nanocrystal nucleates and grows from a spherical primary particle, additives such as proteins^{16,17} or smaller compounds¹⁸ may interact with the forming magnetite surface. Adsorption of an additive to a crystal face lowers the interfacial energy of that facet, and crystal growth along that axis is slowed, ensuring this face dominates the final particle morphology.

Research into magnetotactic bacteria,¹⁹ and subsequently their biomineralisation proteins^{20,21} and derivatives such as magnetite interacting Adhirons (MIA)²² has furthered our understanding of how highly faceted magnetite forms in nature under ambient conditions. Drawing inspiration from MIA, the use of small molecular additives incorporating amine functionalities have been found to modulate the shape of

^a Department of Chemistry, The University of Sheffield, Dainton Building, Brook Hill, Sheffield, S3 7HF, United Kingdom

^b School of Physics and Astronomy, University of Edinburgh, James Clerk Maxwell Building, Peter Guthrie Tait Road, Edinburgh, EH9 3FD, United Kingdom

^c Department of Chemical and Biological Engineering, The University of Sheffield, Mappin Street, Sheffield, S1 3JD, United Kingdom

Electronic Supplementary Information (ESI) available: See DOI: 10.1039/x0xx00000x

MNPs.²³ Ethylenediamine homologues have successfully been used to produce octahedral particles in both batch and large-scale flow co-precipitation reactions, with tetraethylenepentamine (TEPA) being the most successful of this series.²³

Further investigation into the impact and function of TEPA as an additive is important to build on the understanding of how the morphology of MNPs are affected by the addition of TEPA to RTCP reactions, which can help design MNPs for desired applications.

Previous studies aiming to understand the factor-response relationship of MNPs were often carried out utilising a variation of the one-factor-at-a-time (OFAT) approach. However, univariate methods are unsuited to understand the complex nature of MNP synthesis, and for optimisation of multiple responses such as shape and magnetism simultaneously. Instead, multivariate methods such as those within the Design of Experiments (DoE) framework are popular and allow product and process optimisation via statistical evidence. The DoE methodology provides efficient designs that designate a combination (treatment) of reaction synthesis parameters (factors) and their physical values (factor levels) according to which experimental results (observations) are collected and statistically analysed.

Generally, designs fall into several categories, two of which will be discussed in this paper: 1) Screening designs are used to segregate significant from insignificant factors and for obtaining preliminary indication of the direction of response improvement, while lacking precision due to their design simplicity. 2) Optimisation frequently employs more elaborate models to obtain an increasingly precise map of the behaviour of the chemical system, at the cost of being more resource intensive. Greater experimental efficiency can be obtained with a combination of these two approaches as we recently demonstrated elsewhere.²⁴

For MNPs both screening and optimisation designs have previously been used to gain a better understanding of the input-output relationship between synthesis factors and

size, magnetite yield, and magnetisation for electrochemical-, microwave-, and Mössbauer-synthesised magnetite.^{25–28} Magnetite via co-precipitation was screened using Plackett-Burman and uniform 2⁶ fractional factorial designs.^{29,30}

A range of optimisation studies have been conducted including central composite designs, Box-Behnken designs, and optimal designs to accurately map particle size, yield, and magnetisation for hydrothermal and co-precipitation magnetite syntheses.^{31–36} However, previous studies reveal several drawbacks: all studies performed a single standalone design and did not optimise the system beyond their one-off experiment, with the exception of Medinger et al.³⁶, who used a feedback loop to refine the response surface methodology. Moreover, studies attempted to optimise only a single response at a time. Instead, we report a sequential strategy consisting of two factorial screening designs, followed by a path of steepest ascent (PSA) optimisation (Figure 1).

The factorial screening design allows construction of simple polynomial regression models at low experimental cost. The maximum (or minimum) response can be assumed to be in the direction in which the regression model increases (or decreases), although the optimum point may lie outside of the initial screening design space. The path of steepest ascent (or descent) can then be calculated and experiments carried out at regular intervals to locate the maximum (or minimum) response. PSA optimisation is reported for biological^{37–42} and organic synthesis,^{43,44} but has rarely been employed for inorganic synthesis,^{45,46} and is entirely unreported for magnetite synthesis.

In the synthesis of MNP, multiple input parameters affect the output product properties (responses) to various extents, resulting in an inherently complex reaction landscape. Future scale-up and optimisation depend on the ability to identify the significant from the insignificant factors and to map how the response changes with a change in the identified significant factors.

Previous research has shown the importance of the Fe³⁺/Fe²⁺ iron ratio on the size and composition of MNPs formed

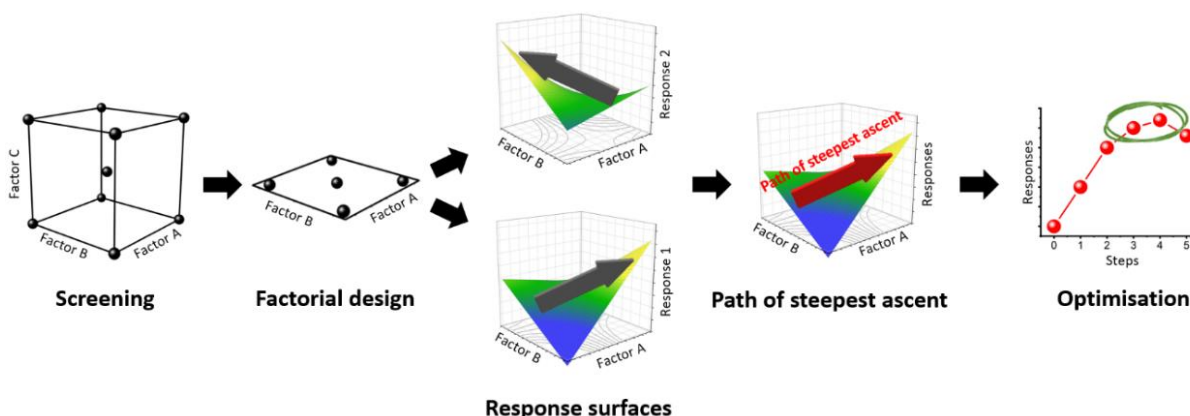


Figure 1. Sequential Design of Experiments strategy consisting of a factorial screening design followed by a path of steepest ascent to optimise two responses simultaneously.

physicochemical properties. For screening, 2³ and 2⁴ full factorial designs (FFD) were employed to evaluate nanoparticle

under RTCP conditions. Particles formed at lower ratios are typically larger in size, with higher polydispersity and a lower

proportion of magnetite. Biomineralisation proteins have shown the ability to influence ferrous iron, promoting the formation of magnetite in ferrous-rich environments which would usually be unfavourable for the formation of this desired iron oxide, inspiring the investigation into the potential for additives to alter the proportion of magnetite formed at lower ferric ratios. Varying the ratio from the established ideal of 0.6 allows for the effect of the additive across a spectrum of conditions to be investigated.

pH titrations of the reaction system have shown times at which the RTCP is significantly chemically distinct, leading to the selection of three distinct timepoints; T_1 , the start of the reaction, T_2 , after all soluble iron (III) is consumed, and T_3 , after all soluble iron (II) is consumed. The equivalence points at which the ferric/ferrous ions were consumed were taken from Rawlings et al and were determined based on the ferric ratio for each reaction.¹⁶

Our previous concentration study suggested the ideal Fe/additive ratio to be around 125.²³ Performing reactions above and below this tested value allows the influence of additive concentration to be screened across a range. We are seeking to further improve upon the previously identified optimal conditions, and investigate a wider range of concentrations than those previously studied.

Both magnetism and particle shape play an important role in the potency of MNPs as a potential biomedical treatment, and as such both these responses are measured, and further iterations of DoE optimised for.

A total of three iterations of DoE were completed, with two factorial designs, the first of which covering all three factors, the second considering ferric ratio and additive:iron ratio, and finally a path of steepest ascent compromising between optimising both magnetism and the proportion of faceted particles formed.

The complete study of three iterative designs is the first account of systematic optimisation of additive controlled bioinspired magnetite nanoparticle synthesis using a sequential statistical strategy.

Materials and Methods

Chemicals

Iron (II) sulphate, iron (III) sulphate, sodium hydroxide and tetraethylenepentamine were purchased from Sigma-Aldrich and used without further purification. Iron contents of the iron salts were assessed via inductively coupled plasma optical emission spectrometry analysis when calculation iron solution molarities. Ultrapure water (Milli-Q) (Merck, Milli-Q integral purification system) was used for all experiments.

Magnetite Nanoparticle Synthesis

To favour the formation of magnetite nanoparticles, all reactions were carried out under an inert atmosphere of N_2 . All solutions were sparged with N_2 for a minimum of 30 minutes prior to use. An Ultrapure water (Milli-Q) (Merck, Milli-Q integral purification system) was used.

Particles were formed using a room temperature co-precipitation technique. Iron(II) sulphate and iron(III) sulphate were dissolved in N_2 sparged MilliQ (20 mL), under an inert atmosphere of N_2 to form a 1 mM Fe solution in a two-necked round bottom flask (quantities of iron(II) sulphate and iron(III) sulphate were calculated relative to the desired Fe^{3+}/Fe^{2+} ratio). A set amount of TEPA was calculated relative to the iron content, added to the reaction mixture, and left to stir to ensure dissolution of TEPA and iron salts. N_2 sparged 0.5 M NaOH (8 mL) was added at a rate of 50 μ L a minute with magnetic stirring, for a total of 160 minutes using a Harvard Apparatus 11 plus syringe pump driver.

A schematic of the reaction set-up is shown in supplementary figure S10.

The reaction was then left to age for an hour under the inert atmosphere with stirring maintained. The reaction mixture was then magnetically separated, washed 5 times with sparged MilliQ to remove any non-magnetic iron oxides and NaOH, and the particles dried in a vacuum oven at 40 °C overnight. The particles were then ground with a pestle and mortar for analysis.

Magnetite Nanoparticle Characterisation

Transmission Electron Microscopy (TEM): For TEM analysis of magnetic nanoparticles, a 10 μ L of a 1mg/mL suspension of nanoparticles was sonicated for 1 minute in hexane and dropped onto a carbon coated copper TEM grid and allowed to dry down for a minimum of 1 hour. Grids were imaged using a FEI Tecnai G2 Spirit electron microscope (Thermo Scientific, Waltham, MA, United States) and the TEM images were analysed using Image-J software (v1.52, public domain, National Institute of Health, MD, USA). >200 particles per sample were randomly selected for measurement. Further details on the shape and size analysis from TEM images can be found in the supplementary.

Vibrating Sample Magnetometry (VSM): Magnetic susceptibility was performed on a known quantity (1–5 mg) of dry iron oxide nanoparticles on a MPMS 3 SQUID magnetometer (Quantum Design, Surrey, United Kingdom) in vibrating sample mode, with the samples packed in size 3 gelatine capsules. The samples were run at 300 K between –3 and 3 T with a sweep rate of 0.01 T/s. The data shown is cropped at saturation magnetisation.

X-Ray Diffraction (XRD): For XRD data of samples was collected by analysis of dry iron oxide nanoparticles in a Bruker D8 powder diffractometer (Bruker, Coventry, United Kingdom). Diffraction images were collected at 0.022-degree increments from 20–80 degrees, with a fixed wavelength at $\lambda = 1.54178 \text{ \AA}$ at 1.2 seconds per step from a Cu K α -ray source.

Table 1. Input parameters and experimental results of the factorial design. Experiments were carried out as duplicates.

Factors				Responses	
Fe/additive ratio, x_1 (mol/mol)		Fe ³⁺ /Fe ²⁺ ratio, x_2 (mol/mol)		Shape (% isotropically faceted)	Saturation magnetisation (emu g ⁻¹)
Coded	Uncoded	Coded	Uncoded		
-1	50	-1	0.2	39, 41	41.7, 69.1
+1	500	-1	0.2	58, 54	31.3, 38.3
-1	50	+1	0.6	87, 92	75.7, 78.0
+1	500	+1	0.6	11, 13	66.9, 74.2
0	275	0	0.4	14, 18	59.2, 78.0

Factorial Design

Initially, a 2³ FFD with a centre point was utilised (data shown in supplementary information). The preliminary study identified the time point of additive addition to be insignificant for the MNP properties, hence this factor was removed from future experiments. Thus, we proceeded with a 2² full factorial design with center point to investigate the Fe/additive ratio (factor x_1) between the boundaries 50-500 mol/mol, and the Fe³⁺/Fe²⁺ ratio (factor x_2) between 0.2-0.6 mol/mol, as identified suitable from the literature review above, and tabulated in Table 1. The use of coded variables, essentially rescaling the x inputs between -1 and +1, has found merit for its orthogonality and is applied here where appropriate. Equations 1 and 2 were used to convert between coded and uncoded variables (see Table 1) for the Fe/additive (x_1) and Fe³⁺/Fe²⁺ (x_2) factors respectively:

$$x_{1,\text{coded}} = \frac{x_{1,\text{uncoded}} - 275}{225} \quad (1)$$

$$x_{2,\text{coded}} = \frac{x_{2,\text{uncoded}} - 0.4}{0.2} \quad (2)$$

Based on the factorial design, first-order linear regression models were constructed for visualisation and response optimisation purposes according to equation 3:

$$y = \beta_0 + \sum \beta_i x_i + \sum \beta_{ij} x_i x_j \quad (3)$$

where y is the response, β_0 is the average, β_i are the regression coefficients of the main factors, β_{ij} are the regression coefficients of the factor interactions, and x_i and x_j are the regressor variables of the factors or factor interactions.

Path of Steepest Ascent (PSA)

Using the first-order model established during the screening experiment (equation 3), the path of steepest ascent was evaluated for each response from:

$$\nabla y|_{(0,0)} = \frac{\partial}{\partial x_i} (\beta_0 + \sum \beta_i x_i + \sum \beta_{ij} x_i x_j)|_{(0,0)}, \frac{\partial}{\partial x_j} (\beta_0 + \sum \beta_i x_i + \sum \beta_{ij} x_i x_j)|_{(0,0)} \quad (4)$$

where ∂ are partial derivatives evaluated at (0,0), resulting in a straight line with the origin at the center point of the factorial design. Because the paths of steepest ascent for the shape and magnetisation responses diverged in different directions an optimised line between the two was taken as the final PSA in an

Table 2. Treatment steps and experimental results along the path of steepest ascent. Experiments were carried out as duplicates.

Step	Factors				Responses	
	Fe/additive ratio, x_1 (mol/mol)		Fe ³⁺ /Fe ²⁺ ratio, x_2 (mol/mol)		Shape (% isotropically faceted)	Saturation magnetisation (emu g ⁻¹)
	Coded	Uncoded	Coded	Uncoded		
0	0	275	0	0.40	19, 17	62.8.3, 61.6
1	-0.24	221	0.24	0.45	26, 31	67.8, 73.4
2	-0.48	167	0.47	0.49	20, 25	86.4, 90.6
3	-0.72	113	0.71	0.54	16, 16	91.1, 84.5
4	-0.96	59	0.95	0.59	96, 94	67.7, 63.0
5	-1.2	5	1.19	0.64	45, 54	67.4, 76.8

endeavour to optimise both responses simultaneously. The PSA was then divided into five equal segments between the center point and the physical limits of MNP synthesis of Fe/additive ≥ 5.0 and Fe³⁺/Fe²⁺ ≤ 0.64 , resulting in six steps (Table 2).

Results

Response Consideration

When considering the quality of particles desired for biomedical applications, two key points of potential optimisation were identified: i) the percentage of faceted particles, and ii) the saturation magnetisation. As elongated nanorods have been previously found to exhibit cytotoxic effects,⁴⁷ the focus was kept on isotropic (equal size along each axis) faceted particles. Due to the nature of TEM imaging returning a two-dimensional image, particle shapes are assigned by the presence of defined facets (figure S13, supplementary) with a large number (> 300) of particles being inspected for shape analysis. Saturation magnetisation is highly indicative of the magnetic purity of particles formed, with pure magnetite exhibiting a saturation magnetisation of 92 emu g⁻¹. High magnetic saturation is desired for industrial applications.

An initial scouting experiment found the time point of additive addition to be an insignificant factor in both the shape and magnetism responses of MNP and was hence deleted from further experiments (see supplementary information). The two remaining factors Fe/additive ratio and Fe³⁺/Fe²⁺ ratio were used to simultaneously optimise the shape (% isotropic faceted particles) and saturation magnetisation (emu g⁻¹) responses by employment of a factorial design followed by a path of steepest ascent optimisation.

Table 3. Regression models and analysis of variance for the shape and magnetisation response based on a confidence interval of 95%.

	Shape (% isotropic faceted particles)					Saturation magnetisation (emu g ⁻¹)				
Uncoded ^a	$y = 1.3 + 0.14x_1 + 150x_2 - 0.52x_1x_2$					$y = 49.5 - 0.0615x_1 + 49.8x_2 + 0.0792x_1x_2$				
Coded ^b	$y = 42.51 - 15.34x_1 + 1.39x_2 - 23.4x_1x_2$					$y = 61.24 - 6.71x_1 + 14.31x_2 + 3.57x_1x_2$				
Source	DF ^c	SS ^d	MS ^e	F-Value ^f	p-Value ^g	DF ^c	SS ^d	MS ^e	F-Value ^f	p-Value ^g
Fe/additive	1	1882	1882	6.34	0.045*	1	360	360	2.91	0.139
Fe ³⁺ /Fe ²⁺	1	15	15	0.05	0.827	1	1638	1638	13.27	0.011*
Fe/additive × Fe ³⁺ /Fe ²⁺	1	4382	4382	14.75	0.009*	1	101.7	101.7	0.82	0.339
Residual ^h	6	1782	297			6	741	123		
Curvature ⁱ	1	1750	1750	270.83	0.000	1	135	135	1.11	0.34
Pure error ^j	5	32	6			5	606	121		
Total	9	8062				9	2840			
R ² ^k	0.78					0.74				
Adjusted R ² ^l	0.67					0.61				
Prediction R ² ^m	0.62					0.29				

a: Model with factors in original units of mol/mol

b: Model with factors rescaled between -1 and +1

c: Degrees of Freedom (DF)

d: Sum of squares (SS)

e: Mean square (MS)

f: The MS of a factor divided by the residual MS

g: Source is statistically significant if p-value < α (0.05)

h: Error

i: Presence of significant interaction terms causing bending or curvature of the response surface

j: Residual or error calculated from replicated observations

k: Coefficient of multiple determination

l: R² accounting for statistically significant terms in the model

m: R² evaluating the predictability of a missing observation

* Statistically significant factor or interaction

Factorial Design

Table 1 tabulates the experimental results for the factorial design. For each response, a first-order linear regression model was constructed according to equation 3 with the Minitab 19 Software⁴⁸ (Table 3). Analysis of variance (ANOVA) was performed to evaluate the adequacy and predictability of the models (also Table 3), as well as to segregate significant from insignificant factors with a level of significance of α = 0.05.

The ANOVA shows several key findings; i) Fe/additive ratio is significant for the shape response, but not magnetism, ii) Fe³⁺/Fe²⁺ is significant for magnetism but not shape, iii) the interaction of Fe/additive ratio and Fe³⁺/Fe²⁺ is significant for shape but not magnetism.

Previously conducted research has shown the importance of additive concentration on the proportion of faceted particles, with a higher % of particles appearing faceted as the Fe/additive ratio increases.⁴⁹ As more additive is present, a greater inhibition of growth may occur on developing crystal facets,

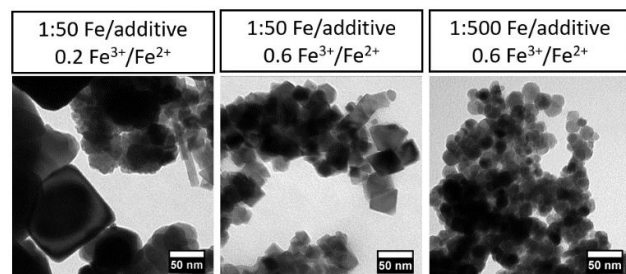


Figure 2. Representative TEM images of particles formed under stated conditions in the factorial design of magnetite synthesis with TEPA additive.

resulting in an increased proportion of shape-controlled particles. This is shown in Figure 2, with the proportion of isotropic faceted particles being highest at a 1:50 Fe/additive ratio and 0.6 ferric ratio (87 and 92 % faceted for the two repeats). This improved morphology is not observed at the equivalent 1:500 Fe/additive ratio, instead producing the lowest proportion of isotropic faceted particles (11 and 13 %). As the interaction between Fe/additive ratio and Fe³⁺/Fe²⁺ was found to be significant for shape, this synergy results in the effect of one factor being dependent on the level of the other factor. This means that as a consistent Fe/additive ratio fails to produce identical results at different ferric ratios, the shape depends on the levels of both factors, which is termed an interaction. Thus, the shape is influenced by a coupled effect between both the Fe/additive and Fe³⁺/Fe²⁺ ratio.

The addition of higher concentrations of additive were not found to significantly influence saturation magnetisation within these experimental parameters.

The key influencing factor for particle magnetism was found to be Fe³⁺/Fe²⁺. This ratio is responsible for the iron oxides formed, with magnetite formation being favoured at the optimal 2:1 ratio. At lower ferric ratios ferrous-rich non-magnetic iron oxides are formed, leading to a product of mixed iron oxides containing non-magnetic iron oxides, and reduced saturation magnetisation.

When the path of steepest ascent is constructed mathematically, higher-order terms are neglected, making complex models redundant at an early stage of optimisation. Nevertheless, the ANOVA shows that curvature is significant for

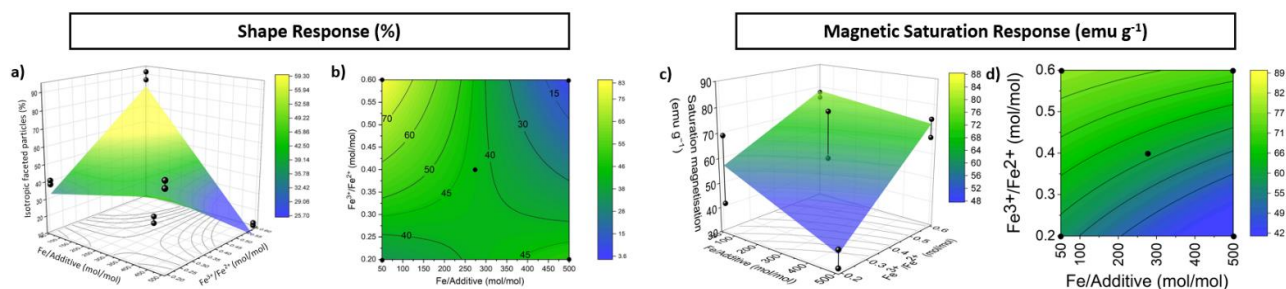


Figure 3. Three-dimensional response surfaces for a) the shape and c) the magnetism response, and contour plots for b) the shape and d) the magnetism response, each based on the first-order regression models from the FFD.

the shape of MNP, suggesting that a model based on main effects only is inappropriate to explain the trend fully. According to the non-hierarchy principle, it is indeed possible for a factor to be insignificant on its own but to be part of a large interaction.^{50,51} On the other hand, the insignificance of curvature for magnetism could suggest that a simple model is sufficient in this case. However, significant deviation from the predictions of the models was observed, making the PSA optimisation beyond the original design promising.

The R^2 values of 0.78 and 0.74 for shape and magnetism respectively indicate that 78 and 74 % of the trend in shape and magnetism can be explained by the model. Moreover, most types of R^2 statistics were above 0.6, giving confidence in the models for development of the following PSA.

Figure 3 shows three-dimensional (3D) response surfaces and contour plots of the regression models for the shape and magnetisation respectively. A contour plot is essentially a top-down view of the 3D model, in which lines of constant response are drawn.

Path of Steepest Ascent

As the factorial design did not identify a maximum response, the search for optimum synthesis conditions is required to move beyond the initial design in the most efficient direction, which is generally assumed to be the direction in which the responses increase steepest.⁵²

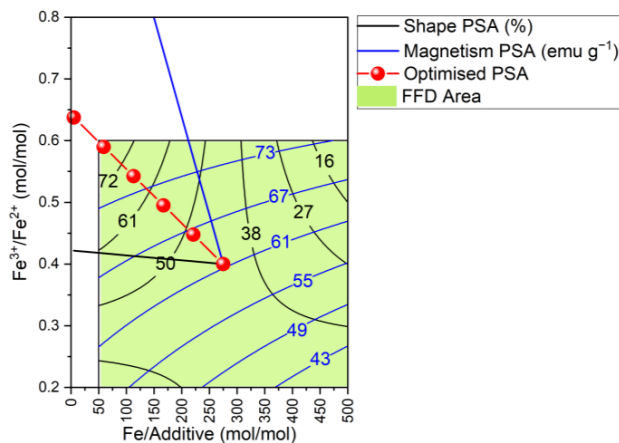


Figure 4. Contour plot depicting direction of increasing response for the shape (black) and magnetism response (blue), leading to the optimised path of steepest ascent (red) with 6 steps.

Using coded regression models (Table 3), individual paths of steepest ascent were calculated for the shape and saturation magnetisation respectively in coded units:

$$x_2 = -0.0906x_1 \quad (4)$$

$$x_2 = -2.1326x_1 \quad (5)$$

From comparison of equations 4 and 5, and likewise from the responses shown in Figure 3, it was observed that the shape and magnetism responses increased in differing directions. In pursuit of the best compromise between the two responses, an optimised PSA was constructed with equation $x_2 = -1.0108x_1$ dividing the sector between the two individual PSAs in two.

This path was then divided by 6 steps between the midpoint (Fe/additive = 275 mol/mol, Fe³⁺/Fe²⁺ = 0.4 mol/mol) and the physical limits of MNP synthesis (Fe/additive \geq 5.0 and Fe³⁺/Fe²⁺ \leq 0.8), resulting in the PSA extending beyond the initial factorial design shown in the contour plot in Figure 4 with the steps illustrated in red.

The coded variables were converted to uncoded according to equations 1 and 2 and are tabulated alongside the experimental results in Table 2.

For the shape and magnetism responses respectively, Figure 5 shows the actual results and the values predicted by the first-order models along the optimised PSA. The discrepancies between predicted and actual values reinforce the fact that factorial designs may indicate the direction of a global maximum, but a sequential strategy is required to identify its precise location and local minima or maxima in its vicinity.

The maximum % isotropic faceted particles occurred with 95% (average of both experimental values) at the fourth step, and the maximum saturation magnetisation occurred at the third step with 88.5 emu g⁻¹.

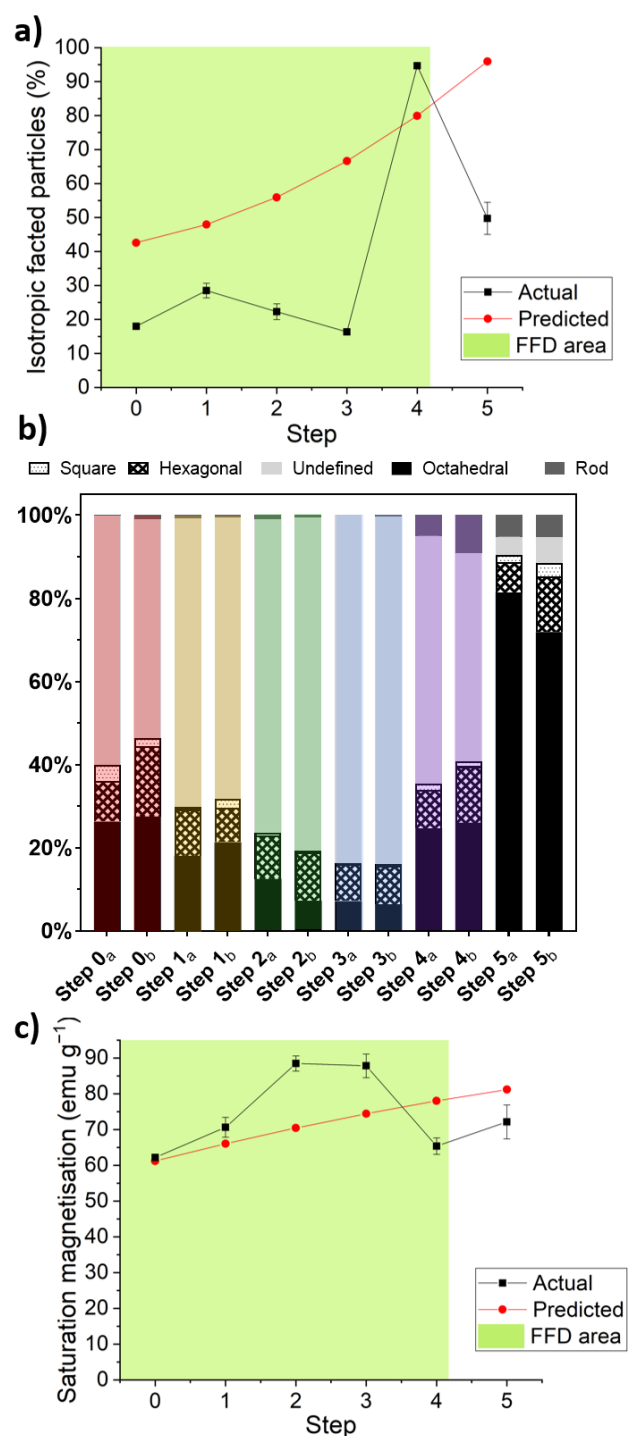


Figure 5. Actual results and values predicted by the optimised PSA for a) the shape; b) shape frequency graph of particles; and c) the saturation magnetisation responses. Error bars are range of duplicate experiments

Discussion

The co-precipitation of magnetite from solution is a complex reaction, which proceeds through a series of intermediary ferric and ferrous based iron oxides to form magnetite.⁵³ As such, the experimental landscape may not be straightforward, and

different levels of factors interacting may considerably alter the morphology and magnetism of particles formed in a non-linear manner. Many co-precipitation particle syntheses factor in mild oxidation to obtain the final magnetite product, hence syntheses with $\text{Fe}^{3+}/\text{Fe}^{2+}$ ratios of > 0.66 are still successful at producing magnetic particles despite an excess of ferrous ions.

The process of iterative DoE has taken steps toward mapping said experimental landscape, with several experimental conditions being identified as points of interest for further study which will be discussed below.

From the first scouting FFD the time point of additive addition was found to be an insignificant factor. This suggests the function of TEPA as an additive under these conditions was to interact with forming magnetite surfaces, influencing particle growth via inhibition of facet growth rather than via interaction with aqueous iron ions. This is concurrent with molecular dynamics simulations suggesting TEPA has an exothermic binding energy at the [111] octahedral magnetite surface.⁴⁹ Deletion of the time variable also allowed for future designs to be simplified, as the addition of TEPA at the beginning of the reaction did not appear to impair the formation of the desired product.

The first FFD also considered size as a response, with size being influenced significantly by both the $\text{Fe}^{3+}/\text{Fe}^{2+}$ and $\text{Fe}/\text{additive}$ ratios. Higher concentrations of TEPA led to a reduction in particle size at a low ferric ratio (0.2), producing particles in accordance (closer to 20 nm) with those produced at a more ideal ferric ratio (0.6). The ferric ratio has previously been found to drastically influence the size of particles formed, with particles formed at higher ratios (0.5-0.7) being significantly smaller in size than those formed at lower ratios (0.2-0.4). This was seen alongside a significant increase in saturation magnetisation suggesting that as well as particle size decreasing, the addition of TEPA also promoted the formation of greater proportions of magnetite at sub-optimal $\text{Fe}^{3+}/\text{Fe}^{2+}$ ratios. As the experiments progressed through further iterations it was decided to focus on shape tuning and optimising magnetic response to simplify the designs and streamline optimisation.

The second FFD identified the $\text{Fe}/\text{additive}$ ratio as significant for the proportion of isotropic faceted particles formed, with Figure 3 exemplifying the difference in particles formed at the same $\text{Fe}^{3+}/\text{Fe}^{2+}$ ratio with varied $\text{Fe}/\text{additive}$ ratio. This increase in proportion of isotropic faceted particles is likely due to the larger quantity of additive having an increased inhibition effect on specific facet growth. A concentration study has been previously conducted which found a $\text{Fe}/\text{additive}$ ratio of 125:1 was preferred to a lower iron concentration of 12.5:1.⁴⁹ This study tested an intermediate value of 50:1 between the previously explored experimental values, which was found to produce highly optimal particles (~90% faceted and 80.9 emu g^{-1}). Notably, these particles are the best compromise between performance of both the shape and magnetic response and are hence deemed as the preferred conditions for further investigation into the effect of TEPA as an additive on magnetite co-precipitations. As the PSA varied two factors simultaneously, it is not possible to draw parallels between all points of the

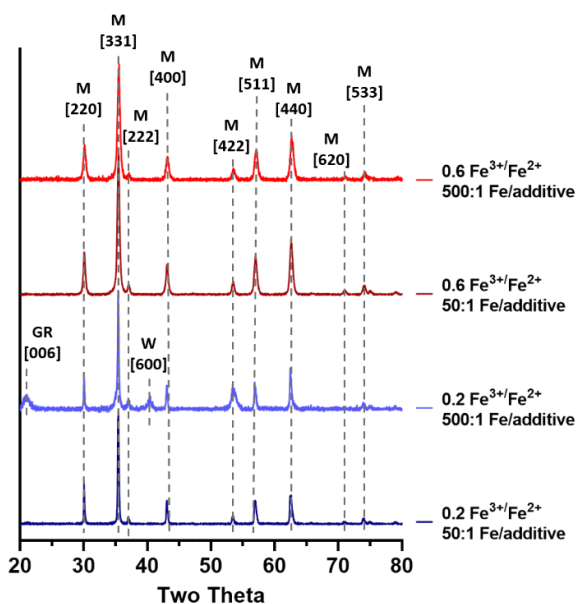


Figure 6. Annotated XRD data for magnetic particles formed with high and low levels of $\text{Fe}^{3+}/\text{Fe}^{2+}$ ratio and Fe/additive ratio, where M = magnetite, GR = Green rust, and W = Wüstite.

previous concentration study due to the effect of also varying the $\text{Fe}^{3+}/\text{Fe}^{2+}$ ratio simultaneously, and the resultant effect this may have on the proportion of faceted particles formed.

Figure 3 also draws a contrast to the effect of the lower (0.2) $\text{Fe}^{3+}/\text{Fe}^{2+}$ ratio on particles formed. Whilst particle size is not analysed as a response in these designs, the particles are visibly less consistent with reduced magnetism relative to the particles formed at a 0.6 ratio. This reduction in saturation magnetisation can occur due to the formation of other non-magnetic iron oxides being favoured the further from the ideal ratio of 2:1 $\text{Fe}^{3+}/\text{Fe}^{2+}$ ions. This is supported by XRD data (Figure 6) showing that the XRD of particles formed at a low ferric ratio with a low concentration of additive exhibited a ferrous rich green rust and wüstite impurity peaks. These peaks were not observed in the sample formed at the same low ferric ratio with a higher Fe/additive ratio, supporting the theory that at highly sub-optimal ratios, high concentrations of TEPA may be aiding the formation of magnetite.

Interestingly, a lower $\text{Fe}^{3+}/\text{Fe}^{2+}$ ratio can lead to more faceted particles. This effect can occur for two reasons: i) when a particle is larger in size their facets have had longer to grow and mature compared to smaller particles, and ii) not all particles present at lower ferric ratios will be magnetite. The presence of iron oxide impurities with different morphologies may explain the greater proportion of faceted particles forming at the lower ferric ratio compared to the particles synthesised at a 0.6 ratio with 50:1 additive ratio. A similar pattern has been observed prior with the formation of hexagonal plates of green rust, which is also observed in the XRD of the 0.2 $\text{Fe}^{3+}/\text{Fe}^{2+}$ 500:1 Fe/additive ratio reaction.⁵⁴

In contrast to the considerable change observed in shape response with the Fe/additive ratio, saturation magnetisation was not found to be significantly influenced by a change in Fe/additive ratio. This suggests in contrast with the first design

that TEPA is neither promoting the formation of higher quality magnetite, nor lowering the particle quality, which can occur when an additive is embedded in the forming nanoparticle structure lowering the overall particle crystallinity. As the first FFD included $\text{Fe}^{3+}/\text{Fe}^{2+}$ ratios further from the 2:1 stoichiometric ratio of ferrous and ferric ions natively found within magnetite, it is possible the improved magnetic response is only observed at ratios very far from the ideal. Any assumption made cannot be extrapolated to all concentrations of additive and can only be considered the case for the conditions tested within the experimental design, as the effects of higher proportions of additive were found to lower particle magnetism in the PSA.

The particles formed at a 0.6 $\text{Fe}^{3+}/\text{Fe}^{2+}$ ratio and 50:1 Fe/additive ratio were significantly more faceted than those formed under any of the other conditions, highlighting the interaction between the two factors. TEPA is less effective at tuning the shape of particles formed at lower $\text{Fe}^{3+}/\text{Fe}^{2+}$ ratios, perhaps due to the formation of other iron oxides. The higher Fe/additive ratio produced less faceted particles than the lower ratio at the 0.2 $\text{Fe}^{3+}/\text{Fe}^{2+}$ ratio possibly due to the previously mentioned effect of an increased TEPA concentration producing smaller particles which are often generally less faceted at lower ferric ratios.

The PSA design successfully identified a maximum for both the shape and magnetic response, albeit not at the same step. While it is difficult to maximise both responses simultaneously, as the individual maxima occur at different steps (shape maximum at step 4, magnetism maximum at step 3), it is still possible to evaluate an optimum operating range between both responses. A midpoint between step 3 and 4 is likely to offer the best agreement, predicted to produce 75 % isotropic faceted particles with 75 emu g^{-1} saturation magnetisation.

Consistent with prior research,⁴⁹ Fe/additive ratios appear to have a peak concentration at which they are most effective, above which there are diminishing returns. Above this concentration the additional TEPA may act to alter the pH of the reaction in a manner which is unfavourable.

This diminishing returns effect also appears in the magnetic data, with magnetism generally increasing until step 3, at which point it drops. When comparing the second FFD and the PSA, it was found that similar conditions (FFD - Fe/additive: 50:1, $\text{Fe}^{3+}/\text{Fe}^{2+}$: 0.6) (PSA - Fe/additive: 59:1, $\text{Fe}^{3+}/\text{Fe}^{2+}$: 0.59) produced particles with lower magnetism of 65.4 emu g^{-1} (FFD) compared to 76.9 emu g^{-1} (PSA). The sensitive nature of coprecipitations may have led to a small less controllable change in conditions (room temperature, humidity, etc.) forming less magnetic particles.

Several data points within the second FFD and PSA show a discrepancy in magnetic data (Table 1 and Table 2) with one repeat producing more highly magnetic particles. For future work, further control over these discrepancies may be prudent. A magnetic reading of > 60 is still deemed highly magnetic, with one laboratory using superparamagnetic particles with a saturation magnetisation of 25–35 emu g^{-1} (BioMag®),⁵⁵ hence suggesting the particles synthesised in these designs would be sufficiently magnetic for biomedical use.

From the experimental conditions covered in the three designs, the optimal particles were produced at a 0.6 Fe³⁺/Fe²⁺ ratio and 50:1 Fe/additive ratio. Whilst the PSA did not reveal an improvement in particle properties over the second FFD, it is important to push the boundaries of experimental design in the search for optimal MNP synthesis in the event ideal conditions are outside the previously tested ranges.

Conclusions

DoE has been utilised through three iterations of experiments to investigate the previously unexplored reaction landscape of additive addition to MNP co-precipitation. By seeking to optimise the shape and magnetic response simultaneously through a combination of FFD and PSA, several findings have been identified.

The time-point of TEPA addition was not found to play a significant role, suggesting it can be added to the reaction at a later point if required without detrimental effect to particle quality. This allows for the potential of future synthesis to be simplified, whilst further building on our understanding of how TEPA functions as an additive.

The upper and lower limitations of high quality isotropic faceted MNP synthesis have been explored, with reduced magnetism observed at lower Fe³⁺/Fe²⁺ ratios, showcasing the importance of a close to 2:1 stoichiometric ratio, with a ratio of 0.6 generally producing the particles with the highest magnetic properties. Optimal isotropic faceted particle formation was observed at 59:1 and 50:1 Fe/additive ratios, at 0.59/0.6 Fe³⁺/Fe²⁺ ratios respectively, further highlighting the importance of a ferric ratio close to 0.6.

This work is a compelling step on the pathway to statistically guided and tunable MNP synthesis, with the shape control of MNP having not yet been extensively researched under RTCP conditions. By building upon the prior studies of the influence of TEPA in the co-precipitation system, we have furthered our understanding of how additive concentration and ferric ratio influence the properties of MNP formed and identified a potential starting point for batch scale-up of isotropic faceted MNP.

Abbreviations

3D: Three-dimensional
ANOVA: Analysis of variance
DF: Degrees of Freedom
DoE: Design of Experiments
FFD: Full factorial design
MIA: Magnetite interacting Adhiron
MNP: Magnetite nanoparticles
MS: Mean square
OFAT: One-factor-at-a-time
RTCP: Room temperature co-precipitation
SS: Sum of squares
TEM: Transmission electron microscopy
TEPA: Tetraethylenepentamine

VSM: Vibrating sample magnetometry

XRD: X-Ray diffraction

Conflicts of interest

There are no conflicts to declare.

Acknowledgements

This work was supported by funding from the EPSRC (grant number EP/P006892/1) and the University of Sheffield's EPSRC DTP allowance (grant number EP/M508135/1) funds Laura Norfolk's PhD. We thank S. Tsokov, C. Hill (Sheffield Electron Microscopy unit) for TEM training, Nicola Morley and Zhao Leong for VSM training, Heather Grieveson for ICP measurements, and Craig Robertson for support with powder XRD.

References

- 1 A. E. Rawlings, L. A. Somner, M. Fitzpatrick-Milton, T. P. Roebuck, C. Gwyn, P. Liravi, V. Seville, T. J. Neal, O. O. Mykhaylyk, S. A. Baldwin and S. S. Staniland, *Nat. Commun.*, 2019, **10**, 1–9.
- 2 S. M. Bird, A. E. Rawlings, J. M. Galloway and S. S. Staniland, *RSC Adv.*, 2016, **6**, 7356–7363.
- 3 R. E. Rosensweig, *Sci. Am.*, 1982, 136–145.
- 4 D. Yuvarajan and M. V. Ramanan, *Arab. J. Sci. Eng.*, 2016, **41**, 2023–2030.
- 5 K. Mahmoudi, A. Bouras, D. Bozec, R. Ivkov and C. Hadjipanayis, *Int. J. Hyperth.*, 2018, **0**, 1–13.
- 6 Q. A. A. Pankhurst, J. Connolly, J. S. K and J. Dobson, *J. Phys. D ...*, 2003, **36**, 167–181.
- 7 R. Weissleder, D. D. Stark, B. L. Engelstad, B. a Bacon, D. L. White, P. Jacobs and J. Lewis, *Am. J. Roentgenol.*, 1989, **152**, 167–173.
- 8 Wahajuddin and S. Arora, *Int. J. Nanomedicine*, 2012, **7**, 3445–3471.
- 9 A. E. Rawlings, J. P. Bramble, A. A. S. Tang, L. A. Somner, A. E. Monnington, D. J. Cooke, M. J. McPherson, D. C. Tomlinson and S. S. Staniland, *Chem. Sci.*, 2015, **6**, 5586–5594.
- 10 A. G. Roca, L. Gutiérrez, H. Gavilán, M. E. Fortes Brollo, S. Veintemillas-Verdaguer and M. del P. Morales, *Adv. Drug Deliv. Rev.*, 2019, **138**, 68–104.
- 11 J. Mohapatra, A. Mitra, M. Aslam and D. Bahadur, *IEEE Trans. Magn.*, 2015, **51**, 3–6.
- 12 S. V Patwardhan, J. R. H. Manning and M. Chiacchia, *Curr. Opin. Green Sustain. Chem.*, 2018, **12**, 110–116.
- 13 D. Maity, S. N. Kale, R. Kaul-Ghanekar, J. M. Xue and J. Ding, *J. Magn. Magn. Mater.*, 2009, **321**, 3093–3098.
- 14 M. Unni, A. M. Uhl, S. Savliwala, B. H. Savitzky, R. Dhavalikar, N. Garraud, D. P. Arnold, L. F. Kourkoutis, J. S. Andrew and C. Rinaldi, *ACS Nano*, 2017, **11**, 2284–2303.
- 15 S. V Patwardhan and S. S. Staniland, *Green Nanomaterials*, 2019.

- 16 A. E. Rawlings, J. P. Bramble, A. M. Hounslow, M. P. Williamson, A. E. Monnington, D. J. Cooke and S. S. Staniland, *Chem. - A Eur. J.*, 2016, **22**, 7885–7894.
- 17 A. E. Rawlings, J. P. Bramble, R. Walker, J. Bain, J. M. Galloway and S. S. Staniland, *Proc. Natl. Acad. Sci.*, 2014, **111**, 16094–16099.
- 18 Y. Kuwahara, T. Miyazaki, Y. Shirosaki, G. Liu and M. Kawashita, *Ceram. Int.*, 2016, **42**, 6000–6004.
- 19 R. Blakemore, *Science (80-)*, 1975, **190**, 377–379.
- 20 A. Arakaki, J. Webb and T. Matsunaga, *J. Biol. Chem.*, 2003, **278**, 8745–8750.
- 21 D. Murat, V. Falahati, L. Bertinetti, R. Csencsits, A. Körnig, K. Downing, D. Faivre and A. Komeili, *Mol. Microbiol.*, 2012, **85**, 684–699.
- 22 A. E. Rawlings, J. P. Bramble, A. A. S. Tang, L. A. Somner, A. E. Monnington, D. J. Cooke, M. J. McPherson, D. C. Tomlinson and S. S. Staniland, *Chem. Sci.*, 2015, **6**, 5586–5594.
- 23 L. Norfolk, K. Kapusta, D. J. Cooke and S. S. Staniland, *Green Chem.*, 2021, 1–12.
- 24 L. Dewulf, M. Chiacchia, A. S. Yeardley, R. A. Milton, S. F. Brown and S. V. Patwardhan, *Mol. Syst. Des. Eng.*, 2021, **6**, 293–307.
- 25 A. Rodríguez-López, A. Paredes-Arroyo, J. Mojica-Gomez, C. Estrada-Arteaga, J. J. Cruz-Rivera, C. G. Elías Alfaro and R. Antaño-López, *J. Nanoparticle Res.*, 2012, **14**, 1–9.
- 26 E. Mohammad, E. I. Reza and N. Bahram, *Asian J. Chem.*, 2008, **20**, 3857–3865.
- 27 T. Raut, B. Shrivastava, P. Sharma, P. Gide, G. Deokar, S. Rahane and K. Erande, *Part. Sci. Technol.*, 2016, **34**, 509–516.
- 28 K. Al-Saad, A. A. Issa, S. Idoudi, B. Shomar, M. A. Al-Ghouti, N. Al-Hashimi and M. El-Azazy, *Molecules*, 2020, **25**, 1–20.
- 29 N. C. V. Rost, F. M. Broca, G. C. Gonçalves, M. A. Cândido, M. L. Castilho and L. J. Raniero, *Brazilian J. Phys.*, 2019, **49**, 22–27.
- 30 M. Mahmoudi, A. Simchi, M. Imani, A. S. Milani and P. Stroeve, *J. Phys. Chem. B*, 2008, **112**, 14470–14481.
- 31 A. González Moreno, M. M. López Guerrero, E. Vereda Alonso, A. García De Torres and J. M. C. Pavón, *New J. Chem.*, 2017, **41**, 8804–8811.
- 32 H. C. Roth, S. P. Schwaminger, M. Schindler, F. E. Wagner and S. Berensmeier, *J. Magn. Magn. Mater.*, 2015, **377**, 81–89.
- 33 N. Mizutani, T. Iwasaki and S. Watano, *Nanomater. Nanotechnol.*, 2015, **5**, 1–7.
- 34 D. Forge, A. Roch, S. Laurent, H. Tellez, Y. Gossuin, F. Renaux, L. Vander Elst and R. N. Muller, *J. Phys. Chem. C*, 2008, **112**, 19178–19185.
- 35 S. P. Schwaminger, C. Syhr and S. Berensmeier, *Crystals*, 2020, **10**, 1–12.
- 36 J. Medinger, M. Nedyalkova and M. Lattuada, *Nanomaterials*, 2021, **11**, 1–19.
- 37 G. Fan, Y. Zhu, Z. Fu, B. Sun, C. Teng, R. Yang and X. Li, *3 Biotech*, 2020, **10**, 1–15.
- 38 C. Li, L. Li, H. Zhou, C. Xia and L. He, *J. Braz. Chem. Soc.*, 2015, **26**, 247–254.
- 39 X. J. Jiang, Y. Hu, L. Jiang, B. Zou, P. Song and H. Huang, *Biotechnol. Bioprocess Eng.*, 2013, **18**, 350–357.
- 40 S. Zhang and J. D. Cui, *Biotechnol. Biotechnol. Equip.*, 2012, **26**, 3418–3423.
- 41 C. L. Yao, C. H. Liu, I. M. Chu, T. B. Hsieh and S. M. Hwang, *Enzyme Microb. Technol.*, 2003, **33**, 343–352.
- 42 E. R. El-Helow and A. M. El-Ahawany, *Enzyme Microb. Technol.*, 1999, **24**, 325–331.
- 43 C. Jiang, G. Sun, Z. Zhou, Z. Bao, X. Lang, J. Pang, Q. Sun, Y. Li, X. Zhang, C. Feng and X. Chen, *Int. J. Biol. Macromol.*, 2019, **121**, 293–300.
- 44 C. Pizarro, M. A. Fernández-Torroba, C. Benito and J. M. González-Sáiz, *Biotechnol. Bioeng.*, 1997, **53**, 497–506.
- 45 Y.-C. Hsiao and C.-C. Hu, *J. Electrochem. Soc.*, 2013, **160**, H279–H284.
- 46 B. Ghosh, D. C. Agrawal and S. Bhatia, *Ind. Eng. Chem. Res.*, 1994, **33**, 2107–2110.
- 47 N. Doshi and S. Mitragotri, *J. R. Soc. Interface*, 2010, **7**, 1–8.
- 48 Minitab, *Getting Started with Minitab Statistical Software*, 2020.
- 49 S. S. S. Laura Norfolk, Klaudia Kapusta, David Cooke, .
- 50 D. C. Montgomery, R. H. Myers, W. H. Carter and G. G. Vining, *Qual. Reliab. Eng. Int.*, 2005, **21**, 197–201.
- 51 B. E. Ankenman and A. M. Dean, *Handb. Stat.*, 2003, **22**, 263–317.
- 52 D. C. Montgomery, *Design and Analysis of Experiments: 8th Edition*, 2440.
- 53 A. E. Rawlings, J. P. Bramble, A. M. Hounslow, M. P. Williamson, A. E. Monnington, D. J. Cooke and S. S. Staniland, *Chem. - A Eur. J.*, 2016, **22**, 7885–7894.
- 54 L. Norfolk, A. E. Rawlings, J. P. Bramble, K. Ward, N. Francis, R. Waller, A. Bailey and S. S. Staniland, *Nanomaterials*, 2019, **9**, 1729.
- 55 B. L. Inc, *Magnetic Properties of Magnetic Particles*, 2017.

A Design of Experiment (DoE) approach to the optimisation of bioinspired magnetite nanoparticles using an affordable amine additive

Laura Norfolk,^{*a} Luc Dewulf^b, Mauro Chiacchia^c, Siddharth Patwardhan^c, and Sarah Staniland

Design 1

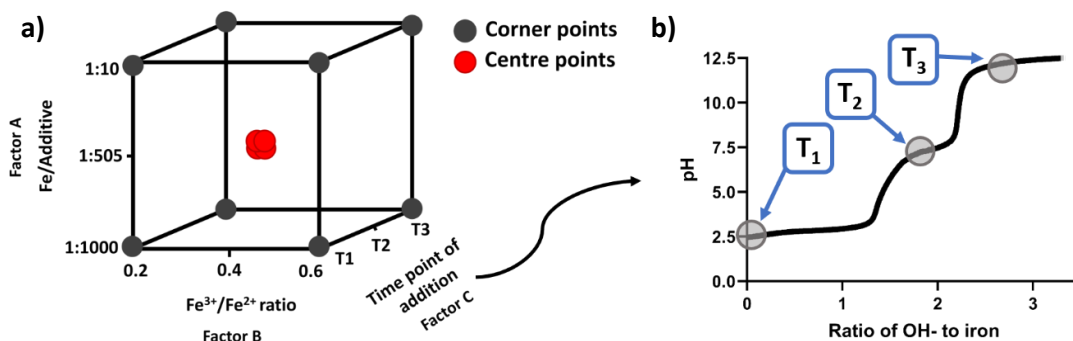


Figure S1. a) Three-factor study varying (A) Additive:iron ratio, (B) Fe^{3+} :Total Fe, and (C) additive time-point of addition, with the grey and red circles representing reaction conditions tested. b) pH titration curve from a 0.6 ratio reaction, showing the timepoints at which TEPA was added.

Table S1. Summary of the synthesis conditions with the experimental results from the first iteration of the factorial design

Experiment number	Block	Factor A TEPA:iron ratio (mol/mol)	Factor B Fe(III):total Fe ratio (mol/mol)	Factor C Time of TEPA addition	% Faceted particles	Average size (nm)	Saturation magnetism (emu g^{-1})
1	1	1:1000	0.2	T1	17.3	35.3	34.2
2	1	1:10	0.6	T1	44.5	21.0	70.6
3	1	1:10	0.2	T3	6.2	19.9	53.4
4	1	1:1000	0.6	T3	36.5	18.6	68.6
5	1	1:505	0.4	T2	22.7	33.9	62.0
6	1	1:505	0.4	T2	48.6	30.0	64.0
7	2	1:10	0.2	T1	35.7	24.4	67.5
8	2	1:1000	0.6	T1	72.6	21.7	75.0
9	2	1:1000	0.2	T3	23.0	27.4	67.2
10	2	1:10	0.6	T3	55.0	17.2	72.3
11	2	1:505	0.4	T2	46.5	31.2	72.6
12	2	1:505	0.4	T2	48.4	27.8	82.6

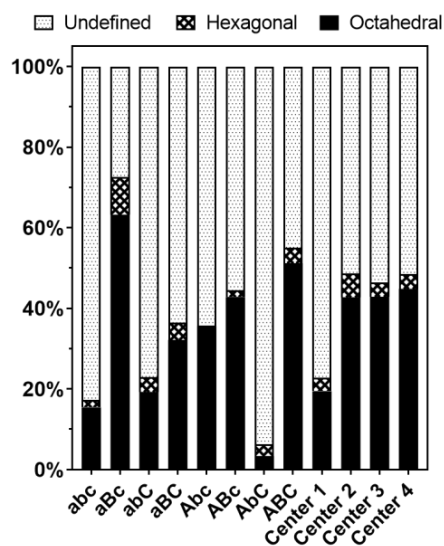


Figure S2. Shape distribution of particles formed at various response levels as detailed in Table 1. The three factors are denoted by the letters a-c where a = Fe/additive ratio, b = Fe^{3+}/Fe^{2+} ratio, and c = time point of TEPA addition. Capital letters denotes a high factor level, whereas lowercase represents a low factor level (in the case of Fe/additive a high level denotes more additive present).

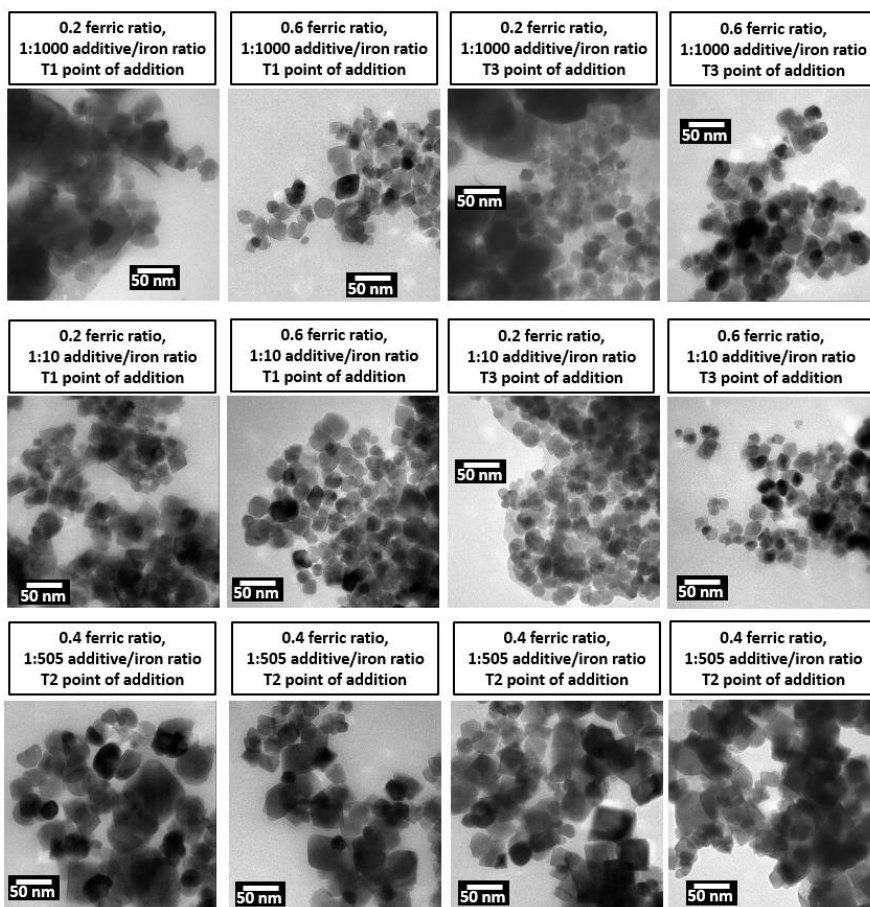


Figure S3. Representative TEM images of the particles formed in the first DoE iteration in order of experiment number

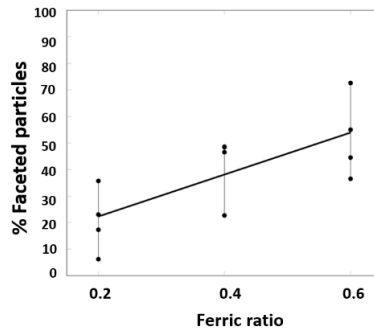


Figure S4. Variation of % faceted particles with ferric ratio for the first iteration of DoE. Black dots are the experimental values.

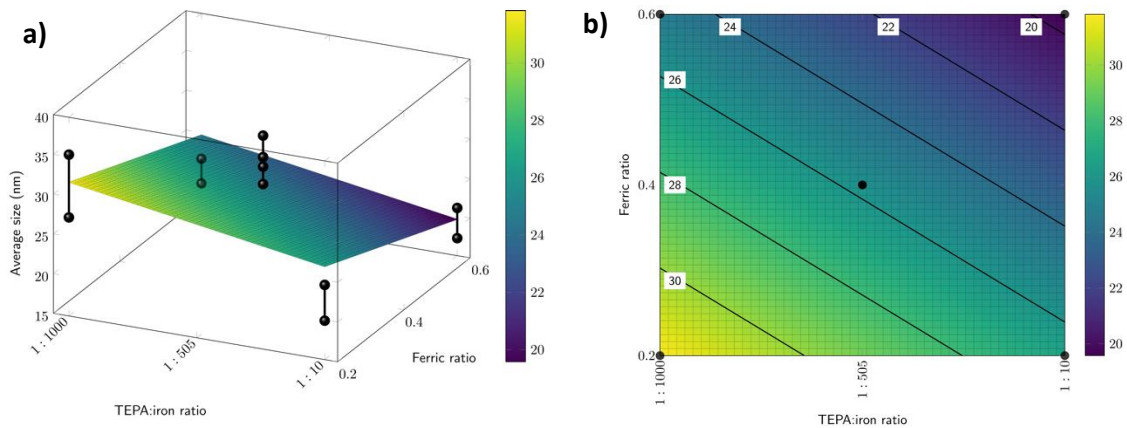


Figure S5. a) Surface plot of variation of average size with additive concentration and ferric ratio. Black spheres are experimental values; b) Contour plot of variation of average size with additive concentration and ferric ratio. Contour lines shown in black represent constant average size indicated in white box.

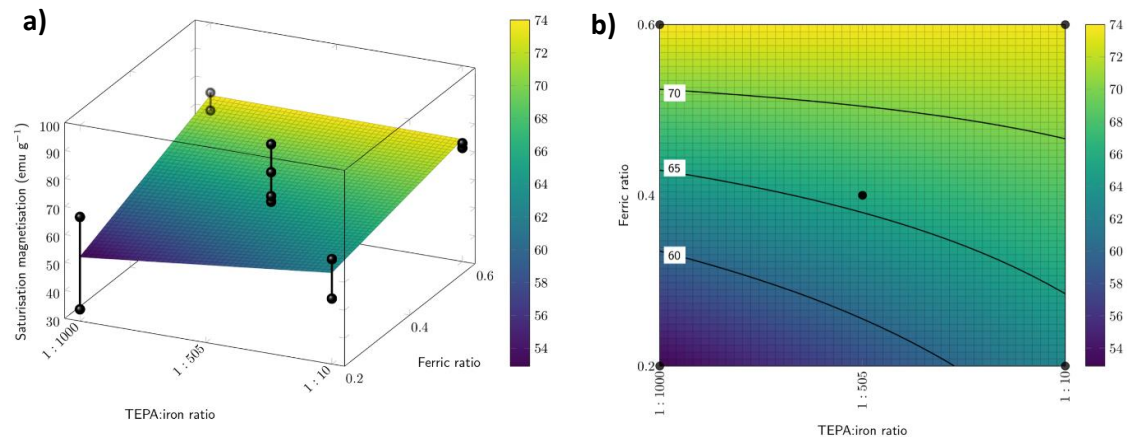


Figure S6. a) Surface plot of variation of saturation magnetisation with additive concentration and ferric ratio. Black spheres are experimental values; b) Contour plot of variation of saturation magnetisation with additive concentration and ferric ratio. Contour lines shown in black represent constant saturation magnetisation indicated in white box.

Table S2. Analysis of variance for the response isotropic faceted particles (%) of the first DoE iteration

Source	Sum of Squares	Degrees of Freedom	Mean Squares	F-Value	P-Value
A (tepa:fe)	8.00	1	8	0.06	0.819
B (ferricratio)	1997.12	1	1997.12	15.48	0.029
C (time)	305.04	1	305.04	2.36	0.222
AB	15.68	1	15.68	0.12	0.750
AC	16.24	1	16.24	0.13	0.746
BC	0.40	1	0.40	0.00	0.959
Blocks (ABC)	925.76	1	925.76	7.17	0.075
Residual	387.09	3	129.03		
Lack-of-fit	49.88	1	49.88	0.30	0.641
Pure Error	337.21	2	168.61		
Total	3727.46	11			

Table S3. Analysis of variance for the response saturation magnetism (emu/g) of the first DoE iteration

Source	Sum of Squares	Degrees of Freedom	Mean Squares	F-Value	P-Value
A (tepa:fe)	44.69	1	44.686	2.53	0.21
B (ferricratio)	514.52	1	514.516	29.14	0.012
C (time)	25.38	1	25.376	1.44	0.317
AB	50.89	1	50.886	2.88	0.188
AC	190.07	1	190.069	10.77	0.046
BC	70.61	1	70.609	4	0.139
Blocks (ABC)	593.64	1	593.644	33.62	0.01
Residual	52.97	3	17.656		
Lack-of-fit	0.47	1	0.474	0.02	0.905
Pure Error	52.49	2	26.247		
Total	1663.49	11			

Table S4. Analysis of variance for the response average particle size (nm) of the first DoE iteration

Source	Sum of Squares	Degrees of Freedom	Mean Squares	F-Value	P-Value
A (tepa:fe)	433.65	1	433.65	30.05	0.012
B (ferricratio)	1881.91	1	1881.91	130.42	0.001
C (time)	87.78	1	87.78	6.08	0.090
AB	686.35	1	686.35	47.56	0.006
AC	44.65	1	44.65	3.09	0.177
BC	98.70	1	98.70	6.84	0.079
Blocks (ABC)	2.34	1	2.34	0.16	0.714
Residual	43.29	3	14.43		
Lack-of-fit	18.55	1	18.55	1.5	0.345
Pure Error	24.74	2	12.37		
Total	3711.33	11			

Design 2

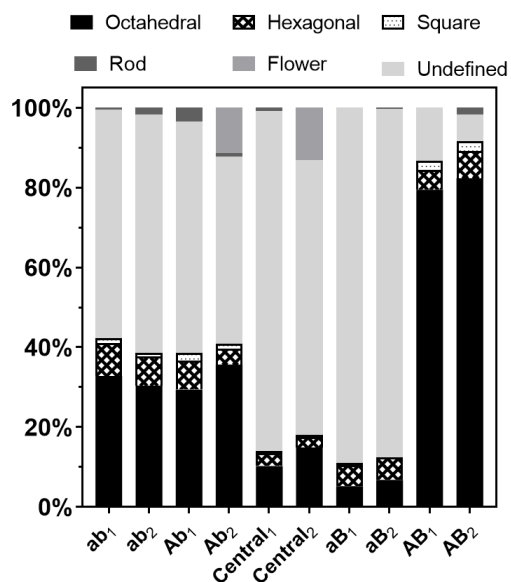


Figure S7. Shape distribution of particles formed in the second factorial design. The two factors are denoted by the letters a-b where a = Fe/additive ratio, b = Fe³⁺/Fe²⁺ ratio. Capital letters denotes a high factor level, whereas lowercase represents a low factor level (in the case of Fe/additive a high level denotes more additive present and subscript 1 and 2 represent the two repeats of the experiments).

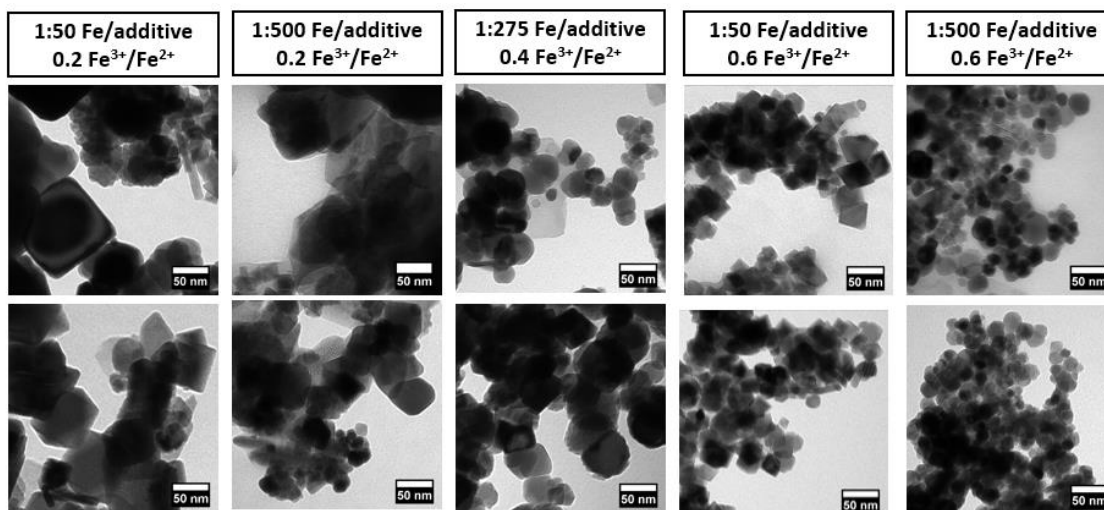


Figure S8. Representative TEM images of the particles formed in the second DoE iteration.

Design 3

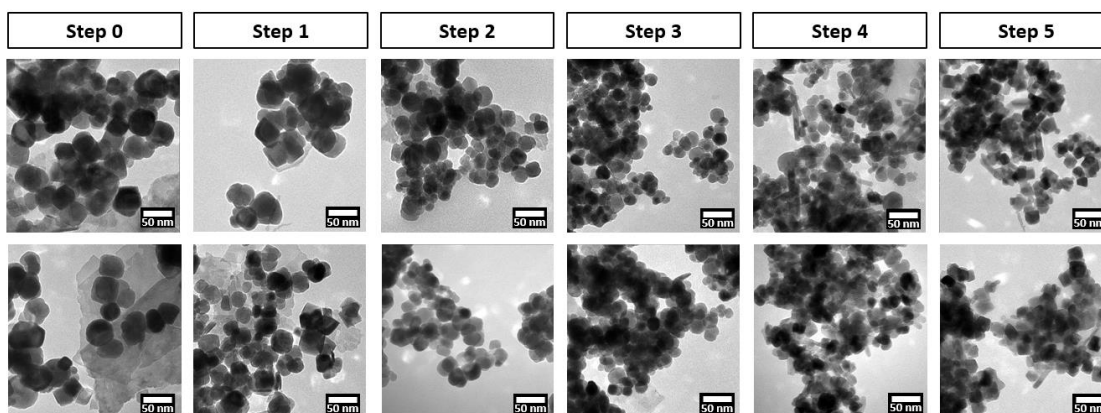


Figure S9. Representative TEM images of the particles formed in the third DoE iteration.

Miscellaneous

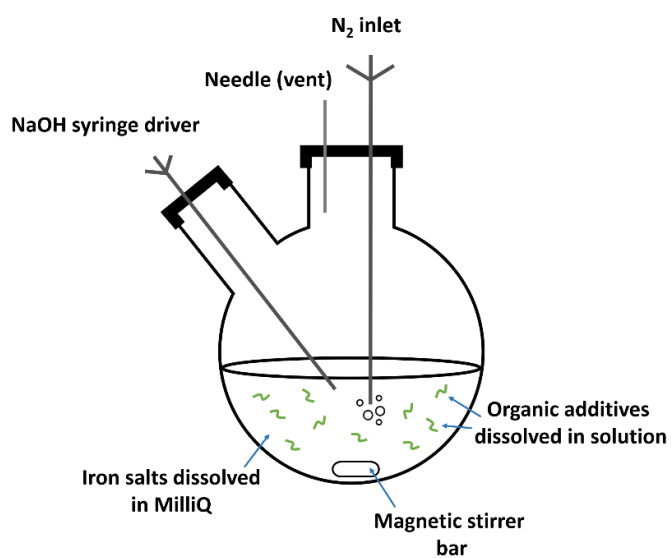


Figure S10. Schematic of the reaction set-up used to synthesise magnetic nanoparticles in each co-precipitation reaction.

Particle Sizing Methodology:

Particle measurements are taken across the longest axis of each particle to ensure consistency between measurements using ImageJ software. Approximately 200 measurements are taken from each sample to get an accurate measure of mean size given the variety in particles per sample. To avoid human bias in which particles are selected for analysis, particles are analysed from a single “area” of a TEM image to prevent small or large particles being selectively measured. Several images are analysed for each sample to ensure a representative sample is taken.

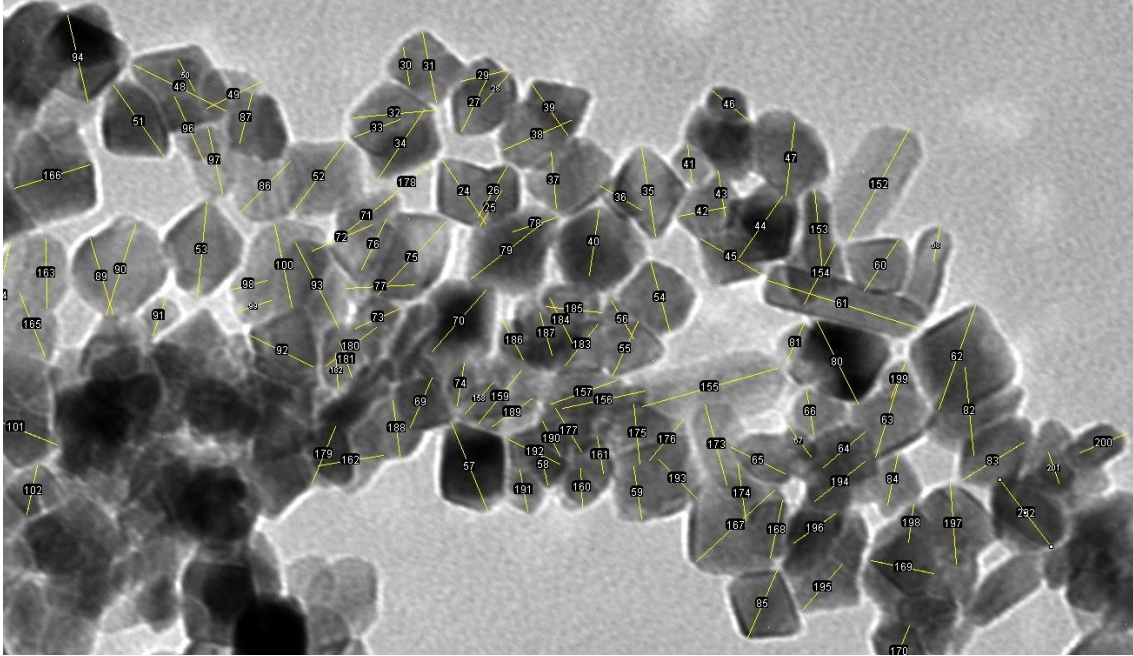


Figure S11. Screenshot of ImageJ particle sizing showing particles are analysed in clusters.

Particle Shape Analysis Methodology:

Images are manually analysed using drawing software (Inkscape, Paint.net, etc) by marking each particle a shape with a set colour (figure S12). A minimum of 300 samples are marked from several different images to ensure a representative sample is selected. The particles are then counted, at which point the shape assignment is checked a secondary time to maximise accuracy. Sample particle shapes can be seen in figure S13.

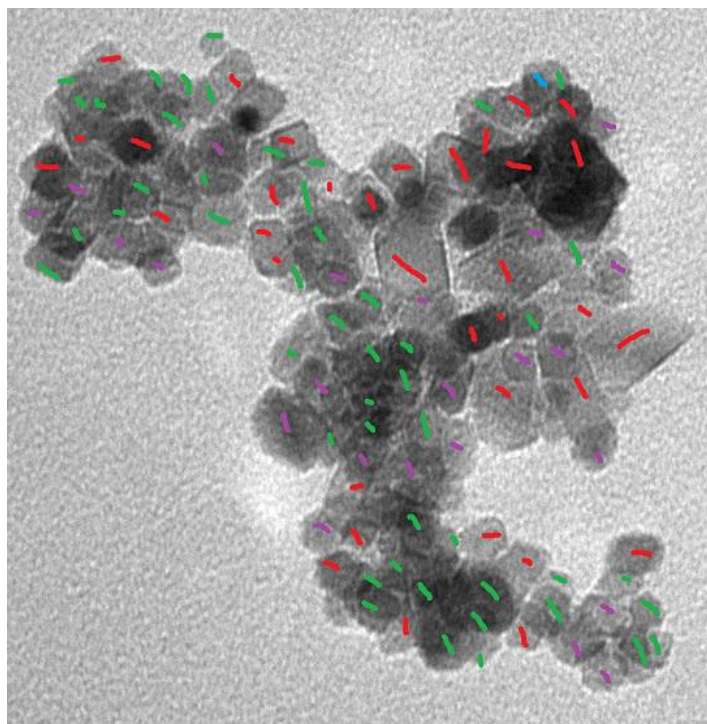


Figure S12. Example image analysis showing octahedral (red), undefined (green), and hexagonal (purple) particles.

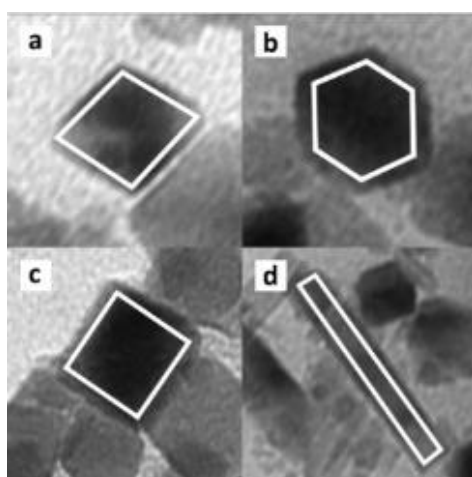
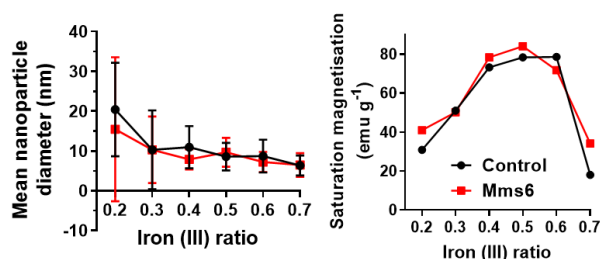
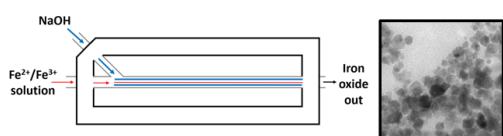


Figure S13. Sample particle shapes from TEM analysis; **a)** Octahedral; **b)** Hexagonal; **c)** square; **d)** rod/elongated.

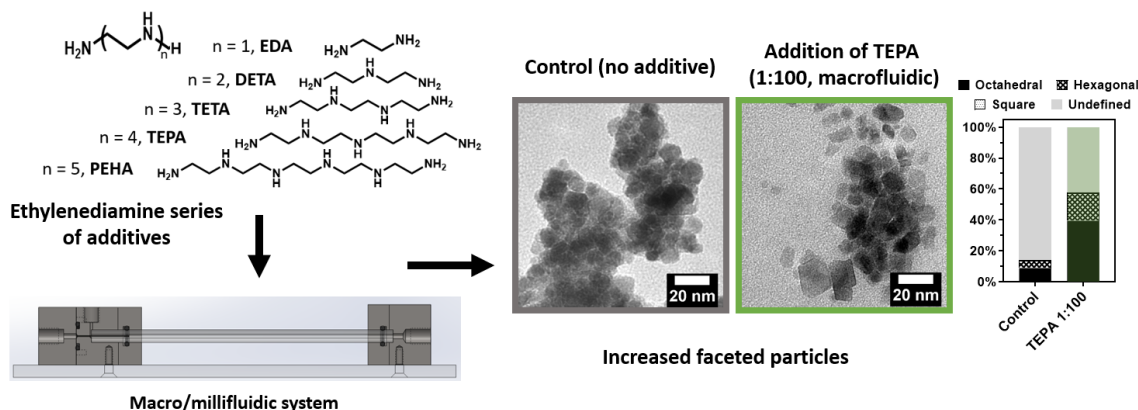
Chapter 6.

Millifluidics

Millifluidic paper 1:



Millifluidic paper 2:



This chapter covers two papers: The first is a published paper in MDPI, titled 'Macrofluidic Coaxial Flow Platforms to Produce Tunable Magnetite Nanoparticles: A Study of the Effect of Reaction Conditions and Biomineralisation Protein Mms6'. The second paper is to be submitted, and is titled "Adapting the morphology of magnetite nanoparticles synthesised in a coaxial flow device using affordable amine additives".

Millifluidic paper 1 DOI: 10.3390/nano9121729

6.1 Macrofluidic Coaxial Flow Platforms to Produce Tunable Magnetite Nanoparticles: A Study of the Effect of Reaction Conditions and Biomineralisation Protein Mms6

6.1.1 Author Contributions

Laura Norfolk (first author): Organised the design and manufacture of the PEEK macrofluidic device, troubleshot the PEEK macrofluidic device, synthesised the two sets of particles used in the main paper, analysed the particles (XRD, TEM, VSM, shape and size analysis), designed and created Figures 1a, 1d, 2, 3, 4, 5, and 6, prepared the first paper draft, reviewed and edited the paper, and supervised Katy Ward.

Andrea Rawlings (first author): Conceptualised the research, designed the methodology, acquired initial data, performed all protein expression and purification, wrote the protein expression/purification methods, aided with paper review and editing, and supervised multiple Masters students.

Jonathan Bramble (first author): Conceptualised the research, designed and organised the manufacture of the PTFE block for the PDMS device, designed the methodology, optimised the macrofluidic system flow rates, acquired initial data, modelled the macrofluidic system in COMSOL, created Figure 1 b and 1c, and supervised Masters students.

Katy Ward: SURE summer student who aided in the development of the reaction conditions used for the final paper and troubleshot the PEEK macrofluidic device.

Noel Francis: Masters student who aided in the development of the reaction conditions used for the final paper, and adapted the outlet of the PDMS co-axial device to incorporate a magnetic trap.

Rachel Waller: Masters student who aided in the development of the reaction conditions used for the final paper.

Ashley Bailey: Masters student who aided in the development of the reaction conditions used for the final paper.

Sarah Staniland (principal investigator): Conceptualised the research, prepared the first paper draft, and aided with review and editing.



Article

Macrofluidic Coaxial Flow Platforms to Produce Tunable Magnetite Nanoparticles: A Study of the Effect of Reaction Conditions and Biomineralisation Protein Mms6

Laura Norfolk ^{1,†}, Andrea E. Rawlings ^{1,2,†} , Jonathan P. Bramble ^{1,2,†}, Katy Ward ¹, Noel Francis ¹, Rachel Waller ¹, Ashley Bailey ² and Sarah S. Staniland ^{1,2,*}

¹ Department of Chemistry, University of Sheffield, Brook Hill, Sheffield S3 7HF, UK; lnorfolk1@sheffield.ac.uk (L.N.); a.rawlings@sheffield.ac.uk (A.E.R.); klward2@sheffield.ac.uk (K.W.); nfrancis1@sheffield.ac.uk (N.F.); rwaller2@sheffield.ac.uk (R.W.)

² School of Physics and Astronomy, University of Leeds, Leeds LS2 9JT, UK; bailey272@hotmail.co.uk

* Correspondence: s.s.staniland@sheffield.ac.uk; Tel.: +44-(0)114-222-9539

† These authors contributed equally to this work.

Received: 14 October 2019; Accepted: 20 November 2019; Published: 4 December 2019



Abstract: Magnetite nanoparticles' applicability is growing extensively. However, simple, environmentally-friendly, tunable synthesis of monodispersed iron-oxide nanoparticles is challenging. Continuous flow microfluidic synthesis is promising; however, the microscale results in small yields and clogging. Here we present two simple macrofluidics devices (cast and machined) for precision magnetite nanoparticle synthesis utilizing formation at the interface by diffusion between two laminar flows, removing aforementioned issues. Ferric to total iron was varied between 0.2 (20:80 Fe³⁺:Fe²⁺) and 0.7 (70:30 Fe³⁺:Fe²⁺). X-ray diffraction shows magnetite in fractions from 0.2–0.6, with iron-oxide impurities in 0.7, 0.2 and 0.3 samples and magnetic susceptibility increases with increasing ferric content to 0.6, in agreement with each other and batch synthesis. Remarkably, size is tuned (between 20.5 nm to 6.5 nm) simply by increasing ferric ions ratio. Previous research shows biomineralisation protein Mms6 directs magnetite synthesis and controls size, but until now has not been attempted in flow. Here we report Mms6 increases magnetism, but no difference in particle size is seen, showing flow reduced the influence of Mms6. The study demonstrates a versatile yet simple platform for the synthesis of a vast range of tunable nanoparticles and ideal to study reaction intermediates and additive effects throughout synthesis.

Keywords: fluidic; magnetite; magnetic nanoparticle; flow synthesis; Mms6

1. Introduction

The design and synthesis of precise monodispersed iron oxide magnetic nanoparticles (MNP) is a growing research field due to their applicability in nanotechnologies, particularly in the biomedical sector [1]. In nanomedicine, MNPs comprised of the magnetic iron oxides magnetite (Fe₃O₄) or maghemite (γ-Fe₂O₃) are considered very attractive due to their low toxicity and cheap precursors. They can act as contrast agents in MRI and can also be heated by an alternating magnetic field or laser light to provide hyperthermia as a remote, switchable therapy for cancer treatment [2–4]. MNP can be functionalised with probes (like fluorescent tags for imaging), drugs and targeting or a combination of all of these to form smart theranostic that can be targeted to a specific region of the body by a magnetic field.

However, “green” (ambient, non-toxic conditions) synthesis of iron oxides is notoriously difficult to control. Minor changes to any number of reaction conditions (iron precursors, choice of base, ratio of iron oxidation states of the precursors etc.) will lead to the production of a range of iron oxides [1]. For example, the partial oxidation of ferrous hydroxide using an excess of NaOH under N₂ at 90 °C will precipitate octahedral magnetite particles approximately 20–80 nm in size. Changing the base used can result in needle-shaped FeOOH by-products [5]. Furthermore, if the excess of NaOH is reduced to stoichiometric base:ferrous ions concentrations the particle size increases dramatically up to approximately 1 µm, as the excess of ferrous ions increases the particle products reduce to 400 nm diameter as the excess of ferrous ions increases [6]. A co-precipitation of ferric and ferrous ions at room temperature under N₂ with KOH base results in mostly small MNP of poor crystallinity, with a heterogeneous shape and size population ranging from <5 nm up to micrometre scales [2,5]. Although this does allow scope to synthesise various morphologies and sizes, the overwhelming drawback is that it is near impossible to synthesise a mono-dispersed and reproducible product with respect to consistent and monodispersed size and shape. Furthermore, ferric oxide impurities are common (which represent a large proportion of the heterogeneity observed in the co-precipitation synthesis).

A key challenge for the green synthesis of magnetite is the reproducibility of batch nanoparticle synthesis. Very subtle changes in conditions can have huge effects on the final MNP product, which is more exaggerated and difficult to address in batch synthesis, with batch to batch variations being inevitable.

Micro and macro fluidic systems offer a unilaminar controlled fluid environment, where the fluid flow and dynamics can be quantified, modelled, controlled, and reproduced with higher accuracy, allowing a more reproducible synthesis compared to batch synthesis [7]. Furthermore, defining and achieving precise reaction environments enables a more detailed analysis of the synthesis process, such as the possibility of adding probes for analysis or reagents at precise reaction points. An additional benefit of a continuous fluidic system is that the reaction time points equate to channel position, allowing screening and monitoring of the synthesis at every stage in situ. Such systems can be readily modified to incorporate characterisation instrumentation such as spectroscopy, microscopy and filming to analyse reactions as they occur in real-time at the microscale [8].

Microfluidics have been investigated for the synthesis of inorganic nanoparticles for over a decade [9], but this research has concentrated on the synthesis of quantum dots and noble metal (Ag, Au) nanoparticles [7–11]. To date there have only been two studies that use a fluidics system to fabricate iron-oxide MNP [12,13], which may be surprising considering the obvious benefits controlling the reaction environment has on fastidious iron-oxide synthesis. Abou-Hassen et al. reported some preliminary results for a co-precipitation of magnetite [12]. They reported issues with clogging so utilised a millimetric system, but could not obtain magnetite even when coated with a surfactant to prevent oxidation, instead producing 7 nm sized maghemite coated nanoparticles. In the same year Frenz et al. reported a more sophisticated microfluidic synthesis of iron oxide [13]. Again, the aim was to produce magnetite but they noted it readily oxidises to maghemite on contact with air. They utilised aqueous microdroplets of reagents in an organic solvent, where an electric voltage initiates reagent mixing of the droplets to nucleate the formation of 4 nm sized nanoparticles.

While this method is elegant, yields and overall outputs were found to be low. In general, while the small volumes of microfluidic synthesis offer excellent control and reproducibility over batch synthesis, the drawbacks are that these smaller scale syntheses offer smaller quantities of product and issues with clogging of the tubing requires elaborate solutions leading to more complex fabrication of the devices.

In this work we present a simple (easily castable from PDMS) millimetric macro fluidics device for the synthesis of magnetite MNP's, and improve on this with a more sophisticated fluidic device machined out of polyether ethyl ketone (PEEK) utilising a glass capillary as the reaction vessel, but of the same simple design (Figure 1a). With the aim of attaining simple green reaction conditions we do

not use droplets, organic solvents or surfactants. We explore tuning the particle formation by varying the ratio of ferrous ions to ferric ions in the fluidic synthesis. This demonstrates an excellent simple platform technology for the synthesis of a vast range of nanoparticles with the ability to tune their properties with further development.

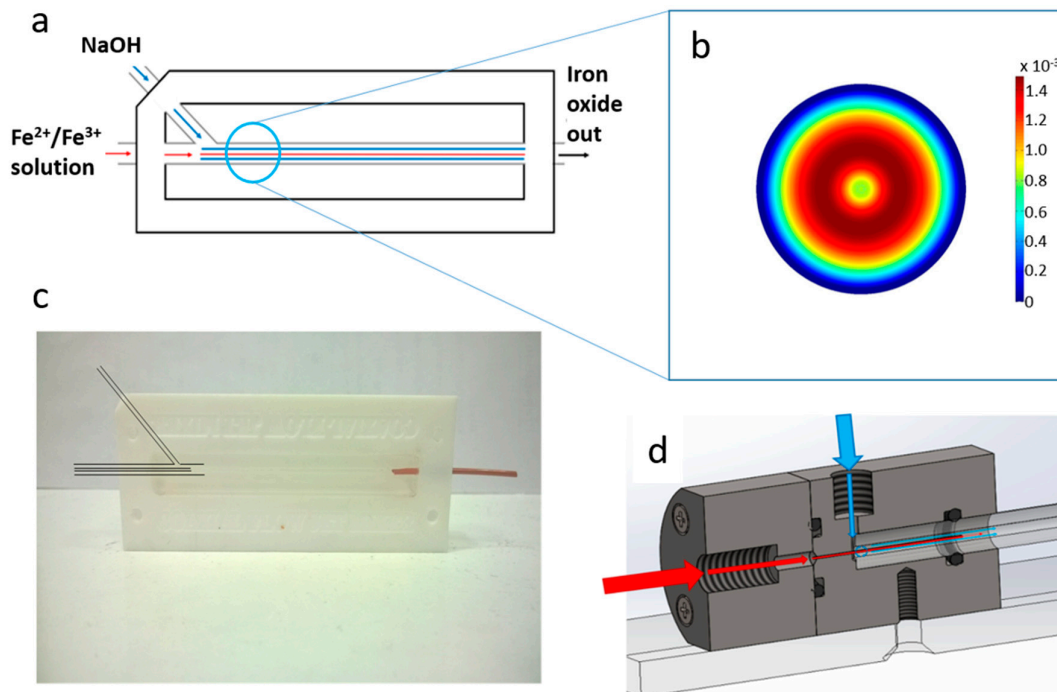


Figure 1. (a) schematic of the design of the co-axial fluidic device, showing the fluidic junction between the two streams of reactants. (b) Cross-sectional velocity of sheath flow around a core flow in a tube after the junction, (c) Photograph of the polydimethylsiloxane (PDMS) device with inlets highlighted for clarity, (d) cross-sectional view of polyether ethyl ketone (PEEK) device. For (a,d) iron/NaOH inlet with red arrows representing the flow of iron solution and blue arrows representing the flow of NaOH solution.

Control over the formation of magnetite MNPs have also been achieved in the natural world through biomineralisation using biological additives. In nature many inorganic minerals are formed with exceptional precision over the mineral composition, size and morphology, utilising a range of biomineralisation proteins. One such example is the biomineralisation of magnetite MNP by Magnetotactic bacteria within liposomes in their cells known as magnetosomes [14,15]. Magnetosome membrane specific (Mms) biomineralisation proteins embedded in this liposome are responsible for nucleation of the iron oxide mineral and crystallisation to a precise size and shape [14,15]. Previously, Mms6 has been shown to control the formation of magnetite MNP in vitro when added to green co-precipitation chemical synthesis, showing a promising new methodology of controlling nanoparticle synthesis with biological additives [16–18]. It is thought that Mms6 is a nucleating protein for magnetite MNPs [19,20].

In this work we also demonstrate how the fluidics device we produced can be used in conjunction with a biomineralisation protein additive to control the particle formation further. The addition of an Mms protein is a proof-of-concept to demonstrate how such a simple fluidics system could be utilised as a platform to help to understand how proteins (or indeed any other nanomaterial additive) function in vitro in a controlled fluidic environment.

2. Materials and Methods

2.1. Reagents

Iron (II) sulphate, iron (III) sulphate and sodium hydroxide were purchased from Sigma-Aldrich (Gillingham, United Kingdom) and used without further purification. Iron contents were confirmed via ICP-MS prior to experimentation. PDMS was prepared from Dow Corning (Midland, MI, United States) kit sylgard 184 in the standard ratio 1:10 curing agent:polymer.

2.2. Macrofluidics Device Fabrication

2.2.1. PDMS Device

The device was constructed from a PTFE hollowed out block with a long channel milled from the centre. Initially a stiff metal wire with a diameter of 1.6 mm was pushed through the two holes along the axis of the device. A second input hole, intersected the main channel at an angle of 45° as shown in Figure 1a,c. The blunt end of a needle was shaped using a drill bit to meet and fit the shape of the central wire. Triton X-100 was wiped over the wires/needle so they could be easily removed from the device after casting. The space was then filled with liquid PDMS and cured at 60 °C for 24 h. When cured, the central wire and needle was carefully removed, leaving behind a central channel and side inlet in PDMS. The materials and equipment required to create this device are cheap and readily available, and the PTFE block is reusable for many castings. The block was fastened to a heavy object to prevent lateral movement when connected to stiff fluidic tubes. The fluid from the central channel was fed into a PEEK tube with an inner diameter of 0.02". The internal hole was expanded using a shaped drill bit to ensure a smooth transition in diameter.

2.2.2. PEEK Device

The device was designed and modelled in SolidWorks, comprising of 6 individual components; (i) Fe inlet, (ii) NaOH inlet, (iii) inlet faceplate, (iv) capillary, (v) outlet faceplate, (vi) outlet (Figure 2).

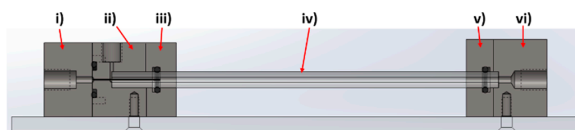


Figure 2. Cross section of PEEK system illustrating the different components.

The rig was machined from PEEK, with o-ring seals between components i–ii, ii–iii, and v–vi to ensure no leakage of solution, a problem often observed in PDMS cast systems. A 27-gauge blunt-end needle (0.41 mm OD, 0.016 ID) was set through component i) with the use of epoxy resin. This needle was sprayed with Teflon spray to aid flow. The capillaries used were 0.5 m in length, with a 5 mm outer diameter and 1.5 mm internal diameter. The capillary tube was inserted between components ii/iii (inlet) and components v/vi (outlet). The system was locked in position with clamp stands to prevent movement when connected to the fluidic tubing.

Fluidic connections for both devices (Upchurch Scientific, purchased from Kinesis (Cambridge, UK) or Fischer Scientific (Loughborough, United Kingdom)) and PEEK tubing with an outer diameter 1/16" and inner diameter of 0.02" were used. Glass capillaries were initially used but were replaced, to reduce problems with clogging, with PEEK capillaries. All tubes were cut with tube cutters (Upchurch Scientific A-327, A-350) to ensure clean and perpendicular cuts. Two syringe drivers (Harvard Apparatus, Cambridge, United Kingdom) were used to control the flow rate of iron and base into the mixer. Glass syringes (SGE Europe Ltd., Milton Keynes, United Kingdom) with volumes of 1 mL and 10 mL were used for the inner and outer flows respectively. Luer fittings were used to connect PEEK tubing to syringes.

2.3. Protein Expression and Purification

The *mms6* sequence from *Magnetospirillum magneticum* AMB-1 was introduced into a pTTQ8 based expression vector by cohesive end cloning with the resulting plasmid, pHis8mms6, encoding N-terminally octahistidine tagged Mms6. The protein was produced in *E. coli* BL21 star (DE3) cells (Invitrogen, Waltham, MA, United States) harbouring a pRARE (Merck, Nottingham, United Kingdom) plasmid to compensate for codon bias in the *mms6* sequence. Cells were cultured in autoinducing Superbroth (Formedium, Hunstanton, United Kingdom) at 37 °C with shaking for 24 h in the presence of carbenicillin and chloramphenicol to select for the pHis8mms6 and pRARE plasmids respectively. Cells were lysed by sonication in 25 mM Tris pH 7.4, 100 mM NaCl. The insoluble material, containing the His8-Mms6 inclusion bodies, was collected by centrifugation at 16,000× *g* and resuspended in 6 M Guanidine Hydrochloride, 25 mM Tris pH 7.4 to solubilise the proteins. Further centrifugation at 16,000× *g* was performed to remove any material not solubilised by the Guanidine treatment. The supernatant was mixed with nickel charged nitrilotriacetic acid (NTA) resin (Amintra resin, Expedeon, Cambridge, United Kingdom) to allow binding of the histidine tagged Mms6. The resin was subsequently packed into a gravity flow column and washed extensively with Wash Buffer (6 M Guanidine hydrochloride, 25 mM Tris pH 7.4, 10 mM Imidazole) before elution of the bound protein in 300 mM Imidazole supplemented Wash Buffer. The eluted protein was refolded by rapidly diluting into a large volume of Refolding Buffer (500 mM NaCl, 25 mM tris pH 7.4) before being concentrated using a 10 kDa molecular weight cut off centrifugal concentrator (Sartorius, Binbrook, United Kingdom). The concentrated material was subjected to centrifugation to remove any small amounts of precipitated protein before dialysis against 500 mM NaCl using a 3.5 kDa molecular weight cut off slide-a-lyser (Thermo Scientific, Waltham, MA, United States). The refolded His8-Mms6 was quantified by absorbance at 280 nm and stored at 193 K.

2.4. Continuous Flow MNP Synthesis

The device was cleaned with ultrapure water, then dilute hydrochloric acid (1 M) followed by ultrapure water again by pumping 10 mL through both ports.

All reagents were prepared with ultrapure water, and deoxygenated by sparging with N₂ for 30 min. The outer flow syringe driver was loaded with a 10 mL luer lock syringe of NaOH (1 M) and connected to the co-axial fluidic device via capillary tubing. This was set at a continuous rate of 360 µL/min. The inner flow syringe driver was loaded with a 1 mL luer lock syringe of a mixed ratio of Fe²⁺ and Fe³⁺ salts (ferrous sulphate pentahydrate and ferric sulphate heptahydrate) varied from a 4:1 (0.2 ferric) to 1:2 (0.7 ferric) Fe²⁺:Fe³⁺ ratio with a total iron concentration of (0.05 M) and connected to the co-axial fluidic device via capillary tubing. This was set at a continuous rate of 90 µL/min (although these rates were varied (see results) these were found to be optimum). The solutions were prepared immediately prior to the experiment.

The iron oxide material formed and flowed to the end of the device where it reached the exit port and dripped into a round bottom flask which was kept under an atmosphere of nitrogen. The iron oxide product was magnetically separated and washed 3× in deoxygenated ultrapure water and subsequently dried in a vacuum oven overnight.

Further improvements to the PDMS device included magnetically collecting the iron oxide as it exited the device using a magnetic trap. This was also washed 3× with deoxygenated ultrapure water and dried under vacuum.

2.5. Continuous Flow MNP Synthesis Modified with Mms6

The iron oxide synthesis was further modified with the addition of Mms proteins, where 50 µg of protein was added to the 1 mL Fe salt solution before the reaction. The experiment then proceeded as before.

2.6. Characterisation

2.6.1. Magnetic Susceptibility

Magnetic susceptibility was measured on a known amount of dry iron oxide nanoparticles using a bench-top Bartington MS2G magnetic susceptometer (Bartington Instruments, Witney, United Kingdom) at room temperature. The sample was loaded into the instrument in an eppendorf (a blank was subtracted of an empty eppendorf tube). A reading in emu was recorded. Each sample was analysed in triplicate.

2.6.2. Magnetometry

Magnetic susceptibility was performed on a known quantity (1–5 mg) of dry iron oxide nanoparticles on a MPMS 3 SQUID magnetometer (Quantum Design, Surrey, United Kingdom) in vibrating sample mode, with the samples packed in size 3 gelatine capsules. The samples were run at 300 K between -7 and 7 T with a sweep rate of 0.01 T/s. Preliminary magnetic susceptibility measurements were performed on a known quantity (approx. 5 mg) of dry iron oxide nanoparticles using a bench-top Bartington MS2G magnetic susceptometer at room temperature. The sample was loaded into the instrument in an eppendorf (a blank was subtracted of an empty eppendorf tube). A reading in emu was recorded. Each sample was analysed in triplicate.

2.6.3. Transmission Electron Microscopy

10 μ L of a 1 mg/mL suspension of nanoparticles in hexane was dropped onto a carbon coating copper TEM grid and allowed to dry down. Grids were imaged using a FEI Tecnai G2 Spirit electron microscope (Thermo Scientific, Waltham, MA, United States) and the TEM images were analysed using Image-J software (v1.52 a, public domain, National Institute of Health, Md, USA). >200 particles per samples were randomly selected and measured.

2.6.4. X-Ray Diffraction (XRD)

XRD data collected by analysis of dry iron oxide nanoparticles in a Bruker D8 powder diffractometer (Bruker, Coventry, United Kingdom). Diffraction images were collected at 0.022 degree increments from 20 – 80 degrees, with a fixed wavelength at $\lambda = 1.54178$ Å from a Cu K α X-ray source.

3. Results

3.1. Design Experimental Set-Up and Optimisation of the Coaxial Flow Device

The co-axial flow device design was based on the work of Abous-Hassen [12], operating under the principle of MNP forming in a sheath flow of sodium hydroxide (NaOH), with a core flow of mixed valence iron salt solution resulting in an axial diffusion gradient between the iron ions and NaOH solution in the centre of the channel. The velocity profile for this coaxial geometry was modelled using the fluid dynamics package in COMSOL Multiphysics. (Supplementary Figure S1). Recent literature gives further detail to support our modelling, describing how increasing the flow rate of the outer flow, focuses the jet to the centre and thus increases diffusion at the interface [21]. Figure 1b shows the resulting solution to the model showing the cross-sectional velocity in a tube after the junction. It is important to note that the flow regime remains laminar by selecting the correct fluid flow rates. The nanoparticles are formed at the interface which remains stable, no turbulent mixing is required.

The first device was simply cast from polydimethylsiloxane (PDMS) within a Polytetrafluoroethylene (PTFE) holder using a wire and needle to template the channels (Figure 1a,c). In this set up the molten PDMS is simply poured into the PTFE mould and cured over 24 h, then the wire and needle are simply removed. While the PDMS coaxial flow mixer device was based on the example by Hassan et al. [12], a number of design modifications were introduced (see Section 2). The improvements to the construction of the device led to greater ease of use, reliability, and a

reduction in the occurrence of blockages and leaking (which are reported across the literature for PDMS microfluidic platforms). Such devices were standardly used for a one to two years timeframe. Over this time, the devices would handle approximately a litre of solution per year. We did not notice any abrasion or cavitation forming in the device over this time and the reproducibility and quality of the data remained consistent over the time. New casting was usually required due to leakage at the junctions. A second generation microfluidic device was produced to the same simple fluidic system design but builds and improves on this by machining the system out of polyether ether ketone (PEEK) to remove the need to re-cast from PDMS which in turn removed the variations between fluidic devices, for greater consistency between reactions (Figure 1d). The junctions in the new device are also designed to reduce/eliminate leakage. Furthermore, by incorporating a glass capillary as the channel through which the reaction occurs, it is possible to vary the retention time of the iron solution in the sheath flow of NaOH solution by altering the capillary length. It is important to note that while the improved machined fluidics device had less issues with clogging and leaking, the profile of the results that follow were reproducible and consistent across both devices (Supplementary Figure S2).

3.2. Optimisation of Coaxial Flow Devices

It is crucial when utilising a sheath flow system for the formation of iron oxide nanoparticles to develop laminar flow of the outer stream (NaOH), allowing it to diffuse into and react with the core stream (iron solution) at the interface. This is achieved by running the NaOH inlet at a faster rate than that of the Fe inlet to ensure an excess of NaOH that can develop into laminar flow before the core stream point of entry. The concentrations of both the NaOH solution and Fe solution can also be varied, meaning the conditions had to be balanced to find both optimum concentrations and flow rates for each of the reagents and inlets.

When the Fe solution had a concentration of 10 mM, an undeveloped inner stream was observed, due to the low amounts of iron. 20 mM, 50 mM, and 100 mM Fe solutions were also tested and found to produce a cohesive flow. 100 mM was selected due to producing the greatest yield of particles in the shortest run time. NaOH concentration was tested at 0.1 M, 0.3 M, 0.5 M, and 1 M with 1 M producing black particles along the length of the reaction capillary.

A minimum Fe/inner flow rate of $\sim 60 \mu\text{L}/\text{min}$ was found to be necessary, as below this rate magnetic particles would begin to form at either the entry to the system in the case of the PDMS moulded device, or at the tip of the needle in the PEEK system, with both cases resulting in clogging and fouling of the system. Incidences of clogging were reduced at an increased inner flow rate of $\sim 90 \mu\text{L}/\text{min}$. It was found for both devices that when a lower NaOH/outer flow rates was employed (<4:1 ratio between the rates of the two streams), a consistent stream of particles did not develop, with clumps of non-magnetic iron material travelling through the systems instead. A ratio of 4:1 between the outer and inner inlets was found to work optimally (summarised in Table S1), with black iron oxide particles forming in a stream.

3.3. Varying the Ferric: Ferrous Ion Ratio to Tune MNP Magnetism and Size

When synthesising iron oxide MNP's, the ratio between ferric and ferrous ions have a significant influence on the reaction environment. We have previously found that when the fraction (X) of ferric iron of the total iron (both ferrous and ferric) is varied between $X = 0.2$ – 0.7 in a batch synthesis, the iron-oxides produced change, with ferrous rich oxides (such as amorphous ferrous hydroxide and wüstite) being favoured at the lowest ratio, and ferric-rich oxides (such as schwertmannite) being favoured at the higher ratio, with magnetite formation favoured at 0.5–0.6 ferric content [19,22].

In this study we performed the reaction in both fluidic devices varying the fraction of ferric ions from $X = 0.2$ to 0.7 in line with our previous work [19]. In both cases the 0.6 ratio ($3\text{Fe}^{3+}:2\text{Fe}^{2+}$) gave the highest magnetisation. This was 78.7 emug^{-1} , and the 0.5 ($1\text{Fe}^{3+}:1\text{Fe}^{2+}$) ratio producing particles of similar magnetisation at 78.4 emug^{-1} for the PEEK system (see Table 1, Supplementary Table S1 and Figure S2 for comparison with PDMS device), suggesting magnetite was successfully synthesised

in the flow system. This is very high for nanoparticles of this size compared with the literature [23], showing the samples to be high quality and purity magnetite. This was confirmed by X-ray diffraction analysis of the resulting particles (Figure 3). The question as to whether or not the particles analysed were formed in the fluidic device or matured in the collection vessel afterwards was addressed by using a magnetic trap to collect the magnetic material straight from the exit of the fluidics channel (see schematic in Supplementary Figure S3a). The nanoparticles from the PDMS device which were initially magnetic and collected in the magnetic trap (primary product) and those collected in the final collection vial (secondary product) were then compared with the total unseparated products. It was clear that there was only negligible magnetism in the secondary product, showing the magnetite nanoparticles were indeed produced in the fluidic system, not matured later in the collection vial (Supplementary Figure S3b). It is interesting to note that the magnetism of the magnetically trapped primary product was virtually the same as the profile for the unseparated product. This means that the non-magnetic iron oxides are also being trapped in such samples, presumably because they are intrinsically aggregated to the magnetite iron-oxides. Importantly, however the samples are not maturing (becoming more magnetic) in the collection vial. The composition of the particles at different ferric/ferric ion ratios was analysed by X-ray diffraction (Figure 3) and compared to the predicted theoretical iron-oxide composition.

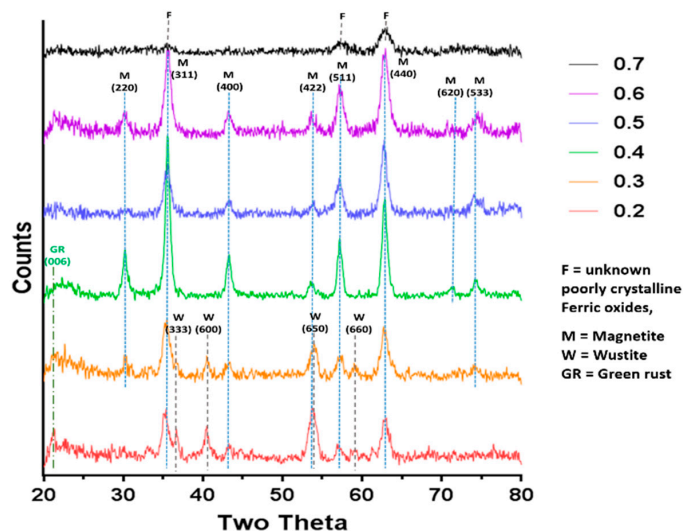


Figure 3. Annotated X-Ray Diffraction (XRD) data of the control samples across the range of ferric to ferrous ratio.

Table 1. Tables of characterization of all the control samples from 0.2–0.7 ferric ion fraction to total ferric and ferrous ion.

Sample	Major Crystalline Iron Species	Particle Size XRD (nm)	Particle Size TEM (nm)	Sat. Magnetic Moment (emu/g)
0.2	Magnetite, Wüstite, Green rust	9.32	13.1 ± 9.6 (35.7 ± 19.4) Mean 20.5 ± 11.8	30.89
0.3	Magnetite, Wüstite, Green rust	9.32	6.9 ± 4.9 (31.2 ± 10.2) Mean 10.9 ± 10.3	51.06
0.4	Magnetite, Green rust	13.31	10.9 ± 5.3	73.27
0.5	Magnetite	10.36	8.6 ± 3.5	78.44
0.6	Magnetite	9.32	7.4 ± 4.1	78.67
0.7	Poorly crystalline ferric oxides	N/A	6.5 ± 3.0	18.08

The XRD in Figure 3 clearly shows that Magnetite is the main crystalline component for samples at ratio 0.4, 0.5 & 0.6. These data also reveal an absence of contaminating crystalline iron oxides,

and this is in agreement with the magnetic data which are all high and similar for these samples. As expected, 0.7 is too high a ratio to produce magnetite as the main product, and as such we observed small, poorly crystalline/amorphous particles. It should be noted that any amorphous products in the sample will not be detectable by XRD. It is impossible to assign a mineral phase to the small, broad, poorly resolved peaks observed, but they could be due to ferric oxides such as schwertmannite, ferrihydrite and ferroxhyte, and to some small quantity of magnetite or maghemite (to account for the small saturation magnetism recorded).

In the more ferrous rich ratios, magnetite is seen alongside ferrous oxides such wüstite and mixed valance oxide green rust. Due to the unknown presence of amorphous oxides ratios of minerals present cannot be extracted from the XRD data, but it can be clearly seen that there is a large proportion of wüstite (and potential green rust) compared to magnetite. Again, the presence of these minerals is responsible for the lower magnetic saturation. The X-ray diffraction pattern could also be used to calculate the average crystalline diameters using the full width half maximum (FWHM) of the $2\theta = 35.5^\circ$ peak data in the Scherrer equation, which are shown in Table 1. Note the 0.7 sample could not be analysed in this way due to the irregularly shaped small peaks. The samples were also analysed by transmission electron microscopy (TEM) and the particles were measured in ImageJ to produce size distributions (Figure 4). We found the average size of the particles formed ranged from 6.5–20.5 nm depending on the initial X-value used, with the lower ratios (0.2–0.3) forming heterogeneous particles with a large variation in sizes observed. Much of this variation is due to the different ferrous-oxide species in these samples. Green rust and ferrous hydroxide forms plates (some of which can be seen in the control X = 0.3 sample in Figure 4). For clarity of sizing, the sizes of these plates were not counted as they would distort the average size of the remaining particles. Wüstite forms irregular shaped particles across a wide size range, which is more difficult reliably recognise to remove from the data, so was not subtracted and so we believe this is responsible for the very large size distribution in these samples. However, there is a visibly bi-modal distribution of smaller and larger particles in the 0.2 and 0.3 samples giving a larger mean size than the higher ratios (Figure 4 and Supplementary Figure S4) including the magnetite particles. This is not however seen in the XRD sizing. This discrepancy could be due to two factors. The first could be the inclusion of materials that are not magnetite in the TEM sizing as discussed above. The second could be inaccuracies in measuring the XRD peak due to masking. In the XRD the $2\theta = 35.5^\circ$ peak has contributions from both magnetite and wüstite that will serve to artificially broaden the peak, reducing the calculated size of the particles. The particles formed at 0.4–0.6 ratios were found to be the most homogeneous with a reduced standard deviation, and this was expected as these are favourable conditions, with the ratios closest to the natural ratio at which magnetite forms. The magnetic and XRD data show these samples clearly contain majority magnetite and happily also show close agreement between the XRD sizing and the TEM sizing (Table 1), showing the crystallite size is the same as the particle size, indicating single crystalline particles. What is most interesting is that particle size reduces as the X value increases. This is clearly seen in both TEM and XRD sizing for this magnetite dominated samples. This shows that (with careful optimisation) the size of magnetite nanoparticles could be subtly tuned by varied starting ratio of ferric to ferrous iron precursors within this 0.4–0.6 range. It should be noted that particle size also affected the saturation magnetisation. However, recent studies show small size difference between 13 and 9 nm will have little effect in the superparamagnetic regime [23]. Furthermore, the trend is the opposite of what we observe in our data. Identical samples show increased magnetic saturation with increasing particle size, whereas our samples show increasing magnetic saturation as size decreases as ratio goes from 0.4–0.6. As such, the difference in magnetic saturation seen can only be due to increased quality and quantities of magnetite nanoparticles present. Particles formed at the 0.7 ratio were the smallest 6.5 ± 3.0 nm, however, the significant reduction in magnetism of this sample suggests the majority is not magnetite but non-magnetic iron oxides, so while it still follows the trend, the size of this sample is not as relevant when considering tuning the size of magnetite particles.

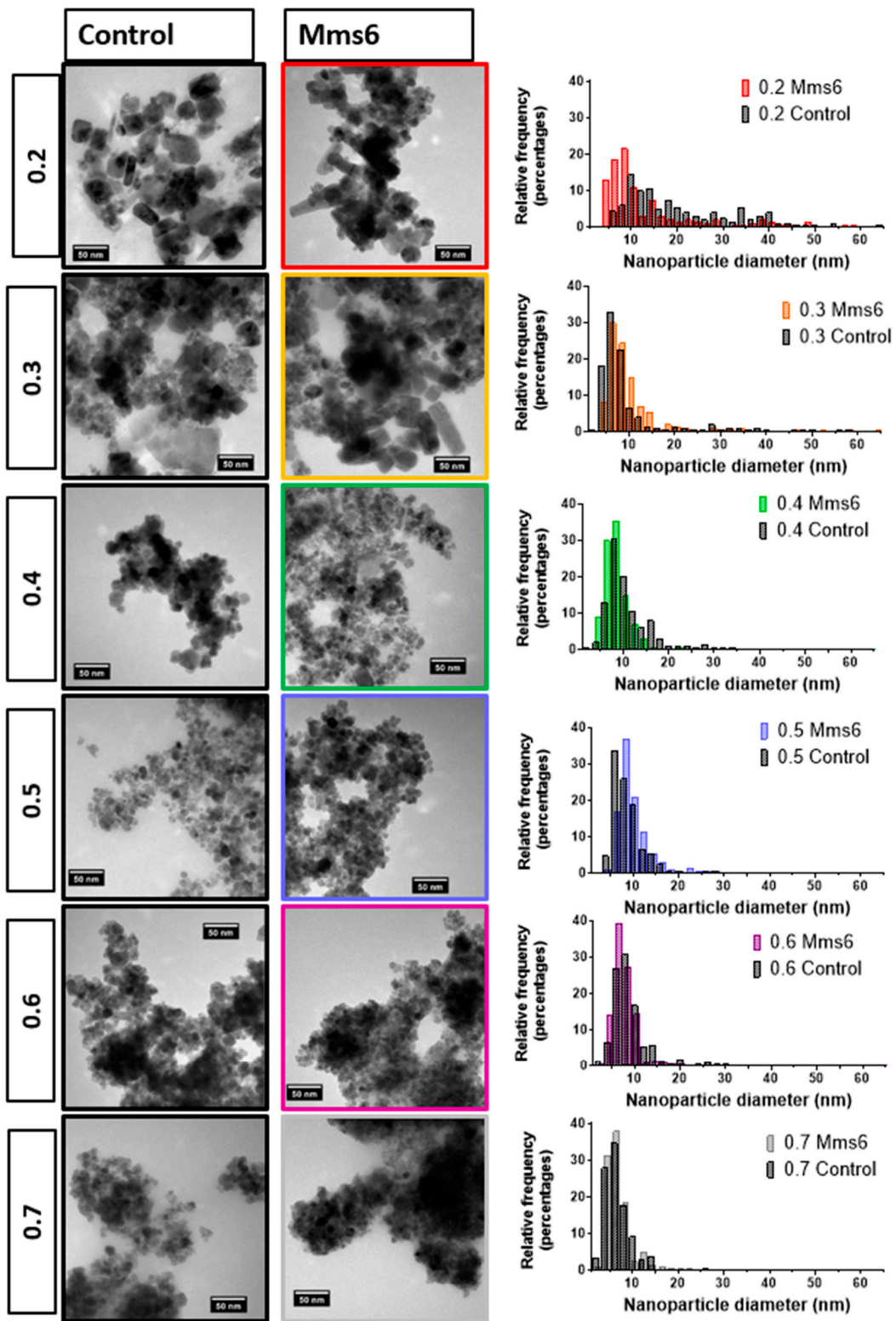


Figure 4. Representative transmission electron microscopy (TEM) image of the particles formed in the fluid device over the 0.2–0.7 ratio of ferric iron:total iron. Left column control samples and right column with the addition of 50 μg Mms6.

3.4. Addition of Mms6

Mms6 has previously been found to influence the phase and size of particles formed in a batch co-precipitation of magnetite. Extensive research of this protein has shown it to self-assemble into micelles in solution, displaying an acidic C-terminal surface to nucleate the forming iron oxides. We thus investigated if Mms6 would have the same controlling effect in a fluidic synthesis. Again, the synthesis was conducted across the 0.2–0.7 X ratio to draw a comparison between control particles and those formed in the presence of Mms6 protein. In this synthesis 50 μg of Mms6 was added to the 50 mM iron solution (1 mL) before flowing through the device. Very little difference was seen in morphology between those particles formed with and without Mms6 (Figure 4). This was also true of the size (Figure 5a, see Supplementary Table S2 for detailed particle size data) showing no notable difference, except with the 0.2 samples. Here we see more control towards smaller particles more similar to higher ratio samples. However, more difference is observed in the magnetic properties of the particles formed (Figure 5b). Interestingly, particles formed in the presence of Mms6 showed increased magnetic saturation for all initial iron ratios than the control, except for the 0.6 ratio. As there is no difference in size, this difference is solely due to the improved quality in Mms6 mediated samples from 0.2–0.5 over controls for additional/larger TEM images of all samples see Supplementary Figure S4c. This is in complete agreement with our previous studies in a batch synthesis [19]. XRD analysis of these samples shows that there is indeed more magnetite present in the most extreme ratios of 0.2 and 0.7 (Figure 6).

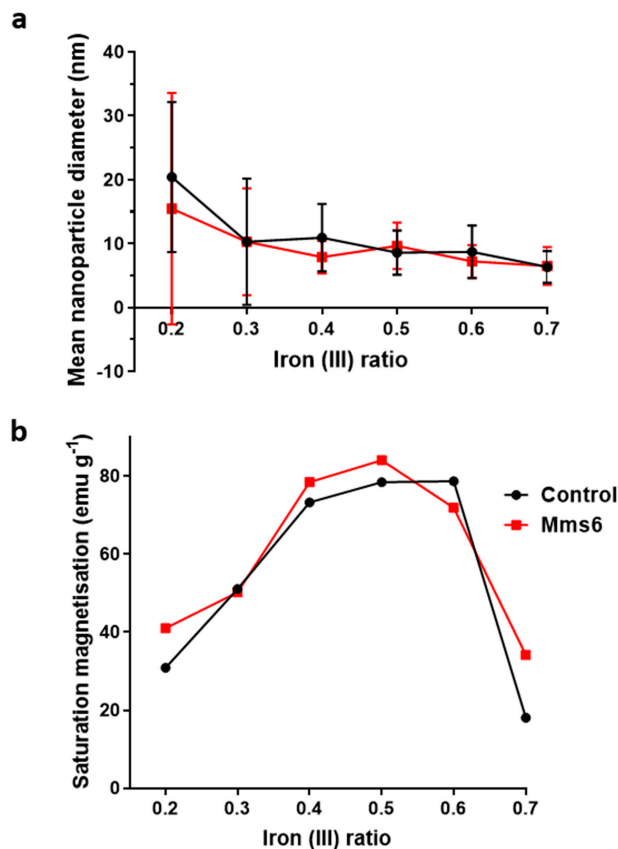


Figure 5. Comparison of control particles to those formed in the presence of 50 μg of Mms6 within the fluidic system. (a) Variation of particle size with increasing initial ratio of ferric ions. (b) Variation of saturated magnetic moment with increasing initial ratio of ferric ions.

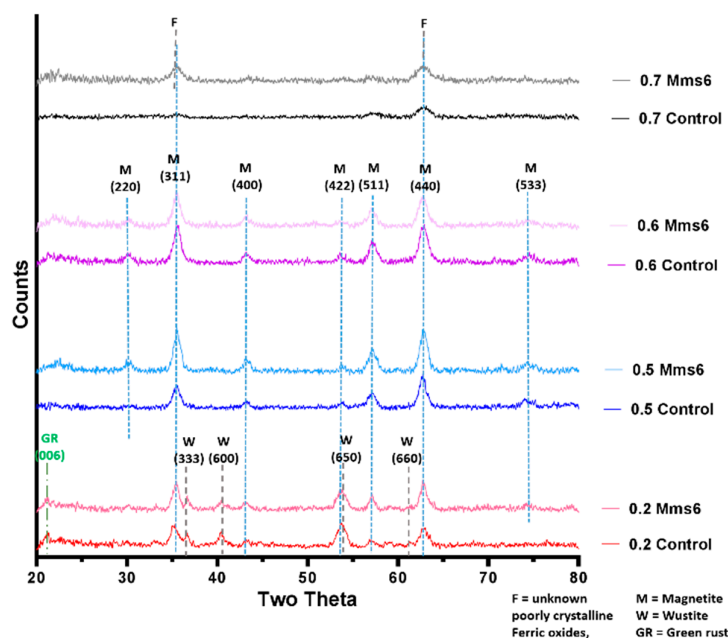


Figure 6. XRD of particles formed in control and Mms6 reactions for 0.2, 0.5, 0.6 and 0.7 X ratio reactions, annotated to show iron oxide.

The X-ray diffraction data correlates well with the magnetic data, showing a now visible peak at the dominant magnetite 311 reflection of $2\theta = 35.5^\circ$ in the Mms6 0.7 ratio sample along with close to doubled increase in saturation magnetisation (from 10 to 34 emu/g). Furthermore, the magnetite peaks are clearly larger than the wüstite peak in the 0.2 Mms6 sample compared to the 0.2 control sample. This again is matched by an increase in saturated magnetic moment from 30.9 to 41 emu/g, suggesting that Mms6 is aiding the formation of magnetite at unfavourable X ratios, with a similar trend observed to our previous studies [19].

4. Discussion

A key issue that occurs in many microfluidic systems is clogging and fouling, and in the case of PDMS systems, leakage. The problem of clogging is exacerbated by the magnetic nature of the formed iron oxide products, resulting in magnetic aggregation which leads to clogging and obstruction of laminar flow. These issues were addressed in PDMS systems by increasing the diameter of tubing, ensuring the fluidic channel is as straight as possible, and by shaping the needle used to cast the device for a smoother co-axial junction. However, this system was still prone to leaking so the design of a second PEEK system addressed this issue by utilising a capillary as the reaction vessel joined to the inlets by specifically machined connectors, sealed with o-rings. The transparent nature of the material of the PEEK system also allows the reaction lifetime to be potentially monitored with optical microscopic or spectroscopic techniques with greater ease. Both devices showed consistent results from run to run within the same device and also across the two devices (once the flow rates were optimised) (see Supplementary Table S1), showing the formation of magnetite in this simple fluidic system has good reaction control.

Magnetite is stoichiometrically formed of $2 \text{Fe}^{3+} : 1 \text{Fe}^{2+}$ giving an X ratio of 0.667. Oxidation is known to occur when performing this reaction so initial precursor ratios of 0.5 and 0.6 are commonly used. It is clear from this study that $X = 0.4\text{--}0.6$ give a good yield of magnetite, demonstrated by the magnetism, TEM and XRD, with lower X-values contaminated with ferrous iron oxides such as wüstite and green rust (0.2 and 0.3). It is also worth acknowledging that XRD only detects crystalline materials so amorphous phases could also be present. There has been detailed theoretic and experimental

research into the iron oxides that form at different ferrous:ferric precursor ratios [19,22]. The results in this paper tally well with previous findings where mixtures of ferrous hydroxides, ferrous oxides, green rust and a small amount of magnetite can be formed at lower ratios while mixtures of magnetite and ferric-oxides such as schwertmannite and goethite are seen in higher ratios (above the stoichiometric ratio). It is excellent to see the fluidic system reproduces the results from previous batch studies and tally well with theoretical work. However, what has not been seen before is the ability to tune the size with varying X . It is not clear from searching the literature if this has not been explored before in all synthetic forms of precipitating magnetite, batch, fluidic or otherwise, or whether this effect is something only seen in a flow synthesis. In the flow the iron solution is been fed the base at the interface at a continuous rate at the interface were the crystals will be seeded. Perhaps at ratios closer to stoichiometric, the nucleation is so rapid that the particles do not have the capacity to grow quite as much before all the iron solution is used up, forming smaller particles. However, in the lower ratios, fewer particles can be nucleated giving more iron feedstock to grow the smaller number of particles more.

We developed the experiment further by adding the biomineralisation protein Mms6 to the flow synthesis. In agreement with our previous study this aided the formation of magnetite at ratios where the control showed less magnetite [19]. This is thought to be possible as the acidic rich DEEVE amino acid motif on the C-terminus of the protein is exposed and is capable of binding iron ions [19,20,24,25]. The N-terminus is hydrophobic and as such causes the protein to self-assemble into rafts within the native environment or micelles in aqueous solution, displaying the acidic residues as a negative charged nucleation surface for iron binding. Importantly it has been show to bind ferrous ions in some sites and ferric ions less specifically but in abundance, encouraging the nucleation of magnetite specifically [20]. Previous work has also shown that Mms6 controls the size of the particles to be 20 nm when formed in solution. However, we did not see this control in the flow synthesis. We hypothesis that the synthesis in flow increases the effect of the chemical kinetics of particle formation over slower additive modified crystal growth giving little room for Mms6 to be effective, especially with respect to particle size control. However interestingly, it has been previously reported that the curvature of the charged surface may be key to size controlling aspect of Mms6. When Mms6 is displayed on a flat surface the particles formed are larger (90 nm) compared to 20 nm in solution, so it could also be the case that Mms6 in the flow system cannot form the correct size-controlling surface [26].

Finally, this device, experiments and results demonstrates how this system could be a beneficial platform for the study of nanoparticle formation more generally. The reaction vessel is long so time points can be equated to distance. This can be useful in both experiment design (introducing additive such as Mms6 at different reaction points) and analysis (studying the reaction intermediates in situ). Similarly, this could be universally extended to study the action and effect of a full range of different additive and at different stages in a wet chemistry synthesis of any nanoparticles.

5. Conclusions

We have successfully built a simple and reliable fluidic system that reproducibly formed magnetite nanoparticles. Magnetite is the major product in the synthesis where the ferric to total iron ratio of the precursor solution was 0.4–0.6, demonstrated by both the XRD and the magnetic data. The size of the nanoparticles can be tuned simply by varying this ratio, however consistent magnetite and thus tuning is best achieved between ferric fractions of 0.4–0.6 (with larger particles at higher ferrous content ($X = 0.4$) and smaller particles with higher ferric content ($X = 0.6$). Outside this range other iron oxides were obtained, reducing the homogeneity in terms of size, and morphology, as well as reducing the magnetic saturation. The more ferrous rich ratios ($X = 0.2$ – 0.3) contained wüstite and green rust, while the phases of the more ferric rich $X = 0.7$ ratio were unidentifiable from our characterisation. Addition of Mms6, a magnetite nucleation protein, helped to produce more magnetite within all samples (except $X = 0.6$) with the most profound effect at the 0.2 and 0.7 extremes. Mms6 was not able to affect the particle size in the fluidic system, which it is able to do in a batch synthesis. We speculate

this may be due to the complex competing effects of the dominance of kinetics on synthesis in dynamic flow, coupled with the flow conditions affecting the Mms6 assembly. This study shows a promising proof-of-concept for using a simple fluidic system for the formation of and detailed in situ analysis of the formation of a full range of inorganic nanomaterials, and their interaction with crystallization additives, such as Mms6.

Supplementary Materials: The following are available online at <http://www.mdpi.com/2079-4991/9/12/1729/s1>, Figure S1: Demonstration of the fluidic dynamic modelled performed in COMSOL, x and y axis are length in metres (x is $\times 10^{-3}$): A. shows the mesh used for the modelling. Note this is a radial symmetry model with the centre at 0, so only half the tube is shown. B. shows the surface radial velocity. The yellow colour = 0 m/s showing negligible or no radial velocity indicating laminar flow (red at the end is an artifact of the boundary conditions), Figure S2: Variation of (a) magnetic saturation and (b) nanoparticle size verse the initial ferric to ferrous iron composition for both the first generation PDMS fluidic system and the second generation PEEK fluidic system. Ratio is of ferric iron to total ferric + ferrous iron precursor. (a) obtained from sizing > 200 particle per sample using image], (b) was measured on a benchtop magnetometer for the PDMS device and on the VSM for the PEEK system, Figure S3: (a) Adapted outlet of PDMS co-axial flow device, incorporating a magnetic trap. (b) Magnetic susceptibility of primary and secondary products measured on a benchtop magnetometer, Figure S4a: Histogram series for the TEM size analysis of control samples, Figure S4b: Histogram series for the TEM size analysis of Mms6 mediated samples, Figure S4c: Larger TEM Images of all samples, Table S1: Comparison of the specification of the two devices: tubing measurements and flow rates, Table S2: Mean particle sizes of the control and Mms6 mediated particles produced in the PEEK system.

Author Contributions: Research conceptualization, J.P.B., A.E.R. and S.S.S.; methodology, J.P.B., A.E.R.; data acquisition, L.N., A.E.R., J.P.B., K.W., N.F., R.W., A.B.; formal analysis, L.N., A.E.R., J.P.B., K.W., N.F., R.W., A.B.; writing—original draft preparation, L.N., S.S.S.; writing—review and editing, L.N., S.S.S., A.E.R.; supervision, S.S.S., A.E.R., J.P.B., L.N.; funding acquisition, S.S.S.

Funding: This research was funded by the BBSRC (grant number BB/H005412/1 & 2) and the EPSRC (grant number EP/P006892/1). The University of Sheffield's ESPRC DTP allowance (grant number EP/M508135/1) funds Laura Norfolk's PhD.

Acknowledgments: We would like to thank Andrew Norfolk and Stefan Waterson from the Cambridge Design Partnership for their assistance in the design and preparation of the PEEK microfluidic system. Thank you also goes to Garry Turner and Richard Truswell for assistance in any additional machining and adjustments required. We would also like to thank the following people for assistance and training: Chris Hill and Svetomir Tzokov for TEM, Nicola Morley and Zhao Yuan Leong for magnetometry and Craig Robertson for XRD.

Conflicts of Interest: The authors declare no conflict of interest.

References

1. Meng Lin, M.; Kim, H.-H.; Kim, H.; Muhammed, M.; Kyung Kim, D. Iron oxide-based nanomagnets in nanomedicine: Fabrication and applications. *Nano Rev.* **2010**, *1*, 4883. [[CrossRef](#)] [[PubMed](#)]
2. Laurent, S.; Forge, D.; Port, M.; Roch, A.; Robic, C.; Vander Elst, L.; Muller, R.N. Magnetic Iron Oxide Nanoparticles: Synthesis, Stabilization, Vectorization, Physicochemical Characterizations, and Biological Applications. *Chem. Rev.* **2008**, *108*, 2064–2110. [[CrossRef](#)] [[PubMed](#)]
3. Pankhurst, Q.A.; Connolly, J.; Jones, S.K.; Dobson, J. Applications of magnetic nanoparticles in biomedicine. *J. Phys. D Appl. Phys.* **2003**, *36*, R167–R181. [[CrossRef](#)]
4. Plan Sangnier, A.; Preveral, S.; Curcio, A.; Silva, A.K.; Lefèvre, C.T.; Pignol, D.; Lalatonne, Y.; Wilhelm, C. Targeted thermal therapy with genetically engineered magnetite magnetosomes@RGD: Photothermia is far more efficient than magnetic hyperthermia. *J. Control. Release* **2018**, *279*, 271–281. [[CrossRef](#)] [[PubMed](#)]
5. Regazzoni, A.E.; Urrutia, G.A.; Blesa, M.A.; Maroto, A.J.G. Some observations on the composition and morphology of synthetic magnetites obtained by different routes. *J. Inorg. Nucl. Chem.* **1981**, *43*, 1489–1493. [[CrossRef](#)]
6. Sugimoto, T.; Matijevic, E. Formation of uniform spherical magnetite particles by crystallization from ferrous hydroxide gels. *J. Colloid Interface Sci.* **1980**, *74*, 227–243. [[CrossRef](#)]
7. Marre, S.; Jensen, K.F. Synthesis of micro and nanostructures in microfluidic systems. *Chem. Soc. Rev.* **2010**, *39*, 1183–1202. [[CrossRef](#)]
8. Phillips, T.W.; Lignos, I.G.; Maceiczky, R.M.; deMello, A.J.; deMello, J.C. Nanocrystal synthesis in microfluidic reactors: Where next? *Lab Chip* **2014**, *14*, 3172–3180. [[CrossRef](#)]

9. Edel, J.B.; Fortt, R.; deMello, J.C.; deMello, A.J. Microfluidic routes to the controlled production of nanoparticles. *Chem. Commun.* **2002**, 1136–1137. [[CrossRef](#)]
10. Baber, R.; Mazzei, L.; Thanh, N.T.K.; Gavriilidis, A. Synthesis of silver nanoparticles in a microfluidic coaxial flow reactor. *RSC Adv.* **2015**, *5*, 95585–95591. [[CrossRef](#)]
11. Mirhosseini Moghaddam, M.; Baghbanzadeh, M.; Sadeghpour, A.; Glatter, O.; Kappe, C.O. Continuous-Flow Synthesis of CdSe Quantum Dots: A Size-Tunable and Scalable Approach. *Chem. Eur. J.* **2013**, *19*, 11629–11636. [[CrossRef](#)] [[PubMed](#)]
12. Abou Hassan, A.; Sandre, O.; Cabuil, V.; Tabeling, P. Synthesis of iron oxide nanoparticles in a microfluidic device: Preliminary results in a coaxial flow millichannel. *Chem. Commun.* **2008**, 1783–1785. [[CrossRef](#)] [[PubMed](#)]
13. Frenz, L.; El Harrak, A.; Pauly, M.; Bégin-Colin, S.; Griffiths, A.D.; Baret, J.-C. Droplet-Based Microreactors for the Synthesis of Magnetic Iron Oxide Nanoparticles. *Angew. Chem. Int. Ed.* **2008**, *47*, 6817–6820. [[CrossRef](#)] [[PubMed](#)]
14. Uebe, R.; Schuler, D. Magnetosome biogenesis in magnetotactic bacteria. *Nat Rev Micro* **2016**, *14*, 621–637. [[CrossRef](#)] [[PubMed](#)]
15. Komeili, A. Molecular mechanisms of magnetosome formation. *Annu. Rev. Biochem.* **2007**, *76*, 351–366. [[CrossRef](#)]
16. Amemiya, Y.; Arakaki, A.; Staniland, S.S.; Tanaka, T.; Matsunaga, T. Controlled formation of magnetite crystal by partial oxidation of ferrous hydroxide in the presence of recombinant magnetotactic bacterial protein Mms6. *Biomaterials* **2007**, *28*, 5381–5389. [[CrossRef](#)]
17. Arakaki, A.; Webb, J.; Matsunaga, T. A novel protein tightly bound to bacterial magnetic particles in *Magnetospirillum magneticum* strain AMB-1. *J. Biol. Chem.* **2003**, *278*, 8745–8750. [[CrossRef](#)]
18. Rawlings, A.E.; Bramble, J.P.; Walker, R.; Bain, J.; Galloway, J.M.; Staniland, S.S. Self-assembled MmsF proteinosomes control magnetite nanoparticle formation in vitro. *Proc. Natl. Acad. Sci. USA* **2014**, *111*, 16094–16099. [[CrossRef](#)]
19. Rawlings, A.E.; Bramble, J.P.; Hounslow, A.M.; Williamson, M.P.; Monnington, A.E.; Cooke, D.J.; Staniland, S.S. Ferrous iron key to Mms6 magnetite biomineralisation: A mechanistic study to understand magnetite formation using pH titration and NMR. *Chem. A Eur. J.* **2016**, *22*, 7885–7894. [[CrossRef](#)]
20. Staniland, S.S.; Rawlings, A.E. Crystallizing the function of the magnetosome membrane mineralization protein Mms6. *Biochem. Soc. Trans.* **2016**, *44*, 883–890. [[CrossRef](#)]
21. Andreev, V.P.; Koleshko, S.B.; Holman, D.A.; Scampavia, L.D.; Christian, G.D. Hydrodynamics and Mass Transfer of the Coaxial Jet Mixer in Flow Injection Analysis. *Anal. Chem.* **1999**, *71*, 2199–2204. [[CrossRef](#)] [[PubMed](#)]
22. Ruby, C.; Géhin, A.; Abdelmoula, M.; Génin, J.-M.R.; Jolivet, J.-P. Coprecipitation of Fe(II) and Fe(III) cations in sulphated aqueous medium and formation of hydroxysulphate green rust. *Solid State Sci.* **2003**, *5*, 1055–1062. [[CrossRef](#)]
23. Li, Q.; Kartikowati, C.W.; Horie, S.; Ogi, T.; Iwaki, T.; Okuyama, K. Correlation between particle size/domain structure and magnetic properties of highly crystalline Fe₃O₄ nanoparticles. *Sci. Rep.* **2017**, *7*, 9894. [[CrossRef](#)] [[PubMed](#)]
24. Wang, L.; Prozorov, T.; Palo, P.E.; Liu, X.; Vaknin, D.; Prozorov, R.; Mallapragada, S.; Nilsen-Hamilton, M. Self-Assembly and Biphasic Iron-Binding Characteristics of Mms6, A Bacterial Protein That Promotes the Formation of Superparamagnetic Magnetite Nanoparticles of Uniform Size and Shape. *Biomacromolecules* **2012**, *13*, 98–105. [[CrossRef](#)]
25. Zhang, H.; Liu, X.; Feng, S.; Wang, W.; Schmidt-Rohr, K.; Akinc, M.; Nilsen-Hamilton, M.; Vaknin, D.; Mallapragada, S. Morphological Transformations in the Magnetite Biomineralizing Protein Mms6 in Iron Solutions: A Small-Angle X-ray Scattering Study. *Langmuir* **2015**, *31*, 2818–2825. [[CrossRef](#)]
26. Bird, S.M.; Rawlings, A.E.; Galloway, J.M.; Staniland, S.S. Using a biomimetic membrane surface experiment to investigate the activity of the magnetite biomineralisation protein Mms6. *RSC Adv.* **2016**, *6*, 7356–7363. [[CrossRef](#)]





Supplementary information

Macrofluidic Coaxial Flow Platforms to Produce Tunable Magnetite Nanoparticles: A Study of the Effect of Reaction Conditions and Biomineralisation Protein Mms6

Laura Norfolk ^{1,†}, Andrea E Rawlings ^{1,2,†}, Jonathan P Bramble ^{1,2,†}, Katy Ward ¹, Noel Francis ¹, Rachel Waller ¹, Ashley Bailey ² and Sarah S. Staniland ^{1,2,*}

¹ Department of Chemistry, University of Sheffield, Brook Hill, Sheffield S3 7HF, UK; lnorfolk1@sheffield.ac.uk (L.N.); a.rawlings@sheffield.ac.uk (A.R.); jbramble82@gmail.com (J.B.); klward2@sheffield.ac.uk (K.W.); nfrancis1@sheffield.ac.uk (N.F.); rwaller2@sheffield.ac.uk (R.W.)

² School of Physics and Astronomy, University of Leeds, Leeds LS2 9JT, UK; bailey272@hotmail.co.uk

* Correspondence: s.s.staniland@sheffield.ac.uk; Tel.: +44-(0)114-222-9539

† These authors contributed equally to this work.

S1. Fluid dynamics modelling using COMSOL Multiphysics.

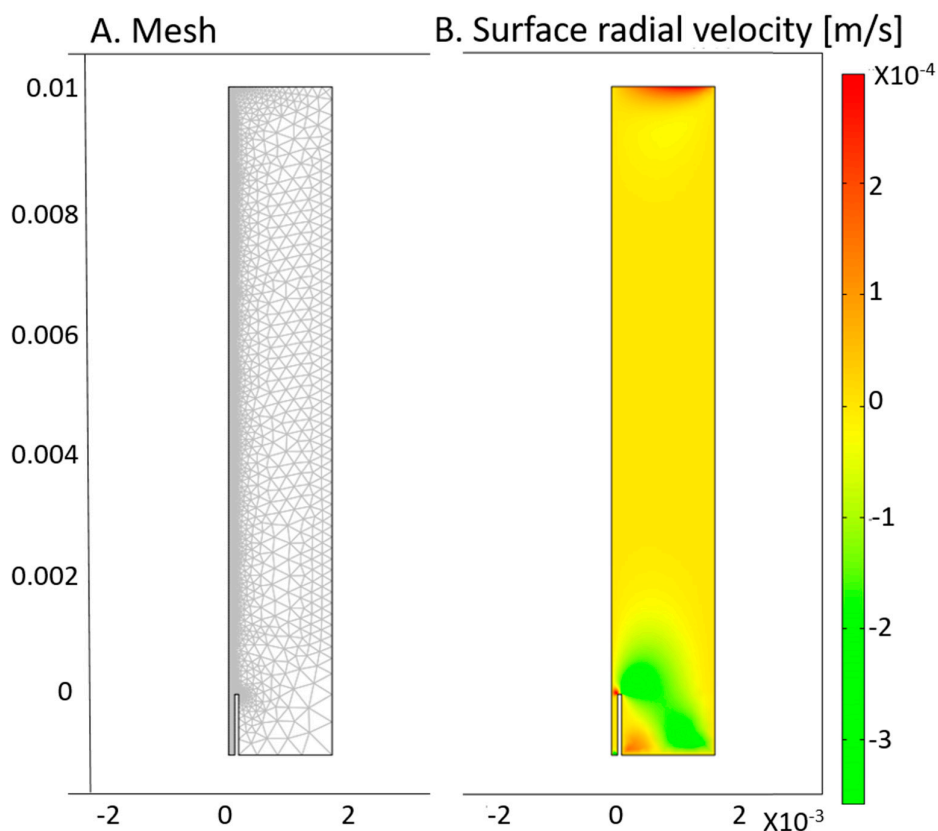


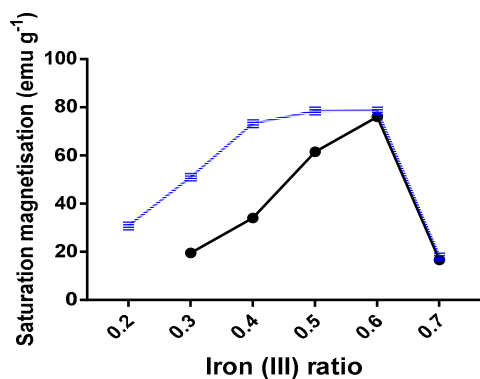
Figure S1. Demonstration of the fluidic dynamic modelled performed in COMSOL, x and y axis are length in metres (x is $\times 10^{-3}$): A. shows the mesh used for the modelling. Note this is a radial symmetry model with the centre at 0, so only half the tube is shown. B. shows the surface radial velocity. The

yellow colour = 0 m/s showing negligible or no radial velocity indicating laminar flow (red at the end is an artifact of the boundary conditions).

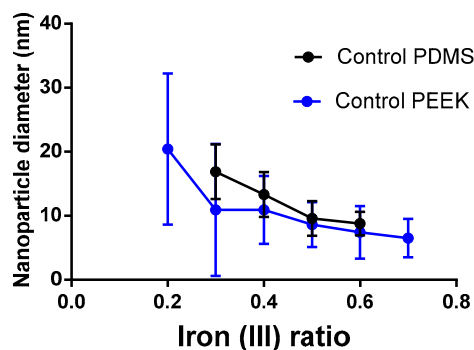
S2. Comparison of both 1st generation PDMS and 2nd generation PEEK systems along with their resulting particles produced.

Table S1. Comparison of the specification of the two devices: tubing measurements and flow rates.

	Iron Solution (100 mM)		Sodium Hydroxide solution (IM)	
	Tube diameter	Flow rate	Tube diameter	Flow rate
1 st generation PDMS device (Tube length 10 cm)	0.5 mm (0.02")	60-70 $\mu\text{l min}^{-1}$	1.6 mm	300 $\mu\text{l min}^{-1}$
2 nd generation PEEK device (Tube length 50 cm)	0.5 mm (0.02")	60-90 $\mu\text{l min}^{-1}$	1.5 mm	240-360 $\mu\text{l min}^{-1}$ (1:4 ratio)



(a)



(b)

Figure S2. Variation of a) magnetic saturation and b) nanoparticle size verse the initial ferric to ferrous iron composition for both the first generation PDMS fluidic system and the second generation PEEK fluidic system. Ratio is of ferric iron to total ferric + ferrous iron precursor. a) obtained from sizing > 200 particle per sample using imageJ, b) was measured on a benchtop magnetometer for the PDMS device and on the VSM for the PEEK system.

S3. PDMS coaxial flow device modified with a Magnetic trap

A magnetic trap was introduced to the PDMS device to investigate whether MNP were formed inside the device or matured into MNP in the collection vessel. All other conditions remained unchanged. The nanoparticles which were initially magnetic and collected in the magnetic trap (primary products) and those collected in the final collection vial (secondary products) could then be compared with the total produce from the earlier unmodified study. It was clear to see visually that most of the magnetic sample was indeed trapped and was thus formed in the device and not subsequently.

There was a small amount of magnetic material in the secondary product, but it is difficult to say whether these particles were magnetic when leaving the device and failed to be trapped due to high flow rate or if they matured to become magnetic at a later stage. Nevertheless, the quantities are so minimal that we are confident that the main magnetic iron oxide product is produced *within the co-axial flow device*.

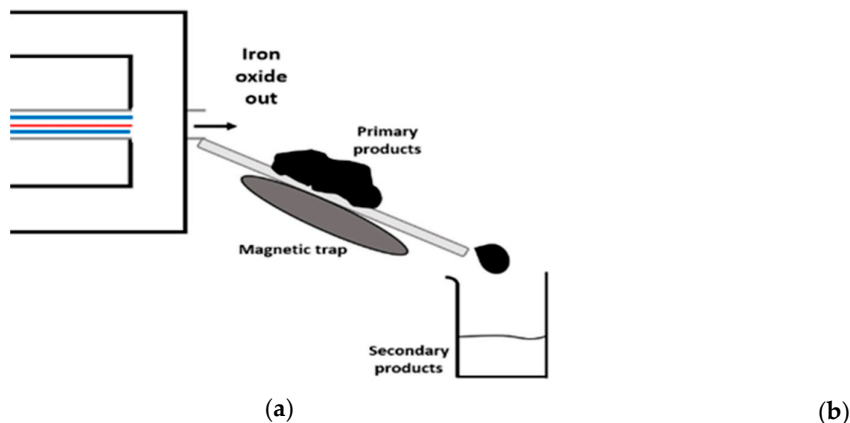


Figure S3. a) Adapted outlet of PDMS co-axial flow device, incorporating a magnetic trap. b) Magnetic susceptibility of primary and secondary products measured on a benchtop magnetometer.

S4. Detailed analysis of particle sizes for the PEEK 2nd generation system.

Table S2. Mean particle sizes of the control and Mms6 mediated particles produced in the PEEK system.

Sample	Mms6	
	Control Particle size TEM (nm)	Particle size TEM (nm)
0.2	13.1 ± 9.6 (35.7 ± 19.4) Mean 20.5 ± 11.8	10.1 ± 9.0 (36.1 ± 11.4) Mean 15.5 ± 18.1
0.3	6.9 ± 4.9 (31.2 ± 10.2) Mean 10.9 ± 10.3	10.3 ± 8.4
0.4	10.9 ± 5.3	7.9 ± 2.5
0.5	8.6 ± 3.5	9.7 ± 3.6
0.6	7.4 ± 4.1	7.2 ± 2.5
0.7	6.5 ± 3.0	6.5 ± 3.0

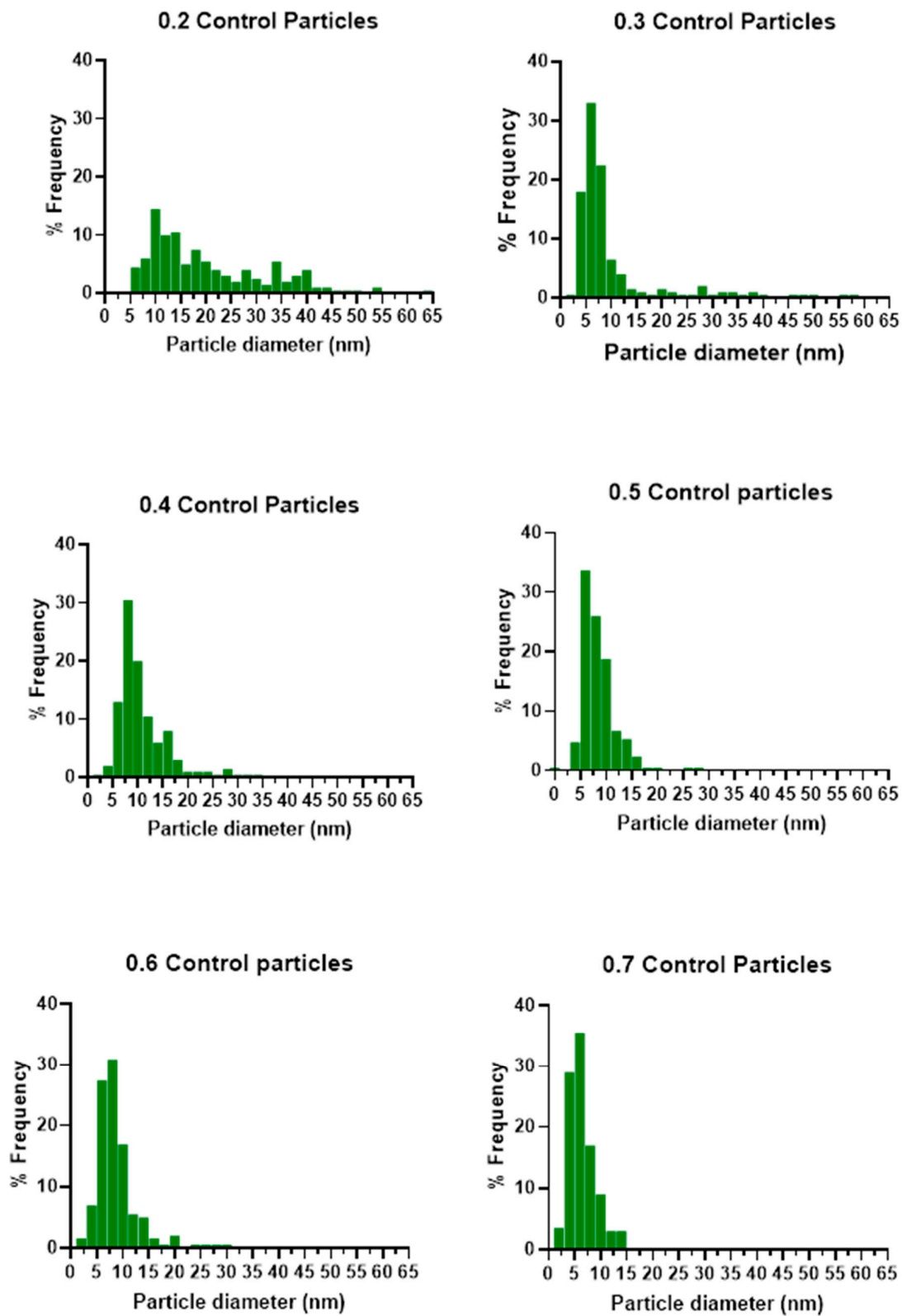


Figure S4a. Histogram series for the TEM size analysis of control samples.

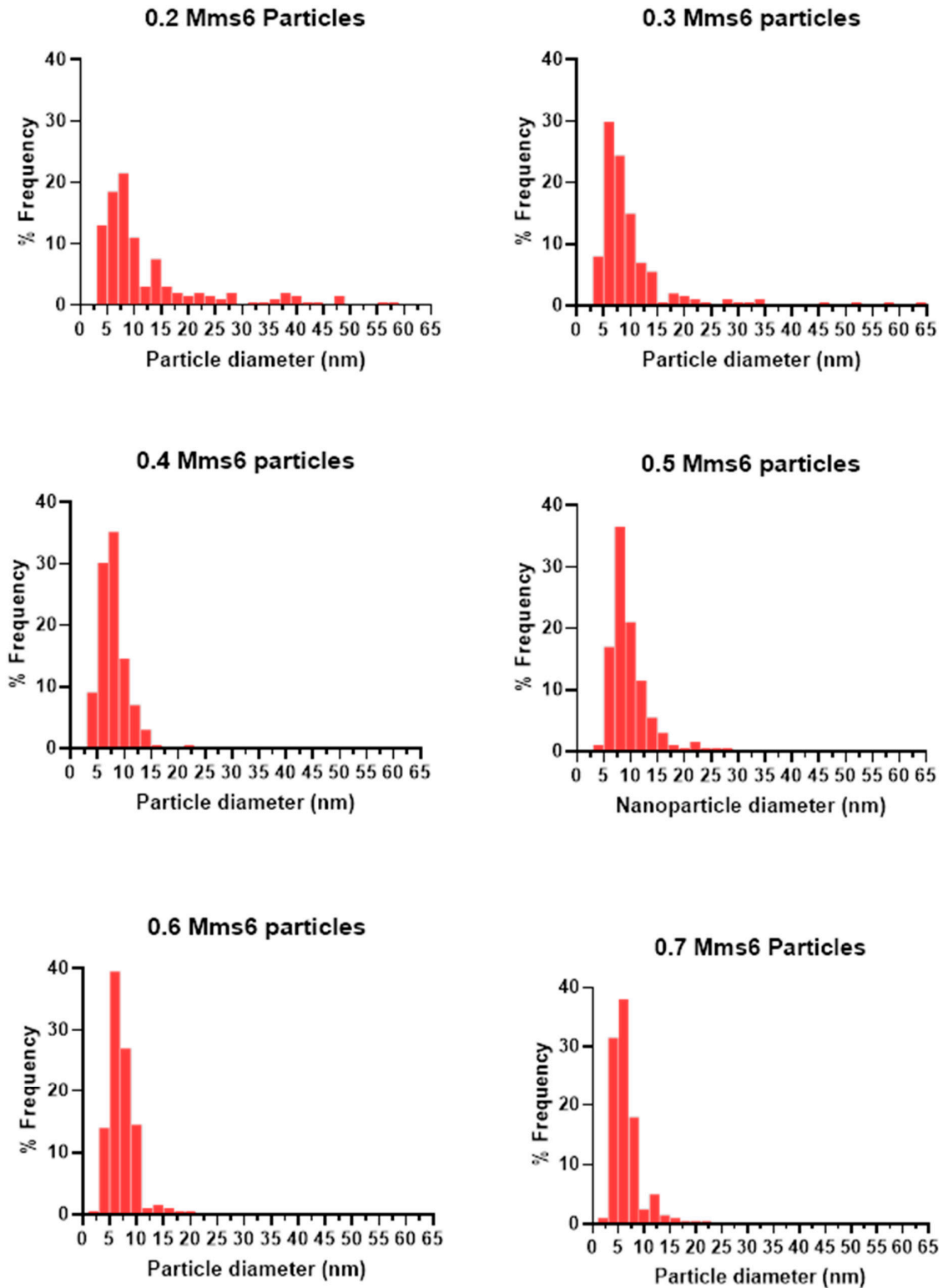
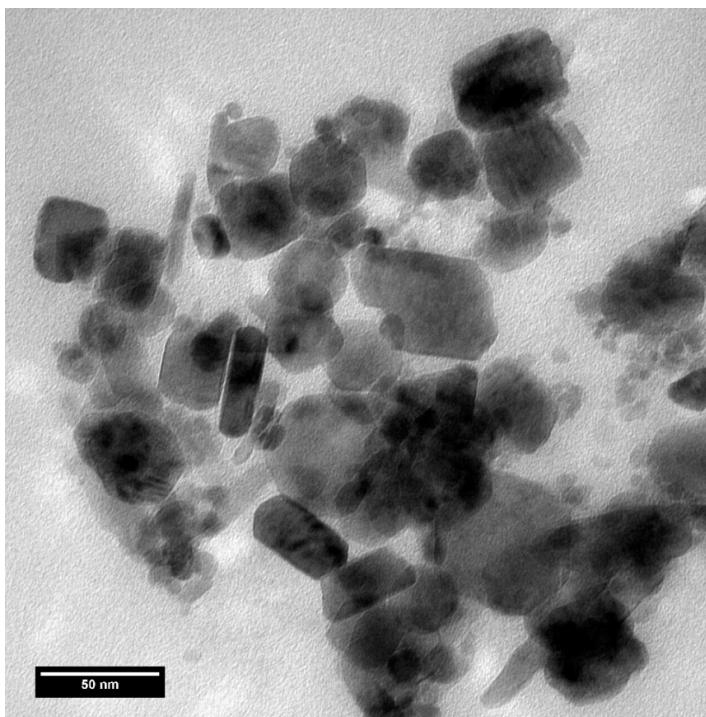
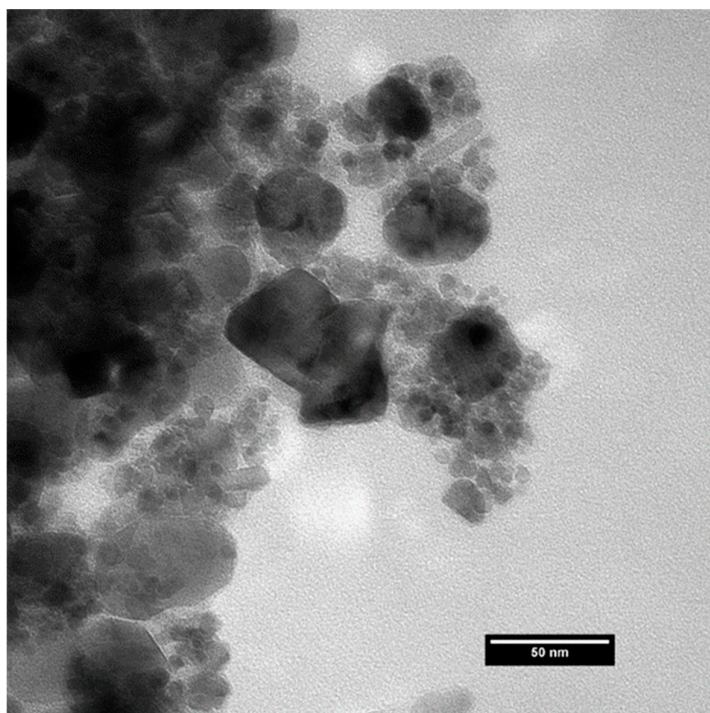


Figure S4b. Histogram series for the TEM size analysis of Mms6 mediated samples.

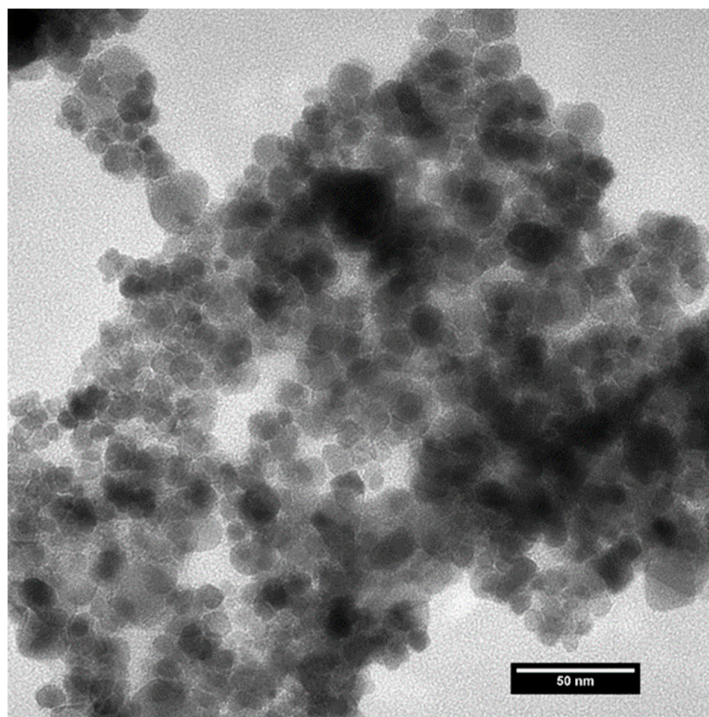
0.2 Control:



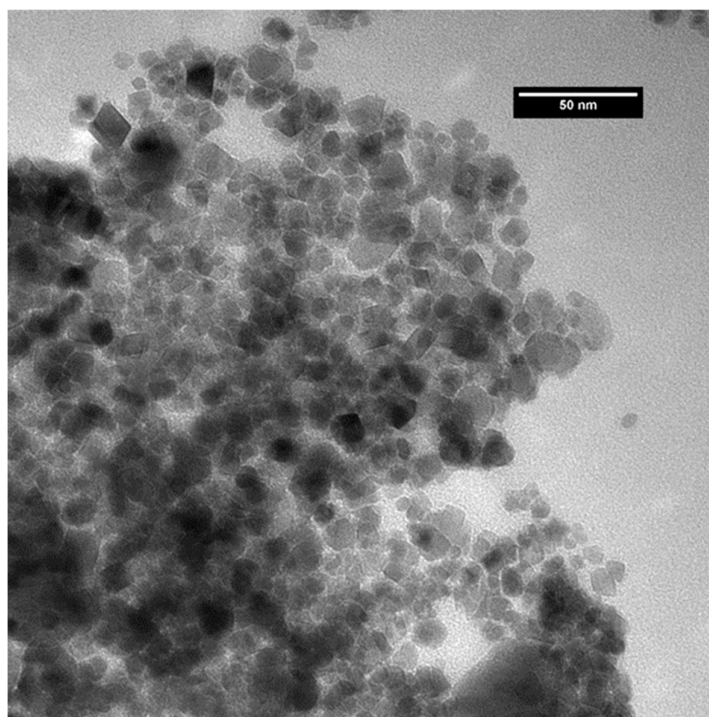
0.3 Control:



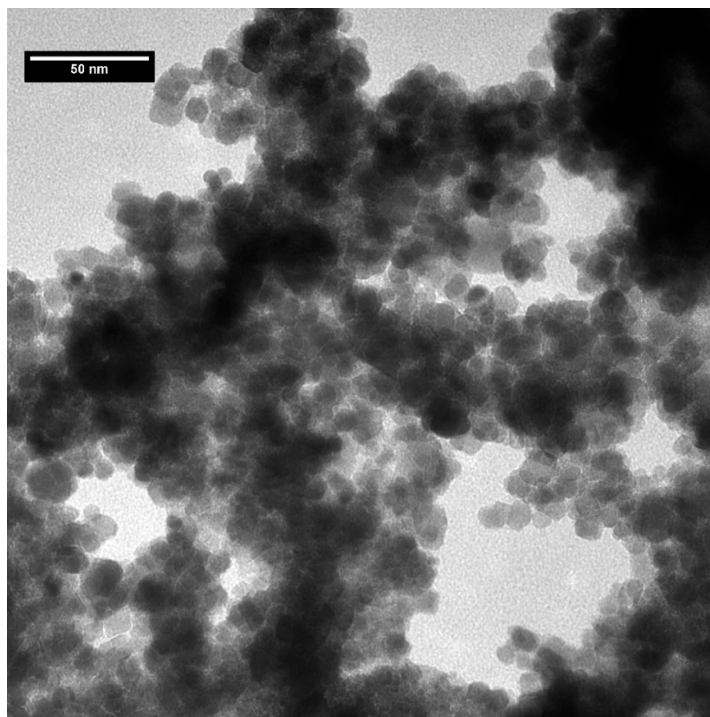
0.4 control:



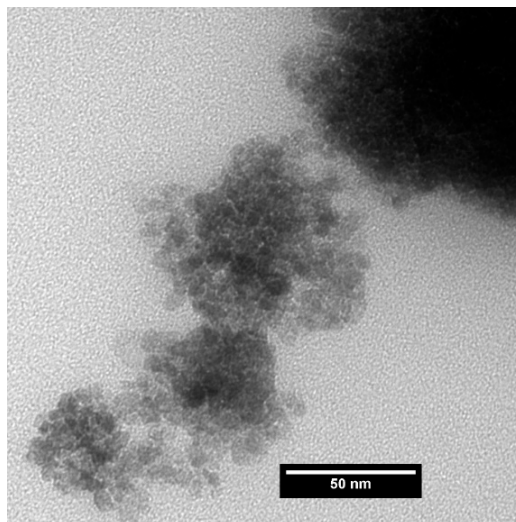
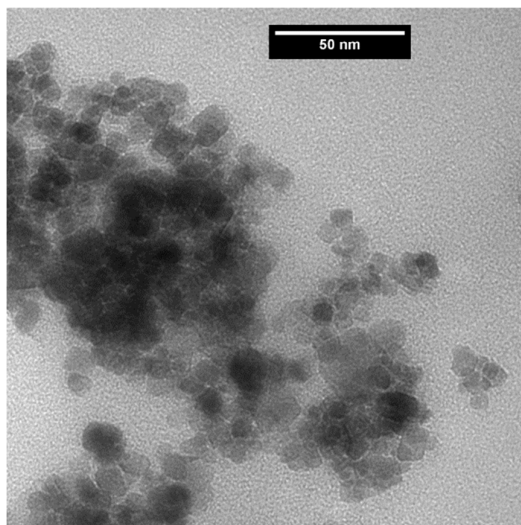
0.5 control:



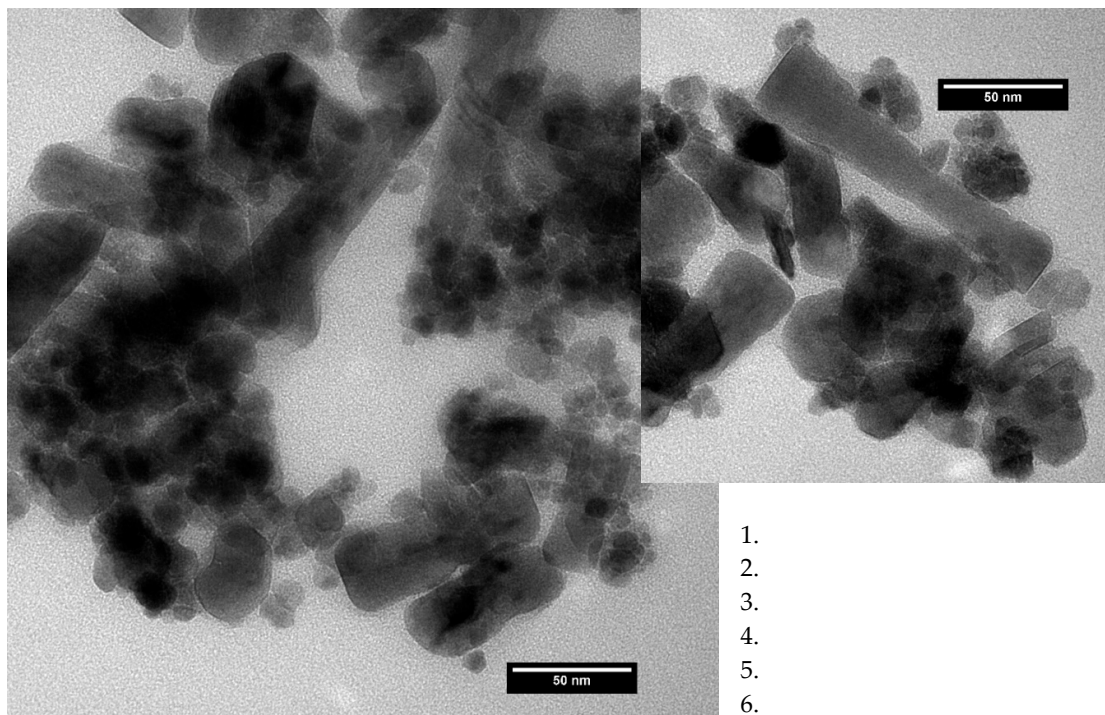
0.6 control:



0.7 control:

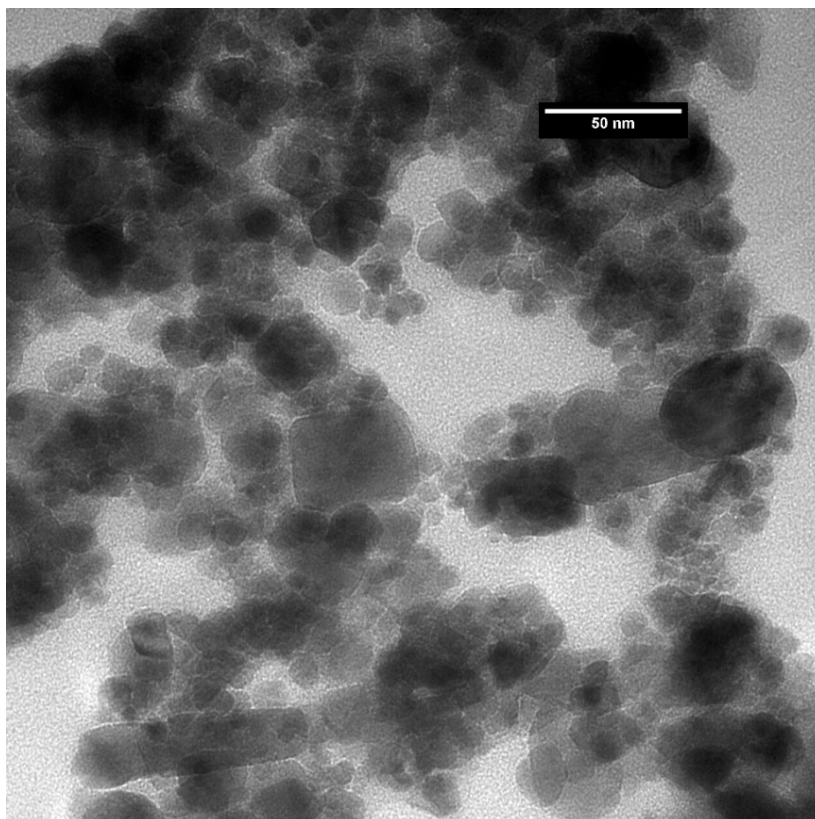


0.2 Mms6:

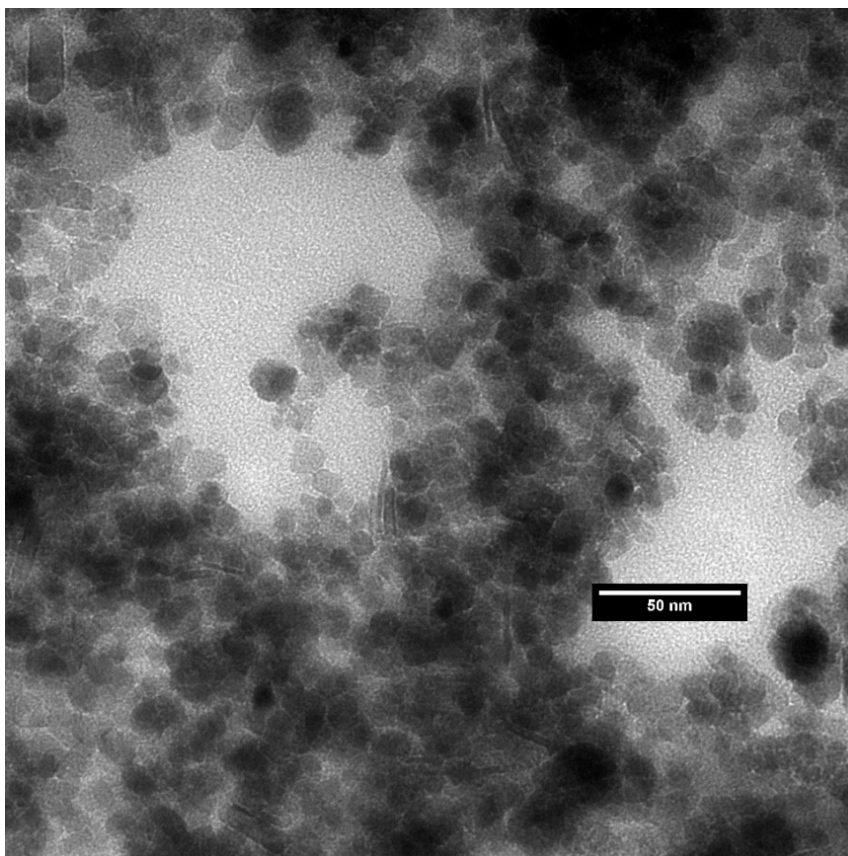


- 1.
- 2.
- 3.
- 4.
- 5.
- 6.
- 7.

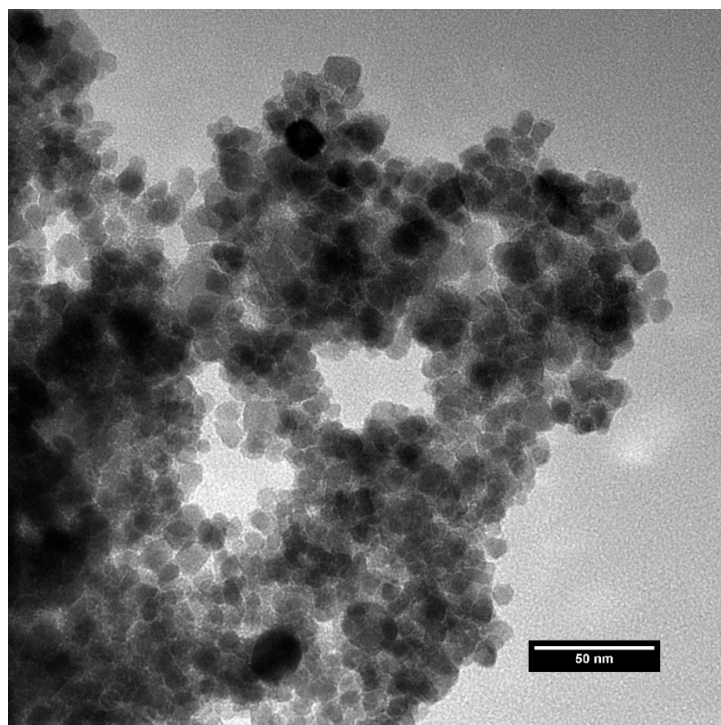
0.3 Mms6:



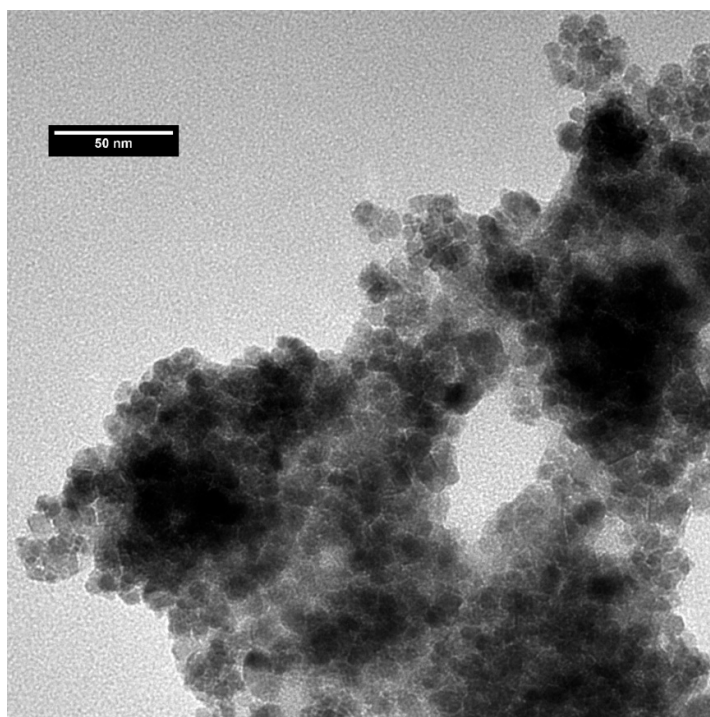
0.4 Mms6:



0.5 Mms6:



0.6 Mms6:



0.7 Mms6:

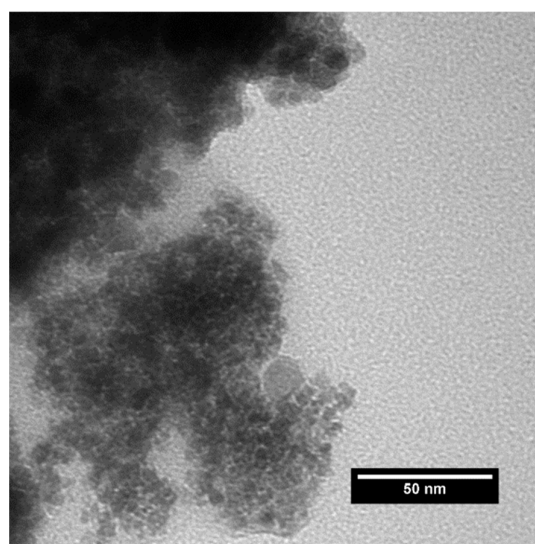
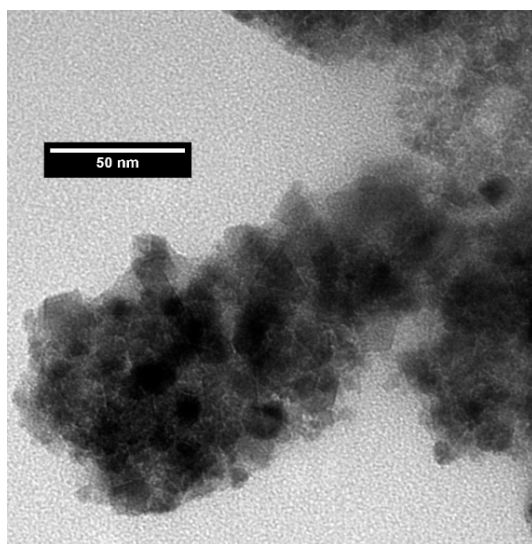


Figure S4c. Larger TEM Images of all samples.

6.2 Adapting the Morphology of Magnetite Nanoparticles Synthesised in a Coaxial Flow Device Using Affordable Amine Additives

6.2.1 Author Contributions

Laura Norfolk (first author): Designed the study, synthesised the 15 sets of particles, analysed the particles (XRD, TEM, VSM, shape and size analysis), designed and created all figures and supplementary, prepared the first paper draft, reviewed and edited the paper.

Sarah Staniland (principal investigator): Supervisor, acquired funding for the project, reviewed the first paper draft.

ARTICLE

Adapting the morphology of magnetite nanoparticles synthesised in a coaxial flow device with affordable amine additives

Laura Norfolk,^a and Sarah Staniland^{*a}

Received 00th January 20xx,
Accepted 00th January 20xx

DOI: 10.1039/x0xx00000x

Fluidic synthesis of magnetic nanoparticles (MNP) is a promising way to produce particles of tailored shape and tunable size. An ethylenediamine (EDA) series of amines have been used as additives in an attempt to modify the morphology of magnetic nanoparticles (MNP) formed. Previous results from batch synthesis show the EDA series to control MNP shape. Here we demonstrate this can be extended to a macrofluidic co-axial laminar flow synthesis system, showcasing their robustness at tailoring the morphology of particles. The addition of tetraethylenepentamine (TEPA) controls the morphology of particles formed under laminar flow, producing 58% faceted particles at a 1:100 additive/iron ratio. This is significantly higher than 14% in control particles, but this however a much lower proportion than seen in batch synthesis demonstrating the limits of additive applicability within macrofluidic flow.

Introduction

Inorganic nanomaterials such as magnetite, Fe_3O_4 , are seeing increased industrial use, with applications in water purification,¹ high-density data storage,² magnetic fluids,³ and the biomedical industry.^{4–6} Industrial specifications of nanomaterials are stringent, with the need to produce highly tailored magnetite nanoparticles (MNP) with tightly controlled physical properties becoming a necessity.

The physical properties of a MNP govern the particles magnetic properties, with shape and size both being key parameters. When a MNP is sufficiently small, typically less than 20 nm, they lose their bulk magnetism and develop superparamagnetic behaviour.⁷ Superparamagnetic iron oxide nanoparticles (SPIONs) are highly desirable due to their “switchable” magnetism, where applying an external field switches the SPIONs on and removing it switches them off. Hence, particles of low mean diameter may be favoured in many industries.⁸

In fields such as the biomedical industry, particles of certain particle shapes have been found to offer enhanced properties over their spherical counterparts.⁹ Octahedral particles of 6–12 nm diameter were found to exhibit improved specific absorbance rates for magnetic hyperthermia and increased efficacy as magnetic resonance imaging (MRI) contrast agents.¹⁰ Octahedral MNP have also been shown to exhibit enhanced magnetic properties,¹¹ highlighting the importance of MNP shape control.

Current methodologies for the synthesis of highly tailored nanomaterials are environmentally unsustainable, utilising

high-boiling organic solvents, toxic pre-cursors, and sustained heating and vacuum use to obtain high quality MNP. Whilst these techniques can produce highly faceted particles of set morphologies such as cubic,¹² pyramidal,¹³ octahedral,¹⁴ and nanoflowers,¹⁵ the methodologies are unsuitable for sustainable production of “green” MNP. Room-temperature co-precipitation (RTCP) uses water as a solvent and requires no use of heat or vacuum for the formation of particles. However, poor control is afforded over the particles formed, with a high degree of polydispersity and little morphological control over the shape distribution of synthesised MNP. A small change in reaction conditions can result in vastly different iron oxides and particles forming due to the complicated system by which magnetite co-precipitates.¹⁶

One potential solution to this is the use of fluidic synthesis. The unilaminar controlled environment offers a high degree of reproducibility over batch environments, minimising the batch to batch variations found within typical RTCP syntheses.¹⁷ Hassan et al. designed a co-axial flow device operating under laminar sheath flow, whereby an inner flow of mixed valence iron solution is precipitated via diffusion¹⁸ with an outer flow of base.¹⁹ Utilising the principle of sheath co-axial flow to synthesise MNP, we have previously investigated the effect of ferric ratio on the particles formed within a macrofluidic co-axial system.¹⁷ This study revealed the ability to tune the size of particle within the macrofluidic formed by simply increasing the ratio of ferric ions, offering a unique method of tailoring MNP.¹⁷

One key method by which MNP shape can be tailored during synthesis is via the addition of an additive, an extra reagent which enables the formation of particles with a desired property. The adsorption of an additive to a crystal surface lowers that surface’s interfacial energy, and consequently slows

^a Department of Chemistry, The University of Sheffield, Dainton Building, Brook Hill, Sheffield, S3 7HF, United Kingdom

Electronic Supplementary Information (ESI) available: [details of any supplementary information available should be included here]. See DOI: 10.1039/x0xx00000x

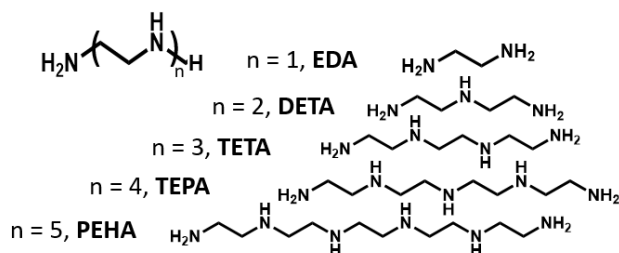


Figure 1. The abbreviated names and structures of the EDA series of additives, showing their increasing chain length and repeat unit structure.

the growth of the face.²⁰ An additive that selectively binds a specific crystal face will suppress growth of this face, allowing it to dominate the final morphology.²¹

A bioinspired range of amine additives consisting of ethylenediamine (EDA) chains of increasing length were found to drastically influence the morphology of particles formed in batch RTCF reactions, producing up to 97% faceted particles upon their addition, compared to only 6% in controls.²² The amines consist of amine groups along an aliphatic ethylene backbone (Figure 1), with the chain length increasing by a single $-\text{CH}_2\text{CH}_2-$ unit to form the series: $n = 1$, ethylenediamine (EDA); $n = 2$, diethylenetriamine (DETA); $n = 3$, triethylenetetramine (TETA); $n = 4$, tetraethylenepentamine (TEPA); and $n = 5$, pentaethylenhexamine (PEHA). Molecular dynamics modelling (MD) revealed a preference for this series of amines to bind to the [111] surface of magnetite over the [100] face, facilitating the formation of particles with predominantly octahedral morphology.²²

Whilst these additives are highly proficient in controlling the shape of MNP in batch conditions, the diffusion-based nature of co-axial macrofluidic flow may yield different results. The addition of a biomineralisation protein, Mms6, observed to increase particle size and shape-control of MNP formed when used as an additive in batch co-precipitation reactions²³ was found in our previous study to not impart this size controlling effect within the co-axial flow system.¹⁷ It is important to determine whether this system of laminar flow is compatible with the addition of additives for particle shape control.

In this study we demonstrate the activity of additives within a macrofluidic co-axial flow system by observing the effects of the addition of amines known to markedly increase the proportion of faceted particles in a non-flow system when used under a diffusion-based laminar flow regime.

Experimental

Materials and methods

All reactions were carried out under an inert atmosphere of N_2 , and all solutions sparged with N_2 for 30 minutes prior to use. Ultrapure Milli-Q water (Merck Milli-Q integral purification system) was used. All reagents were purchased from Sigma Aldrich.

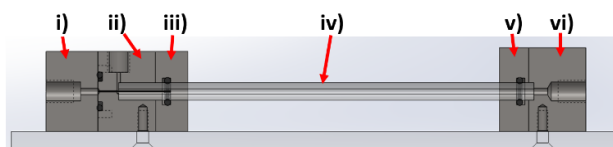


Figure 2. Cross section of PEEK system illustrating the different components. (i) Fe inlet, (ii) NaOH inlet, (iii) inlet faceplate, (iv) capillary, (v) outlet faceplate, (vi) outlet.

Laminar flow MNP synthesis

A polyether ether ketone co-axial device (Figure 2) was designed, produced and operated as in ref 17 was cleaned with ultrapure water, then dilute hydrochloric acid (1 M) followed by ultrapure water again by pumping 10 mL through both ports.

The outer flow syringe driver was loaded with a 10 mL Luer lock syringe of NaOH (1 M) and connected to the co-axial fluidic device via capillary tubing. The outer flow was set at a continuous rate of $360 \mu\text{L min}^{-1}$. When the NaOH within the syringe was depleted, the syringe was replaced with another syringe containing 1 M NaOH.

The inner flow syringe driver was loaded with a 10 mL Luer lock syringe filled with 8 mL of a 0.6 ratio of Fe^{3+} and Fe^{2+} salts (ferrous sulphate pentahydrate (44 mg) and ferric sulphate heptahydrate (61 mg)) with a total iron concentration of (0.05 M) and a set amount of additive, relative to the ratio (1:100 (0.76 μL for TEPA), 1:1000 (0.076 μL for TEPA), or 1:10000 (0.0076 μL for TEPA) being used (example volumes given for clarity). This syringe was then connected to the co-axial fluidic device via capillary tubing with inner flow set at a continuous rate of $90 \mu\text{L min}^{-1}$.

The iron oxide product was magnetically separated and washed three times in deoxygenated ultrapure water and subsequently dried in a vacuum oven overnight.

Characterisation

Transmission electron microscope (TEM): For sample analysis of magnetic nanoparticles, a 1mg mL^{-1} suspension of nanoparticles was sonicated for 1 minute in hexane, after which a $10 \mu\text{L}$ sample was dropped onto a carbon coated copper TEM grid and allowed to dry down for a minimum of one hour. Grids were imaged using a FEI Tecnai G2 Spirit electron microscope (Thermo Scientific, Waltham, MA, United States) and the TEM images were analysed using ImageJ software (v1.52, public domain, National Institute of Health, MD, USA). For each sample over 200 particles were randomly selected for measurement. For details on particles size and shape analysis see supplementary information S1 (size) and S2 (shape).

X-ray diffraction (XRD): XRD data of samples was collected by analysis of dry iron oxide nanoparticles in a Bruker D8 powder diffractometer (Bruker, Coventry, United Kingdom). Diffraction images were collected at 0.022-degree increments from 20–80 degrees, using a fixed wavelength of $\lambda = 1.54178 \text{ \AA}$ from a $\text{Cu K}\alpha$ X-ray source. For XRD data see supplementary.

Vibrating sample magnetometry (VSM): Magnetic susceptibility and saturation magnetisation were measured on

a known quantity (1-5 mg weighed with an accurate mass balance) of dry iron oxide nanoparticles using a MPMS 3 SQUID magnetometer (Quantum Design, Surrey, United Kingdom) in vibrating sample mode, with the samples packed in size 3 polycarbonate capsules and immobilised with polytetrafluorethylene (PTFE) tape. The samples were run at 300 K between -3 and 3 T with a sweep rate of 0.01 T s⁻¹. The control data is capped at 3 T for comparative purposes.

Results and Discussion

A range of additive modified MNP were synthesised using a co-axial flow device. The range of EDA additives of increasing length previously screened in our batch RTCP study have been used to ascertain their effectiveness at modulating the shape of MNP formed under a laminar flow regime.

Control particles formed at a 0.6 ferric ratio with no additive present were found to be mostly undefined in shape, with 14% of particles appearing faceted in shape (Table 1, Figure 3). A saturation magnetisation of 74.3 emu g⁻¹ was achieved, with an average particle size of 8.7 ± 4 nm.

The addition of the EDA series of additives produced particles with a size range of 6.7 - 9.7 nm in diameter Figure 3a) showing no significant difference to each other or to the controls. It is interesting to note that particles formed with higher concentration of additives are generally slightly larger (Figure 3a).

The main trend observed across the additive series in the saturation magnetisation (for the highest two additive concentrations) is inverse to the quantity of faceted particles (shape control), with the control particles with no additive present showing the highest magnetisation. For the 1:1000 concentrations, samples formed with EDA have a similar value to controls (72.3 emu g⁻¹) steadily declining to TEPA (49.2 emu g⁻¹), to increase slightly for PEHA (60.1 emu g⁻¹)

Table 1. Table of characterisation of control particles and particles formed with the addition of an ethylenediamine series of additives.

Sample	Additive/Fe ratio	Particle size (nm)	% Faceted particles	Saturation magnetisation (emu g ⁻¹)
Control	N/A	8.7 ± 4.2	8	73.4
EDA	1:100	9.5 ± 2.6	5	70.6
	1:1000	7.4 ± 1.8	14	72.3
	1:10000	9.1 ± 2.5	21	61.9
DETA	1:100	8.0 ± 3.3	28	59.9
	1:1000	8.1 ± 2.7	22	65.1
	1:10000	7.0 ± 2.3	21	54.5
TETA	1:100	9.2 ± 3.4	36	62.7
	1:1000	7.0 ± 2.4	31	58.8
	1:10000	7.7 ± 2.5	28	54.4
TEPA	1:100	7.9 ± 2.8	58	48.0
	1:1000	7.8 ± 2.4	47	49.2
	1:10000	6.7 ± 2.5	28	53.1
PEHA	1:100	9.2 ± 3.6	10	53.2
	1:1000	8.7 ± 2.6	18	60.1
	1:10000	8.7 ± 2.6	17	52.6

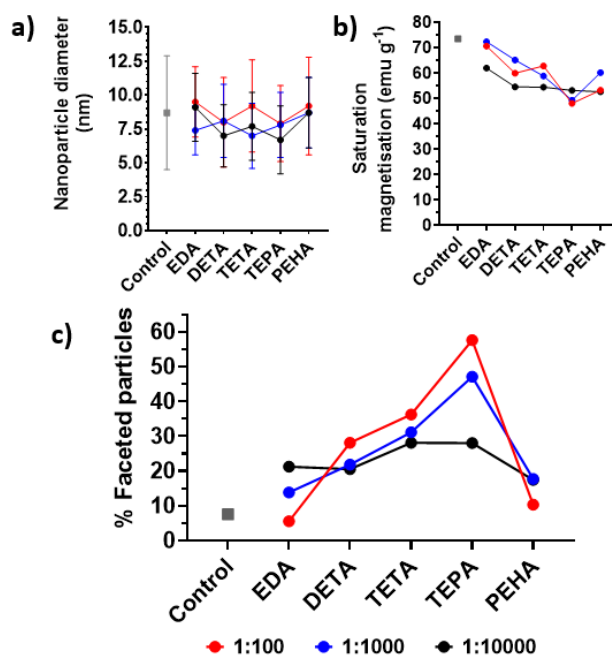


Figure 3. Effect of additive to iron ratios across the EDA series of additives: a) effect on saturation magnetisation; b) effect on mean particle diameter; c) effect on percentage of faceted particles.

(Figure 3b). It seems that the strongest additive binding has a negative effect on the magnetism, suggesting perhaps that the binding may alter the crystal and magnetic structure of the forming particle, lowering the magnetism. For the lowest concentration of additive (1:1000) a lower more linear magnetic response was recorded. With the exception of EDA, all other samples give a constant saturation magnetisation between 53 and 55 emu g⁻¹. A different mechanism seems responsible for these lower quantities compared to controls, with such small amounts of additive present it could be the additive acts to adversely affect the chemistry, so more mixed oxides are formed, without seeing the competing benefit of controlling crystallisation.

The most notable effect of the additive series on the particles formed was the change in morphology (Figure 3c). Across the series and range of concentrations 5-58% faceted particles were observed (compared to 8% with no additives). Notably, the addition of the higher concentration of EDA resulted in the formation of the least defined particles, with only 5% of particles formed being faceted, a decrease from the control particles. EDA exhibited a reversed effect compared to each of the other amine additives, with the higher concentrations appearing to have a detrimental effect on the proportion of faceted particles formed. The short chain structure of EDA may lead to non-specific binding of magnetite facets, therefore lowering the presence of defined facets rather than promoting them. Our previous study modelling the effects of DETA-PEHA revealed that the longer amines in the EDA series (TETA-PEHA) exhibit exothermic (favourable) binding at the [111] magnetite surface. The longer amine additives can lie flat on the [111] surface, allowing for additional binding interactions. DETA however due to its short length has no

preference for interaction between the [100] and [111] magnetite faces and exhibits less preference for the formation of octahedral MNP.²⁴ It follows that EDA would also be able to lie flat on both the [100] and [111] magnetite facets, hence showing no ability to selectively inhibit the growth of a magnetite face to tailor the morphology of particles formed.

As such, a rise in faceted particles is observed as amine chain length increases, consistent with our previous studies.²⁴ As amine chain length increases, longer additives will have a greater number of Fe-N and O-H interactions with the forming magnetite surface, enabling greater growth suppression of the crystal facet.²²

TEPA produced the highest percentage of faceted particles at each of the three tested additive concentrations, producing 58% MNP with defined facets (at the highest concentration). This is in line with our previous research, suggesting the efficacy of the EDA series of additives increases with chain length, peaking at TEPA before seeing a reduction in morphological control with PEHA. On addition of PEHA a significant decrease in faceted morphology was observed from 58% faceted for TEPA 1:100 to 10% at PEHA 1:100. Whilst PEHA manages to produce 18% faceted particles at a 1:1000 ratio, this decrease in shape-control efficacy is observed across each concentration of PEHA compared to TEPA, with the lowest concentration of TEPA outperforming the highest of PEHA. This suggests that more

factors are involved than mere amine group concentration, as efficacy is also reduced at the lowest concentration. Notably, only a small decrease in additive performance was noted in a batch system,²² suggesting PEHA is rendered ineffective as an additive under the laminar flow regime.

For each of the other additives in the series (DETA, TETA, and TEPA), the 1:100 ratio produced the highest percentage of faceted particles. As the mode of action of these additives is believed to be by interaction and binding of the amine to the forming particle surface, a higher concentration of additive allows for greater inhibition of facet growth, hence resulting in the development of more defined particle morphologies. The proportion of faceted particles formed at the 1:100 ratio is ~20% higher than at the 1:1000 ratio. This is not as high as would be desired considering a 10 x increase in additive concentration is required for this effect.

In a batch RTCP system, TETA, TEPA, and PEHA produced 96, 97, and 91% faceted particles respectively, while the co-axial laminar flow device does offer some level of control, it falls short of the control offered in the batch synthesis, failing to produce particles with an equivalent degree of shape control.²² Figure 4 shows a comparison of particles formed under various conditions to compare and contrast the influence of additives on MNP formed, as well as particles formed using TEPA as an additive within the batch RTCP system. Whilst over half the particles formed are of faceted morphology when using a 1:100 TEPA ratio within the macrofluidic device (Figure 4c), it is clear that the additive is not as effective as when used under batch conditions. TETA and PEHA also each exhibited a significant drop in the percentage of faceted particles formed compared to batch reactions, with both additives exhibiting a significant decrease in efficacy within the macrofluidic system. The short-time scale of reaction within the capillary coupled with the diffusion-based mixing may not allow for efficient mixing of the additives with developing particles, with additives potentially struggling to interact with forming magnetite surfaces under the flow regime.

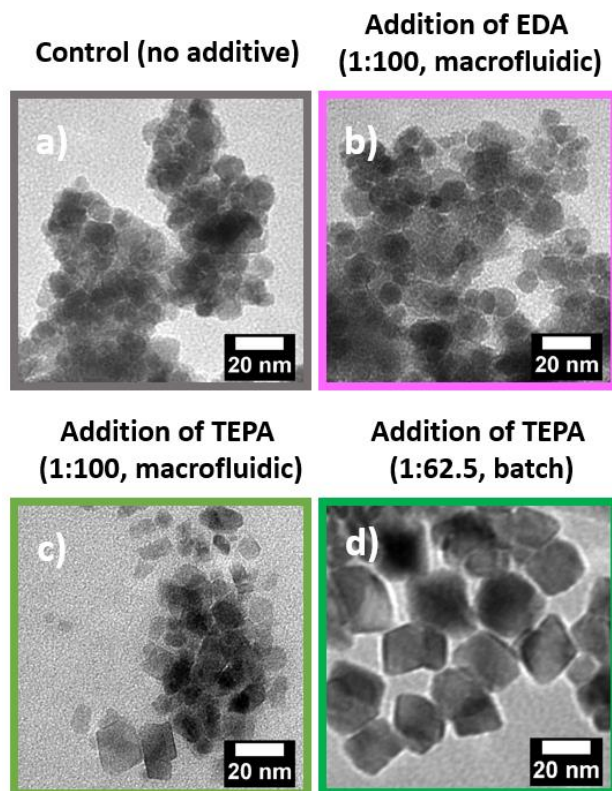


Figure 4. Comparison of representative TEM images of particles formed with a) No additive (macrofluidic); b) addition of EDA (1:100 additive/Fe ratio, macrofluidic); c) addition of TEPA (1:100 additive/Fe ratio, macrofluidic), d) addition of TEPA in a batch co-precipitation reaction (1:62.5 additive/Fe ratio).

Conclusions

This study investigated the efficacy of an EDA series of additives, some of which were effective at producing MNP with mostly faceted morphology, when utilised in a macrofluidic co-axial flow device. TEPA was found to produce 58% faceted particles at a compared to the 97% formed in a batch system.²² TEPA appears to be of optimum additive length of the EDA series, producing the highest proportion of faceted particles at both the 1:100 and 1:1000 ratios, further showcasing its strengths at tailoring the morphology of particles formed at low additive concentrations.

However, within the macrofluidic co-axial flow device, there appears to be a decrease in magnetism observed as the proportion of faceted particles increases. A counter-effect of additive molecules being embedded within forming particles lowering their crystallinity and additives enhancing the crystallinity of forming MNP may be at play, leading to a general decrease in magnetism as additive chain length increases, and

improved magnetism at the middle additive concentration rather than the lowest.

Whilst a high degree of shape-control was successfully exerted over particles within the macrofluidic system using TEPA as an additive, the behaviour of additives was found to vary significantly from our previous observations within a batch system, with TETA and PEHA no longer producing highly defined particles.

The TEPA-enhanced synthesis of MNP using a macrofluidic co-axial device is achievable, with TEPA exerting control over the morphology of particles formed, producing a substantial increase in MNP with octahedral morphology. Considering the reduced influence of both the biomineralisation protein Mms6, and TEPA within the macrofluidic system, however, our results suggest additive efficacy is lessened when directly compared to the results achievable within a batch synthesis due to the effect of flow synthesis.

Conflicts of interest

There are no conflicts to declare.

Abbreviations

DETA: diethylenetriamine

EDA: ethylenediamine

MNP: magnetic nanoparticle

MRI: magnetic resonance imaging

TETA: triethylenetetramine

TEPA: tetraethylenepentamine

PEEK: polyether ethyl ketone

PEHA: pentaethylenehexamine

RTCP: room-temperature co-precipitation

SPION: super paramagnetic iron oxide nanoparticle

Acknowledgements

We would like to thank Andrew Norfolk and Stefan Waterson from the Cambridge Design Partnership for their assistance in the design and preparation of the PEEK macrofluidic system. Thank you also goes to Garry Turner and Richard Truswell for assistance with additional machining and adjustments. This work was supported by funding from the EPSRC (grant number EP/P006892/1) and the University of Sheffield's EPSRC DTP allowance (grant number EP/M508135/1) funds Laura Norfolk's PhD. We thank S. Tsokov, C. Hill (Sheffield Electron Microscopy unit) for TEM training, Nicola Morley and Zhao Leong for VSM training, and Craig Robertson for support with powder XRD.

References

- 1 R. Gregory, R. J. Maloney and M. Stockley, *Water Environ. J.*, 1988, **2**, 532–544.
- 2 X. Sun, Y. Huang and D. E. Nikles, *Int. J. Nanotechnol.*, 2004, **1**, 328.
- 3 R. E. Rosensweig, *Sci. Am.*, 1982, 136–145.

- 4 J. Estelrich and M. Antònia Busquets, *Molecules*, 2018, **23**, 1–26.
- 5 R. E. E. Rosensweig, *J. Magn. Magn. Mater.*, 2002, **252**, 370–374.
- 6 A. F. Alves, S. G. Mendo, L. P. Ferreira, M. H. Mendonça, P. Ferreira, M. Godinho, M. M. Cruz and M. D. Carvalho, *J. Nanoparticle Res.*, 2016, **18**, 1–13.
- 7 C. P. Bean, *J. Appl. Phys.*, 1955, **26**, 1381–1383.
- 8 J. Dulińska-Litewka, A. Łazarczyk, P. Hałubiec, O. Szafranski, K. Karnas and A. Karewicz, *Materials (Basel)*, 2019, **12**, 1–26.
- 9 G. Zhen, B. W. Muir, B. a. Moffat, P. Harbour, K. S. Murray, B. Moubaraki, K. Suzuki, I. Madsen, N. Agron-Olshina, L. Waddington, P. Mulvaney and P. G. Hartley, *J. Phys. Chem. C*, 2011, **115**, 327–334.
- 10 J. Mohapatra, A. Mitra, M. Aslam and D. Bahadur, *IEEE Trans. Magn.*, 2015, **51**, 3–6.
- 11 A. Mitra, J. Mohapatra, S. S. Meena, C. V. Tomy and M. Aslam, *J. Phys. Chem. C*, 2014, **118**, 19356–19362.
- 12 C. H. Ho, C. P. Tsai, C. C. Chung, C. Y. Tsai, F. R. Chen, H. J. Lin and C. H. Lai, *Chem. Mater.*, 2011, **23**, 1753–1760.
- 13 L. Zhang, Q. Li, S. Liu, M. Ang, M. O. Tade and H. C. Gu, *Adv. Powder Technol.*, 2011, **22**, 532–536.
- 14 A. G. Roca, L. Gutiérrez, H. Gavilán, M. E. Fortes Brollo, S. Veintemillas-Verdaguer and M. del P. Morales, *Adv. Drug Deliv. Rev.*, 2019, **138**, 68–104.
- 15 P. Hugounenq, M. Levy, D. Alloyeau, L. Lartigue, E. Dubois, V. Cabuil, C. Ricolleau, S. Roux, C. Wilhelm, F. Gazeau and R. Bazzi, *J. Phys. Chem. C*, 2012, **116**, 15702–15712.
- 16 A. E. Rawlings, J. P. Bramble, A. M. Hounslow, M. P. Williamson, A. E. Monnington, D. J. Cooke and S. S. Staniland, *Chem. - A Eur. J.*, 2016, **22**, 7885–7894.
- 17 L. Norfolk, A. E. Rawlings, J. P. Bramble, K. Ward, N. Francis, R. Waller, A. Bailey and S. S. Staniland, *Nanomaterials*, 2019, **9**, 1729.
- 18 J. B. Knight, A. Vishwanath, J. P. Brody and R. H. Austin, 1998, 1–4.
- 19 A. Abou Hassan, O. Sandre, V. Cabuil and P. Tabeling, *Chem. Commun.*, 2008, 1783–1785.
- 20 S. Mann, D. D. Archibald, J. M. Didymus, T. Douglas, B. R. Heywood, F. C. Meldrum and N. J. Reeves, *Science (80-.)*, 1993, **261**, 1286–1292.
- 21 S. V Patwardhan and S. S. Staniland, *From Bioinspired Synthesis to Sustainable Manufacturing of Inorganic Nanomaterials*, .
- 22 L. Norfolk, K. Kapusta, D. J. Cooke and S. S. Staniland, *Green Chem.*, 2021, 1–12.
- 23 Y. Amemiya, A. Arakaki, S. S. Staniland, T. Tanaka and T. Matsunaga, *Biomaterials*, 2007, **28**, 5381–5389.
- 24 S. S. S. Laura Norfolk, Klaudia Kapusta, David Cooke, .

Adapting the morphology of magnetite nanoparticles synthesised in a coaxial flow device using affordable amine additives

Laura Norfolk,^a and Sarah Staniland^{*a}

Supplementary Information

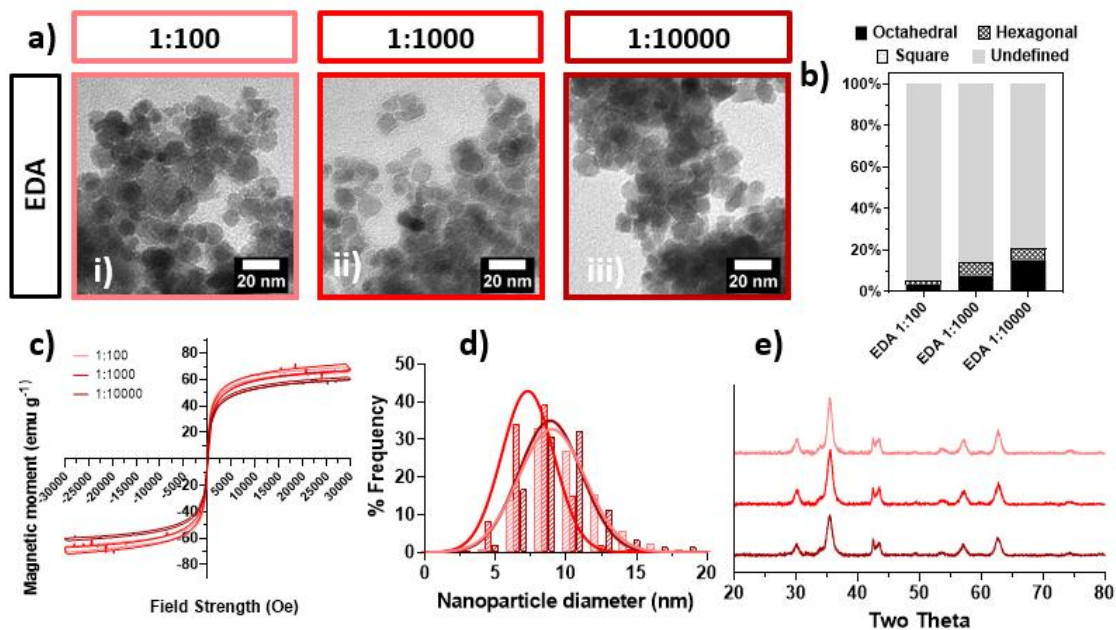


Figure S1. EDA additive data compilation: **a) i-iii.** TEM images; **b)** shape analysis; **c)** magnetic data; **d)** size frequency distribution; **e)** XRD data where 1:100 (pale red), 1:1000 (red) and 1:10000 (dark red) additive/iron ratios.

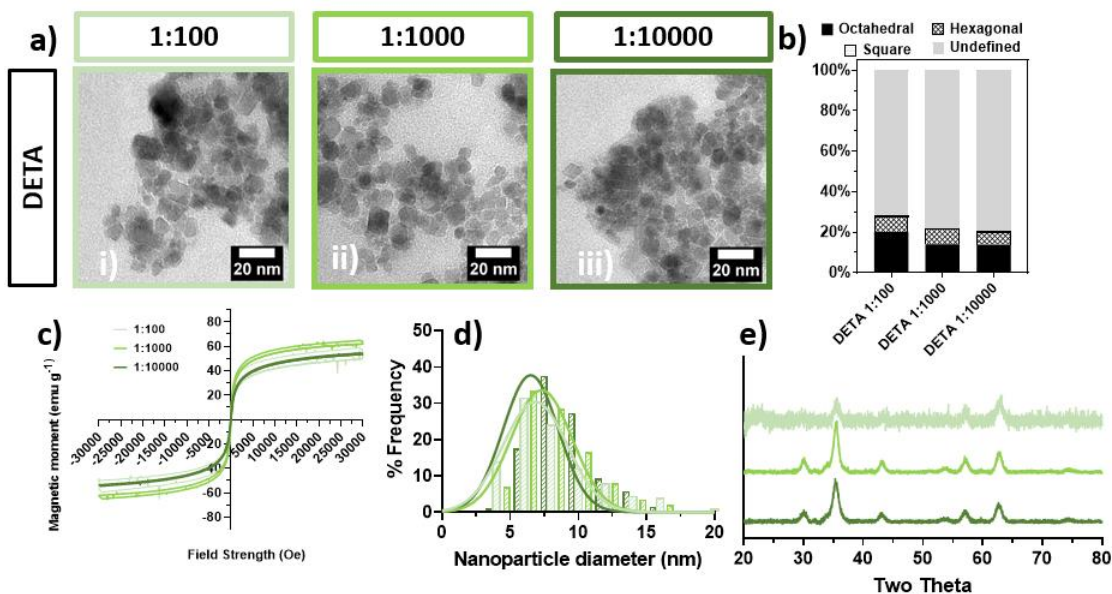


Figure S2. DETA additive data compilation: **a) i-iii.** TEM images; **b)** shape analysis; **c)** magnetic data; **d)** size frequency distribution; **e)** XRD data where 1:100 (pale green), 1:1000 (green) and 1:10000 (dark green) additive/iron ratios.

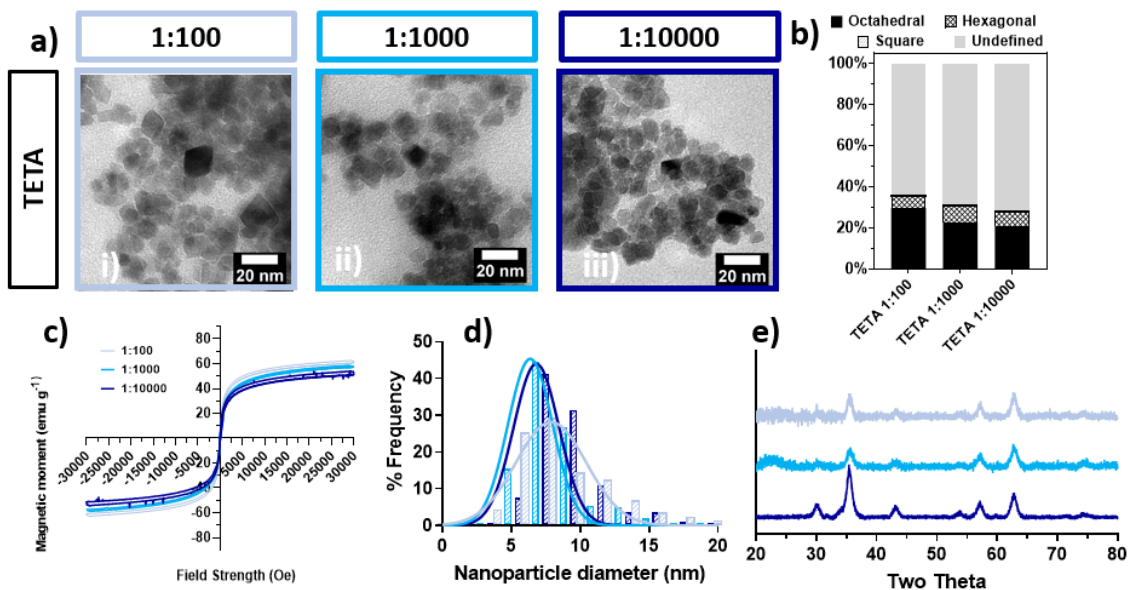


Figure S3. TETA additive data compilation: **a) i-iii.** TEM images; **b)** shape analysis; **c)** magnetic data; **d)** size frequency distribution; **e)** XRD data where 1:100 (pale blue), 1:1000 (blue) and 1:10000 (dark blue) additive/iron ratios.

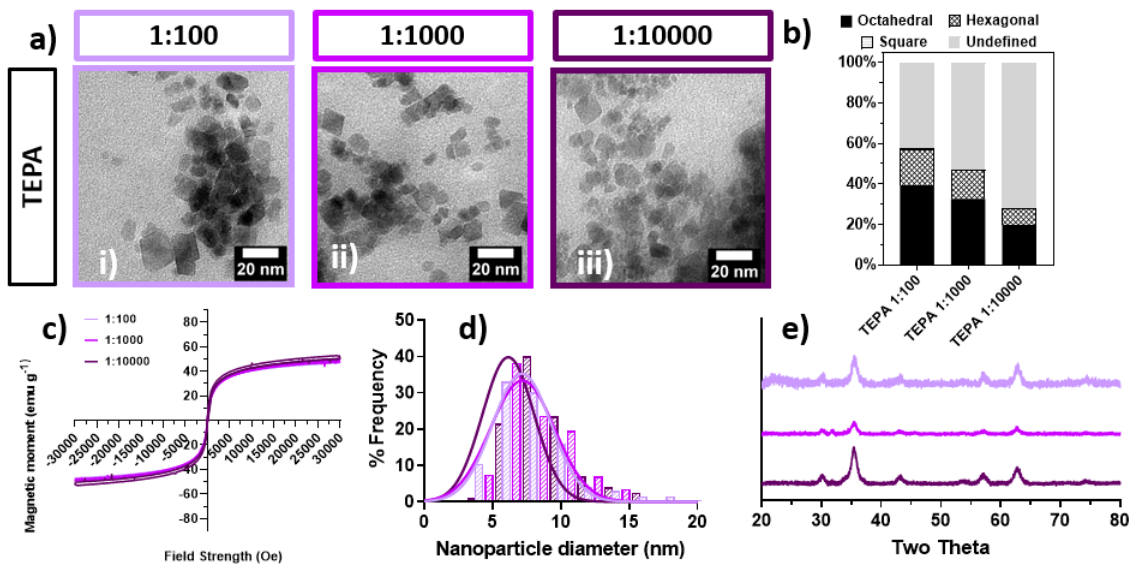


Figure S4. TEPA additive data compilation: **a) i-iii.** TEM images; **b)** shape analysis; **c)** magnetic data; **d)** size frequency distribution; **e)** XRD data where 1:100 (pale purple), 1:1000 (purple) and 1:10000 (dark purple) additive/iron ratios.

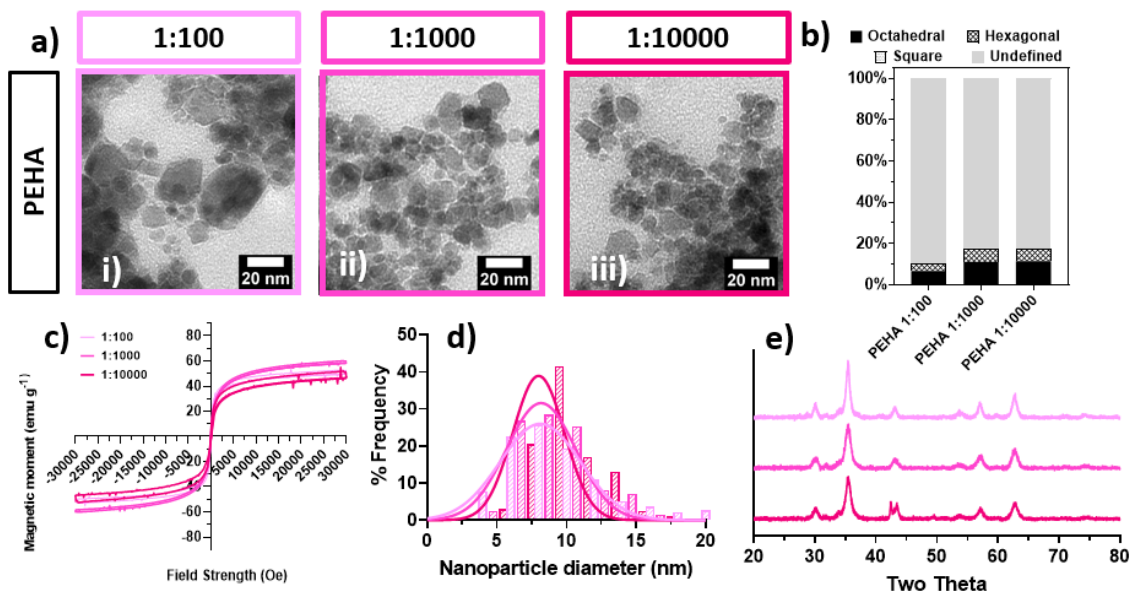
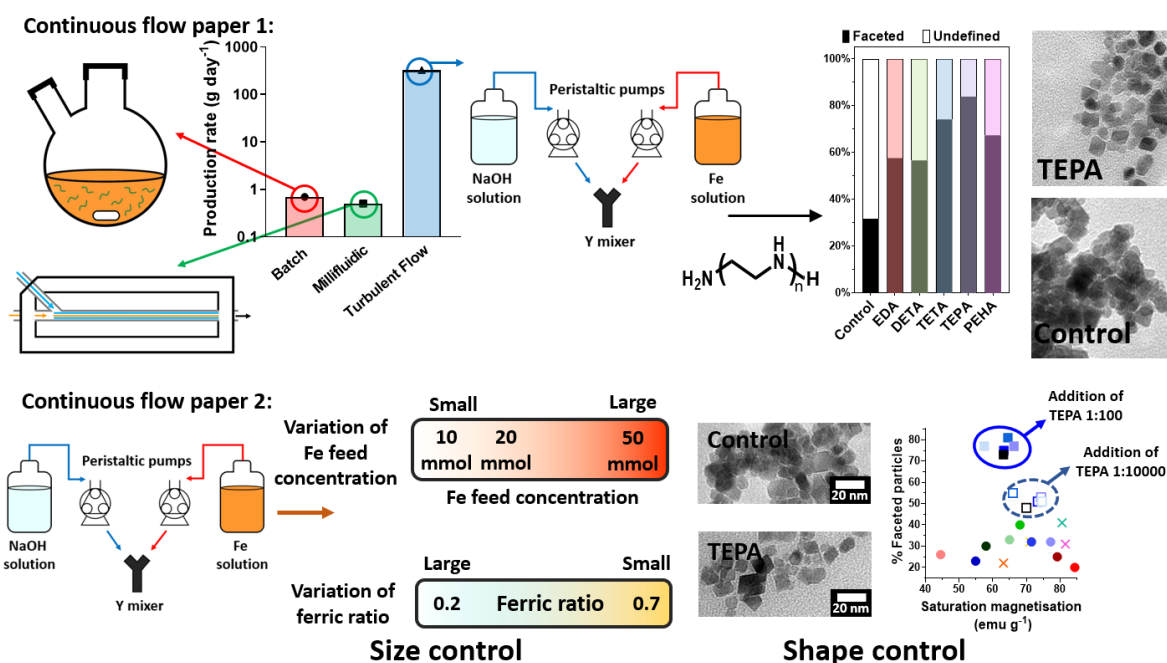


Figure S5. PEHA additive data compilation: **a) i-iii.** TEM images; **b)** shape analysis; **c)** magnetic data; **d)** size frequency distribution; **e)** XRD data where 1:100 (pale pink), 1:1000 (pink) and 1:10000 (dark pink) additive/iron ratios

Chapter 7.

Large Scale Flow Mixing and Optimisation



This chapter consists of two papers based on the use of a continuous flow static mixer to tailored produce MNP on a larger scale. The first paper is titled "Robust Scalable Continuous Flow Bioinspired Synthesis of Magnetite Nanoparticles using Ethylenediamine Additives". The second paper is titled "Optimisation of a scalable continuous flow synthesis of magnetite nanoparticles using tetraethylenepentamine as an additive".

7.1 Robust Scalable Continuous Flow Bioinspired Synthesis of Magnetite Nanoparticles Using Ethylenediamine Additives

7.1.1 Author Contributions

Laura Norfolk (first author): Designed the study and synthesised particles alongside Georgina Zimbitas, analysed the particles (XRD, TEM, VSM, shape and size analysis) created all figures, assisted in writing first draft (abstract, introduction, methods, results, discussion, and conclusions), reviewed and edited.

Georgina Zimbitas (first author): Designed the study and synthesised particles alongside Laura Norfolk, assembled and tested the continuous flow static mixer, assisted in writing first draft (abstract, introduction, methods, results and discussion), reviewed and edited, Reynold's number calculation, created graphical abstract.

Jan Sefcik: Conceptualised the use of a continuous flow static mixer, designed the continuous flow static mixer alongside Georgina Zimbitas, assisted in writing first draft (introduction and discussion).

Sarah Staniland (principal investigator): Supervisor, assisted in writing first draft (abstract, introduction, results and discussion, conclusions) assisted in editing Figure 1, acquired funding, created Table of Contents image.

Robust Scalable Continuous Flow Bioinspired Synthesis of Magnetite Nanoparticles using Ethylenediamine Additives

Laura Norfolk,^a Georgina Zimbitas^b, Jan Sefcik^{b,c}, and Sarah Staniland^{a*}

Keywords: Magnetite, nanoparticles, scale-up, fluidic synthesis, bioinspired

Highlights (3-5 points needed):

- Ethylenediamine additives were used to control the shape of faceted, octahedral SPIONs.
- A continuous flow static mixing setup demonstrated production rates five times higher than reported in the previous literature.
- The method allows for further scale up for industrial production of tailored faceted SPIONs.

Abstract

Superparamagnetic iron-oxide nanoparticles (SPIONs) are of great interest for a wide range of applications whereby precise control of particle properties is essential. Tunable synthetic routes leading to monodisperse particles of desired properties (magnetism, size, shape, etc.) are essential and there are growing demands on their robust highly scalable production. Recently developed “greener” bioinspired additive methods for SPION synthesis revealed promising results with respect to size and shape tunability but had low production rates and limited scalability. Here we show that bioinspired synthesis of highly faceted magnetite nanoparticle can be robustly achieved with a wide range of ethylenediamine additives that control the shape of SPIONs, resulting in a higher proportion of faceted, predominately octahedral, particles. All 5 additives irrespective of chain length increased the proportion of faceted particles (between 38 - 84 % faceted across the range of additives and concentrations) compared to the control (32% faceted), indicating that the ethylenediamines exhibit favourable binding to the [111] face of magnetite, while the best morphological control was achieved with the longer additives. Using additive-enhanced, continuous flow static mixing set-up at laboratory scale, production rates of up to 311 g day⁻¹ have been achieved, which is five times higher than previously reported for magnetite nanoparticle synthesis. Continuous flow static mixing is inherently scalable in terms of flow rates, allowing further scale up for industrial production of tailored faceted SPIONs.

1. Introduction

Magnetic nanoparticles (MNPs) have seen an explosion of interest recently, with a large body of research dedicated to their applications across a wide range of applications including ferrofluids,¹ carbon capture,² high-density data storage,³ magnetic drug delivery,⁴ magnetic resonance imaging,⁵⁻⁸ and as therapeutic agents in cancer treatment.⁹ MNPs can be adapted through coatings or surface functionalisation to be water-soluble,¹⁰ highly biocompatible,¹¹ or biodegradable depending on the coating used.¹²

Spherical nanocrystalline magnetite (Fe_3O_4) and maghemite ($\gamma\text{-Fe}_2\text{O}_3$) with diameters less than 20 nm exhibit superparamagnetic behaviour wherein their magnetisation can randomly flip direction due to the thermal energy available at room temperature, and as such have been termed SPIONs (superparamagnetic iron oxide nanoparticles). The result of this effect is that unlike larger particles or bulk iron-oxide, SPIONs do not have remnant magnetisation in the absence of a magnetic field, with the particles instead behaving as if they were paramagnetic.¹³ This “switchable” magnetism is especially attractive in nanomedicine as it allows for particles to be magnetically directed to desired sites (such as tumours)⁴ under an applied magnetic field. Once the field is removed the particles are less likely to agglomerate due to their paramagnetic nature, increasing their half-life in the human body.¹⁴

SPIONs have other useful properties that lend themselves to biomedical applications: their nanoscale nature offers a high surface area which can be readily functionalised in various manners,¹⁵ high magnetic saturation,¹⁶ and low toxicity. As such, the potential of SPIONs is being realised across the biomedical industry.

It is clear from research that physicochemical properties such as magnetism, magnetic heating, and biological properties such as toxicity, circulation time, and uptake of the SPIONs are chiefly affected by their physical attributes of size, shape, and the SPIONs' homogeneity.^{15,17–20} The size of particles is critical, as large or aggregated clumps of particles in the bloodstream can block capillaries causing embolisms,²¹ as well as influencing circulation time in the blood and uptake into cells.²² For example, the size range for SPIONs needs to be within the correct range to be uptaken by cells, but outside the size range that is targeted for destruction by macrophages.^{23,24} Furthermore, the body concentrates different sized SPIONs to different organs of the body, offering a further mode of targeting if size can be selectively synthesised for.²¹

Many synthetic methodologies and biomedical studies have focused on the use of spherical SPIONs as these are easily synthesised. However, varying the shape leads to different magnetic and biocompatibility properties.²⁵ Literature involving the use of non-spherical particles has been rapidly growing based on wide research interested in highly faceted SPIONs. Octahedral magnetite particles have been found to exhibit an enhanced specific absorption rate for magnetic hyperthermia, and increased performance as MRI contrast agents compared to spherical particles.²⁶ It is thus crucial to understand and develop techniques by which non-spherical particles can be synthesised, and to tailor both shape and size of particles to create bespoke SPIONs for specific applications.

Nanoparticle production is a huge industry, with the global market share estimated as being approximately \$80 billion in 2019,²⁷ and demand for SPIONs specifically is rising more rapidly. The sector of nanomedicine is a vast potential growth area, however tailoring and precision of particle properties need to be achieved before this can be fully realised. With growing demand comes the growing requirement to ensure manufacture is as green and sustainable as possible. While various synthetic methods such as oxidative precipitation,²⁸ hydrothermal synthesis,²⁹ and thermal decomposition³⁰ can produce highly defined particles with specific shapes such as cubic,^{31,32} nanoflowers,³³ and octahedral,³⁴ many of these techniques utilise toxic precursors, large quantities of organic solvents, and/or extensive heating and vacuum use, making SPION manufacture wasteful and harmful to the environment.

Environmentally friendly synthesis methods with scale-out potential exist for the production of precisely tailored SPIONs,^{35–37} however they are not easily amenable to scale-up. Common green methods to produce MNPs are usually variants on room-temperature co-precipitation (RTCP), an aqueous technique that requires no organic solvents. The pH of a mixed valence iron salt solution is slowly raised by addition of a base, resulting in the precipitation of magnetite (and potentially other iron oxides). A pH titration study of the RTCP system revealed a strong dependence on the ferric ratio, with lower ratios producing higher proportions of non-magnetite iron oxides.³⁸ However, this process is difficult to finely control, with small variations in reaction conditions resulting in significant changes to the reaction products such as formation of a broad distribution of SPIONs, being of mostly undefined morphology.³⁹ Reproducibility of the product formed and product quality are both crucial factors for a synthetic route to be of industrial importance.

Despite the pressing need for alternative green synthetic production routes that can be industrially scaled-up, very little research has been conducted in this area for nanomaterial production. A promising way to exert control over particle formation in this green synthesis regime is to use an additive. This has been achieved in nature with the assistance of proteins.

A type of bacteria known as magnetotactic bacteria can produce exceptionally homogeneous particles under ambient conditions in a process known as biomineralisation.⁴⁰ Utilising a suite of proteins that serve to induced controlled biomineralisation, lipid bound nanoparticles are formed in organelles known as magnetosomes. Research has revealed biomineralisation proteins, such as Mms6, are key to controlling the nucleation of magnetite,⁴¹ via iron ions binding to a negatively charged protein surface.⁴⁰

Magnetite interacting Adhirons (MIAs) are peptide display scaffold proteins discovered through iterations of phage display biopanning⁴² to target cubic nanoparticles of magnetite.⁴³ The protein sequence of the binding region revealed a preference for basic residues, specifically lysine. Molecular dynamics (MD) simulations identified lysine as having the lowest adsorption energy to the [100] magnetite surface, showing basic groups are strong binders to the magnetite surface. Bound proteins or additives lower the surface energy of a developing crystal face, stabilising that surface and slowing its growth, resulting in it dominating the final particle morphology.⁴³

We have shown the success of the additive approach using both MIAs and Mms6 as additives in RTCP reactions, with a marked increase in morphological and phase/size control, respectively, over particles formed *in vitro*.^{40,43} Whilst several proteins and peptides have shown promise as biological additives for sustainable nanoparticle synthesis, many of the effective proteins are expensive and time-consuming to purify and isolate, making them unsuitable for scale-up due to the large quantity of protein required. The concept of additives can be extended to simpler molecules which are more compatible with scale-up (can be readily purchased or synthesised) to develop a range of bioinspired additives containing functionalities found to be highly effective in nature.

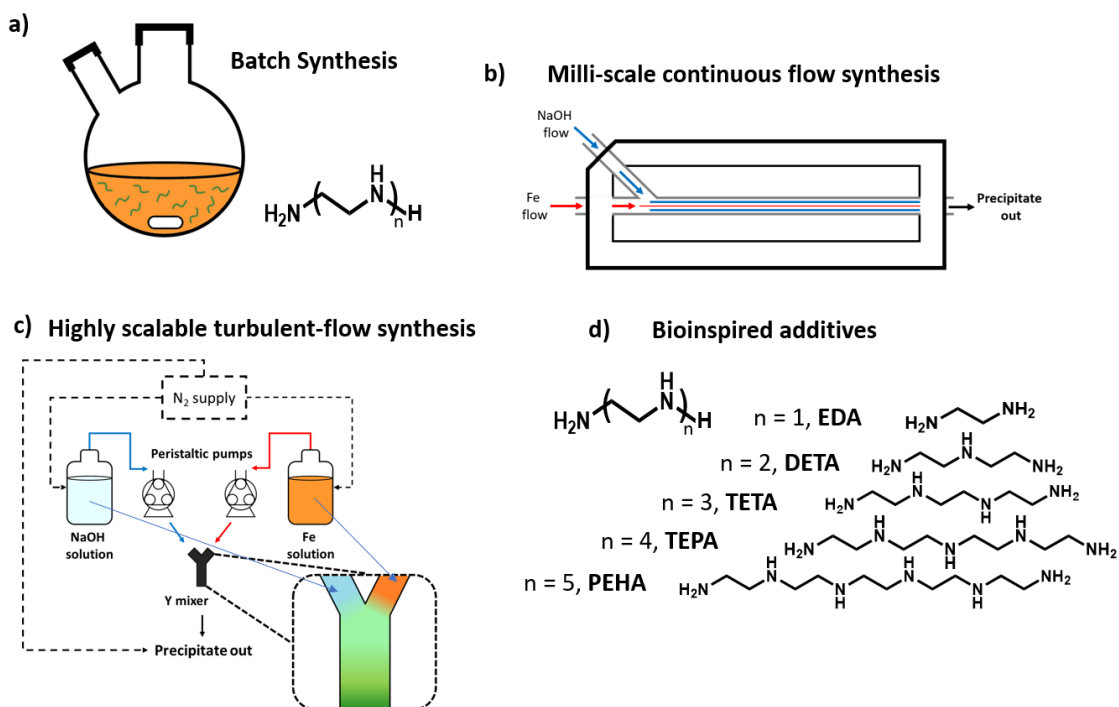


Fig 1. Schematics to demonstrate the concept of developing progressive “green” (RTCP) magnetite synthesis systems: **a)** depicts previous optimised batch synthesis of magnetite with and without bioinspired additives;⁴⁴ **b)** Schematic representation of the milli-scale laminar continuous flow synthesis method; **c)** Schematic representation of the continuous flow mixing set-up, including 2 pumps, 2 feed solutions, a collected precipitate solution, and a Y-mixer. Supply routes are designated with arrows: feed and collected routes are solid lines and N₂ gas supply in dashed lines; **d)** shows the abbreviated names and chemical structures of the bioinspired additive ethylenediamine series with arrows showing they could be added to either the NaOH or Fe inlet of the continuous flow system.

Seeking inspiration from knowledge that amine rich lysine proteins bind strongly to magnetite surfaces to control the morphology of nanoparticles, we recently investigated a green synthesis route of magnetite nanoparticle production utilising as additives bioinspired ethylenediamine-based compounds consisting of amine groups spaced out on an aliphatic -CH₂CH₂- backbone (Figure 1a), with the series used being: Ethylenediamine (EDA), Diethylenetriamine (DETA), Triethylenetetramine (TETA), Tetraethylenepentamine (TEPA), and Pentaethylenhexamine (PEHA), increasing in length by one ethylenediamine unit per molecules (Figure 1d). In a batch RTCP environment these amines were found to significantly increase the proportion of octahedral/ faceted particles formed.⁴⁴

While batch manufacturing often relies on simpler, widely available equipment, continuous manufacturing is very attractive in terms of ensuring reproducibility, consistency and precision in achieving critical quality attributes of particulate products under steady state operating conditions.^{45–48} Several synthetic methodologies for making magnetic nanoparticles, particularly SPIONs, have been implemented using continuous processing, including ambient temperature precipitation,^{49–53} hydrothermal synthesis,^{53,54} thermal decomposition,⁵⁵ oxidative precipitation,⁵⁶ and high temperature precipitation⁵⁷ in the presence of surfactants. Fluidic synthesis has been utilised for SPIONs on the small scale, with maghemite⁵⁸ and magnetite^{39,59,60} particles both being synthesised on a millifluidic scale (Figure 1b). In one of these millifluidic systems particles were also modified using Mms6,³⁹ however yields were

found to be low due to the small scale of the system and this sheath flow system renders itself unsuitable for scale-up since millimetric channels are required to ensure laminar flow. The highest production rate reported to date for magnetite nanoparticles has been 2.6 g hr^{-1} or 62 g day^{-1} , using high temperature precipitation⁵³ with the addition of surfactants.

The key challenge in scaling up RTCP processes is to increase the space-time-yield of the overall process, which requires much shorter residence times while achieving the same end-product quality. This in turn requires much more efficient mixing, which is typically a rate limiting step in precipitation processes. Very efficient mixing can be achieved under certain continuous flow conditions using static mixers,^{61,62} with mixing times on the order of 10-100 ms at typical flow conditions. Continuous flow static mixing is also inherently scalable in terms of flow rates, allowing relatively straightforward scale up towards industrial scale manufacturing.

In this paper, green RTCP additive-enhanced synthesis is employed using a continuous flow static mixing set-up, resulting in the production rate of SPIONs orders of magnitude higher compared to batch and millifluidic systems, while achieving the same end-product quality. Allowing. This approach is used to push the boundaries of SPION production rates more than five times higher than reported in the previous literature. As continuous flow static mixing is inherently scalable in terms of flow rates, this approach can facilitate further scale up for industrial production of tailored faceted SPIONs.

2. Materials and methods

Ultrapure MilliQ water (Merck MilliQ integral purification system) was used. All reagents were purchased from Sigma Aldrich unless otherwise stated and used as purchased.

2.1 Batch room temperature co-precipitation (RTCP)

A solution of ferrous sulphate (0.4 mmol) and ferric sulphate (0.3 mmol) was made via addition of salts to deoxygenated MilliQ water (20 mL) that had been sparged with N_2 for at least 30 minutes in a two-neck round bottom flask. The solution was left to stir for 5 minutes using magnetic stirring to ensure dissolution of the iron salts. N_2 sparged 500 mmol NaOH (8 mL) was added at a rate of $50 \mu\text{L min}^{-1}$ for a total of 160 minutes using a Harvard Apparatus 11 plus syringe pump driver under an atmosphere of N_2 . The reaction was left to age for an hour under the inert atmosphere, and the reaction mixture was then magnetically separated and washed at least three times with N_2 sparged MilliQ water to remove any non-magnetic iron oxide by-products. The particles were dried in a $40 \text{ }^\circ\text{C}$ oven overnight, and then ground with a pestle and mortar for analysis.⁴⁴

2.2 Millifluidic flow

For the full synthetic methodology and device fabrication details please refer to Norfolk et al.³⁹ The device was cleaned prior to use with 500 mM HCl, and then with MilliQ water for several minutes. A solution of 50 mM mixed valence (ferrous and ferric sulphate) iron salts (0.6 ferric ratio) and a solution of 1M NaOH were deoxygenated via sparging with N_2 for a minimum of 30 minutes. A Harvard Apparatus 11 plus syringe pump driver was connected to the outer sheath flow inlet loaded with a 10 mL Luer lock syringe of NaOH and connected to a millimetric co-axial fluidic device via polyether ether ketone (PEEK) capillary tubing. This outer flow was

set at a flow rate of $360 \mu\text{L min}^{-1}$. A second syringe pump driver was connected to the inner core flow and loaded with a 10mL Luer lock syringe filled with 8mL of 0.6 ferric ratio Fe salt solution and connected via PEEK capillary tubing. This was set at a flow rate of $90 \mu\text{L min}^{-1}$. The NaOH syringe was refilled as required.

The iron oxide material formed and flowed to the end of the device where it reached the exit port and dripped into a round bottom flask which was kept under an atmosphere of N_2 . The iron oxide product was magnetically separated and washed three times with deoxygenated MilliQ water and subsequently dried in a vacuum oven at $40 \text{ }^\circ\text{C}$ overnight. The particles were then ground with a pestle and mortar for analysis.

2.3 Continuous flow static mixing

Two Watson Marlow 520DuN (Zwijnaarde, Belgium) cased peristaltic pumps were used, with one attached to the NaOH feed and the other attached to the Fe solution feed. Mixing and instantaneous precipitation both occur in a plastic Y-shaped static mixer which was connected to an outlet tube leading to the collection vessel. Both pumps were set to 10 rounds per minute. When both pumps were running concurrently this setup resulted in a residence time of approximately 2s for the mixed solution in the outlet tube.

Fe solution was fed through one pump, whereas NaOH solution was co-currently fed through the other pump (Figure 1c) in a 1:1 volumetric flow ratio. Feed solutions each contained a magnetic stirrer bar, with the solutions placed on magnetic plates to be under constant mild stirring throughout the experimental run. All solutions (feeds and product output) were constantly supplied with N_2 throughout the run to ensure the solutions were sparged of oxygen, thus minimising the possibility of unwanted oxidation occurring at any stage of the precipitation process. The feed solutions were left to stir for at least 5 minutes under a constant atmosphere of N_2 prior to mixing to ensure deoxygenation was complete.

Modified lids were used to avoid the re-dissolution of O_2 into any of the three solutions (Fe solution stock, NaOH stock, collection vessel) during the experimental runs. These modified lids incorporated 3 openings: one for the pump feed tubing, one for the N_2 supply, and the third with tubing that allowed for gas/pressure to escape the vessel.

Table 1. Additives and additive:iron ion molar ratios used for magnetite precipitation with 500 mmol NaOH and 50 mmol total Fe at a 0.6 ferric ratio

Additive: iron ion ratio	1:100	1:1000	1:10000	Additive added to solution:
	Experimental number			
<i>No additive</i>	1			N/A
<i>TEPA</i>	2	3	4	50 mM Fe
	5	6	7	500 mM NaOH
<i>TETA</i>	8	9	10	50 mM Fe
	11	12	13	500 mM NaOH
<i>PEHA</i>	14	15	16	50 mM Fe
	17	18	19	500 mM NaOH
<i>DETA</i>	20	21	22	50 mM Fe
	23	24	25	500 mM NaOH
<i>EDA</i>	26	27	28	50 mM Fe
	29	30	31	500 mM NaOH

Once the initial 5 minutes of stirring of the feed solutions was complete, both peristaltic pumps were turned on (counterclockwise flow) for mixing to occur. Mixed solution was collected only after the flow became constant. Timing the collection of 15-20 mL of mixed solution resulted in a calculated flow rate of 110-120 mL min⁻¹ from both pumps combined with an average of 112 ml min⁻¹ across the 31 experiments.

In between precipitation runs to minimise the possibility of cross-contamination from previous runs, the system was flushed out with in-house ultrapure MilliQ water until the fluid ran clear from the collection tube. The flow was then reversed on both pumps (clockwise) and MilliQ water was then left to flow out of the feeding tubes, again, until the water ran clear.

32 experiments are included in this study with effects of the amine additive, additive-to-total iron ratio, and additive addition point. The experiments were run at a ferric ratio of 0.6 - previously established as the optimal ratio for magnetite formation due to its proximity to the stoichiometric ratio of ferric and ferrous iron in Fe₃O₄ (2:1) - and using total iron concentration of 50 mM and NaOH concentration of 500 mM, to remain consistent with previously conducted research.⁴⁴

Each additive was tested at three different additive:total iron ratios; 1:100, 1:1000, and 1:10000. The additive was introduced via either the Fe solution or NaOH inlet (referred to as addition points), resulting in a total of six experiments for each additive.

The full list of conditions can be seen in Table 1, with the amines used being TEPA (experiments 2-7), TETA (experiments 8-13), PEHA (experiments 14-19), DETA (experiments 20-25) and EDA (experiments 26-31). In addition, a control experiment, with no additive present, was also performed for comparison (experiment 1). The collected particles were magnetically separated, washed three times with deoxygenated MilliQ water, and dried in a vacuum oven at 40 °C overnight. The particles were then ground with a pestle and mortar for analysis.

2.4 Characterisation

2.4.1 Transmission electron microscope (TEM). For sample analysis of magnetic nanoparticles, a 1mg mL⁻¹ suspension of nanoparticles was sonicated for 1 minute in hexane, after which a 10 µL sample was dropped onto a carbon coated copper TEM grid and allowed to dry down for a minimum of one hour. Grids were imaged using a FEI Tecnai G2 Spirit electron microscope (Thermo Scientific, Waltham, MA, United States) and discrete particles of the TEM images were analysed using ImageJ software (v1.52, public domain, National Institute of Health, MD, USA). For each sample over 200 particles were randomly selected for measurement. For details on particles size and shape analysis see supplementary information of Norfolk et al.⁴⁴

2.4.2 X-ray diffraction (XRD). XRD data of samples was collected by analysis of dry iron oxide nanoparticles in a Bruker D8 powder diffractometer (Bruker, Coventry, United Kingdom). Diffraction images were collected at 0.022-degree increments from 20–80 degrees, using a fixed wavelength of $\lambda = 1.54178 \text{ \AA}$ from a Cu K α X-ray source

2.4.3 Vibrating sample magnetometry (VSM). Magnetic susceptibility and saturation magnetisation were measured on a known quantity (1-5 mg weighed with an accurate mass balance) of dry iron oxide nanoparticles using a MPMS 3 SQUID magnetometer (Quantum Design, Surrey, United Kingdom) in vibrating sample mode, with the samples packed in size 3 gelatine capsules and immobilised with polytetrafluoroethylene (PTFE) tape. The samples were run at 300 K between -3 and 3 T with a sweep rate of 0.01 T s⁻¹. The data presented is cropped at saturation magnetisation for ease of viewing.

3. Results and Discussion

3.1 Comparison of continuous flow static mixing system with batch and millifluidic systems: scale-up in the absence of additives

Three systems were investigated: batch room-temperature co-precipitation, millifluidic sheath flow, and continuous flow static mixing. All three used the same room-temperature co-precipitation (RTCP) synthesis where the pH of a solution of mixed valence ferrous/ferric iron ions is raised to precipitate out the iron oxide nanoparticles under an inert atmosphere. Varying

the ferrous/ferric ratio results in different iron oxides being formed. Magnetite (Fe_3O_4) is the desired product and is most readily formed (according to the literature and our previous work) at a ratio of 0.6 ferric ions, which is close to the stoichiometric 2:1 ratio of $3^+/2^+$ ions in the structure of magnetite.

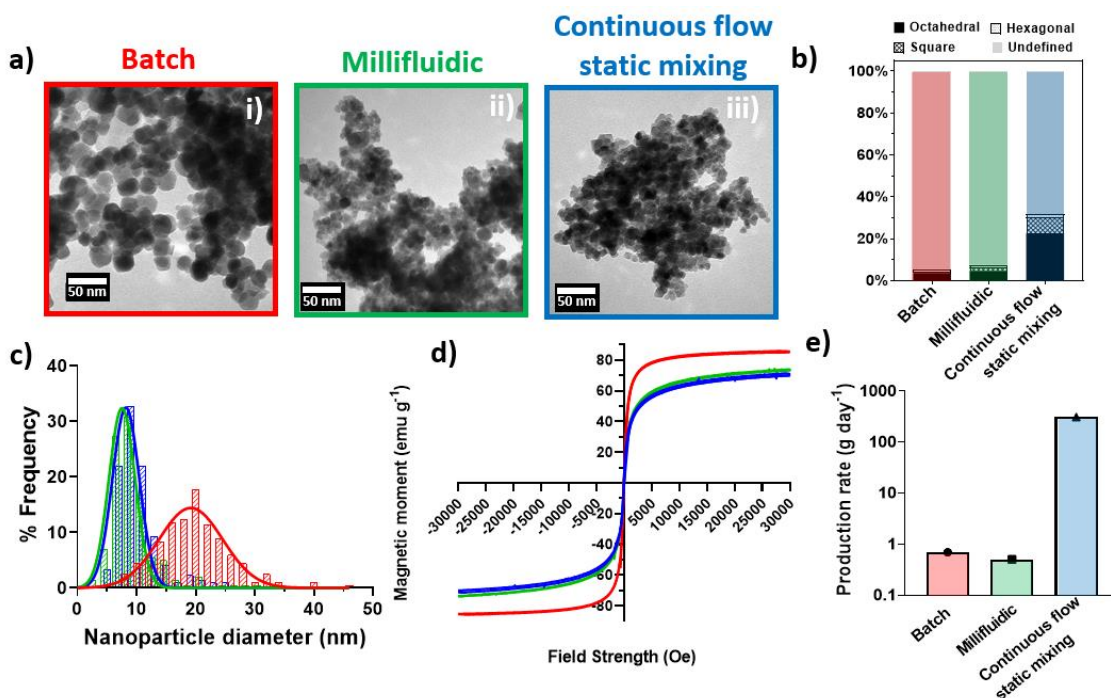


Fig 2. Results for the MNPs formed at the 0.6 ferric ratio. Colour codes used: batch RTCP (red), millifluidic (green),³⁹ continuous flow mixing (blue). **a)** representative TEM images; **b)** comparison of shape analysis results; **c)** particle size frequency distribution; **d)** magnetic data; **e)** production rate comparison of the three synthetic methods.

In this study the iron species were all fixed to this 0.6 ratio. A 50 mmol mixed valence iron solution was used for all three systems while the concentration of NaOH was set at 500 mmol for the batch and continuous flow static mixing set-up (as this was previously optimised for the batch system). 1M NaOH was found to be optimum in the millifluidic system as 500 mmol NaOH resulted in non-magnetic iron oxides,³⁹ which was not found to be an issue with the continuous flow static mixing system.

Each sample has been analysed by TEM imaging to ascertain shape and size of particles formed, XRD for crystallinity and phase identification, and VSM for magnetic data.

For each system control reactions were carried out to ascertain the morphology and quality of particles formed when no additive was present. The millifluidic 0.6 control reaction has previously been published,³⁹ and this reaction has been selected to act as a comparison between the three systems. TEM images of the particles formed across each of these three set-up systems are shown in Figure 2a. The particles formed in the millifluidic and batch reaction systems were found to exhibit minimal shape control, as shown in Figure 2b, with undefined particles being the primary constituent of the two reactions. The proportion of undefined particles varied from 92% for the millifluidic to 94% for the batch RTCP systems. The continuous flow static mixing system however exhibited a higher degree of shape control,

producing 32% faceted particles. A significant variation was observed in particle size, shown in Figure 2c. The millifluidic and continuous flow static mixing systems produced particle sizes of 8.7 ± 4.1 nm and 9.2 ± 3.6 nm respectively, whereas the batch RTCP reaction resulted in particle sizes of 19.5 ± 6.2 nm, thus resulting in particles almost double the size of those produced in the two flow systems, and with a much broader size distribution. This is to be expected as nucleation under flow is faster due to the rapid rise in pH compared to the slow addition of base over time utilised in the batch reactions.

Magnetic data gathered from the three systems shows a relatively high magnetic moment (emu g^{-1}) of material from each reaction, having values of 85.8 emu g^{-1} (batch), 73.8 emu g^{-1} (millifluidic), and 71.4 emu g^{-1} (continuous flow static mixing) at a field strength of 3 T, with pure magnetite having a value of 92 emu g^{-1} by comparison. Both millifluidic and continuous flow static mixing produced slightly less magnetic particles than those formed in the batch system. XRD data (supplementary figure S1) for each reaction was found to be consistent with magnetite. Lesser magnetic particles could be due to the oxidation of the nanoparticles. Whereas precautions were taken to minimise the degree of oxidation the possibility of it occurring remained. For the millifluidic system the solutions were pre-sparged with N_2 , however they were then loaded into syringes which are not perfectly airtight thus possibly allowing a small amount of oxidation to occur throughout the reaction process, leading to the production of less magnetic particles. In the continuous flow static mixing system each stock solution and the resultant mixed solution are consistently sparged with N_2 throughout the experiment, with the retention time in the system being significantly lower than the time required in the millifluidic system due to the disparity in the flow rates. Despite this, the collected nanoparticles in this case remained in solution for an extended period of time as they needed to be transported for analysis, again possible resulting in a slight degree of oxidation and, subsequently slightly lower magnetisation compared to the batch system.

In summary, both flow systems show a consistency in size of particles produced, being of ~ 10 nm, while batch synthesis offers particles of ~ 20 nm. When comparing the two flow systems the continuous flow static mixing systems produces similar highly magnetic magnetite particles at a far greater production rate, with the promise and potential for further scale-up. A production rate calculation for the three systems run over a 24-hour period (Figure 2e) shows the impressive improvement the continuous flow static mixing system offers in particle production capacity, potentially producing over 311 g of bespoke nanoparticles per day (Supplementary information S2).

Properties of the nanocrystals are, however, not only associated with their size but also their shape.^{63–65} As such there is a need to achieve a narrow particle size distribution of a uniform shape in order to obtain high-quality nanoparticle production.

3.2 Effect of EDA series of additives in the continuous flow static mixing system

A series of amines (Figure 1d and Table 1) were selected for use as additives in the continuous flow static mixing system. DETA-PEHA additives have been shown to influence the morphology of particles formed in RTCP reactions via adsorption to the [111] crystal face of developing magnetite nanocrystals producing octahedral nanocrystals.⁴⁴ Computational modelling has shown this is due to preferential adsorption to the [111] crystal face (over [100])

of the forming magnetite nanocrystals, increasing its dominance in the final crystal habit. Here we test if such additives can influence the morphology of magnetite nanoparticles formed in the large-scale continuous flow static mixing system.

Each ethylenediamine additive from chain length (number of ethylene units) $n = 1 - 5$ (EDA ($n = 1$); DETA ($n = 2$); TETA ($n = 3$); TEPA ($n = 4$); PEHA ($n = 5$)) was added at various concentrations (additive:iron ratios 1:100, 1:1000, and 1:10000) and tested with addition in each of the iron and NaOH channel inlets. For consistency with results from the previous section, and so the continuous flow static mixing results without additives can be used as a control, the reaction conditions were identical to those of previous sections (0.6 ferric ion ratio with iron solution of 50mmol and NaOH solution of 500mmol concentration).

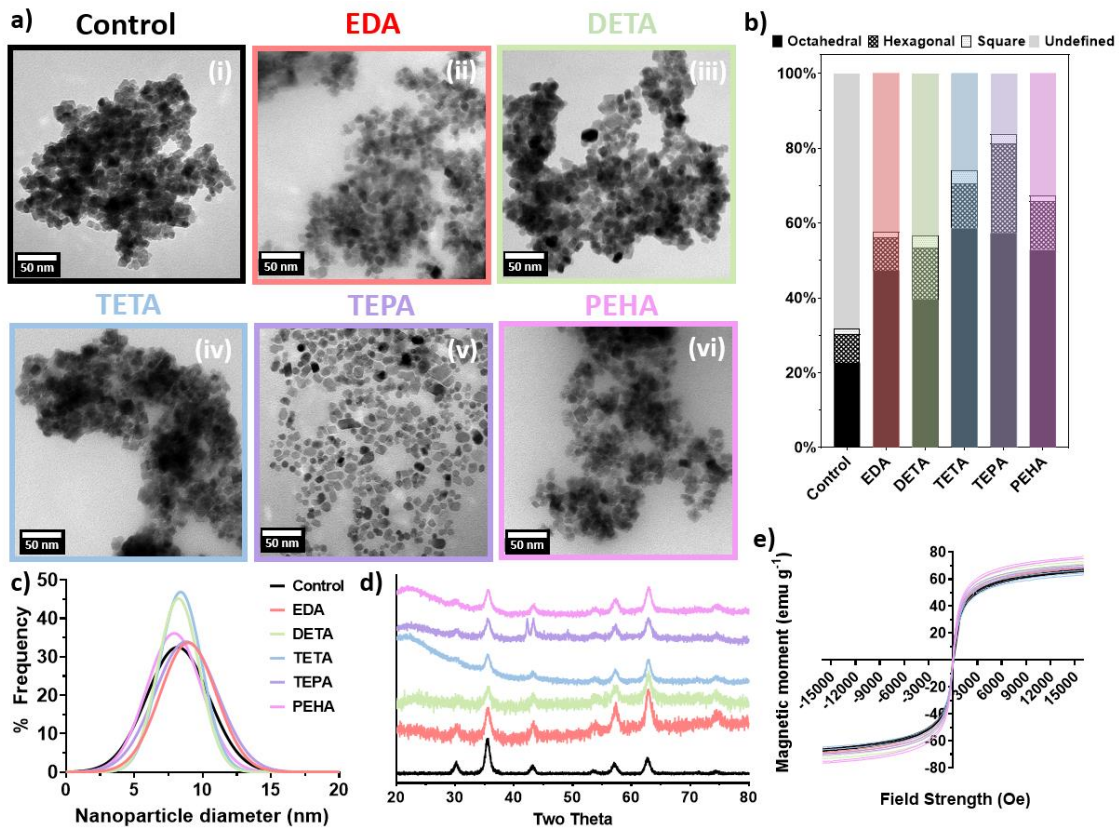


Fig 3. Comparison of effect of additives on magnetite nanoparticles formed with continuous flow mixing at 1:100 additive:iron ratios (Fe inlet) (coloured) and RTCP batch control (black). **a)** TEM images; **b)** shape analysis; **c)** particle size distribution; **d)** XRD; **e)** magnetic data.

Figure 3 shows the results for the particles formed when an additive was added to the iron solution inlet at the highest additive:iron ion ratio, that being 1:100. TEM images (Figure 3a) show the morphology is significantly improved with the addition of any of the selected ethylenediamine-based additives, resulting in clearly more faceted and angular nanoparticles from ~32% (control) to 58-84% with additives (Figure 3b). Notably, the faceted particles are predominantly diamond shaped with a proportion appearing hexagonal. It is important to note here that when a 3D shape is visualised in 2D, an octahedral particle most commonly appears to be diamond shaped but can also appear hexagonal or even square if viewed down different axes. Under these conditions, TEPA shows the most control with 84% faceted particles compared to 57% for EDA and 58% for DETA, both of which offer the least control. Figure 3c

shows the size of particles is not significantly affected by the addition of the ethylenediamine additives.

These results generally agree with a previous batch set-up study with the same additive series, where crystallisation was directed to octahedral particles.⁴¹ Previously TETA, TEPA, and PEHA were observed to offer excellent morphological control, which is reflected similarly in these results. Notable differences are that the additive could not offer quite the same level of morphological control here as that achieved in a batch process (batch process previously produced ~ 1.2x more octahedral/faceted particles relative to each additive).⁴⁴

3.3 Effect of process conditions in the continuous flow static mixing system

All additives were used in further studies to investigate the effect of additive concentration and addition points. The ratios of 1:100, 1:1000, and 1:1000 of additive:iron ions were selected to investigate additive effectiveness as well as additive addition location (introduced in either the iron or base reagent solution). The 1:10 ratio of TEPA to iron yielded poor quality particles in the batch reaction system and was hence not investigated further in this study.⁴⁴ The 3 different concentrations with 2 different addition points resulted in 6 different particle samples to analyse for each additive (total of 30 data sets, see Supplementary figures S3-S7 for TEM, size and shape analysis, XRD and magnetism for each additive individually).

Reactions with PEHA each exert similarly good control, with DETA less so.⁴⁴ This was explained through prior molecular dynamics simulations that DETA shows no preference for either the [111] or [100] face of magnetite, and hence does not as efficiently promote octahedral particle morphology. We propose there is the same advantage of longer chains and increasing number of amine groups as that which we reported for the batch system. Modelling showed the longer molecules can bind strongly to the [111] surface, with increased numbers of both Fe-N and O-H interactions.⁴⁴

The addition of additives in any proportion resulted in an increase in proportion of faceted (square, diamond, hexagonal) particles observed, with a minimum of 38% and a maximum of 84% being observed (Figure 4a) compared to 32% in the comparable control. Generally, there is a trend that the more control is exerted over forming faceted particles using additives at the longer amine lengths. This follows the trend previously observed wherein TETA, TEPA, and

There is an exception to this trend; for the highest concentration of additives (1:100) added to either the iron or NaOH solution we see TEPA has the highest quality particles, then a reduction for PEHA (for the same conditions) (Figure 4a). This, again, is very interesting and suggests there is an optimum number of amine groups beyond which control over crystal habit is reduced. The concentration is the ratio of additive to the iron ion concentration and as such PEHA will have more amine groups present than TEPA at the same additive:iron ratio. At this highest concentration the quantity of amines PEHA introduces may go beyond the optimum amines required. As such, the highest quantity of faceted particles is achieved for PEHA at the middle concentration of 1:1000, producing 70% faceted particles compared to 67% at the 1:100 ratio.

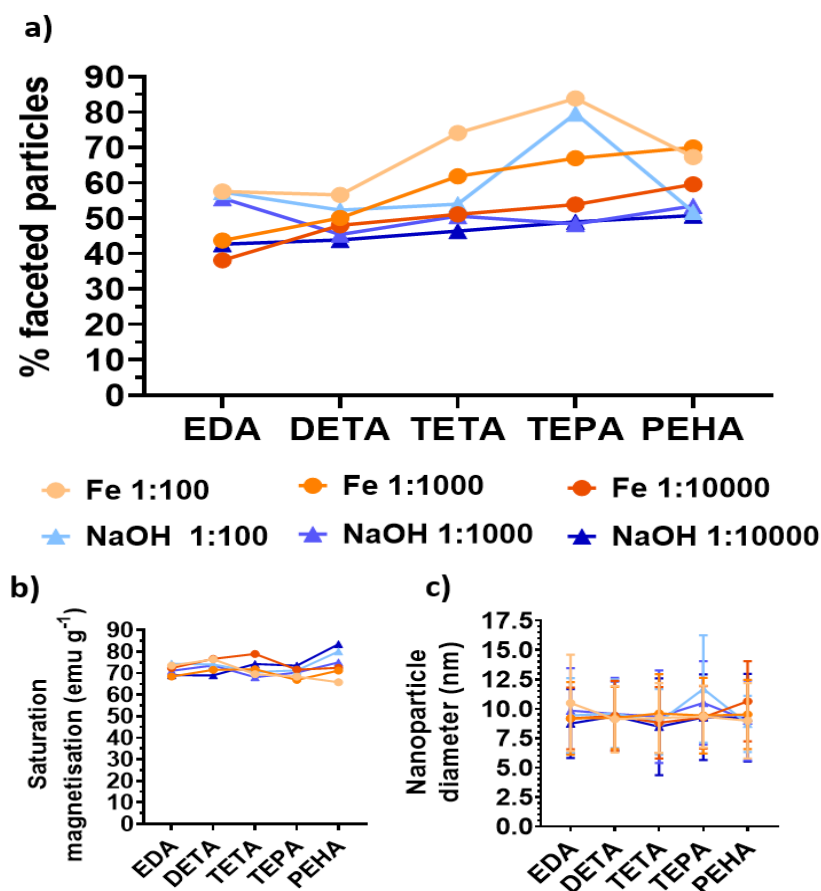


Fig 4. Effect of additive to iron ratios and additive feed (addition to Fe or NaOH inlet) for each additive. **a)** Effect on percentage faceted particles; **b)** effect on saturation magnetisation; **c)** effect on mean particle diameter.

While the main difference in faceted particle formation is seen by varying additives, there are some trends seen with respect to the reagent inlet the additive is introduced in and the additive:iron ion ratio. There is a higher percentage of faceted particles produced with the smallest additive (EDA) when added to the NaOH solution inlet, compared with those produced where the additive is present in the iron solution. This is reversed for the longest additive (PEHA), where additive present in the iron solution produces a greater proportion of faceted particles. However, the difference is not so clear for the mid-length additives with variations presented being too small to be of any significance. This behaviour could hint to a small advantage of protonating the longer amines, which would only occur in the more acidic iron solution. This could be expected to be attractive to a negatively charged magnetite surface. It is not clear why the neutral EDA in basic conditions would produce more faceted particles than the EDA introduced to the reaction in the acidic iron solution. The continuous flow static mixing environment is much more effective in homogenising local concentrations compared to more heterogeneous environments in mixed flasks or under laminar flow conditions, so that local concentrations of positive and negative ions are much more uniform.

When TEPA was used at the highest concentration of 1:100, a high percentage of faceted particles were produced from use in either inlet (84% with additive added via Fe solution compared to 80% via NaOH solution). Despite the efficacy of longer chain amine additives

appearing reduced when added through the NaOH solution, TEPA appears to be highly effective at the 1:100 concentration. This effect rapidly falls off at the medium and lowest concentrations, producing a similar proportion of faceted particles (~50%) as the other additives.

Higher quantities of faceted particles occur with higher concentrations of additives across the full range of additives and regardless of inlet solution (Figure 4a and Supplementary figure S8) with the exception of PEHA and TETA 1:100 (NaOH inlet), as already discussed. For example, EDA at a 1:100 additive:iron ion ratio produces 58% faceted particles compared to 38% at the 1:10000 concentration when added via the iron solution, showing approximately 20% difference. Similarly, for EDA added via the NaOH solution, the 1:100 ratio yields 57% faceted particles versus 43% at the 1:10000 ratio, again showing approximately 15-20% difference. There is a much smaller difference with concentration for DETA (insignificant for DETA in the NaOH solution) and a larger difference observed for TETA and TEPA (excluding the TEPA 1:100 result discussed prior) (Figure 4a). While this trend is consistent it is worth noting that the additive concentration increased by 100-fold between the lowest and highest concentration for only a marginal 15-20% improvement. These marginal improvements in particle shape would not be likely to offset additional costs of using 10- or 100-times larger amounts of additives per unit mass of particles produced, meaning it would appear to be most cost effective to use the lower additive concentration. Furthermore, it is worth highlighting the most faceted SPIONs (70%) are achieved with PEHA at the mid-concentration of 1:1000 introduced through the iron ion channel (Figure 4a), demonstrating that there is a more significant difference seen by varying the additive used rather than varying additive concentration.

The effect of the additive is predominantly confined to altering the particle morphology, with no significant difference observed in magnetism (Figure 4b and supplementary information S9) or size (Figure 4c and supplementary information S9) across all additives, concentrations, and addition inlet. The magnetic saturation of all samples lies between 83.5 emu g^{-1} (for PEHA NaOH 1:10000) and 65.8 emu g^{-1} (for PEHA Fe 1:100) (supplementary figure S9). It is noteworthy that PEHA magnetic saturation is highest (higher than control sample) for the lowest concentration of additive in base, with magnetic saturation reducing as the concentration of additive increases, then reducing furthermore with additive added in the iron channel at the lowest concentrations to highest concentration giving the lowest magnetic saturation (Figure 4b). There is a small increase in magnetic saturation in samples produced with increasing length of additives, added in NaOH, whereas the magnetic saturation of samples produced with additives in the iron solution see a peak at DETA and TETA. The highest saturation quantities are from samples produced with the lowest concentration of additives. There is no difference in size across all particles, in keeping with the data from the batch study and the hypothesis that the amine is not nucleating particles but is solely a shape controlling additive.

4. Conclusions

Particles formed using RTCP conditions across three different systems (batch, millifluidic, and larger-scale continuous flow static mixing) without the addition of additives were found to each produce particles with poor shape control, with particles of such undefined morphology making up 68% (continuous flow static mixing) to 94% (batch) of the particles present. The batch

system produces particles approximately twice the diameter (~20 nm) of those formed in the other two fluidic systems (~9 – 11 nm). Each system produces highly magnetic particles, with the most magnetic being formed in the batch system.

The inclusion of ethylenediamine-based additives significantly affected the morphology of the resultant particles with the addition of any of the additives increasing the proportion of faceted particles from ~32 % to 50%, ranging from 38-84 %. The majority of faceted (square, diamond, hexagonal) particles formed in each reaction appeared to be octahedral in nature. These results suggest additives play a key role in shape direction of the forming magnetite particles. The addition of additive in any proportion led to a substantial increase in ratio of faceted particles observed, with a general trend of more additive resulting in a higher proportion of faceted particles. PEHA showed to be a notable exception to this, showing slightly more faceted particle control at the mid-concentration, possibly due to the amount of amine groups being too high from the combined effect of longer chain and high concentration, thus causing a detrimental effect on the forming particles. Overall, the increase in octahedral particles present due to additive addition supports the hypothesis that the amines exhibit favourable binding via adsorption to the [111] face of magnetite. Using an additive-enhanced synthesis in a continuous flow static mixing system we demonstrated robust scalable production of highly faceted magnetite nanoparticles with production rates of 311 g day⁻¹ which far exceed those previously reported in the literature. This approach is inherently amenable to both scale up and scale out, facilitating translation of magnetite synthesis to continuous manufacturing at kilogram scale per day using green chemistry. Finally, this versatile process provides an alternative, “greener” bioinspired additive method, where minute amounts of additives are needed, water is used as a solvent, and the reactions are all performed at room temperature.

Conflicts of interest

There are no conflicts of interest to declare.

Abbreviations

DETA, diethylenetriamine; EDA, ethylenediamine; MIA, magnetite interacting Adhiron; MNP, magnetic nanoparticle; MD, molecular dynamics; MTB, magnetotactic bacteria; PEEK, polyethyl ethyl ketone; RTCP, room temperature co-precipitation; SPION, superparamagnetic iron oxide nanoparticle; TEPA, tetraethylenepentamine; TETA, triethylenetetramine; PEHA, pentaethylenehexamine

Acknowledgements

This work was supported by funding from the EPSRC (grant number EP/P006892/1) and the University of Sheffield's EPSRC DTP allowance (grant number EP/M508135/1) funds Laura Norfolk's PhD. We thank S. Tsokov, and C. Hill (Sheffield Electron Microscopy unit) for TEM training and HRTEM, Nicola Morley and Zhao Leong for support with VSM, and Craig Robertson for support with powder XRD.

References

1. Rosensweig, R. E. Heating magnetic fluid with alternating magnetic field. *Journal of magnetism and magnetic materials* **252**, 370–374 (2002).
2. Mendoza, E. Y. M. *et al.* Iron oxides as efficient sorbents for CO₂ capture. *Journal of Materials Research and Technology* **8**, 2944–2956 (2019).
3. Bird, S. M., Galloway, J. M., Rawlings, A. E., Bramble, J. P. & Staniland, S. S. Taking a hard line with biotemplating: cobalt-doped magnetite magnetic nanoparticle arrays. *Nanoscale* **7**, 7340–7351 (2015).
4. Mody, V. V. *et al.* Magnetic nanoparticle drug delivery systems for targeting tumor. *Applied Nanoscience* **4**, 385–392 (2014).
5. Sharma, P., Brown, S., Walter, G., Santra, S. & Moudgil, B. Nanoparticles for bioimaging. *Advances in colloid and interface science* **123**, 471–485 (2006).
6. Yallapu, M. M., Foy, S. P., Jain, T. K. & Labhasetwar, V. PEG-functionalized magnetic nanoparticles for drug delivery and magnetic resonance imaging applications. *Pharmaceutical research* **27**, 2283–2295 (2010).
7. Reddy, G. R. *et al.* Vascular targeted nanoparticles for imaging and treatment of brain tumors. *Clinical Cancer Research* **12**, 6677–6686 (2006).
8. Zhen, G. *et al.* Comparative study of the magnetic behavior of spherical and cubic superparamagnetic iron oxide nanoparticles. *The Journal of Physical Chemistry C* **115**, 327–334 (2011).
9. Li, Z. *et al.* Magnetite nanoparticles with high heating efficiencies for application in the hyperthermia of cancer. *Materials Science and Engineering: C* **30**, 990–996 (2010).
10. Maity, D., Kale, S. N., Kaul-Ghanekar, R., Xue, J.-M. & Ding, J. Studies of magnetite nanoparticles synthesized by thermal decomposition of iron (III) acetylacetonate in tri (ethylene glycol). *Journal of Magnetism and magnetic Materials* **321**, 3093–3098 (2009).
11. Gonzales-Weimuller, M., Zeisberger, M. & Krishnan, K. M. Size-dependant heating rates of iron oxide nanoparticles for magnetic fluid hyperthermia. *Journal of magnetism and magnetic materials* **321**, 1947–1950 (2009).

12. Zhao, H., Saatchi, K. & Häfeli, U. O. Preparation of biodegradable magnetic microspheres with poly (lactic acid)-coated magnetite. *Journal of Magnetism and Magnetic Materials* **321**, 1356–1363 (2009).
13. Stephen, Z. R., Kievit, F. M. & Zhang, M. Magnetite nanoparticles for medical MR imaging. *Materials Today* **14**, 330–338 (2011).
14. Wahajuddin, S. A. Superparamagnetic iron oxide nanoparticles: magnetic nanoplateforms as drug carriers. *International journal of nanomedicine* **7**, 3445–3471 (2012).
15. Mahmoudi, M., Sant, S., Wang, B., Laurent, S. & Sen, T. Superparamagnetic iron oxide nanoparticles (SPIONs): development, surface modification and applications in chemotherapy. *Advanced drug delivery reviews* **63**, 24–46 (2011).
16. Kemp, S. J., Ferguson, R. M., Khandhar, A. P. & Krishnan, K. M. Monodisperse magnetite nanoparticles with nearly ideal saturation magnetization. *RSC advances* **6**, 77452–77464 (2016).
17. Mahmoudi, M., Hofmann, H., Rothen-Rutishauser, B. & Petri-Fink, A. Assessing the in vitro and in vivo toxicity of superparamagnetic iron oxide nanoparticles. *Chemical reviews* **112**, 2323–2338 (2012).
18. Jana, N. R., Chen, Y. & Peng, X. Size-and shape-controlled magnetic (Cr, Mn, Fe, Co, Ni) oxide nanocrystals via a simple and general approach. *Chemistry of materials* **16**, 3931–3935 (2004).
19. Smith, B. R. & Gambhir, S. S. Nanomaterials for in vivo imaging. *Chemical reviews* **117**, 901–986 (2017).
20. Wu, W., He, Q. & Jiang, C. Magnetic iron oxide nanoparticles: synthesis and surface functionalization strategies. *Nanoscale research letters* **3**, 397–415 (2008).
21. Chen, K.-H. *et al.* Nanoparticle distribution during systemic inflammation is size-dependent and organ-specific. *Nanoscale* **7**, 15863–15872 (2015).
22. Ma, N. *et al.* Influence of nanoparticle shape, size, and surface functionalization on cellular uptake. *Journal of nanoscience and nanotechnology* **13**, 6485–6498 (2013).

23. Owens III, D. E. & Peppas, N. A. Opsonization, biodistribution, and pharmacokinetics of polymeric nanoparticles. *International journal of pharmaceutics* **307**, 93–102 (2006).
24. Champion, J. A., Katare, Y. K. & Mitragotri, S. Particle shape: a new design parameter for micro-and nanoscale drug delivery carriers. *Journal of controlled release* **121**, 3–9 (2007).
25. Roca, A. G. *et al.* Design strategies for shape-controlled magnetic iron oxide nanoparticles. *Advanced drug delivery reviews* **138**, 68–104 (2019).
26. Mohapatra, J., Mitra, A., Aslam, M. & Bahadur, D. Octahedral-shaped Fe₃O₄ nanoparticles with enhanced specific absorption rate and R₂ relaxivity. *IEEE Transactions on Magnetics* **51**, 1–3 (2015).
27. Nambiar, R. B., Perumal, A. B., Sadiku, E. R. & Sellamuthu, P. S. Chapter 3 - Bacterial Synthesis of Nanoparticles and Their Applications. in *Biological Synthesis of Nanoparticles and Their Applications* (CRC Press, 2019).
28. Wang, B., Wei, Q. & Qu, S. Synthesis and characterization of uniform and crystalline magnetite nanoparticles via oxidation-precipitation and modified co-precipitation methods. *Int. J. Electrochem. Sci* **8**, 3786–3793 (2013).
29. Haw, C. Y. *et al.* Hydrothermal synthesis of magnetite nanoparticles as MRI contrast agents. *Ceramics International* **36**, 1417–1422 (2010).
30. Willis, A. L., Turro, N. J. & O'Brien, S. Spectroscopic characterization of the surface of iron oxide nanocrystals. *Chemistry of materials* **17**, 5970–5975 (2005).
31. Nikitin, A. *et al.* Synthesis, characterization and MRI application of magnetite water-soluble cubic nanoparticles. *Journal of Magnetism and Magnetic Materials* **441**, 6–13 (2017).
32. Fatima, H., Lee, D.-W., Yun, H. J. & Kim, K.-S. Shape-controlled synthesis of magnetic Fe₃O₄ nanoparticles with different iron precursors and capping agents. *RSC advances* **8**, 22917–22923 (2018).
33. Shaw, S. K. *et al.* Synthesis of exchange coupled nanoflowers for efficient magnetic hyperthermia. *Journal of Magnetism and Magnetic Materials* **484**, 437–444 (2019).

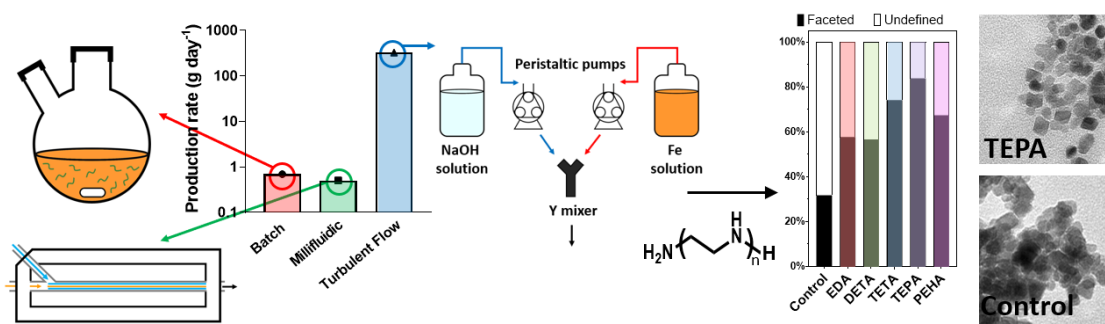
34. Li, W., Lee, S. S., Wu, J., Hinton, C. H. & Fortner, J. D. Shape and size controlled synthesis of uniform iron oxide nanocrystals through new non-hydrolytic routes. *Nanotechnology* **27**, 324002 (2016).
35. Chin, S. F., Iyer, K. S. & Raston, C. L. Fabrication of carbon nano-tubes decorated with ultra fine superparamagnetic nano-particles under continuous flow conditions. *Lab on a Chip* **8**, 439–442 (2008).
36. Chen, X., Smith, N. M., Iyer, K. S. & Raston, C. L. Controlling nanomaterial synthesis, chemical reactions and self assembly in dynamic thin films. *Chemical Society Reviews* **43**, 1387–1399 (2014).
37. D'Alonzo, N. J., Eggers, P. K. & Raston, C. L. Vortex fluidics synthesis of polymer coated superparamagnetic magnetite nanoparticles. *New Journal of Chemistry* **41**, 552–558 (2017).
38. Rawlings, A. E. *et al.* Ferrous iron binding key to Mms6 magnetite biomineralisation: a mechanistic study to understand magnetite formation using pH titration and NMR spectroscopy. *Chemistry (Weinheim an der Bergstrasse, Germany)* **22**, 7885 (2016).
39. Norfolk, L. *et al.* Macrofluidic coaxial flow platforms to produce tunable magnetite nanoparticles: A study of the effect of reaction conditions and biomineralisation protein mms6. *Nanomaterials* **9**, 1729 (2019).
40. Staniland, S. S. & Rawlings, A. E. Crystallizing the function of the magnetosome membrane mineralization protein Mms6. *Biochemical Society Transactions* **44**, 883–890 (2016).
41. Galloway, J. M. *et al.* Magnetic bacterial protein Mms6 controls morphology, crystallinity and magnetism of cobalt-doped magnetite nanoparticles in vitro. *Journal of Materials Chemistry* **21**, 15244–15254 (2011).
42. McGuire, M. J., Li, S. & Brown, K. C. Biopanning of phage displayed peptide libraries for the isolation of cell-specific ligands. *Biosensors and Biodetection* 291–321 (2009).
43. Rawlings, A. E. *et al.* Phage display selected magnetite interacting Adhirons for shape controlled nanoparticle synthesis. *Chemical Science* **6**, 5586–5594 (2015).

44. Norfolk, L., Kapusta, K., Cooke, D. & Staniland, S. S. Ethylenediamine Series as Additives to Control the Morphology of Magnetite Nanoparticles. *Green Chemistry* (2021) doi:10.1039/D1GC01539G, 1-12
45. Brown, C. J. *et al.* Enabling precision manufacturing of active pharmaceutical ingredients: workflow for seeded cooling continuous crystallisations. *Molecular Systems Design & Engineering* **3**, 518–549 (2018).
46. Svoboda, V. *et al.* Continuous cocrystallization of benzoic acid and isonicotinamide by mixing-induced supersaturation: exploring opportunities between reactive and antisolvent crystallization concepts. *Crystal Growth & Design* **17**, 1902–1909 (2017).
47. MacFhionnghaile, P., Svoboda, V., McGinty, J., Nordon, A. & Sefcik, J. Crystallization diagram for antisolvent crystallization of lactose: using design of experiments to investigate continuous mixing-induced supersaturation. *Crystal growth & design* **17**, 2611–2621 (2017).
48. Raza, S. A. *et al.* Rapid continuous antisolvent crystallization of multicomponent systems. *Crystal Growth & Design* **18**, 210–218 (2018).
49. Simmons, M., Wiles, C., Rocher, V., Francesconi, M. G. & Watts, P. The preparation of magnetic iron oxide nanoparticles in microreactors. *Journal of Flow Chemistry* **3**, 7–10 (2013).
50. Haseidl, F., Müller, B. & Hinrichsen, O. Continuous-Flow Synthesis and Functionalization of Magnetite: Intensified Process for Tailored Nanoparticles. *Chemical Engineering & Technology* **39**, 2051–2058 (2016).
51. Suryawanshi, P. L. *et al.* Synthesis of iron oxide nanoparticles in a continuous flow spiral microreactor and Corning® advanced flow™ reactor. *Green Processing and Synthesis* **7**, 1–11 (2018).
52. Bemetz, J. *et al.* Microfluidic-based synthesis of magnetic nanoparticles coupled with miniaturized NMR for online relaxation studies. *Analytical chemistry* **90**, 9975–9982 (2018).

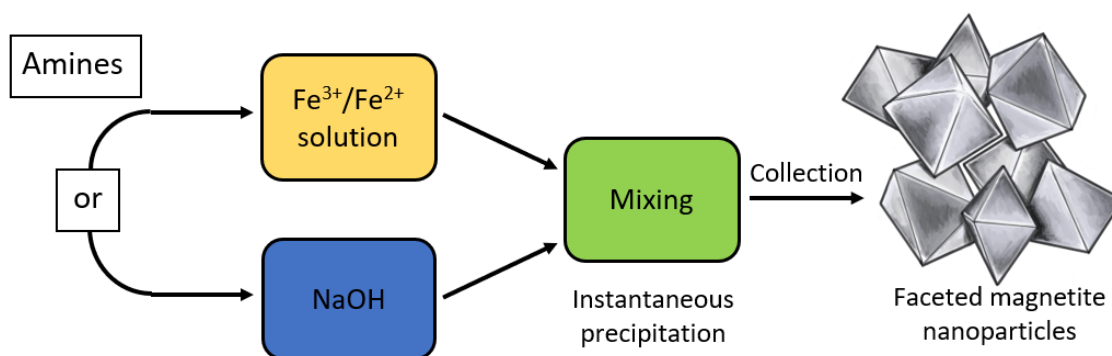
53. Besenhard, M. O. *et al.* Co-precipitation synthesis of stable iron oxide nanoparticles with NaOH: New insights and continuous production via flow chemistry. *Chemical Engineering Journal* **399**, 125740 (2020).
54. Maurizi, L. *et al.* One step continuous hydrothermal synthesis of very fine stabilized superparamagnetic nanoparticles of magnetite. *Chemical Communications* **47**, 11706–11708 (2011).
55. Glasgow, W. *et al.* Continuous synthesis of iron oxide (Fe₃O₄) nanoparticles via thermal decomposition. *Particuology* **26**, 47–53 (2016).
56. Asimakidou, T. *et al.* Continuous production of magnetic iron oxide nanocrystals by oxidative precipitation. *Chemical Engineering Journal* **393**, 124593 (2020).
57. Mahin, J. & Torrente-Murciano, L. Continuous synthesis of monodisperse iron@ iron oxide core@ shell nanoparticles. *Chemical Engineering Journal* **396**, 125299 (2020).
58. Abou Hassan, A., Sandre, O., Cabuil, V. & Tabeling, P. Synthesis of iron oxide nanoparticles in a microfluidic device: preliminary results in a coaxial flow millichannel. *Chemical Communications* 1783–1785 (2008).
59. LaGrow, A. P. *et al.* Unravelling the growth mechanism of the co-precipitation of iron oxide nanoparticles with the aid of synchrotron X-Ray diffraction in solution. *Nanoscale* **11**, 6620–6628 (2019).
60. Panariello, L. *et al.* A Modular Millifluidic Platform for the Synthesis of Iron Oxide Nanoparticles with Control over Dissolved Gas and Flow Configuration. *Materials* **13**, 1019 (2020).
61. Lindenberg, C., Schöll, J., Vicum, L., Mazzotti, M. & Brozio, J. Experimental characterization and multi-scale modeling of mixing in static mixers. *Chemical Engineering Science* **63**, 4135–4149 (2008).
62. Falk, L. & Commenge, J.-M. Performance comparison of micromixers. *Chemical Engineering Science* **65**, 405–411 (2010).
63. Mirabello, G., Lenders, J. J. & Sommerdijk, N. A. Bioinspired synthesis of magnetite nanoparticles. *Chemical Society Reviews* **45**, 5085–5106 (2016).

64. Majidi, S., Zeinali Sehrig, F., Farkhani, S. M., Soleymani Goloujeh, M. & Akbarzadeh, A. Current methods for synthesis of magnetic nanoparticles. *Artificial cells, nanomedicine, and biotechnology* **44**, 722–734 (2016).
65. Guardia, P., Labarta, A. & Batlle, X. Tuning the size, the shape, and the magnetic properties of iron oxide nanoparticles. *The Journal of Physical Chemistry C* **115**, 390–396 (2011).

TOC:



Graphical abstract:



Robust Scalable Continuous Flow Bioinspired Synthesis of Magnetite Nanoparticles using Ethylenediamine Additives

Laura Norfolk,^{*a} Georgina Zimbitas^b, Jan Sefcik^{b,c}, and Sarah Staniland^a

SUPPLEMENTARY INFORMATION

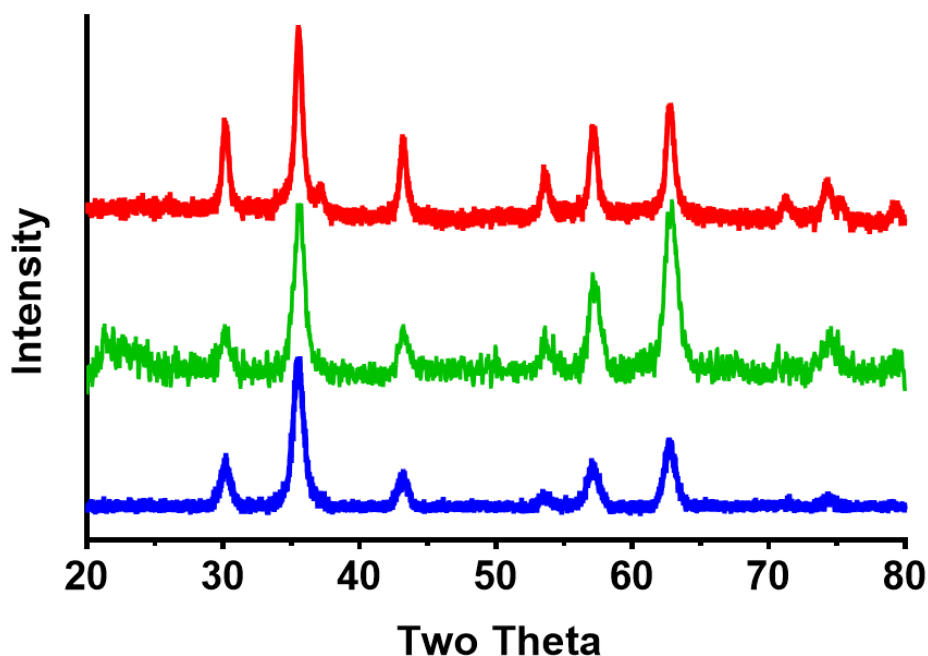


Figure S1. XRD data of control (no additive) RTCP reactions for each set-up system: batch (red), millifluidic (green), and turbulent flow (blue).

Supplementary information S2. Theoretical production rate (g day^{-1} of nanoparticles) calculation

Reaction information used:

***Batch:** 1 mmol of iron salts produces 0.333 mmol of magnetite per reaction

Millifluidic: $90 \mu\text{L min}^{-1}$ flow rate of 50 mmol iron solution

Turbulent flow: Average flow rate of 112 mL min^{-1} (from 31 measurements) for both NaOH and Fe solution. As they flow in a 1:1 ratio the flow rate of only the Fe solution can be assumed to be half the overall flow rate - 56 mL min^{-1}

Assumptions:

1. Time for system set-up and particle extraction from the batch system between batches is not accounted for
2. All batch synthesis is run directly after one another for a 24-hour period (9 batches)
3. Millifluidic and turbulent flow run continuously for a 24-hour period
4. 100% conversion of iron salt to magnetite (Fe_3O_4 molecular weight = $231.531 \text{ g mol}^{-1}$, 3 mol of iron salt produces 1 mol of magnetite)

Calculations:

Batch: $3 \times 10^{-3} \text{ mol of magnetite} \times 231.531 \text{ g mol}^{-1} = \mathbf{0.69 \text{ g day}^{-1}}$

Millifluidic: $1440 \text{ (mins day}^{-1}) \times 90 \text{ }\mu\text{L min}^{-1} = 0.1296 \text{ L day}^{-1}$

$0.1296 \text{ L} \times (0.05/3) \text{ Mol of magnetite formed} \times 231.531 \text{ g mol}^{-1} = \mathbf{0.50 \text{ g day}^{-1}}$

Turbulent flow: $1440 \text{ (mins day}^{-1}) \times 56 \text{ mL min}^{-1} = 80.64 \text{ L day}^{-1}$ of iron solution processed

$80.64 \text{ L} \times (0.05/3) \text{ Mol of magnetite formed} \times 231.531 \text{ g mol}^{-1} = \mathbf{311.2 \text{ g day}^{-1}}$

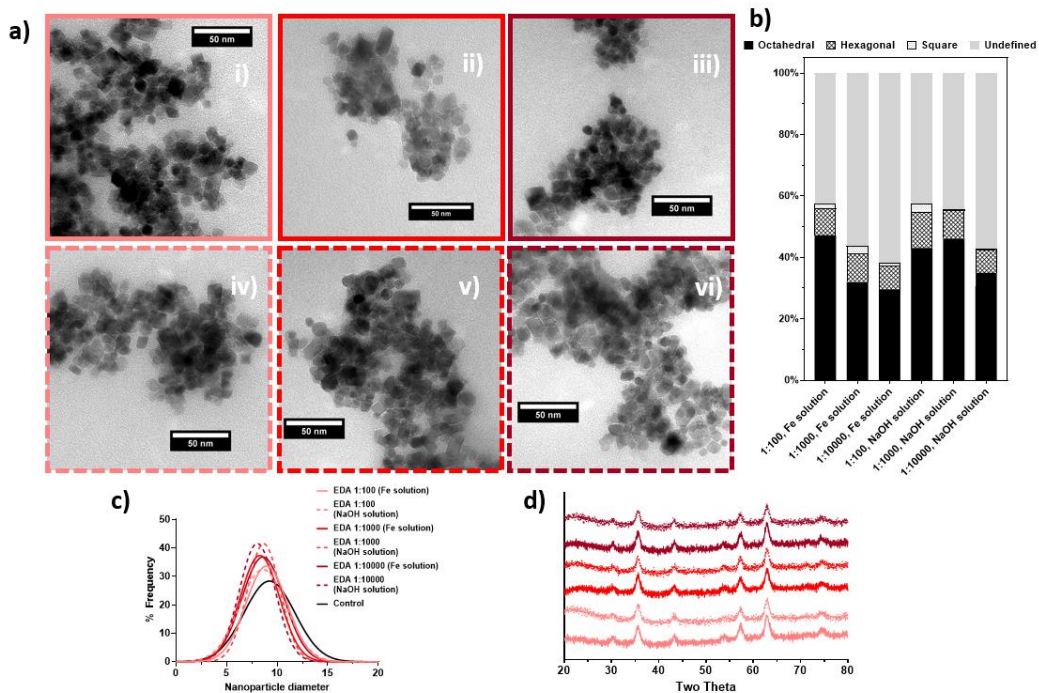


Figure S3. EDA additive data compilation: a) i-vi. TEM images; b) shape analysis; c) frequency distribution; d) XRD; e) magnetic data of particles formed at 1:100 (pale red), 1:1000 (red) and 1:10000 (dark red) EDA:iron ion ratios Solid lines indicate additive added through Fe inlet, and dashed lines indicate through NaOH inlet.

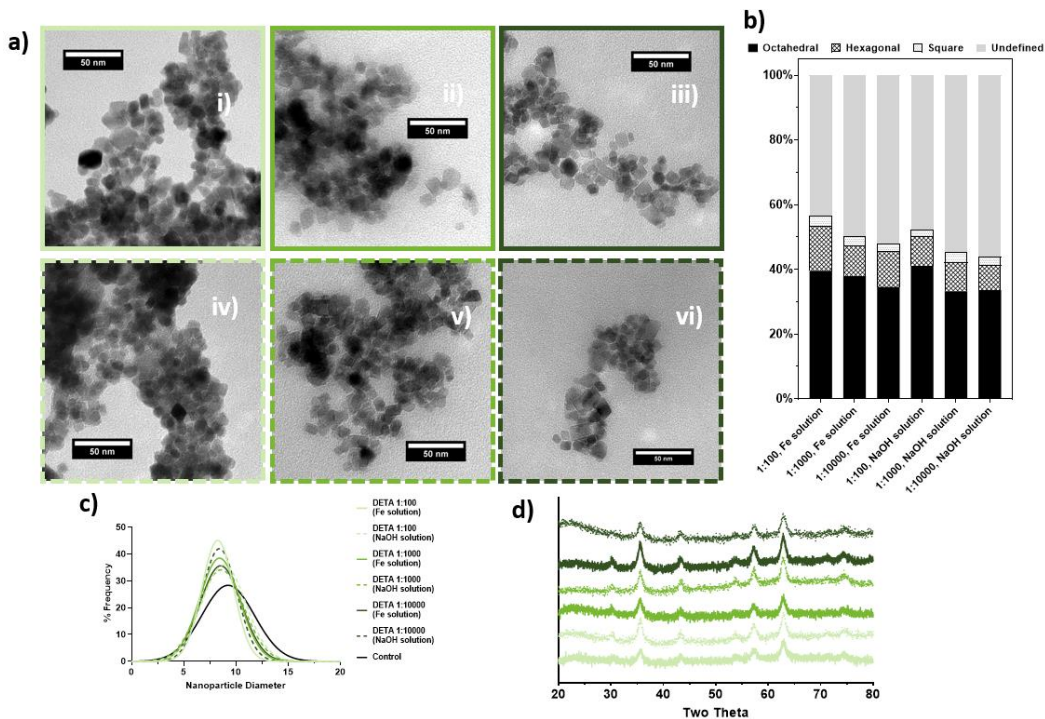


Figure S4. DETA additive data compilation: a) i-vi. TEM images; b) shape analysis; c) frequency distribution; d) XRD; e) magnetic data of particles formed at 1:100 (pale green), 1:1000 (green) and 1:10000 (dark green) DETA:iron ion ratios Solid lines indicate additive added through Fe inlet, and dashed lines indicate through NaOH inlet.

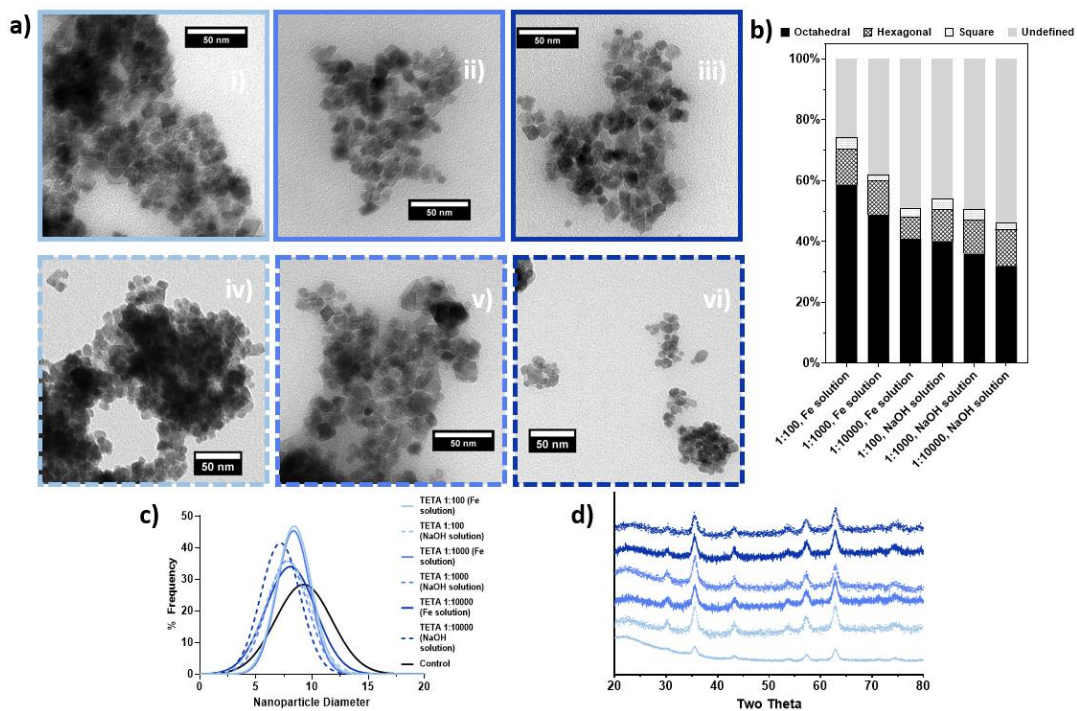


Figure S5. TETA additive data compilation: a) TEM images; b) shape analysis; c) frequency distribution; d) XRD; e) magnetic data of particles formed at 1:100 (pale red), 1:1000 (red) and 1:10000 (dark red) TETA:iron ion ratios Solid lines indicate additive added through Fe inlet, and dashed lines indicate through NaOH inlet.

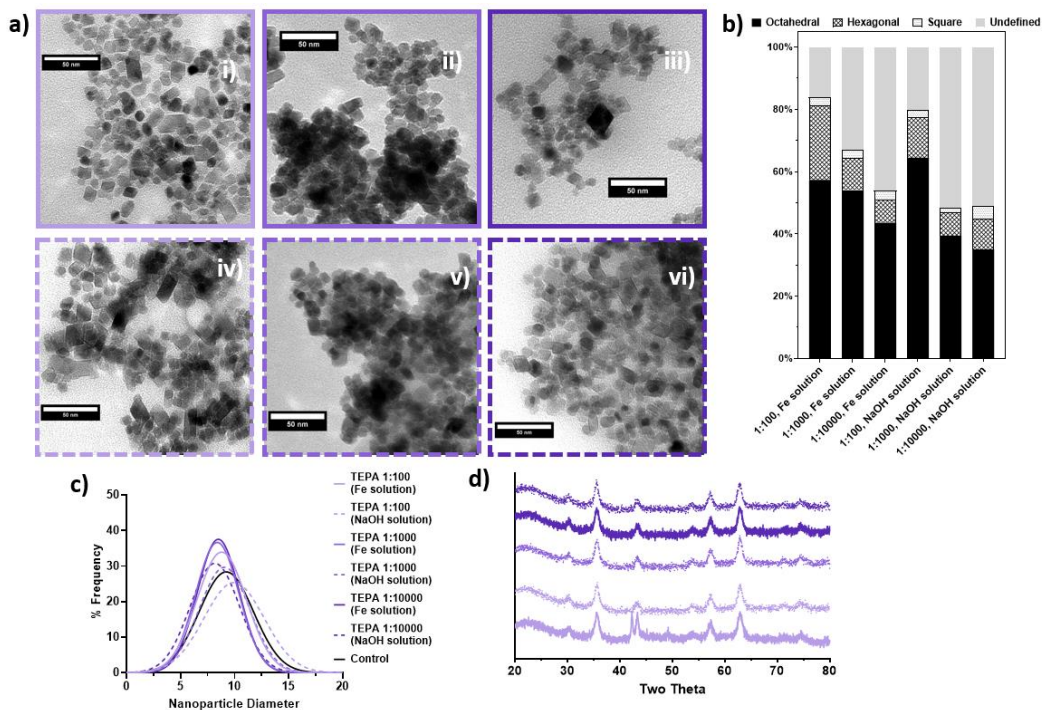


Figure S6. TEPA additive data compilation: a) TEM images; b) shape analysis; c) frequency distribution; d) XRD; e) magnetic data of particles formed at 1:100 (pale purple), 1:1000 (purple) and 1:10000 (dark purple) TEPA:iron ion ratios Solid lines indicate additive added through Fe inlet, and dashed lines indicate through NaOH inlet.

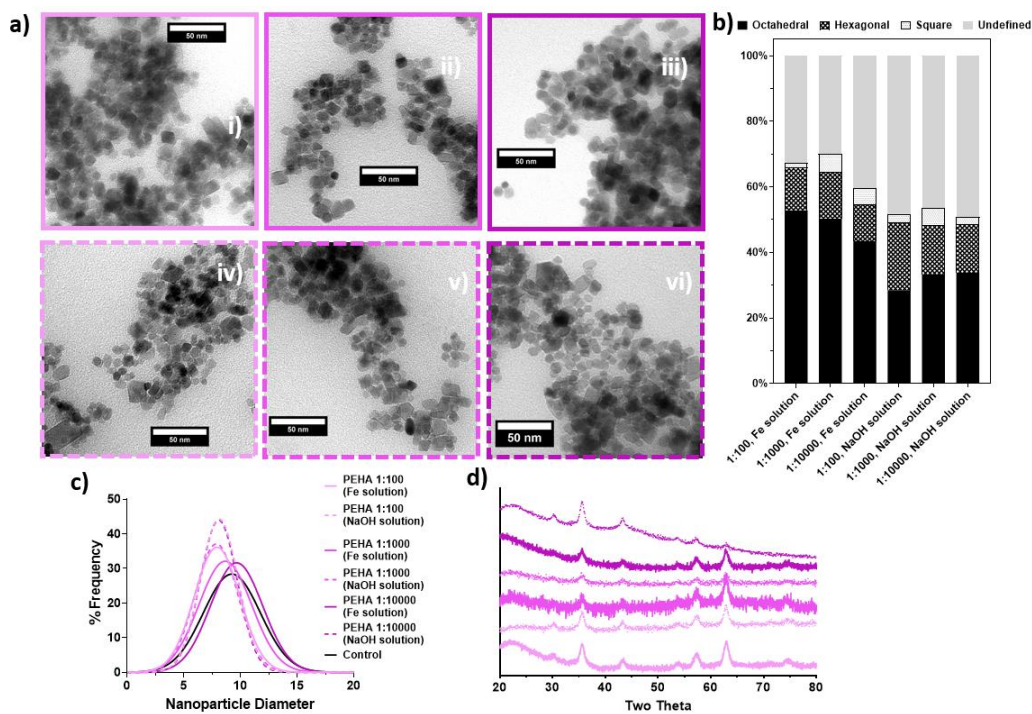


Figure S7. PEHA additive data compilation: a) TEM images; b) shape analysis; c) frequency distribution; d) XRD; e) magnetic data of particles formed at 1:100 (pale pink), 1:1000 (pink) and 1:10000 (dark pink) PEHA:iron ion ratios. Solid lines indicate additive added through Fe inlet, and dashed lines indicate through NaOH inlet.

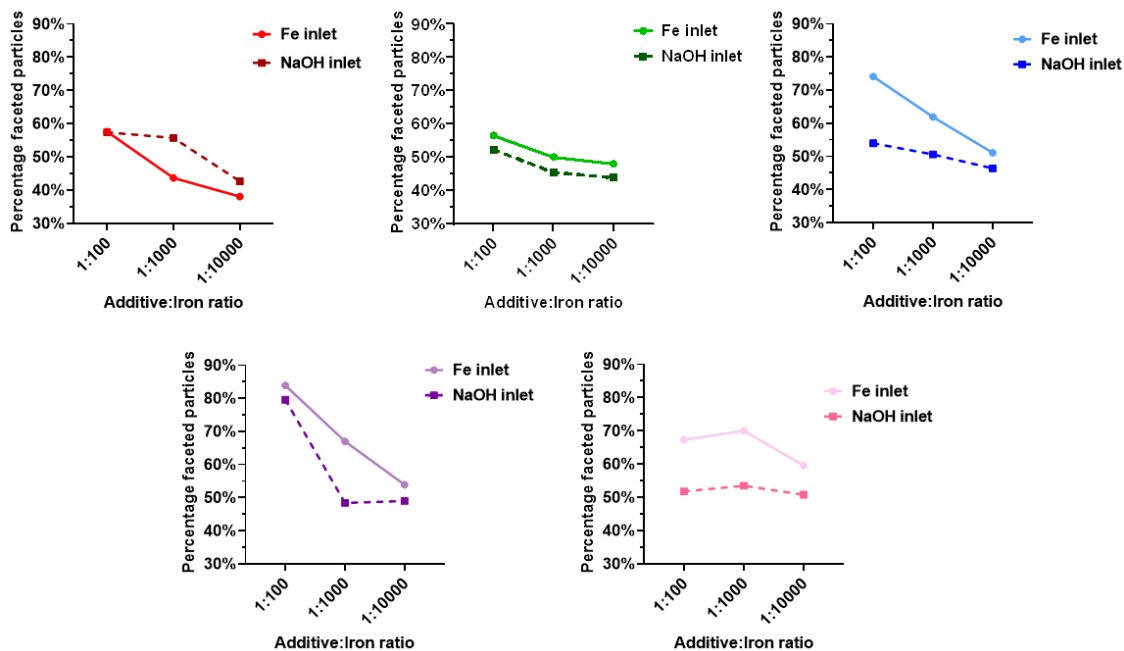


Figure S8. Graphs showing percentage faceted particles against additive:iron ratio for EDA (red), DETA (green), TETA (blue), TEPA (purple), and PEHA (pink)

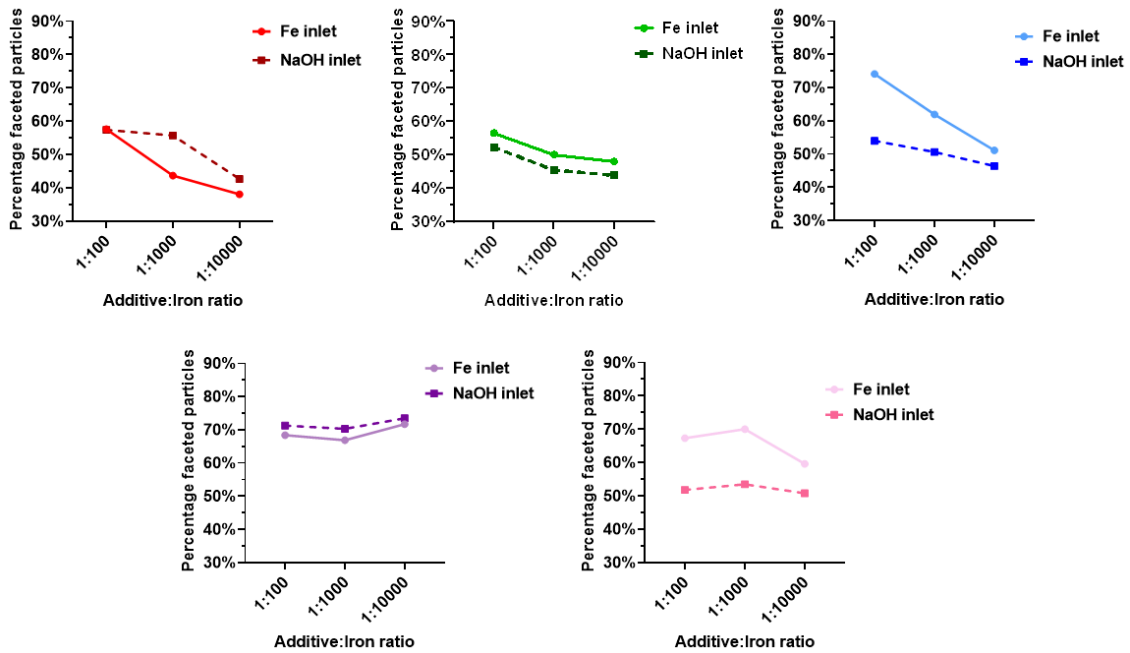


Figure S9. Saturation magnetisation against iron: additive ratio for EDA-PEHA additives added through **a) Fe inlet** and **b) NaOH inlet**.

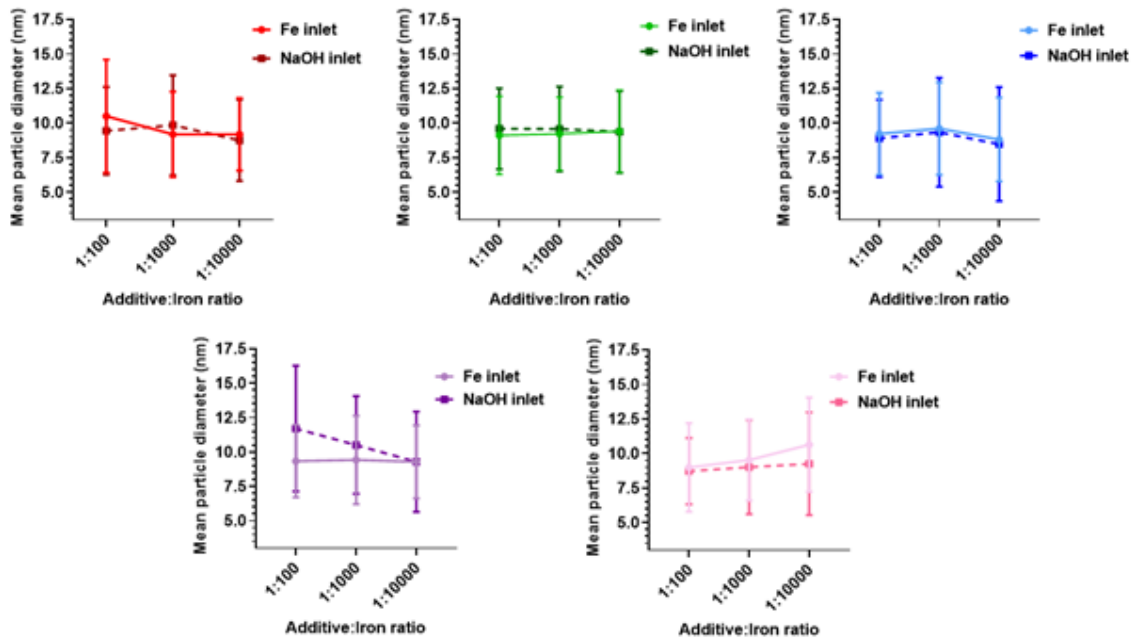


Figure S10. Graphs showing mean particle size against additive:iron ratio for EDA (red), DETA (green), TETA (blue), TEPA (purple), and PEHA (pink).

7.2 Optimisation of a Scalable Continuous Flow Synthesis of Magnetite Nanoparticles Using Tetraethylenepentamine as an Additive

7.2.1 Author Contributions

Laura Norfolk (first author): Synthesised 13 of the samples alongside Georgina Zimbitas, analysed all particles (XRD, TEM, VSM, shape and size analysis), created all figures and supplementary document, wrote the first draft,

Georgina Zimbitas (first author): Synthesised all particles, assisted in writing the first draft (introduction, methods, results, and discussion), aided in analysis of results.

Jan Sefcik: Conceptualised the use of a continuous flow static mixer, designed the continuous flow static mixer alongside Georgina Zimbitas, and assisted in the design of Figure 6.

Sarah Staniland (principal investigator): Acquired funding for the project, assisted with reviewing and editing.

ARTICLE

Optimisation of a scalable continuous flow synthesis of magnetite nanoparticles using tetraethylenepentamine as an additive

Laura Norfolk,^a Georgina Zimbitas^b, Jan Sefcik^{b,c} and Sarah Staniland^a

Received 00th January 20xx,
Accepted 00th January 20xx

DOI: 10.1039/x0xx00000x

The synthesis of superparamagnetic iron-oxide (SPIONs) has increasingly become of research importance due to their rising applications in industries which depend on precise control of particle properties, such as the biomedical industry. The current synthetic methodologies utilised to form the morphologically consistent particles desired for industrial use are energy intensive and utilise toxic pre-cursors and high boiling organic solvents. To address the environmentally unfriendly nature of these syntheses, room-temperature co-precipitation (RTCP) of magnetite has been investigated however in most studies it proved to offer poor control over the morphology of particles formed. In contrast, our previous study presented a RTCP synthetic method that not produced faceted magnetite nanoparticles, but also did so at high yields of approximately 300 g / day. In this paper we optimise our previous study, selecting the additive previously found to produce the highest amount of faceted particles within the smallest range of size distribution. Particle size was found to be tunable via the concentration of the Fe feed used, with an average particle size of 6.8 nm formed with a 10 mmol Fe solution, increasing to 8.7 nm at a 50 mmol Fe solution. Further size control can be exerted over a wider range of particle sizes via simply adjusting the Fe³⁺/Fe²⁺ ratio, producing highly magnetic particles of > 70 emu g⁻¹ spanning 22.7 to 9.2 nm particle diameter between a 0.2 - 0.6 ferric ratio. TEPA was found to exert control over the morphology of particles formed between a 0.4 – 0.6 ferric range at a 1:100 additive/Fe ratio, producing 73-81% faceted particles. This showcases the robustness of the continuous flow static mixing system and its reproducibility in synthesising highly faceted particles under environmentally sustainable reaction conditions.

Introduction

The rise of the inorganic nanomaterial industry has been apparent over the past decade, with both funding and publications increasing with each passing year. Nanomaterial syntheses, however, are exceedingly wasteful. Up to 1000 kg of waste material is produced in the synthesis of 1 kg of desired product,¹ with devastating long-term effects on the environment. This highlights the urgent need for producing these materials under “greener” conditions if the industry is to maintain its growth in a sustainable manner.²

Magnetite, Fe₃O₄, nanoparticles are no exception to this commercial interest, seeing applications in multiple industries spanning high-density data storage,³ carbon capture,⁴ and crucially, biomedical applications requiring precision magnetic nanoparticles (MNP) such as in magnetic drug delivery⁵, magnetic hyperthermia for cancer treatment,^{6–8} and as contrast agents in magnetic resonance imaging.⁹

Many synthetic methods of forming MNP are reliant on high boiling organic solvents,¹⁰ extended heating times, and use of toxic pre-cursors such as iron pentacarbonyl and iron acetylacetonate.¹¹ These syntheses however remain in use due to their ability to form highly morphologically consistent particles, with defined shapes possible such as cubic,^{12,13} octahedral,¹⁴ and nanoflower^{15,16} particles.

The co-precipitation of MNP is a preferred synthesis of the nanomaterial due to its ambient temperature and aqueous solvent being more environmentally friendly than other magnetite syntheses.¹⁷ However, RTCP fails to replicate the fine tuning and control of particle morphology achieved in thermal decomposition and hydrothermal syntheses. RTCP reactions produce inconsistent particles with a high degree of polydispersity,¹⁸ and other undesired iron oxides forming.^{18,19}

One example by which highly homogeneous MNP have been formed under ambient conditions occurs in nature within magnetotactic bacteria (MTB). MTB utilise a suite of biomineralisation proteins, such as Mms6 and MmsF, which interact with aqueous iron ions and growing magnetite surfaces, leading to the formation of larger, more highly faceted particles.^{18,20,21}

Mms6¹⁸ and MmsF²¹ have been both successfully used *in vitro* as additives under RTCP conditions, resulting in the formation of larger, more consistent nanoparticles. However, it is both labour intensive and costly to isolate and purify these proteins, eliminating the realistic possibility of these

^a Department of Chemistry, The University of Sheffield, Dainton Building, Brook Hill, Sheffield, S3 7HF, United Kingdom

^b Department of Chemical & Process Engineering, University of Strathclyde, James Weir Building, 75 Montrose Street, Glasgow G1 1XJ, United Kingdom

^c Future Manufacturing Research Hub in Continuous Manufacturing and Advanced Crystallisation, University of Strathclyde, Technology and Innovation Centre, 99 George Street, Glasgow G1 1RD, United Kingdom.

Electronic Supplementary Information (ESI) available: [details of any supplementary information available should be included here]. See DOI: 10.1039/x0xx00000x

biomineralisation proteins seeing immediate industrial scale use.

Robust, well-expressing proteins have also been developed for highly specific molecular recognition applications. Adhirons, for example, are peptide display scaffold proteins that were initially developed as effective alternatives to traditional antibody binding proteins. Magnetite interacting Adhirons (MIAs) were discovered through iterations of phage display biopanning²² with the purpose of targeting magnetite cubic nanoparticles.²³ The binding region is made up of a protein sequence that shows a preference for residues of a basic nature, such as lysine. Molecular dynamics (MD) simulations revealed that lysine had an affinity for a specific magnetite face, namely the [100] magnetite surface, indicating that basic groups are strong binders to the magnetite surface. In general, additives such as bound proteins can lower the surface energy of a developing crystal face, leading to the stabilisation of that face and deceleration of its growth.²⁴ This, in turn, results in the specific face affecting the final particle morphology.

By adapting our understanding of the function of MIA and biomineralisation proteins, it is possible to dope reactions with 'additives', compounds added for the purpose of influencing the magnetite product formation, whether that be in the production of homogeneous particles with a tight size distribution or controlling the shape of the MNP.

Equipped with the knowledge that amine-rich lysine binds strongly to the magnetite surface leading to control over the morphology of the forming particles, attention was then drawn upon utilisation of bioinspired compounds consisting of amine groups. Specifically, our previous study focused on the effect of an ethylenediamine (EDA) series of additives in a continuous flow mixing system,²⁵ one of which being Tetraethylenepentamine (TEPA). This EDA has been studied as an additive via MD modelling and experimental data of batch RTCP, revealing its ability to inhibit growth of the [111] crystal face of magnetite, slowing its growth, and thus resulting in well-defined octahedral particles.²⁴

TEPA is an ethylenediamine based alkylamine that has been studied as an additive, with molecular dynamics (MD) modelling and experimental data of batch RTCP revealing the amine's ability to inhibit growth of the [111] crystal face of magnetite, slowing its growth and resulting in well-defined octahedral particles.²⁴ The addition of TEPA has been found to be highly effective in producing morphologically consistent octahedral MNP, exhibiting a high degree of shape control in co-precipitation reactions.²⁴

Batch manufacturing is often preferred as it requires simpler, cheaper, and widely available equipment. Continuous manufacturing, however, can ensure higher reproducibility, consistency, and precision of critical quality attributes of products under steady state operating conditions.^{26–29} Magnetic nanoparticles, such as SPIONs (superparamagnetic iron oxide nanoparticles), have been produced under a variety of synthesis methodologies that involve continuous processing, including ambient temperature precipitation^{30–33} oxidative precipitation,³⁴ hydrothermal synthesis,³⁵ thermal decomposition³⁶ and high temperature precipitation.³⁷

When operating on the small scale, SPION production is often done using fluidic synthesis. For example, millifluidics have been employed to successfully produce both maghemite³⁸ and magnetite³⁹ particles. In the latter case, Mms6 was also utilised to modify magnetite precipitation leading to faceted nanoparticle production, however due to the small scale of the set-up yields were predictably low. Small scale production and the need for millifluidic set-ups to use millimetric channels to ensure laminar flow render this flow system unsuitable for industrial scale-up. Alternatives are thus needed to ensure quality product manufacture at higher yields.

Scaling up of RTCP processes requires increase of the space-time-yield of the overall process, meaning shorter residence times are needed while maintaining the quality of the end product. To accomplish this, mixing - recognised as the rate limiting step in precipitation processes - needs to be more efficient. Static mixers are often utilised for this purpose as they can provide very efficient mixing under certain continuous flow conditions. In addition, continuous flow static mixing is inherently scalable with regards to flow rates, thus allowing for direct scale up for applications in industrial scale production.

Whereas high temperature precipitation using surfactants³⁷ had shown the highest reported magnetite production rate of 2.6 g h⁻¹ (62 g day⁻¹) to date, our previous study utilised both the benefits of continuous flow static mixing and the implementation of a series of EDA additives to surpass this by achieving yields of over 310 g day⁻¹, while still producing high-quality, magnetic, faceted magnetite nanoparticles.²⁵

In the study presented in this paper focus is on optimising the reaction conditions by which particles are formed under co-precipitation conditions by systematically varying both the iron and base concentrations. From there, we systematically vary the ferric ratio between 0.2 - 0.7 to ascertain the influence on magnetic quality of particles formed. We then further research the effect of TEPA on particles formed alongside a variation in ferric ratio to further establish optimum conditions for scaled-up production of highly faceted MNP.

Materials and Methods

Ultrapure MilliQ water (Merck MilliQ integral purification system) was used. All reagents were purchased from Sigma Aldrich unless stated otherwise and used as purchased.

Continuous Flow Mixing

Two Watson Marlow 520DuN (Zwijnaarde, Belgium) cased peristaltic pumps were used, with one attached to the NaOH feed and the other attached to the Fe solution feed. Mixing occurred in a plastic Y connector which led to the collection vessel. Both pumps were set to 10 rounds per minute. When both pumps were running concurrently this setup resulted in a residence time of approximately 2s for the mixed solution.

Fe solution was fed through one pump, whereas NaOH solution was co-currently fed through the other pump (Figure 1

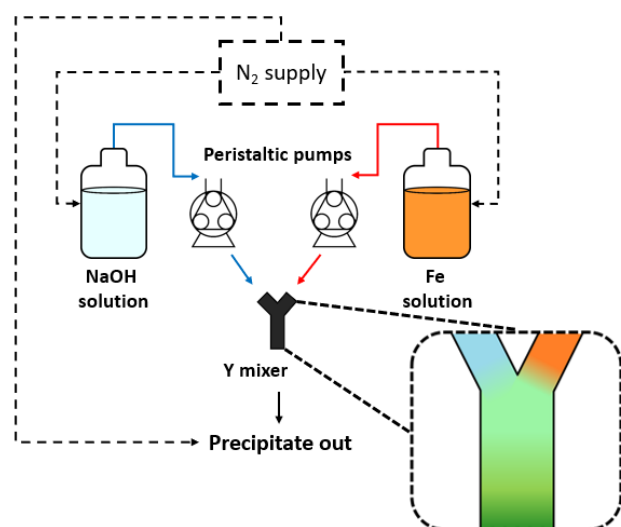


Figure 1. Schematic of experimental set-up for the continuous flow mixing set-up including 2 pumps, 2 feed solutions, a collected precipitate solution, and a Y-mixer. Supply routes are designated with arrows; feed and collected routes are solid lines and N₂ gas supply in dashed lines.

in a 1:1 flow ratio. Feed solutions each contained a magnetic stirrer bar, with the solutions placed on magnetic plates so as to be under constant mild stirring throughout the experimental run. All solutions (feeds and product output) were constantly supplied with N₂ throughout the run to ensure the solutions were sparged of oxygen, thus minimising the possibility of unwanted oxidation occurring at any stage of the precipitation process. The feed solutions were left to stir for at least 5 minutes under a constant atmosphere of N₂ prior to mixing to ensure deoxygenation was complete.

Modified lids were used to avoid the re-dissolution of O₂ into any of the three solutions (Fe solution stock, NaOH stock, collection vessel) during the experimental runs. These modified lids incorporated 3 openings: one for the pump feed tubing, one for the N₂ supply, and the third with tubing that allowed for gas/pressure to escape the vessel.

Once the initial 5 minutes of stirring of the feed solutions was complete, both peristaltic pumps were turned on (counterclockwise flow) for mixing to occur.

The collected particles were magnetically separated, washed three times with deoxygenated MilliQ water, and dried in a vacuum oven at 40 °C overnight. The particles were then ground with a pestle and mortar for analysis.

To minimise the possibility of cross-contamination from previous runs the system was flushed out with in-house ultrapure MilliQ water until the fluid ran clear from the

Table 2. Experimental conditions for the optimisation of TEPA concentration with ferric ratio

Ferric ratio	0.40	0.45	0.50	0.55	0.60	Experimental Number
TEPA						
1:100	1	2	3	4	5	
1:10000	6	7	8	9	10	

collection tube. The flow was then reversed on both pumps (clockwise) and MilliQ water was then left to flow out of the feeding tubes, again, until the water ran clear.

Characterisation

Transmission electron microscope (TEM): For sample analysis of magnetic nanoparticles, a 1 mg mL⁻¹ suspension of nanoparticles was sonicated for 1 minute in hexane, after which a 10 µL sample was dropped onto a carbon coated copper TEM grid and allowed to dry down for a minimum of one hour. Grids were imaged using a FEI Tecnai G2 Spirit electron microscope (Thermo Scientific, Waltham, MA, United States) and the TEM images were analysed using ImageJ software (v1.52, public domain, National Institute of Health, MD, USA). For each sample over 200 particles were randomly selected for measurement. For details on particles size and shape analysis see supplementary information of Norfolk et al.²⁴

X-ray diffraction (XRD): XRD data of samples was collected by analysis of dry iron oxide nanoparticles in a Bruker D8 powder diffractometer (Bruker, Coventry, United Kingdom). Diffraction images were collected at 0.022-degree increments from 20–80 degrees, using a fixed wavelength of $\lambda = 1.54178 \text{ \AA}$ from a Cu K α X-ray source.

Vibrating sample magnetometry (VSM): Magnetic susceptibility and saturation magnetisation were measured on a known quantity (1–5 mg weighed with an accurate mass balance) of dry iron oxide nanoparticles using a MPMS 3 SQUID magnetometer (Quantum Design, Surrey, United Kingdom) in vibrating sample mode, with the samples packed in size 3 gelatine capsules and immobilised with polytetrafluorethylene (PTFE) tape. The samples were run at 300 K between -3 and 3 T with a sweep rate of 0.075 T s⁻¹.

Results

Co-precipitation of MNP generally offers poor control over the morphology of particles formed compared to less green synthetic methods. As biomineralisation proteins are capable of drastically altering the morphology of MNP formed under ambient conditions, it follows that compounds containing similar active functionalities may exert similar influence over the morphology of synthesised particles.

Our previous study revealed that the addition of EDA additives raised the percentage of faceted (defined diamond,

Table 1. Experimental conditions for the optimisation of Fe and NaOH feed concentration.

mM Fe	Control – No additive		
	Experimental Number		
10	1	2	3
20	4	5	6
30	7	8	9
NaOH	300	500	1000

hexagonal, or square shaped) particles formed under co-precipitation conditions utilising a continuous flow static mixer, forming 84% faceted particles, a significant increase on the 34% observed in the control reaction.²⁵ We intend to build upon this work, identifying optimal conditions by which highly faceted MNP may be facilitated by the addition of TEPA, the most effective of the EDA based additives, and produce particles which are both highly defined and exhibit the highest saturation magnetisation possible.

Optimisation of Fe and NaOH feed concentrations

Previous fluidic experiments under millifluidic conditions were found to require optimisation to produce the highest quality

particles.³⁹ Varying the Fe and NaOH feed concentrations altered the quality of MNP product formed, with an optimum being established prior to the full study being conducted.³⁹

In the journey to establishing the ideal conditions for the large-scale production of co-precipitated magnetite, it is important to screen for conditions which produce the highest quality MNP.

Three different concentrations of iron and NaOH have been tested to cover each possible variation. The iron concentrations tested were 10, 20, and 50 mmol Fe with 50 mmol Fe previously being the standard concentration used for each of our batch,²⁴ millifluidic,³⁹ and continuous flow static mixing work. The representative TEM images and data for these reactions can be seen in Figure 2a-e.

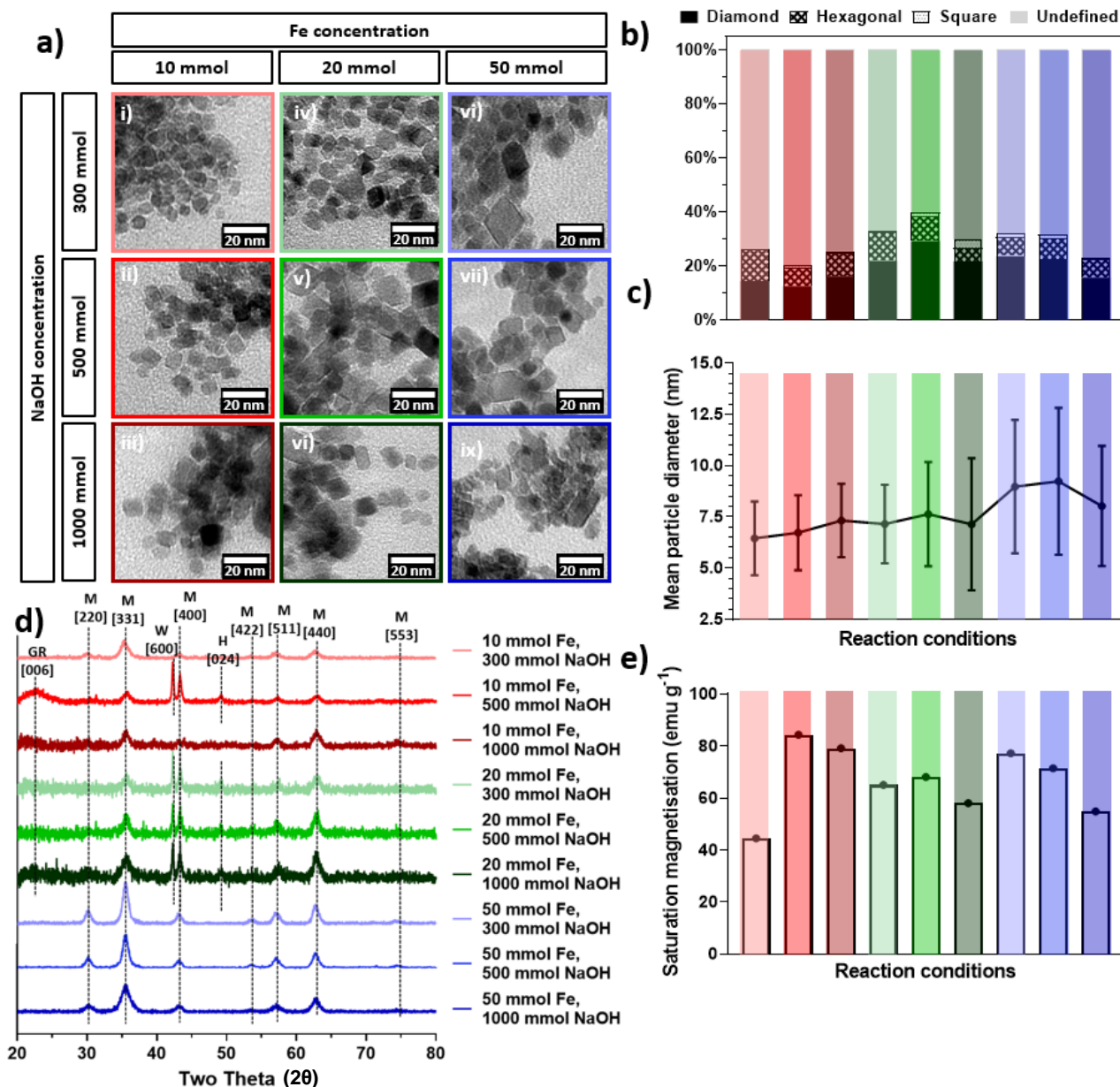


Figure 2. Comparison of effect of changing ferric ratio at high (1:100, solid) and low (1:10000, dashed outline) TEPA:Fe ratios. **a)** Representative TEM images; **b)** XRD data where M = magnetite, H = hematite, and GR = green rust **c)** comparison of shape analysis results; **d)** comparison of mean particle size and standard deviation; **e)** saturation magnetisation data.

The shape distribution in Figure 2b showed each reaction formed between 23-44% faceted particles. The lower iron concentration of 10 mmol produced particles with the least defined shape, however variability between each of the reaction conditions was not significant, with undefined particles being the major constituent of each sample. This system has been noted to produce the most defined MNP with no addition of additives, producing 34% faceted particles in our prior work.²⁵ As the [111] crystallographic plane of magnetite has the lowest surface energy, these facets are favoured during fast reactions where particle nucleation and growth rates are high, which facilitate the formation of the most energetically favourable morphology.⁴⁰ In contrast, slower reaction rates have been observed to promote the equilibrium growth of facets, producing less defined morphologies.⁴¹ Consequently, the rapid timescale (< 2 s) of the continuous flow static mixer may promote the formation of octahedral particles incorporating energetically favourable [111] facets.

The size of particles formed (Figure 2c) ranged from 6.4 ± 1.8 nm (10 mmol Fe, 300 mmol NaOH) to 9.2 ± 3.6 nm (50 mmol Fe, 500 mmol NaOH). Particle size increased with iron concentration, with larger particles forming at higher iron concentrations as more iron is available for the formation of MNP.

XRD of the reactions (Figure 2d) suggested a higher level of particle purity was observed for the higher Fe concentration of 50mM, whereas lower iron concentrations (20, 10 mmol) exhibited the presence of non-magnetite iron oxide impurities of green rust, wüstite and hematite, appearing as additional peaks observed for $2\theta = 28.8, 42.3,$ and 49.2 respectively.

Whereas most of the particles formed were highly magnetic (> 65 emu g^{-1}), the effect of impurities may have been reflected in the saturation magnetisation. For all three Fe concentrations, saturation magnetisation dropped when going from 500mmol to 1000mmol NaOH, with 20mmol and 50mmol Fe showing similar saturation magnetisation values (app. 70 emu gr^{-1} to 60 emu gr^{-1}), and 10mmol Fe being significantly higher (app. 85 emu g^{-1} to 70 emu g^{-1}). The presence of impurities may have affected the 20mmol Fe set, lowering its saturation

magnetisation to values observed for 50mmol Fe. Saturation magnetisation values at 300mmol NaOH decreased with decreasing Fe concentration, with the highest value being 77.3 emu g^{-1} for 50mmol Fe, dropping to 65 and 45 emu gr^{-1} for 20mmol and 10mmol Fe respectively (Figure 2e).

Our next studies were conducted at a Fe ratio of 50 mmol to maximise output of particles within a given time (the space-time-yield), whilst selecting the NaOH concentration which consistently produced highly magnetic particles, 500 mmol.

Optimisation of Fe^{3+}/Fe^{2+} ratio

Another manner by which the properties of MNP can be either tailored or optimised without the addition of further additives is by altering the ratio of ferric to ferrous iron within the reaction solution.⁴² RTCP is a complex reaction system whereby magnetite is formed through a series of intermediate ferric and ferrous iron oxides as the pH of the reaction increases.¹⁸ As magnetite natively contains a 2:1 stoichiometric ratio of ferric (Fe^{3+}) and ferrous (Fe^{2+}) iron, the highest proportion of magnetite is formed close to a ferric ratio of 0.66. However, the synthesis is sensitive to oxidation. In this study the ferric ratio was systematically varied with each reaction containing the same total concentration of iron ions, however the Fe^{3+}/Fe^{2+} ratio was varied from 0.2 (ferrous rich) to 0.7 (ferric rich). Each reaction was conducted using a 50 mmol Fe solution and representative TEM images, size, shape, magnetism, and XRD data for each sample are shown in Figure 3.

The size of particles formed changed drastically across the varying ferric ratios, with the size and standard deviation (SD) generally decreasing as the ferric ratio increased. Figure 3b reveals the smallest particles (7.7 ± 2.2 nm) formed at a 0.7 ratio, with the largest forming at the 0.2 ratio (22.7 ± 11.5 nm). This trend has previously been observed in a millifluidic system, whereby it was concluded that variation of the ferric ratio could be utilised as a powerful tool to tailor the mean particle size formed.³⁹

The percentage of faceted particles present varied between reactions, with generally 29 – 41 % faceted particles being

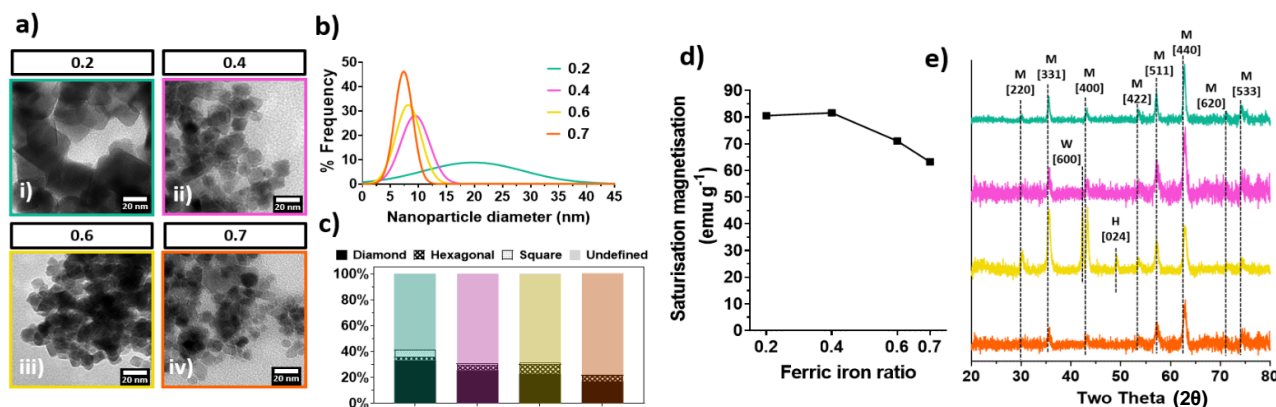


Figure 3. Comparison of effect of changing Fe^{3+}/Fe^{2+} ratio between the 0.2 - 0.7 range. a) Representative TEM images; b) frequency distribution of nanoparticle size; c) shape distribution; d) saturation magnetisation e) Annotated X-ray Diffraction (XRD) data of the samples formed across the 0.2 - 0.7 ferric ratio range, where M = magnetite, W = wüstite, and H = hematite.

formed across each sample. These results are comparable to the particles formed in our prior study.²⁵

Notably, highly magnetic particles are formed from the lower ferric ratios, which was previously not observed in the millifluidic system.⁴² Saturation magnetism remains reasonably consistent across the 0.2 - 0.5 ferric range, between 79.7 – 81.6 emu g^{-1} . Saturation magnetism begins to decline past the 0.5 ratio, with the 0.7 ratio producing particles with a saturation magnetisation of 63.2 emu g^{-1} . In the millifluidic system magnetism rose until 0.5 - 0.6 then declined significantly, producing particles with an 18.1 saturation magnetisation at a 0.7 ferric ratio.

XRD of each of the varying ferric ratio samples (Figure 3e) showed magnetite was the primary constituent for each of the

reactions. At the 0.7 ratio the XRD was less defined, with a high signal to noise ratio suggesting less crystalline material present. Interestingly, the 0.2 ferric ratio contained minimal impurities, with wüstite and hematite peaks appearing in the later reactions. This contrasts with previous studies suggesting the highest purity magnetite occurs at ratios closer to the ideal 2:1 ratio observed in nature. A range of ferric ratios are viable for magnetite production from this system, offering the potential to tune particle size via simple adjustment of the $\text{Fe}^{3+}/\text{Fe}^{2+}$ ratio.

Optimisation of TEPA concentration with ferric ratio

Building upon our study of the effect of ferric ratio on the properties of MNP formed within the continuous flow static mixer, we selected a tighter range of ferric ratios to ascertain

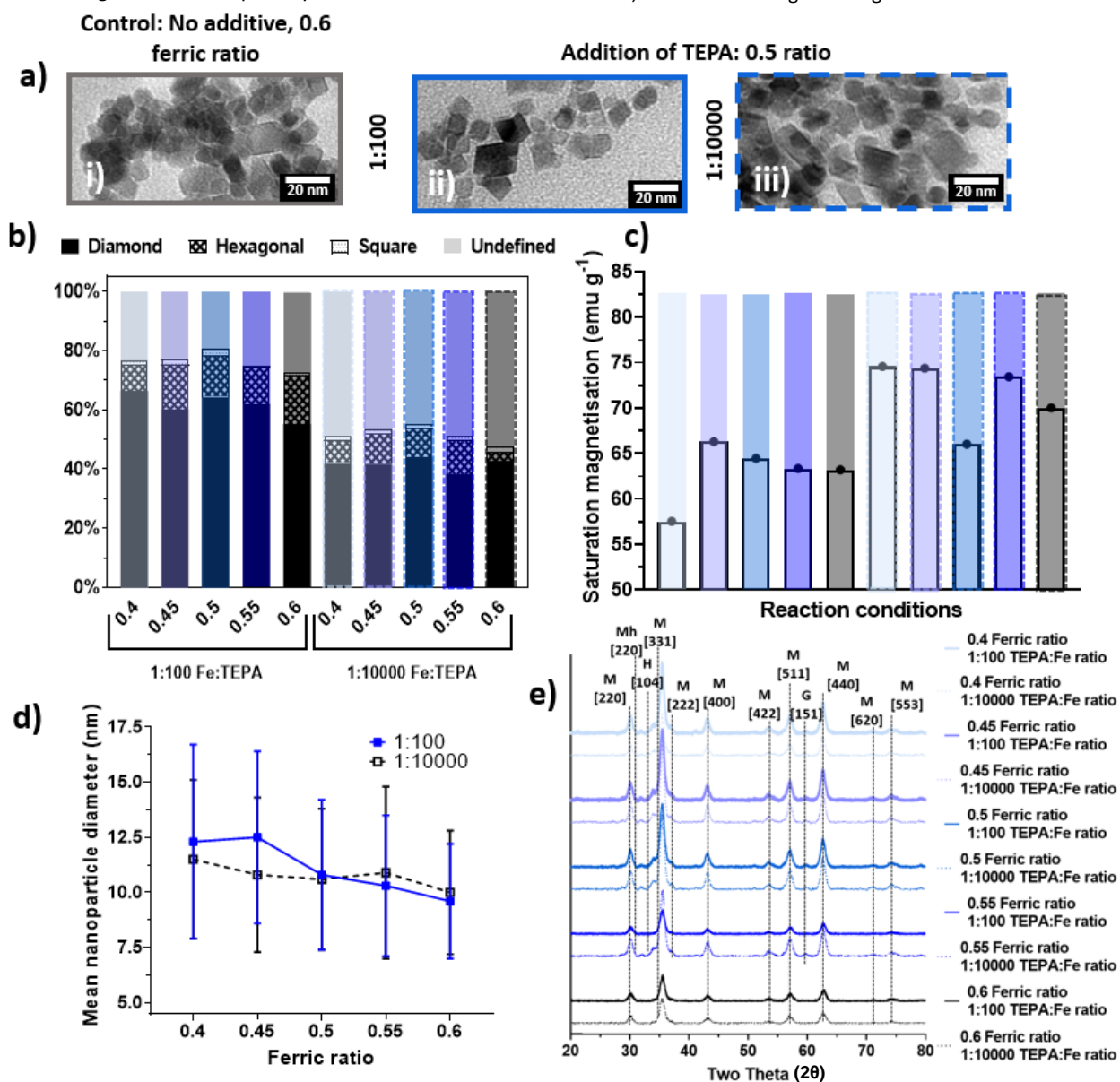


Figure 4. Comparison of effect of changing ferric ratio (0.4 – 0.6) at high (1:100, solid) and low (1:10000, dashed outline) TEPA:Fe ratios. **a)** Comparative TEM images of **i)** control particles, **ii)** 0.5 $\text{Fe}^{3+}/\text{Fe}^{2+}$ ratio 1:100 additive/Fe, **iii)** 0.5 $\text{Fe}^{3+}/\text{Fe}^{2+}$ ratio 1:10000 additive/Fe; **b)** comparison of shape analysis data **c)** comparison of saturation magnetisation; **d)** comparison of mean particle size and standard deviation; **e)** XRD data where M = magnetite, Mh = maghemite, H = hematite, and G = goethite.

the influence of additives around the previously believed ideal ferric ratio, at smaller increments than previously tested (0.4, 0.45, 0.5, 0.55, and 0.6).

Throughout our previous studies, the concentration of additive has been observed to significantly influence the amount of faceted particles precipitated.²⁴ Our previous study into the result of additive addition alongside the effect of increasing additive length revealed that additive effectiveness increases with chain length, up to the point of pentaethylenhexamine at which point diminishing returns were observed as the excess amine functionalities were deemed to poison the reaction. As such, TEPA was selected to produce the highest proportion of faceted particles. As it is economically favourable to use little additive while maximising additive efficacy, two additive/Fe ratios have been tested: high (1:100) and low (1:10000). This allows us to observe the difference in percentage of faceted particles formed with a 100-fold difference in additive concentration. In our previous study, a difference of 15–20% faceted particles was observed between the use of a 1:100 and 1:10000 ratio.²⁵

The percentage of faceted particles, particle size, XRD, magnetic data, and select TEM images can be seen in Figure 4. As the ferric ratio increased the particles were observed to decrease in size and polydispersity, with tighter size distributions occurring between the 0.4 and 0.6 range. This trend was also seen for the control system. Of interest here is the fact that both samples with additives had comparable particle sizes to those of the control sample at the same ferric ratio, indicating towards the presence of TEPA having a minimal effect on the overall particle size, with the size being more influenced by the ferric ratio.

The addition of TEPA, however, does appear to affect the amount of faceted particle formed (Figure 4b) and the degree of magnetism (Figure 4c). Indeed, the control samples showed the lowest overall percentage of faceted particles (22–42%) and had the highest saturation magnetisation (app. 62–83 emu g⁻¹). The 1:10000 TEPA:Fe system followed, having a higher overall percentage of faceted particles (48–56%), and lower saturation magnetisation (app. 65–75 emu g⁻¹). The 1:100 TEPA:Fe system had the highest amount of additive present, leading to the highest percentage of faceted particles (73–81%), but also had the lowest saturation magnetisation (app. 58–66 emu g⁻¹). In any case, the magnetism remained high (> 65 emu g⁻¹) for almost all of the samples measured. The above further solidify the idea of using additives for tailoring the degree of magnetism and of faceted MNP formed.

XRD data revealed each sample consisted primarily of magnetite with minor maghemite, hematite, and goethite impurities in some of the samples. The 0.6 ratio XRD again appears to contain the smallest proportion of impurities, however, did not offer improved magnetic properties.

Discussion

From the three studies conducted varying Fe and NaOH feed concentration, ferric ratio, and finally ferric ratio in conjunction

with the addition of TEPA as an additive at high and low concentration, several key findings have been identified.

The Fe feed concentration appears to play a more significant role than the NaOH feed concentration, which is in line with expectations as the Fe is the limiting factor in the amount of product formed due to NaOH being in excess. Changes in NaOH concentration had small effects on the particle sizes formed, with average sizes increasing slightly from 6.4 to 9.3 nm as NaOH concentration went from 300mmol to 1000mmol. As expected, the supply of Fe to the magnetite formation had a much more dramatic effect on particle size, whereby size and size variability dropped with increasing ferric ratio. Sizes varied from app. 23 to 8nm as ferric ratio went from 0.2 to 0.7. This behaviour was seen irrespective of the presence and concentration of additive, indicating that overall particle size is mostly driven by Fe availability.

Magnetisation measurements notably revealed that within the 0.2–0.7 ferric ratio reactions magnetism was high at the low ratios, which has previously not been observed. The larger particle size of the lower ratio reactions suggests the particles may have had longer to mature. As the reactions were left to develop, mineral dehydration can occur with ferrous rich iron oxides converting to magnetite with time.¹⁸ This occurs over a longer time-scale than magnetite which is precipitated within the timescale of the reaction, and may explain the larger particles. As the lower ratio sample (0.2) was not immediately magnetic on exit from the continuous flow static mixer (dark green and non-magnetic, later developing to black and magnetic), this lowers its viability for scale-up despite its high magnetism as additional time would be required for MNP maturation to form the desired product. In the case of reactions closer to the “optimal” ferric ratio, the MNP formed were fully nucleated and grown within the timeframe of the reaction, being magnetic on formation. Due to transport in solution for analysis, it is likely some oxidation occurred which may account for the drop in magnetism observed at the 0.6 ratio, which produced the highest magnetism within the millifluidic system.⁴² For the system varying NaOH concentration, a drop in magnetism was observed for all 3 of the mmol Fe samples with increase of NaOH concentration from 500 mmol to 1000 mmol, suggesting there is an optimal ratio of Fe/NaOH to be determined, requiring further investigation.

Our previous work has found TEPA to be highly effective at promoting the formation of octahedral MNP via inhibition of the [111] surface of magnetite during the growth face of particle development.²⁴ TEPA has previously successfully been utilised as an additive within the continuous flow static mixer system, producing 84% faceted particles at a 0.6 ferric ratio with a 1:100 additive/Fe ratio. TEPA exhibited a similar degree of effectiveness across the TEPA optimisation study, 73 - 81% showcasing the robustness of additive assisted MNP synthesis. As TEPA operates by selective binding to the [111] magnetite surface, higher additive concentrations allows greater growth inhibition, with an optimal concentration of 1:62.5 TEPA/Fe producing 97% faceted particles within a batch RTCP.²⁴ This ideal concentration may vary in a system which produces smaller particles, as a larger proportion of additive would be required to form a

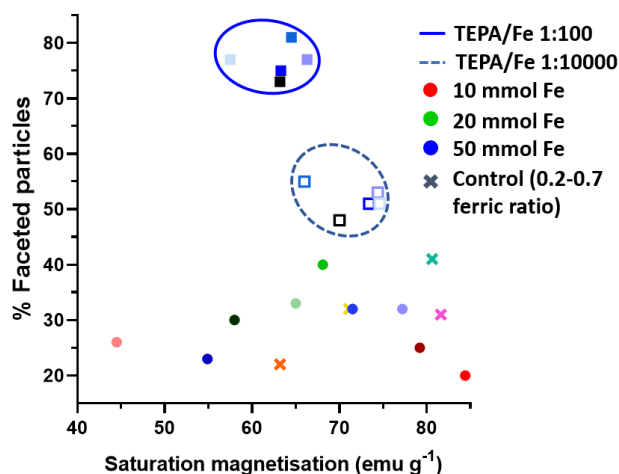


Figure 5. Saturation magnetisation plotted against percentage of faceted particles for the Fe/NaOH feed concentration optimisation and the TEPA concentration with ferric ratio optimisation.

monolayer due to the increased surface area of particles forming. As such, a greater quantity of additive may be required than the 1:100 currently tested to produce octahedral particles.

Figure 5 depicts the relationship between TEPA addition, saturation magnetisation, and faceted particles formed for the Fe/NaOH feed concentration optimisation and the TEPA concentration with the ferric ratio. From the graph it is clear that the addition of TEPA increases the percentage of faceted particles formed. Notably, saturation magnetisation decreases on addition of the higher additive concentration, with an average decrease of 8.7 emu g^{-1} . This inverse proportionality of increasing percentage of faceted particles with decreasing saturation magnetisation may occur as the result of TEPA contaminating the forming particles, becoming incorporated within their structure, and disrupting uniform crystal structure. However, the particles formed on addition of 1:10000 TEPA/Fe appear highly magnetic, outperforming many of the samples formed with no additive. Faceted particles exhibiting defined morphologies such as octahedral may be more crystalline than undefined particles, raising their saturation magnetisation. As such, these two competing factors may result in an interplay between particle properties, with a compromise between percentage faceted particles and particle magnetism being required.

Conclusions

Continuing our study on the use of additives within RTCP systems, in this body of work we sought to further our understanding of the synthesis of highly faceted MNP utilising a continuous flow static mixer and TEPA as an additive.

From this work we have identified two methods by which the size of particles formed can be tuned within the continuous flow static mixer. Varying the concentration of the Fe feed solution limits the amount of iron available for particle growth within the short residence time of the continuous flow system, allowing control over particle growth. Variation of the ferric ratio. As the size of MNP has a significant influence on the

magnetic properties of the nanoparticle product, it is key to be able to exert control over this.

The addition of TEPA was observed to have a marked effect on the proportion of faceted particles formed at both a 1:100 and 1:10000 ratio, with the ferric ratio of the reaction (between 0.4-0.6) having minimal impact on the proportion of faceted particles present. This opens the field to synthesising octahedral shaped particles of tailored size, whether it be by selective use of lower ferric ratios within the continuous flow static mixing system, or utilising a batch RTCP system to produce larger particles.²⁴

These studies showcase the strength of TEPA in modulating the morphology of particles formed under RTCP conditions. The ability to produce $\sim 300 \text{ g}$ of tailored nanomaterials whilst tailoring the size of particles formed is a promising prospect and a significant breakthrough in the journey to scalable green magnetite.

Conflicts of interest

There are no conflicts to declare.

Abbreviations

- EDA:** ethylenediamine
- MD:** molecular dynamics
- MIA:** magnetite interacting Adhirons
- MNP:** magnetite nanoparticles
- MTB:** magnetotactic bacteria
- RTCP:** room temperature co-precipitation
- SPION:** superparamagnetic iron oxide nanoparticle
- TEM:** transmission electron microscopy
- TEPA:** tetraethylenepentamine
- VSM:** vibrating-sample magnetometry
- XRD:** X-ray diffraction

Acknowledgements

This work was supported by funding from the EPSRC (grant number EP/P006892/1) and the University of Sheffield's EPSRC DTP allowance (grant number EP/M508135/1) funds Laura Norfolk's PhD. We thank S. Tsokov, and C. Hill (Sheffield Electron Microscopy unit) for TEM training and HRTEM, Nicola Morley and Zhao Leong for support with VSM, and Craig Robertson for support with powder XRD.

References

- 1 M. J. Eckelman, J. B. Zimmerman and P. T. Anastas, *J. Ind. Ecol.*, 2008, **12**, 316–328.
- 2 S. V Patwardhan, J. R. H. Manning and M. Chiacchia, *Curr. Opin. Green Sustain. Chem.*, 2018, **12**, 110–116.
- 3 S. S. S. Scott M. Bird, Johanna M. Galloway, Andrea E. Rawlings, Jonathan P. Bramble, *J. Mater. Chem. Nanoscale*, 2015, **7**, 1–12.
- 4 E. Y. Mora Mendoza, A. Sarmiento Santos, E. Vera López, V.

- Drozd, A. Durygin, J. Chen and S. K. Saxena, *J. Mater. Res. Technol.*, 2019, **8**, 2944–2956.
- 5 S. Mornet, S. Vasseur, F. Grasset and E. Duguet, *J. Mater. Chem.*, 2004, **14**, 2161–2175.
- 6 J. P. Fortin, C. Wilhelm, J. Servais, C. Ménager, J. C. Bacri and F. Gazeau, *J. Am. Chem. Soc.*, 2007, **129**, 2628–2635.
- 7 Z. Li, M. Kawashita, N. Araki, M. Mitsumori, M. Hiraoka and M. Doi, *Mater. Sci. Eng. C*, 2010, **30**, 990–996.
- 8 J. H. Park, G. Saravanakumar, K. Kim and I. C. Kwon, *Adv. Drug Deliv. Rev.*, 2010, **62**, 28–41.
- 9 P. Sharma, S. Brown, G. Walter, S. Santra and B. Moudgil, *Adv. Colloid Interface Sci.*, 2006, **123**, 471–485.
- 10 D. Maity, S. N. Kale, R. Kaul-Ghanekar, J. M. Xue and J. Ding, *J. Magn. Magn. Mater.*, 2009, **321**, 3093–3098.
- 11 M. Unni, A. M. Uhl, S. Savliwala, B. H. Savitzky, R. Dhavalikar, N. Garraud, D. P. Arnold, L. F. Kourkoutis, J. S. Andrew and C. Rinaldi, *ACS Nano*, 2017, **11**, 2284–2303.
- 12 A. Nikitin, M. Fedorova, V. Naumenko, I. Shchetinin, M. Abakumov, A. Erofeev, P. Gorelkin, G. Meshkov, E. Beloglazkina, Y. Ivanenkov, N. Klyachko, Y. Golovin, A. Savchenko and A. Majouga, *J. Magn. Magn. Mater.*, 2017, **441**, 6–13.
- 13 H. Fatima, D. W. Lee, H. J. Yun and K. S. Kim, *RSC Adv.*, 2018, **8**, 22917–22923.
- 14 A. G. Roca, L. Gutiérrez, H. Gavilán, M. E. Fortes Brollo, S. Veintemillas-Verdaguer and M. del P. Morales, *Adv. Drug Deliv. Rev.*, 2019, **138**, 68–104.
- 15 P. Hugouenq, M. Levy, D. Alloyeau, L. Lartigue, E. Dubois, V. Cabuil, C. Ricolleau, S. Roux, C. Wilhelm, F. Gazeau and R. Bazzi, *J. Phys. Chem. C*, 2012, **116**, 15702–15712.
- 16 S. K. Shaw, A. Biswas, A. Gangwar, P. Maiti, C. L. Prajapat, S. Singh and N. K. Prasad, *J. Magn. Magn. Mater.*, 2019, **484**, 437–444.
- 17 A. H. Lu, E. L. Salabas and F. Schüth, *Angew. Chemie - Int. Ed.*, 2007, **46**, 1222–1244.
- 18 A. E. Rawlings, J. P. Bramble, A. M. Hounslow, M. P. Williamson, A. E. Monnington, D. J. Cooke and S. S. Staniland, *Chem. - A Eur. J.*, 2016, **22**, 7885–7894.
- 19 M. C. Mascolo, Y. Pei and T. A. Ring, *Materials (Basel)*, 2013, **6**, 5549–5567.
- 20 S. S. Staniland and A. E. Rawlings, *Biochem. Soc. Trans.*, 2016, **44**, 883–90.
- 21 A. E. Rawlings, J. P. Bramble, R. Walker, J. Bain, J. M. Galloway and S. S. Staniland, *Proc. Natl. Acad. Sci.*, 2014, **111**, 16094–16099.
- 22 M. J. Mcguire, S. Li and K. C. Brown, in *Biosensors & Biodetection*, 2009, pp. 291–321.
- 23 A. E. Rawlings, J. P. Bramble, A. A. S. Tang, L. A. Somner, A. E. Monnington, D. J. Cooke, M. J. McPherson, D. C. Tomlinson and S. S. Staniland, *Chem. Sci.*, 2015, **6**, 5586–5594.
- 24 L. Norfolk, K. Kapusta, D. J. Cooke and S. S. Staniland, *Green Chem.*, 2021, **23**, 1–12.
- 25 S. S. Laura Norfolk, Georgina Zimbitas, Jan Sefcik, .
- 26 C. J. Brown, T. Mcglone, S. Yerdelen, V. Srirambhatla, F. Mabbott, R. Gurung, M. L. Briuglia, B. Ahmed, H. Polyzois, J. McGinty, F. Perciballi, D. Fysikopoulos, P. Macfhionnghaile, H. Siddique, V. Raval, T. S. Harrington, A. D. Vassileiou, M. Robertson, E. Prasad, A. Johnston, B. Johnston, A. Nordon, J. S. Srai, G. Halbert, J. H. Ter Horst, C. J. Price, C. D. Rielly, J. Sefcik and A. J. Florence, *Mol. Syst. Des. Eng.*, 2018, **3**, 518–549.
- 27 V. Svoboda, P. Macfhionnghaile, J. McGinty, L. E. Connor, I. D. H. Oswald and J. Sefcik, *Cryst. Growth Des.*, 2017, **17**, 1902–1909.
- 28 P. MacFhionnghaile, V. Svoboda, J. McGinty, A. Nordon and J. Sefcik, *Cryst. Growth Des.*, 2017, **17**, 2611–2621.
- 29 S. A. Raza, U. Schacht, V. Svoboda, D. P. Edwards, A. J. Florence, C. R. Pulham, J. Sefcik and I. D. H. Oswald, *Cryst. Growth Des.*, 2018, **18**, 210–218.
- 30 M. Simmons, C. Wiles, V. Rocher, M. G. Francesconi and P. Watts, *J. Flow Chem.*, 2013, **3**, 7–10.
- 31 F. Haseidl, B. Müller and O. Hinrichsen, *Chem. Eng. Technol.*, 2016, **39**, 2051–2058.
- 32 P. L. Suryawanshi, S. H. Sonawane, B. A. Bhanvase, M. Ashokkumar, M. S. Pimlapure and P. R. Gogate, *Green Process. Synth.*, 2018, **7**, 1–11.
- 33 J. Bemetz, A. Wegemann, K. Saatchi, A. Haase, U. O. Häfeli, R. Niessner, B. Gleich and M. Seidel, *Anal. Chem.*, 2018, **90**, 9975–9982.
- 34 T. Asimakidou, A. Makridis, S. Veintemillas-Verdaguer, M. P. Morales, I. Kellartzis, M. Mitrakas, G. Vourlias, M. Angelakeris and K. Simeonidis, *Chem. Eng. J.*, 2020, **393**, 124593.
- 35 L. Maurizi, F. Bouyer, J. Paris, F. Demoisson, L. Saviot and N. Millot, *Chem. Commun.*, 2011, **47**, 11706–11708.
- 36 W. Glasgow, B. Fellows, B. Qi, T. Darroudi, C. Kitchens, L. Ye, T. M. Crawford and O. T. Mefford, *Particuology*, 2016, **26**, 47–53.
- 37 J. Mahin and L. Torrente-Murciano, *Chem. Eng. J.*, 2020, **396**, 125299.
- 38 A. Abou Hassan, O. Sandre, V. Cabuil and P. Tabeling, *Chem. Commun.*, 2008, 1783–1785.
- 39 L. Norfolk, A. E. Rawlings, J. P. Bramble, K. Ward, N. Francis, R. Waller, A. Bailey and S. S. Staniland, *Nanomaterials*, 2019, **9**, 1729.
- 40 Z. L. Wang, *J. Phys. Chem. B*, 2000, **104**, 1153–1175.
- 41 A. Mitra, J. Mohapatra, S. S. Meena, C. V. Tomy and M. Aslam, *J. Phys. Chem. C*, 2014, **118**, 19356–19362.
- 42 L. Norfolk, A. E. Rawlings, J. P. Bramble, K. Ward, N. Francis, R. Waller, A. Bailey and S. S. Staniland, *Nanomaterials*, 2019, **9**, 1–15.

Optimisation of a scalable continuous flow synthesis of magnetite nanoparticles using tetraethylenepentamine as an additive

Laura Norfolk,^a Georgina Zimbitas,^b Jan Sefcik^{b,c} and Sarah Staniland^a

Table 1. Table of characterisation for the optimisation of Fe and NaOH feed concentrations.

NaOH concentration (mmol)	Particle size (nm)	% Faceted particles	Saturation magnetisation (emu g ⁻¹)
10 mmol Fe			
300	6.4 ± 1.8	26	44.5
500	6.7 ± 1.8	20	84.4
1000	7.3 ± 1.8	25	79.2
20 mmol Fe			
300	7.1 ± 1.9	33	65.0
500	7.6 ± 2.5	40	68.1
1000	7.1 ± 3.2	30	58.0
50 mmol Fe			
300	9.0 ± 3.3	32	77.2
500	9.2 ± 3.6	32	71.5
1000	8.0 ± 2.9	23	54.9

Table 2. Table of characterisation for the optimisation of ferric ratio.

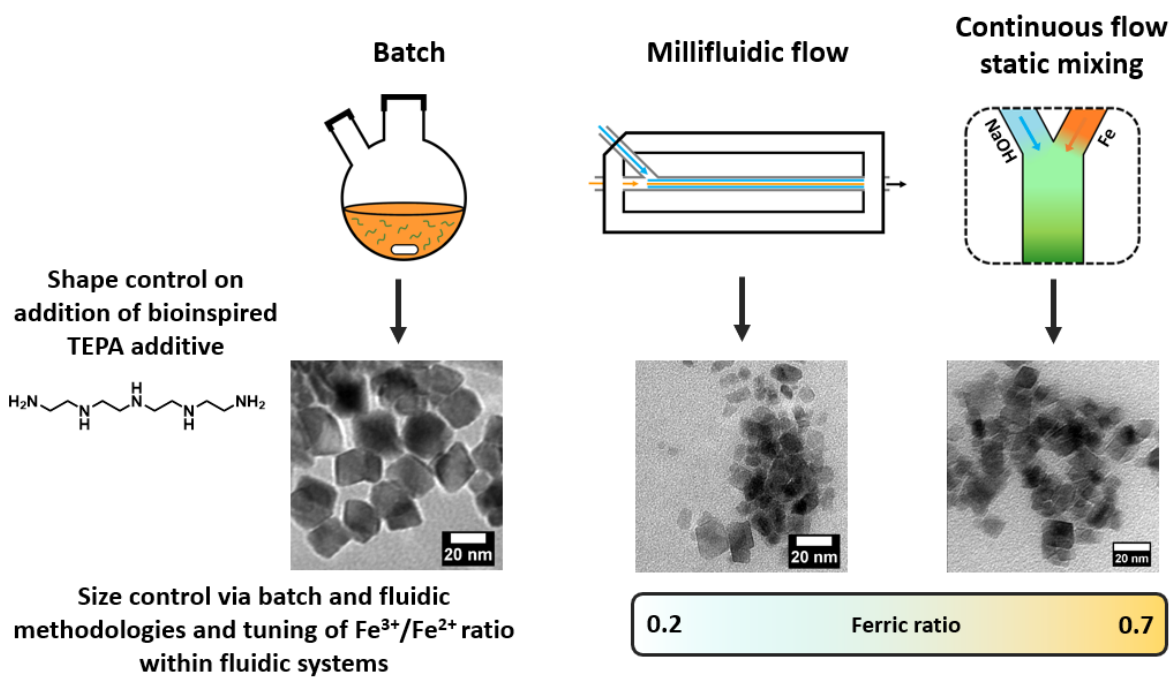
Ferric ratio	Particle size (nm)	% Faceted particles	Saturation magnetisation (emu g ⁻¹)	XRD impurities
0.2	22.7 ± 11.5	41	80.6	N/A
0.4	11.0 ± 4.7	31	81.6	Wüstite, hematite
0.6	9.2 ± 3.6	32	71.1	Wüstite, hematite
0.7	7.7 ± 2.2	22	63.2	Undefined ferric oxides

Table 3. Table of characterisation for the optimisation of TEPA concentration with ferric ratio.

Ferric ratio	Particle size (nm)	% Faceted particles	Saturation magnetisation (emu g ⁻¹)	XRD impurities
1:100 Fe/additive				
0.4	12.3 ± 4.4	77	57.5	Maghemite, hematite, goethite
0.45	12.5 ± 3.9	77	66.3	Maghemite, hematite, goethite
0.5	10.8 ± 3.4	81	64.5	Maghemite, hematite, goethite
0.55	10.3 ± 3.2	75	63.3	Maghemite, hematite, goethite
0.6	9.6 ± 2.6	73	63.2	Maghemite, hematite
1:10000 Fe/additive				
0.4	11.5 ± 3.6	51	74.6	Maghemite, hematite, goethite
0.45	10.8 ± 3.5	53	74.4	Maghemite, hematite, goethite
0.5	10.6 ± 3.2	55	66.0	Maghemite, hematite, goethite
0.55	10.9 ± 3.9	51	73.4	Maghemite, hematite, goethite
0.6	10.0 ± 2.8	48	70.0	Maghemite, hematite

Chapter 8.

Conclusions and Future Work



This chapter concludes the thesis, revisiting the original aims and hypotheses and reflecting on the success of the project. Future work and directions are also discussed, as well as the real world importance of this body of work.

8.1 Conclusions

Throughout this thesis, the idea of drawing inspiration from the forms and functions observed within biomineralisation proteins and their derivatives has been a constant. Starting from the acidic biomineralisation proteins, Mms6 and MmsF, and delving into magnetite interacting Adhirons heavily enriched with basic amino acids, additives inspired by these biomolecules have been curated for use as magnetite control agents. Each of the aims set out within the introduction will be addressed, discussing how they were met and further work which would allow for each research aim to be further explored.

8.1.1 Screening Additives

The first aim of this project was the screening of prospective additive compounds which could be utilised to tailor the properties of MNPs formed under ambient RTCP conditions. This was successfully achieved through the screening of a range of 30 compounds spanning acidic, basic, and mixed-functionality (containing both acidic and basic groups) compounds, alongside amino acids, homopeptides, and polymers such as polysaccharides and carbon backbone-based compounds with varying degrees of backbone flexibility. By investigating a wide range of additives with varying backbone flexibilities and functionalities, a greater understanding of the influence of additives within a RTCP system was established. As particle nucleation and growth operate under two differing mechanisms, current understanding suggests that acidic functionalities are key to the control of nucleation, whereas basic functionalities influence the growth regime of particles.

Prior to this study, several compounds had been identified which were suitable for influencing the size of particles formed under co-precipitation conditions. However, fewer compounds were readily known to tailor the shape of particles formed. Whilst oleylamine and oleic acid, two well-studied additives, found success in producing cubic particles using thermal decomposition conditions,¹⁹⁹ these compounds are insoluble in water rendering them unsuitable for use in RTCP reactions.

This study revealed several starting points for further research by identifying additives

which exhibited a marked effect on the shape of particles formed. TETA, TEPA, and PEHA produced 96, 97, and 91 % faceted particles respectively, showing near homogeneous control over the morphological control of particles formed. The success of these amines at modulating the shape properties of MNPs supports the understanding built upon from MIA proteins that the interaction between basic amines and magnetite surfaces is key to tailoring the shape of particles formed.

The mixed functionality additive L-lysine, containing both an acidic carboxyl group and two amine groups, was found to aid the formation of particles with the lowest polydispersity of each of the additives screened, producing particles of reduced size and standard deviation of 14.3 ± 4.3 nm compared to the 6.5 nm observed in an additive-free control. Shape control was also exhibited, producing 55 % faceted particles. This aspect of influencing both desired morphological properties (shape and size) is promising for the simultaneous control of both the shape and size of MNP with the addition of only a singular additive. 7-Aminoheptanoic acid and 12-aminododecanoic acid each also produced a greater proportion of faceted particles compared to control reactions with reduced mean particle diameter. As each of these compounds were tested at the relatively low amount of 8×10^{-8} mol of additive per 20 mL reaction, their effectiveness at simultaneously tailoring shape and size may be inhibited. As such, future concentration studies on these three additives would reveal further information on both their mode of action and efficacy as additives.

Notably, high-acyl (HA) gellan gum (GG) was found to control the shape of MNPs formed, producing 74 % faceted particles despite no amine groups being present. There are two suspected mechanisms by which HA-GG may exert this effect. As the glycerate sidechains of the polysaccharide backbone exhibit structural similarity to the ethylenediamine series of additives, instead containing ethylenediol groups, these alcohol groups may interact with forming magnetite surfaces in a comparable manner. Secondly, the polysaccharide backbone itself contains multiple ethylenediol groups, meaning the backbone of the polysaccharide may instead be binding to forming particles. By using low-acyl (LA) GG (Figure 8.1) as an additive, these sidechains are removed as a factor and a comparison could be drawn between the additives structure and effect.

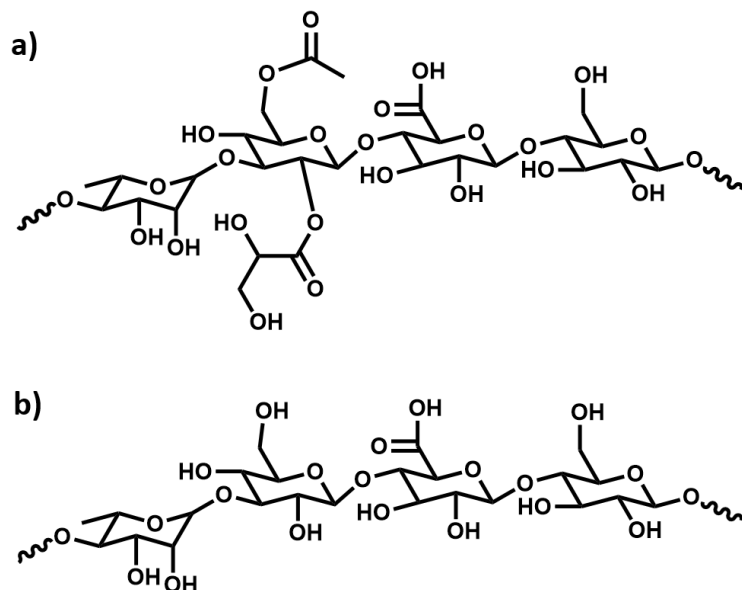


Figure 8.1: Chemical structures of **a)** High-acyl gellan gum (HA-GG), **b)** Low-acyl gellan gum (LA-GG).

To ascertain whether active functionalities spaced out with ethylene groups are ideal for shape control further studies into additives utilising an ethylene spacer between active functionalities must be conducted. By investigating additives such as EDTA and analogous compounds (Figure 8.2), understanding of the effect of this spacer group could be deepened.

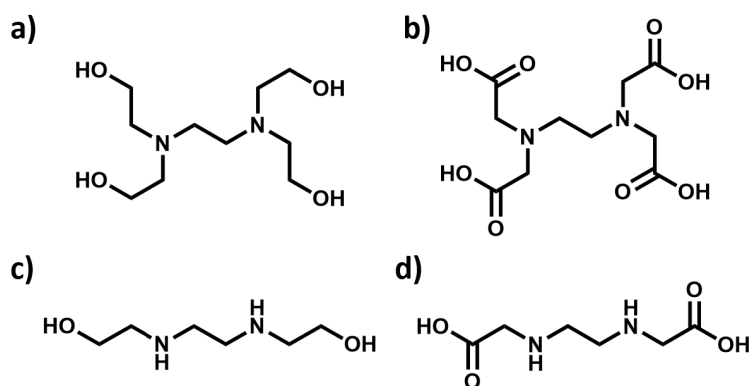


Figure 8.2: Chemical structures of **a)** Ethylenediamine tetracetic acid (EDTA), **b)** N,N,N',N'-Tetrakis(2-hydroxyethyl)ethylenediamine, **c)** Ethylenediamine-N,N'-diacetic acid, **d)** N,N-Bis(2-hydroxyethyl)ethylenediamine.

Interestingly, some additives found to exert influence over MNP formation in prior research such as citric acid were not observed to have a notable effect within this study. As the concentrations selected were in line with the concentration of Mms6 required to exert morphological control *in vitro*, this concentration may not be ideal for additives which do not self assemble. As such, this study could be further developed by screening each additive across a range of concentrations. This is supported by the spermine concentration study which showed an improvement in additive effectiveness as the additive concentration increases. Repeating each additive across a range of concentrations may yield results which are more consistent with the literature.

8.1.2 Additive Optimisation and Understanding

The second aim of this work was upon identification of additives which could significantly tune the morphology of MNPs, to further study their mode of action and utilise DoE principals to develop understanding of how an additive may interact with the RTCP system. As the EDA series produced the most homogeneous shape-controlled particles these additives were selected for further optimisation.

MD modelling of DETA-PEHA was conducted on the [100] (cubic) and [111] (octahedral) surfaces of magnetite to develop understanding of why these additives direct to a primarily octahedral morphology. TETA, TEPA, and PEHA were found to preferentially bind to the [111] magnetite surface, with these amines able to lie flat against this face, binding with multiple amine groups simultaneously which was not seen on the [100] surface. The shorter chain amine, DETA, was found to bind unselectively to both the [100] and [111] surface, consistent with its reduced effectiveness at morphological control, producing 42 % faceted particles compared to >90 % for TETA-PEHA.

This application of MD modelling crucially sheds light on the mechanism by which the EDA series of additives direct the morphology of growing MNPs towards octahedral. Further study into other additives found to be effective would be beneficial, with MD modelling offering potential insight into the binding and efficacy of other compounds. L-lysine has previously been modelled against the [100] face of magnetite, revealing the strong binding

of basic amino acids compared to acidic amino acids.¹²³ Modelling L-lysine alongside other additives such as alkylamines with differing C:N ratios and spacing between amines would allow for the importance of active functionality spacing to be better understood. Due to the structurally more complicated nature of both LA-GG and HA-GG, these additives would not be readily suitable for modelling. Instead, either comparative studies between the two compounds or modelling of individual sugar rings rather than polymeric forms may allow the function of GG to be identified.

DoE was implemented across three iterations of experiments to study the influence of TEPA addition on the formation of MNPs under co-precipitation conditions. DoE had previously not been applied using the addition of an additive as a factor, leaving a key gap in the understanding of how additive addition may influence the properties of MNPs formed. Two full-factorial designs (FFDs) and a path of steepest ascent (PSA) optimisation were conducted, with each design building upon the findings of the prior designs.

The time-point of TEPA addition was found to be an insignificant factor, supporting the idea of amine-based additives not impacting particle nucleation but instead interacting with already nucleated magnetite and directing particle growth. As the other two factors investigated (ferric ratio, and Fe/additive ratio) were found to be significant in the first FFD, they remained as factors throughout each subsequent study.

Notably, higher concentrations of TEPA were found to promote the formation of magnetite at sub-optimal ferric ratios, producing particles which were both more magnetic and closer in morphology to particles typically seen at ratios closer to the 2:1 ratio observed in magnetite. The second FFD and PSA identified two similar Fe/additive ratios at which an optimal proportion of faceted particles is formed, 50:1 and 59:1, producing 90 and 95 % isotropic faceted particles (faceted particles excluding rods as these are not ideal for many industrial purposes). This was in agreement with a concentration study conducted on TEPA which found 62.5:1 and 125:1 Fe/additive ratios produced 97 % and 81 % faceted particles respectively.

However it must be noted that in the PSA design many of the reactions performed worse than predicted, producing lower proportions of faceted particles than predicted by the model.

The batch co-precipitation system is highly sensitive to small environmental changes such as room temperature and humidity, as well as more controllable variables such as stirring rate. Further validation and work on the use of TEPA within batch RTCP is required to understand the discrepancies observed within batches of particles formed to truly develop a robust method by which morphologically controlled MNPs can be consistently produced. Due to the slow nature of the RTCP reactions conducted (160 minutes for the addition of NaOH) the influence of environmental conditions may exert a greater effect than would be observed in a short time-scale reaction. Future DoE experiments conducted within a more tightly controlled environment such as utilising a water bath to maintain consistent temperatures would allow for the cause of these differences to be determined.

8.1.3 Fluidic Systems and Scale-up

The final aim of the project was to produce MNPs in a range of systems with the goal of increasing reproducibility between syntheses, and to enable the large-scale synthesis of magnetic nanoparticles with enhanced properties. Previously, RTCP has been noted to be highly sensitive to small changes in reaction environment with differences in saturation magnetism and percentage of faceted particles formed being noted. As such, the exploration of alternative synthetic techniques was of great importance to ascertain a robust methodology for the production of consistent high quality MNPs.

A macrofluidic/millifluidic system, henceforth referred to as the millifluidic system, was designed to combat the issue of reproducibility issues within batch RTCP reactions. The effect of Mms6, a biomineralisation protein found to strongly control the size and shape of magnetite particles formed when used as an additive in batch RTCP, was studied within this system at a range of ferric ratios. Whilst Mms6 was found to be unable to tailor the morphology of particles formed under millifluidic conditions, saturation magnetism was higher at lower ferric ratios (0.2-0.3) compared to additive-free controls. This suggests Mms6 still aided the formation of magnetite, even if it could not exert a shape-control effect under laminar flow conditions.

Crucially, by simply adjusting the ferric ratio between 0.2-0.7, particle size could be

tuned to produce particles between 20.5 and 6.5 nm diameter. This reveals a methodology by which particle size can be controlled, without even requiring the use of an additive.

This system was further tested with the addition of the EDA series of additives, spanning from EDA-PEHA to cover the full range of readily available EDA-based amines. Three additive to iron ratios were selected (1:100, 1:1000, and 1:10000), with the intention of determining an optimal balance between additive effect and the reduced economy of using more additive. TEPA once again produced the highest percentage of faceted particles, producing 58 % faceted particles at a 1:100 ratio compared to 47 % at a 1:1000 ratio. This is not a significant difference for a 10-fold increase in additive concentration, suggesting lower additive concentrations may be more economically viable if this methodology were to be scaled out.

The incorporation of a clear glass capillary into the design allows for both the *in situ* analysis of product formation using methodologies such as colour analysis of the iron stream to monitor reaction progress, as well as readily being able to adapt the length of the capillary to optimise residence time within the system. The system could be adapted further via machining additional inlets to allow for the introduction of additives at various reaction points.

However, the millifluidic system has flaws which make it unsuitable for large-scale particle production. The iron oxide products are prone to oxidation due to the inability to sparge the Fe and NaOH feed solutions with an inert gas throughout the reaction, as the solutions are required to be within a syringe for the system to operate. Despite the reasonably low residence time (~1 minute) of iron solution within the millifluidic device, small amounts of particles are produced due to the low volume of the reaction channel. Careful calibration is required to ensure the Fe inlet needle is central, as the capillary is prone to fouling if the needle is askew. It was also found that additives do not appear as effective under the laminar flow regime, with both Mms6 and TEPA not performing as well as observed under batch conditions.

A continuous flow static mixer was designed to overcome the shortcomings observed with regard to additive mixing within the millifluidic system. The use of a continuous flow

static mixer allows for rapid mixing of the reagents, whilst minimising residence time within the system for efficient production of particles and a simple route to industrial scale MNP production. This continuous flow system is capable of producing $> 300 \text{ g day}^{-1}$ of MNP, an increase of greater than five times the highest production rate previously been stated in the literature for MNP synthesis.

Each of the EDA-PEHA series of additives was used at three concentrations (1:100, 1:1000, and 1:10000) within this continuous flow system. The addition of additives increased the percentage of faceted particles from 34 % in an additive-free control, to 38-84 % on addition of EDA-PEHA across each of the three concentration. The 1:100 additive/Fe ratio formed the most faceted particles, with TEPA producing the highest proportion of each of the amine additives (84 %).

Optimisation of the continuous flow static mixer revealed two manners by which MNP size could be tuned, with both the concentration of the Fe feed and the ferric ratio found to influence particle diameter. When varying the ferric ratio between 0.2-0.7, mean particle diameter ranged from 22.7 nm at the lowest ratio to 7.7 nm at the highest. Interestingly, magnetism is maintained at lower ferric ratios, despite being non-magnetic on exiting the continuous flow static mixer and requiring time to mature. This size tuning effect was maintained in a further study on the addition of TEPA between a 0.4-0.6 ferric ratio, with a high degree (73-81 %) of faceted morphology being noted across the ferric range. This is a critical finding, as it allows for the size and morphology of the particles to be tailored in tandem with the addition of only a single affordable additive.

Future studies into the use of TEPA as an additive at the lowest ferric ratios (0.2-0.35) would reveal whether shape-control is maintained at typically less ideal ratios within the continuous flow system, which would allow for octahedral particles spanning a wide range of sizes to be formed within a system which is readily amenable to scale-up.

Notably, both fluidic systems produce smaller MNP ($\sim 10 \text{ nm}$) than those synthesised within a batch system ($\sim 20 \text{ nm}$). This provides another approach to tailoring the size of particles produced, with the addition of TEPA to different systems allowing the production of octahedral particles of either size.

Whilst the potential for scale-up has been explored as a continuous concept, batch manufacture is still deemed preferable across many industries. The current batch RTCP methodology uses the slow addition of $50 \mu\text{L min}^{-1}$ of base, limiting the speed at which MNPs are formed. The rapid addition of base requires both rapid and consistent stirring throughout the vessel to ensure homogeneous particle formation. Poor mixing results in steeper pH gradients within the reaction mixture, allowing some particles to nucleate before others and altering the size distribution of MNPs formed. The use of a more controllable system, such as a reactor vessel with overhead stirring, would allow for the fast mixing required to avoid significant pH gradients and lay the foundations of additive-assisted batch RTCP on larger scales.

Throughout this body of work, TEM, XRD, VSM have been used as the primary means of analysing the particles formed across the range of RTCP synthesis methods. At the stage of research where additives are being identified and initially optimised, this analysis is adequate. However, other methods may offer additional information required for future development of the particle synthesis methods and their subsequent characterisation.

Dynamic Light Scattering (DLS) is one method commonly used to analyse the size of nanoparticles. The magnetic nature of MNP causes particles to aggregate, which causes inaccuracy in the measurements compared to TEM. As such, the human error attributed to TEM analysis is an improvement on the measurements gathered from DLS. Atomic force microscopy (AFM) is another technique which has applications in the measurement of nanoscale materials. Once again, TEM offers superior resolution, and if cost is not an issue, offers superior size information. Zeta potential readings measuring the electrical potential of MNP is key information when developing suspensions of nanoparticles and would be crucial when the formed MNP are being further developed into potential medical formulations. Ultraviolet visible (UV-vis) spectroscopy measures the absorbance of specific wavelengths of light. Standard spectra are available of a range of compounds, including magnetite. UV-vis spectroscopy of magnetite formed in the presence of organic additives may shed light on the binding and presence of additives to particle surfaces, allowing another means of characterising the binding of additives, similar to FTIR. Electron paramagnetic resonance

(EPR) allows for the study of materials with unpaired electrons. Maghemite exhibits a broadening of peaks compared to magnetite and use of this technique may allow for more precise characterisation of magnetite and maghemite in samples.

When considering future changes to the synthesis of MNP utilising continuous flow techniques, the methodology could be expanded in several manners. The use of online measurement to continuously monitor the synthesis of particles would be a significant step toward industrial synthesis of continuously produced MNP. Whilst the continuous flow methodology produces high quality MNP on a massively reduced timescale compared to the original batch RTCP methodology utilised, TEM, XRD, and VSM are not typically automatable analysis techniques.

8.2 Final Remarks

Within this thesis, a significant body of work has been developed and presented on the use of bioinspired additives to tailor MNPs, particularly pertaining to the use of TEPA as a morphological control agent. The robustness of this additive has been demonstrated, showing effectiveness at modulating the shape of MNPs formed within RTCP reactions across three synthetic systems. As well as displaying the efficacy of TEPA within co-precipitation reactions, the use of TEPA has been understood and optimised through DoE and modelling studies. It has been demonstrated that bioinspired additives have the potential to offer near homogeneous control over the morphology of particles formed within co-precipitation reactions, directing the syntheses to octahedral morphology.

This work has been a major step towards the bioinspired large-scale production of additive-mediated MNP synthesis. The combination of the ability to control particle size by utilising fluidic and batch methodologies whilst directing the shape of MNPs formed to octahedral allows for bespoke particles to be produced. With the development of the continuous flow static mixer, it is feasible to synthesise over 300 g day^{-1} of primarily octahedral MNPs whilst controlling the size of particle formed via adjustment of the ferric ratio. With further optimisation and development of the continuous flow static mixer, this finding could significantly impact how MNPs are synthesised on an industrial scale. The ability to

produce large quantities of MNPs with both tailored shape and size, without the use of environmentally unsustainable practices, is a substantial step towards the development of sustainable MNPs produced on an industrial scale.

The bioinspired large-scale production of MNPs may be within reach as the industrial community becomes more aware of environmental issues surrounding the production of nanomaterials, leading to the selection of greener alternatives. By developing these alternative green methodologies, the sustainable manufacture of MNPs becomes an attractive and viable option for industry.

Bibliography

1. J. M. Galloway, J. P. Bramble, A. E. Rawlings, G. Burnell, S. D. Evans and S. S. Staniland, *Small*, 2012, **8**, 204–208.
2. Z. Li, M. Kawashita, N. Araki, M. Mitsumori, M. Hiraoka and M. Doi, *Materials Science and Engineering C*, 2010, **30**, 990–996.
3. Z. R. Stephen, F. M. Kievit and M. Zhang, *Materials Today*, 2011, **14**, 330–338.
4. Q. A. Pankhurst, J. Connolly, S. K. Jones and J. Dobson, *Journal of Physics D: Applied Physics*, 2003, **36**, 167–181.
5. J. Wolfram, M. Zhu, Y. Yang, J. Shen, E. Gentile, D. Paolino, M. Fresta, G. Nie, C. Chen, H. Shen, M. Ferrari and Y. Zhao, *Current Drug Targets*, 2015, **16**, 1671–1681.
6. S. Majidi, F. Z. Sehrig, S. M. Farkhani, M. S. Goloujeh and A. Akbarzadeh, *Artificial Cells, Nanomedicine and Biotechnology*, 2016, **44**, 722–734.
7. E. Inshakova and O. Inshakov, *MATEC Web of Conferences*, 2017, **129**, 1–5.
8. M. J. Eckelman, J. B. Zimmerman and P. T. Anastas, *Journal of Industrial Ecology*, 2008, **12**, 316–328.
9. S. Mann, D. D. Archibald, J. M. Didymus, T. Douglas, B. R. Heywood, F. C. Meldrum and N. J. Reeves, *Science*, 1993, **261**, 1286–1292.
10. S. V. Patwardhan and S. S. Staniland, *Green Nanomaterials*, Institute of Physics Publishing, 2019.
11. R. P. Feynman, *Engineering and Science*, 1960, **23**, 22–36.
12. K. E. Drexler, *Engines of Creation: The Coming Era of Nanotechnology*, Anchor Books, 1986.
13. P. H. Abelson, *Science*, 2000, **288**, 269.
14. E. Ruska and H. Rohrer, *Science*, 2013, **234**, 821–822.
15. M. von Ardenne, *Zeitschrift für Physik*, 1938, **109**, 553–572.

16. B. J. Inkson, *Scanning Electron Microscopy (SEM) and Transmission Electron Microscopy (TEM) for Materials Characterization*, 2016, pp. 17–43.
17. G. L. Hornyak and J. J. Moore, *Fundamentals of Nanotechnology*, CRC Press, 2009.
18. O. C. Farokhzad and R. Langer, *ACS Nano*, 2009, **3**, 16–20.
19. W. J. Stark, P. R. Stoessel, W. Wohlleben and A. Hafner, *Chemical Society Reviews*, 2015, **44**, 5793–5805.
20. N. Doshi and S. Mitragotri, *Journal of the Royal Society Interface*, 2010, **7**, 403–410.
21. Y. Lalatonne, J. Richardi and M. P. Pileni, *Nature Materials*, 2004, **3**, 121–125.
22. D. Maity, S. N. Kale, R. Kaul-Ghanekar, J. M. Xue and J. Ding, *Journal of Magnetism and Magnetic Materials*, 2009, **321**, 3093–3098.
23. E. M. Hotze, T. Phenrat and G. V. Lowry, *Journal of Environmental Quality*, 2010, **39**, 1909–1924.
24. M. Fittipaldi, C. Innocenti, P. Ceci, C. Sangregorio, L. Castelli, L. Sorace and D. Gatteschi, *Physical Review B: Condensed Matter and Materials Physics*, 2011, **83**, 1–10.
25. R. C. Popescu, E. Andronescu and B. S. Vasile, *Nanomaterials*, 2019, **9**, 1–31.
26. C. S. C. Santos, B. Gabriel, M. Blanchy, O. Menes, D. García, M. Blanco, N. Arconada and V. Neto, *Materials Today: Proceedings*, 2015, **2**, 456–465.
27. J. Lee, S. Mahendra and P. J. Alvarez, *ACS Nano*, 2010, **4**, 3580–3590.
28. P. Tartaj, P. Morales, S. Veintemillas-Verdaguer and T. Gonz, *In Vivo*, 2003, **182**, 182–197.
29. J. Jeevanandam, A. Barhoum, Y. S. Chan, A. Dufresne and M. K. Danquah, *Beilstein Journal of Nanotechnology*, 2018, **9**, 1050–1074.
30. M. E. Vance, T. Kuiken, E. P. Vejerana, S. P. McGinnis, M. F. H. Jr., D. Rejeski and M. S. Hull, *Beilstein Journal of Nanotechnology*, 2015, **6**, 1769–1780.
31. DTU Environment, Danish Ecological Council, Danish Consumer Council, *The Nanodatabase*, <https://nanodb.dk/>, date accessed: 2020-11-10.

32. M. A. Gattoo, S. Naseem, M. Y. Arfat, A. Mahmood Dar, K. Qasim and S. Zubair, *BioMed Research International*, 2014, **2014**, 1–8.
33. A. Weir, P. Westerhoff, L. Fabricius and N. von Goetz, *Environmental Science and Technology*, 2012, **46**, 2242–2250.
34. M. C. Roco, *Journal of Nanoparticle Research*, 2005, **7**, 707–712.
35. S. Davidson, D. A. Lamprou, A. J. Urquhart, M. H. Grant and S. V. Patwardhan, *ACS Biomaterials Science and Engineering*, 2016, **2**, 1493–1503.
36. D. V. Dao, K. Nakamura, T. T. Bui and S. Sugiyama, *Advances in Natural Sciences: Nanoscience and Nanotechnology*, 2010, **1**, 1–10.
37. G. R. Reddy, M. S. Bhojani, P. McConville, J. Moody, B. A. Moffat, D. E. Hall, G. Kim, Y. E. L. Koo, M. J. Woolliscroft, J. V. Sugai, T. D. Johnson, M. A. Philbert, R. Kopelman, A. Rehemtulla and B. D. Ross, *Clinical Cancer Research*, 2006, **12**, 6677–6686.
38. P. Sharma, S. Brown, G. Walter, S. Santra and B. Moudgil, *Advances in Colloid and Interface Science*, 2006, **123**, 471–485.
39. G. A. Bhaduri and L. Šiller, *Catalysis Science & Technology*, 2013, **3**, 1234–1239.
40. X. Sun, Y. Huang and D. E. Nikles, *International Journal of Nanotechnology*, 2004, **1**, 328–346.
41. M. Gaumet, A. Vargas, R. Gurny and F. Delie, *European Journal of Pharmaceutics and Biopharmaceutics*, 2008, **69**, 1–9.
42. S. J. Klaine, P. J. Alvarez, G. E. Batley, T. F. Fernandes, R. D. Handy, D. Y. Lyon, S. Mahendra, M. J. McLaughlin and J. R. Lead, *Environmental Toxicology and Chemistry*, 2008, **27**, 1825–1851.
43. V. L. Colvin, *Nature Biotechnology*, 2004, **22**, 1166–1170.
44. E. S. Bernhardt, B. P. Colman, M. F. Hochella, B. J. Cardinale, R. M. Nisbet, C. J. Richardson and L. Yin, *Journal of Environmental Quality*, 2010, **39**, 1954–1965.
45. S. M. Louie, R. Ma and G. V. Lowry, *Frontiers of Nanoscience*, 2014, **7**, 55–87.

46. G. Pallas, W. J. Peijnenburg, J. B. Guinée, R. Heijungs and M. G. Vijver, *Sustainability*, 2018, **10**, 1–17.
47. B. P. Isaacoff and K. A. Brown, *Nano Letters*, 2017, **17**, 6508–6510.
48. H. J. Jung, Y. Sohn, H. G. Sung, H. S. Hyun and W. G. Shin, *Powder Technology*, 2014, 1–29.
49. S. V. Patwardhan, J. R. H. Manning and M. Chiacchia, *Current Opinion in Green and Sustainable Chemistry*, 2018, **12**, 110–116.
50. M. Niederberger and H. Cölfen, *Physical Chemistry Chemical Physics*, 2006, **8**, 3271–3287.
51. C.-M. H. Tak-Sing Wong, Branden Brough, *Molecular & Cellular Biomechanics*, 2009, **23**, 1–55.
52. R. S. Varma, *Current Opinion in Chemical Engineering*, 2012, **1**, 123–128.
53. Y. Lu and S. Ozcan, *Nano Today*, 2015, 1–4.
54. K. J. M. Matus, W. C. Clark, P. T. Anastas and J. B. Zimmerman, *Environmental Science and Technology*, 2012, **46**, 10892–10899.
55. J. R. H. Manning, T. W. S. Yip, A. Centi, M. Jorge and S. V. Patwardhan, *ChemSusChem*, 2017, **10**, 1683–1691.
56. S. V. P. Claire Forsyth, *Journal of Materials Chemistry B*, 2013, **1**, 1164–1174.
57. K. Shimizu, J. Cha, G. D. Stucky and D. E. Morse, *Proceedings of the National Academy of Sciences of the United States of America*, 1998, **95**, 6234–6238.
58. I. E. Pamirsky and K. S. Golokhvast, *BioMed Research International*, 2013, **2013**, 1–7.
59. D. J. Belton, S. V. Patwardhan and C. C. Perry, *Journal of Materials Chemistry*, 2005, **15**, 4629–4638.
60. D. J. Belton, S. V. Patwardhan, V. V. Annenkov, E. N. Danilovtseva and C. C. Perry, *Proceedings of the National Academy of Sciences of the United States of America*, 2008, **105**, 5963–5968.

61. S. V. Patwardhan, *Chemical Communications*, 2011, **47**, 7567–82.
62. William Gilbert, *De Magnete*, 1600.
63. B. Cullity and C. D. Graham, *Introduction to Magnetic Materials, Second Edition*, Wiley-IEEE Press, 2008.
64. Florida State University High Energy Physics Group, *The Hysteresis Loop and Magnetic Properties*, <http://www.hep.fsu.edu/wahl/phy3802/expinfo/hysteresis/HysteresisLoop.htm>, date accessed: 2021-03-17.
65. J. S. Lee, J. M. Cha, H. Y. Yoon, J. K. Lee and Y. K. Kim, *Scientific Reports*, 2015, **5**, 1–7.
66. G. Concas, F. Congiu, G. Muscas and D. Peddis, *Journal of Physical Chemistry C*, 2017, **121**, 16541–16548.
67. V. Reichel, A. Kovács, M. Kumari, É. Bereczk-Tompa, E. Schneck, P. Diehle, M. Pósfai, A. M. Hirt, M. Duchamp, R. E. Dunin-Borkowski and D. Faivre, *Scientific Reports*, 2017, **7**, 1–8.
68. C. P. Bean, *Journal of Applied Physics*, 1955, **26**, 1381–1383.
69. R. H. Kodama, *Journal of Magnetism and Magnetic Materials*, 1999, **200**, 359–372.
70. M. Friák, A. Schindlmayr and M. Scheffler, *New Journal of Physics*, 2007, **9**, 1–15.
71. J. P. Wright, J. P. Attfield and P. G. Radaelli, *Physical Review B*, 2002, **66**, 1–15.
72. J. B. Moussy, *Journal of Physics D: Applied Physics*, 2013, **46**, 1–27.
73. P. W. Anderson, *Physical Review*, 1950, **79**, 350–356.
74. B. Wang, Q. Wei and S. Qu, *International Journal of Electrochemical Science*, 2013, **8**, 3786–3793.
75. E. Lima, A. L. Brandl, A. D. Arelaro, G. F. Goya, E. Lima, A. L. Brandl, A. D. Arelaro and G. F. Goya, *Journal of Applied Physics*, 2006, **99**, 1–10.
76. N. Mahmed, O. Heczko and S.-P. Hannula, *IOP Conference Series: Materials Science and Engineering*, 2011, **18**, 1–4.

77. D. Maity and D. C. Ā. Agrawal, *Journal of Magnetism and Magnetic Materials*, 2007, **308**, 46–55.
78. M. Munoz, Z. M. de Pedro, J. A. Casas and J. J. Rodriguez, *Applied Catalysis B: Environmental*, 2015, **176-177**, 249–265.
79. L. Carlos, F. S. G. Einschlag, M. C. González and D. O. Màrtire, in *Waste Water - Treatment Technologies and Recent Analytical Developments*, 2013, pp. 63–77.
80. D. Yuvarajan and M. V. Ramanan, *Arabian Journal for Science and Engineering*, 2016, **41**, 2023–2030.
81. S. Mornet, S. Vasseur, F. Grasset and E. Duguet, *Journal of Materials Chemistry*, 2004, **14**, 2161–2175.
82. J. Chakma, G. H. Sun, J. D. Steinberg, S. M. Sammut and R. Jagsi, *The New England Journal of Medicine*, 2014, **370**, 3–6.
83. M. Mahmoudi, S. Sant, B. Wang, S. Laurent and T. Sen, *Advanced Drug Delivery Reviews*, 2011, **63**, 24–46.
84. W. H. De Jong and P. J. Borm, *International Journal of Nanomedicine*, 2008, **3**, 133–149.
85. J. P. Fortin, C. Wilhelm, J. Servais, C. Ménager, J. C. Bacri and F. Gazeau, *Journal of the American Chemical Society*, 2007, **129**, 2628–2635.
86. C. Sun, K. Du, C. Fang, N. Bhattarai, O. Veisoh, F. Kivitt, Z. Stephen, D. Lee, R. G. Ellenbogen and B. Ratner, *In Vivo*, 2011, **4**, 2402–2410.
87. R. Weissleder, D. D. Stark, B. L. Engelstad, B. a. Bacon, D. L. White, P. Jacobs and J. Lewis, *American Journal of Roentgenology*, 1989, **152**, 167–173.
88. C. Lang, D. Schüler and D. Faivre, *Macromolecular Bioscience*, 2007, **7**, 144–151.
89. R. E. E. Rosensweig, *Journal of Magnetism and Magnetic Materials*, 2002, **252**, 370–374.
90. S. Laurent, S. Dutz, U. O. Häfeli and M. Mahmoudi, *Advances in Colloid and Interface Science*, 2011, **166**, 8–23.

91. J. Motoyama, T. Hakata, R. Kato, N. Yamashita, T. Morino, T. Kobayashi and H. Honda, *BioMagnetic Research and Technology*, 2008, **6**, 1–9.
92. Wahajuddin and S. Arora, *International Journal of Nanomedicine*, 2012, **7**, 3445–3471.
93. J. H. Park, G. Saravanakumar, K. Kim and I. C. Kwon, *Advanced Drug Delivery Reviews*, 2010, **62**, 28–41.
94. Y. H. Deng, C. C. Wang, J. H. Hu, W. L. Yang and S. K. Fu, *Colloids and Surfaces A: Physicochemical and Engineering Aspects*, 2005, **262**, 87–93.
95. M. Mandal, S. Kundu, S. K. Ghosh, S. Panigrahi, T. K. Sau, S. M. Yusuf and T. Pal, *Journal of Colloid and Interface Science*, 2005, **286**, 187–194.
96. X. Zhang and J. Wang, *Solid State Sciences*, 2018, **75**, 14–20.
97. J. Dobson, *Drug Development Research*, 2006, **67**, 55–60.
98. A. H. Lu, E. L. Salabas and F. Schüth, *Angewandte Chemie - International Edition*, 2007, **46**, 1222–1244.
99. C. Chouly, D. Pouliquen, I. Lucet, J. J. Jeune and P. Jallet, *Journal of Microencapsulation*, 1996, **13**, 245–255.
100. A. K. Gupta and S. Wells, *IEEE Transactions on Nanobioscience*, 2004, **3**, 66–73.
101. X. Huang, L. Li, T. Liu, N. Hao, H. Liu, D. Chen and F. Tang, *ACS Nano*, 2011, **5**, 5390–5399.
102. B. Fadeel and Garcia-Bennett, *Advanced Drug Delivery Reviews*, 2010, **62**, 362–374.
103. A. Nikitin, M. Fedorova, V. Naumenko, I. Shchetinin, M. Abakumov, A. Erofeev, P. Gorelkin, G. Meshkov, E. Beloglazkina, Y. Ivanenkov, N. Klyachko, Y. Golovin, A. Savchenko and A. Majouga, *Journal of Magnetism and Magnetic Materials*, 2017, **441**, 6–13.
104. G. Zhen, B. W. Muir, B. a. Moffat, P. Harbour, K. S. Murray, B. Moubaraki, K. Suzuki, I. Madsen, N. Agron-Olshina, L. Waddington, P. Mulvaney and P. G. Hartley, *The Journal of Physical Chemistry C*, 2011, **115**, 327–334.

105. A. Mitra, J. Mohapatra, S. S. Meena, C. V. Tomy and M. Aslam, *Journal of Physical Chemistry C*, 2014, **118**, 19356–19362.
106. J. Mohapatra, A. Mitra, M. Aslam and D. Bahadur, *IEEE Transactions on Magnetics*, 2015, **51**, 1–4.
107. S. Karthika, T. K. Radhakrishnan and P. Kalaichelvi, *Crystal Growth and Design*, 2016, **16**, 6663–6681.
108. N. T. K. Thanh, N. Maclean and S. Mahiddine, *Chemical Reviews*, 2014, **114**, 7610–7630.
109. V. K. Lamer and R. H. Dinegar, *Journal of the American Chemical Society*, 1950, **72**, 4847–4854.
110. E. C. Vreeland, J. Watt, G. B. Schober, B. G. Hance, M. J. Austin, A. D. Price, B. D. Fellows, T. C. Monson, N. S. Hudak, L. Maldonado-Camargo, A. C. Bohorquez, C. Rinaldi and D. L. Huber, *Chemistry of Materials*, 2015, **27**, 6059–6066.
111. S. Mann, *Biomineralization: Principles and Concepts in Bioinorganic Materials Chemistry*, Oxford University Press, U.S.A, 2001.
112. P. Hartman and W. G. Perdok, *Acta Crystallographica*, 1955, **8**, 525–529.
113. P. W. Voorhees, *Journal of Statistical Physics*, 1985, **38**, 231–252.
114. U. Dahmen and A. P. Alivisatos, *Science*, 2009, **324**, 1309–1313.
115. R. L. Penn and J. A. Soltis, *CrystEngComm*, 2014, **16**, 1409–1418.
116. H. Cölfen and S. Mann, *Angewandte Chemie - International Edition*, 2003, **42**, 2350–2365.
117. L. C. Soare, P. Bowen, J. Lemaitre and H. Hofmann, *Journal of Physical Chemistry B*, 2006, **110**, 17763–17771.
118. D. B. DeOliveira and R. A. Laursen, *Journal of the American Chemical Society*, 1997, **7863**, 10627–10631.
119. R. Q. Song and H. Cölfen, *CrystEngComm*, 2011, **13**, 1249–1276.

120. J. R. H. Manning, E. Routoula and S. V. Patwardhan, *Journal of Visualized Experiments*, 2018, **2018**, 1–9.
121. W. K. Park, S. J. Ko, S. W. Lee, K. H. Cho, J. W. Ahn and C. Han, *Journal of Crystal Growth*, 2008, **310**, 2593–2601.
122. D. Zhang, J. Zheng and Z. Tong, *Journal of Experimental Nanoscience*, 2010, **5**, 162–168.
123. A. E. Rawlings, J. P. Bramble, A. A. S. Tang, L. A. Somner, A. E. Monnington, D. J. Cooke, M. J. McPherson, D. C. Tomlinson and S. S. Staniland, *Chemical Science*, 2015, **6**, 5586–5594.
124. L. Addadi and S. Weiner, *Angewandte Chemie - International Edition*, 1992, **31**, 153–169.
125. M. Unni, A. M. Uhl, S. Savliwala, B. H. Savitzky, R. Dhavalikar, N. Garraud, D. P. Arnold, L. F. Kourkoutis, J. S. Andrew and C. Rinaldi, *ACS Nano*, 2017, **11**, 2284–2303.
126. W. Li, S. S. Lee, J. Wu, C. H. Hinton and J. D. Fortner, *Nanotechnology*, 2016, **27**, 1–7.
127. L. Hu, A. Percheron, D. Chaumont and C. H. Brachais, *Journal of Sol-Gel Science and Technology*, 2011, **60**, 198–205.
128. S. F. Chin, S. C. Pang and C. H. Tan, *Journal of Materials and Environmental Science*, 2011, **2**, 299–302.
129. L. Liebermann, J. Clinton, D. M. Edwards and J. Mathon, *Physical Review Letters*, 1970, **25**, 232–235.
130. R. Kaiser and G. Miskolczy, *Journal of Applied Physics*, 1970, **41**, 1064–1072.
131. C. Y. Haw, F. Mohamed, C. H. Chia, S. Radiman, S. Zakaria, N. M. Huang and H. N. Lim, *Ceramics International*, 2010, **36**, 1417–1422.
132. A. Kogan and N. Garti, *Advances in Colloid and Interface Science*, 2006, **123-126**, 369–385.

133. D. Langevin, *Annual Review of Physical Chemistry*, 1992, **43**, 341–369.
134. Z. L. Liu, X. Wang, K. L. Yao, G. H. Du, Q. H. Lu, Z. H. Ding, J. Tao, Q. Ning, X. P. Luo, D. Y. Tian and D. Xi, *Journal of Materials Science*, 2004, **39**, 2633–2636.
135. M. C. Mascolo, Y. Pei and T. A. Ring, *Materials*, 2013, **6**, 5549–5567.
136. T. Ahn, J. H. Kim, H. M. Yang, J. W. Lee and J. D. Kim, *The Journal of Physical Chemistry C*, 2012, **116**, 6069–6076.
137. A. E. Rawlings, J. P. Bramble, A. M. Hounslow, M. P. Williamson, A. E. Monnington, D. J. Cooke and S. S. Staniland, *Chemistry - A European Journal*, 2016, **22**, 7885–7894.
138. R. Massart, J. Roger and V. Cabuil, *Brazilian Journal of Physics*, 1995, **25**, 135–141.
139. J. P. Jolivet, P. Belleville, E. Tronc and J. Livage, *Clays and Clay Minerals*, 1992, **40**, 531–539.
140. E. Tronc, P. Belleville, J.-P. Jolivet and J. Livage, *Langmuir*, 1992, **16**, 313–319.
141. S. Laurent, D. Forge, M. Port, A. Roch, C. Robic, L. Vander Elst and R. N. Muller, *Chemical Reviews*, 2008, **108**, 2064–2110.
142. J. Baumgartner, A. Dey, P. H. H. Bomans, C. Le Coadou, P. Fratzl, N. A. J. M. Sommerdijk and D. Faivre, *Nature Materials*, 2013, **12**, 310–314.
143. R. Valenzuela, M. Cecilia Fuentes, C. Parra, J. Baeza, N. Duran, S. K. Sharma, M. Knobel and J. Freer, *Journal of Alloys and Compounds*, 2009, **488**, 227–231.
144. X. Q. Qiu, L. Lv, G.-S. Li, W. Han, X.-J. Wang and L.-P. Li, *Journal of Thermal Analysis and Calorimetry*, 2008, **91**, 873–878.
145. S. P. Schwaminger, D. Bauer, P. Fraga-García, F. E. Wagner and S. Berensmeier, *CrystEngComm*, 2017, **19**, 246–255.
146. D. K. Kim, Y. Zhang, W. Voit, K. V. Rao and M. Muhammed, *Journal of Magnetism and Magnetic Materials*, 2001, **225**, 30–36.
147. H. Aono, H. Hirazawa, T. Naohara, T. Maehara, H. Kikkawa and Y. Watanabe, *Materials Research Bulletin*, 2005, **40**, 1126–1135.

148. R. B. Frankel and D. A. Bazylinski, *Reviews in Mineralogy and Geochemistry*, 2003, **54**, 95–114.
149. H. Vali, B. Weiss, Y.-L. Li, S. K. Sears, S. S. Kim, J. L. Kirschvink and C. L. Zhang, *Proceedings of the National Academy of Sciences*, 2004, **101**, 16121–16126.
150. C. T. Lefèvre, M. L. Schmidt, N. Vioria, D. Trubitsyn, D. Schüler and D. A. Bazylinski, *Applied and Environmental Microbiology*, 2012, **78**, 7238–7248.
151. G. Mirabello, J. J. M. Lenders and N. A. J. M. Sommerdijk, *Chemical Society Reviews*, 2016, **45**, 5085–5106.
152. F. E. Round, R. M. Crawford and D. G. Mann, *The Diatoms: Biology and Morphology of the Genera*, Cambridge University Press, 1990.
153. A. E. Rawlings, J. P. Bramble and S. S. Staniland, *Soft Matter*, 2012, **8**, 6675–6679.
154. J. M. Galloway, J. P. Bramble and S. S. Staniland, *Chemistry - A European Journal*, 2013, **19**, 8710–8725.
155. B. K. Ahn, S. Das, R. Linstadt, Y. Kaufman, N. R. Martinez-Rodriguez, R. Mirshafian, E. Kesselman, Y. Talmon, B. H. Lipshutz, J. N. Israelachvili and J. H. Waite, *Nature Communications*, 2015, **6**, 1–7.
156. M. R. Wasielewski, *Chemical Reviews*, 1992, **92**, 435–461.
157. U. C. Banerjee, R. K. Sani, W. Azmi and R. Soni, *Process Biochemistry*, 1999, **35**, 213–219.
158. R. B. Frankel, in *Iron Biominerals*, Springer, 1991, pp. 1–6.
159. S. M. Bird, A. E. Rawlings, J. M. Galloway and S. S. Staniland, *RSC Advances*, 2016, **6**, 7356–7363.
160. G. O. Walters, F. M. Miller and M. Worwood, *Journal of Clinical Pathology*, 1973, **26**, 770–772.
161. G. A. Ordway and D. J. Garry, *Journal of Experimental Biology*, 2004, **207**, 3441–3446.
162. R. J. Geider and J. La Roche, *Photosynthesis Research*, 1994, **39**, 275–301.

163. A. Komeili, *FEMS Microbiology Reviews*, 2012, **36**, 232–255.
164. F. Müller, *Microbiologists solve the mystery of the compass needle in magnetic bacteria*, 2019, <https://phys.org/news/2019-07-microbiologists-mystery-compass-needle-magnetic.html>, date accessed: 2021-02-04.
165. W. Lin, K. Benzerara, D. Faivre and Y. Pan, *Frontiers in Microbiology*, 2014, **5**, 6–7.
166. C. Jogler and D. Schüler, *Annual Review of Microbiology*, 2009, **63**, 501–521.
167. R. Blakemore, *Science*, 1975, **190**, 377–379.
168. M. Hildebrand, M. J. Doktycz and D. P. Allison, *Pflügers Archiv - European Journal of Physiology*, 2008, **456**, 127–137.
169. J. L. Kirschvink and J. W. Hagadorn, in *The Biomineralisation of Nano- and Micro-Structures*, Wiley, 2000, ch. 10, pp. 139–149.
170. S.-B. R. Chang and J. L. Kirschvink, *Annual Review of Earth and Planetary Sciences*, 1989, **17**, 169–195.
171. S. L. Simmons, S. M. Sievert, R. B. Frankel, D. A. Bazylinski and K. J. Edwards, *Applied and Environmental Microbiology*, 2004, **70**, 6230–6239.
172. D. A. Bazylinski, *Chemical Geology*, 1996, **132**, 191–198.
173. B. Issa, I. M. Obaidat, B. A. Albiss and Y. Haik, *International Journal of Molecular Sciences*, 2013, **14**, 21266–21305.
174. I. Šafařík and M. Šafaříková, *Monatshefte für Chemie*, 2002, **133**, 737–759.
175. L. Yan, S. Zhang, P. Chen, H. Liu, H. Yin and H. Li, *Microbiological Research*, 2012, **167**, 507–519.
176. A. Stintzi, C. Barnes, J. Xu and K. N. Raymond, *Proceedings of the National Academy of Sciences*, 2000, **97**, 10691–10696.
177. Y. Amemiya, A. Arakaki, S. S. Staniland, T. Tanaka and T. Matsunaga, *Biomaterials*, 2007, **28**, 5381–5389.
178. S. S. Staniland and A. E. Rawlings, *Biochemical Society Transactions*, 2016, **44**, 883–90.

179. L. Wang, T. Prozorov, P. E. Palo, X. Liu, D. Vaknin, R. Prozorov, S. Mallapragada and M. Nilsen-Hamilton, *Biomacromolecules*, 2012, **13**, 98–105.
180. D. Murat, V. Falahati, L. Bertinetti, R. Csencsits, A. Körnig, K. Downing, D. Faivre and A. Komeili, *Molecular Microbiology*, 2012, **85**, 684–699.
181. D. Murat, A. Quinlan, H. Vali and A. Komeili, *Proceedings of the National Academy of Sciences*, 2010, **107**, 5593–5598.
182. A. E. Rawlings, J. P. Bramble, R. Walker, J. Bain, J. M. Galloway and S. S. Staniland, *Proceedings of the National Academy of Sciences*, 2014, **111**, 16094–16099.
183. M. Sternke, K. W. Tripp and D. Barrick, *Proceedings of the National Academy of Sciences*, 2019, **166**, 11275–11284.
184. C. Tiede, R. Bedford, S. J. Heseltine, G. Smith, I. Wijetunga, R. Ross, D. Alqallaf, A. P. E. Roberts, A. Balls, A. Curd, R. E. Hughes, H. Martin, S. R. Needham, L. C. Zanetti-Domingues, Y. Sadigh, T. P. Peacock, A. A. Tang, N. Gibson, H. Kyle, G. W. Platt, N. Ingram, T. Taylor, L. P. Coletta, I. Manfield, M. Knowles, S. Bell, F. Esteves, A. Maqbool, R. K. Prasad, M. Drinkhill, R. S. Bon, V. Patel, S. A. Goodchild, M. Martin-Fernandez, R. J. Owens, J. E. Nettleship, M. E. Webb, M. Harrison, J. D. Lippiat, S. Ponnambalam, M. Peckham, A. Smith, P. K. Ferrigno, M. Johnson, M. J. McPherson and D. C. Tomlinson, *eLife*, 2017, **6**, 1–35.
185. Y. Kuwahara, T. Miyazaki, Y. Shirozaki, G. Liu and M. Kawashita, *Ceramics International*, 2016, **42**, 6000–6004.
186. J. J. M. Lenders, H. R. Zope, A. Yamagishi, P. H. H. Bomans, A. Arakaki, A. Kros, G. De With and N. A. J. M. Sommerdijk, *Advanced Functional Materials*, 2015, **25**, 711–719.
187. M. Nakaya, R. Nishida and A. Muramatsu, *Molecules*, 2014, **19**, 11395–11403.
188. Y. Li, M. Afzaal and P. O'Brien, *Journal of Materials Chemistry*, 2006, **16**, 2175–2180.
189. A. G. Shtukenberg, M. D. Ward and B. Kahr, *Chemical Reviews*, 2017, **117**, 14042–14090.

190. K. Sangwal, *Additives and Crystallization Processes*, John Wiley & Sons, 2007.
191. F. Jones and M. I. Ogden, *CrystEngComm*, 2010, **12**, 1016–1023.
192. E. Ruiz-Agudo, C. V. Putnis and C. Rodriguez-Navarro, *Crystal Growth and Design*, 2008, **8**, 2665–2673.
193. F. Jones, W. R. Richmond and A. L. Rohl, *Journal of Physical Chemistry B*, 2006, **110**, 7414–7424.
194. A. L. Rohl, D. H. Gay, R. J. Davey and C. R. A. Catlow, *Journal of the American Chemical Society*, 1996, **118**, 642–648.
195. A. G. Roca, L. Gutiérrez, H. Gavilán, M. E. Fortes Brollo, S. Veintemillas-Verdaguer and M. del Puerto Morales, *Advanced Drug Delivery Reviews*, 2019, **138**, 68–104.
196. A. Gal, K. Kahil, N. Vidavsky, R. T. Devol, P. U. P. A. Gilbert, P. Fratzl, S. Weiner and L. Addadi, *Advanced Functional Materials*, 2014, **24**, 5420–5426.
197. A. L. Willis, N. J. Turro and S. O'Brien, *Chemistry of Materials*, 2005, **17**, 5970–5975.
198. S. Mourdikoudis and L. M. Liz-Marzán, *Chemistry of Materials*, 2013, **25**, 1465–1476.
199. S. Sun and H. Zeng, *Journal of the American Chemical Society*, 2002, **124**, 8204–8205.
200. V. M. Lenart, S. L. Gómez, M. P. Calatayud and G. R. F. Goya, <http://arxiv.org/abs/1402.1134>, 2014, date accessed: 2020-12-03, 1–2.
201. R. Lopez-Moreno, A. Fernández-Vivas, C. Valverde-Tercedor, A. I. Azuaga Fortes, S. Casares Atienza, A. B. Rodriguez-Navarro, R. Zarivach and C. Jimenez-Lopez, *Crystal Growth and Design*, 2017, **17**, 1620–1629.
202. V. Dmitrović, J. J. M. Lenders, H. R. Zope, G. De With, A. Kros and N. A. J. M. Sommerdijk, *Biomacromolecules*, 2014, **15**, 3687–3695.
203. J. Bain and S. S. Staniland, *Physical Chemistry Chemical Physics*, 2015, **17**, 15508–15521.

204. N. Mobarra, M. Shanaki, H. Ehteram, H. Nasiri, M. Sahmani, M. Saeidi, M. Goudarzi, H. Pourkarim and M. Azad, *International Journal of Hematology-Oncology and Stem Cell Research*, 2016, **10**, 239–247.
205. I. Gautier-Luneau, P. Bertet, A. Jeunet, G. Serratrice and J. L. Pierre, *BioMetals*, 2007, **20**, 793–796.
206. V. L. Kirillov, D. A. Balaev, S. V. Semenov, K. A. Shaikhutdinov and O. N. Martyanov, *Materials Chemistry and Physics*, 2014, **145**, 75–81.
207. A. Bee, R. Massart and S. Neveu, *Journal of Magnetism and Magnetic Materials*, 1995, **149**, 6–9.
208. H. Kazamzadeh, A. Ataie and F. Rashchi, *International Journal of Modern Physics: Conference Series*, 2012, **5**, 160–167.
209. V. V. Makarov, A. J. Love, O. V. Sinitsyna, S. S. Makarova, I. V. Yaminsky, M. E. Taliansky and N. O. Kalinina, *Acta Naturae*, 2014, **6**, 35–44.
210. Y. P. Yew, K. Shameli, M. Miyake, N. Kuwano, N. B. Bt Ahmad Khairudin, S. E. Bt Mohamad and K. X. Lee, *Nanoscale Research Letters*, 2016, **11**, 1–7.
211. A. M. Awwad and N. M. Salem, *Nanoscience and Nanotechnology*, 2013, **2**, 208–213.
212. I. P. Sari and Y. Yulizar, *IOP Conference Series: Materials Science and Engineering*, 2017, **191**, 1–5.
213. C. Li, Y. Wei, A. Liivat, Y. Zhu and J. Zhu, *Journal of Nanomaterials*, 2014, **2014**, 1–9.
214. A. Trepte, *Montmorillonite*, 2007, <https://commons.wikimedia.org/wiki/File:Montmorillonite-en.svg>, date accessed: 2020-10-27.
215. L. Ternent, D. A. Mayoh, M. R. Lees and G. L. Davies, *Journal of Materials Chemistry B*, 2016, **4**, 3065–3074.
216. W. L. Tan and M. A. Bakar, *Journal of Physical Science*, 2006, **17**, 37–50.
217. M. Mahdavi, M. B. Ahmad, M. J. Haron, F. Namvar, B. Nadi, M. Z. Ab Rahman and J. Amin, *Molecules*, 2013, **18**, 7533–7548.

218. A. Mukhopadhyay, N. Joshi, K. Chattopadhyay and G. De, *ACS Applied Materials and Interfaces*, 2012, **4**, 142–149.
219. M. F. Tai, C. W. Lai and S. B. Abdul Hamid, *Journal of Nanomaterials*, 2016, **2016**, 1–7.
220. J. J. Zhu, Q. F. Qiu, H. Wang, J. R. Zhang, J. M. Zhu and Z. Q. Chen, *Inorganic Chemistry Communications*, 2002, **5**, 242–244.
221. J. Griffiths, in *Animal Cell Culture and Production of Biologicals*, Kluwer Academic Publishers, 1991, pp. 401–410.
222. M. B. Plutschack, B. Pieber, K. Gilmore and P. H. Seeberger, *Chemical Reviews*, 2017, **117**, 11796–11893.
223. S. D. Schaber, D. I. Gerogiorgis, R. Ramachandran, J. M. B. Evans, P. I. Barton and B. L. Trout, *Industrial and Engineering Chemistry Research*, 2011, **50**, 10083–10092.
224. A. Sanchez-Martinez, O. Ceballos-Sanchez, C. Koop-Santa, E. R. López-Mena, E. Orozco-Guareño and M. García-Guaderrama, *Ceramics International*, 2018, **44**, 5273–5283.
225. Y. V. Kolen'Ko, M. Bañobre-López, C. Rodríguez-Abreu, E. Carbó-Argibay, A. Sailsman, Y. Piñeiro-Redondo, M. F. Cerqueira, D. Y. Petrovykh, K. Kovnir, O. I. Lebedev and J. Rivas, *Journal of Physical Chemistry C*, 2014, **118**, 8691–8701.
226. S. J. Arteaga-Díaz, S. I. Meramo-Hurtado, J. León-Pulido, A. Zuorro and A. D. González-Delgado, *MDPI Applied Sciences*, 2019, **9**, 1–10.
227. W. Wu, Q. He and C. Jiang, *Nanoscale Research Letters*, 2008, **3**, 397–415.
228. F. Mirasol, *BioPharm International*, 2020, **33**.
229. H. Ashiba, M. Fujimaki, K. Awazu, T. Tanaka and M. Makishima, *Sensing and Bio-Sensing Research*, 2016, **7**, 121–126.
230. C. W. Shields IV and C. D. Reyes and G. P. López, *Lab on a Chip*, 2015, **15**, 1230–1249.
231. L. Guo, J. Feng, Z. Fang, J. Xu and X. Lu, *Trends in Food Science and Technology*, 2015, **46**, 252–263.

232. J. Happel and H. Brenner, *Low Reynolds number hydrodynamics - with special applications to particulate media*. Springer, 1983.
233. A. Abou Hassan, O. Sandre, V. Cabuil and P. Tabeling, *Chemical Communications*, 2008, 1783–1785.
234. M. James, R. A. Revia, Z. Stephen and M. Zhang, *Nanomaterials*, 2020, **10**, 1–19.
235. P. L. Suryawanshi, S. H. Sonawane, B. A. Bhanvase, M. Ashokkumar, M. S. Pimplapure and P. R. Gogate, *Green Processing and Synthesis*, 2018, **7**, 1–11.
236. L. Frenz, A. El Harrak, M. Pauly, S. Bégin-Colin, A. D. Griffiths and J. C. Baret, *Angewandte Chemie - International Edition*, 2008, **47**, 6817–6820.
237. A. Larrea, V. Sebastian, A. Ibarra, M. Arruebo and J. Santamaria, *Chemistry of Materials*, 2015, **27**, 4254–4260.
238. C. H. Yang, C. Y. Wang, K. S. Huang, C. P. Kung, Y. C. Chang and J. F. Shaw, *International Journal of Pharmaceutics*, 2014, **463**, 155–160.
239. D. C. Montgomery, *Design and Analysis of Experiments: 8th Edition*, John Wiley & Sons, 2012.
240. M. Tanco, E. Viles, L. Ilzarbe and M. J. Álvarez, *World Congress on Engineering*, 2007, **20**, 1108–1112.
241. A. Rodríguez-López, A. Paredes-Arroyo, J. Mojica-Gomez, C. Estrada-Arteaga, J. J. Cruz-Rivera, C. G. Elías Alfaro and R. Antaño-López, *Journal of Nanoparticle Research*, 2012, **14**, 1–9.
242. E. Mohammad, E. I. Reza and N. Bahram, *Asian Journal of Chemistry*, 2008, **20**, 3857–3865.
243. T. Raut, B. Shriwastava, P. Sharma, P. Gide, G. Deokar, S. Rahane and K. Erande, *Particulate Science and Technology*, 2016, **34**, 509–516.
244. M. Mahmoudi, A. Simchi, M. Imani, A. S. Milani and P. Stroeve, *Journal of Physical Chemistry B*, 2008, **112**, 14470–14481.
245. N. Mahmed, O. Heczko, A. Lancok and S. P. Hannula, *Journal of Magnetism and Magnetic Materials*, 2014, **353**, 15–22.

246. H. C. Roth, S. P. Schwaminger, M. Schindler, F. E. Wagner and S. Berensmeier, *Journal of Magnetism and Magnetic Materials*, 2015, **377**, 81–89.
247. T. Iwasaki, N. Mizutani, S. Watano, T. Yanagida and T. Kawai, *Journal of Experimental Nanoscience*, 2010, **5**, 251–262.
248. D. Forge, A. Roch, S. Laurent, H. Tellez, Y. Gossuin, F. Renaux, L. V. Elst and R. N. Muller, *Journal of Physical Chemistry C*, 2008, **112**, 19178–19185.
249. L. Norfolk, A. E. Rawlings, J. P. Bramble, K. Ward, N. Francis, R. Waller, A. Bailey and S. S. Staniland, *Nanomaterials*, 2019, **9**, 1729.
250. G. Cao and Y. Wang, *Nanostructures and Nanomaterials: Synthesis, Properties, and Applications*, World Scientific Publishing, 2011.
251. R. W. Kelsall, I. W. Hamley and M. Geoghegan, *Nanoscale Science and Technology*, John Wiley & Sons, 2005.
252. H. H. Rose, *Science and Technology of Advanced Materials*, 2008, **9**, 1–30.
253. D. B. Williams and C. B. Carter, *Transmission Electron Microscopy: A Textbook for Materials Science*, Springer, 2009.
254. H. Stanjek and W. Häusler, *Hyperfine Interactions*, 2004, **154**, 107–119.
255. J. Epp, in *Materials Characterization Using Nondestructive Evaluation (NDE) Methods*, Woodhead Publishing, 2016, pp. 81–124.
256. A. L. Patterson, *Physical Review*, 1939, **56**, 978–982.
257. S. Foner, *Review of Scientific Instruments*, 1959, **30**, 548–557.
258. Author unknown, *VSM Schematic*, 2011, https://commons.wikimedia.org/wiki/File:VSM_en.svg, date accessed: 2021-07-22.
259. M. Huang and G. M. Hieft, *Spectrochimica Acta Part B: Atomic Spectroscopy*, 1989, **44**, 739–749.
260. C.-P. S. Hsu, in *Handbook of Instrumental Techniques for Analytical Chemistry*, Prentice Hall, 1997, ch. 15, pp. 247–282.
261. M. M. Blum and H. John, *Drug Testing and Analysis*, 2012, **4**, 298–302.

262. J. D. Schuttlefield and V. H. Grassian, *Journal of Chemical Education*, 2008, **85**, 279–281.
263. L. Norfolk, K. Kapusta, D. J. Cooke and S. S. Staniland, *Green Chemistry*, 2021, **23**, 1–12.